CARDIAC PACEMAKING IN HEALTH AND DISEASE: FROM GENES TO FUNCTION

EDITED BY: Pietro Mesirca, Alicia D'Souza, Futoshi Toyoda and Gerard J. J. Boink
PUBLISHED IN: Frontiers in Physiology and Frontiers in Cardiovascular Medicine

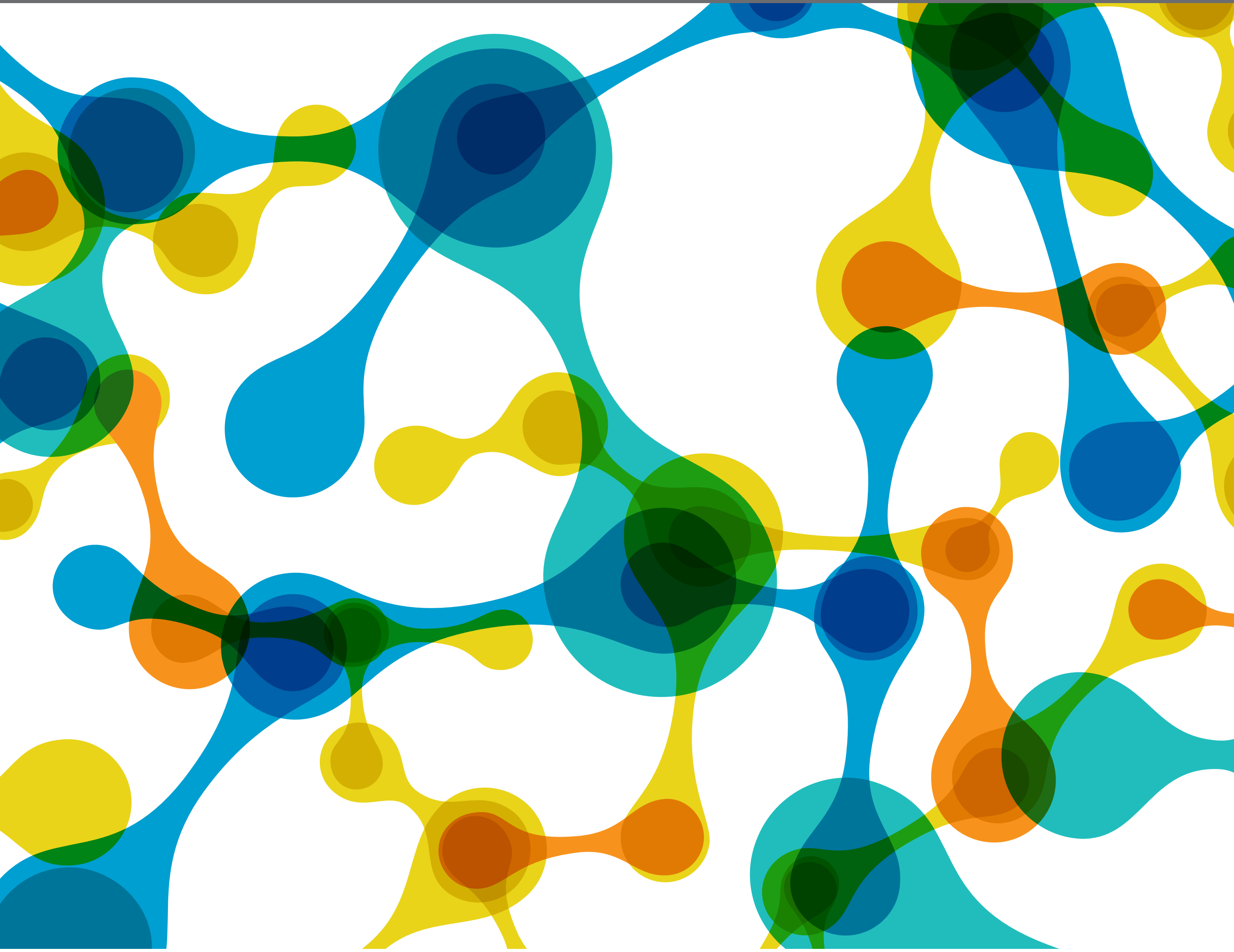

frontiers Research Topics

ISSN 1664-8714
ISBN 978-2-88976-025-1
DOI 10.3389/978-2-88976-025-1

About Frontiers

Frontiers is more than just an open-access publisher of scholarly articles: it is a pioneering approach to the world of academia, radically improving the way scholarly research is managed. The grand vision of Frontiers is a world where all people have an equal opportunity to seek, share and generate knowledge. Frontiers provides immediate and permanent online open access to all its publications, but this alone is not enough to realize our grand goals.

Frontiers Journal Series

The Frontiers Journal Series is a multi-tier and interdisciplinary set of open-access, online journals, promising a paradigm shift from the current review, selection and dissemination processes in academic publishing. All Frontiers journals are driven by researchers for researchers; therefore, they constitute a service to the scholarly community. At the same time, the Frontiers Journal Series operates on a revolutionary invention, the tiered publishing system, initially addressing specific communities of scholars, and gradually climbing up to broader public understanding, thus serving the interests of the lay society, too.

Dedication to Quality

Each Frontiers article is a landmark of the highest quality, thanks to genuinely collaborative interactions between authors and review editors, who include some of the world's best academicians. Research must be certified by peers before entering a stream of knowledge that may eventually reach the public - and shape society; therefore, Frontiers only applies the most rigorous and unbiased reviews.
Frontiers revolutionizes research publishing by freely delivering the most outstanding research, evaluated with no bias from both the academic and social point of view.
By applying the most advanced information technologies, Frontiers is catapulting scholarly publishing into a new generation.

What are Frontiers Research Topics?

Frontiers Research Topics are very popular trademarks of the Frontiers Journals Series: they are collections of at least ten articles, all centered on a particular subject. With their unique mix of varied contributions from Original Research to Review Articles, Frontiers Research Topics unify the most influential researchers, the latest key findings and historical advances in a hot research area! Find out more on how to host your own Frontiers Research Topic or contribute to one as an author by contacting the Frontiers Editorial Office: frontiersin.org/about/contact

CARDIAC PACEMAKING IN HEALTH AND DISEASE: FROM GENES TO FUNCTION

Topic Editors:
Pietro Mesirca, INSERM U1191 Institut de Génomique Fonctionnelle (IGF), France
Alicia D'Souza, The University of Manchester, United Kingdom
Futoshi Toyoda, Shiga University of Medical Science, Japan
Gerard J. J. Boink, University of Amsterdam, Netherlands

Citation: Mesirca, P., D'Souza, A., Toyoda, F., Boink, G. J. J., eds. (2022). Cardiac Pacemaking in Health and Disease: From Genes to Function.
Lausanne: Frontiers Media SA. doi: 10.3389/978-2-88976-025-1

Table of Contents

frontiers | Frontiers in Physiology

EDITORIAL
published: 30 May 2022
doi: 10.3389/fphys.2022.913506

Editorial: Cardiac Pacemaking in Health and Disease: From Genes to Function

Alicia D'Souza[1]*, *Gerard J. J. Boink*[2,3], *Futoshi Toyoda*[4] *and Pietro Mesirca*[5,6]*

[1]*Division of Cardiovascular Sciences, University of Manchester, Manchester, United Kingdom,* [2]*Departments of Cardiology and Medical Biology, Amsterdam University Medical Centers, Location University of Amsterdam, Amsterdam, Netherlands,* [3]*Amsterdam Cardiovascular Sciences, Research Program: Heart Failure and Arrhythmias, Amsterdam, Netherlands,* [4]*Department of Physiology, Shiga University of Medical Science, Otsu, Japan,* [5]*Institut de Génomique Fonctionnelle, Université de Montpellier, CNRS, INSERM, Montpellier, France,* [6]*LabEx Ion Channels Science and Therapeutics, Montpellier, France*

Keywords: pacemaker tissue, ion channels, atrial arrhythmia, channelopathies, heart

Editorial on the Research Topic

Cardiac Pacemaking in Health and Disease: From Genes to Function

OPEN ACCESS

Edited and reviewed by:
John D. Imig,
Medical College of Wisconsin,
United States

Correspondence:
Alicia D'Souza
alicia.dsouza@manchester.ac.uk
Pietro Mesirca
pietro.mesirca@igf.cnrs.fr

Specialty section:
This article was submitted to Cardiac Electrophysiology, a section of the journal Frontiers in Physiology

Received: *05 April 2022*
Accepted: *06 May 2022*
Published: *30 May 2022*

Citation:
D'Souza A, Boink GJJ, Toyoda F and Mesirca P (2022) Editorial: Cardiac Pacemaking in Health and Disease: From Genes to Function. Front. Physiol. 13:913506. doi: 10.3389/fphys.2022.913506

The origin of the heartbeat and the intricacies of cardiac pacemaker automaticity have captivated the interest of physiologists for over 70 years. This continues to be a vibrant and innovative area of research, where state-of-the-art imaging, genomic, transgenic and bioengineering modalities, coupled with classical electrophysiological and computational techniques have enabled unprecedented insight into the fundamentals of automaticity. This Research Topic is intended to hold up a mirror to the current activities in the field; we invited commentaries and original contributions from leading experts on themes relating to the functional or developmental aspects of pacemaker activity and its dysregulation in the context of conduction system disease.

In this Research Topic, DiFrancesco evocatively considers landmark discoveries that underscored the concept of "funny" (f-) current (I_f)-based pacemaking and summarises the current and future clinical applications of these findings. These include the development of Ivabradine (Procolaran©), an I_f blocker widely prescribed as a heart rate lowering therapy for stable angina and heart failure, and the potential for biological pacemaking based on transfer of HCN channels (the molecular basis of the I_f current) in the diseased conduction system. An important characteristic of I_f is its direct regulation by cyclic adenosine monophosphate (cAMP), and in the second article, Porro et al. review our current understanding of the structure-function relationships that underlie cAMP-mediated changes in HCN conformation and gating. The authors contextualise their exciting recent advances in deciphering how binding of cAMP to the Cyclic Nucleotide-Binding Domain changes HCN-channel conformation via interaction with cytoplasmic C-terminal C-linker. Moreover they highlight how detailed insight into channel structure has led to the development of novel peptide tools such as TRIP8b$_{nano}$ (Saponaro et al., 2018) enabling selective inhibition of cAMP dependent HCN regulation, sparing inhibition of channels' conductance compared to traditional pore blockers. In the same field, Hennis et al. provide a contemporary review on heart rate modulation in the sinus node. The authors cite a large body of evidence contrasting the traditional view that cAMP-dependent HCN4 regulation mediates chronotropic responses, and instead postulate upon a role for cAMP-mediated PKA-dependent phosphorylation of Ca^{2+} clock proteins integral to pacemaker activity in this process. Based on their recent elegant work (Fenske et al., 2020) the authors propose that the role of HCN4 is not to orchestrate the heart rate response to autonomic input, as commonly thought, but rather to determine the intrinsic HR and stabilise it. In this work, firing and non-firing/dormant myocytes were detected in the mouse sinus node and it was determined that cAMP-dependent HCN4 activation regulates a "tonic entrainment" process between firing and dormant cells that can slow down the predominant rhythm. The concept that dormant sinus node myocytes have a physiological relevance is an intriguing one that has received attention in recent years (Kim et al., 2018; Tsutsui et al., 2018; Bychkov et al., 2020) and in this Research Topic the Lakatta group in Tsutsui et al. delve further into their study. The team confirm and expand their previous observation that adrenergic stimulation revives spontaneous activity in dormant sinus node myocytes, to maximum firing rate similar to that of spontaneously firing myocytes. Mechanistically, this work demonstrates an underlying role for cAMP-mediated augmentation of I_{CaL}, I_{K} and I_{f} densities, an increase in diastolic local calcium release, alongside phosphorylation of the critical SR "Ca^{2+}-clock" protein phospholamban for obtaining high rates of firing in previously dormant myocytes. These data offer new insight into how the sinus node reaches high pacemaking frequencies by synchronising dormant and firing cell activity.

Outside cAMP-dependent regulation, new signalling pathways that modulate heart rate independently from the autonomic nervous system have been uncovered in recent years. In this regard, new roles for protein kinase-dependent pathways in the regulation of HCN channel availability are described in a research paper by Ira Cohens' team (Lu et al.). Building upon their previous work determining a role for phosphatidylinositol-3-phosphate kinase (PI3K) in sinus node rate by modulation of basal I_f half-activation (Lin et al., 2019), the team demonstrate PI3K-dependent AKT phosphorylation of HCN2 channels at the Serine 861 residue positively regulates HCN2-mediated I_f.

Another important factor potentially regulating pacemaker activity on a beat-to-beat basis–independently of autonomic input–is mechanical force. Cyclical stretching of atrial tissue during the cardiac cycle is predicted to regulate stretch-activated channels in several cell types in the sinus node, including pacemaker cells, fibroblasts and endothelium (MacDonald et al., 2020; Quinn and Kohl, 2012, 2021). The article by Turner et al. reports, for the first time, the expression profile of mechanosensitive ion channels in murine sinus node indicating potential effectors of fast acting mechanical forces: Piezo-1, Trek1 and Ca^{2+} activated K^+ (BK) channels that show significant expression in the sinus node in comparison to its molecular marker Hcn4. In addition, the article suggests new potential candidates for stretch-dependent regulation of pacemaker activity and discusses the possible mechanisms of interplay between mechanosensitive channels and the current model of sinoatrial automaticity in relation to the proposal of the "mechanical clock" by Quinn and Kohl (2021).

The functional role of K^+ channels in pacemaker activity has been hotly debated. Indeed, K^+ channels critically contribute to the balance between inward and outward currents during the automatic action potential cycle. Small-conductance calcium activated K^+ (SK1-3) channels play an important role in automaticity by matching necessary outward current with intracellular calcium dynamics. However, excessive calcium release can induce inhibition of pacemaking by over-activation of SK channels. Next, a review article by Weisbrod discusses expression and pathophysiological roles of SK channes in the heart - an important summary of the known functional properties of these channels, also highlighting their therapeutic potential in cardiac arrhythmias and in heart failure.

Numerical modelling of pacemaker activity has proved to be an important tool to widen mechanistic understanding of automaticity by *in silico* manipulation of ion channels and proteins controlling intracellular calcium dynamics. Five computational articles in this Research Topic provide new insights into pacemaker activity. First, the study by Yang et al. addresses an important question arising from the existence of electrical and calcium dependent oscillators in pacemaker cells. This manuscript suggests that the degree of self-organisation of RyR-dependent calcium release sites underlies variability in the pacemaker interbeat, by generating oscillations of the $\mathrm{Na}^+/\mathrm{Ca}^{2+}$ exchanger current ($\mathrm{I}_{\mathrm{NCX}}$). The activity of NCX thus reflects the degree of organisation of the calcium oscillator. Since NCX also couples to membrane voltage, this phenomenon explains the intrinsic variability of sinus node cell firing under both basal conditions and autonomic activation.

Next, two articles by the Zhang group combine mathematical models with previously reported experimental data to provide mechanistic insight into the physiological modulation of sinus node function across the lifespan. Presenting an updated computational model for neonatal rabbit sinus node myocytes, Alghamdi et al. investigate how ion channel remodelling may explain differences in pacemaking between neonatal and adult sinus node myocytes and their response to acetylcholine. In follow on studies the authors utilize a mathematical model of the rat sinus node action potential to interrogate the mechanisms by which sinus node function slows in advanced age, arriving at a predominant role for $I_{Ca,L}$, remodelling in age-related sinus bradycardia (Alghamdi et al.). Zhang and colleagues also demonstrate the utility of multiscale modelling in improving understanding of atrial fibrillation susceptibility following a gain-of-function mutation in the transcription factor Pitx2c (Bai et al.) and in an additional article (Bai et al.) the authors apply numerical simulations and theoretical analysis to provide new insight into the mode of action of I_{f} block with clinical concentrations of ivabradine.

The range and scope of approaches in the aforementioned articles demonstrate the advanced resolution and level of detail at which the electrophysiological basis of pacemaker automaticity is currently interpreted. Less well-established are the precise transcriptional and epigenetic mechanisms that underpin pacemaker cell development and function–an important knowledge gap given that genetic variation in regulatory elements modifies developmental and disease gene expression patterns and phenotypes. In this Research Topic Mandla et al. explore how recent progress in chromatin biology, bioinformatics, and human genetics has enabled unique insight into transcriptional regulators and genomic loci critical for pacemaker cell development. The authors discuss recent exceptional work defining the sinus node cis-regulatory landscape (Fernandez-Perez et al., 2019; Van Eif et al., 2019; Galang et al., 2020) and the validation of novel enhancers, such as the pacemaker cell-specific enhancer for Islet1 (Galang et al., 2020), essential for development and function of the sinus node.

Further dissection and insight into such regulatory pathways may have important implications in stratifying patients at risk for rhythm disturbances and pacemaker implant, aid understanding of sinus node dysfunction (SND) pathophysiology and identify novel approaches for sinus node regeneration and therapy.

SND mechanisms and new therapies for its rescue are of considerable interest in the field, and the focus of three original research articles in this Research Topic. Végh et al. explored stem cell based delivery of the well-established biological pacemaker transgene combination HCN2/SkM1 (Boink et al., 2013). Here, HCN2 is overexpressed to augment diastolic depolarization rate, while the skeletal muscle sodium channel, SkM1, can hyperpolarize action potential threshold, thereby accelerating and stabilizing the induced biological pacemaker rhythm. In the current study the authors used cardiac myocyte progenitor cells (CMPCs) as a new gene delivery platform to potentially induce long-term biological pacing (Végh et al., 2019). In doing so they optimized non-viral, electroporation-based manipulation of CMPCs, which appeared to be superior over *ex vivo* lentiviral transduction. Moreover, their computational simulation studies identified an SkM1-mediated increase in final stage diastolic depolarization as a novel mechanism-of-action for biological pacing based on HCN2/SkM1. Soattin et al. investigated subsidiary atrial pacemakers in a large animal (goat) model of SND. Radiofrequency ablation of the sinus node resulted in pacemaking from subsidiary sites in a proportion of animals, leading the authors to speculate upon its role as a dominant pacemaker in SND. Finally, Bidaud et al. demonstrate that genetic ablation of G-protein-gated inwardly rectifying potassium channels (responsible for I_{KAch} current) counteracts slowed pacemaking induced by exercise training in mice by preventing transcriptional and electrical remodelling of pacemaking ion channels. This work builds on findings by D'Souza and Boyett demonstrating that a microRNA network orchestrates reduced sinus node ion channel expression in a range of situations where dysfunctional pacemaking is observed, including exercise training (D'Souza et al., 2014; D'Souza et al., 2017; Mesirca et al., 2021) and heart failure (Yanni et al., 2020). Based on the observations ranging from the whole animal to the microRNA, coupled with previous work by the team (Mesirca et al., 2014; Mesirca et al., 2016) it is concluded that I_{KAch} modulation may be an effective pharmacological strategy for SND rescue.

In sum, the articles in this Research Topic offer a wealth of insight into basic sinus node automaticity while highlighting new themes in its development, physiology and adaptation to disease. The challenge for the field (as for writing concluding remarks!), is how to distil diverging and ever-evolving appreciation of fundamental sinus node biology into the major outstanding questions that preclude identification of new therapeutic targets for SND–a disease that will become increasingly more common as the population ages, and for which palliation by pacemaker implant is the only available therapeutic option. The articles in this Research Topic reiterate that normal pacemaking arises from interactions between the ion channel/Ca^{2+-} handling ensemble, signal transduction pathways (e.g., PI3K) and genetic/epigenetic influences. Further adding to the complexity are interactions between dormant and firing myocytes and increasingly well-recognized myocyte-nonmyocyte (e.g., fibroblast and macrophage) crosstalk. In the era of precision medicine, our ability to integrate and follow these networks *in vivo* in refined SND models with multiomics technologies and multiscale computer modelling will become as important as our capacity to dissect the role of each component. In the meantime, gene therapy (with HCN2/SkM1 or microRNAs) and pharmacological I_{KAch} inhibition show particular promise as emergent therapies for SND management.

AUTHOR CONTRIBUTIONS

AD'S and PM drafted the manuscript; GB and FT edited and approved the manuscript.

FUNDING

AD'S was supported by a British Heart Foundation (BHF) Intermediate Fellowship (FS/19/1/34035) and BHF grants (PG/14/24/30626, RG/11/18/29257, PG/13/99/30233). GB was supported by a European Research Council (ERC Starting Grant 714866 and Proof-of-Concept grant 899422), Horizon 2020 Eurostars (E114245 and E115484), Dutch Research Council (Open Technology Program; 18485), and Health Holland (LentiPace II).

REFERENCES

Boink, G. J., Duan, L., Nearing, B. D., Shlapakova, I. N., Sosunov, E. A., Anyukhovsky, E. P., et al. (2013). HCN2/SkM1 Gene Transfer into Canine Left Bundle Branch Induces Stable, Autonomically Responsive Biological Pacing at Physiological Heart Rates. *J. Am. Coll. Cardiol.* 61, 1192–1201. doi:10.1016/j.jacc.2012.12.031

Bychkov, R., Juhaszova, M., Tsutsui, K., Coletta, C., Stern, M. D., Maltsev, V. A., et al. (2020). Synchronized Cardiac Impulses Emerge from Heterogeneous Local Calcium Signals within and Among Cells of Pacemaker Tissue. *JACC Clin. Electrophysiol.* 6, 907–931. doi:10.1016/j.jacep.2020.06.022

D'Souza, A., Bucchi, A., Johnsen, A. B., Logantha, S. J., Monfredi, O., Yanni, J., et al. (2014). Exercise Training Reduces Resting Heart Rate via Downregulation of the Funny Channel HCN4. *Nat. Commun.* 5, 3775. doi:10.1038/ncomms4775

D'Souza, A., Pearman, C. M., Wang, Y., Nakao, S., Logantha, S. J. R. J., Cox, C., et al. (2017). Targeting miR-423-5p Reverses Exercise Training-Induced HCN4 Channel Remodeling and Sinus Bradycardia. *Circ. Res.* 121, 1058–1068. doi:10.1161/CIRCRESAHA.117.311607

Fenske, S., Hennis, K., Rötzer, R. D., Brox, V. F., Becirovic, E., Scharr, A., et al. (2020). cAMP-Dependent Regulation of HCN4 Controls the Tonic Entrainment Process in Sinoatrial Node Pacemaker Cells. *Nat. Commun.* 11, 5555. doi:10.1038/s41467-020-19304-9

Fernandez-Perez, A., Sathe, A. A., Bhakta, M., Leggett, K., Xing, C., and Munshi, N. V. (2019). Hand2 Selectively Reorganizes Chromatin Accessibility to Induce

Pacemaker-like Transcriptional Reprogramming. *Cell Rep.* 27, 2354–2369. doi:10.1016/j.celrep.2019.04.077

Galang, G., Mandla, R., Ruan, H., Jung, C., Sinha, T., Stone, N. R., et al. (2020). ATAC-seq Reveals an Isl1 Enhancer that Regulates Sinoatrial Node Development and Function. *Circ. Res.* 127, 1502–1518. doi:10.1161/circresaha.120.317145

Kim, M. S., Maltsev, A. V., Monfredi, O., Maltseva, L. A., Wirth, A., Florio, M. C., et al. (2018). Heterogeneity of Calcium Clock Functions in Dormant, Dysrhythmically and Rhythmically Firing Single Pacemaker Cells Isolated from SA Node. *Cell Calcium* 74, 168–179. doi:10.1016/j.ceca.2018.07.002

Lin, R. Z., Lu, Z., Anyukhovsky, E. P., Jiang, Y.-P., Wang, H. Z., Gao, J., et al. (2019). Regulation of Heart Rate and the Pacemaker Current by Phosphoinositide 3-kinase Signaling. *J. Gen. Physiol.* 151, 1051–1058. doi:10.1085/jgp.201812293

MacDonald, E. A., Madl, J., Greiner, J., Ramadan, A. F., Wells, S. M., Torrente, A. G., et al. (2020). Sinoatrial Node Structure, Mechanics, Electrophysiology and the Chronotropic Response to Stretch in Rabbit and Mouse. *Front. Physiol.* 11, 809. doi:10.3389/fphys.2020.00809

Mesirca, P., Bidaud, I., Briec, F., Evain, S., Torrente, A. G., Le Quang, K., et al. (2016). G Protein-Gated IKACh Channels as Therapeutic Targets for Treatment of Sick Sinus Syndrome and Heart Block. *Proc. Natl. Acad. Sci. U. S. A.* 113, E932–E941. doi:10.1073/pnas.1517181113

Mesirca, P., Nakao, S., Nissen, S. D., Forte, G., Anderson, C., Trussell, T., et al. (2021). Intrinsic Electrical Remodeling Underlies Atrioventricular Block in Athletes. *Circ. Res.* 129, e1–e20. doi:10.1161/CIRCRESAHA.119.316386

Mesirca, P., Alig, J., Torrente, A. G., Müller, J. C., Marger, L., Rollin, A., et al. (2014). Cardiac Arrhythmia Induced by Genetic Silencing of 'funny Channels Is Rescued by GIRK4 Inactivation. *Nat. Commun.* 5, 4664. doi:10.1038/ncomms5664

Quinn, T. A., and Kohl, P. (2021). Cardiac Mechano-Electric Coupling: Acute Effects of Mechanical Stimulation on Heart Rate and Rhythm. *Physiol. Rev.* 101, 37–92. doi:10.1152/physrev.00036.2019

Quinn, T. A., and Kohl, P. (2012). Mechano-sensitivity of Cardiac Pacemaker Function: Pathophysiological Relevance, Experimental Implications, and Conceptual Integration with Other Mechanisms of Rhythmicity. *Prog. Biophysics Mol. Biol.* 110, 257–268. doi:10.1016/j.pbiomolbio.2012.08.008

Saponaro, A., Cantini, F., Porro, A., Bucchi, A., Difrancesco, D., Maione, V., et al. (2018). A Synthetic Peptide that Prevents cAMP Regulation in Mammalian Hyperpolarization-Activated Cyclic Nucleotide-Gated (HCN) Channels. *eLife* 7, e35753. doi:10.7554/eLife.35753

Tsutsui, K., Monfredi, O. J., Sirenko-Tagirova, S. G., Maltseva, L. A., Bychkov, R., Kim, M. S., et al. (2018). A Coupled-Clock System Drives the Automaticity of Human Sinoatrial Nodal Pacemaker Cells. *Sci. Signal* 11, 7608. doi:10.1126/scisignal.aap7608

Van Eif, V. W. W., Stefanovic, S., Van Duijvenboden, K., Bakker, M., Wakker, V., De Gier-De Vries, C., et al. (2019). Transcriptome Analysis of Mouse and Human Sinoatrial Node Cells Reveals a Conserved Genetic Program. *Development* 146, 173161. doi:10.1242/dev.173161

Végh, A. M. D., den Haan, A. D., Cócera Ortega, L., Verkerk, A. O., Sluijter, J. P. G., Bakker, D., et al. (2019). Cardiomyocyte Progenitor Cells as a Functional Gene Delivery Vehicle for Long-Term Biological Pacing. *Molecules* 24, 181. doi:10.3390/molecules24010181

Yanni, J., D'Souza, A., Wang, Y., Ning, L., Hansen, B. J., Zakharkin, S. O., et al. (2020). Silencing miR-370 Rescues Funny Current and Sinus Node Function and Improves Survival in Heart Failure. *Sci. Rep.* 10, 11279. doi:10.1038/s41598-020-67790-0

Conflict of Interest: GB reports ownership interest in PacingCure B.V.

The remaining authors declare that the research was conducted in the absence of any commercial or financial relationships that could be construed as a potential conflict of interest.

frontiers
in Physiology

MINI REVIEW
published: 22 January 2020
doi: 10.3389/fphys.2019.01599

A Brief History of Pacemaking

Dario DiFrancesco*

Department of Biosciences, University of Milano, IBF-CNR University of Milano Unit, Milan, Italy

Cardiac pacemaking is a most fundamental cardiac function, thoroughly investigated for decades with a multiscale approach at organ, tissue, cell and molecular levels, to clarify the basic mechanisms underlying generation and control of cardiac rhythm. Understanding the processes involved in pacemaker activity is of paramount importance for a basic physiological knowledge, but also as a way to reveal details of pathological dysfunctions useful in the perspective of a therapeutic approach. Among the mechanisms involved in pacemaking, the "funny" (I_f) current has properties most specifically fitting the requirements for generation and control of repetitive activity, and has consequently received the most attention in studies of the pacemaker function. Present knowledge of the basic mechanisms of pacemaking and the properties of funny channels has led to important developments of clinical relevance. These include: (1) the successful development of heart rate-reducing agents, such as ivabradine, able to control cardiac rhythm and useful in the treatment of diseases such as coronary artery disease, heart failure and tachyarrhythmias; (2) the understanding of the genetic basis of disorders of cardiac rhythm caused by HCN channelopathies; (3) the design of strategies to implement biological pacemakers based on transfer of HCN channels or of stem cell-derived pacemaker cells expressing I_f, with the ultimate goal to replace electronic devices. In this review, I will give a brief historical account of the discovery of the funny current and the development of the concept of I_f-based pacemaking, in the context of a wider, more complex model of cardiac rhythmic function.

Keywords: pacemaker, funny current, I_f current, HCN channels, cardiac rate, ivabradine, HCN channelopathies

OPEN ACCESS

Edited by:
Pietro Mesirca,
INSERM U1191 Institut
de Génomique Fonctionnelle (IGF),
France

Reviewed by:
Flavien Charpentier,
INSERM U1087 L'Unité de Recherche
de l'Institut du Thorax, France
Elisabetta Cerbai,
University of Florence, Italy

****Correspondence:***
Dario DiFrancesco
dario.difrancesco@unimi.it

Specialty section:
This article was submitted to
Cardiac Electrophysiology,
a section of the journal
Frontiers in Physiology

Received: *31 October 2019*
Accepted: *20 December 2019*
Published: *22 January 2020*

Citation:
DiFrancesco D (2020) A Brief
History of Pacemaking.
Front. Physiol. 10:1599.
doi: 10.3389/fphys.2019.01599

EARLY MEMBRANE-LIMITED PACEMAKER THEORIES

Early theories of pacemaking (Noble, 1960) were based on the assumption of the "decay" of a K^+ current, a concept originally proposed in 1951 by Silvio Weidmann on the basis of conductance measurements during diastolic depolarization (DD) in Purkinje fibers (Weidmann, 1951).

The idea received strong support in 1968 with the recording in Purkinje fibers of a pure K current (I_{K2}) with properties fitting perfectly those required for a "pacemaker" current (Noble and Tsien, 1968). This, and a bulk of experimental and theoretical data collected since its original proposal crystallized the K^+ current-decay hypothesis for almost 30 years, with no one having the slightest doubt about its validity.

DISCOVERY OF AN INTRUDER: THE FUNNY CURRENT

In 1979 novel, apparently confounding evidence appeared in the shape of a new ion current recorded from rabbit SAN preparations (Brown et al., 1979). The "funny" (I_f) current was so baptized because it displayed unusual properties, such as a previously unreported nature of *inward* current activated on *hyperpolarization*. This feature gave it the ability to start the DD following an action potential (AP), hence to *generate* spontaneous activity, fitting nicely the requirement of a perfect pacemaker current. Furthermore, we realized that the acceleration caused by adrenaline was due to an increased DD slope, and asked whether I_f could be responsible; to answer this we simply perfused with adrenaline a preparation and watched what happened to I_f. What a beautiful experiment! I_f increased in agreement with the increased steepness of DD. So not only had we discovered a novel mechanism for pacemaker generation, we also had found that it controlled cardiac rate!

The finding of I_f introduced a novel concept in the pacemaking scenario: pacemaking depended upon activation of an inward current at the termination of an AP. This notion was exactly the opposite of the classical one based on deactivation of an outward current. Could we really have two distinct pacemaker mechanisms, one in the SAN and one in the Purkinje fibers?

POTASSIUM ION ACCUMULATION/DEPLETION PHENOMENA CAN MAKE VOLTAGE-CLAMPING A DECEITFUL AFFAIR

New theories revolutionizing established concepts often depend on new techniques.

A new technique developed in the mid-late 70's to voltage-clamp mammalian SAN, the natural cardiac pacemaker region, rather than Purkinje fibers (Noma and Irisawa, 1976), indeed made a big difference. Voltage-clamp of Purkinje fibers, but not of SAN preparations, had in fact a serious and deceitful limitation, one that could make, as discussed below, an inward current look like an outward current: extracellular depletion of K^+ ions.

Anatomy matters. Purkinje fibers are composed of large, tightly packed cells electrically connected along the longitudinal, but not the transverse direction; restricted extracellular spaces, called clefts, separate each cell from the neighboring ones. SAN cells, on the other hand, are loosely connected to each other, without a preferential direction of signal propagation, and are not surrounded by clefts.

The K^+-ionic nature of the I_{K2} current had been based on evidence for a reversal potential near the K^+ equilibrium, as measured by applying large negative steps (Noble and Tsien, 1968). A few years later, however, several studies showed the presence of K^+ accumulation/depletion phenomena in Purkinje fibers (Attwell et al., 1979; Brown et al., 1980; DiFrancesco and Noble, 1980). In fact, stimulated by premonitory curiosity, Carlos Ojeda, Mitsuyoshi Ohba and myself had found that even the measurement of the I_{K2} reversal potential was distorted by cleft K^+ depletion (DiFrancesco et al., 1979).

Driven by intuitive curiosity, further studies highlighted the striking resemblances between I_f and I_{K2} (Brown and DiFrancesco, 1980; DiFrancesco and Ojeda, 1980). Yet the Purkinje fiber I_{K2} reversed at negative voltages, but I_f did not. So where did the solution to the puzzle lay?

I_{K2} REINTERPRETATION: A UNIFYING MODEL OF PACEMAKING

The idea that the best described and most famous cardiac current could have been wrongly interpreted and described, in a way that had misled the whole of the scientific community for such a long time, was not to be admitted easily. A systematic study of the properties of I_{K2} eventually led to the, by then half-expected, shocking result: I_{K2} was not an outward, but an inward current! (DiFrancesco, 1981). This was shown by three lines of evidence: block by Cs^+, conductance measurement during negative steps, and the most impressive bit of evidence: by blocking K^+-depletion, barium ions blocked a large, inward-decreasing component which overlapped the inward increasing I_f, in such a way as to determine a "fake" reversal.

In other words, the I_{K2} current was in fact a camouflaged I_f! The apparent reversal near the K^+- equilibrium potential was the result of two distinct overlapping events: activation of I_f and an inward-decaying K^+ current due to K^+ depletion in extracellular clefts. The nature of the pacemaker process in cardiac cells had therefore baffled the scientific community for over a decade, and the I_K-decay hypothesis had remained undisputed for almost three decades.

Feeling uneasily as a young physiologist who was challenging a central dogma of cardiac physiology, established decades before, fully accepted by the scientific community and supported by world-leading labs, I hardly knew how to best communicate this to the scientific community. I eventually decided to share this knowledge with Denis Noble, and called him over the telephone to reveal my findings. This further strengthened our collaborative relation and resulted a few years later in a numerical model published by Philosophical Transactions of the Royal Society (DiFrancesco and Noble, 1985). The model incorporated the I_f current and other new data, and accounted for essentially all previous experimental data in Purkinje fibers. It was a landmark work in the field of numerical reconstruction and laid the basis for future numerical modeling. It received an important recognition when in 2015 the Royal Society (London) celebrated its 350 year-anniversary and selected the 33 most influential papers published in 350 years by the Philosophical Transactions. Along with papers by Newton, Faraday, Joule, Maxwell, Turing, Medawar, and other giants, Denis and I found that our 1985 model paper had also been listed, to our great honor and gratification.

The discovery of I_f and the reinterpretation of I_{K2} showed that the mechanism generating pacemaker activity was the same in different myocytes and represented a unifying theory of pacemaking.

THE I_F PROPERTIES ARE WELL SUITED FOR A PACEMAKER CURRENT

The I_f discovery in 1979 and the reinterpretation of I_{K2} in 1981 paved the way for a large number of worldwide studies which, in the course of about four decades, investigated the properties of this current.

This part has been amply covered by many review articles (DiFrancesco, 1985, 1987, 1993, 1995, 2006, 2010; DiFrancesco and Camm, 2004; Baruscotti et al., 2005; Barbuti et al., 2007; Bucchi et al., 2012; DiFrancesco and Noble, 2012) and only the most relevant findings are mentioned here.

Kinetics and ionic nature of the current were first investigated and revealed that the current activates slowly, without inactivation, upon hyperpolarization to the diastolic range of voltages (DiFrancesco, 1981; DiFrancesco et al., 1986). Its mixed Na^+ and K^+ ionic nature, another unusual property for a voltage-dependent channel, ensures that I_f is inward in its activation range (DiFrancesco, 1981).

These properties are well designed for a pacemaker current, since slow activation of an inward current at the termination of an action potential, when the voltage enters the pacemaker range, is bound to contribute to a depolarizing process such as diastolic depolarization.

I_f single-channel activity was first recorded in 1986 using an experimentally demanding protocol, involving the use of two pipettes on the same cell to increase single-channel resolution. This was necessary because of what would eventually result one of the smallest ever recorded single channels, with a conductance of about 1 pS (DiFrancesco, 1986). Because channel opening during activity is a stochastic process, low conductance of f-channels is useful to avoid too large Heart Rate Variability (HRV).

Also essential was the finding that not only is I_f activated by adrenergic stimulation, it is also strongly inhibited by muscarinic stimulation (DiFrancesco and Tromba, 1988a,b). This endowed the I_f current with a significant physiological role not only in the process of generation of pacemaker activity, but also in the autonomic regulation of cardiac rate.

The relevance of muscarinic I_f modulation was further strengthened by the finding that low ACh concentrations slow heart rate by I_f inhibition and not, as previously believed, by activation of an ACh-activated K^+ current (I_{KACh}) (DiFrancesco et al., 1989). Thus, normal vagal tone keeps a relatively low heart rate at rest by means of a basal ACh-induced I_f inhibition.

How did autonomic transmitters modulate I_f? Experimental data indicated the presence of a shift of the activation curve (positive with adrenergic, negative with vagal stimulation), with no change of fully-activated currents. Recording of I_f from giant inside-out patches containing hundreds of channels, another demanding protocol, led to the discovery that f-channels are directly activated by binding of intracellular cAMP, via a positive shift of the activation curve (DiFrancesco and Tortora, 1991). Other known channels had this property (typically the cGMP-activated channels of the retina), but f-channels had the unique feature of being *dually* activated by both voltage (hyperpolarization) and cAMP. These data completed the full range of processes involved in the I_f-mediated autonomic rate modulation.

At the turn of the century/millennium, a new era developed for the funny current, following the cloning of the HCN (hyperpolarization-activated, cyclic nucleotide-gated) channel family (Gauß et al., 1998; Santoro et al., 1998; Vaccari et al., 1999). Of the 4 isoforms cloned (HCN1-4), the HCN4 isoform is the most highly expressed in pacemaker tissue.

Cloning of HCN channels allowed investigating the molecular basis of the properties of I_f originally discovered decades before. More recently, the molecular structure first of portions (Saponaro et al., 2014) and finally of the entire α-subunit of HCN channels [HCN1 (Lee and MacKinnon, 2017)] has been resolved. It is quite satisfactory to find that all the features described some 40 years before, such as activation on hyperpolarization, cAMP-dependent activation, mixed Na^+/K^+ permeability, have eventually found a perfectly fitting molecular interpretation.

PRACTICAL APPLICATIONS OF THE FUNCTIONAL PROPERTIES OF FUNNY/HCN4 CHANNELS

The discovery of I_f was initially important as a basic concept in cardiac (and non-cardiac) physiology, but progressively more detailed knowledge of its role in pacemaker generation and cardiac rate control has led more recently to the development of practical applications of clinical relevance.

An important application concerns the pharmacological control of heart rate. Pharmacological research has been long seeking for substances able to slow heart rate specifically, without the side effects of β-blockers and Ca^{++} antagonists. Several "heart rate-inhibiting" substances have been developed to this aim. Ivabradine, the only such drug having reached the market, is a selective f-channel blocker which slows heart rate with little or no cardiovascular side effects, now successfully used in the therapy of Coronary Artery Disease and heart failure (DiFrancesco and Camm, 2004; DiFrancesco and Borer, 2007). Ivabradine directly validates the important contribution of I_f to control of DD and heart rate.

A second application concerns the genetics of arrhythmias. As expected from the I_f role in pacemaking, several HCN4 mutations have been identified in patients with alterations of cardiac rhythm (DiFrancesco, 2013). Arrhythmias associated with HCN4 mutations can be complex, but the majority of reported mutations are loss-of-function and are associated with bradycardia, in agreement with the funny channel involvement in rate control. Interestingly, the only tachyarrhythmia-associated HCN4 mutation found is gain-of-function, which again fits perfectly the I_f role in pacemaking (Baruscotti et al., 2015). Thus HCN4 mutation-linked arrhythmias, too, provide evidence confirming the pacemaking role of I_f.

A final example of clinically relevant application concerns the development of biological pacemakers. Several attempts have shown that *in situ* delivery of funny channels to defective cardiac muscle by gene- or cell-based methods can be employed in the attempt to develop biological pacemakers, with the aim to replace electronic devices. Exhaustive review work covers this important subject (Robinson et al., 2006; Rosen et al., 2011; Chauveau et al., 2014).

The underlying idea is that f-channels can transfer their "pacemaking" ability, so that silent cells made to express f-channels become spontaneously active. Early studies showed for example that HCN2 transfer to neonatal ventricular myocytes accelerates DD and spontaneous rate (Qu et al., 2001), and other attempts used adenoviral-mediated HCN infection, HCN-channel expressing mesenchymal stem cells, fusion between HCN1-expressing fibroblasts and myocytes (Qu et al., 2003; Plotnikov et al., 2004; Potapova et al., 2004; Bucchi et al., 2006; Kashiwakura et al., 2006; Cho et al., 2007; Plotnikov et al., 2008). Cardiomyocytes derived from embryonic stem cells, known to express I_f (Barbuti et al., 2009), have also been adopted to pace cultured cardiomyocytes and *in vivo* hearts when properly grafted (Kehat et al., 2004; Xue et al., 2005; Ionta et al., 2015; Protze et al., 2017). HCN-expressing induced Pluripotent Stem Cell (iPSC)-derived cardiomyocytes have also been used to successfully pace immunosuppressed dog hearts (Chauveau et al., 2017). Though still mainly as proof-of-concept, these data show that HCN transfer can be a viable method to generate biological pacemakers.

A NEW CONTENDER: THE CA CLOCK

Pacemaking involves a large number of events, both at the membrane and inside the cell, which are tuned together to achieve reliable generation and modulation of spontaneous rhythm. This does not exclude that any single mechanism in this network may have a specific function.

For example, the relevance of I_f activation does not imply that no K+-flow occurs during diastole; indeed the I_{Kr} current has been shown to contribute importantly to pacemaking, while having at the same time a major role in repolarization (Clark et al., 2004).

As discussed above, the properties of the funny current are fit for a mechanism contributing substantially to the DD process, generation of cyclic repetitive electrical activity and, ultimately, control of cardiac rate. Clearly, however, all participating mechanisms, not only funny channels, cycle rhythmically during pacemaker activity, and an obvious question arises if other mechanisms with a *specific* role in generating pacemaker activity exist.

Among the important cycling elements are Ca^{++} ions. Ca^{++} ions are released cyclically from the Sarcoplasmic Reticulum (SR) according to a Ca^{++}-dependent Ca^{++}-release mechanism, leading to rhythmic fluctuations of the intracellular Ca^{++} concentration, a mechanism directly responsible for mechanical contraction.

In rabbit SAN cells, Lakatta and collaborators reported that the Ca^{++} concentration increased in sub-sarcolemmal spaces due to opening of Ryanodine Receptors (RyR) which occurred rhythmically during the final fraction of the diastolic depolarization, just before AP upstroke (Bogdanov et al., 2001; Vinogradova et al., 2002, 2004). Since these Local Calcium Releases (LCRs) could generate Ca^{++} waves via Ca^{++}-dependent Ca^{++}-release, thus activating the Na-Ca exchange (NCX) and associated inward depolarizing current, they contributed to accelerate the late phase of diastolic depolarization. This set of events was termed "Ca^{++} clock" and proposed to represent an alternative pacemaker mechanism.

Several studies have investigated the properties of the "Ca^{++} clock" mechanism in order to address its functional role in generating spontaneous activity in pacemaker cells.

Lakatta's group has reported that LCRs are roughly periodic with a rate similar to the SAN beating rate, and can be recorded in permeabilized cells and under V-clamp (Vinogradova et al., 2004). Based on this and other evidence, the Ca^{++} clock model predicts that pacemaker repetitive activity is not caused by "membrane" processes but rather by intracellular Ca^{++} cycling coupled to the NCX current, and that late diastolic Ca^{++} releases are an obligatory rhythmic process in pacemaking [Lakatta in Lakatta and DiFrancesco (2009)].

Whether the Ca^{++} clock is a pacemaking mechanism and how this relates to the I_f –based "membrane clock" mechanism are debated questions (DiFrancesco and Robinson, 2002; Lakatta et al., 2003; Lipsius and Bers, 2003; Lakatta and DiFrancesco, 2009; Robinson, 2011).

A first obvious difficulty for the "Ca^{++} clock" hypothesis is that it completely lacks any degree of specificity for pacemaker tissue. Local Ca^{++} releases and more in general Ca^{++} transients are involved in mechanical contraction, which obviously occurs in all cardiac myocytes. Funny channels, on the other hand, are expressed physiologically only in the SAN and conduction tissue, i.e., only in the myocytes able to beat spontaneously.

There are other problems with the assumption that the Ca^{++} clock is a main determinant of the timing of cardiac rhythm [see DiFrancesco in Lakatta and DiFrancesco (2009), DiFrancesco and Noble (2012)].

For example, disruption of intracellular Ca^{++} dynamics obtained by intracellular perfusion with the Ca^{++} chelator BAPTA totally removes Ca^{++} transients, but leaves repetitive electrical activity to continue undisturbed for tens of second in a single SAN cell (Himeno et al., 2011). This cannot be reconciled with the assumption that LCRs are an obligatory pacing process.

Also, a recent study of intracellular Ca^{++} transients in pacemaker myocytes from mice lacking the L-type Ca^{++} channels Cav1.3 has shown that in these myocytes, the rate of LCRs is greatly reduced; further, in the presence of β-adrenergic stimulation, residual LCRs are asynchronous and not concentrated in the last fraction of the diastolic depolarization (Torrente et al., 2016). These data agree with the hypothesis that LCRs are caused by Ca^{++} entry through Cav1.3 channels typical of pacemaker cells, in contrast with the Ca^{++}-clock assumption that they are caused by spontaneous, rhythmic release from ryanodine receptors.

As mentioned, pacemaking is a composite phenomenon and any process directly or indirectly modifying the diastolic depolarization will affect rate. Furthermore, several recent studies have highlighted new complexities in the pacemaker scenario. While a full discussion of these studies is not presented here, it is important to stress that pacemaking is also modulated by various enzymes (DiFrancesco, 2019; Lin et al., 2019) and mechanical stretch (Quinn and Kohl, 2012). Further, investigations of genetically modified mouse models have shown that $Ca_v1.3$ channels, specifically expressed in pacemaker tissue, contribute directly to pacemaker depolarization (Mesirca et al., 2015), and underlie a persistent Na current (Toyoda et al., 2017), identifiable with the Na-background current hypothesized in early numerical reconstructions.

Also importantly, GIRK4 channel inactivation has been shown to rescue bradyarrhythmias of HCN4-deficient mice (Mesirca et al., 2014), highlighting a previously unsuspected role of I_{KACh} in counterbalancing I_f changes. Complexities in the autonomic modulation of rate have also been described by use of genetically modified mice (Kozasa et al., 2018). These studies suggest that funny channels act to limit excessive bradycardia caused by potent parasympathetic activity.

Existing pacemaker models will clearly need to be extended to comprise this fuller set of novel acquisitions.

CONCLUSION

The initial major impact of the discovery of the funny current was that it revolutionized the old, well-established, worldwide-accepted model of the origin of pacemaking and provided a rational explanation of how pacemaker activity is generated and controlled by the autonomic nervous system.

The I_f -based pacemaking model has since advanced from the original, basic concept mostly relevant to textbook cardiovascular physiology, to a practical concept that can be exploited to generate many useful clinical applications valuable for the development of new therapies.

Pacemaking is a complex mechanism and needs the co-operation of many elementary processes, each of which is unable, by itself, to generate a robust and secure action potential at a stable rate. Still, each of these mechanisms has a specific role. In agreement with their unique functioning role, funny channels are specifically expressed, under physiological conditions, in pacing cells only. Local Calcium Releases occurring in late diastole in subsarcolemmal spaces of pacemaker cells appear to depend upon entry of Ca^{++} ions through Cav1.3 channels and may thus represent a mechanism apt to boost the action potential upstroke, rather than autonomously timing pacemaker rate.

AUTHOR CONTRIBUTIONS

The author confirms being the sole contributor of this work and has approved it for publication.

FUNDING

This work is supported by the Fondation Leducq TNE 19CVD03.

REFERENCES

Attwell, D., Eisner, D., and Cohen, I. S. (1979). Voltage clamp and tracer flux data: effects of a restricted extracellular space. *Q. Rev. Biophys.* 12, 213–261. doi: 10.1017/s0033583500005448

Barbuti, A., Baruscotti, M., and DiFrancesco, D. (2007). The pacemaker current: from basics to the clinics. *J. Cardiovasc. Electrophysiol.* 18, 342–347. doi: 10.1111/j.1540-8167.2006.00736.x

Barbuti, A., Crespi, A., Capilupo, D., Mazzocchi, N., Baruscotti, M., and DiFrancesco, D. (2009). Molecular composition and functional properties of f-channels in murine embryonic stem cell-derived pacemaker cells. *J. Mol. Cell Cardiol.* 46, 343–351. doi: 10.1016/j.yjmcc.2008.12.001

Baruscotti, M., Bucchi, A., and DiFrancesco, D. (2005). Physiology and pharmacology of the cardiac pacemaker ("funny") current. *Pharmacol. Ther.* 107, 59–79. doi: 10.1016/j.pharmthera.2005.01.005

Baruscotti, M., Bucchi, A., Milanesi, R., Paina, M., Barbuti, A., Gnecchi-Ruscone, T., et al. (2015). A gain-of-function mutation in the cardiac pacemaker HCN4 channel increasing cAMP sensitivity is associated with familial Inappropriate Sinus Tachycardia. *Eur. Heart J.* 38, 280–288. doi: 10.1093/eurheartj/ehv582

Bogdanov, K. Y., Vinogradova, T. M., and Lakatta, E. G. (2001). Sinoatrial nodal cell ryanodine receptor and Na(+)-Ca(2+) exchanger: molecular partners in pacemaker regulation. *Circ. Res.* 88, 1254–1258. doi: 10.1161/hh1201.092095

Brown, H., and DiFrancesco, D. (1980). Voltage-clamp investigations of membrane currents underlying pace-maker activity in rabbit sino-atrial node. *J. Physiol.* 308, 331–351. doi: 10.1113/jphysiol.1980.sp013474

Brown, H., DiFrancesco, D., Noble, D., and Noble, S. (1980). The contribution of potassium accumulation to outward currents in frog atrium. *J. Physiol.* 306, 127–149. doi: 10.1113/jphysiol.1980.sp013388

Brown, H. F., DiFrancesco, D., and Noble, S. J. (1979). How does adrenaline accelerate the heart? *Nature* 280, 235–236. doi: 10.1038/280235a0

Bucchi, A., Barbuti, A., DiFrancesco, D., and Baruscotti, M. (2012). Funny current and cardiac rhythm: insights from HCN knockout and transgenic mouse models. *Front. Physiol.* 3:240. doi: 10.3389/fphys.2012.00240

Bucchi, A., Plotnikov, A. N., Shlapakova, I., Danilo, P. Jr., Kryukova, Y., Qu, J., et al. (2006). Wild-type and mutant HCN channels in a tandem biological-electronic cardiac pacemaker. *Circulation* 114, 992–999. doi: 10.1161/circulationaha.106.617613

Chauveau, S., Anyukhovsky, E. P., Ben-Ari, M., Naor, S., Jiang, Y. P., Danilo, P. Jr., et al. (2017). Induced pluripotent stem cell-derived cardiomyocytes provide in vivo biological pacemaker function. *Circ. Arrhythm. Electrophysiol.* 10:e004508. doi: 10.1161/circep.116.004508

Chauveau, S., Brink, P. R., and Cohen, I. S. (2014). Stem cell-based biological pacemakers from proof of principle to therapy: a review. *Cytotherapy* 16, 873–880. doi: 10.1016/j.jcyt.2014.02.014

Cho, H. C., Kashiwakura, Y., and Marban, E. (2007). Creation of a biological pacemaker by cell fusion. *Circ. Res.* 100, 1112–1115. doi: 10.1161/01.res.0000265845.04439.78

Clark, R. B., Mangoni, M. E., Lueger, A., Couette, B., Nargeot, J., and Giles, W. R. (2004). A rapidly activating delayed rectifier K+ current regulates pacemaker activity in adult mouse sinoatrial node cells. *Am. J. Physiol. Heart Circ. Physiol.* 286, H1757–H1766. doi: 10.1152/ajpheart.00753.2003

DiFrancesco, D. (1981). A new interpretation of the pace-maker current in calf Purkinje fibres. *J. Physiol.* 314, 359–376. doi: 10.1113/jphysiol.1981.sp013713

DiFrancesco, D. (1985). The cardiac hyperpolarizing-activated current, if. Origins and developments. *Prog. Biophys. Mol. Biol.* 46, 163–183. doi: 10.1016/0079-6107(85)90008-2

DiFrancesco, D. (1986). Characterization of single pacemaker channels in cardiac sino-atrial node cells. *Nature* 324, 470–473. doi: 10.1038/324470a0

DiFrancesco, D. (1987). The pacemaker current in the sinus node. *Eur. Heart J.* 8(Suppl. L), 19–23. doi: 10.1093/eurheartj/8.suppl_l.19

DiFrancesco, D. (1993). Pacemaker mechanisms in cardiac tissue. *Annu. Rev. Physiol.* 55, 455–472. doi: 10.1146/annurev.ph.55.030193.002323

DiFrancesco, D. (1995). The onset and autonomic regulation of cardiac pacemaker activity: relevance of the f current. *Cardiovasc. Res.* 29, 449–456. doi: 10.1016/s0008-6363(96)88518-x

DiFrancesco, D. (2006). Serious workings of the funny current. *Prog. Biophys. Mol. Biol.* 90, 13–25. doi: 10.1016/j.pbiomolbio.2005.05.001

DiFrancesco, D. (2010). The role of the funny current in pacemaker activity. *Circ. Res.* 106, 434–446. doi: 10.1161/CIRCRESAHA.109.208041

DiFrancesco, D. (2013). Funny channel gene mutations associated with arrhythmias. *J. Physiol.* 591, 4117–4124. doi: 10.1113/jphysiol.2013.253765

DiFrancesco, D. (2019). Comparing pathways for long-term heart rate modulation by the funny current. *J. Gen. Physiol.* 151, 1066–1069. doi: 10.1085/jgp.201912409

DiFrancesco, D., and Borer, J. S. (2007). The funny current: cellular basis for the control of heart rate. *Drugs* 67(Suppl. 2), 15–24. doi: 10.2165/00003495-200767002-00003

DiFrancesco, D., and Camm, J. A. (2004). Heart rate lowering by specific and selective I(f) current inhibition with ivabradine: a new therapeutic perspective in cardiovascular disease. *Drugs* 64, 1757–1765. doi: 10.2165/00003495-200464160-00003

DiFrancesco, D., Ducouret, P., and Robinson, R. B. (1989). Muscarinic modulation of cardiac rate at low acetylcholine concentrations. *Science* 243, 669–671. doi: 10.1126/science.2916119

DiFrancesco, D., Ferroni, A., Mazzanti, M., and Tromba, C. (1986). Properties of the hyperpolarizing-activated current (if) in cells isolated from the rabbit sino-atrial node. *J. Physiol.* 377, 61–88. doi: 10.1113/jphysiol.1986.sp016177

DiFrancesco, D., and Noble, D. (1980). The time course of potassium current following potassium accumulation in frog atrium: analytical solutions using a linear approximation. *J. Physiol.* 306, 151–173. doi: 10.1113/jphysiol.1980.sp013389

DiFrancesco, D., and Noble, D. (1985). A model of cardiac electrical activity incorporating ionic pumps and concentration changes. *Philos. Trans R. Soc. Lond. B Biol. Sci.* 307, 353–398. doi: 10.1098/rstb.1985.0001

DiFrancesco, D., and Noble, D. (2012). The funny current has a major pacemaking role in the sinus node. *Heart Rhythm* 9, 299–301. doi: 10.1016/j.hrthm.2011.09.021

DiFrancesco, D., Ohba, M., and Ojeda, C. (1979). Measurement and significance of the reversal potential for the pace- maker current (iK2) in sheep Purkinje fibres. *J. Physiol.* 297, 135–162. doi: 10.1113/jphysiol.1979.sp013032

DiFrancesco, D., and Ojeda, C. (1980). Properties of the current if in the sino-atrial node of the rabbit compared with those of the current iK2, in Purkinje fibres. *J. Physiol.* 308, 353–367. doi: 10.1113/jphysiol.1980.sp013475

DiFrancesco, D., and Robinson, R. B. (2002). Beta-modulation of pacemaker rate: novel mechanism or novel mechanics of an old one? *Circ. Res.* 90:e69.

DiFrancesco, D., and Tortora, P. (1991). Direct activation of cardiac pacemaker channels by intracellular cyclic AMP. *Nature* 351, 145–147. doi: 10.1038/351145a0

DiFrancesco, D., and Tromba, C. (1988a). Inhibition of the hyperpolarization-activated current (if) induced by acetylcholine in rabbit sino-atrial node myocytes. *J. Physiol.* 405, 477–491. doi: 10.1113/jphysiol.1988.sp017343

DiFrancesco, D., and Tromba, C. (1988b). Muscarinic control of the hyperpolarization-activated current (if) in rabbit sino-atrial node myocytes. *J. Physiol.* 405, 493–510. doi: 10.1113/jphysiol.1988.sp017344

Gauß, R., Seifert, R., and Kaupp, B. U. (1998). Molecular identification of a hyperpolarization-activated channel in sea urchin sperm. *Nature* 393, 583–587. doi: 10.1038/31248

Himeno, Y., Toyoda, F., Satoh, H., Amano, A., Cha, C. Y., Matsuura, H., et al. (2011). Minor contribution of cytosolic Ca2+ transients to the pacemaker rhythm in guinea pig sinoatrial node cells. *Am. J. Physiol. Heart Circ. Physiol.* 300, H251–H261. doi: 10.1152/ajpheart.00764.2010

Ionta, V., Liang, W., Kim, E. H., Rafie, R., Giacomello, A., Marban, E., et al. (2015). SHOX2 overexpression favors differentiation of embryonic stem cells into cardiac pacemaker cells, improving biological pacing ability. *Stem. Cell Rep.* 4, 129–142. doi: 10.1016/j.stemcr.2014.11.004

Kashiwakura, Y., Cho, H. C., Barth, A. S., Azene, E., and Marban, E. (2006). Gene transfer of a synthetic pacemaker channel into the heart: a novel strategy for biological pacing. *Circulation* 114, 1682–1686. doi: 10.1161/circulationaha.106.634865

Kehat, I., Khimovich, L., Caspi, O., Gepstein, A., Shofti, R., Arbel, G., et al. (2004). Electromechanical integration of cardiomyocytes derived from human embryonic stem cells. *Nat. Biotechnol.* 22, 1282–1289.

Kozasa, Y., Nakashima, N., Ito, M., Ishikawa, T., Kimoto, H., Ushijima, K., et al. (2018). HCN4 pacemaker channels attenuate the parasympathetic response and stabilize the spontaneous firing of the sinoatrial node. *J. Physiol.* 596, 809–825. doi: 10.1113/jp275303

Lakatta, E. G., and DiFrancesco, D. (2009). What keeps us ticking: a funny current, a calcium clock, or both? *J. Mol. Cell Cardiol.* 47, 157–170. doi: 10.1016/j.yjmcc.2009.03.022

Lakatta, E. G., Maltsev, V. A., Bogdanov, K. Y., Stern, M. D., and Vinogradova, T. M. (2003). Cyclic variation of intracellular calcium: a critical factor for cardiac pacemaker cell dominance. *Circ. Res.* 92, e45–e50.

Lee, C. H., and MacKinnon, R. (2017). Structures of the Human HCN1 Hyperpolarization-Activated Channel. *Cell* 168, 111–20e11. doi: 10.1016/j.cell.2016.12.023

Lin, R. Z., Lu, Z., Anyukhovsky, E. P., Jiang, Y. P., Wang, H. Z., Gao, J., et al. (2019). Regulation of heart rate and the pacemaker current by phosphoinositide 3-kinase signaling. *J. Gen. Physiol.* 151, 1051–1058. doi: 10.1085/jgp.201812293

Lipsius, S. L., and Bers, D. M. (2003). Cardiac: pacemaking I(f) vs. Ca(2+), is it really that simple? *J. Mol. Cell Cardiol.* 35, 891–893. doi: 10.1016/s0022-2828(03)00184-6

Mesirca, P., Alig, J., Torrente, A. G., Muller, J. C., Marger, L., Rollin, A., et al. (2014). Cardiac arrhythmia induced by genetic silencing of 'funny' (f) channels is rescued by GIRK4 inactivation. *Nat. Commun.* 5:4664. doi: 10.1038/ncomms5664

Mesirca, P., Torrente, A. G., and Mangoni, M. E. (2015). Functional role of voltage gated Ca(2+) channels in heart automaticity. *Front. Physiol.* 6:19. doi: 10.3389/fphys.2015.00019

Noble, D. (1960). Cardiac action and pacemaker potentials based on the Hodgkin-Huxley equations. *Nature* 188, 495–497. doi: 10.1038/188495b0

Noble, D., and Tsien, R. W. (1968). The kinetics and rectifier properties of the slow potassium current in cardiac Purkinje fibres. *J. Physiol.* 195, 185–214. doi: 10.1113/jphysiol.1968.sp008454

Noma, A., and Irisawa, H. (1976). Membrane currents in the rabbit sinoatrial node cell as studied by the double microelectrode method. *Pflugers Arch.* 366, 45–52. doi: 10.1007/bf01062910

Plotnikov, A. N., Bucchi, A., Shlapakova, I., Danilo, P. Jr., Brink, P. R., Robinson, R. B., et al. (2008). HCN212-channel biological pacemakers manifesting ventricular tachyarrhythmias are responsive to treatment with I(f) blockade. *Heart Rhythm* 5, 282–288. doi: 10.1016/j.hrthm.2007.09.028

Plotnikov, A. N., Sosunov, E. A., Qu, J., Shlapakova, I. N., Anyukhovsky, E. P., Liu, L., et al. (2004). Biological pacemaker implanted in canine left bundle branch provides ventricular escape rhythms that have physiologically acceptable rates. *Circulation* 109, 506–512. doi: 10.1161/01.cir.0000114527.10764.cc

Potapova, I., Plotnikov, A., Lu, Z., Danilo, P. Jr., Valiunas, V., Qu, J., et al. (2004). Human mesenchymal stem cells as a gene delivery system to create cardiac pacemakers. *Circ. Res.* 94, 952–959. doi: 10.1161/01.res.0000123827.60210.72

Protze, S. I., Liu, J., Nussinovitch, U., Ohana, L., Backx, P. H., Gepstein, L., et al. (2017). Sinoatrial node cardiomyocytes derived from human pluripotent cells function as a biological pacemaker. *Nat. Biotechnol.* 35, 56–68. doi: 10.1038/nbt.3745

Qu, J., Barbuti, A., Protas, L., Santoro, B., Cohen, I. S., and Robinson, R. B. (2001). HCN2 overexpression in newborn and adult ventricular myocytes: distinct effects on gating and excitability. *Circ .Res.* 89, E8–E14.

Qu, J., Plotnikov, A. N., Danilo, P. Jr., Shlapakova, I., Cohen, I. S., Robinson, R. B., et al. (2003). Expression and function of a biological pacemaker in canine heart. *Circulation* 107, 1106–1109. doi: 10.1161/01.cir.0000059939.97249.2c

Quinn, T. A., and Kohl, P. (2012). Mechano-sensitivity of cardiac pacemaker function: pathophysiological relevance, experimental implications, and conceptual integration with other mechanisms of rhythmicity. *Prog. Biophys. Mol. Biol.* 110, 257–268. doi: 10.1016/j.pbiomolbio.2012.08.008

Robinson, R. B. (2011). The long and short of calcium-dependent automaticity in the sinoatrial node. *Am. J. Physiol. Heart Circ. Physiol.* 300, H31–H32. doi: 10.1152/ajpheart.01083.2010

Robinson, R. B., Brink, P. R., Cohen, I. S., and Rosen, M. R. I. (2006). (f) and the biological pacemaker. *Pharmacol.Res.* 53, 407–415.

Rosen, M. R., Robinson, R. B., Brink, P. R., and Cohen, I. S. (2011). The road to biological pacing. *Nat. Rev.Cardiol.* 8, 656–666. doi: 10.1038/nrcardio.2011.120

Santoro, B., Liu, D. T., Yao, H., Bartsch, D., Kandel, E. R., Siegelbaum, S. A., et al. (1998). Identification of a gene encoding a hyperpolarization-activated pacemaker channel of brain. *Cell* 93, 717–729. doi: 10.1016/s0092-8674(00)81434-8

Saponaro, A., Pauleta, S. R., Cantini, F., Matzapetakis, M., Hammann, C., Donadoni, C., et al. (2014). Structural basis for the mutual antagonism of cAMP and TRIP8b in regulating HCN channel function. *Proc. Natl. Acad. Sci. U.S.A.* 111, 14577–14582. doi: 10.1073/pnas.1410389111

Torrente, A. G., Mesirca, P., Neco, P., Rizzetto, R., Dubel, S., Barrere, C., et al. (2016). L-type Cav1.3 channels regulate ryanodine receptor-dependent Ca2+

release during sino-atrial node pacemaker activity. *Cardiovasc. Res.* 109, 451–461. doi: 10.1093/cvr/cvw006

Toyoda, F., Mesirca, P., Dubel, S., Ding, W. G., Striessnig, J., Mangoni, M. E., et al. (2017). CaV1.3 L-type Ca(2+) channel contributes to the heartbeat by generating a dihydropyridine-sensitive persistent Na(+) current. *Sci. Rep.* 7:7869. doi: 10.1038/s41598-017-08191-8

Vaccari, T., Moroni, A., Rocchi, M., Gorza, L., Bianchi, M. E., Beltrame, M., et al. (1999). The human gene coding for HCN2, a pacemaker channel of the heart. *Biochim. Biophys. Acta* 1446, 419–425. doi: 10.1016/s0167-4781(99)00092-5

Vinogradova, T. M., Bogdanov, K. Y., and Lakatta, E. G. (2002). beta-Adrenergic stimulation modulates ryanodine receptor Ca(2+) release during diastolic depolarization to accelerate pacemaker activity in rabbit sinoatrial nodal cells. *Circ. Res.* 90, 73–79. doi: 10.1161/hh0102.102271

Vinogradova, T. M., Zhou, Y. Y., Maltsev, V., Lyashkov, A., Stern, M., and Lakatta, E. G. (2004). Rhythmic ryanodine receptor Ca2+ releases during diastolic depolarization of sinoatrial pacemaker cells do not require membrane depolarization. *Circ. Res.* 94, 802–809. doi: 10.1161/01.res.0000122045.55331.0f

Weidmann, S. (1951). Effect of current flow on the membrane potential of cardiac muscle. *J. Physiol.* 115, 227–236. doi: 10.1113/jphysiol.1951.sp004667

Xue, T., Cho, H. C., Akar, F. G., Tsang, S. Y., Jones, S. P., Marban, E., et al. (2005). Functional integration of electrically active cardiac derivatives from genetically engineered human embryonic stem cells with quiescent recipient ventricular cardiomyocytes: insights into the development of cell-based pacemakers. *Circulation* 111, 11–20. doi: 10.1161/01.cir.0000151313.18547.a2

Conflict of Interest: The author declares that the research was conducted in the absence of any commercial or financial relationships that could be construed as a potential conflict of interest.

frontiers in Physiology

MINI REVIEW
published: 07 July 2020
doi: 10.3389/fphys.2020.00771

cyclic AMP Regulation and Its Command in the Pacemaker Channel HCN4

*Alessandro Porro[1], Gerhard Thiel[2], Anna Moroni[1] and Andrea Saponaro[1]**

[1]Department of Biosciences, University of Milan, Milan, Italy, [2]Department of Biology, Technische Universität Darmstadt, Darmstadt, Germany

Direct regulation of the pacemaker “funny” current (I_f) by cyclic AMP (cAMP) underlies heart rate modulation by the autonomic nervous system. At the molecular level, cAMP activates hyperpolarization-activated cyclic nucleotide-gated (HCN) channels that drive I_f in sinoatrial node (SAN) myocytes. Even though HCN channel genes were identified more than 20 years ago, the understanding of how cAMP regulates their gating is still fragmented. Here we summarize present understanding on how the cAMP signal is transmitted from the cytosolic to the transmembrane (TM) domain in HCN4. We further discuss how detailed structural knowledge prompted the development of pharmacological/genetic tools for the control of cAMP regulation in these channels.

Keywords: cyclic AMP, hyperpolarization-activated cyclic nucleotide-gated (HCN) channels, regulation, structure, “funny” current, heart rate

Edited by:
Alicia D’Souza,
University of Manchester,
United Kingdom

Reviewed by:
Elisabetta Cerbai,
University of Florence, Italy
Robert Alan Rose,
University of Calgary, Canada

****Correspondence:***
Andrea Saponaro
andrea.saponaro@unimi.it

Specialty section:
This article was submitted to
Cardiac Electrophysiology,
a section of the journal
Frontiers in Physiology

Received: *30 March 2020*
Accepted: *11 June 2020*
Published: *07 July 2020*

Citation:
Porro A, Thiel G, Moroni A and Saponaro A (2020) cyclic AMP Regulation and Its Command in the Pacemaker Channel HCN4.
Front. Physiol. 11:771.
doi: 10.3389/fphys.2020.00771

INTRODUCTION

Automaticity of heartbeat originates in the sinoatrial node (SAN), where specialized cardiomyocytes initiate spontaneous impulses in the absence of external stimuli. A main player of cardiac automaticity is the “funny” current (I_f) that, unique among voltage-gated channels, is activated by hyperpolarization of membrane voltage. I_f is a mixed Na^+/K^+ inward current that slowly depolarizes pacemaker cells to the threshold for action potential firing (DiFrancesco, 1993). In addition to voltage, I_f is modulated by the second messenger cyclic AMP (cAMP), which enhances channel open probability, shifting the voltage-dependency of opening to more positive values and increasing the amount of current at any given voltage (DiFrancesco and Tortora, 1991). This mechanism is of crucial physiological relevance as it contributes to the autonomic regulation of heart rate by adrenaline and acetylcholine, which modulate cAMP concentration of SAN myocytes. It is indeed worth noting that cAMP controls different pathways in SAN myocytes, all converging to the modulation of heart rate (Behar et al., 2016).

The molecular determinants of I_f are hyperpolarization-activated cyclic nucleotide-gated (HCN) channels (Santoro et al., 1998; Ludwig et al., 1999; Wainger et al., 2001). HCN channels are encoded by four distinct genes in mammals (HCN1–HCN4). The four closely related isoforms each express a hyperpolarization-activated cation current, whose kinetics range from fast (HCN1) to very slow (HCN4). HCN isoforms also differ in their voltage-dependence with HCN1 opening at the most depolarized and HCN4 at the most hyperpolarized potentials (as assessed by their half-activation voltage or $V_{1/2}$ value). The channels further differ in their cAMP response with HCN1 displaying the smallest and HCN4 the largest maximal voltage shift with saturating concentrations of ligand (Wahl-Schott and Biel, 2009). HCN4 is the main subunit expressed in SAN (Brioschi et al., 2009), and the characteristic properties of HCN4, slow activation kinetics and the strong response to cAMP, closely match those of I_f (Baruscotti and Difrancesco, 2004). Noteworthy, HCN1 and HCN2 have been found in the SAN as well, but the levels of expression are usually much lower compared to HCN4 and vary a lot among different species. Despite their poor presence, there is evidence that they contribute to the cardiac pacemaking I_f (Herrmann et al., 2011; Bucchi et al., 2012; Fenske et al., 2013).

As for the role of HCN in heart rate acceleration during sympathetic stimulation, there are controversial reports on the role of HCN4. Two initial studies performed in mice deleted of HCN4 in a temporally controlled manner showed that the cAMP regulation of HCN4 is not required for the modulation of the heart rate, as the ECG recordings in freely moving HCN4 knockout (KO) mice did not reveal major alterations of the cardiac electrical activity (Herrmann et al., 2007; Hoesl et al., 2008). However, further studies highlighted the essential role of HCN4 in establishing the basal heart rate and its cAMP-dependent regulation and in reaching the maximal heart rate (Alig et al., 2009; Baruscotti et al., 2011). Therefore, the relevance of HCN4 for the regulation of heart rate is clear, though HCN4 may not contribute to all the phenomena involved in this process. The role of HCN4 in the different levels of modulation of heart rate has been already analyzed in detail in a review (Bucchi et al., 2012) and it is beyond the purpose of our review, which, as already stated, is specifically focused on the molecular details of cAMP regulation of HCN4.

Here, we review current knowledge on how cAMP binds to HCN channels and affects their gating mechanism. Taking HCN4 as a paradigm, we will further show how the precise knowledge of this mechanism leads to the discovery of modalities to interfere with it, paving the way to future therapeutic and pharmacological interventions for the control of heart rate.

INSIGHT INTO cAMP REGULATION COMES FROM THE STRUCTURES OF HCN CHANNELS

To date, the available structural information on HCN channels include the full length model of HCN1 (Lee and MacKinnon, 2017, 2019) and several detailed structures of the cytosolic domain, which host the cAMP binding sites of HCN4, HCN2, and HCN1 (Zagotta et al., 2003; Xu et al., 2010; Lolicato et al., 2011, 2014; Akimoto et al., 2014; Saponaro et al., 2014).

The full length structure of the human HCN1 channels was recently solved using cryo-electron microscopy single particle analysis (cryo-EM) in the presence and absence of bound cAMP (Lee and MacKinnon, 2017, 2019). The overall structure of HCN channels is similar to that of other members [EAG (Whicher and MacKinnon, 2016) and hERG (Wang and MacKinnon, 2017)] of the superfamily of voltage-gated K^+ channel to which HCN belongs.

HCN channels are composed of four subunits assembled around a central pore. **Figure 1A** displays only two opposite subunits in the membrane and four in the cytosolic side, for clarity. Each monomer is composed of six transmembrane (TM) domains, of which S1–S4 form the voltage sensor domain (VSD) and S5–S6 form the pore domain (PD) that hosts the selectivity filter (SF). The N and C termini are cytosolic, the N-terminus contains the HCN domain (HCND) and the C terminus contains the cyclic nucleotide binding domain (CNBD), which is connected to the S6 in the PD *via* a C-linker. The C-linker contains two helix-turn-helix motifs (formed by helices A', B' and C', D', respectively) that form the gating ring of the tetramer by resting as "an elbow on the shoulder" of the neighbor subunit (Zagotta et al., 2003).

Binding of cAMP occurs at the CNBD and initiates the signal that is transmitted *via* the C-linker to the TM part of the channel, where it increases pore open probability by reducing the energetic request of the VSD. **Figure 1B** shows the response of HCN4 currents to the addition of saturating concentrations (30 μM) of cytosolic cAMP. Ligand binding increases the amount of current recorded at intermediate voltage (−90 mV in this example) without affecting the maximal current recorded at saturating voltage (−135 mV). This effect of the ligand on voltage-dependency of the channel is reflected in a right shift (about 20 mV) of the half activating voltage ($V_{1/2}$), as shown in the activation curve that describes channel open probability as a function of voltage (**Figure 1C**).

The comparison of the available HCN1 structures, obtained in the cAMP-free (apo) and -bound (holo) form, provides little mechanistic information on how pore gating may be modulated by cAMP. Minimal differences in the conformation of the C-linker are observed between the apo and holo structures of HCN1 (Lee and Mackinnon, 2017), despite a large body of literature arguing that movements of the CNBD transfer force to the TMD portion of the channel through a rearrangement in the C-linker, leading to a rotation of the elbow (Craven and Zagotta, 2004; Craven et al., 2008; Weissgraeber et al., 2017; Gross et al., 2018). This finding is somehow not surprising considering the known minimal response of HCN1 to cAMP (Porro et al., 2019), and highlights the expectation for other structures of HCN isoforms with a larger cAMP response to come.

Present knowledge on the intramolecular pathway of cAMP effect in HCN channels, thus relies on a large amount of previous work performed on the isolated cytosolic portion of the channel that comprises only the CNBD or the C-linker/CNBD (Zagotta et al., 2003; Xu et al., 2010; Lolicato et al., 2011, 2014; Puljung and Zagotta, 2013; Akimoto et al., 2014; Puljung et al., 2014; Saponaro et al., 2014). It is nonetheless to be mentioned that, despite the above numerous studies showing that the cAMP modulation in HCN is mediated by direct binding of the molecule to the CNBD, it has been reported that the channel can be also regulated by a cAMP-dependent mechanism through protein kinase A (PKA; Liao et al., 2010).

THE CONFORMATIONAL CHANGES INDUCED BY cAMP IN THE CNBD

The CNBD has the conserved motif of a per-ARNT-sim (PAS) domain composed by a beta roll (beta sheets 1–7)

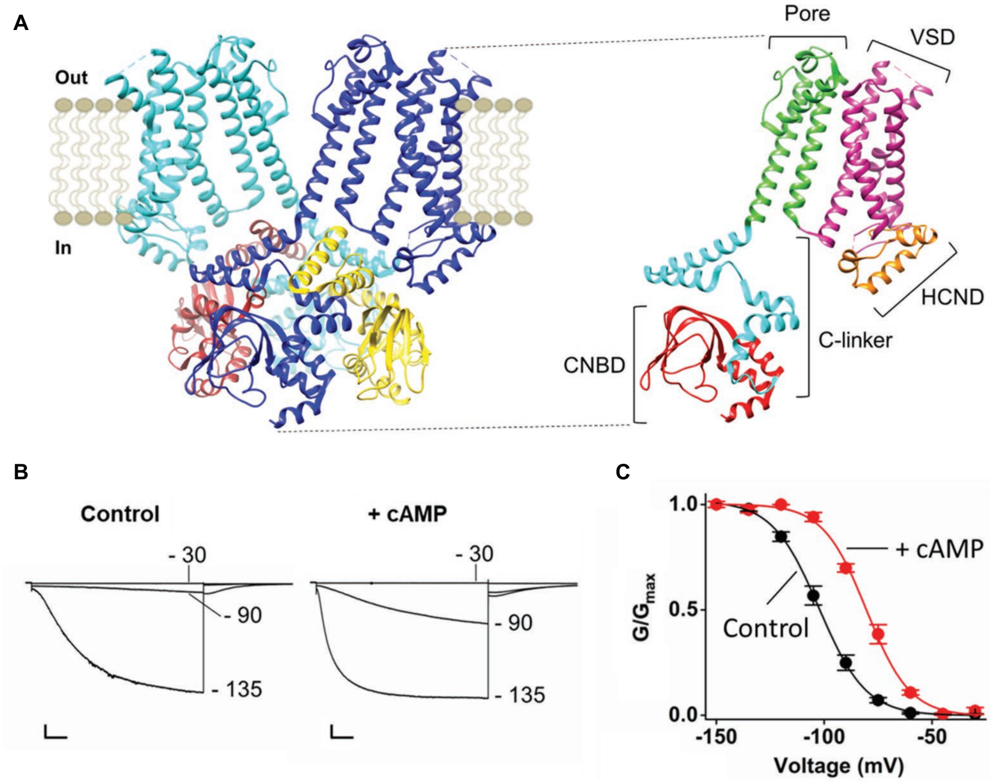

FIGURE 1 | (A) Left, ribbon representation (side view) of two opposite subunits of HCN1 (PDB_ID: 5U6O) colored in blue and light blue. The four cytoplasmic C-terminal regions of HCN1 are shown and colored in blue, brown, light blue, and yellow. Right, ribbon representation (side view) of one subunit of HCN1. The domains of the protein are labeled: The Cytoplasmic N-terminal hyperpolarization-activated cyclic nucleotide-gated domain (HCND) in orange, the voltage sensor domain (VSD) in magenta, the pore domain (PD) in green, the cytoplasmic C-terminal C-linker in light blue, and the cyclic nucleotide binding domain (CNBD) in red. **(B)** Representative whole-cell currents of HCN4 recorded at the indicated voltages in control solution (left) and in the presence of saturating cyclic AMP [cAMP; right; adapted from Porro et al. (2019) with permission]. Scale bar is 200 pA × 500 ms. **(C)** Mean activation curves of HCN4 in control solution (black) and in the presence of saturating cAMP [red; adapted from Porro et al. (2019) with permission]. Values of the activation curves are shown as mean ± SEM.

and alpha helices (E', F', A, B, P, and C). It contains a cAMP binding pocket at the interface between the beta roll and the alpha helices. Binding of cAMP induces most changes in the C-helix. The C-helix undergoes a translational movement toward the beta roll and establishes crucial contacts with the cAMP moiety. During this process the C-terminal end of the C-helix folds and the overall length of the helix increases, thus becoming a sort of a "lid" on the binding pocket. The other relevant movement occurring in the CNBD upon cAMP binding is the upward displacement of helices E' and F' (Saponaro et al., 2014). These two helices are directly connected to the C-linker. Their movement thus transmits the cAMP signal to the C-linker, initiating the conformational changes that will eventually affect pore opening. It is therefore expected that blocking cAMP-induced movements in the CNBD will prevent the effect of the ligand on the current. Indeed, in the nervous system, HCN channels have a cytosolic regulatory subunit, TRIP8b, that inhibits channel response to cAMP by physically interacting with the CNBD (Santoro et al., 2004; Hu et al., 2013; Saponaro et al., 2014, 2018). The minimal portion of TRIP8b that recapitulates the effect of the full length protein on channel gating is 40 residues long (named TRIP8b$_{nano}$) and comprises two short alpha helices, which fold upon binding to the CNBD (Saponaro et al., 2018). The structural model of the complex between HCN2 CNBD and TRIP8b$_{nano}$ was obtained by NMR, and is shown in **Figure 2B**. TRIP8b$_{nano}$ (in green) binds to the CNBD in the cAMP-unbound (apo) state (in gray) and its interaction is predominately driven by electrostatic contacts with the CNBD C-helix.

The structural model of the complex fully explains the articulated mechanism through which TRIP8b antagonizes cAMP binding to the CNBD. cAMP and TRIP8b share the same binding sites on the C-helix and this accounts for the direct competition previously highlighted by functional studies (Han et al., 2011; Deberg et al., 2015; Bankston et al., 2017). On the other hand, TRIP8b interacts with the loop between E'-F' helices (N-bundle loop, colored in yellow in **Figure 2B**), which constitutes an allosteric regulative element for cAMP binding (Saponaro et al., 2018). This accounts for the allosteric inhibition component of the antagonistic action of TRIP8b on the cAMP effect previously proposed (Hu et al., 2013).

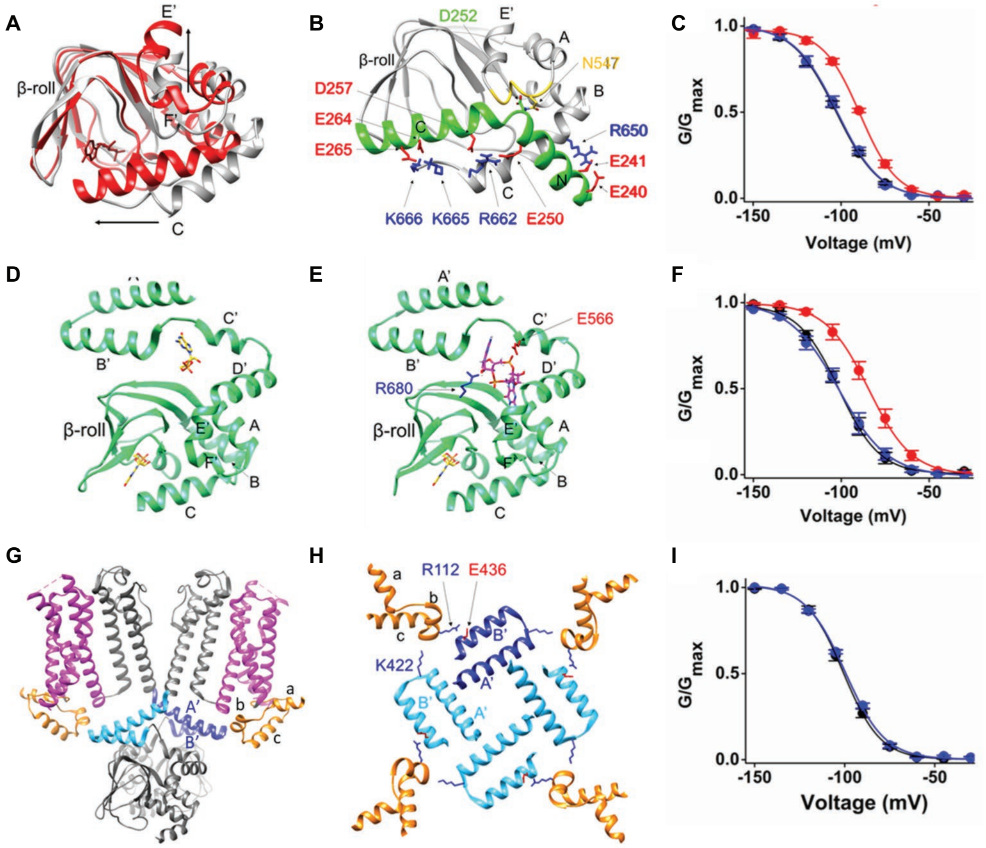

FIGURE 2 | (A) Superimposition of the two structures of HCN2 CNBD, represented as ribbons, solved in the absence (gray, PDB_ID: 2MPF) and in the presence of cAMP (red, PDB_ID: 3U10). cAMP, represented as red sticks, is shown within the beta roll. The structural elements involved in the principal movements induced by cAMP are labeled. The black arrows indicate the direction of such movements. **(B)** Ribbon representation of HCN2 CNBD (gray) in complex with TRIP8b$_{nano}$ peptide [green; adapted from Saponaro et al. (2018) with permission]. The structural elements of both proteins are labeled. The N-bundle loop of the CNBD is colored in yellow. The crucial residues involved in the interaction are shown as sticks and labeled. In particular, the negative residues of TRIP8b$_{nano}$ are colored in red, while in blue the positive residues of HCN2 CNBD. **(C)** Mean activation curves of HCN4 in control solution (black), in the presence of cAMP (red) and in the presence of cAMP and TRIP8b$_{nano}$ [blue; adapted from Saponaro et al. (2018) with permission]. **(D)** Ribbon representation of HCN4 C-linker/CNBD (green) solved in the presence of cGMP (PDB_ID: 4KL1). The two cyclic GMP (cGMP) molecules, represented as sticks, are shown and colored in yellow. **(E)** Docking simulation of c-di-GMP (magenta stick) molecule in the structure of HCN4 C-linker/CNBD (green) solved in the presence of cGMP [PDB_ID: 4KL1; adapted from Lolicato et al. (2014) with permission]. The crucial residues involved in the interaction with c-di-GMP are shown, labeled and colored based on their chemical nature: blue and red for the positively and negatively charged residues, respectively. The cGMP molecule bound to CNBD is represented as sticks and colored in yellow. **(F)** Mean activation curves of HCN4 in control solution (black), in the presence of cAMP (red) and in the presence of cAMP and c-di-GMP [blue; adapted from Lolicato et al. (2014) with permission]. **(G)** Ribbon representation (side view) of two opposite subunits of HCN1 (gray, PDB_ID: 5U6O). The HCNDs are colored in orange, the VSDs are colored in magenta, and the C-linker "elbow" elements (A' and B' helices) are colored in blue and light blue in the two subunits. **(H)** Top view of the HCNDs (orange) and the C-linker "elbow" elements (one subunit in blue and the other three in light blue). The structural elements forming the HCND and the C-linker "elbow" elements are labeled. The residues involved in the interaction between the HCND and two adjacent C-linker "elbows" are shown as sticks, labeled and colored-coded based on their chemical nature as in panels **(B,E)**. **(I)** Mean activation curves of HCN4 wt (black) and K543A-E557A double mutant [blue; adapted from Porro et al. (2019) with permission]. Values of the activation curves shown in panels **(C,F,I)** are shown as mean ± SEM.

Thus, even though cAMP can still bind to the pocket inside the beta roll, the presence of TRIP8b$_{nano}$ prevents cAMP-induced movements in the C-helix and in the E'-F' helices (shown in **Figure 2A**), thus inhibiting cAMP effect on the current (**Figure 2C**).

TRIP8b$_{nano}$ has been used as a peptide tool to selectively prevent adrenergic regulation of I_f in SAN myocytes, reducing the action potential firing rate in isolated myocytes by about 30% (Saponaro et al., 2018). TRIP8b$_{nano}$ is also available in a cell-penetrating form, obtained by fusing the viral TAT peptide sequence at its N-terminus (Saponaro et al., 2018). In this form, TRIP8b$_{nano}$ can be added directly to the external solution, widening its range of applications as a research tool as well as a potential peptide drug whenever the response of HCN channels to cAMP needs to be dampened.

TRANSMISSION OF cAMP EFFECT THROUGH THE C-LINKER

X-ray crystallography has been successfully used to obtain the structure of the cytosolic portion of HCN channels that include the C-linker and the CNBD (C-linker/CNBD; Zagotta et al., 2003; Xu et al., 2010; Lolicato et al., 2011, 2014). In these structures, the C-linker adopts a tetrameric configuration known as "elbow on shoulder," in which the elbow of one subunit, formed by helices A' and B', rests on the shoulder, formed by helices C' and D' of the adjacent subunit. Such a configuration has been confirmed by the full length structure of HCN1 (Lee and MacKinnon, 2017, 2019). Several hydrophilic and hydrophobic contacts connect the elbow and the shoulder creating a network of interactions that can easily propagate the CNBD-initiated movements toward the TM domains. In the specific case of HCN4, in which the C-linker/CNBD was crystallized in the presence of the agonist cyclic GMP (cGMP), the ligand was found to be bound to a second pocket, besides the canonical ligand binding site in the CNBD (Lolicato et al., 2014). This result led to the discovery of a regulatory pocket at the interface between the CNBD and the C-linker, the C-linker pocket (CLP; **Figure 2D**). *In silico* docking performed in the CLP, identified a class of potential binders, cyclic-di-nucleotides (c-di-nucleotide; **Figure 2E**). This is a class of regulatory molecules originally discovered in bacteria (c-di-GMP and c-di-AMP) but more recently found also in mammals (cGAMP; Wu et al., 2013). When tested in patch clamp experiments, c-di-GMP, c-di-AMP, and cGAMP, all efficiently prevented cAMP effect in HCN4 channels with micromolar (c-diGMP and c-di-AMP) and submicromolar (cGAMP) affinity (Lolicato et al., 2014). Several mutations introduced in the CLP, prevented c-di-nucleotide action allowing normal cAMP response of the mutants channels (**Figure 2F**; Lolicato et al., 2014). It is believed that the occupancy of the CLP by c-di-nucleotides blocks the transmission of the movement from the CNBD to the C-linker inasmuch as the CLP corresponds to the flexible link between the two movable parts of the C-linker, the elbow and the shoulder. In this way, the upward movement of the E' and F' helices of the CNBD (see **Figure 2A**) cannot be converted into the expected rotation of the upper part of the C-linker.

Notably, this effect is isoform-specific as only HCN4 responds to c-di-nucleotides (Lolicato et al., 2014). This is remarkable, given the high degree of amino acid conservation in the critical residues of the CLP among different HCN subunits. At the same time, this is very exciting because c-di-nucleotides constitute the only HCN-specific inhibitors available so far. C-di-nucleotides have been shown to reduce cAMP response and firing rate in isolated myocytes of the SAN of mouse (Lolicato et al., 2014). It is worth noting that, even though there is no direct evidence of c-di-nucleotides in the heart, it is known that the key enzyme for cGAMP production, cyclic-GMP-AMP synthase (cGAS), is highly expressed in human cardiac tissues (Uhlen et al., 2010). Moreover, it was demonstrated that c-di-nucleotides can be also transferred from producing cells to neighboring cells through gap junctions, thus rapidly spreading them in a horizontal manner (Ablasser et al., 2013). So far, c-dinucleotides as second messengers in mammals have been associated to the immune system (Li et al., 2013), but the findings reported above allow to hypothesize a possible role of endogenous c-di-nucleotides in the control of I_f, either because of their direct production in cardiomyocytes, or because of their spreading *via* gap junctions following the activation of the immune response.

THE TRANSMISSION OF THE cAMP EFFECT TO THE TM DOMAIN

The full length structure of HCN1 has shown for the first time in the presence of three helical folded domains (helices A–C, see **Figures 2G,H**), termed HCND, at the cytosolic N-terminus of the channel, right before TM1 (Lee and MacKinnon, 2017). In the 3D structure, the HCND wedges in between the C-linker and the VSD possibly establishing contacts with both of them (**Figure 2G**). In a recent work, Porro et al. (2019) highlighted the network of hydrophobic and hydrophilic interactions that physically connect the HCND to the C-linker and the VSD, and underscored their crucial role in mechanically transmitting the cAMP effect from the cytosolic to the TM domain (Porro et al., 2019). **Figure 2H** shows a top view of the tetrameric arrangement of the HCND and the C-linker. Each HCND, in orange, establishes, *via* the top part, hydrophobic contacts with the VSD, in magenta, of its own subunit in the membrane (not shown) and with the lower part electrostatic interactions with the C-linkers of the adjacent (light blue) and opposite (blue) subunits. The HCND thus forms a physical continuum between the cytosolic C-linker and the TM VSD domain.

Mutations of the two resides on the C-linker, E436 and K422 (human HCN1 numbering), completely abolish the response of the channel to cAMP, leaving the properties of the channel unaltered. This result was reproduced in all HCN isoforms tested, HCN1, HCN2, and HCN4 (**Figure 2I** shows the effect of the double mutation in HCN4; Porro et al., 2019), confirming the hypothesis that the HCND is involved in the transmission of the cAMP-induced movement from the cytosolic to the TM domain. In particular, on the basis of molecular dynamic (MD) simulations and linear response theory calculations, it was concluded that the HCND acts as a transmission crank converting the circular rotation of the C-linker into a vertical displacement in the VSD (Porro et al., 2019).

These data provide structural-based support to the view that the C-linker must be physically connected to the VSD to transmit cAMP-induced movements originating in the CNBD. Experimental evidences came originally from a study of Kusch et al. (2010) showing that, in HCN2, the movement of the voltage sensor changes the affinity for cAMP in the CNBD without involving the PD. This result was obtained by simultaneous recording of currents and fluo-cAMP binding, a technique that goes under the name of patch-clamp fluorometry.

Even though the precise allosteric pathway is not yet defined in full detail, it is nonetheless expected that this communication pathway works in both directions, and that the signal of the presence of cAMP and the signal of the presence of voltage will travel along the same pathway through the HCN tetramer, although in opposite directions.

In conclusion, recent advancement in the comprehension of how cAMP regulates gating in HCN channels came from structural studies of the full length as well as from cytosolic portions of the channel. Reconstruction of the allosteric pathway from the CNBD to the VSD allows the control and the command over cAMP effect in the channel providing new tools for research and future pharmacological intervention.

AUTHOR CONTRIBUTIONS

All authors critically reviewed the literature. AM and AS wrote the text and prepared the figures. All authors contributed to the article and approved the submitted version.

FUNDING

This work has been supported by fondazione CARIPLO grant 2018–0231 to AS.

REFERENCES

Ablasser, A., Schmid-Burgk, J. L., Hemmerling, I., Horvath, G. L., Schmidt, T., Latz, E., et al. (2013). Cell intrinsic immunity spreads to bystander cells via the intercellular transfer of cGAMP. *Nature* 503, 530–534. doi: 10.1038/nature12640

Akimoto, M., Zhang, Z., Boulton, S., Selvaratnam, R., VanSchouwen, B., Gloyd, M., et al. (2014). A mechanism for the auto-inhibition of hyperpolarization-activated cyclic nucleotide-gated (HCN) channel opening and its relief by cAMP. *J. Biol. Chem.* 289, 22205–22220. doi: 10.1074/jbc.M114.572164

Alig, J., Marger, L., Mesirca, P., Ehmke, H., Mangoni, M. E., and Isbrandt, D. (2009). Control of heart rate by cAMP sensitivity of HCN channels. *Proc. Natl. Acad. Sci. U. S. A.* 106, 12189–12194. doi: 10.1073/pnas.0810332106

Bankston, J. R., DeBerg, H. A., Stoll, S., and Zagotta, W. N. (2017). Mechanism for the inhibition of the cAMP dependence of HCN ion channels by the auxiliary subunit TRIP8b. *J. Biol. Chem.* 292, 17794–17803. doi: 10.1074/jbc.M117.800722

Baruscotti, M., Bucchi, A., Viscomi, C., Mandelli, G., Consalez, G., Gnecchi-Rusconi, T., et al. (2011). Deep bradycardia and heart block caused by inducible cardiac-specific knockout of the pacemaker channel gene Hcn4. *Proc. Natl. Acad. Sci. U. S. A.* 108, 1705–1710. doi: 10.1073/pnas.1010122108

Baruscotti, M., and Difrancesco, D. (2004). Pacemaker channels. *Ann. N. Y. Acad. Sci.* 1015, 111–121. doi: 10.1196/annals.1302.009

Behar, J., Ganesan, A., Zhang, J., and Yaniv, Y. (2016). The autonomic nervous system regulates the heart rate through cAMP-PKA dependent and independent coupled-clock pacemaker cell mechanisms. *Front. Physiol.* 7:419. doi: 10.3389/fphys.2016.00419

Brioschi, C., Micheloni, S., Tellez, J. O., Pisoni, G., Longhi, R., Moroni, P., et al. (2009). Distribution of the pacemaker HCN4 channel mRNA and protein in the rabbit sinoatrial node. *J. Mol. Cell. Cardiol.* 47, 221–227. doi: 10.1016/j.yjmcc.2009.04.009

Bucchi, A., Barbuti, A., Difrancesco, D., and Baruscotti, M. (2012). Funny current and cardiac rhythm: insights from HCN knockout and transgenic mouse models. *Front. Physiol.* 3:240. doi: 10.3389/fphys.2012.00240

Craven, K. B., Olivier, N. B., and Zagotta, W. N. (2008). C-terminal movement during gating in cyclic nucleotide-modulated channels. *J. Biol. Chem.* 283, 14728–14738. doi: 10.1074/jbc.M710463200

Craven, K. B., and Zagotta, W. N. (2004). Salt bridges and gating in the COOH-terminal region of HCN2 and CNGA1 channels. *J. Gen. Physiol.* 124, 663–677. doi: 10.1085/jgp.200409178

Deberg, H. A., Bankston, J. R., Rosenbaum, J. C., Brzovic, P. S., Zagotta, W. N., and Stoll, S. (2015). Structural mechanism for the regulation of HCN ion channels by the accessory protein TRIP8b. *Structure* 23, 734–744. doi: 10.1016/j.str.2015.02.007

DiFrancesco, D. (1993). Pacemaker mechanisms in cardiac tissue. *Annu. Rev. Physiol.* 55, 455–472. doi: 10.1146/annurev.ph.55.030193.002323

DiFrancesco, D., and Tortora, P. (1991). Direct activation of cardiac pacemaker channels by intracellular cyclic AMP. *Nature* 351, 145–147. doi: 10.1038/351145a0

Fenske, S., Krause, S. C., Hassan, S. I. H., Becirovic, E., Auer, F., Bernard, R., et al. (2013). Sick sinus syndrome in HCN1-deficient mice. *Circulation* 128, 2585–2594. doi: 10.1161/CIRCULATIONAHA.113.003712

Gross, C., Saponaro, A., Santoro, B., Moroni, A., Thiel, G., and Hamacher, K. (2018). Mechanical transduction of cytoplasmic-to-transmembrane-domain movements in a hyperpolarization-activated cyclic nucleotide-gated cation channel. *J. Biol. Chem.* 293, 12908–12918. doi: 10.1074/jbc.RA118.002139

Han, Y., Noam, Y., Lewis, A. S., Gallagher, J. J., Wadman, W. J., Baram, T. Z., et al. (2011). Trafficking and gating of hyperpolarization-activated cyclic nucleotide-gated channels are regulated by interaction with tetratricopeptide repeat-containing Rab8b-interacting protein (TRIP8b) and cyclic AMP at distinct sites. *J. Biol. Chem.* 286, 20823–20834. doi: 10.1074/jbc.M111.236125

Herrmann, S., Layh, B., and Ludwig, A. (2011). Novel insights into the distribution of cardiac HCN channels: an expression study in the mouse heart. *J. Mol. Cell. Cardiol.* 51, 997–1006. doi: 10.1016/j.yjmcc.2011.09.005

Herrmann, S., Stieber, J., Stöckl, G., Hofmann, F., and Ludwig, A. (2007). HCN4 provides a "depolarization reserve" and is not required for heart rate acceleration in mice. *EMBO J.* 26, 4423–4432. doi: 10.1038/sj.emboj.7601868

Hoesl, E., Stieber, J., Herrmann, S., Feil, S., Tybl, E., Hofmann, F., et al. (2008). Tamoxifen-inducible gene deletion in the cardiac conduction system. *J. Mol. Cell. Cardiol.* 45, 62–69. doi: 10.1016/j.yjmcc.2008.04.008

Hu, L., Santoro, B., Saponaro, A., Liu, H., Moroni, A., and Siegelbaum, S. (2013). Binding of the auxiliary subunit TRIP8b to HCN channels shifts the mode of action of cAMP. *J. Gen. Physiol.* 142, 599–612. doi: 10.1085/jgp.201311013

Kusch, J., Biskup, C., Thon, S., Schulz, E., Nache, V., Zimmer, T., et al. (2010). Interdependence of receptor activation and ligand binding in hcn2 pacemaker channels. *Neuron* 67, 75–85. doi: 10.1016/j.neuron.2010.05.022

Lee, C. -H., and MacKinnon, R. (2017). Structures of the human HCN1 hyperpolarization-activated channel. *Cell* 168, 111–120.e11. doi: 10.1016/j.cell.2016.12.023

Lee, C. -H., and MacKinnon, R. (2019). Voltage sensor movements during hyperpolarization in the HCN channel. *Cell* 179, 1582–1589.e7. doi: 10.1016/j.cell.2019.11.006

Li, X. -D., Wu, J., Gao, D., Wang, H., Sun, L., and Chen, Z. J. (2013). Pivotal roles of cGAS-cGAMP signaling in antiviral defense and immune adjuvant effects. *Science* 341, 1390–1394. doi: 10.1126/science.1244040

Liao, Z., Lockhead, D., Larson, E. D., and Proenza, C. (2010). Phosphorylation and modulation of hyperpolarization-activated HCN4 channels by protein kinase A in the mouse sinoatrial node. *J. Gen. Physiol.* 136, 247–258. doi: 10.1085/jgp.201010488

Lolicato, M., Bucchi, A., Arrigoni, C., Zucca, S., Nardini, M., Schroeder, I., et al. (2014). Cyclic dinucleotides bind the C-linker of HCN4 to control channel cAMP responsiveness. *Nat. Chem. Biol.* 10, 457–462. doi: 10.1038/nchembio.1521

Lolicato, M., Nardini, M., Gazzarrini, S., Moller, S., Bertinetti, D., Herberg, F. W., et al. (2011). Tetramerization dynamics of C-terminal domain underlies isoform-specific cAMP gating in hyperpolarization-activated cyclic nucleotide-gated channels. *J. Biol. Chem.* 286, 44811–44820. doi: 10.1074/jbc.M111.297606

Ludwig, A., Zong, X., Stieber, J., Hullin, R., Hofmann, F., and Biel, M. (1999). Two pacemaker channels from human heart with profoundly different activation kinetics. *EMBO J.* 18, 2323–2329. doi: 10.1093/emboj/18.9.2323

Porro, A., Saponaro, A., Gasparri, F., Bauer, D., Gross, C., Pisoni, M., et al. (2019). The HCN domain couples voltage gating and cAMP response in hyperpolarization-activated cyclic nucleotide-gated channels. *Elife* 8:e49672. doi: 10.7554/eLife.49672

Puljung, M. C., DeBerg, H. A., Zagotta, W. N., and Stoll, S. (2014). Double electron-electron resonance reveals cAMP-induced conformational change in HCN channels. *Proc. Natl. Acad. Sci. U. S. A.* 111, 9816–9821. doi: 10.1073/pnas.1405371111

Puljung, M. C., and Zagotta, W. N. (2013). A secondary structural transition in the C-helix promotes gating of cyclic nucleotide-regulated ion channels. *J. Biol. Chem.* 288, 12944–12956. doi: 10.1074/jbc.M113.464123

Santoro, B., Liu, D. T., Yao, H., Bartsch, D., Kandel, E. R., Siegelbaum, S. A., et al. (1998). Identification of a gene encoding a hyperpolarization-activated pacemaker channel of brain. *Cell* 93, 717–729. doi: 10.1016/S0092-8674(00)81434-8

Santoro, B., Wainger, B. J., and Siegelbaum, S. A. (2004). Regulation of HCN channel surface expression by a novel C-terminal protein-protein interaction. *J. Neurosci.* 24, 10750–10762. doi: 10.1523/JNEUROSCI.3300-04.2004

Saponaro, A., Cantini, F., Porro, A., Bucchi, A., DiFrancesco, D., Maione, V., et al. (2018). A synthetic peptide that prevents cAMP regulation in mammalian hyperpolarization-activated cyclic nucleotide-gated (HCN) channels. *Elife* 7:e35753. doi: 10.7554/eLife.35753

Saponaro, A., Pauleta, S. R., Cantini, F., Matzapetakis, M., Hammann, C., Donadoni, C., et al. (2014). Structural basis for the mutual antagonism of cAMP and TRIP8b in regulating HCN channel function. *Proc. Natl. Acad. Sci. U. S. A.* 111, 14577–14582. doi: 10.1073/pnas.1410389111

Uhlen, M., Oksvold, P., Fagerberg, L., Lundberg, E., Jonasson, K., Forsberg, M., et al. (2010). Towards a knowledge-based human protein atlas. *Nat. Biotechnol.* 28, 1248–1250. doi: 10.1038/nbt1210-1248

Wahl-Schott, C., and Biel, M. (2009). HCN channels: structure, cellular regulation and physiological function. *Cell. Mol. Life Sci.* 66, 470–494. doi: 10.1007/s00018-008-8525-0

Wainger, B. J., DeGennaro, M., Santoro, B., Siegelbaum, S. A., and Tibbs, G. R. (2001). Molecular mechanism of cAMP modulation of HCN pacemaker channels. *Nature* 411, 805–810. doi: 10.1038/35081088

Wang, W., and MacKinnon, R. (2017). Cryo-EM structure of the open human ether-à-go-go-related K(+) channel hERG. *Cell* 169, 422–430.e10. doi: 10.1016/j.cell.2017.03.048

Weissgraeber, S., Saponaro, A., Thiel, G., and Hamacher, K. (2017). A reduced mechanical model for cAMP-modulated gating in HCN channels. *Sci. Rep.* 7:40168. doi: 10.1038/srep40168

Whicher, J. R., and MacKinnon, R. (2016). Structure of the voltage-gated K(+) channel Eag1 reveals an alternative voltage sensing mechanism. *Science* 353, 664–669. doi: 10.1126/science.aaf8070

Wu, J., Sun, L., Chen, X., Du, F., Shi, H., Chen, C., et al. (2013). Cyclic GMP-AMP is an endogenous second messenger in innate immune signaling by cytosolic DNA. *Science* 339, 826–830. doi: 10.1126/science.1229963

Xu, X., Vysotskaya, Z. V., Liu, Q., and Zhou, L. (2010). Structural basis for the cAMP-dependent gating in the human HCN4 channel. *J. Biol. Chem.* 285, 37082–37091. doi: 10.1074/jbc.M110.152033

Zagotta, W. N., Olivier, N. B., Black, K. D., Young, E. C., Olson, R., and Gouaux, E. (2003). Structural basis for modulation and agonist specificity of HCN pacemaker channels. *Nature* 425, 200–205. doi: 10.1038/nature01922

Conflict of Interest: The authors declare that the research was conducted in the absence of any commercial or financial relationships that could be construed as a potential conflict of interest.

frontiers
in Physiology

REVIEW
published: 27 May 2021
doi: 10.3389/fphys.2021.669029

Speeding Up the Heart? Traditional and New Perspectives on HCN4 Function

Konstantin Hennis[1], René D. Rötzer[1], Chiara Piantoni[2], Martin Biel[1,3], Christian Wahl-Schott[2,3]* and Stefanie Fenske[1,3]*

[1] Center for Drug Research, Department of Pharmacy, Ludwig-Maximilians-Universität München, Munich, Germany, [2] Institute for Neurophysiology, Hannover Medical School, Hanover, Germany, [3] German Center for Cardiovascular Research (DZHK), Partner Site Munich Heart Alliance, Munich, Germany

Edited by:
Pietro Mesirca,
INSERM U1191 Institut de Génomique Fonctionnelle (IGF), France

Reviewed by:
Tatiana M. Vinogradova,
National Institute on Aging, National Institutes of Health (NIH), United States
Anna Moroni,
University of Milan, Italy
Wayne Rodney Giles,
University of Calgary, Canada

****Correspondence:***
Stefanie Fenske
stefanie.fenske@cup.uni-muenchen.de
Christian Wahl-Schott
wahl-schott.christian@mh-hannover.de

Specialty section:
This article was submitted to Cardiac Electrophysiology, a section of the journal Frontiers in Physiology

Received: *17 February 2021*
Accepted: *19 April 2021*
Published: *27 May 2021*

Citation:
Hennis K, Rötzer RD, Piantoni C, Biel M, Wahl-Schott C and Fenske S (2021) Speeding Up the Heart? Traditional and New Perspectives on HCN4 Function. Front. Physiol. 12:669029. doi: 10.3389/fphys.2021.669029

The sinoatrial node (SAN) is the primary pacemaker of the heart and is responsible for generating the intrinsic heartbeat. Within the SAN, spontaneously active pacemaker cells initiate the electrical activity that causes the contraction of all cardiomyocytes. The firing rate of pacemaker cells depends on the slow diastolic depolarization (SDD) and determines the intrinsic heart rate (HR). To adapt cardiac output to varying physical demands, HR is regulated by the autonomic nervous system (ANS). The sympathetic and parasympathetic branches of the ANS innervate the SAN and regulate the firing rate of pacemaker cells by accelerating or decelerating SDD–a process well-known as the chronotropic effect. Although this process is of fundamental physiological relevance, it is still incompletely understood how it is mediated at the subcellular level. Over the past 20 years, most of the work to resolve the underlying cellular mechanisms has made use of genetically engineered mouse models. In this review, we focus on the findings from these mouse studies regarding the cellular mechanisms involved in the generation and regulation of the heartbeat, with particular focus on the highly debated role of the hyperpolarization-activated cyclic nucleotide-gated cation channel HCN4 in mediating the chronotropic effect. By focusing on experimental data obtained in mice and humans, but not in other species, we outline how findings obtained in mice relate to human physiology and pathophysiology and provide specific information on how dysfunction or loss of HCN4 channels leads to human SAN disease.

Keywords: sinoatrial node, pacemaking, chronotropic effect, heart rate regulation, autonomic nervous system, HCN4 channel, cyclic nucleotide-gated (HCN) channels, hyperpolarization-activated cation channel

---

Abbreviations: ANS, autonomic nervous system; CaMKII, Ca^{2+}/calmodulin-dependent protein kinase II; cAMP, cyclic adenosine monophosphate; CNBD, cyclic nucleotide-binding domain; ECG, electrocardiogram; FRET, Förster resonance energy transfer; GIRK, G protein-coupled inwardly rectifying potassium channel; HCN channel, hyperpolarization-activated cyclic-nucleotide gated cation channel; HR, heart rate; LCR, local calcium release; NCX, sodium-calcium exchanger; PKA, protein kinase A; RyR, ryanodine receptor; SAN, sinoatrial node; SDD, slow diastolic depolarization; SERCA, sarco-/endoplasmic reticulum Ca^{2+} ATPase; SR, sarcoplasmic reticulum; WT, wild type.

INTRODUCTION

Anatomy and Structure of the Sinoatrial Node and Sinoatrial Node Network

The sinoatrial node (SAN) is a spindle-shaped structure located at the posterior side of the right atrium of the heart (**Figure 1**). It runs from the superior vena cava along the sulcus terminalis toward the inferior vena cava (Liu et al., 2007). The cranial portion is referred to as the sinus node "head," the middle portion as the "body," and the caudal portion as the "tail" (Sanchez-Quintana et al., 2005). In the mouse, the SAN is extremely small with a longitudinal dimension along the crista terminalis of about 500–1000 μm and a width of approximately 150 μm (Verheijck et al., 2001; Liu et al., 2007). In humans, the dimensions of the SAN are naturally larger with a length along the crista terminalis of approximately 14–15 mm, a width of 6–7 mm, and a thickness of about 1 mm (Fedorov et al., 2010).

The SAN network is composed of different cell types comprising spontaneously active pacemaker cells that are interspersed with fibroblasts and embedded within a matrix of fibrous connective tissue, predominately consisting of elastin and collagen (Monfredi et al., 2010; Ho and Sanchez-Quintana, 2016). Pacemaker cells are electrically coupled to each other via gap junctions. In addition, there are electrical connections between pacemaker cells, atrial cardiomyocytes and macrophages residing in the SAN. The pacemaker cells also have synaptic contacts with the nerve endings of the sympathetic nerve and vagus nerve, through which the activity of the cells can be changed and controlled (Verheijck et al., 2002; Camelliti et al., 2004; Pauza et al., 2014; Hulsmans et al., 2017). It is now known that the functional interactions of individual pacemaker cells in this cellular network with each other and with the other cell types in the network are of general importance for electrical synchronization to a common electrical rhythm of the sinus node. The slow diastolic depolarization (SDD) is a unique feature of pacemaker cells that drives generation of spontaneous and rhythmic action potentials (**Figure 2**). After completion of the repolarization, pacemaker cells in the SAN do not remain at a stable resting membrane potential but instead slowly depolarize the membrane toward a threshold potential at which the next

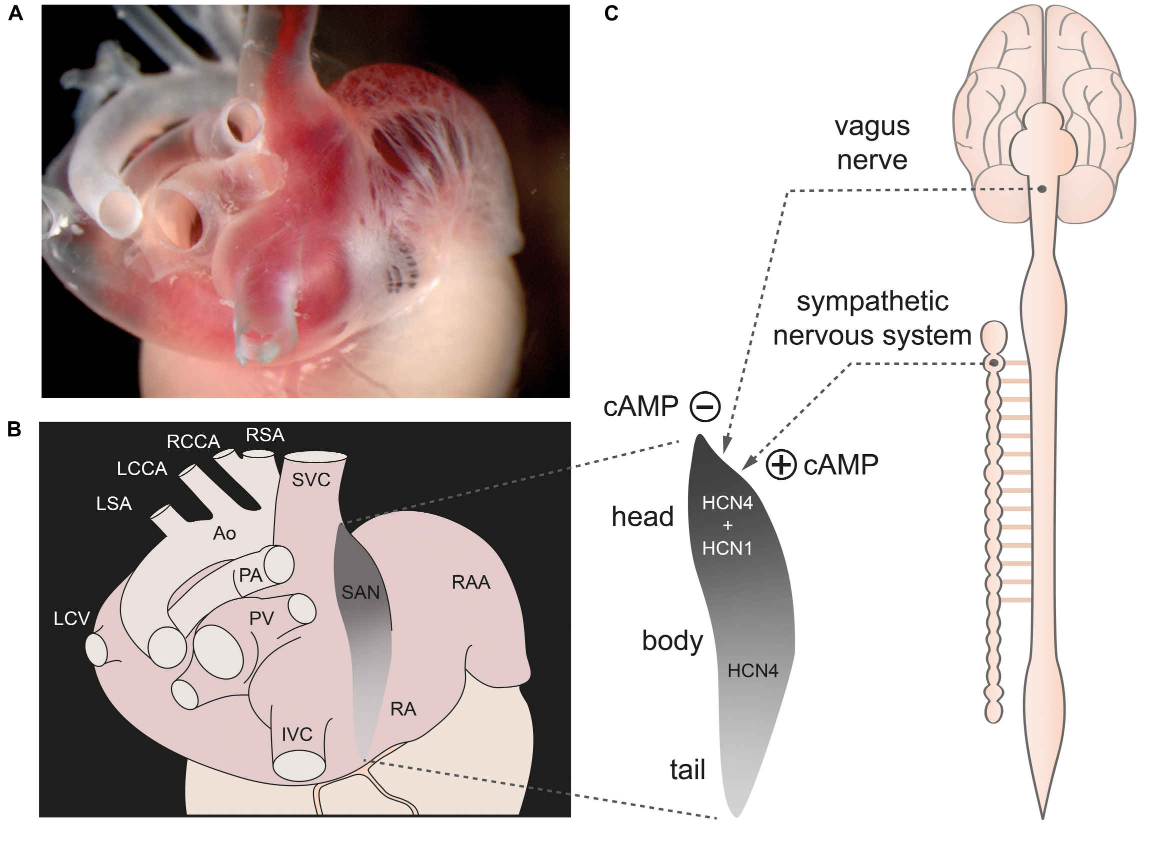

FIGURE 1 | The sinoatrial node. **(A)** Dorsolateral view of the sinoatrial node region of a gelatine-filled mouse heart. **(B)** Schematic illustration of the heart shown in panel **(A)**, depicting the location of the sinoatrial node (SAN) (gray) within the right atrium (RA). **(C, left)** Magnification of the SAN region. The cranial portion is referred to as the sinus node "head," the middle portion as the "body," and the caudal portion as the "tail." HCN1 channels are only expressed in the head region whereas HCN4 channels are expressed throughout the whole SAN. **(C, right)** The SAN is innervated by the sympathetic and parasympathetic nervous system (dashed lines). Activity of both ANS branches tightly controls cAMP concentration in SAN cells. Abbreviations: Ao, Aorta; IVC, inferior vena cava; LCCA, left common carotid artery; LCV, left cranial vein; LSA; left subclavian artery; PA, pulmonary arteries; PV, pulmonary veins; RAA, right atrial appendage; RCCA, right common carotid artery; RSA, right subclavian artery; SVC, superior vena cava. Figure is adapted from Hennis et al., 2021.

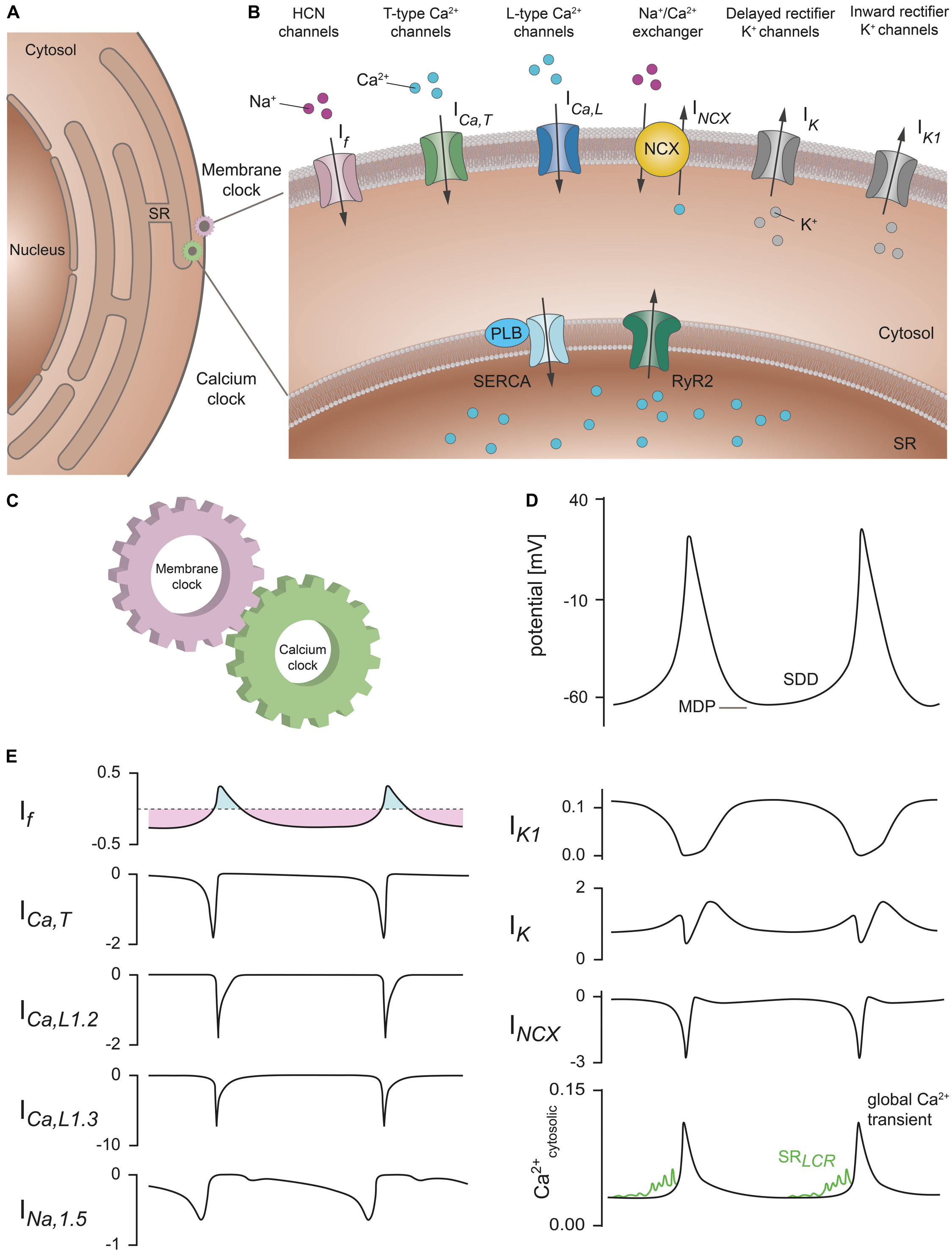

FIGURE 2 | Membrane and calcium clock contribute to the generation of SDD. **(A)** Schematic representation of a SAN cell containing the nucleus, cytosol, and sarcoplasmic reticulum (SR). **(B)** Section of the cell with a magnified view of the plasma membrane and SR membrane. Various proteins that contribute to SDD and are localized in the plasma membrane are collectively described as the *membrane clock*. These include hyperpolarization-activated cyclic-nucleotide gated (HCN) cation channels (pink), T-type Ca^{2+} channels (green), L-type Ca^{2+} channels (blue), Na^+/Ca^{2+} exchanger proteins (NCX, yellow), rapid and slow delayed rectifier K^+ channels (gray), and inward rectifier K^+ channels (gray). The corresponding ionic currents (I) are indicated. Intracellular Ca^{2+} cycling events that contribute to the pacemaker process are summarized as *calcium clock*. Among them are sarco-/endoplasmic reticulum Ca^{2+} ATPases (SERCA) (light blue) associated with the regulatory protein phospholamban (PLB) and ryanodine receptors (RyR2) (dark green) located in the SR membrane. **(C)** Functional interaction of the membrane

(Continued)

FIGURE 2 | Continued
clock and calcium clock is required to ensure regular and rhythmic excitation of the cells. **(D)** Spontaneous SAN action potentials with the characteristic slow diastolic depolarization phase (SDD). The maximum diastolic potential (MDP) is indicated. **(E)** Relative contribution of the ionic currents responsible for SDD and spontaneous action potential firing in mouse SAN cells according to the mathematical model published by Kharche et al. (2011). Current amplitudes are normalized to the cell capacitance (in units of pA/pF). (Upper left panel) I_f manifests as a mainly time-independent, but bidirectionally flowing current. The inward (light purple) and outward component (light blue) are indicated. (Lower right panel) Sarcoplasmic reticulum local calcium releases (SR_{LCR}) (green) that characteristically occur during late SDD have been added to the model data for cytosolic Ca^{2+} transients according to Lakatta et al. (2010). Abbreviations: I_f, hyperpolarization-activated cyclic nucleotide-gated (HCN) current; $I_{Ca,T}$, T-type Ca^{2+} current; $I_{Ca,L1.2}$, L-type Ca^{2+} channel isoform $Ca_v1.2$ current; $I_{Ca,L1.3}$, L-type Ca^{2+} channel isoform $Ca_v1.3$ current; $I_{Na,1.5}$, Na^+ channel isoform $Na_v1.5$ current; I_{K1}, inward rectifying K^+ current; I_K, delayed rectifying K^+ current; I_{NCX}, Na^+/Ca^{2+} exchanger current; $Ca^{2+}{}_{cytosolic}$, cytosolic Ca^{2+} concentration; LCR, local calcium release. For further details see text. Figure is adapted from Lakatta et al. (2010), Kharche et al. (2011), Cingolani et al. (2018).

action potential is generated (**Figure 2D**). The slope of SDD essentially determines the duration of the pacemaker cycle and thus the heart rate (HR).

HCN Channels Are Markers for the SAN

Marker proteins for pacemaker cells within the SAN are hyperpolarization-activated cyclic nucleotide-gated (HCN) channels, of which four isoforms (HCN1-4) exist in mammals. HCN channels belong to the superfamily of voltage-gated cation channels. Four HCN subunits are assembled around a central ion-conducting pore. Each of the subunits consists of six α-helical transmembrane segments (S1-6) and the intracellular N- and C-termini. HCN channels are opened by hyperpolarization and are the molecular determinants of the ionic current I_f in pacemaker cells (Ludwig et al., 1998; Mangoni and Nargeot, 2008; Biel et al., 2009; Li et al., 2015). The channel properties can be modulated by binding of the cyclic nucleotide cyclic adenosine monophosphate (cAMP) to a cyclic nucleotide-binding domain (CNBD) in the C-terminus of the channel (Zagotta et al., 2003), thereby facilitating channel opening. The different isoforms are characterized by some different features, such as kinetics, voltage dependence and cAMP modulation. For example, HCN4 displays the slowest activation and deactivation kinetics and opens at more negative potentials than the other isoforms (Wahl-Schott and Biel, 2009). In contrast, HCN1 displays the fastest kinetics and opens at more positive potentials. Furthermore, HCN4 is the most sensitive to the second messenger cyclic AMP, while the subtype HCN1 is only weakly affected by cAMP (Wahl-Schott and Biel, 2009).

In the mouse, HCN4 is the predominant isoform expressed in pacemaker cells throughout the SAN, whereas HCN1 channels are expressed only in the head region (Fenske et al., 2013). HCN2 channels are expressed only very weakly and are anatomically restricted to the periphery of the SAN (Liu et al., 2007; Herrmann et al., 2011; Fenske et al., 2013).

In humans, HCN4, HCN1, and HCN2 channels are expressed uniformly throughout the SAN without any of the isoforms being restricted to a particular region (Li et al., 2015). Importantly, HCN1 is almost exclusively expressed in the SAN, while HCN2 and HCN4 are present both in SAN pacemaker cells and surrounding right atrial myocytes. Therefore, despite being the predominant isoform also in human SAN, HCN4 cannot be used as a unique marker to identify human SAN pacemaker cells (Chandler et al., 2009; Kalyanasundaram et al., 2019).

Since its first discovery, the I_f current and its role in cardiac pacemaking have been highly debated, leading to controversial views on the importance of I_f in pacemaker activity. On the one side, several groups have questioned a direct involvement of I_f in the generation of action potentials because of its negative threshold of activation and slow time constant (Noma et al., 1980; Yanagihara and Irisawa, 1980), suggesting that the purpose of the current is more likely to maintain a low membrane potential in pacemaker cells. Furthermore, Noma and collaborators showed that Cs^+ reversibly blocks I_f but does not significantly affect the rate of pacemaking (Noma et al., 1983). On the other side, Denyer and Brown (1990) strongly suggested that the I_f current normally makes an important contribution to the depolarization of all SAN pacemaker cells, while the groups of Kreitner (1985); Nikmaram et al. (1997) described a possible different role of I_f in different SAN regions with a greater influence in the periphery than in the center of the SAN.

SPONTANEOUS ACTIVITY OF SINOATRIAL NODE PACEMAKER CELLS

The ability of SAN pacemaker cells to generate SDD and spontaneous action potentials has been attributed to the interplay of two major cellular mechanisms named *membrane clock* and *calcium clock* (**Figures 2A–C**; Lakatta et al., 2010). Insights into these mechanisms are derived from experimental data obtained in mice, which are also the basis for mathematical models of action potential firing in mouse SAN cells (**Figures 2D,E**; Kharche et al., 2011).

The *membrane clock* comprises the activity of all ion channels and transporters that are localized in the cell membrane and contribute to the membrane potential characteristics of SDD (**Figures 2D,E**). Following termination of an action potential, when the membrane potential is most negative (maximum diastolic potential), the early phase of SDD is initiated by the depolarizing inward current I_f that is mediated by constitutively open HCN channels and persists throughout the range of SDD (DiFrancesco et al., 1986; DiFrancesco, 1993; Mangoni and Nargeot, 2008; Biel et al., 2009). The I_f current drives the membrane potential toward the threshold potential at which voltage-gated T-type ($Ca_V3.1$) and L-type ($Ca_V1.3$) Ca^{2+} channels are activated. In addition, voltage-gated sodium channels ($I_{Na,1.5}$, **Figure 2E**) contribute to membrane depolarization during late SDD and the action potential upstroke.

Sodium currents have been shown to be involved in both pacemaking and impulse conduction within the SAN of mice as well as humans, although there seem to be profound species-dependent differences regarding the contribution of different sodium channel isoforms (Lei et al., 2004, 2007; Li et al., 2020). The combination of all inward currents further depolarizes the membrane during late SDD, which leads to an additional opening of voltage-gated L-type $Ca_V1.2$ channels. $I_{Ca,L}$ mainly generates the action potential upstroke and is responsible for coupling excitation to contraction (electromechanical coupling): Ca^{2+} entering cardiomyocytes via $Ca_V1.2$ activates ryanodine receptor 2 (RyR2) which initiates global intracellular Ca^{2+} release from the sarcoplasmic reticulum (SR) (calcium-induced calcium release) and triggers myofibril contraction. Depolarization of the membrane inactivates voltage-gated calcium currents and activates delayed rectifier potassium channels, which conduct the outward currents $I_{K,r}$ and $I_{K,s}$ that are responsible for membrane repolarization and action potential termination (**Figure 2B,E**; Mangoni and Nargeot, 2008; Mesirca et al., 2021). At the beginning of the following pacemaker cycle, the decay of outward potassium currents due to time- and voltage-dependent inactivation of $I_{K,r}$ and $I_{K,s}$ allows the inward pacemaker currents to depolarize the membrane and thus represents another key component of early SDD (Irisawa et al., 1993). Moreover, the inward rectifier potassium current I_{K1} is prominently expressed in murine SAN cells (**Figures 2B,E**), whereas I_{K1} is small or absent in human SAN (Chandler et al., 2009). This might be a reason why membrane potentials in human SAN cells are more positive, which would indirectly support pacemaking (Dobrev, 2009).

In addition to the *membrane clock*, intracellular Ca^{2+} cycling events take place that may significantly contribute to the pacemaker process and are summarized as *calcium clock* (**Figures 2A–C**; Lakatta et al., 2010). During late SDD, periodically occurring, rhythmic local calcium release events (LCRs) from the SR are mediated by spontaneous opening of RyR2 (Vinogradova et al., 2004). The resulting increase in the intracellular Ca^{2+} concentration activates the sodium-calcium exchanger (NCX), a transporter located in the cell membrane that extrudes one Ca^{2+} ion out of the cell in exchange for three Na^+ ions entering the cell when operating in its forward mode (**Figures 2B,E**; Mangoni and Nargeot, 2008). Since in cardiac myocytes the reversal potential of NCX is about −20 mV (Bers et al., 1988; Baartscheer et al., 2011), the outward transport of Ca^{2+} coupled to inward transport of Na^+ (forward mode) is favored in the diastolic range of membrane potentials. This causes a net inward current (I_{NCX}) which further depolarizes the membrane and is responsible for the exponential increase in membrane potential during the late phase of SDD, immediately prior to the action potential upstroke (**Figures 2D,E**; Bogdanov et al., 2006). The extent of LCRs critically depends on SR Ca^{2+} load, which in turn is regulated by the activity of the sarco-/endoplasmic reticulum Ca^{2+} ATPase (SERCA) that refills the SR Ca^{2+} stores after action potential termination (Vinogradova et al., 2010). The Ca^{2+} reuptake into the SR is significantly regulated by phospholamban, a 52-amino acid peptide directly inhibiting SERCA activity (Vinogradova et al., 2018). This *calcium clock* concept was mainly derived from confocal calcium imaging experiments in isolated cells of the SAN. Recently, it was strengthened by combined calcium imaging and electrophysiological experiments in human primary SAN pacemaker cells (Tsutsui et al., 2018). Together, the proper function of both the *membrane clock* and *calcium clock* processes as well as functional coupling of the underlying mechanisms are indispensable for the pacemaker process (Tsutsui et al., 2018). In addition, several proteins associated with the *membrane clock* or *calcium clock* are modulated by activity of the autonomic nervous system (ANS). Therefore, there are many potential candidates that could be involved in or mediate the chronotropic effect and HR regulation.

DOES cAMP-DEPENDENT REGULATION OF HCN4 MEDIATE THE CHRONOTROPIC EFFECT?

The ANS consists of the sympathetic nervous system and parasympathetic nervous system. Both branches of the ANS innervate the SAN (Pauza et al., 2014) and activate intracellular signal transduction cascades in SAN pacemaker cells that regulate HR (**Figure 3**). Following activation of the sympathetic nervous system, the neurotransmitter norepinephrine is released from nerve terminals and activates G_s protein-coupled receptors. The subsequent stimulation of adenylyl cyclases increases the cytoplasmic concentration of the second messenger cAMP (Behar et al., 2016). cAMP binds to a variety of target proteins in the cell, which finally results in acceleration of SDD and consequently the firing rate of pacemaker cells and HR increase (positive chronotropic effect). In contrast, release of acetylcholine from parasympathetic nerve terminals inhibits adenylyl cyclase activity via activation of G_i protein-coupled receptors, followed by a reduction in the cytoplasmic cAMP concentration. In addition, acetylcholine-dependent $G_{\beta\gamma}$ signaling activates G protein-coupled inwardly rectifying potassium channels (GIRK1 and GIRK4) that conduct an outward current ($I_{K,ACh}$) which leads to membrane hyperpolarization. Together, this reduces the maximum diastolic potential and slope of SDD and as a consequence the firing rate and HR decrease (negative chronotropic effect). However, the exact signaling pathway by which alterations in intracellular cAMP mediate an increase or decrease in the firing frequency is still incompletely understood.

HCN4 channels, the main HCN channel isoform in the SAN, display several characteristics which make them an ideal target for HR regulation by the ANS. First, the channels are opened by hyperpolarization and conduct a depolarizing inward current (I_f) throughout the time course of SDD, i.e., at membrane potentials negative to the channel's reversal potential (Mangoni and Nargeot, 2008; Biel et al., 2009). Second, activity of HCN4 is directly regulated by binding of cAMP (DiFrancesco and Tortora, 1991) to a CNBD (Zagotta et al., 2003) in the intracellular C-terminus of the channel (cAMP-dependent regulation, CDR) and is, hence, tightly controlled by the ANS. Consequently, it has been postulated for a long time that CDR of HCN4

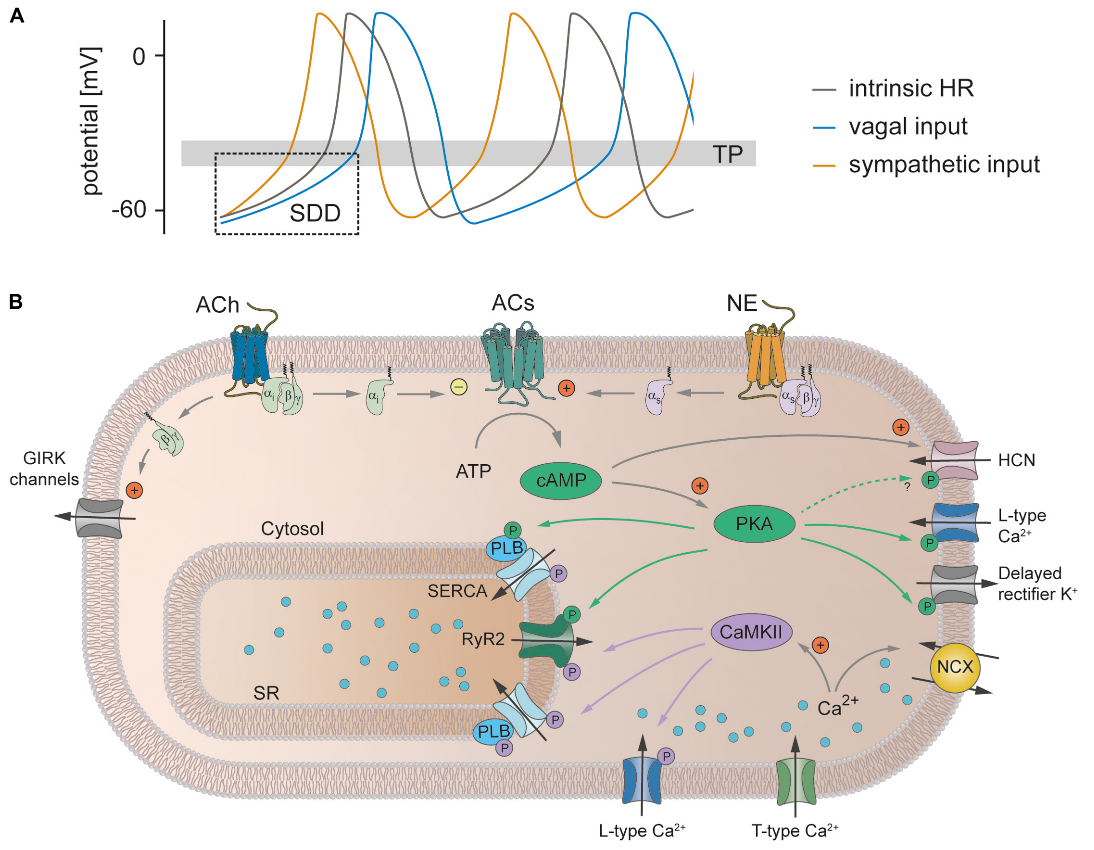

FIGURE 3 | Heart rate regulation by the autonomic nervous system. **(A)** SAN cell action potentials. The intrinsic action potential rate is depicted in gray. Activity of the sympathetic nervous system (orange) leads to a steeper SDD, decreases the time to reach the threshold potential (TP) for the next action potential thereby increasing action potential frequency and consequently also heart rate (positive chronotropic effect). Vagal input flattens SDD, lowers the maximum diastolic potential and thereby increases the time to reach the TP. Action potential frequency and hence HR decrease (negative chronotropic effect). **(B)** Signaling cascades underlying the chronotropic effect. Release of norepinephrine (NE) from sympathetic nerve terminals leads to activation of Gs protein-coupled β-receptors. Subsequent stimulation of adenylyl cyclases (ACs) increases the cytoplasmic concentration of cAMP. cAMP directly facilitates the opening of HCN channels and activates PKA, which in turn phosphorylates various proteins (indicated by green arrows and green circles), thereby increasing their activity. In addition, sympathetic activity increases the intracellular Ca^{2+} concentration, which increases the activity of NCX and CaMKII. This in turn phosphorylates various target proteins (indicated by purple arrows and circles). Taken together, this steepens the SDD, increases the repolarization rate and thereby increases the action potential frequency (see text for further details). In contrast, the release of acetylcholine (ACh) during vagal activity leads to the activation of Gi protein-coupled M-receptors. ACs are inhibited by the Gi protein and thus the opposite effect of sympathetic activation unfolds. In addition, the β/γ-subunit activates GIRK channels that make the maximum diastolic potential more negative. Abbreviations: ACh, acetylcholine; ACs, adenylyl cyclases; ATP, adenosine triphosphate; CaMKII, Ca^{2+}/calmodulin-dependent protein kinase II; GIRK, G protein-coupled inwardly rectifying potassium channels; HCN, hyperpolarization-activated cyclic nucleotide-gated cation channel; NE, norepinephrine; PKA, protein kinase A; PLB, phospholamban; RyR2, ryanodine receptor 2; SERCA, sarco-/endoplasmic reticulum Ca^{2+} ATPase; SR, sarcoplasmic reticulum.

mediates the regulation of HR by the ANS. This hypothesis assumes that upon activation of the sympathetic nervous system, a cAMP-dependent increase in the I_f current is responsible for the acceleration of SDD that increases the firing rate of pacemaker cells and consequently the HR (Brown et al., 1979). On the other hand, a decrease in cAMP caused by activation of the parasympathetic nervous system would reduce HCN4 activity and slow down HR. However, until now this concept could not be validated *in vivo* and therefore remained controversially discussed. Moreover, it has been shown that, especially in the mouse SAN, the gating kinetics of HCN channels are much too slow to open and close the channels during successive action potentials, because the very high sinus rhythm and thus the firing rate of murine SAN pacemaker cells are markedly faster than the channel kinetics (Fenske et al., 2011, 2020; Hennis et al., 2021; Peters et al., 2021). As a result, HCN4-mediated current will manifest mainly as a nearly time-independent but bidirectionally flowing background current during the pacing cycle (**Figure 2E**), strongly arguing against a role for HCN4 in adjusting the slope of SDD and altering HR.

ROLE OF HCN4 IN HR REGULATION: INSIGHTS FROM MOUSE MODELS AND HUMAN PATIENTS

In the past 20 years, different groups have been investigating several mouse models targeting HCN4 (**Table 1**; Bucchi et al.,

TABLE 1 | Phenotypic manifestation of HCN4 mouse models.

References	Model	Tissue specificity	Baseline	Stimulation
HCN4 knockout				
Stieber et al. (2003)	HCN4 knockout	Global	Embryonic lethality	
		Cardiac specific	Embryonic lethality	
			Isolated embryonic cardiomyocytes: immature pacemaker potentials	cAMP: no increase in firing rate
			Isolated embryonic hearts: beating rate ↓	cAMP: no increase in beating rate
Herrmann et al. (2007)	HCN4 knockout	Global inducible, tamoxifen	Isolated SAN cells: large fraction of quiescent cells with hyperpolarized membrane potential	Iso: quiescent SAN cells rescued
			Isolated hearts: sinus pauses	
			In vivo adult mice: sinus pauses, HR unchanged	Iso: preserved max. HR, preserved chronotropic effect Carbachol or CCPA: HR ↓
Hoesl et al. (2008)	HCN4 knockout	Conduction system specific inducible, tamoxifen	Isolated SAN cells: large fraction of quiescent cells with hyperpolarized membrane potential	
			In vivo adult mice: sinus pauses, HR unchanged	Iso: preserved max. HR, preserved chronotropic effect Carbachol or CCPA: HR ↓
Baruscotti et al. (2011)	HCN4 knockout	Cardiac specific inducible, tamoxifen	Isolated SAN cells: firing rate ↓	Iso: max. firing rate ↓, preserved chronotropic action
			In vivo adult mice: bradycardia, AV-blocks, sinus arrest	Iso: max. HR ↓, preserved chronotropic effect
Mesirca et al. (2014)	hHCN4-AYA dominant-negative	Cardiac specific inducible, dox-withdrawal	Isolated SAN cells: firing rate ↓	Iso: max. firing rate ↓, preserved chronotropic action
			In vivo adult mice: bradycardia, sinus pauses, AV blocks, ventricular tachycardia	Iso: max. HR ↓, preserved chronotropic effect
HCN4 overexpression and knockdown				
Kozasa et al. (2018)	HCN4 overexpression	Global HZ without dox	Embryonic lethality (homozygous with and w/o dox)	
			Isolated SAN cells: firing rate unchanged	ACh: beating rate reduction ↓
			In vivo adult mice: HR unchanged, HRV ↓	Iso: preserved max. HR VNS: beating rate reduction ↓
	HCN4 knockdown	Global inducible, HZ with dox	Isolated SAN cells: firing rate ↓	ACh: beating rate reduction ↑
			In vivo adult mice: bradycardia, sinus arrhythmia, HRV ↑	Iso: preserved max. HR VNS: beating rate reduction ↑
cAMP-insensitive HCN4 channels				
Harzheim et al. (2008)	HCN4 R669Q knock-in	Global	Embryonic lethality (homozygous)	
			Isolated embryonic cardiomyocytes: firing rate ↓	
			Isolated embryonic hearts: beating rate ↓	Iso: absence of chronotropic effect
			Isolated adult hearts (HZ): unchanged beating rate	
			In vivo adult mice (HZ): unchanged HR	
Alig et al. (2009)	hHCN4-573X transgenic	Cardiac specific inducible, dox-withdrawal	Isolated SAN cells: quiescent and intermittent beating cells, beating rate ↓	Iso: rescues quiescent and interm beating cells, max. beating rate ↓, preserved chronotropic action
			In vivo adult mice: bradycardia, HR regulation preserved	
Fenske et al. (2020)	HCN4FEA Y527F, R669E, T670A knock-in	Global	Isolated SAN cells: cells alternate between firing and non-firing mode	Iso: time spent in non-firing mode ↓, preserved chronotropic action
			Isolated hearts: beating rate ↓	VNS: sinus pauses
			In vivo adult mice: bradycardia, sinus dysrhythmia, preserved chronotropic effect	

Abbreviations: ACh, acetylcholine; cAMP, cyclic adenosine monophosphate; CCPA, 2-Chloro-N6-cyclopentyladenosine; dox, doxycycline; HR, heart rate; HZ, heterozygous; HRV, heart rate variability; Iso; isoproterenol; max., maximum; SAN, sinoatrial node; VNS, vagus nerve stimulation; ↓ decreased compared to WT condition, ↑ increased compared to WT condition.

2012; Herrmann et al., 2012). The findings of these studies led to conflicting hypotheses about the role of HCN4 CDR in HR regulation. Stieber et al. (2003) created HCN4 knockout mice by generating a non-functional construct lacking the pore, which prevents translation of a functional protein and thereby results in complete absence of HCN4. Loss of HCN4 in these mice led to embryonic lethality due to a strongly diminished I_f during cardiac development. By studying embryonic HCN4$^{-/-}$ hearts and isolated cardiomyocytes the authors found that HR was markedly reduced by about 40% and that HR and action potential firing rate could not be accelerated by cAMP. Surprisingly, a further study revealed that mice carrying only a point mutation in the CNBD of HCN4 also die during embryonic development (Harzheim et al., 2008). A single amino acid exchange (R669Q), which results in abolished CDR but otherwise unaltered channel function, caused embryonic lethality. This indicates that binding of cAMP to HCN4 is a general pre-requisite for the physiological function of the channel. Furthermore, the authors reported significantly reduced HRs and absent responses to catecholaminergic stimulation in embryonic hearts. Taken together, these studies suggest an important role of HCN4 CDR in mediating the chronotropic effect, although insights are restricted to findings from embryonic states in which the SAN and cardiac conduction system are not yet fully developed.

In order to overcome the limitations caused by embryonic lethality, Baruscotti et al. (2011) generated a mouse model in which cardiac-specific knockout of HCN4 was achieved in a temporally controlled manner, thereby enabling investigation of adult mice lacking HCN4 channels in the heart. In these mice, loss of HCN4 led to progressively developing bradycardia and AV block, which finally resulted in sinus arrest and cardiac death. However, HR response to beta-adrenergic stimulation was not affected by the tamoxifen-induced knockout of HCN4. In 2014, the findings were supported by a further study investigating heart-specific silencing of I_f by transgenic expression of a dominant-negative, non-conductive HCN4-channel subunit (hHCN4-AYA) in adult mice (Mesirca et al., 2014). The animals showed significant SAN dysfunction reflected by frequent sinus pauses and reduced HR, while sympathetic regulation of HR was unaltered. Unexpectedly, another study reported that diminished I_f due to a comparable approach of tamoxifen-induced, global knockout of HCN4 gave rise to cardiac arrhythmia in the form of recurrent sinus pauses, whereas the mice showed no signs of bradycardia under baseline conditions (Herrmann et al., 2007). However, HR acceleration induced by exercise or injection of isoproterenol was normal, which demonstrates preserved beta-adrenergic HR regulation also in these animals. Significantly lower HRs were only detected after application of carbachol or CCPA, an A1 adenosine receptor agonist, indicating overshooting parasympathetic responses of the SAN in the absence of HCN4. On the single cell level, knockout of HCN4 resulted in a quiescent phenotype of pacemaker cells characterized by a hyperpolarized maximum diastolic potential that was reversible upon application of isoproterenol. A further study by the same group, in which HCN4 was deleted explicitly in pacemaker cells of the sinoatrial and atrioventricular node, confirmed these results (Hoesl et al., 2008). Kozasa et al. (2018) investigated the contribution of HCN4 to the autonomic regulation of the SAN by transgenic overexpression or knockdown of HCN4 channels in mice. Surprisingly, overexpression of HCN4 did not induce tachycardia, but reduced HR variability, possibly due to excessively attenuated ANS input. This was evident in HR histograms derived from 24 h telemetric electrocardiogram (ECG) recordings. Histograms from HCN4-overexpressing mice were characterized by a unimodal distribution with a single peak in the intermediate frequency range and a symmetrically reduced total HR range. In contrast, HRs in WT histograms were bimodally distributed with a considerably broader frequency range. Furthermore, conditional knockdown of HCN4 induced pronounced bradycardia and gave rise to sinus arrhythmia and enhanced parasympathetic responses to cervical vagus nerve stimulation. Following injection of isoproterenol, bradycardia induced by cervical vagus nerve stimulation was attenuated in HCN4-overexpressing mice. Remarkably, neither overexpression nor knockdown of HCN4 altered the HR response of the SAN to beta-adrenergic stimulation. Taken together, this study suggests that HCN4 is responsible for stabilizing the spontaneous firing of the SAN mainly by attenuating the parasympathetic response. Thus, HCN4 channels protect the SAN network during parasympathetic regulation while the cAMP-dependent activation of HCN4 seems to enhance this protective effect. A few years ago, further insight into CDR of HCN4 was provided by Baruscotti et al. (2017), who identified the first gain-of-function mutation in HCN4 in a patient with inappropriate sinus tachycardia. The R524Q mutation is located in the C-linker, a region that couples cAMP binding to channel activation. Heterologous expression of R524Q mutant HCN4 channels revealed increased sensitivity to cAMP, and rat neonatal cardiomyocytes transfected with the mutant channel construct displayed enhanced spontaneous beating rates. Accordingly, the symptoms in human patients included prolonged periods of sinus tachycardia and frequent palpitations at rest and during exercise. This suggests that overactive CDR of HCN4 may lead to excessive responses of the SAN network to sympathetic stimulation, but unfortunately these observations were not further investigated mechanistically as no mouse model with this particular mutation is available to date.

To study the role of HCN4 CDR more specifically, a transgenic mouse model was generated by Alig et al. (2009). The mice were created with a mutation (573X) that was initially identified in a human patient with sinus node dysfunction (Schulze-Bahr et al., 2003). The structure of HCN4 is highly conserved between different species, including mice and humans, which in principle justifies the use of the mouse as a model organism for the study of HCN4 CDR. The mutation results in a truncation of the C-terminus of HCN4 that includes the CNBD and thereby causes cAMP insensitivity of the channel. Transgenic, cardiac-specific overexpression of the mutant construct (hHCN4-573X) in adult mice suppressed cAMP sensitivity of HCN4 in a dominant-negative manner. The cardiac phenotype of these mice was characterized by a marked reduction in HR at rest and during exercise, while the relative range of HR regulation was unchanged. On the single cell level, the mutation caused a heterogeneous phenotype with isolated pacemaker cells being arrhythmic, alternating between spontaneous firing and subthreshold membrane potential oscillations, or completely lacking electrical automaticity. These observations widely match with the symptoms of the human patient, which include bradycardia and chronotropic incompetence due to idiopathic sinus node dysfunction (Schulze-Bahr et al., 2003). The findings provide important insights into the physiological role of HCN4 in the SAN and further support the theory that HR regulation by the ANS is not mediated by CDR of HCN4. However, the mutation in this model causes a C-terminal truncation involving a total of 630 amino acids. Since the sequence of the CNBD comprises only 119 amino acids (Ludwig et al., 1999), it is obvious that the truncation eliminates not only the CNBD but also many other structural domains, including potential phosphorylation sites and binding domains for various modulators in addition to cAMP. Therefore, the cardiac phenotype of the mice cannot be directly attributed to absent CDR of HCN4.

To particularly investigate the physiological implication of HCN4 CDR, our group created a knock-in mouse model with two amino acid exchanges in the CNBD and one in the C-linker, which result in loss of CDR of the channel while embryonic lethality is prevented (HCN4FEA mouse line) (Fenske et al., 2020). These mice displayed pronounced bradycardia, whereas the entire range of HR regulation was preserved. The findings strongly support the theory that, in contrast to previous assumptions, CDR of HCN4 is not required for the classical chronotropic effect. In addition, several other human HCN4 channelopathies have been reported that result in loss of HCN4 function (Verkerk and Wilders, 2015). The mutations lead to diverse cardiac syndromes, the majority of which include bradycardia. However, in some of these channelopathies HR modulation by beta-adrenergic stimulation is preserved. Unfortunately, a straight forward interpretation of these cardiac phenotypes on HCN4 function is compromised by the fact that all patients identified so far display heterozygous mutations and thus also express an unmodified copy of HCN4.

In summary, evidence is growing that the role of HCN4 in the SAN is different to the originally postulated HR regulation by the ANS and that the classical chronotropic effect is mainly carried out by pacemaker mechanisms other than HCN4. Instead, it seems more likely that HCN4 is involved in setting the intrinsic HR (i.e., HR in the absence of autonomic regulation) and, in particular, in determining the lower part of the HR range. Furthermore, the channel appears to exert a protective effect on the SAN network especially during parasympathetic activity, thereby suppressing bradycardia. In contrast, HR modulation by the ANS is still possible in the absence of HCN4. It remains unclear why a minor part of the mouse studies did not report occurrence of bradycardia after deletion of HCN4 (Herrmann et al., 2007; Hoesl et al., 2008). Possible explanations might include that some HCN4 channels remain present after application of tamoxifen due to insufficient Cre activation. Furthermore, differences in the genetic background of the (sub-) strains of mice used in the studies could also contribute to these functional discrepancies (Bucchi et al., 2012).

NON-FIRING PACEMAKER CELLS IN THE SINOATRIAL NODE

Several mouse studies have shown that inhibition of various components involved in cardiac automaticity gives rise to the presence of quiescent states in isolated pacemaker cells. For example, pacemaker cells isolated from atrial-specific NCX knockout mice are completely quiescent, which leads to intermittent burst pacemaker activity of the SAN network. This is characterized by frequent, short pauses of a few seconds, reminiscent of human sinus node dysfunction and "tachy-brady" syndrome (Torrente et al., 2015). Furthermore, as outlined above, knockout of HCN4 as well as truncation of the HCN4 C-terminus cause quiescent phenotypes of isolated SAN pacemaker cells (Herrmann et al., 2007; Alig et al., 2009). However, it has only recently been discovered that non-firing pacemaker cells are also present and functionally relevant *in vivo* in the intact SAN of WT animals, especially during HR regulation by the ANS (Fenske et al., 2020). These findings reported by our group revealed that HCN4 channels indeed play an important role in HR regulation, but that this is based on a completely different mechanism than originally postulated. In this study, we found that isolated pacemaker cells expressing cAMP-insensitive HCN4FEA channels, but also WT cells, can spontaneously switch into a non-firing mode that is characterized by a hyperpolarized membrane potential and lasts for up to 1 min. Non-firing was more pronounced in HCN4FEA cells but could also reliably be induced in WT cells by application of carbachol or TAT-TRIP8b$_{\text{nano}}$, a synthetic peptide that prevents CDR in HCN channels (Saponaro et al., 2018). Strikingly, *ex vivo* confocal calcium imaging of intact SAN preparations revealed that non-firing pacemaker cells are also present in the intact SAN and significantly modify SAN network activity. This is in line with findings from another recent study which reported presence of markedly heterogeneous calcium signals in adjacent cells within the SAN network (Bychkov et al., 2020), indicating that not all pacemaker cells in the SAN generate full-scale action potentials at a given time.

What is the exact functional relevance of non-firing pacemaker cells in the SAN? From our experimental findings we derived the hypothesis that a tonic electrical interaction via gap junctions takes place between cells in the non-firing mode and neighboring cells in the firing mode. During non-firing, pacemaker cells are significantly more hyperpolarized than firing cells for a period of up to 1 min. Through tonic interaction, these cells act as "brakes" in the network of the SAN and inhibit the activity of neighboring pacemaker cells in the firing mode. This interaction lowers the maximum diastolic potential and slows down the SDD of the firing cells, and thus slows down basal HR. In addition, tonic inhibition seems to increase during vagal activity and decrease during beta-adrenergic stimulation, probably because more cells switch to the non-firing mode or firing mode, respectively. This process is very important for setting the intrinsic HR and stabilizing SAN network activity, but not for changing HR *per se*. However, because the mechanism is dependent on cAMP and CDR of HCN4, it also contributes substantially to the regulation of SAN network activity by the ANS. According to this new hypothesis, CDR of HCN4 determines the number of pacemaker cells in the non-firing mode and is essential to ensure a safe and stable transition between different HRs during sympathetic and/or vagal activity, while it appears to be particularly important in fine-tuning the HR-lowering effect of the parasympathetic nervous system. During high vagal activity, HCN4 effectively counteracts hyperpolarizing changes in the membrane potential. This effect is due to the well-known properties of HCN channels to dampen inhibitory and excitatory stimuli, thereby stabilizing the membrane potential (Robinson and Siegelbaum, 2003; Nolan et al., 2004; Narayanan and Johnston, 2008; Biel et al., 2009; Wahl-Schott et al., 2014). Via CDR of HCN4, the extent of this antagonizing effect, i.e., the gain of negative feedback, can be adjusted according to the situation, which effectively stabilizes HR. Conversely, in the absence of CDR, responses of the SAN to ANS activity are exaggerated which results in extreme HR fluctuations, sinus dysrhythmia and instability of mean HR [for review see also: (Hennis et al., 2021)].

It is known that, in general, inhibitory elements increase the stability of electrically active networks. For example, inhibitory interneurons in the brain provide a mechanism to balance the activity of otherwise unstable neuronal networks (Markram et al., 2004; Sadeh and Clopath, 2021). Our work shows that inhibitory control of excitability is also essential in the SAN to ensure a stable function of the pacemaker process and to protect the SAN network during ANS activity. Taken together, CDR counteracts parasympathetic override, inappropriate HR decreases and the occurrence of bradycardia, which is completely different to the originally postulated HR regulation by the ANS and the classical chronotropic effect (Kozasa et al., 2018; Fenske et al., 2020).

ALTERNATIVE CONCEPTS FOR CLASSICAL CHRONOTROPIC RESPONSE

It is becoming more and more accepted that the role of HCN4 in the SAN is to set the intrinsic HR and stabilize the SAN network during input from the ANS. Therefore, the question arises as to which molecular component(s) of SAN pacemaking actually mediate(s) the chronotropic effect. It is well known that beta-adrenergic signaling in the SAN activates the stimulating adenylyl cyclase–cAMP–protein kinase A (PKA) cascade (**Figure 3B**; Behar et al., 2016). Besides direct effects, e.g., on HCN4, cAMP binds to and activates PKA, which in turn phosphorylates and activates numerous target proteins in the cell, many of them involved in pacemaker activity (MacDonald et al., 2020). These targets include L-type Ca^{2+} channels (van der Heyden et al., 2005), phospholamban (Vinogradova et al., 2010), RyR (Shan et al., 2010), delayed rectifier potassium channels (Lei et al., 2000), Na^{+}/K^{+}-ATPase (Gao et al., 1994), and HCN channels (Liao et al., 2010). In addition, there is also evidence that sympathetic stimulation activates Ca^{2+}/calmodulin-dependent protein kinase II (CaMKII) (Wu et al., 2009; Grimm and Brown, 2010; Wu and Anderson, 2014), which shares a number of downstream targets with PKA, i.e., L-type Ca^{2+} channels (Vinogradova et al., 2000), phospholamban and RyR2 (Li et al., 2016). Accordingly, voltage-gated Ca^{2+} channels are a component of the *membrane clock* different to HCN4 that could possibly mediate the chronotropic effect. While a potential isoproterenol-induced effect on $I_{Ca,T}$ in the SAN is not completely resolved (Hagiwara et al., 1988; Li et al., 2012), $I_{Ca,L}$ is enhanced following PKA-dependent (van der Heyden et al., 2005; Mangoni and Nargeot, 2008) and CaMKII-dependent phosphorylation (Dzhura et al., 2000; Vinogradova et al., 2000; Mangoni and Nargeot, 2008). In line with this, knockout of L-type $Ca_V1.3$ channels in mice slowed the firing rate of isolated SAN pacemaker cells and reduced the slopes of both the early and late phase of SDD (Mangoni et al., 2003; Baudot et al., 2020). However, it has been indicated that $I_{Ca,L}$ augmentation alone is not sufficient to achieve the normal increase in action potential firing rate upon beta-adrenergic stimulation (Vinogradova et al., 2002; Lakatta et al., 2010).

It is therefore possible that modulation of the *calcium clock* could play a key role in HR regulation by the ANS (**Figure 3B**). In this concept, activation of PKA and/or CaMKII would increase LCRs from the SR due to (A) accelerated Ca^{2+} reuptake into the SR following either direct CaMKII-dependent stimulation of SERCA (Narayanan and Xu, 1997) or disinhibition of SERCA by PKA/CaMKII-dependent phosphorylation of phospholamban (Vinogradova et al., 2010; Li et al., 2016) and/or (B) increased release of Ca^{2+} from the SR due to phosphorylation of RyR2 by PKA and/or CaMKII (Vinogradova et al., 2002; Bers, 2006; Shan et al., 2010). This would lead to enhanced LCRs that also occur earlier in the pacemaker cycle. Since LCRs activate NCX by elevating intracellular Ca^{2+}, the consequences would include an increase in depolarizing I_{NCX} current with an onset earlier in SDD, thereby accelerating SDD and reducing the pacemaker cycle length, i.e., increasing the firing frequency (Bogdanov et al., 2006; Maltsev and Lakatta, 2009; Lakatta et al., 2010).

There are several aspects that argue in favor of this theory. First, Förster resonance energy transfer (FRET) experiments showed that PKA activity in isolated SAN pacemaker cells is tightly linked to action potential firing rate in response to either adrenergic or cholinergic stimulation (Behar et al., 2016). In addition, beta-adrenergic stimulation of PKA activity enhances LCRs, whereas inhibition of PKA abolishes LCRs and significantly interferes with cellular automaticity (Vinogradova et al., 2006). Furthermore, it has been shown that also CaMKII activity is essential for stimulating LCRs to cause a physiological HR increase (Wu et al., 2009; Swaminathan et al., 2011). This indicates that (possibly common) downstream targets of PKA and CaMKII, which are attributable to the *calcium clock*, could be responsible for mediating the chronotropic response.

Second, there is evidence that the rate of refilling the SR Ca^{2+} storage during diastole has a direct influence on the chronotropic state of the SAN. It has been demonstrated that direct pharmacological inhibition of SERCA prolongs the spontaneous cycle length of isolated SAN pacemaker cells, whereas changes in PKA/CaMKII-dependent phospholamban phosphorylation, which lead to successive disinhibition of SERCA, are paralleled by a reduction of the LCR period and pacemaker cycle length (Vinogradova et al., 2010; Li et al., 2016).

Third, it has been indicated that modulation of RyR2 function is indispensable for physiological HR adaption (Vinogradova et al., 2006; Eschenhagen, 2010; Shan et al., 2010). Accordingly, when RyRs in SAN pacemaker cells are blocked by ryanodine, or when phosphorylation of RyR2 by PKA is genetically inhibited, augmentation of I_{NCX}, acceleration of SDD and increase in firing frequency following beta-adrenergic stimulation are diminished (Rigg et al., 2000; Lakatta et al., 2010; Shan et al., 2010).

Fourth, there is evidence that the Na^+-Ca^{2+} exchanger (NCX) plays a fundamental role in SAN automaticity and contributes significantly to the positive chronotropic modulation of the SAN (Zhou and Lipsius, 1993; Bogdanov et al., 2001, 2006). NCX knockout mice and numerical I_{NCX} and Ca^{2+} dynamics model simulations revealed decreased or completely abolished responsiveness to isoproterenol stimulation (Bogdanov et al., 2006; Gao et al., 2013; Maltsev et al., 2013), suggesting that I_{NCX} is a crucial contributor to the *fight-or-flight* response in the SAN.

In conclusion, it has become clear that HCN4 is not required for mediating the classical chronotropic effect, but rather contributes to determining the intrinsic HR and protecting the stability of the SAN network during ANS activity. Instead, it is more likely that one or several components of the *calcium clock* are the key mediators of HR regulation by the ANS. However, since there are numerous redundant processes involved in this cascade, with some of them possibly representing backup mechanisms to ensure proper chronotropic responses in the case of dysfunction of other components, the major contributor to HR adaption in the SAN remains yet to be identified.

AUTHOR CONTRIBUTIONS

KH, SF, and CW-S wrote the manuscript. SF and RR composed the figures. RR, CP, and MB revised the manuscript. All authors carefully revised the literature and approved the final version of the manuscript.

FUNDING

Open Access funding enabled and organized by Projekt DEAL. This work was supported by the German Research Foundation [FE 1929/1-1, WA 2597/3-1, BI 484/5-1, and TRR152].

ACKNOWLEDGMENTS

We thank Dainius Pauza and Audrys Pauza for their help in establishing the preparation of gelatine-inflated hearts to visualize the anatomy of the sinoatrial node region.

REFERENCES

Alig, J., Marger, L., Mesirca, P., Ehmke, H., Mangoni, M. E., and Isbrandt, D. (2009). Control of heart rate by cAMP sensitivity of HCN channels. *Proc. Natl. Acad. Sci. U.S.A.* 106, 12189–12194. doi: 10.1073/pnas.0810332106

Baartscheer, A., Schumacher, C. A., Coronel, R., and Fiolet, J. W. (2011). The driving force of the Na/Ca-exchanger during metabolic inhibition. *Front. Physiol.* 2:10. doi: 10.3389/fphys.2011.00010

Baruscotti, M., Bucchi, A., Milanesi, R., Paina, M., Barbuti, A., Gnecchi-Ruscone, T., et al. (2017). A gain-of-function mutation in the cardiac pacemaker HCN4 channel increasing cAMP sensitivity is associated with familial Inappropriate Sinus Tachycardia. *Eur. Heart J.* 38, 280–288. doi: 10.1093/eurheartj/ehv582

Baruscotti, M., Bucchi, A., Viscomi, C., Mandelli, G., Consalez, G., Gnecchi-Rusconi, T., et al. (2011). Deep bradycardia and heart block caused by inducible cardiac-specific knockout of the pacemaker channel gene Hcn4. *Proc. Natl. Acad. Sci. U.S.A.* 108, 1705–1710. doi: 10.1073/pnas.1010122108

Baudot, M., Torre, E., Bidaud, I., Louradour, J., Torrente, A. G., Fossier, L., et al. (2020). Concomitant genetic ablation of L-type Cav1.3 (alpha1D) and T-type Cav3.1 (alpha1G) Ca(2+) channels disrupts heart automaticity. *Sci. Rep.* 10:18906. doi: 10.1038/s41598-020-76049-7

Behar, J., Ganesan, A., Zhang, J., and Yaniv, Y. (2016). The autonomic nervous system regulates the heart rate through cAMP-PKA dependent and independent coupled-clock pacemaker cell mechanisms. *Front. Physiol.* 7:419. doi: 10.3389/fphys.2016.00419

Bers, D. M. (2006). Cardiac ryanodine receptor phosphorylation: target sites and functional consequences. *Biochem. J.* 396:e1. doi: 10.1042/BJ20060377

Bers, D. M., Christensen, D. M., and Nguyen, T. X. (1988). Can Ca entry via Na-Ca exchange directly activate cardiac muscle contraction? *J. Mol. Cell. Cardiol.* 20, 405–414. doi: 10.1016/s0022-2828(88)80132-9

Biel, M., Wahl-Schott, C., Michalakis, S., and Zong, X. (2009). Hyperpolarization-activated cation channels: from genes to function. *Physiol. Rev.* 89, 847–885. doi: 10.1152/physrev.00029.2008

Bogdanov, K. Y., Maltsev, V. A., Vinogradova, T. M., Lyashkov, A. E., Spurgeon, H. A., Stern, M. D., et al. (2006). Membrane potential fluctuations resulting from submembrane Ca2+ releases in rabbit sinoatrial nodal cells impart an exponential phase to the late diastolic depolarization that controls their chronotropic state. *Circ. Res.* 99, 979–987. doi: 10.1161/01.RES.0000247933.66532.0b

Bogdanov, K. Y., Vinogradova, T. M., and Lakatta, E. G. (2001). Sinoatrial nodal cell ryanodine receptor and Na(+)-Ca(2+) exchanger: molecular partners in pacemaker regulation. *Circ. Res.* 88, 1254–1258. doi: 10.1161/hh1201.092095

Brown, H. F., Difrancesco, D., and Noble, S. J. (1979). How does adrenaline accelerate the heart? *Nature* 280, 235–236. doi: 10.1038/280235a0

Bucchi, A., Barbuti, A., Difrancesco, D., and Baruscotti, M. (2012). Funny current and cardiac rhythm: insights from HCN knockout and transgenic mouse models. *Front. Physiol.* 3:240. doi: 10.3389/fphys.2012.00240

Bychkov, R., Juhaszova, M., Tsutsui, K., Coletta, C., Stern, M. D., Maltsev, V. A., et al. (2020). Synchronized cardiac impulses emerge from heterogeneous local calcium signals within and among cells of pacemaker tissue. *JACC Clin. Electrophysiol.* 6, 907–931. doi: 10.1016/j.jacep.2020.06.022

Camelliti, P., Green, C. R., Legrice, I., and Kohl, P. (2004). Fibroblast network in rabbit sinoatrial node: structural and functional identification of homogeneous and heterogeneous cell coupling. *Circ. Res.* 94, 828–835. doi: 10.1161/01.RES.0000122382.19400.14

Chandler, N. J., Greener, I. D., Tellez, J. O., Inada, S., Musa, H., Molenaar, P., et al. (2009). Molecular architecture of the human sinus node: insights into the function of the cardiac pacemaker. *Circulation* 119, 1562–1575. doi: 10.1161/CIRCULATIONAHA.108.804369

Cingolani, E., Goldhaber, J. I., and Marban, E. (2018). Next-generation pacemakers: from small devices to biological pacemakers. *Nat. Rev. Cardiol.* 15, 139–150. doi: 10.1038/nrcardio.2017.165

Denyer, J. C., and Brown, H. F. (1990). Pacemaking in rabbit isolated sino-atrial node cells during Cs+ block of the hyperpolarization-activated current if. *J. Physiol.* 429, 401–409. doi: 10.1113/jphysiol.1990.sp018264

DiFrancesco, D. (1993). Pacemaker mechanisms in cardiac tissue. *Annu. Rev. Physiol.* 55, 455–472. doi: 10.1146/annurev.ph.55.030193.002323

DiFrancesco, D., Ferroni, A., Mazzanti, M., and Tromba, C. (1986). Properties of the hyperpolarizing-activated current (if) in cells isolated from the rabbit sino-atrial node. *J. Physiol.* 377, 61–88. doi: 10.1113/jphysiol.1986.sp016177

DiFrancesco, D., and Tortora, P. (1991). Direct activation of cardiac pacemaker channels by intracellular cyclic AMP. *Nature* 351, 145–147. doi: 10.1038/351145a0

Dobrev, D. (2009). Ion channel portrait of the human sinus node: useful for a better understanding of sinus node function and dysfunction in humans? *Circulation* 119, 1556–1558. doi: 10.1161/CIRCULATIONAHA.108.836866

Dzhura, I., Wu, Y., Colbran, R. J., Balser, J. R., and Anderson, M. E. (2000). Calmodulin kinase determines calcium-dependent facilitation of L-type calcium channels. *Nat. Cell Biol.* 2, 173–177. doi: 10.1038/35004052

Eschenhagen, T. (2010). Is ryanodine receptor phosphorylation key to the fight or flight response and heart failure? *J. Clin. Invest.* 120, 4197–4203. doi: 10.1172/JCI45251

Fedorov, V. V., Glukhov, A. V., Chang, R., Kostecki, G., Aferol, H., Hucker, W. J., et al. (2010). Optical mapping of the isolated coronary-perfused human sinus node. *J. Am. Coll. Cardiol.* 56, 1386–1394. doi: 10.1016/j.jacc.2010.03.098

Fenske, S., Hennis, K., Rotzer, R. D., Brox, V. F., Becirovic, E., Scharr, A., et al. (2020). cAMP-dependent regulation of HCN4 controls the tonic entrainment process in sinoatrial node pacemaker cells. *Nat. Commun.* 11:5555. doi: 10.1038/s41467-020-19304-9

Fenske, S., Krause, S. C., Hassan, S. I., Becirovic, E., Auer, F., Bernard, R., et al. (2013). Sick sinus syndrome in HCN1-deficient mice. *Circulation* 128, 2585–2594. doi: 10.1161/CIRCULATIONAHA.113.003712

Fenske, S., Mader, R., Scharr, A., Paparizos, C., Cao-Ehlker, X., Michalakis, S., et al. (2011). HCN3 contributes to the ventricular action potential waveform in the murine heart. *Circ. Res.* 109, 1015–1023. doi: 10.1161/CIRCRESAHA.111.246173

Gao, J., Cohen, I. S., Mathias, R. T., and Baldo, G. J. (1994). Regulation of the beta-stimulation of the Na(+)-K+ pump current in guinea-pig ventricular myocytes by a cAMP-dependent PKA pathway. *J. Physiol.* 477(Pt 3), 373–380. doi: 10.1113/jphysiol.1994.sp020199

Gao, Z., Rasmussen, T. P., Li, Y., Kutschke, W., Koval, O. M., Wu, Y., et al. (2013). Genetic inhibition of Na+-Ca2+ exchanger current disables fight or flight sinoatrial node activity without affecting resting heart rate. *Circ. Res.* 112, 309–317. doi: 10.1161/CIRCRESAHA.111.300193

Grimm, M., and Brown, J. H. (2010). Beta-adrenergic receptor signaling in the heart: role of CaMKII. *J. Mol. Cell. Cardiol.* 48, 322–330. doi: 10.1016/j.yjmcc.2009.10.016

Hagiwara, N., Irisawa, H., and Kameyama, M. (1988). Contribution of two types of calcium currents to the pacemaker potentials of rabbit sino-atrial node cells. *J. Physiol.* 395, 233–253. doi: 10.1113/jphysiol.1988.sp016916

Harzheim, D., Pfeiffer, K. H., Fabritz, L., Kremmer, E., Buch, T., Waisman, A., et al. (2008). Cardiac pacemaker function of HCN4 channels in mice is confined to embryonic development and requires cyclic AMP. *EMBO J.* 27, 692–703. doi: 10.1038/emboj.2008.3

Hennis, K., Biel, M., Wahl-Schott, C., and Fenske, S. (2021). Beyond pacemaking: HCN channels in sinoatrial node function. *Prog. Biophys. Mol. Biol.* doi: 10.1016/j.pbiomolbio.2021.03.004 [Epub ahead of print].

Herrmann, S., Hofmann, F., Stieber, J., and Ludwig, A. (2012). HCN channels in the heart: lessons from mouse mutants. *Br. J. Pharmacol.* 166, 501–509. doi: 10.1111/j.1476-5381.2011.01798.x

Herrmann, S., Layh, B., and Ludwig, A. (2011). Novel insights into the distribution of cardiac HCN channels: an expression study in the mouse heart. *J. Mol. Cell. Cardiol.* 51, 997–1006. doi: 10.1016/j.yjmcc.2011.09.005

Herrmann, S., Stieber, J., Stockl, G., Hofmann, F., and Ludwig, A. (2007). HCN4 provides a 'depolarization reserve' and is not required for heart rate acceleration in mice. *EMBO J.* 26, 4423–4432. doi: 10.1038/sj.emboj.7601868

Ho, S. Y., and Sanchez-Quintana, D. (2016). Anatomy and pathology of the sinus node. *J. Interv. Card. Electrophysiol.* 46, 3–8. doi: 10.1007/s10840-015-0049-6

Hoesl, E., Stieber, J., Herrmann, S., Feil, S., Tybl, E., Hofmann, F., et al. (2008). Tamoxifen-inducible gene deletion in the cardiac conduction system. *J. Mol. Cell. Cardiol.* 45, 62–69. doi: 10.1016/j.yjmcc.2008.04.008

Hulsmans, M., Clauss, S., Xiao, L., Aguirre, A. D., King, K. R., Hanley, A., et al. (2017). Macrophages facilitate electrical conduction in the heart. *Cell* 169, 510–522.e20. doi: 10.1016/j.cell.2017.03.050

Irisawa, H., Brown, H. F., and Giles, W. (1993). Cardiac pacemaking in the sinoatrial node. *Physiol. Rev.* 73, 197–227. doi: 10.1152/physrev.1993.73.1.197

Kalyanasundaram, A., Li, N., Hansen, B. J., Zhao, J., and Fedorov, V. V. (2019). Canine and human sinoatrial node: differences and similarities in the structure, function, molecular profiles, and arrhythmia. *J. Vet. Cardiol.* 22, 2–19. doi: 10.1016/j.jvc.2018.10.004

Kharche, S., Yu, J., Lei, M., and Zhang, H. (2011). A mathematical model of action potentials of mouse sinoatrial node cells with molecular bases. *Am. J. Physiol. Heart Circ. Physiol.* 301, H945–H963. doi: 10.1152/ajpheart.00143.2010

Kozasa, Y., Nakashima, N., Ito, M., Ishikawa, T., Kimoto, H., Ushijima, K., et al. (2018). HCN4 pacemaker channels attenuate the parasympathetic response and stabilize the spontaneous firing of the sinoatrial node. *J. Physiol.* 596, 809–825. doi: 10.1113/JP275303

Kreitner, D. (1985). Electrophysiological study of the two main pacemaker mechanisms in the rabbit sinus node. *Cardiovasc. Res.* 19, 304–318. doi: 10.1093/cvr/19.5.304

Lakatta, E. G., Maltsev, V. A., and Vinogradova, T. M. (2010). A coupled SYSTEM of intracellular Ca2+ clocks and surface membrane voltage clocks controls the timekeeping mechanism of the heart's pacemaker. *Circ. Res.* 106, 659–673. doi: 10.1161/CIRCRESAHA.109.206078

Lei, M., Brown, H. F., and Terrar, D. A. (2000). Modulation of delayed rectifier potassium current, iK, by isoprenaline in rabbit isolated pacemaker cells. *Exp. Physiol.* 85, 27–35. doi: 10.1111/j.1469-445x.2000.01915.x

Lei, M., Jones, S. A., Liu, J., Lancaster, M. K., Fung, S. S., Dobrzynski, H., et al. (2004). Requirement of neuronal- and cardiac-type sodium channels for murine sinoatrial node pacemaking. *J. Physiol.* 559, 835–848. doi: 10.1113/jphysiol.2004.068643

Lei, M., Zhang, H., Grace, A. A., and Huang, C. L. (2007). SCN5A and sinoatrial node pacemaker function. *Cardiovasc. Res.* 74, 356–365. doi: 10.1016/j.cardiores.2007.01.009

Li, N., Csepe, T. A., Hansen, B. J., Dobrzynski, H., Higgins, R. S., Kilic, A., et al. (2015). Molecular mapping of sinoatrial node HCN channel expression in the human heart. *Circ. Arrhythm. Electrophysiol.* 8, 1219–1227. doi: 10.1161/CIRCEP.115.003070

Li, N., Kalyanasundaram, A., Hansen, B. J., Artiga, E. J., Sharma, R., Abudulwahed, S. H., et al. (2020). Impaired neuronal sodium channels cause intranodal conduction failure and reentrant arrhythmias in human sinoatrial node. *Nat. Commun.* 11:512. doi: 10.1038/s41467-019-14039-8

Li, Y., Sirenko, S., Riordon, D. R., Yang, D., Spurgeon, H., Lakatta, E. G., et al. (2016). CaMKII-dependent phosphorylation regulates basal cardiac pacemaker function via modulation of local Ca2+ releases. *Am. J. Physiol. Heart Circ. Physiol.* 311, H532–H544. doi: 10.1152/ajpheart.00765.2015

Li, Y., Wang, F., Zhang, X., Qi, Z., Tang, M., Szeto, C., et al. (2012). beta-Adrenergic stimulation increases Cav3.1 activity in cardiac myocytes through protein kinase A. *PLoS One* 7:e39965. doi: 10.1371/journal.pone.0039965

Liao, Z., Lockhead, D., Larson, E. D., and Proenza, C. (2010). Phosphorylation and modulation of hyperpolarization-activated HCN4 channels by protein kinase A in the mouse sinoatrial node. *J. Gen. Physiol.* 136, 247–258. doi: 10.1085/jgp.201010488

Liu, J., Dobrzynski, H., Yanni, J., Boyett, M. R., and Lei, M. (2007). Organisation of the mouse sinoatrial node: structure and expression of HCN channels. *Cardiovasc. Res.* 73, 729–738. doi: 10.1016/j.cardiores.2006.11.016

Ludwig, A., Zong, X., Jeglitsch, M., Hofmann, F., and Biel, M. (1998). A family of hyperpolarization-activated mammalian cation channels. *Nature* 393, 587–591. doi: 10.1038/31255

Ludwig, A., Zong, X., Stieber, J., Hullin, R., Hofmann, F., and Biel, M. (1999). Two pacemaker channels from human heart with profoundly different activation kinetics. *EMBO J.* 18, 2323–2329. doi: 10.1093/emboj/18.9.2323

MacDonald, E. A., Rose, R. A., and Quinn, T. A. (2020). Neurohumoral control of sinoatrial node activity and heart rate: insight from experimental models and findings from humans. *Front. Physiol.* 11:170. doi: 10.3389/fphys.2020.00170

Maltsev, A. V., Yaniv, Y., Stern, M. D., Lakatta, E. G., and Maltsev, V. A. (2013). RyR-NCX-SERCA local cross-talk ensures pacemaker cell function at rest and during the fight-or-flight reflex. *Circ. Res.* 113, e94–e100. doi: 10.1161/CIRCRESAHA.113.302465

Maltsev, V. A., and Lakatta, E. G. (2009). Synergism of coupled subsarcolemmal Ca2+ clocks and sarcolemmal voltage clocks confers robust and flexible pacemaker function in a novel pacemaker cell model. *Am. J. Physiol. Heart Circ. Physiol.* 296, H594–H615. doi: 10.1152/ajpheart.01118.2008

Mangoni, M. E., Couette, B., Bourinet, E., Platzer, J., Reimer, D., Striessnig, J., et al. (2003). Functional role of L-type Cav1.3 Ca2+ channels in cardiac pacemaker activity. *Proc. Natl. Acad Sci. U.S.A.* 100, 5543–5548. doi: 10.1073/pnas.0935295100

Mangoni, M. E., and Nargeot, J. (2008). Genesis and regulation of the heart automaticity. *Physiol. Rev.* 88, 919–982. doi: 10.1152/physrev.00018.2007

Markram, H., Toledo-Rodriguez, M., Wang, Y., Gupta, A., Silberberg, G., and Wu, C. (2004). Interneurons of the neocortical inhibitory system. *Nat. Rev. Neurosci.* 5, 793–807. doi: 10.1038/nrn1519

Mesirca, P., Alig, J., Torrente, A. G., Muller, J. C., Marger, L., Rollin, A., et al. (2014). Cardiac arrhythmia induced by genetic silencing of 'funny' (f) channels is rescued by GIRK4 inactivation. *Nat. Commun.* 5:4664. doi: 10.1038/ncomms5664

Mesirca, P., Fedorov, V. V., Hund, T. J., Torrente, A. G., Bidaud, I., Mohler, P. J., et al. (2021). Pharmacologic approach to sinoatrial node dysfunction. *Annu. Rev. Pharmacol. Toxicol.* 61, 757–778. doi: 10.1146/annurev-pharmtox-031120-115815

Monfredi, O., Dobrzynski, H., Mondal, T., Boyett, M. R., and Morris, G. M. (2010). The anatomy and physiology of the sinoatrial node–a contemporary review. *Pacing Clin. Electrophysiol.* 33, 1392–1406. doi: 10.1111/j.1540-8159.2010.02838.x

Narayanan, N., and Xu, A. (1997). Phosphorylation and regulation of the Ca(2+)-pumping ATPase in cardiac sarcoplasmic reticulum by calcium/calmodulin-dependent protein kinase. *Basic Res. Cardiol.* 92(Suppl. 1), 25–35. doi: 10.1007/BF00794065

Narayanan, R., and Johnston, D. (2008). The h channel mediates location dependence and plasticity of intrinsic phase response in rat hippocampal neurons. *J. Neurosci.* 28, 5846–5860. doi: 10.1523/JNEUROSCI.0835-08.2008

Nikmaram, M. R., Boyett, M. R., Kodama, I., Suzuki, R., and Honjo, H. (1997). Variation in effects of Cs+, UL-FS-49, and ZD-7288 within sinoatrial node. *Am. J. Physiol.* 272, H2782–H2792. doi: 10.1152/ajpheart.1997.272.6.H2782

Nolan, M. F., Malleret, G., Dudman, J. T., Buhl, D. L., Santoro, B., Gibbs, E., et al. (2004). A behavioral role for dendritic integration: HCN1 channels constrain spatial memory and plasticity at inputs to distal dendrites of CA1 pyramidal neurons. *Cell* 119, 719–732. doi: 10.1016/j.cell.2004.11.020

Noma, A., Kotake, H., and Irisawa, H. (1980). Slow inward current and its role mediating the chronotropic effect of epinephrine in the rabbit sinoatrial node. *Pflugers Arch.* 388, 1–9. doi: 10.1007/BF00582621

Noma, A., Morad, M., and Irisawa, H. (1983). Does the "pacemaker current" generate the diastolic depolarization in the rabbit SA node cells? *Pflugers Arch.* 397, 190–194. doi: 10.1007/BF00584356

Pauza, D. H., Rysevaite, K., Inokaitis, H., Jokubauskas, M., Pauza, A. G., Brack, K. E., et al. (2014). Innervation of sinoatrial nodal cardiomyocytes in mouse. A combined approach using immunofluorescent and electron microscopy. *J. Mol. Cell. Cardiol.* 75, 188–197. doi: 10.1016/j.yjmcc.2014.07.016

Peters, C. H., Liu, P. W., Morotti, S., Gantz, S. C., Grandi, E., Bean, B. P., et al. (2021). Bi-directional flow of the funny current (If) during the pacemaking cycle in murine sinoatrial node myocytes. *bioRxiv* [Preprint]. doi: 10.1101/2021.03.10.434820

Rigg, L., Heath, B. M., Cui, Y., and Terrar, D. A. (2000). Localisation and functional significance of ryanodine receptors during beta-adrenoceptor stimulation in the guinea-pig sino-atrial node. *Cardiovasc. Res.* 48, 254–264. doi: 10.1016/s0008-6363(00)00153-x

Robinson, R. B., and Siegelbaum, S. A. (2003). Hyperpolarization-activated cation currents: from molecules to physiological function. *Annu. Rev. Physiol.* 65, 453–480. doi: 10.1146/annurev.physiol.65.092101.142734

Sadeh, S., and Clopath, C. (2021). Inhibitory stabilization and cortical computation. *Nat. Rev. Neurosci.* 22, 21–37. doi: 10.1038/s41583-020-00390-z

Sanchez-Quintana, D., Cabrera, J. A., Farre, J., Climent, V., Anderson, R. H., and Ho, S. Y. (2005). Sinus node revisited in the era of electroanatomical mapping and catheter ablation. *Heart* 91, 189–194. doi: 10.1136/hrt.2003.031542

Saponaro, A., Cantini, F., Porro, A., Bucchi, A., Difrancesco, D., Maione, V., et al. (2018). A synthetic peptide that prevents cAMP regulation in mammalian hyperpolarization-activated cyclic nucleotide-gated (HCN) channels. *Elife* 7:e35753. doi: 10.7554/eLife.35753

Schulze-Bahr, E., Neu, A., Friederich, P., Kaupp, U. B., Breithardt, G., Pongs, O., et al. (2003). Pacemaker channel dysfunction in a patient with sinus node disease. *J. Clin. Invest.* 111, 1537–1545. doi: 10.1172/JCI16387

Shan, J., Kushnir, A., Betzenhauser, M. J., Reiken, S., Li, J., Lehnart, S. E., et al. (2010). Phosphorylation of the ryanodine receptor mediates the cardiac fight or flight response in mice. *J. Clin. Invest.* 120, 4388–4398. doi: 10.1172/JCI32726

Stieber, J., Herrmann, S., Feil, S., Loster, J., Feil, R., Biel, M., et al. (2003). The hyperpolarization-activated channel HCN4 is required for the generation of pacemaker action potentials in the embryonic heart. *Proc. Natl. Acad. Sci. U.S.A.* 100, 15235–15240. doi: 10.1073/pnas.2434235100

Swaminathan, P. D., Purohit, A., Soni, S., Voigt, N., Singh, M. V., Glukhov, A. V., et al. (2011). Oxidized CaMKII causes cardiac sinus node dysfunction in mice. *J. Clin. Invest.* 121, 3277–3288. doi: 10.1172/JCI57833

Torrente, A. G., Zhang, R., Zaini, A., Giani, J. F., Kang, J., Lamp, S. T., et al. (2015). Burst pacemaker activity of the sinoatrial node in sodium-calcium exchanger knockout mice. *Proc. Natl. Acad. Sci. U.S.A.* 112, 9769–9774. doi: 10.1073/pnas.1505670112

Tsutsui, K., Monfredi, O. J., Sirenko-Tagirova, S. G., Maltseva, L. A., Bychkov, R., Kim, M. S., et al. (2018). A coupled-clock system drives the automaticity of human sinoatrial nodal pacemaker cells. *Sci. Signal.* 11:eaa7608. doi: 10.1126/scisignal.aap7608

van der Heyden, M. A., Wijnhoven, T. J., and Opthof, T. (2005). Molecular aspects of adrenergic modulation of cardiac L-type Ca2+ channels. *Cardiovasc. Res.* 65, 28–39. doi: 10.1016/j.cardiores.2004.09.028

Verheijck, E. E., Van Kempen, M. J., Veereschild, M., Lurvink, J., Jongsma, H. J., and Bouman, L. N. (2001). Electrophysiological features of the mouse sinoatrial node in relation to connexin distribution. *Cardiovasc. Res.* 52, 40–50. doi: 10.1016/s0008-6363(01)00364-9

Verheijck, E. E., Wilders, R., and Bouman, L. N. (2002). Atrio-sinus interaction demonstrated by blockade of the rapid delayed rectifier current. *Circulation* 105, 880–885. doi: 10.1161/hc0702.104128

Verkerk, A. O., and Wilders, R. (2015). Pacemaker activity of the human sinoatrial node: an update on the effects of mutations in HCN4 on the hyperpolarization-activated current. *Int. J. Mol. Sci.* 16, 3071–3094. doi: 10.3390/ijms16023071

Vinogradova, T. M., Bogdanov, K. Y., and Lakatta, E. G. (2002). beta-Adrenergic stimulation modulates ryanodine receptor Ca(2+) release during diastolic depolarization to accelerate pacemaker activity in rabbit sinoatrial nodal cells. *Circ. Res.* 90, 73–79. doi: 10.1161/hh0102.102271

Vinogradova, T. M., Brochet, D. X., Sirenko, S., Li, Y., Spurgeon, H., and Lakatta, E. G. (2010). Sarcoplasmic reticulum Ca2+ pumping kinetics regulates timing of local Ca2+ releases and spontaneous beating rate of rabbit sinoatrial node pacemaker cells. *Circ. Res.* 107, 767–775. doi: 10.1161/CIRCRESAHA.110.220517

Vinogradova, T. M., Lyashkov, A. E., Zhu, W., Ruknudin, A. M., Sirenko, S., Yang, D., et al. (2006). High basal protein kinase A-dependent phosphorylation drives rhythmic internal Ca2+ store oscillations and spontaneous beating of cardiac pacemaker cells. *Circ. Res.* 98, 505–514. doi: 10.1161/01.RES.0000204575.94040.d1

Vinogradova, T. M., Tagirova Sirenko, S., and Lakatta, E. G. (2018). Unique Ca(2+)-cycling protein abundance and regulation sustains local Ca(2+) releases and spontaneous firing of rabbit sinoatrial node cells. *Int. J. Mol. Sci.* 19:2173. doi: 10.3390/ijms19082173

Vinogradova, T. M., Zhou, Y. Y., Bogdanov, K. Y., Yang, D., Kuschel, M., Cheng, H., et al. (2000). Sinoatrial node pacemaker activity requires Ca(2+)/calmodulin-dependent protein kinase II activation. *Circ. Res.* 87, 760–767. doi: 10.1161/01.res.87.9.760

Vinogradova, T. M., Zhou, Y. Y., Maltsev, V., Lyashkov, A., Stern, M., and Lakatta, E. G. (2004). Rhythmic ryanodine receptor Ca2+ releases during diastolic depolarization of sinoatrial pacemaker cells do not require membrane depolarization. *Circ. Res.* 94, 802–809. doi: 10.1161/01.RES.0000122045.55331.0F

Wahl-Schott, C., and Biel, M. (2009). HCN channels: structure, cellular regulation and physiological function. *Cell. Mol. Life Sci.* 66, 470–494. doi: 10.1007/s00018-008-8525-0

Wahl-Schott, C., Fenske, S., and Biel, M. (2014). HCN channels: new roles in sinoatrial node function. *Curr. Opin. Pharmacol.* 15, 83–90. doi: 10.1016/j.coph.2013.12.005

Wu, Y., and Anderson, M. E. (2014). CaMKII in sinoatrial node physiology and dysfunction. *Front. Pharmacol.* 5:48. doi: 10.3389/fphar.2014.00048

Wu, Y., Gao, Z., Chen, B., Koval, O. M., Singh, M. V., Guan, X., et al. (2009). Calmodulin kinase II is required for fight or flight sinoatrial node physiology. *Proc. Natl. Acad. Sci. U.S.A.* 106, 5972–5977. doi: 10.1073/pnas.0806422106

Yanagihara, K., and Irisawa, H. (1980). Inward current activated during hyperpolarization in the rabbit sinoatrial node cell. *Pflugers Arch.* 385, 11–19. doi: 10.1007/BF00583909

Zagotta, W. N., Olivier, N. B., Black, K. D., Young, E. C., Olson, R., and Gouaux, E. (2003). Structural basis for modulation and agonist specificity of HCN pacemaker channels. *Nature* 425, 200–205. doi: 10.1038/nature01922

Zhou, Z., and Lipsius, S. L. (1993). Na(+)-Ca2+ exchange current in latent pacemaker cells isolated from cat right atrium. *J. Physiol.* 466, 263–285.

Conflict of Interest: The authors declare that the research was conducted in the absence of any commercial or financial relationships that could be construed as a potential conflict of interest.

frontiers
in Physiology

ORIGINAL RESEARCH
published: 09 April 2021
doi: 10.3389/fphys.2021.596832

cAMP-Dependent Signaling Restores AP Firing in Dormant SA Node Cells via Enhancement of Surface Membrane Currents and Calcium Coupling

Kenta Tsutsui[1,2], Maria Cristina Florio[1], Annie Yang[1], Ashley N. Wirth[1], Dongmei Yang[1], Mary S. Kim[1], Bruce D. Ziman[1], Rostislav Bychkov[1], Oliver J. Monfredi[1,3], Victor A. Maltsev[1] and Edward G. Lakatta[1]*

[1] Laboratory of Cardiovascular Science, Biomedical Research Center, Intramural Research Program, National Institute on Aging, NIH, Baltimore, MD, United States, [2] Department of Cardiovascular Medicine, Faculty of Medicine, Saitama Medical University International Medical Center, Saitama, Japan, [3] Heart and Vascular Center, University of Virginia, Charlottesville, VA, United States

OPEN ACCESS

Edited by:
*Alicia D'Souza,
The University of Manchester,
United Kingdom*

Reviewed by:
*Ana M. Gomez,
Institut National de la Santé et de la Recherche Médicale (INSERM),
France
Mark Richard Boyett,
University of Copenhagen, Denmark*

***Correspondence:**
*Edward G. Lakatta
lakattae@grc.nia.nih.gov*

Specialty section:
This article was submitted to Cardiac Electrophysiology, a section of the journal Frontiers in Physiology

Received: *20 August 2020*
Accepted: *09 March 2021*
Published: *09 April 2021*

Citation:
Tsutsui K, Florio CM, Yang A, Wirth AN, Yang D, Kim MS, Ziman BD, Bychkov R, Monfredi OJ, Maltsev VA and Lakatta EG (2021) cAMP-Dependent Signaling Restores AP Firing in Dormant SA Node Cells via Enhancement of Surface Membrane Currents and Calcium Coupling. Front. Physiol. 12:596832. doi: 10.3389/fphys.2021.596832

Action potential (AP) firing rate and rhythm of sinoatrial nodal cells (SANC) are controlled by synergy between intracellular rhythmic local Ca^{2+} releases (LCRs) ("Ca^{2+} clock") and sarcolemmal electrogenic mechanisms ("membrane clock"). However, some SANC do not fire APs (dormant SANC). Prior studies have shown that β-adrenoceptor stimulation can restore AP firing in these cells. Here we tested whether this relates to improvement of synchronization of clock coupling. We characterized membrane potential, ion currents, Ca^{2+} dynamics, and phospholamban (PLB) phosphorylation, regulating Ca^{2+} pump in enzymatically isolated single guinea pig SANC prior to, during, and following β-adrenoceptor stimulation (isoproterenol) or application of cell-permeant cAMP (CPT-cAMP). Phosphorylation of PLB (Serine 16) was quantified in the same cells following Ca^{2+} measurement. In dormant SANC LCRs were small and disorganized at baseline, membrane potential was depolarized (−38 ± 1 mV, n = 46), and I_{CaL}, I_f, and I_K densities were smaller vs SANC firing APs. β-adrenoceptor stimulation or application of CPT-cAMP led to *de novo* spontaneous AP generation in 44 and 46% of dormant SANC, respectively. The initial response was an increase in size, rhythmicity and synchronization of LCRs, paralleled with membrane hyperpolarization and small amplitude APs (rate ∼1 Hz). During the transition to steady-state AP firing, LCR size further increased, while LCR period shortened. LCRs became more synchronized resulting in the growth of an ensemble LCR signal peaked in late diastole, culminating in AP ignition; the rate of diastolic depolarization, AP amplitude, and AP firing rate increased. I_{CaL}, I_K, and I_f amplitudes in dormant SANC increased in response to β-adrenoceptor stimulation. During washout, all changes reversed in order. Total PLB was higher, but the ratio of phosphorylated PLB (Serine 16) to total PLB was lower in dormant SANC. β-adrenoceptor stimulation increased this ratio in AP-firing cells. Thus, transition of dormant SANC to AP firing is linked to the increased functional coupling of membrane and Ca^{2+} clock proteins. The transition occurs via (i) an increase in cAMP-mediated phosphorylation of PLB accelerating Ca^{2+} pumping, (ii) increased spatiotemporal LCR synchronization, yielding a larger diastolic LCR ensemble signal resulting in an earlier increase in diastolic I_{NCX}; and (iii) increased current densities of I_f, I_{CaL}, and I_K.

Keywords: cardiac automaticity, pacemaker mechanism, dormant cells, coupled-oscillator system, sinoatrial nodal cells

INTRODUCTION

Spontaneous electrical impulses that drive the heartbeat originate in the sinoatrial node (SAN). Early studies have discovered that automaticity of SAN pacemaker cells (SANC) is mainly driven by a combination of voltage-dependent activation and inactivation of ion channels (Noble, 1984). Pacemaker mechanism was interpreted initially as the time-dependent decline of K^+ conductance, which unmasked a background inward Na^+ current (Noble, 1962). This was followed by the discovery of the "funny current," (DiFrancesco et al., 1986), i.e., an inward current I_f which is activated by membrane hyperpolarization, and was next believed to be the pacemaker current. Although this interpretation was later revealed to be oversimplified: other sarcolemmal ion channels, in addition to I_f and K^+ channels, were shown to be crucial for SANC automaticity (Wilders et al., 1991; Irisawa et al., 1993; Noma, 1996; Mangoni and Nargeot, 2008; Mesirca et al., 2015). In reality, these ion channels' functions are tightly integrated. For example, openings of low-voltage activated L-type Ca^{2+} channels $Ca_{v1.3}$ (Mangoni and Nargeot, 2008) occur during diastolic depolarization and subsequent activation of $Ca_{v1.2}$ channels generates an action potential (AP) upstroke. The resultant membrane depolarization activates voltage-activated K^+ channels leading to AP repolarization. This chain reaction of ion channel activation has been referred as to "membrane clock" or "M clock" (Lakatta et al., 2010).

Recent progress in understanding mechanisms of SANC automaticity has revealed even more complexity in the pacemaker mechanisms that involve intracellular Ca^{2+} cycling (Rubenstein and Lipsius, 1989; Rigg and Terrar, 1996; Huser et al., 2000; Bogdanov et al., 2001). Spontaneous AP generation is contributed by roughly periodic, spontaneous diastolic local Ca^{2+} releases (LCRs), generated via spontaneous activation of ryanodine receptors (RyR2) of the sarcoplasmic reticulum (SR), i.e., "Ca^{2+} clock" coupled to the M clock. Diastolic activation of the Na^+-Ca^{2+}-exchanger (NCX) by LCRs, results in larger net inward current (I_{NCX}) that, in the context of actiavated I_f and decaying K^+ conductance, accelerates diastolic depolarization toward the AP threshold, review (Lakatta et al., 2010). The most recent conceptualization of these complex interactions among multiple pacemaker mechanisms has been redefined as an ignition process (Lyashkov et al., 2018) that complements aforementioned signaling from LCRs and I_{NCX} to depolarize cell membrane with additional activation of low voltage activated Ca^{2+} channels ($Ca_{v1.3}$ and $Ca_{v3.1}$) generating diastolic Ca^{2+} current (I_{CaL} and I_{CaT}) and attendant Ca^{2+} influx to activate more LCRs via Ca^{2+}-induced-Ca^{2+}-release (Chen et al., 2009; Torrente et al., 2016) that, in turn, generates more I_{NCX} and membrane depolarization, forming an explosive feed-forward loop to insure the attainment of AP threshold and generation of a new pacemaker cycle.

The robust biophysical "engine" of automaticity described above is, in turn, driven and regulated by a biochemical "engine": Ca^{2+}-calmodulin-activated adenylyl cyclase in SANC increases cAMP (Mattick et al., 2007; Younes et al., 2008) that activates I_f [by shifting its activation curve (DiFrancesco and Tortora, 1991)] and cAMP-mediated PKA-dependent and CaMKII-dependent phosphorylation of clocks' proteins resulting in increased Ca^{2+} releases that feed-forward activities of the proteins (L-type Ca^{2+} channels, RyR, PLB (phospholamban), and SERCA). The activation level of the biochemical "engine" under basal conditions is kept near a mid-range by phosphatases and phosphodiesterases (Vinogradova et al., 2008; Lakatta et al., 2010).

Marked variation exists in AP firing intervals among individual isolated SANC (Opthof et al., 1987; Lyashkov et al., 2007; Yaniv et al., 2014). In addition to this cell-to-cell variability of average AP intervals at baseline (inter-SANC variability), beat-to-beat variability in the AP cycle intervals also occurs in each SANC (*intra*-SANC variability) (Wilders and Jongsma, 1993). Emerging evidence suggests that the degree of clock synchronization (i.e., functional coupling between the Ca^{2+}- and M clocks) fluctuates on a beat-to-beat basis, and that this is the basis of intra-SANC variability (Monfredi et al., 2013), with the more effective coupling associated with higher rates and smaller variability (Yaniv et al., 2014). Thus, we define clock coupling as various degrees of synchronization of multiple mechanisms both in the cell membrane and inside the cell with the AP cycle length (CL) and its cycle-to-cycle variability reporting the effectiveness of the coupling.

β-adrenoreceptor (AR) stimulation of isolated SANC enhances clock synchronization and coupling in part via both direct cAMP effects and also by phosphorylation of multiple clock proteins to increase the AP firing rate (Lakatta et al., 2010) and reduce the variability of AP firing intervals both within and among isolated SANC (Yaniv et al., 2016; Kim et al., 2018; Yang et al., 2020), while cholinergic receptor stimulation has the opposite effect (Lyashkov et al., 2009). Thus, flexible degrees of effectiveness of clock coupling deviating from its mid-range in SANC determine both the average AP firing intervals and AP firing interval variability harboring the entire physiologic range of steady-state AP firing.

Recent studies of single isolated SANC revealed that cells that do not fire APs (dormant cells) still generate LCRs, and a large proportion of these cells began to fire spontaneous AP-induced Ca^{2+} transients in response to β-AR stimulation (Kim et al., 2018). However, APs, ion currents, and protein phosphorylation were not measured in that study. Here we propose that (i) dormant cells have insufficient clock coupling to fire APs, i.e., their clock coupling extremely deviates from the aforementioned mid-range regulation, even beyond what cholinergic receptor stimulation does in AP firing cells; (ii) in transition to AP firing β-AR stimulation increases key ion currents, phosphorylation, and membrane potential oscillations, in addition to Ca^{2+} signaling to make clock protein functions more synchronized, i.e., enhancing clock coupling.

MATERIALS AND METHODS

SANC Isolation and Selection

All animal studies followed the Guide for the Care and Use of Laboratory Animals published by the National Institutes of Health (NIH Publication no. 85-23, revised 1996). Experimental protocols were approved by the Animal Care and Use Committee of the National Institutes of Health (protocol #034LCS2016). SANC were isolated from guinea pig (Kim et al., 2018). A beating cell was defined as a SANC with apparent spontaneous contractions. On the other hand, a non-beating cell was a SANC lacking contractions. Only SANC with "spindle" "spider" or "rod" appearance (Denyer and Brown, 1990; Verheijck et al., 1998; Boyett et al., 2000) were chosen. Apparently damaged cells on the basis of structure were excluded from this study.

Electrophysiology

All electrophysiological signals, APs and ion currents, were measured by a patch-clamp amplifier Axopatch 200B, digitized with DIGIDATA 1440A, and recorded (on-line) and analyzed (off-line) with pClamp software version 10 (all from Molecular devices, PA, United States).

A perforated patch clamp method was used to measure membrane potentials (Rigg et al., 2000). Briefly, isolated SANC fixed in a heated bath (36 ± 0.5°C) were superfused at a rate of 1 ml/min with the HEPES-based solution of which temperature was kept at 36 ± 0.5°C and consisted of the following composition: 140 NaCl; 5 KCl; 5 HEPES; 0.33 NaH_2PO_4; 5.5 Glucose; 0.5 $MgCl_2$; 1.8 $CaCl_2$, titrated to pH 7.3 with NaOH. Glass micro-pipettes (resistance 3–5 MΩ) were filled to closely emulate intracellular composition (mM): 143 KCl; 10 NaCl; 2 Mg ATP; 5 HEPES; 10 EGTA; pH 7.3 adjusted with KOH. Amphotericin B (250 μM) was used to measure the membrane potential of SANC. The continuous recording was undertaken before, during and after application of either β-AR agonist isoproterenol (100 nM) or cell-permeable CPT-cAMP (300 μM).

To compare the ion current density profile of dormant SANC with that of firing SANC, a whole-cell patch clamp method was used as previously described (Monfredi et al., 2018). In short, the voltage protocols and pipette solution were designed to measure major ionic currents consecutively in the same cell (always in the following order: I_{CaL}, I_f, and I_K). The patch pipettes had resistances ranging between 2 and 3 MΩ, and were filled with the following solution (in mM): K^+ gluconate 100, MgATP 2.5, Na_2ATP, HEPES 5, KCl 20, EGTA 5, $CaCl_2$ 2; titrated to pH 7.2 with KOH. Tetrodotoxin (10 μM) was added to the bathing solution to block Na^+ currents that could otherwise interfere with I_{CaL} measurements. The cell capacitance and series resistance were electronically compensated by the amplifier to the point just preceding positive feedback oscillations. Seal resistance was measured at the beginning of each experiment and was routinely >10 GΩ. If the seal resistance was lower than this, data from the cell were discarded. Capacitance currents were measured by applying a ramp from −60 to −80 mV. We used a ramp with a 10 V/s rate of change of membrane potential (20 mV over 2 ms) and measured resultant current at the end of the ramp, which we used to assess electrical membrane capacitance. Measured ionic currents were normalized to cell capacitance, to yield a current density in pA/pF (Monfredi et al., 2018).

I_{CaL} Measurements

In line with previous studies (Honjo et al., 1996), depolarizing steps lasting 300 ms from a holding potential of −45 mV were undertaken, with a first level of −40 mV, in 5 mV increments, to a final level of +40 mV. IV curves were plotted in each cell, and the I_{CaL} current density was taken to be the peak current at 0 mV.

I_f Measurements

In line with previous studies (Honjo et al., 1996), hyperpolarizing steps lasting 1000 ms from a holding potential of −35 mV were undertaken, with a first level of −40 mV, in −10 mV increments, to a final level of −120 mV. IV curves were plotted in each cell, and the I_f current density was taken to be the mean current at −110 mV over a 50 ms period beginning 300 ms after the hyperpolarizing pulse. This protocol has a short, 300 ms pulse duration that does not fully saturate I_f activation, and aims to quickly evaluate effective I_f magnitude during diastole, rather than its maximum conductance, activation curve, and kinetics. Thus, the I_f magnitude increase in our experiments with β-AR stimulation reflects both the shift of the activation curve to more positive potentials and acceleration of activation kinetics.

I_K Measurements

In line with previous studies (Lei and Boyett, 1999; Lei et al., 2000), depolarizing steps lasting 1000 ms from a holding potential of −60 mV were undertaken, with a first level of −60 mV, in +10 mV increments, to a final level of 50 mV. IV curves were plotted in each cell, and the I_K current density was taken to be the mean current at +40 mV over a 50 ms period beginning 300 ms after the hyperpolarizing pulse.

2D Intracellular Ca^{2+} Signal Measurement

Cells were loaded with 5 μM Fluo-4AM for 20 min at a room temperature before the measurement. During measurement, cells were continuously perfused with HEPES-based saline at 36 ± 0.1°C by temperature controller TC2BIP 2/3Ch (Cell MicroControls, Norfolk, VA, United States). Ca^{2+} signals were imaged with a 2D camera sCMOS PCO edge 4.2 with a 13.2 mm square sensor of 2048 × 2048 pixels resolution. To resolve LCR dynamics, we acquired images at a rate of 100 frames/second that was possible only using a part of the sensor (1280 × 1280). The recording camera was mounted on Zeiss Axiovert 100 inverted microscopes (Carl Zeiss, Inc., Germany) with a ×63 oil immersion lens and a fluorescence excitation light source CoolLED pE-300-W (CoolLED Ltd., Andover, United Kingdom). Fluo-4 fluorescence excitation (470/40 nm) and emission light collection (525/50 nm) were performed using the Zeiss filter set 38 HE. When the Ca^{2+} signals were simultaneously measured with membrane potential, we programmed the patch clamp amplifier to timely shoot out a short TTL signal, wired to the 2D camera that was also set to start recording upon receiving the synchronizing pulse from patch amplifier. The 2D video-recording of intracellular Ca^{2+} dynamics was exported and analyzed by a computer program that detects LCRs and quantifies the size, period (a time interval between the peak of the prior AP-induced Ca^{2+} transient and the onset of an LCR), and the ensemble area of LCRs (the sum area of all detected LCR signals) as previously described (Maltsev et al., 2017). Our previous studies using confocal microscopy in the line-scanning mode demonstrated that β-AR stimulation indeed increases number of LCRs (Figure 4A in Vinogradova et al., 2002). However, in the present study, using 2D non-confocal imaging, we measured and LCR ensemble area. We report this parameter because the total area of all LCRs is what activates NCX current and contributes to the diastolic depolarization.

Dual Immunostaining of Phospholamban

Immediately after Ca^{2+} measurements up to 1 h, the cells were fixed for 10 min at room temperature with 4% formaldehyde in phosphate buffer (PBS), and the samples were stored in 0.1% Triton/PBS at 4°C for subsequent immunostaining and confocal imaging.

Dishes were washed twice with washing solution (0.1% Triton/PBS) and permeabilized with 0.5% Triton-X-100 in PBS for 15 min at room temperature. The samples were again washed twice then blocked by incubating overnight in a solution containing: 2% BSA/PBS, 5% normal goat serum, 0.02% NaN3, and 0.1% Triton. SANC were then incubated with anti-PLB total antibody (mouse, 1:200, Badrilla, Cat. No. A010-14) and anti-phosphorylated phospholamban (PLB) at Ser 16 antibody (rabbit, 1:200, Badrilla, Cat. No. A010-12AP) at 4°C overnight. Cell were then washed 5–10 min followed by labeling with Atto647 goat anti-mouse IgG (1:1000, Sigma, Cat. No. 50185) and Cy3 goat anti-rabbit IgG secondary antibody (1:1000, Jackson ImmunoResearch, Cat. No. 111-165-144) followed by additional incubation for 1 h at room temperature, and finally washed with plain PBS for 5 min. Plates were mounted with ProLong Gold antifade reagent (Thermo Fisher Scientific, Cat. No. P36934).

Confocal Imaging

Fluorescence was imaged by a Zeiss LSM 880 confocal microscope (Carl Zeiss Inc., Germany) using a 40×/1.3 N.A. oil immersion lens. The Atto647 and Cy3 fluorophores were excited with 633 nm (DPSS 10 mW) and 561 nm (He-Ne 5 mW) lasers, respectively. Individual SANC captured in live Ca^{2+} imaging was identified by its grid location and cell morphology. Images were processed and the intensity of immunofluorescent signal was quantified using ZEN 2.3 lite software (Carl Zeiss Inc., Germany). The fluorescence density of phosphorylated phospholamban was normalized to that of the total phospholamban.

Preparation for Live Intracellular Imaging

Laminin (Sigma-Aldrich, St. Louis, MO, United States; Cat. No. L2020) – coated dishes and physiological bathing solution (Tyrode, or HEPES-based saline) were prepared fresh the day of each experiment. Glass bottom gridded dishes (MatTek Corporation, Ashland, MA, United States; Cat. No. P35G-1.5-14-CGRD) were coated with 40 μg laminin/mL PBS + 1.0% PS in the center of the coverslip and incubated for 1 h before aspirating.

Statistical Analysis

Data are presented as mean ± SEM. $p < 0.05$ was considered statistical significance. Unpaired, two-tailed t-test was used to test differences in current densities and AP characteristics between (i) dormant and firing SANC in baseline and (ii) DMSO- and ivabradine (IVA)-pretreated responder dormant SANC. One-way ANOVA with Tukey's multiple comparisons test was used to compare current densities and AP characteristics. Fisher's exact test was used to compare the response% of cyclopiazonic acid (CPA)- or IVA-treated dormant SANC with that of DMSO-pretreated dormant SANC.

RESULTS

Characterization of Membrane Potential, Ion Current Density Profile, and LCRs in Dormant SANC at Baseline

We surveyed AP firing behavior of 34 freshly isolated single SANC from 10 guinea pig hearts. Of the 34 SANC, 11 manifested spontaneous AP firing at baseline ("firing SANC") while 23 did not ("dormant") (**Figure 1A**). In contrast to SANC that fired spontaneous APs at baseline, in which the maximum diastolic potential (MDP) was −58.5 ± 1.2 mV (**Table 1**), the membrane potential of dormant SANC was more depolarized to −39 ± 0.2 mV (**Figure 1B** top left and **Table 1**).

To determine the baseline functional profile of the M clock in dormant and firing SANC, we sequentially measured current density profiles of the L-type Ca^{2+} current (I_{CaL}), funny current (I_f), and summed repolarizing K^+ currents (I_K) in another 7 firing and 15 dormant cells, as previously described (Monfredi et al., 2018). Current-voltage (I–V) relationships of all three currents (**Figure 1C**) reflect a reduction in all three currents in dormant SANC vs those firing spontaneous APs at baseline (**Figure 1C**, $p < 0.05$ indicated as *).

To characterize baseline intracellular Ca^{2+} signaling of dormant and spontaneously firing SANC, we loaded other 14 firing SANC and 45 dormant SANC with Fluo-4, a fluorescent Ca^{2+} indicator. Consistent with our previous study (Kim et al., 2018), all SANC studied, both dormant and those firing spontaneous APs, exhibited LCRs at baseline (**Figure 1B** top).

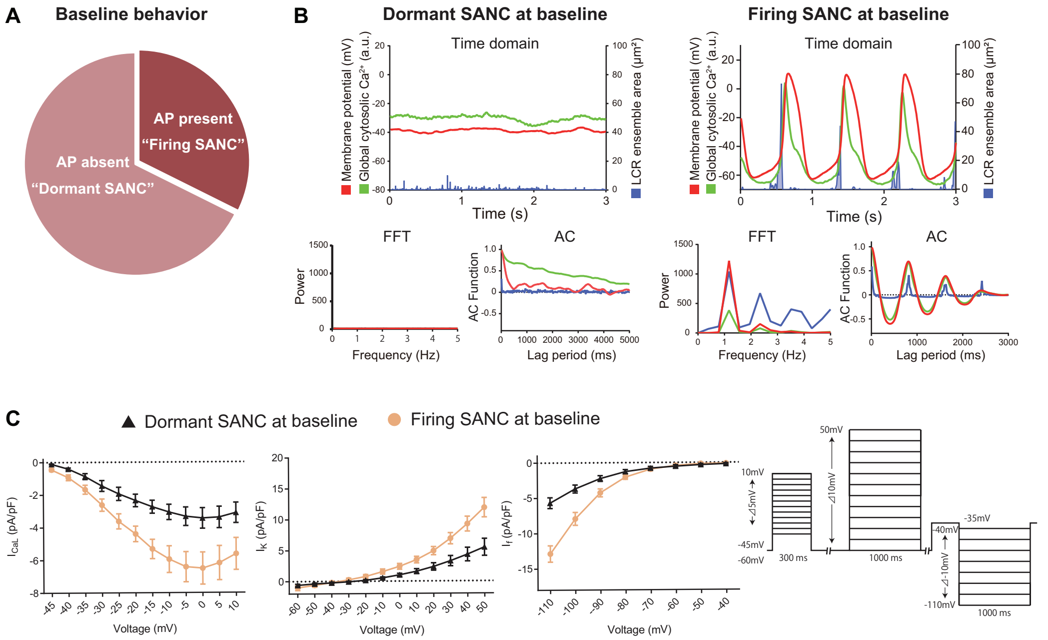

FIGURE 1 | (A) The proportion of baseline behavior of freshly isolated guinea pig SANC we studied total 34 cells. About 1/3 and 2/3 were AP present (firing) and AP absent (dormant), respectively. **(B)** Illustrative examples of simultaneous voltage (magenta), global cytosolic Ca^{2+} (green) and LCR ensemble area (blue) in dormant SANC (left) and firing SANC (right) at baseline. The corresponding frequency analysis by fast Fourier transform (FFT) and autocorrelation analysis (AC) are shown below. **(C)** Major ion current density of voltage-dependent L-type Ca^{2+} channel, voltage-dependent K channel and the funny current in dormant (black) and firing (yellow) SANC at baseline; those of dormant SANC were reduced compared to those of firing SANC. The protocol is shown in the right panel.

TABLE 1 | Membrane potential characteristics of initially firing/dormant guinea pig SANCs.

	AP Firing SANC		Dormant SANC				
			Overall	Responder		Non-responder	
	Baseline	β-AR stimulation	Baseline	Baseline	β-AR stimulation	Baseline	β-AR stimulation
n	7	7	12	6	6	6	6
CL (ms)	892 ± 124	484 ± 39*	NA	NA	509 ± 35*	NA	NA
CV (%)	13.3 ± 3.2	5.5 ± 1.1	NA	NA	5.5 ± 1.2	NA	NA
MDP (mV)	−58.5 ± 1.2	−66.5 ± 0.8*	NA	NA	64.0 ± 1.9*	NA	NA
Dormant potential (mV)	NA	NA	−39.5 ± 0.9#	−40.1 ± 1.5	NA	−39.0 ± 1.2	−39.9 ± 1.3
AP amplitude (mV)	72 ± 3	89 ± 4*	NA	NA	76 ± 6	NA	NA
Ignition period (ms)	802 ± 118	402 ± 46*	NA	NA	426 ± 42*	NA	NA

CL, cycle length; MDP, maximum diastolic potential; NA, not applicable.
**$p < 0.05$ vs those of firing at baseline control by one-way ANOVA with Tukey multiple comparisons.*
#$p < 0.05$ vs MDP of firing at baseline control by unpaired t-test.
CV stands for coefficient of variance (calculated as standard deviation divided by mean).

Fast Fourier transform (FFT) and autocorrelation analyses in SANC firing APs at baseline showed robust rhythmicity in membrane potential, global cytosolic Ca^{2+} signal, and LCR ensemble area, and *vice versa* confirmed a lack of spontaneous rhythmicity of these parameters in dormant SANC (**Figure 1B** bottom). Thus, while firing SANC produce rhythmic ensemble LCR signals synchronized to late diastole, LCRs of dormant SANC were smaller and less organized.

PLB phosphorylation at Serine 16 (**Figure 2A**), a crucial determinant of LCR kinetics and synchronization (Sirenko et al., 2012), was reduced in dormant SANC vs AP firing SANC at baseline ($p < 0.001$, **Figure 2B**).

Dormant SANC Begin to Generate Spontaneous AP in Response to Enhanced cAMP-PKA Signaling

Because enhancing cAMP-PKA signaling by β-AR stimulation increases an AP firing rate in firing SANC via facilitation of the functional coupling between Ca^{2+} and M clocks

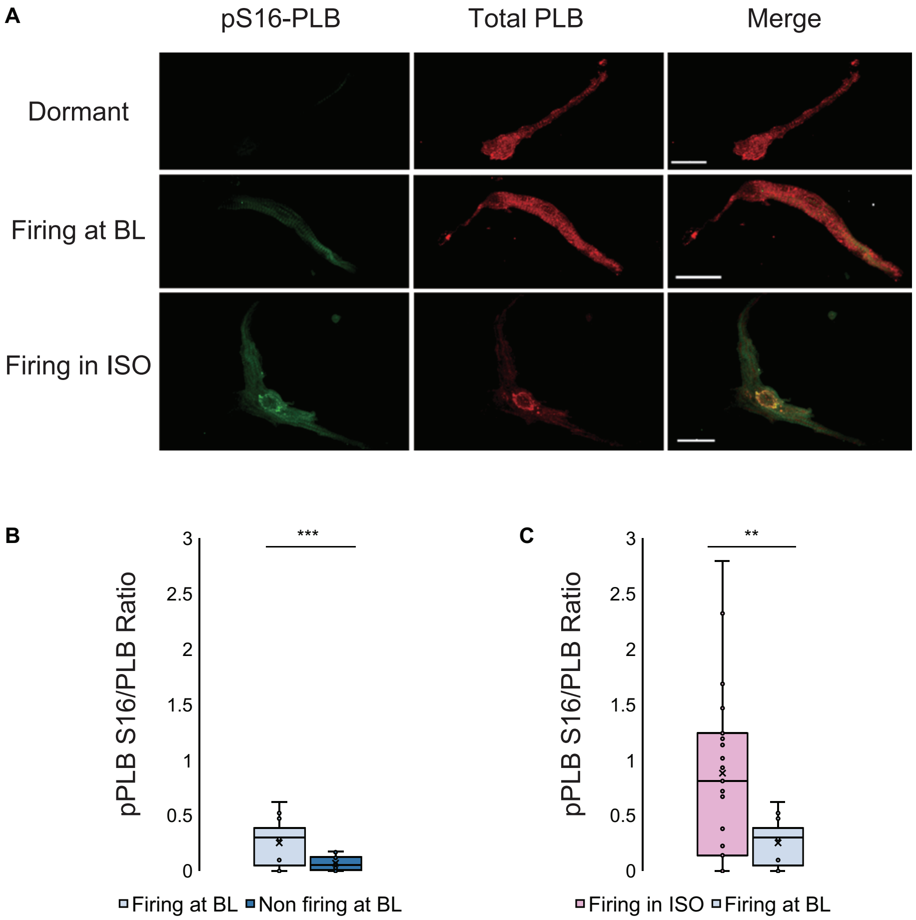

FIGURE 2 | (A) Double immunolabeling of phosphorylated phospholamban (p-PLB) at Serine 16 (green) and total PLB (red) and the merged images of SANC that were dormant at baseline (top), firing at baseline (middle) and dormant at baseline but began firing in response to isoproterenol (bottom). **(B)** The p-PLB/total PLB ratio of SANC firing at baseline ($N = 3/n = 10$) vs dormant at baseline ($N = 3/n = 10$) (At baseline, firing cells have much higher pPLB S16/PLB ratio than non-firing cells)] and **(C)** The p-PLB/total PLB ratio of SANC firing in isoproterenol ($N = 5/n = 15$) vs firing at baseline ($N = 3/n = 10$) (Firing cells in ISO have higher pPLB S16/PLB ratios than firing cells at BL). *t*-test, $^{***}p < 0.001$, $^{**}p < 0.01$.

(Vinogradova et al., 2002; Tsutsui et al., 2018), we sought to discover whether cAMP-PKA signaling was capable of inducing *de novo* spontaneous APs in dormant SANC at baseline.

β-AR stimulation with 100 nM isoproterenol of SANC firing APs at baseline reduced AP CL by 46% (892 ± 39 to 484 ± 39 ms, **Table 1**), accompanied by an increase in AP amplitude and MDP, a reduced ignition period, and a reduction in cycle-to-cycle interval variability (coefficient of variance) (**Figure 3A** and **Table 1**). Among 12 initially dormant SANC, a half (six cells) began to spontaneously fire APs in response to β-AR stimulation ("responder") (**Supplementary Video 1**) while the remainder (six cells) failed to do so ("non-responder") (**Figure 3B** and **Table 1**). Steady state AP firing in the presence of β-AR stimulation in initially dormant SANC at baseline (pre-β-AR stimulation, **Figure 3D**) is comparable to those SANC that fired rhythmic APs at baseline of which rate accelerated in response to β-AR stimulation (**Table 1** "Firing SAN β-AR stimulation" vs "Dormant SANC Responder β-AR stimulation"). Prior to β-AR stimulation, the baseline membrane potential of dormant responders did not differ from those of non-responders (**Table 1**). In some responder dormant SANC, membrane potential spontaneously hyperpolarized prior to the first *de novo* spontaneous AP (**Figure 3C**). The initial APs during β-AR stimulation were small and dysrhythmic. *Bona fide* APs subsequently began to occur within ∼20 s (**Figure 3C**). When β-AR stimulation was disconitinued (isoproterenol washout), the responder cells became dormant again (**Figure 3E**). In non-responder dormant SANC, the membrane potential did not change following β-AR stimulation (**Table 1**).

To determine whether β-AR stimulation-induced activation of dormant SANC was dependent on increased cAMP signaling, we repeated the same experiment with cell-permeable CPT-cAMP. CPT-cAMP recapitulated the β-AR stimulation-induced automaticity in 46% of dormant SANC studied [6/13, $p < 0.05$ vs time control (0/8, 0%), **Figure 3F**], indicating that the resumption of AP firing in initially dormant SANC is indeed caused by cAMP-dependent mechanisms.

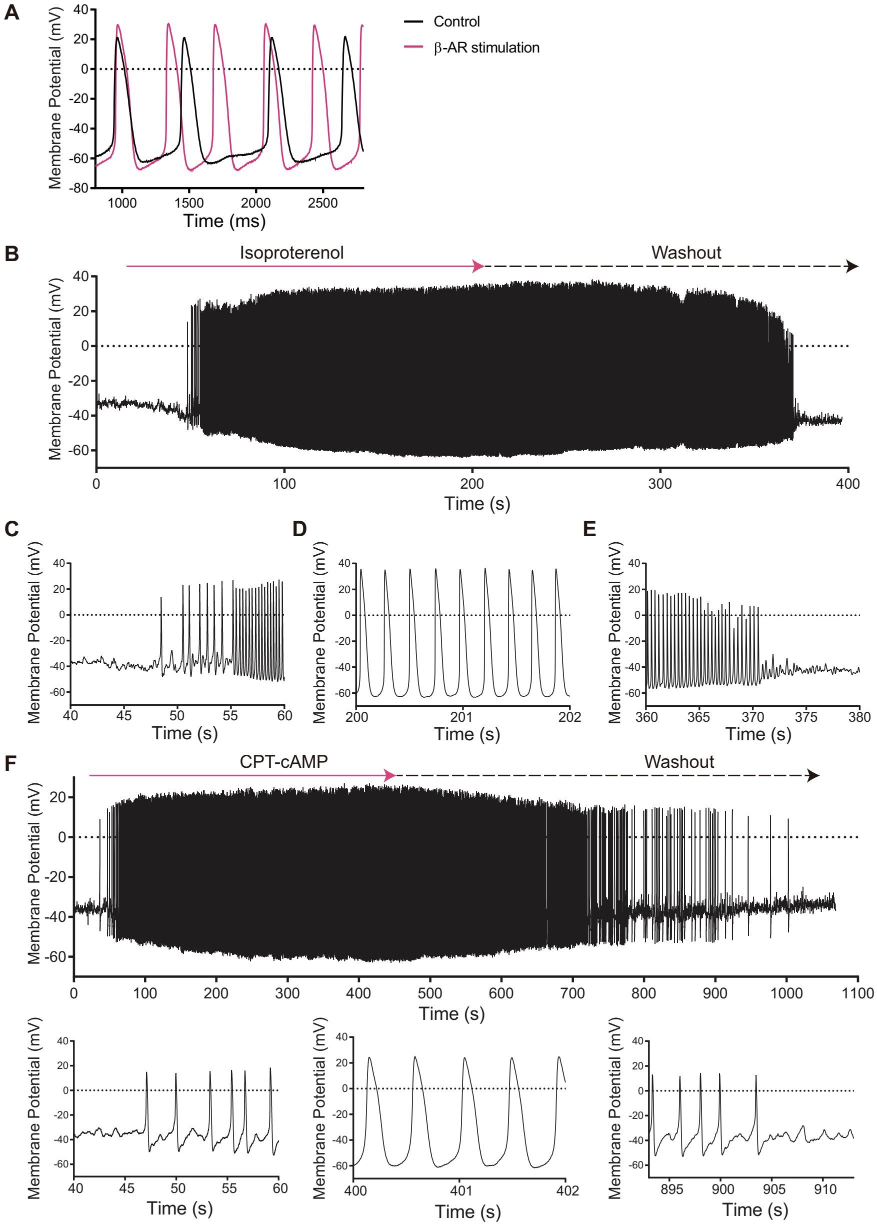

FIGURE 3 | (A) Membrane potential tracings of SANC that fire spontaneous APs at baseline (black) that accelerated in response to isoproterenol (magenta). **(B)** Among 12 initially dormant SANC, 44% fired APs in response to β-AR stimulation ("responder") while 56% failed to do so ("non-responder"). This was significantly different from the corresponding time control group (n = 8) in which spontaneous AP firing did not occur ($p < 0.05$).) When isoproterenol was washed out, the β-AR stimulation-induced APs stopped. Detail of the beginning **(C)**, steady state **(D)** and wash-out **(E)** phases of the β-AR stimulation-induced AP in a SANC that was dormant under initial baseline conditions. **(F)** The cell permeable CPT-cAMP recapitulated the β-AR stimulation-induced APs in other set of SANC that were dormant at baseline. Note the similarity to panel **(B–E)**.

The Full Spectrum of Clock Coupling Emerges in Dormant SANC That Fire APs in Response to an Increase in cAMP

Simultaneous recordings of membrane potential and 2D Ca^{2+} signals (**Figures 4**, **5**) at critical stages of the transition from the dormancy to the spontaneous AP firing state in response to increased intracellular cAMP signaling inform on how enhanced clock coupling evolves in response to cAMP.

At baseline, while the dormant SANC failed to produce rhythmic APs or LCRs (**Figure 4A**), the phase-plane diagram of membrane potential vs global cytosolic Ca^{2+} signal during this sequence depicts stalled fluctuations in membrane potential and whole-cell Ca^{2+} levels in dormant SANC at baseline as a tight cluster of dots (**Figure 4A** right panel). In response to cAMP, the same SANC in **Figure 4A** generated small and slow membrane potential oscillations accompanied by a simultaneous

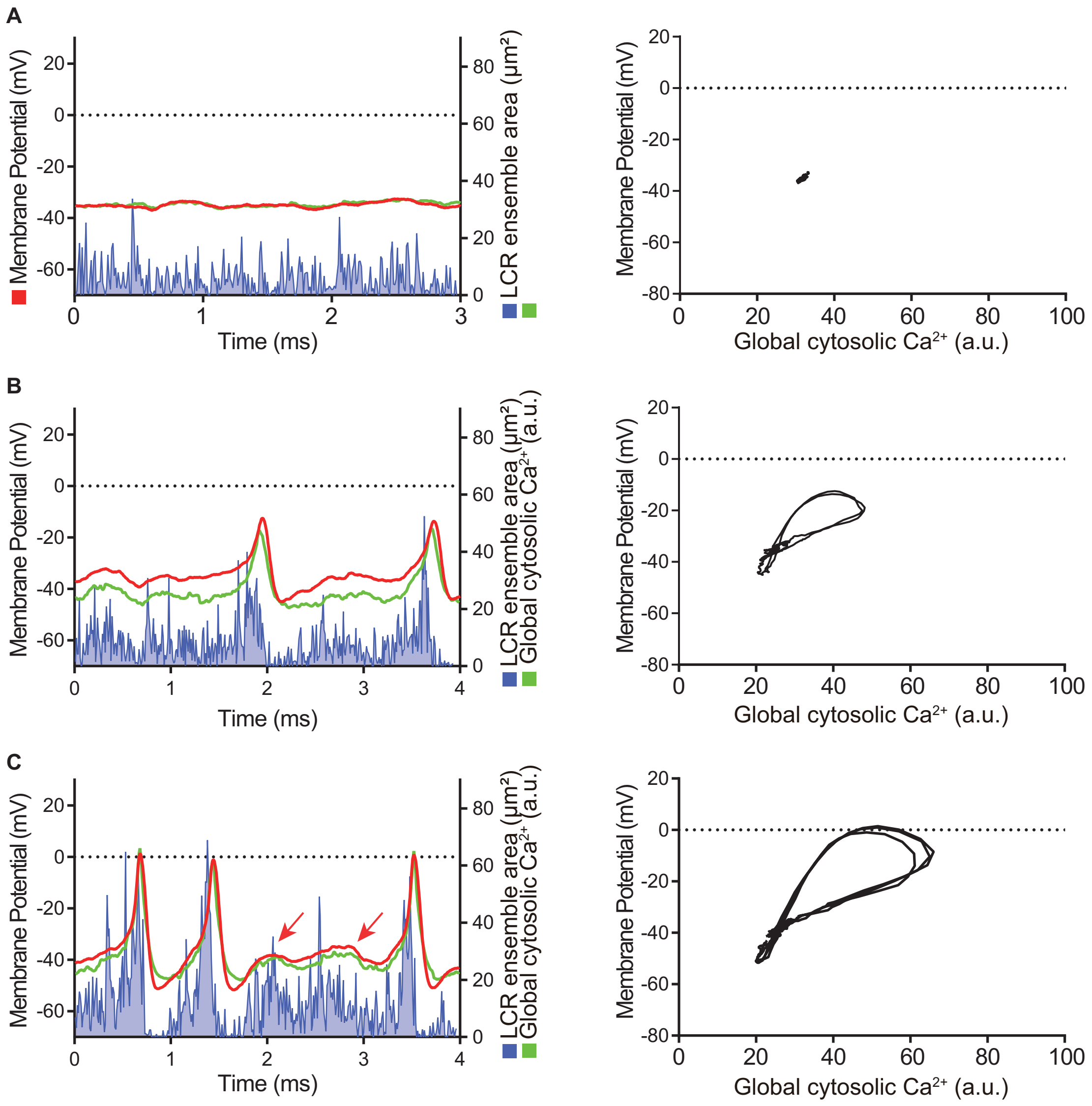

FIGURE 4 | Time domain (left column) and the Ca^{2+}-voltage phase-plot loops (right column) of simultaneous membrane potential (red), whole-cell Ca^{2+} transient (green) and LCR ensemble area (blue) measurement at the early stage of AP induction in response to β-AR stimulation in a SANC that was electrically dormant at baseline. Note that, to minimize both phototoxicity and bleaching of the Ca^{2+} indicator, Ca^{2+} signals could be recorded only for short time window, although membrane potential could be recorded for prolonged periods: **(A)** Baseline, **(B)** The first AP, and **(C)** Following early phase that is characterized by APs with a small amplitude and failed ignition (arrows). Blue line shows the integrated area of detected individual LCRs by our image analysis program (Maltsev et al., 2017).

fluctuation in whole cell Ca^{2+} and LCRs (**Figure 4B** left panel) progressively increasing in amplitude over time (**Figure 4C** left panel). Although some early small-sized APs induced small whole-cell Ca^{2+} transients, at this time the coupling degree of the two clocks failed to produce regular APs (**Figure 4B** left panel). As cAMP exposure time increased, AP failure still occurred but became less frequent. There was an increase in synchronization between membrane potential and Ca^{2+} toward normal size APs and Ca^{2+} transients, shown as an increase in the size of phase-plane loops over time (**Figures 4B** right panel, **4C** right panel). The initiation of self-organizing, mutually interacting electrical and Ca^{2+} oscillations (i.e., Ca^{2+}-induced Ca^{2+} release) and its time-dependent, feed-forward augmentation following exposure to cAMP are clearly observed in another dormant SANC (**Figure 5**). Note two missed ignitions of full APs during **Figure 4C** (the 3rd and 4th "would-be firing," indicated by arrows) were preceded by failed escalation of LCR ensemble area (**Figure 4C** left panel). This finding suggests the possibility that the cAMP-induced APs in initially dormant SANC are caused by emergent coupling between the M- and Ca^{2+}-clocks. Later stages of β-AR activation demonstrated further extended the progressive increase in the "loop" size depicted in the Vm-Ca^{2+} phase plane diagram with associated shortening of CL of cAMP-induced APs, respectively (**Figures 5B–D**). During steady-state

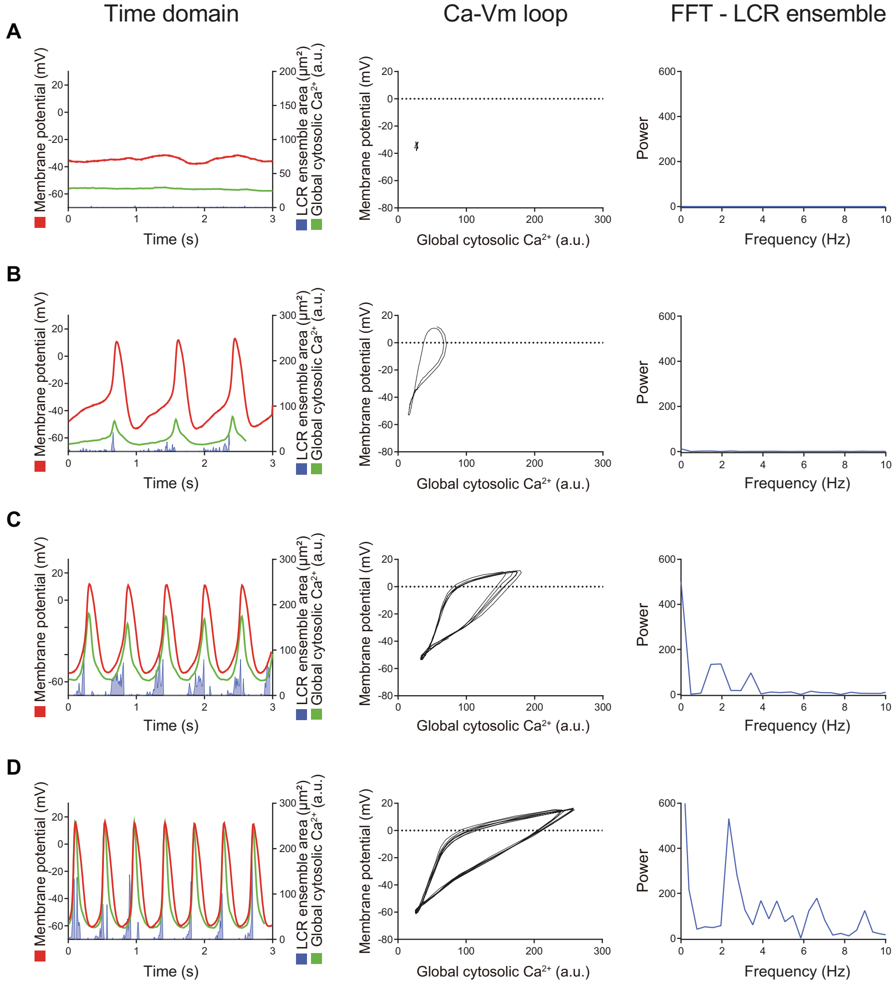

FIGURE 5 | Later stage of the β-AR stimulation-induced AP induction sequence observed in other SANC that was initially dormant at baseline. Time domain (left), Ca^{2+}-Vm loop (middle) and FFT of Ca^{2+} signals (right) during the baseline dormancy **(A)**, early stages **(B,C)**, and steady state **(D)** of AP induction in response to β-AR stimulation. The Ca-Vm loop evolves to expand as the AP cycle length shortens in response to β-AR stimulation.

AP firing (**Figure 5D**), the LCR ensemble is synchronized in time such that the LCR ensemble forms sharp spikes immediately before the AP upstroke. The failed interactions between Ca^{2+}- and M-clocks that resulted in failed AP ignition observed during earlier stages (**Figures 4B,C**) no longer occur, and there is regular AP firing.

The isoproterenol/CPT-AMP wash-out phase is characterized by symmetrical reversal of the steps described above. The SANC gradually fail to maintain regular AP firing and eventually membrane potential depolarized to ~ -40 mV, accompanied by loss of fluctuations in membrane potential. At the same time, the whole-cell Ca^{2+} signal become markedly reduced and LCRs became small and disorganized (**Figure 6**). Note the similarities in the transition during "wash-out" and "wash-in" shown in **Figure 6** and **Figure 4**, respectively.

In summary, these results indicate that clock functions and coupling are severely reduced in dormant SANC at baseline; an increase in clock coupling underlies the cAMP-dependent AP rescue in dormant SANC.

Voltage-Dependent Ca^{2+}, K, and Funny Current Increases in Dormant SANC in Response to Increasing cAMP

To determine the effects of increased cAMP on M clock functions in responder and non-responder SANC, we evaluated ion current densities with voltage-clamp experiments following brief Ca^{2+} imaging (i.e., total light exposure limited to <4 s) to classify the baseline AP firing behavior of each cell and its response to isoproterenol. I_{CaL}, I_K and I_f densities of initially dormant SANC increased in response to isoproterenol in both responder and non-responder cells (**Figure 7**), suggesting that the enhanced cAMP signaling augments M-clock function in all of these dormant cells. However, there was no difference in current density after exposure to isoproterenol between responders and

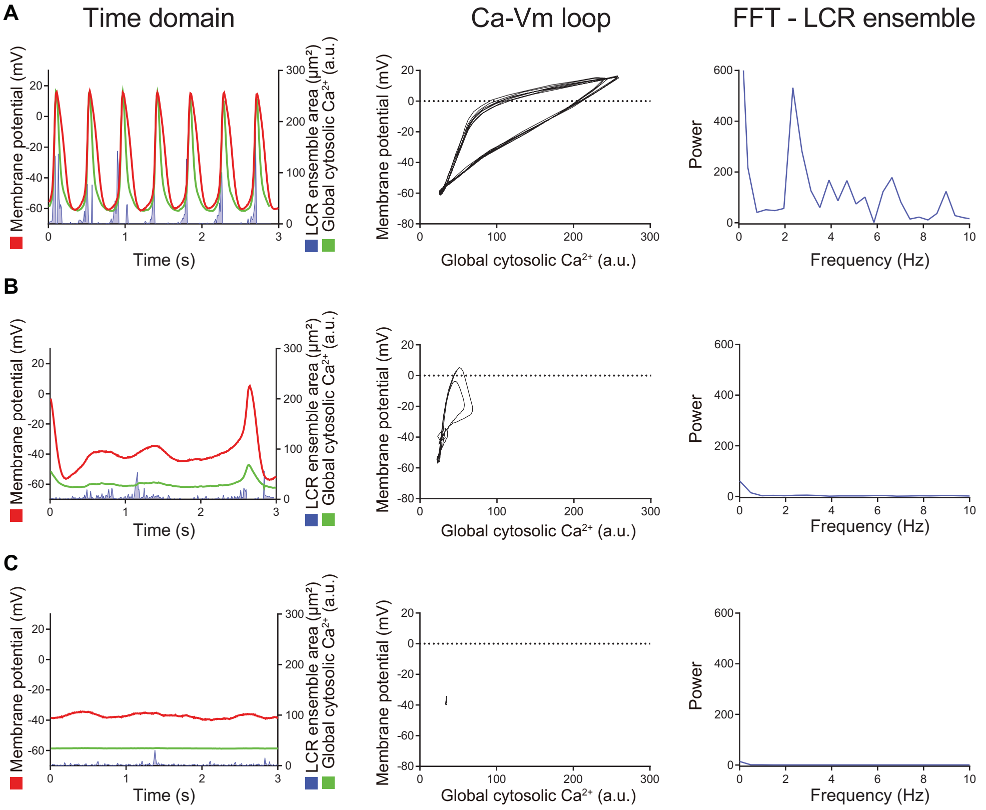

FIGURE 6 | When the intracellular cAMP level decreased by washout of BARs/CPT-cAMP, the changes described in **Figure 5** reversed in order. Compared to the steady state AP firing (panel **A**), the AP cycle length is prolonged and LCR ensemble is decreased (panel **B**), suggesting the disengagement of M- and Ca^{2+}-clocks. Shortly after cAMP washout (the panel **B**), spontaneous AP firing ceased, and the cell returned to dormant state again (panel **C**) in which the membrane potential drifted around –40 mV, ensemble LCR signal area decreased, and the voltage-Ca^{2+} loop demonstrated only very small fluctuation around one point, rather than crating a loop.

non-responders, indicating that the augmentation in M-clock functions did not predict whether dormant SANC at baseline would respond to cAMP.

Selective Independent Blocks of the Ca^{2+} and M Clock Reveal Their Different Roles in Restoration of β-AR-Induced APs in the Dormant SANC

To further characterize the relative roles of M- and Ca^{2+} clock mechanisms in the resumption of automaticity in initially dormant SANC, we compared the inducibility of APs in dormant cells by isoproterenol in the presence of CPA (0.5 µM, n = 11) or IVA (3 µM, n = 7) to that of control group (n = 10).

CPA, a Ca^{2+} clock inhibitor that acts by inhibiting SR Ca^{2+} ATPase (SERCA) and reducing Ca^{2+} pumping into the SR (Vinogradova et al., 2010), reversibly suppressed the LCR ensemble signal in dormant SANC, confirming that LCR signals observed in dormant SANC are SERCA-dependent. In response to subsequent β-AR stimulation, only 9% (1/11) of initially dormant SANC superfused with 0.5 µM CPA generated spontaneous APs, a significantly lower % than the control group ($p < 0.05$), in which 60% (6/10) of initially dormant SANC began to fire spontaneous APs in response to β-AR stimulation (**Table 2**). The baseline membrane potential of non-responder dormant SANC bathed in CPA was around −40 mV with CPA addition, and remained unchanged during and following wash out of β-AR stimulation (**Table 2**).

In contrast to CPA, pretreatment of SANC with selective if inhibitor ivabradine (3 µM) did not affect the success rate (71%, 5/7) of β-AR stimulation in restoring AP firing in initially dormant SANC (**Table 2**). However, the AP CL of the IVA-pretreated responder dormant SANC during β-AR stimulation was longer and more irregular, and the MDP was relatively depolarized, compared to control responder SANC during β-AR stimulation (**Table 2**).

Phosphorylation of Coupled-Clock Proteins Is Reduced in Dormant SANC at Baseline

PLB is a protein that modulates the Ca^{2+} kinetics of the Ca^{2+} clock by controlling the pumping function of SERCA. We analyzed the phosphorylation of PLB

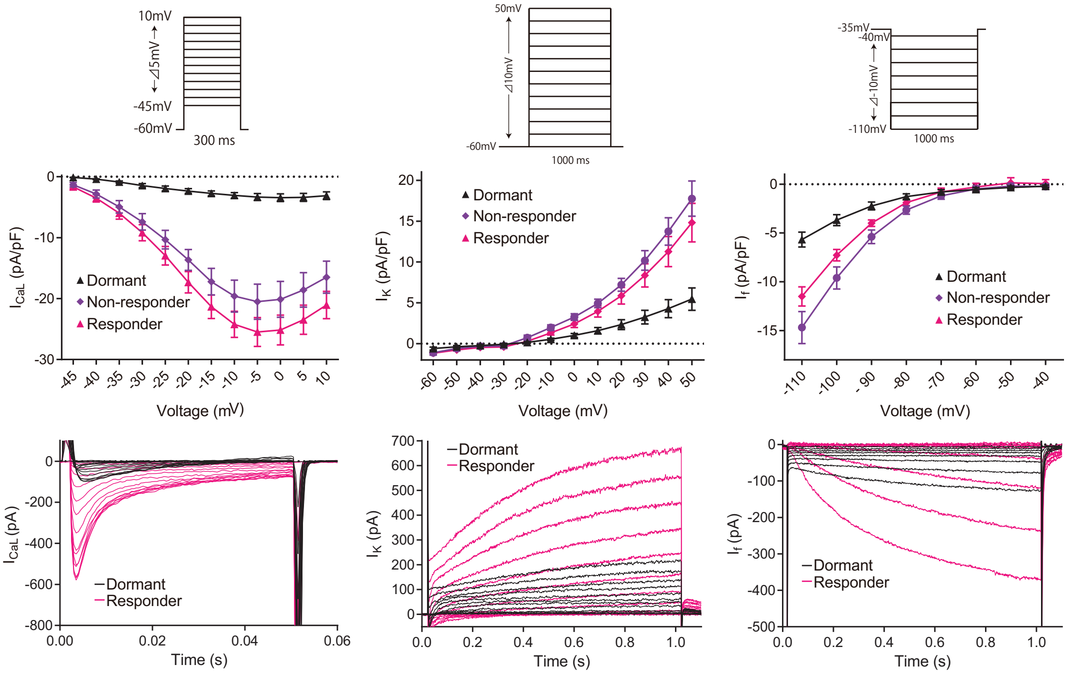

FIGURE 7 | Consecutive in-series measurements of ion-current density of L-type Ca^{2+} current (left panels), K^+ current (center panels) and funny current (right panels) from SANC revealed that M-clock function of both responder (magenta) and non-responder (purple) dormant SANC increases in response to β-AR stimulation by 100 nM isoproterenol. The voltage protocol (same to those for **Figure 1C**) is shown above the I-V curves. Example I–V curves for each current is shown in the bottom raw. The data shown are from different cells, one without isoproterenol (black) and one with isoproterenol (magenta).

TABLE 2 | Membrane potential characteristics of CPA/IVA-pretreated dormant SANC in response to β-AR stimulation.

	DMSO-pretreated *n* = 10	**CPA-pretreated *n* = 11**	**IVA-pretreated *n* = 7**
Responded cells (%)	6 (60%)	1 (9%*)	5 (71%)
Responder			
Dormant potential - Baseline (mV)	−41.3 ± 3.0	−46.2	−38.3 ± 0.8
CL (ms)	435 ± 17	579	1118 ± 340**
CV (%)	0.42 ± 0.04	2.3	3.3 ± 1.0**
MDP (mV)	−65.2 ± 2.0	−65.0	−58.5 ± 2.8**
AP amplitude (mV)	73.5 ± 5.2	70.6	64.7 ± 5.7
Non-responder			
Dormant potential - Baseline (mV)	−44.6 ± 0.6	−42.1 ± 3.2	−37. 9 ± 4.8
- Isoproterenol (mV)	−42.5 ± 1.5	−42.7 ± 3.8	−42.3 ± 2.1

**p* < 0.05 vs DMSO-pretreated group by Fisher's exact test.*
***p* < 0.05 vs DMSO-pretreated group by unpaired t-test.*
CV stands for coefficient of variance (calculated as standard deviation divided by mean).

in Serine 16, the main site of this regulatory protein activated by cAMP-dependent protein kinase A (PKA), by quantifying the phosphorylated-PLB/total PLB ratio (pS16-PLB/total PLB ratio) following measurement of Ca^{2+} dynamics in the same cells. Phosphorylation of Serine 16 was reduced by sixfold in dormant SANC vs SANC firing spontaneous APs in normal Tyrode under basal conditions (**Figures 2A,B**).

Next, we perfused a subgroup of SANC that fired APs at baseline with normal Tyrode supplemented with isoproterenol 100 nM to prove that an increase in AP firing rate in these cells is associated with an increased PLB phosphorylation. In response to β-AR stimulation, the phosphorylation level of PLB increased by an additional twofold over that level observed in the group of cells firing APs at baseline in the absence of β-AR stimulation (**Figures 2A,C**). We further found that in SANC we studied, including those dormant cells (firing rate = 0) the phosphorylated-PLB/total PLB ratios were positively correlated with AP firing rate (**Figure 8A**). In contrast, when the absolute number of PLB counts were plotted as a function of AP firing rate, they were negatively correlated (**Figure 8B**).

DISCUSSION

Our results demonstrate that augmentation of cAMP-PKA signaling is capable of restoring automaticity of dormant cells via enhancements in both M- and Ca^{2+}-clock functions and their coupling, including increases of key membrane currents I_{CaL}, I_K, and I_f and phosphorylation of the critical SR Ca^{2+}-clock protein PLB.

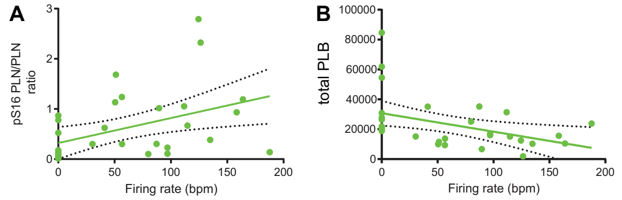

FIGURE 8 | The phosphorylated-PLB/total PLB ratios **(A)** and total PLB number **(B)** and were positively ($n = 32$; $Y = 0.004982X + 0.3209$, $p = 0.0132$; $R^2 = 0.188$) and negatively ($n = 31$; $Y = -123.5X + 30723$, $p = 0.0161$; $R^2 = 0.184$) associated with the firing rate, respectively.

Role of cAMP Signaling in SANC Normal Baseline Automaticity

As we noted in Introduction, in SANC that fire APs at baseline, intracellular cAMP-PKA signaling is maintained around the middle of the range of possible signaling levels (Vinogradova et al., 2008), resulting in a moderate degree of coupling between the roughly periodic SR Ca^{2+}-clock and the membrane-bound, voltage- and time-dependent M clock that together drive basal AP firing. Thus, direct cAMP binding to certain clock proteins (e.g. HCN4) and cAMP mediated-PKA dependent phosphorylation of other clock proteins (e.g., PLB, RyR, K^+-channels and L-type Ca^{2+} channels) is what drives basal SANC automaticity (Lakatta et al., 2010). This spontaneous AP firing and its attendant Ca^{2+} influx maintain cytoplasmic Ca^{2+} at a level sufficient to support the mean basal AP firing rate and rhythm by further activating Ca^{2+}-dependent adenylyl cyclases and CaMKII. To keep this robust feed-forward system of phosphorylation in check, counteracting phosphodiesterases and protein phosphatases are simultaneously activated (Lakatta et al., 2010; Tsutsui et al., 2016). A change in the degree of the clock coupling is accompanied by changes in the mean AP firing CL.

Enhanced Clock Coupling in Response to Increased cAMP-PKA Signaling

To accelerate the mean AP firing rate of single isolated SANC, β-AR stimulation-induced augmentation of clock phosphorylation more precisely synchronizes LCRs in time. This augmented LCR ensemble Ca^{2+} signal produces a larger I_{NCX} earlier in diastole (Maltsev and Lakatta, 2010). This earlier and greater Ca^{2+}-NCX interaction during β-AR stimulation occurs in addition to the cAMP-mediated augmentation of I_f and I_K (Lyashkov et al., 2018). The β-AR-induced reduction in mean AP CL is accompanied by a reduction in the inter-AP interval variability (Monfredi et al., 2014).

Dormant SANC, studied here, however, appear to lack of effective functions M- and Ca^{2+}- clocks and their interactions, producing only small and disorganized LCRs (**Figures 1C**, **5A**). M-clock functions in dormant SANC (I_{CaL}, I_f, and I_K densities and I–V relations) were reduced compared to those in SANC firing spontaneous AP at baseline (**Figure 1B**). We interpret our results to indicate that in the dormant state, a disorganized Ca^{2+} signal occurs but no APs are ignited, this is a manifestation of suppression of both the M- and Ca^{2+}- clocks. The relatively depolarized dormant SANC membrane potential of ∼-38 mV will undoubtedly hamper the voltage-dependent mechanisms within the M-clock.

We observed that, as in SANC spontaneously firing APs at baseline (reviewed in Irisawa et al., 1993 and Mangoni and Nargeot, 2008), β-AR stimulation in initially dormant SANC increased three major inward and outward currents: Ca^{2+}, K^+ and funny currents. Therefore, it is reasonable to speculate that an increase in the M-clock function mediated by augmentation of the currents that we studied plays an important role in the "responder" SANC. With β-AR stimulation, density of ion currents increases, and this is the result of a phosphorylation of the channel and/or a direct action of cAMP on the channel. However, a striking finding was that the effect of β-AR stimulation on these current densities did not differ between responders and non-responders (**Figure 7**), that is this effect of β-AR stimulation is not *sufficient* to guarantee transformation from dormancy to automaticity. This indicates that there must be additional mechanisms for automaticity to be restored in dormant SANC.

Ca^{2+} clock function is also decreased in dormant SANC, compared to SANC that fire spontaneous APs at baseline. The absence of regular AP-induced Ca^{2+} influx leads to a reduction in cytosolic Ca^{2+} level (**Figure 6**) (van Borren et al., 2010; Tsutsui et al., 2018). This low Ca^{2+} level impacts on the robustness and rhythmicity of spontaneous LCRs. However, baseline SR Ca^{2+} content of guinea pig dormant SANC is comparable to that of firing SANC, and it neither increases nor decreases in response to β-AR stimulation (Kim et al., 2018). The absence of increased SR Ca^{2+} load in a dormant SANC demonstrated in our previous research (Kim et al., 2018) may be due to low cytosolic Ca^{2+} that diminishes the ratio of phosphorylated PLB to total PLB suppressing SR function (Sirenko et al., 2012). The metabolic state including ATP production would also be expected to be reduced during dormancy compared to SANC that fire APs at baseline. In such a state, Ca^{2+}-activated AC and PKA and CaMKII signaling, which is activated in basal state in SANC, would also be expected to decrease, causing a reduction in a wide range of cell functions within SANC. Important evidence for critical roles of basal PKA and CaMKII signaling in transition to dormancy is that a selective inhibition of either signaling (AIP or PKI) results in cell dormancy with a membrane potential fluctuating at about −30 mV (Vinogradova et al., 2000; Vinogradova et al., 2006). The important role of Ca^{2+} for cell dormancy have been demonstrated in previous studies: Inhibition of Ca^{2+} cycling (ryanodine or BAPTA-AM) facilitated vagally induced SANC dormancy (van Borren et al., 2010). Our previous studies in permeabilized SANC showed that LCRs are not random openings of RyR2 and they are different from Ca^{2+} sparks in ventricular myocytes (Sirenko et al., 2012). LCRs exhibit a larger spatial extent (appeared manly as locally propagating wavelets) and their occurrence is partially periodic, i.e., LCRs behave as a set of heterogeneous local Ca^{2+} oscillators (or "clocks"), whereas occurrence of Ca^{2+} sparks in ventricular myocytes at the basal state is mainly random. In this regard, it has previously been reported that freshly isolated single permeabilized ventricular myocytes, exhibiting random Ca^{2+} sparks in a physiologic free (Ca^{2+}), manifest a marked self-organization of Ca^{2+} sparks to produce robust and roughly periodic LCRs when PLB becomes highly phosphorylated during PDE and phosphatase inhibition (Sirenko et al., 2012, 2014).

Our results demonstrate that, as a marker of SANC-wide coupled clock protein PLB, phosphorylation at Serine 16 is markedly reduced in dormant SANC vs those that fire spontaneous APs in dormant SANC. Furthermore, the phosphorylated-PLB/total PLB ratios were positively correlated with AP firing rate (**Figure 8A**), whereas the absolute numbers of PLB were negatively correlated (**Figure 8B**), indicating that SR Ca^{2+} pumping in dormant cells is likely to be suppressed by two mechanisms: low PLB phosphorylation and high PLB expression. Insufficient SR Ca^{2+} pumping, in turn, could inhibit Ca^{2+} clock operation and contribute to cell dormancy. Increased cAMP-dependent phosphorylation of PLB enables these dormant cells to fire APs. In response to β-AR stimulation, both the baseline function of Ca^{2+} clock (**Figures 4**, **5**) and M clock (**Figure 7**) in dormant SANC becomes enhanced. As a result, the Ca^{2+}-membrane potential phase plane diagram (**Figures 4–6**), a visual representation of the Ca^{2+}-Na^{+} electro-chemical gradient oscillation that underlies an AP cycle, evolves from a tight cluster of dots at baseline (**Figures 4A**, **5** top) to the narrow, early transition stage, to the steady state, in which the membrane potential fluctuation within the same range is accompanied by larger intracellular Ca^{2+} oscillations (**Figure 5**). This suggests that an increase in clock coupling emerges upon the cAMP-dependent activation of dormant SANC; and that clock coupling continues to increase in the context of the time-dependent increase in intracellular Ca^{2+} and increase in cAMP-PKA signaling that enhances function of proteins of both clocks. Note that the low R^2 values between the AP firing rate and p-/total PLB ratio (**Figure 8**) indicates that the impact of factors that determine AP firing rate varies from cell to cell.

Specific Biophysical Mechanisms

With respect to specific biophysical mechanisms, the transition from dormancy to AP firing may be explained by impact of the enhancement of cAMP-PKA signaling on the ignition process, i.e., I_f, LCRs and feed-forward interactions of Ca^{2+} and M clock, including LCRs, NCX, and I_{CaL} (Lyashkov et al., 2018). Following the ignition theory, increased LCRs and I_{NCX} depolarize cell membrane activating low voltage-activated Ca channels ($Ca_{v1.3}$ and $Ca_{v3.1}$) that generate both respective diastolic Ca currents (I_{CaL} and I_{CaT}) and attendant Ca^{2+} influx to activate more LCRs via Ca^{2+}-induced-Ca^{2+}-release (Chen et al., 2009; Torrente et al., 2016). The additional LCRs, in turn, generate more I_{NCX} and membrane depolarization, forming an explosive feed-forward loop to insure robust ignition of a new pacemaker cycle. Our previous study of dormant cells (Kim et al., 2018) featured a numerical model of this transition from dormancy to AP firing. Numerical simulations of this model illustrated that the diastolic I_{NCX} amplitude substantially increases from a steady level of about −4 pA in dormant cells to oscillations from −9 to −15 pA in firing cells (**Supplementary Figures 1, 2**).

The results of ivabradine and CPA experiments (**Table 2**) suggest that enhanced function of the Ca^{2+}-clock is critical for the majority of responder dormant SANCs to initiate the *bona fide* APs in response to β-AR stimulation, while I_f current, in contrast, appears to have a role in stabilization of the β-AR stimulation-induced *de novo* APs among responder dormant SANC. This interpretation is supported by previous studies (Vinogradova et al., 2006) that demonstrated the obligatory role of basal PKA activation for normal SANC automaticity (that is opposite to dormancy): specific inhibition of PKA-dependent phosphorylation by PKI results in AP firing failure, i.e., cell dormancy. Thus, PKA-insensitive I_f directly regulated by cAMP (DiFrancesco and Tortora, 1991) is expected to remain unchanged under these conditions of selective PKA inhibitions, but it is not sufficient to prevent dormancy.

One important specific question is about why dormant cells have a depolarized membrane potential fluctuating near −38 mV (**Figure 1B**) and what causes membrane hyperpolarization during their transition to AP firing (**Figure 3B**). Previous studies showed that a reduction in the electrochemical gradient by decreasing extracellular Na^{+} or increasing extracellular K^{+}, pharmacological blockade of I_{Kr} (Verheijck et al., 1995) or I_{CaL} (Verheijck et al., 1999), or a brief, subthreshold depolarizing or hyperpolarizing pulse (Jalife and Antzelevitch, 1979) induces dormancy in SANC that otherwise spontaneously fire APs at either the single cell or tissue-ball level. Dormant SANC can be reactivated by reverting the altered extracellular ion composition (Noma and Irisawa, 1975a), adrenergic agonists (Opthof et al., 1987), or subthreshold pacing to cardiac neurons that induce I_{KACh}-driven hyperpolarization to an adjacent dormant SANC (Goto et al., 1983). The predesposition to dormancy can be also linked to substantial functional heterogeneity of key ion current densities, i.e., the M clock side of the system (Honjo et al., 1996; Monfredi et al., 2018).

The existence of "pseudo resting" potential of −30 to −40 mV, when voltage-gated channels are not active, has been thoroughly studied and discussed by Capel and Terrar (2015a,b) who noted that upon cessation of rhythmic AP firing (by multiple different reasons) many SANC fluctuate around a membrane potential in the region of −35 mV. A similar "resting potential" of −38 mV was also observed in rabbit SA node by Noma and Irisawa (1975b). It was suggested that this relatively depolarized level of membrane potential is determined by a balance of numerous ion currents of different nature (Capel and Terrar, 2015b), and I_{NCX} seems to also critically contribute to this balance (Sanders et al., 2006). The relatively depolarized membrane potential of −38 mV in dormant cells could be also explained by the absence of I_{K1} current in SANC combined with a lower amplitude of voltage-activated K^{+} currents (in the absence of their activation by APs). We tested this idea via numerical model simulations (**Supplementary Figure 3**) but found that in a dormant cell I_{Kr} remains relatively high, near 15 pA (blue line), i.e., larger than I_{NCX} amplitude of about 4 pA (**Supplementary Figure 2**), indicating that a lower K^{+} current amplitude is hardly the only reason of the depolarized potential observed in dormant cells.

Future studies should further address the mechanisms that drive the initial hyperpolarization in responding dormant cells.

One possible mechanism is via electrogenic transporters (i.e., not ion channels) such as Na^+/K^+ pump. Hyperpolarization can be also driven by Ca^{2+}-activated K^+ channels [review (Clements et al., 2015)]. All three "small K" isoforms (SK1, SK2, and SK3) were identified in mouse SAN (Torrente et al., 2017) and inhibition of SK channels with apamin prolonged APs in isolated SAN cells, slowed diastolic depolarization, and reduced pacemaker rate in isolated SAN cells and intact SAN tissue (Torrente et al., 2017). Large-conductance Ca^{2+}- and voltage-activated K^+ channels (BK channels or maxi-K^+ channels) also seem to play a prominent role in pacemaker function (Imlach et al., 2010; Lai et al., 2014).

Are Dormant SANC Functional Members of a Heterogeneous Pacemaker Cell Community in Intact SAN Tissue?

It has been reported that most of the SANC enzymatically isolated from guinea pig SAN do not beat spontaneously (Toyoda et al., 2018). This has traditionally been interpreted as a result of damage from the cell isolation process. However, one might consider that the AP firing behavior of a single isolated SANC would not necessarily be identical to that of intact SAN tissue. Rather than representing damaged SANC, recent research (Kim et al., 2018; Tsutsui et al., 2018) and the present study demonstrate that almost half of SANC that do not beat at baseline "wake up" in response to increased cAMP-PKA signaling and began to fire spontaneous APs at a rate that does not differ from that of isolated SANC that fire AP at baseline; and the cells return back to dormant state when the stimulus is removed. While dormant cells studied here would likely behave differently within a cellular network of SAN, the possibility remains that (i) such dormant SANC may exist in intact SAN tissue and can dynamically change the ensemble AP firing behavior, or (ii) AP firing cells become the dominant cells in certain prevailing physiological conditions that may not favor the phenotype of the SANC that beat spontaneously at baseline after isolation.

Previous studies have a bearing on this issue. Studying surgically isolated small SAN tissue preparations, Opthof et al. (1987) observed that, while the majority of small SAN tissues demonstrated spontaneous AP firing at different frequencies, some of the small SAN tissues dissected from the septal side of the SAN were electrically dormant. Some SANC within SAN tissue are electrically quiescent during normal heart function (Noma and Irisawa, 1975a,b; Goto et al., 1983; Opthof et al., 1987; Toyoda et al., 2018). This is believed to reflect a degree of functional redundancy – the SAN of cats contains about 2000 primary pacemaker cells, but can function normally with less than 500 cells (Opthof et al., 1986). A physiological implication of this phenomenon is that not all SANC contribute to all beats; this may be to optimize energy consumption at times when the participation of all SANC within SAN tissue is not required, e.g., in the basal state. Vagal nerve stimulation modulates SAN rate and rhythm and can lead to marked sinus bradycardia or even arrest (van Borren et al., 2010). Non-firing SANC may be able to serve as subsidiary pacemakers by responding differently to external stimuli, thereby resulting in a shift of the "leading pacemaker site" within the SAN (Lang et al., 2011). However, the actual physiological role of non-firing SANC *in vivo* remains unclear.

The function of dormant cells will be better realized within the context of evolution of our understanding of SAN tissue operation. About 40 years ago SANC automaticity has been conceptualized as initiated by small group of "strong" cells (a dictator model) with a concentric propagation from the initiation site toward atria (Sano et al., 1978; Bleeker et al., 1980). Then an idea of mutual entrainment of coupled oscillators (Winfree, 1967) was applied to the coordinated firing of the entire population of SAN cells (Jalife, 1984; Michaels et al., 1987): individual SAN cells that are loosely connected through low resistance junctions generate spontaneous excitations that differ in phase, mutually entrain each other to fire with a common period. Recently, by utilizing a newly developed whole-tissue Ca^{2+} imaging apparatus, we have discovered an extensive, reticular HCN4+/Cx43-cell meshwork across the posterior aspect of murine right atria along the crista terminalis that generates spontaneous *regular* electrical impulses (Bychkov et al., 2020). Within the network, however, we have observed highly heterogeneous AP firing behavior. Some SANC within this network discharge spontaneous APs regularly, while others had dysrhythmic AP firing, and even some subpopulations remain completely dormant. The majority of these SANC had LCRs along with the intricate and complex cell-to-cell heterogeneous Ca^{2+} signals. That study proposed a novel, microscopic signaling paradigm of SAN operation in which synchronized APs emerge from heterogeneous subcellular subthreshold Ca^{2+} signals, resembling multiscale complex processes of impulse generation within clusters of neurons in neuronal networks. Another recent study (Fenske et al., 2020) also detected non-firing cells in mouse SAN and provided evidence that a tonic and mutual interaction process (tonic entrainment) between firing and non-firing cells slows down the overall rhythm of the SAN.

CONCLUSION

Our results demonstrate that cAMP-signaling awakes AP firing of dormant SANC via emergence of a coupled-clock system, i.e., the emergence of self-organized roughly periodic Ca^{2+} clock and concurrent oscillations of membrane potential that informs on an increase in clock synchronization in response to β-AR stimulation. The results of the present study raise, but do not prove, the possibility of the existence of dormant SANC *in vivo*; but if this were the case, dynamic recruitment of these cells *in vivo* would likely depend on cAMP-PKA signaling. In other words, some cells that are embedded in SAN tissue, but do not generate APs all the time (Bychkov et al., 2020; Fenske et al., 2020), may activate to fire APs conditionally, namely in the presence of β-AR stimulation *in vivo*. Other cells may deactivate upon cholinergic receptor stimulation (Goto et al., 1983; Opthof et al., 1987; Fenske et al., 2020).

Limitations and Future Directions

Although substantial evidence has recently emerged to indicate the presence of non-firing cells in intact tissue, we must emphasize that dormant cells we study in isolation are not necessarily the same dormant cells that have been observed in the intact tissue. More experimental and numerical studies are needed to clarify the role of non-firing cells in SA node and biochemical (cAMP, PKA, and CaMKII signaling) and biophysical mechanisms of dormant cell transition to AP firing, including initial hyperpolarization. Multi-cellular and multiscale numerical modeling would include dormant cells and test several new hypotheses of SAN operational paradigm that have been proposed but not validated yet, including the ideas of subthreshold signal summation among neighboring cells (Bychkov et al., 2020), stochastic resonance (Clancy and Santana, 2020), percolating criticality (Weiss and Qu, 2020), and cell silencing at lower rates (Fenske et al., 2020).

DATA AVAILABILITY STATEMENT

The raw data supporting the conclusions of this article will be made available by the authors, without undue reservation.

ETHICS STATEMENT

The animal study was reviewed and approved by the Animal Care and Use Committee of the National Institutes of Health.

AUTHOR CONTRIBUTIONS

KT: perform the experiments, and drafting of the manuscript and critically revising it for important intellectual content, analysis, and interpretation of the data. MF, AY, AW, DY, MK, and BZ: perform the experiments, and critically revising the manuscript for important intellectual content, analysis, and interpretation of the data. RB and OM: analysis and interpretation of the data. VM: project planning, analysis and interpretation of the data, numerical model simulations, and drafting of the manuscript and revising it critically for important intellectual content. EL: project planning, conception and design of the experiments, and drafting of the manuscript and revising it critically for important intellectual content. All authors contributed to the article and approved the submitted version.

FUNDING

This research was supported by the Intramural Research Program of the NIH, National Institute on Aging. KT was supported by Japan Society for the Promotion of Science Research Fellowship for Japanese Biomedical and Behavioral Researchers at NIH. OM was supported by National Institute for Health Research in the United Kingdom.

SUPPLEMENTARY MATERIAL

The Supplementary Material for this article can be found online at: https://www.frontiersin.org/articles/10.3389/fphys.2021.596832/full#supplementary-material

Supplementary Movie 1 | Simultaneous measurement of Ca^{2+} and voltage signals from an initially dormant SANC that began to fire in response to CPT-cAMP. At the baseline, although membrane potential hovers around −40 mV, LCRs are present. During the transitions, the same cell began to fire spontaneous AP (for detailed description, see text and **Figures 5**, **6**). Following the CPT-cAMP washout, the SANC ceases to fire spontaneous AP, turned dormant again.

REFERENCES

Bleeker, W. K., Mackaay, A. J., Masson-Pevet, M., Bouman, L. N., and Becker, A. E. (1980). Functional and morphological organization of the rabbit sinus node. *Circ. Res.* 46, 11–22. doi: 10.1161/01.res.46.1.11

Bogdanov, K. Y., Vinogradova, T. M., and Lakatta, E. G. (2001). Sinoatrial nodal cell ryanodine receptor and Na^{+}-Ca^{2+} exchanger: molecular partners in pacemaker regulation. *Circ. Res.* 88, 1254–1258. doi: 10.1161/hh1201.092095

Boyett, M. R., Honjo, H., and Kodama, I. (2000). The sinoatrial node, a heterogeneous pacemaker structure. *Cardiovasc. Res.* 47, 658–687. doi: 10.1016/s0008-6363(00)00135-8

Bychkov, R., Juhaszova, M., Tsutsui, K., Coletta, C., Stern, M. D., Maltsev, V. A., et al. (2020). Synchronized cardiac impulses emerge from multi-scale, heterogeneous local calcium signals within and among cells of heart pacemaker tissue. *JACC Clin. Electrophysiol.* 6, 907–931. doi: 10.1016/j.jacep.2020.06.022

Capel, R. A., and Terrar, D. A. (2015a). Cytosolic calcium ions exert a major influence on the firing rate and maintenance of pacemaker activity in guinea-pig sinus node. *Front. Physiol.* 6:23. doi: 10.3389/fphys.2015.00023

Capel, R. A., and Terrar, D. A. (2015b). The importance of Ca^{2+}-dependent mechanisms for the initiation of the heartbeat. *Front. Physiol.* 6:80. doi: 10.3389/fphys.2015.00080

Chen, B., Wu, Y., Mohler, P. J., Anderson, M. E., and Song, L. S. (2009). Local control of Ca^{2+}-induced Ca^{2+} release in mouse sinoatrial node cells. *J. Mol. Cell Cardiol.* 47, 706–715. doi: 10.1016/j.yjmcc.2009.07.007

Clancy, C. E., and Santana, L. F. (2020). Evolving discovery of the origin of the heartbeat: a new perspective on sinus rhythm. *JACC Clin. Electrophysiol.* 6, 932–934. doi: 10.1016/j.jacep.2020.07.002

Clements, R. T., Terentyev, D., and Sellke, F. W. (2015). Ca^{2+}-activated K^{+} channels as therapeutic targets for myocardial and vascular protection. *Circ. J.* 79, 455–462. doi: 10.1253/circj.CJ-15-0015

Denyer, J. C., and Brown, H. F. (1990). Rabbit sino-atrial node cells: isolation and electrophysiological properties. *J. Physiol.* 428, 405–424. doi: 10.1113/jphysiol.1990.sp018219

DiFrancesco, D., Ferroni, A., Mazzanti, M., and Tromba, C. (1986). Properties of the hyperpolarizing-activated current (i_f) in cells isolated from the rabbit sino-atrial node. *J. Physiol.* 377, 61–88. doi: 10.1113/jphysiol.1986.sp016177

DiFrancesco, D., and Tortora, P. (1991). Direct activation of cardiac pacemaker channels by intracellular cyclic AMP. *Nature* 351, 145–147. doi: 10.1038/351145a0

Fenske, S., Hennis, K., Rotzer, R. D., Brox, V. F., Becirovic, E., Scharr, A., et al. (2020). cAMP-dependent regulation of HCN4 controls the tonic entrainment process in sinoatrial node pacemaker cells. *Nat. Commun.* 11:5555. doi: 10.1038/s41467-020-19304-9

Goto, J., Toyama, J., and Yamada, K. (1983). Effects of timing of vagal stimulation on the sinoatrial nodal cell discharge. *J. Electrocardiol.* 16, 45–52. doi: 10.1016/s0022-0736(83)80158-7

Honjo, H., Boyett, M. R., Kodama, I., and Toyama, J. (1996). Correlation between electrical activity and the size of rabbit sino-atrial node cells. *J. Physiol.* 496(Pt 3), 795–808. doi: 10.1113/jphysiol.1996.sp021728

Huser, J., Blatter, L. A., and Lipsius, S. L. (2000). Intracellular Ca^{2+} release contributes to automaticity in cat atrial pacemaker cells. *J. Physiol.* 524(Pt 2), 415–422. doi: 10.1111/j.1469-7793.2000.00415.x

Imlach, W. L., Finch, S. C., Miller, J. H., Meredith, A. L., and Dalziel, J. E. (2010). A role for BK channels in heart rate regulation in rodents. *PLoS One* 5:e8698. doi: 10.1371/journal.pone.0008698

Irisawa, H., Brown, H. F., and Giles, W. (1993). Cardiac pacemaking in the sinoatrial node. *Physiol. Rev.* 73, 197–227. doi: 10.1152/physrev.1993.73.1.197

Jalife, J. (1984). Mutual entrainment and electrical coupling as mechanisms for synchronous firing of rabbit sino-atrial pace-maker cells. *J. Physiol.* 356, 221–243. doi: 10.1113/jphysiol.1984.sp015461

Jalife, J., and Antzelevitch, C. (1979). Phase resetting and annihilation of pacemaker activity in cardiac tissue. *Science* 206, 695–697. doi: 10.1126/science.493975

Kim, M. S., Maltsev, A. V., Monfredi, O., Maltseva, L. A., Wirth, A., Florio, M. C., et al. (2018). Heterogeneity of calcium clock functions in dormant, dysrhythmically and rhythmically firing single pacemaker cells isolated from SA node. *Cell Calcium* 74, 168–179. doi: 10.1016/j.ceca.2018.07.002

Lai, M. H., Wu, Y., Gao, Z., Anderson, M. E., Dalziel, J. E., and Meredith, A. L. (2014). BK channels regulate sinoatrial node firing rate and cardiac pacing *in vivo*. *Am. J. Physiol. Heart Circ. Physiol.* 307, H1327–H1338. doi: 10.1152/ajpheart.00354.2014

Lakatta, E. G., Maltsev, V. A., and Vinogradova, T. M. (2010). A coupled SYSTEM of intracellular Ca^{2+} clocks and surface membrane voltage clocks controls the timekeeping mechanism of the heart's pacemaker. *Circ. Res.* 106, 659–673. doi: 10.1161/circresaha.109.206078

Lang, D., Petrov, V., Lou, Q., Osipov, G., and Efimov, I. R. (2011). Spatiotemporal control of heart rate in a rabbit heart. *J. Electrocardiol.* 44, 626–634. doi: 10.1016/j.jelectrocard.2011.08.010

Lei, M., and Boyett, M. R. (1999). Heterogenous expression of the rapid delayed rectifier K^+ current $I_{K,r}$ and the slow delayed rectifier K^+ current $I_{K,s}$ in rabbit sinoatrial node cells. *J. Physiol.* 521, 19–20.

Lei, M., Honjo, H., Kodama, I., and Boyett, M. R. (2000). Characterisation of the transient outward K+ current in rabbit sinoatrial node cells. *Cardiovasc. Res.* 46, 433–441. doi: 10.1016/s0008-6363(00)00036-5

Lyashkov, A. E., Behar, J., Lakatta, E. G., Yaniv, Y., and Maltsev, V. A. (2018). Positive feedback mechanisms among local Ca^{2+} releases, NCX, and ICaL ignite pacemaker action potentials. *Biophys. J.* 114, 1176–1189. doi: 10.1016/j.bpj.2017.12.043

Lyashkov, A. E., Juhaszova, M., Dobrzynski, H., Vinogradova, T. M., Maltsev, V. A., Juhasz, O., et al. (2007). Calcium cycling protein density and functional importance to automaticity of isolated sinoatrial nodal cells are independent of cell size. *Circ. Res.* 100, 1723–1731. doi: 10.1161/circresaha.107.153676

Lyashkov, A. E., Vinogradova, T. M., Zahanich, I., Li, Y., Younes, A., Nuss, H. B., et al. (2009). Cholinergic receptor signaling modulates spontaneous firing of sinoatrial nodal cells via integrated effects on PKA-dependent Ca^{2+} cycling and I_{KACh}. *Am. J. Physiol. Heart Circ. Physiol.* 297, H949–H959.

Maltsev, A. V., Parsons, S. P., Kim, M. S., Tsutsui, K., Stern, M. D., Lakatta, E. G., et al. (2017). Computer algorithms for automated detection and analysis of local Ca^{2+} releases in spontaneously beating cardiac pacemaker cells. *PLoS One* 12:e0179419. doi: 10.1371/journal.pone.0179419

Maltsev, V. A., and Lakatta, E. G. (2010). A novel quantitative explanation for autonomic modulation of cardiac pacemaker cell automaticity via a dynamic system of sarcolemmal and intracellular proteins. *Am. J. Physiol. Heart Circ. Physiol.* 298, H2010–H2023.

Mangoni, M. E., and Nargeot, J. (2008). Genesis and regulation of the heart automaticity. *Physiol. Rev.* 88, 919–982. doi: 10.1152/physrev.00018.2007

Mattick, P., Parrington, J., Odia, E., Simpson, A., Collins, T., and Terrar, D. (2007). Ca^{2+}-stimulated adenylyl cyclase isoform AC1 is preferentially expressed in guinea-pig sino-atrial node cells and modulates the I_f pacemaker current. *J. Physiol.* 582, 1195–1203. doi: 10.1113/jphysiol.2007.133439

Mesirca, P., Torrente, A. G., and Mangoni, M. E. (2015). Functional role of voltage gated Ca^{2+} channels in heart automaticity. *Front. Physiol.* 6:19. doi: 10.3389/fphys.2015.00019

Michaels, D. C., Matyas, E. P., and Jalife, J. (1987). Mechanisms of sinoatrial pacemaker synchronization: a new hypothesis. *Circ. Res.* 61, 704–714. doi: 10.1161/01.res.61.5.704

Monfredi, O., Lyashkov, A. E., Johnsen, A. B., Inada, S., Schneider, H., Wang, R., et al. (2014). Biophysical characterization of the underappreciated and important relationship between heart rate variability and heart rate. *Hypertension* 64, 1334–1343. doi: 10.1161/HYPERTENSIONAHA.114.03782

Monfredi, O., Maltseva, L. A., Spurgeon, H. A., Boyett, M. R., Lakatta, E. G., and Maltsev, V. A. (2013). Beat-to-beat variation in periodicity of local calcium releases contributes to intrinsic variations of spontaneous cycle length in isolated single sinoatrial node cells. *PLoS One* 8:e67247. doi: 10.1371/journal.pone.0067247

Monfredi, O., Tsutsui, K., Ziman, B., Stern, M. D., Lakatta, E. G., and Maltsev, V. A. (2018). Electrophysiological heterogeneity of pacemaker cells in the rabbit intercaval region, including the SA node: insights from recording multiple ion currents in each cell. *Am. J. Physiol. Heart Circ. Physiol.* 314, H403–H414. doi: 10.1152/ajpheart.00253.2016

Noble, D. (1962). A modification of the Hodgkin-Huxley equations applicable to Purkinje fibre action and pace-maker potentials. *J. Physiol.* 160, 317–352. doi: 10.1113/jphysiol.1962.sp006849

Noble, D. (1984). The surprising heart: a review of recent progress in cardiac electrophysiology. *J. Physiol.* 353, 1–50. doi: 10.1113/jphysiol.1984.sp015320

Noma, A. (1996). Ionic mechanisms of the cardiac pacemaker potential. *Jpn. Heart J.* 37, 673–682. doi: 10.1536/ihj.37.673

Noma, A., and Irisawa, H. (1975a). Contribution of an electrogenic sodium pump to the membrane potential in rabbit sinoatrial node cells. *Pflugers Arch.* 358, 289–301. doi: 10.1007/bf00580527

Noma, A., and Irisawa, H. (1975b). Effects of Na+ and K+ on the resting membrane potential of the rabbit sinoatrial node cell. *Jpn. J. Physiol.* 25, 207–302.

Opthof, T., De Jonge, B., Masson-Pevet, M., Jongsma, H. J., and Bouman, L. N. (1986). Functional and morphological organization of the cat sinoatrial node. *J. Mol. Cell Cardiol.* 18, 1015–1031. doi: 10.1016/s0022-2828(86)80290-5

Opthof, T., Vanginneken, A. C., Bouman, L. N., and Jongsma, H. J. (1987). The intrinsic cycle length in small pieces isolated from the rabbit sinoatrial node. *J. Mol. Cell Cardiol.* 19, 923–934. doi: 10.1016/s0022-2828(87)80621-1

Rigg, L., Heath, B. M., Cui, Y., and Terrar, D. A. (2000). Localisation and functional significance of ryanodine receptors during beta-adrenoceptor stimulation in the guinea-pig sino-atrial node. *Cardiovasc. Res.* 48, 254–264. doi: 10.1016/s0008-6363(00)00153-x

Rigg, L., and Terrar, D. A. (1996). Possible role of calcium release from the sarcoplasmic reticulum in pacemaking in guinea-pig sino-atrial node. *Exp. Physiol.* 81, 877–880. doi: 10.1113/expphysiol.1996.sp003983

Rubenstein, D. S., and Lipsius, S. L. (1989). Mechanisms of automaticity in subsidiary pacemakers from cat right atrium. *Circ. Res.* 64, 648–657. doi: 10.1161/01.res.64.4.648

Sanders, L., Rakovic, S., Lowe, M., Mattick, P. A., and Terrar, D. A. (2006). Fundamental importance of Na^+-Ca^{2+} exchange for the pacemaking mechanism in guinea-pig sino-atrial node. *J. Physiol.* 571, 639–649. doi: 10.1113/jphysiol.2005.100305

Sano, T., Sawanobori, T., and Adaniya, H. (1978). Mechanism of rhythm determination among pacemaker cells of the mammalian sinus node. *Am. J. Physiol.* 235, H379–H384. doi: 10.1152/ajpheart.1978.235.4.H379

Sirenko, S., Maltsev, V. A., Maltseva, L. A., Yang, D., Lukyanenko, Y., Vinogradova, T. M., et al. (2014). Sarcoplasmic reticulum Ca^{2+} cycling protein phosphorylation in a physiologic Ca^{2+} milieu unleashes a high-power, rhythmic Ca^{2+} clock in ventricular myocytes: Relevance to arrhythmias and bio-pacemaker design. *J. Mol. Cell Cardiol.* 66C, 106–115. doi: 10.1016/j.yjmcc.2013.11.011

Sirenko, S., Yang, D., Li, Y., Lyashkov, A. E., Lukyanenko, Y. O., Lakatta, E. G., et al. (2012). Ca^{2+}-dependent phosphorylation of Ca^{2+} cycling proteins generates robust rhythmic local Ca^{2+} releases in cardiac pacemaker cells. *Sci. Signal.* 6:ra6. doi: 10.1126/scisignal.2003391

Torrente, A. G., Mesirca, P., Neco, P., Rizzetto, R., Dubel, S., Barrere, C., et al. (2016). L-type Cav1.3 channels regulate ryanodine receptor-dependent Ca^{2+} release during sino-atrial node pacemaker activity. *Cardiovasc. Res.* 109, 451–461. doi: 10.1093/cvr/cvw006

Torrente, A. G., Zhang, R., Wang, H., Zaini, A., Kim, B., Yue, X., et al. (2017). Contribution of small conductance K^+ channels to sinoatrial node pacemaker activity: insights from atrial-specific Na^+/Ca^{2+} exchange knockout mice. *J. Physiol.* 595, 3847–3865. doi: 10.1113/JP274249

Toyoda, F., Ding, W. G., and Matsuura, H. (2018). Heterogeneous functional expression of the sustained inward Na(+) current in guinea pig sinoatrial node cells. *Pflugers Arch.* 470, 481–490. doi: 10.1007/s00424-017-2091-y

Tsutsui, K., Monfredi, O., and Lakatta, E. G. (2016). A general theory to explain heart rate and cardiac contractility changes with age. *Physiol. Mini. Rev.* 9, 9–25.

Tsutsui, K., Monfredi, O., Sirenko-Tagirova, S. G., Maltseva, L. A., Bychkov, R., Kim, M. S., et al. (2018). A coupled-clock system drives the automaticity of human sinoatrial nodal pacemaker cells. *Sci. Signal.* 11:eaa7608.

van Borren, M. M., Verkerk, A. O., Wilders, R., Hajji, N., Zegers, J. G., Bourier, J., et al. (2010). Effects of muscarinic receptor stimulation on Ca^{2+} transient, cAMP production and pacemaker frequency of rabbit sinoatrial node cells. *Basic Res. Cardiol.* 105, 73–87. doi: 10.1007/s00395-009-0048-9

Verheijck, E. E., Van Ginneken, A. C., Bourier, J., and Bouman, L. N. (1995). Effects of delayed rectifier current blockade by E-4031 on impulse generation in single sinoatrial nodal myocytes of the rabbit. *Circ. Res.* 76, 607–615. doi: 10.1161/01.res.76.4.607

Verheijck, E. E., Van Ginneken, A. C., Wilders, R., and Bouman, L. N. (1999). Contribution of L-type Ca^{2+} current to electrical activity in sinoatrial nodal myocytes of rabbits. *Am. J. Physiol.* 276, H1064–H1077.

Verheijck, E. E., Wessels, A., Van Ginneken, A. C., Bourier, J., Markman, M. W., Vermeulen, J. L., et al. (1998). Distribution of atrial and nodal cells within the rabbit sinoatrial node: models of sinoatrial transition. *Circulation* 97, 1623–1631. doi: 10.1161/01.cir.97.16.1623

Vinogradova, T. M., Bogdanov, K. Y., and Lakatta, E. G. (2002). beta-Adrenergic stimulation modulates ryanodine receptor Ca^{2+} release during diastolic depolarization to accelerate pacemaker activity in rabbit sinoatrial nodal cells. *Circ. Res.* 90, 73–79. doi: 10.1161/hh0102.102271

Vinogradova, T. M., Brochet, D. X., Sirenko, S., Li, Y., Spurgeon, H., and Lakatta, E. G. (2010). Sarcoplasmic reticulum Ca^{2+} pumping kinetics regulates timing of local Ca^{2+} releases and spontaneous beating rate of rabbit sinoatrial node pacemaker cells. *Circ. Res.* 107, 767–775. doi: 10.1161/circresaha.110.220517

Vinogradova, T. M., Lyashkov, A. E., Zhu, W., Ruknudin, A. M., Sirenko, S., Yang, D., et al. (2006). High basal protein kinase A-dependent phosphorylation drives rhythmic internal Ca^{2+} store oscillations and spontaneous beating of cardiac pacemaker cells. *Circ. Res.* 98, 505–514. doi: 10.1161/01.res.0000204575.94040.d1

Vinogradova, T. M., Sirenko, S., Lyashkov, A. E., Younes, A., Li, Y., Zhu, W., et al. (2008). Constitutive phosphodiesterase activity restricts spontaneous beating rate of cardiac pacemaker cells by suppressing local Ca^{2+} releases. *Circ. Res.* 102, 761–769. doi: 10.1161/circresaha.107.161679

Vinogradova, T. M., Zhou, Y. Y., Bogdanov, K. Y., Yang, D., Kuschel, M., Cheng, H., et al. (2000). Sinoatrial node pacemaker activity requires Ca^{2+}/calmodulin-dependent protein kinase II activation. *Circ. Res.* 87, 760–767. doi: 10.1161/01.res.87.9.760

Weiss, J. N., and Qu, Z. (2020). The sinus node: still mysterious after all these years. *JACC Clin. Electrophysiol.* 6, 1841–1843. doi: 10.1016/j.jacep.2020.09.017

Wilders, R., and Jongsma, H. J. (1993). Beating irregularity of single pacemaker cells isolated from the rabbit sinoatrial node. *Biophys. J.* 65, 2601–2613. doi: 10.1016/s0006-3495(93)81289-x

Wilders, R., Jongsma, H. J., and Van Ginneken, A. C. (1991). Pacemaker activity of the rabbit sinoatrial node. A comparison of mathematical models. *Biophys. J.* 60, 1202–1216. doi: 10.1016/s0006-3495(91)82155-5

Winfree, A. T. (1967). Biological rhythms and the behavior of populations of coupled oscillators. *J. Theor. Biol.* 16, 15–42. doi: 10.1016/0022-5193(67)90051-3

Yang, Y., Lyashkov, A. E., Morrell, C. H., Zahanich, I., Yaniv, Y., Vinogradova, T., et al. (2020). Self-similar action potential cycle-to-cycle variability of Ca2+ and current oscillators in cardiac pacemaker cells. *bioRxiv* [preprint] doi: 10.1101/2020.09.01.277756

Yaniv, Y., Ahmet, I., Liu, J., Lyashkov, A. E., Guiriba, T. R., Okamoto, Y., et al. (2014). Synchronization of sinoatrial node pacemaker cell clocks and its autonomic modulation impart complexity to heart beating intervals. *Heart Rhythm.* 11, 1210–1219. doi: 10.1016/j.hrthm.2014.03.049

Yaniv, Y., Ahmet, I., Tsutsui, K., Behar, J., Moen, J. M., Okamoto, Y., et al. (2016). Deterioration of autonomic neuronal receptor signaling and mechanisms intrinsic to heart pacemaker cells contribute to age-associated alterations in heart rate variability *in vivo*. *Aging Cell* 15, 716–724. doi: 10.1111/acel.12483

Younes, A., Lyashkov, A. E., Graham, D., Sheydina, A., Volkova, M. V., Mitsak, M., et al. (2008). Ca^{2+}-stimulated basal adenylyl cyclase activity localization in membrane lipid microdomains of cardiac sinoatrial nodal pacemaker cells. *J. Biol. Chem.* 283, 14461–14468. doi: 10.1074/jbc.m707540200

Conflict of Interest: The authors declare that the research was conducted in the absence of any commercial or financial relationships that could be construed as a potential conflict of interest.

frontiers in Physiology

ORIGINAL RESEARCH
published: 09 November 2020
doi: 10.3389/fphys.2020.587040

Regulation of HCN2 Current by PI3K/Akt Signaling

*Zhongju Lu[1,2], Hong Zhan Wang[1], Chris R. Gordon[1,3], Lisa M. Ballou[1], Richard Z. Lin[1,4] and Ira S. Cohen[1]**

[1] Department of Physiology and Biophysics, Stony Brook University, Stony Brook, NY, United States, [2] Department of Medicine, Stony Brook University, Stony Brook, NY, United States, [3] Department of Nephrology, Stony Brook University, Stony Brook, NY, United States, [4] Medical Service, Northport VA Medical Center, Northport, NY, United States

It has long been known that heart rate is regulated by the autonomic nervous system. Recently, we demonstrated that the pacemaker current, I_f, is regulated by phosphoinositide 3-kinase (PI3K) signaling independently of the autonomic nervous system. Inhibition of PI3K in sinus node (SN) myocytes shifts the activation of I_f by almost 16 mV in the negative direction. I_f in the SN is predominantly mediated by two members of the HCN gene family, HCN4 and HCN1. Purkinje fibers also possess I_f and are an important secondary pacemaker in the heart. In contrast to the SN, they express HCN2 and HCN4, while ventricular myocytes, which do not normally pace, express HCN2 alone. In the current work, we investigated PI3K regulation of HCN2 expressed in HEK293 cells. Treatment with the PI3K inhibitor PI-103 caused a negative shift in the activation voltage and a dramatic reduction in the magnitude of the HCN2 current. Similar changes were also seen in cells treated with an inhibitor of the protein kinase Akt, a downstream effector of PI3K. The effects of PI-103 were reversed by perfusion of cells with phosphatidylinositol 3,4,5-trisphosphate (the second messenger produced by PI3K) or active Akt protein. We identified serine 861 in mouse HCN2 as a putative Akt phosphorylation site. Mutation of S861 to alanine mimicked the effects of Akt inhibition on voltage dependence and current magnitude. In addition, the Akt inhibitor had no effect on the mutant channel. These results suggest that Akt phosphorylation of mHCN2 S861 accounts for virtually all of the observed actions of PI3K signaling on the HCN2 current. Unexpectedly, Akt inhibition had no effect on I_f in SN myocytes. This result raises the possibility that diverse PI3K signaling pathways differentially regulate HCN-induced currents in different tissues, depending on the isoforms expressed.

Keywords: HCN2, pacemaker current, PI3K, Akt, sinus node

Edited by:
Pietro Mesirca,
INSERM U1191 Institut de Génomique Fonctionnelle (IGF), France

Reviewed by:
Wayne Rodney Giles,
University of Calgary, Canada
Elisabetta Cerbai,
University of Florence, Italy

Correspondence:
Ira S. Cohen
ira.cohen@stonybrook.edu

Specialty section:
This article was submitted to Cardiac Electrophysiology, a section of the journal Frontiers in Physiology

Received: *24 July 2020*
Accepted: *16 October 2020*
Published: *09 November 2020*

Citation:
Lu Z, Wang HZ, Gordon CR, Ballou LM, Lin RZ and Cohen IS (2020) Regulation of HCN2 Current by PI3K/Akt Signaling. Front. Physiol. 11:587040. doi: 10.3389/fphys.2020.587040

INTRODUCTION

The sinoatrial node (SN) initiates electrical activity in the heart that triggers the cardiac contractions responsible for circulation of the blood. This electrical activity includes action potentials associated with contraction and a period between action potentials called diastolic depolarization. The SN rate is dependent on both voltage-dependent ion channels (called the membrane voltage clock) and triggered release of intracellular Ca^{2+} (called the Ca^{2+} clock) (DiFrancesco, 1993; Lakatta et al., 2010). All of the elements necessary for this electrical event are intrinsic to the SN myocytes.

The membrane voltage clock includes a number of ion channels which generate net inward current during the diastolic interval, driving the SN toward the action potential threshold. One of these diastolic membrane currents is the pacemaker current, I_f. I_f is selective to Na^+ and K^+ and activates slowly on hyperpolarization (DiFrancesco, 1993). The cardiac pacemaker channels are comprised of heteromultimers of three members of the HCN gene family. HCN4 is the dominant isoform in rabbit SN myocytes (81% of the total HCN mRNA), while HCN1 (18%) and HCN2 (0.6%) are present at lower levels (Shi et al., 1999). By contrast, HCN2 is the predominant isoform in ventricular myocytes, and I_f in Purkinje fibers is mediated by HCN2 and HCN4 (Shi et al., 1999; Han et al., 2002).

An increase in I_f increases the SN pacing rate. The sympathetic nervous system increases heart rate in part by shifting the activation of I_f to more positive potentials, allowing greater activation during diastolic depolarization. The parasympathetic nervous system has the opposite effect on both heart rate and the voltage dependence of I_f (DiFrancesco, 1993). Although the details of this rapid sympathetic and parasympathetic regulation of heart rate and I_f have been studied in detail, little is known about other regulatory mechanisms that control intrinsic heart rate over longer time periods of time. One recent study pointed to a potential role for AMPK in this process (Yavari et al., 2017). Our own studies indicated that phosphoinositide 3-kinase (PI3K) regulates both SN rate and I_f independently of the autonomic nervous system (Lin et al., 2019).

Class I PI3Ks produce the lipid second messenger phosphatidylinositol 3,4,5-trisphosphate [$PI(3,4,5)P_3$]. The enzymes are heterodimers containing one of four distinct catalytic subunits bound to one of several regulatory subunits. PI3Ks in the Class IA subgroup can be activated by tyrosine kinases (TKs) *via* binding of the regulatory subunits to tyrosine-phosphorylated proteins. There are multiple downstream effectors of PI3K, including the protein kinase Akt (Ballou et al., 2015). We recently demonstrated that inhibition of PI3K by the pan PI3K isoform inhibitor PI-103 induced a slowing of sinus rate *in situ* and *in vitro* and a negative shift in activation of I_f in SN myocytes. There was no change in the whole cell conductance of I_f (Lin et al., 2019). This work built on a previous study which demonstrated that some TK inhibitors (TKIs) act through inhibition of PI3K signaling to induce an acquired long QT syndrome (Lu et al., 2012). PI3K inhibition caused alterations in a number of cardiac membrane currents, including a reduction in amplitude of I_{Na}, I_{Kr}, and I_{Ks} together with a reduction in I_{CaL} and a positive shift in its activation. An increase in the persistent sodium current I_{NaP} was also observed (Lu et al., 2012). Earlier work showed that TKIs also caused a simple reduction in amplitude of I_f in SN myocytes (Wu and Cohen, 1997). However, the consequences of TK inhibition on heterologously expressed HCN isoforms varied widely, with no effect on HCN1, reduced amplitude and slowed activation kinetics of both HCN2 and HCN4, and a shift in the activation of HCN2 to more negative potentials (Yu et al., 2004). These differences in the effects of TK inhibition on different HCN isoforms, plus the fact that one of the downstream actions of TK inhibition can be a reduction in PI3K activity, induced us to study PI3K regulation of heterologously expressed HCN2, the dominant ventricular isoform (Shi et al., 1999).

MATERIALS AND METHODS

Electrophysiology

Patch Clamp Recording of HCN2 Current Expressed in HEK293 Cells

We used a traditional whole-cell patch clamp (voltage-clamp) recording technique to examine HCN2 currents expressed in HEK293 cells. Experiments in **Figures 1–3** employed a stable cell line expressing mouse HCN2 and GFP. The experiments in **Figure 4** used HEK293 cells transiently transfected with GFP-mHCN2 constructs (see Section 2.2). Whole-cell patch clamp recording was performed using the Axopatch-1D amplifier coupled to the pCLAMP data acquisition and analysis software package (version 10, Axon Instruments, Inc). Patch electrode resistance was 4-6 MΩ and room temperature was 20 ± 1°C. The bath solution was (in mM): NaCl 140, KCl 5.4, $MgCl_2$ 1, $CaCl_2$ 1.8, HEPES 10, and glucose 10 (pH 7.4 with NaOH). The pipette solution contained: aspartate 130, KOH 146, NaCl 10, EGTA-KOH 5, $CaCl_2$ 2, Mg-ATP 2, and HEPES-KOH 10 (pH 7.2 with KOH) (Potapova et al., 2004). The voltage protocol to measure the HCN2 activation curve was to hold the cell at -30 mV and hyperpolarize for 1.5 s to voltages between −30 and −130 mV in 10-mV increments, followed by a 1-s voltage step to + 50 mV to record the tail currents, followed by a step back to −30 mV. The normalized plot of tail current versus test voltage was fit with a Boltzmann function, and then, the voltage at half maximum activation ($V_{1/2}$) and slope factor (K) were calculated from the fit. Current densities are expressed as the value of the time-dependent component of current amplitude measured at the end of the test potential (-120 mV, 1.5-s duration) from a holding potential of -30 mV and normalized to cell membrane capacitance.

Whole-Cell Patch Clamp Recording of I_f in Single SN Myocytes

Single SN myocytes were isolated from rabbit hearts as previously described (Lin et al., 2019). All animal-related procedures were approved by the Stony Brook University Institutional Animal Care and Use Committee. Electrophysiological measurements of I_f were performed at room temperature (20 ± 1°C). The external solution contained (in mM): NaCl 140, KCl 8, $CaCl_2$ 1.8, $MgCl_2$ 1.0, HEPES 5, glucose 10, $MnCl_2$ 2, $CdCl_2$ 0.2, and $BaCl_2$ 8 (pH adjusted to 7.4 with NaOH). The internal solution contained KCl 50, K-aspartate 80, $MgCl_2$ 1, EGTA 10, Mg-ATP 3, and HEPES 10 (pH 7.2). Mn^{2+} and Cd^{2+} were used to reduce Ca^{2+} currents, which can overlap with and obscure I_f tail currents. Ba^{2+} was used to block the background K^+ current (I_{K1}), which activates and inactivates in the same voltage range as I_f. The liquid junction potential (10 mV) between the electrode tip and cell interior was not corrected. The voltage-clamp protocol

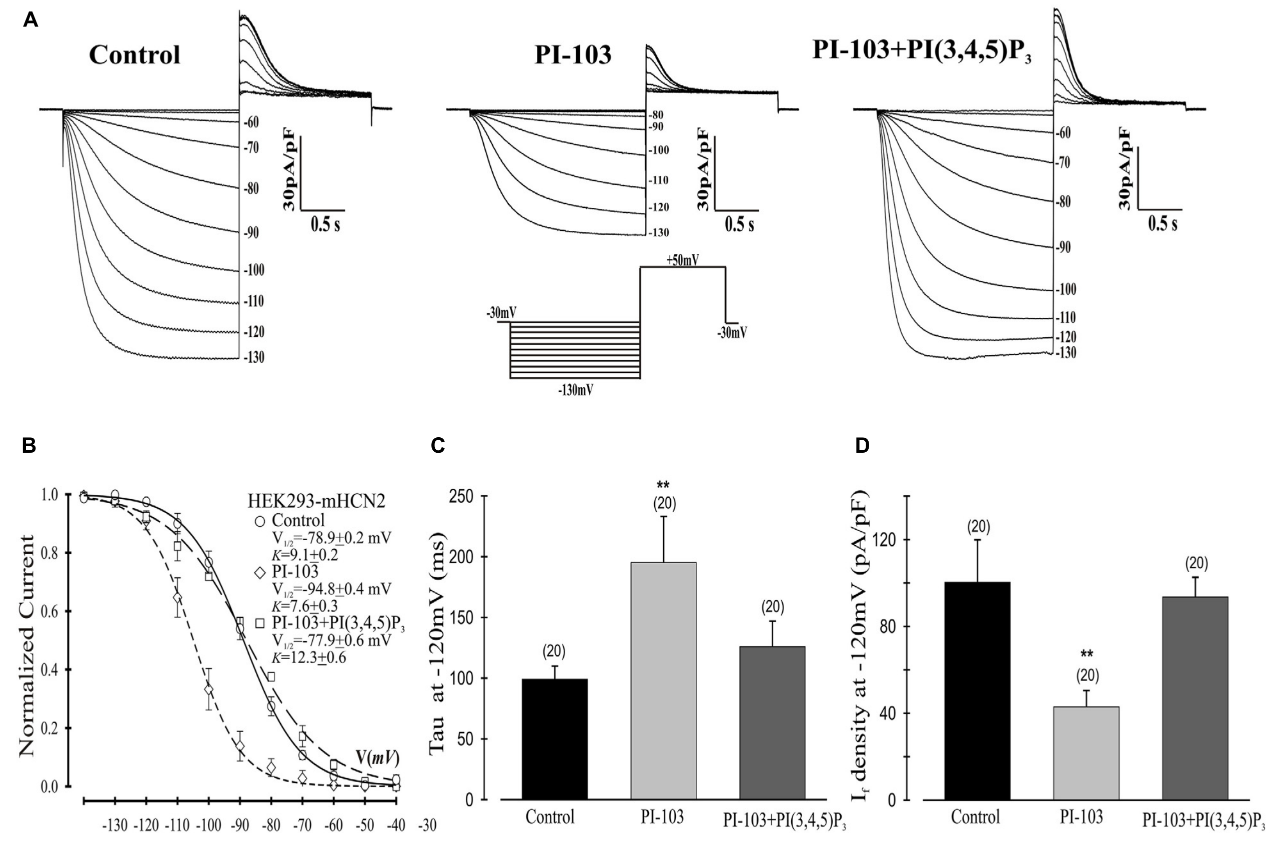

FIGURE 1 | Effects of PI-103 and PI(3,4,5)P_3 on I_f in HEK293 cells stably expressing mHCN2. **(A)** Traces of I_f activation in control cells or cells incubated for 2 h with 1 μM PI-103 or treated with PI-103 plus infusion of 1 μM PI(3,4,5)P_3 in the patch pipette. Inset: Voltage clamp protocol for activating I_f (see text for details). **(B)** Boltzmann fit of 1-s isochronal activation curves for I_f shows that PI-103 negatively shifted the voltage at half-maximal activation and infusion of PI(3,4,5)P_3 reversed the shifted midpoint to near the control level. **(C)** The mean time constants (tau) from a single exponential fit of I_f measured at –120 mV. **(D)** Summary data show a reduction of I_f amplitude by PI-103 which was reversed by PI(3,4,5)P_3. I_f was measured at –120 mV from a holding potential of –30 mV. Numbers above the bars show the number of cells examined. **, $P < 0.05$.

for I_f activation was to apply 1-s hyperpolarizing voltage steps ranging from -30 mV to -110 mV in -10-mV increments from a holding potential of -30 mV and then to apply a depolarizing step to + 50 mV for 0.5 s to record the tail currents, after which the preparation was stepped back to the holding potential. To generate the I_f activation curve, the normalized plot of tail current versus test voltage was fit with a Boltzmann function, and $V_{1/2}$ and K were calculated from the fit.

Cell Treatments

PI(3,4,5)P_3 or control phosphoinositides were diluted in internal solution to a final concentration of 1 μM and infused through the patch pipette. Where indicated, cells were pretreated with PI-103 (1 μM) or Akti (10 μM) for 2 h before patch clamping. HEK293 cells were treated with PI-103 or Akti at 37°C, and isolated SN cells were treated with Akti at room temperature.

Statistical Analysis

When comparing different sets of data, statistical analysis was performed with either Student's t tests or ANOVA; significance was set to $P \leq 0.05$. Results are given as mean ± SEM.

DNA Constructs

Mouse *Hcn2* cDNA was subcloned into pEGFP-C1, and the putative mHCN2 Akt phosphorylation site mutant, S861A, was made by PCR. The 50 μl PCR reaction contained 1x Ultra AD buffer (Stratagene), 200 μM of each dNTP, 30 ng DNA template, 0.25 μM of each primer, 1.5 μl PfuUltra AD DNA polymerase (Stratagene), and 3% dimethylsulfoxide. The PCR program was: (1) 95°C for 1 min; (2) 95°C for 1 min; (3) 68°C for 1 min; (4) 72°C for 9 min; (5) 13x to step 2; (6) 72°C for 10 min; (7) hold at 4°C. The mutation was confirmed by sequencing both DNA strands. The primers (Eurofins Genomics) used for mutagenesis were 5′-CTCGCGCCTCTCTGCCAACTTGTGACC (forward) and 5′-GGTCACAAGTTGGCAGAGAGGCGCGAG (reverse). The constitutively active myristoylated Akt construct (Ballou et al., 2001) was subcloned into pcDNA3.1(−).

Western Blotting and Immunoprecipitation

HEK293 cells were transiently transfected with the appropriate constructs using *Trans*IT-239 transfection reagent (Mirus Bio) and analyzed 2-3 days later. For western blotting, the cell layers were rinsed twice with PBS on ice and then scraped into a lysis buffer containing 50 mM HEPES, pH 7.5, 10 mM sodium pyrophosphate, 50 mM NaCl, 50 mM NaF, 5 mM EDTA, 0.1 mM sodium orthovanadate, 0.25% sodium deoxycholate, 1% IGEPAL CA-630, 200 μM phenylmethylsulfonyl fluoride, 1.7 μg/ml aprotinin and 2 μg/ml leupeptin. After strong vortexing, the lysates were centrifuged for 10 min at 4°C at 18,000 × g. Protein assays (Bio-Rad) were done on the supernatants, and equal amounts of protein were either directly subjected to SDS-PAGE or subjected to immunoprecipitation using GFP antibody. For immunoprecipitation, lysate supernatant was mixed with antibody and left on ice overnight, then protein G-agarose beads (Roche) were added. After rotating at 4°C for 2 h, the beads were washed 4 times with lysis buffer, boiled with SDS sample buffer, and subjected to SDS-PAGE. The proteins were transferred onto PVDF by semi-dry blotting, and signals were detected on film using horseradish peroxidase-linked secondary antibodies (GE Healthcare) and Western Lightning Plus ECL reagent (PerkinElmer). After signal detection, the blot was stripped at 50°C for 30 min in 62.5 mM Tris, 2% SDS, and 100 mM 2-mercaptoethanol, pH 6.7, reblocked in 5% non-fat dry milk in 20 mM Tris, 137 mM NaCl, and 0.1% Tween 20, pH 7.6, and probed with another antibody.

Reagents and Antibodies

Chemical agents employed in the studies include the pan-PI3K inhibitor PI-103 (Cayman Chemical), Akt inhibitor VIII (Akti; Millipore), and the diC8 phosphoinositides PI(3,4,5)P_3, phosphatidylinositol 3,5-bisphosphate (PI(3,5)P_2) and phosphatidylinositol 4,5-bisphosphate (PI(4,5)P_2) from Echelon Biosciences. The antibodies used targeted GFP (Santa Cruz sc-9996), phospho-Ser/Thr Akt substrate sites (Cell Signaling 9614), Akt phospho-Thr308 (Cell Signaling 9275), or HCN2 (Abcam ab19346). Active recombinant Akt1 protein was from Millipore.

RESULTS

We began by investigating the effects of PI-103, which inhibits all four isoforms of class I PI3K, on mHCN2-induced currents. As indicated in **Figure 1**, exposure of cells expressing mHCN2 to PI-103 reduced the amplitude of the mHCN2-induced current (panel A) and shifted the voltage dependence of activation in the negative direction (panel B). The voltage at half-maximal activation ($V_{1/2}$) was -78.9 ± 0.2 mV (control) versus -94.8 ± 0.4 mV (PI-103), a difference of 15.9 mV. These actions were prevented when PI(3,4,5)P_3, the second messenger produced by PI3K, was present in the pipette solution (**Figure 1**). To confirm that this was a specific effect of the PI3K second messenger, we performed additional experiments with control phosphoinositides PI(3,5)P_2 or PI(4,5)P_2 in the pipette solution. The results are provided in **Figure 2**. Panel A shows the raw data. Neither PI(3,5)P_2 nor PI(4,5)P_2 prevented the actions of PI-103. Panel B shows an absence of effect of either control phospholipid on the voltage dependence of activation, as well as an absence of effect on the current amplitude at −120 mV, where activation is nearly complete and the current activates rapidly enough to reach steady state during the test pulse.

Next we examined which downstream elements in the PI3K signaling pathway might mediate the decrease in mHCN2-induced conductance and the shift in the voltage dependence of activation to more negative potentials. We began by examining the actions of an Akt inhibitor (Akti) on mHCN2-induced current. The results are provided in **Figure 3**. Panel A provides raw data which indicate that Akti produced virtually identical effects on the mHCN2-induced currents as PI-103. This result suggested that Akt acts downstream of PI3K to regulate mHCN2 channels. In support of this hypothesis, pipette perfusion of active Akt protein in cells pretreated with PI-103 completely reversed the inhibitory effects of PI-103 (panel B). Panel C illustrates that Akti caused a 15 mV negative shift in $V_{1/2}$ as compared to the control, while panel D demonstrates that active Akt reversed the shift caused by PI-103. Finally, the effects of Akti alone or active Akt in the presence of PI-103 on mHCN2-induced current amplitude is provided in panel E. These results confirm that Akt functions downstream of PI3K to regulate the mHCN2-induced current.

It was possible that the actions of Akt were exerted through direct phosphorylation of the mHCN2 channel. We identified a number of potential Akt phosphorylation sites in HCN proteins, as illustrated in panel A of **Figure 4**. Interestingly, the sequence surrounding S861 at the C terminus of mHCN2 (RSRLSS$_{861}$NL) is identical in human, dog and zebrafish, and similar highly conserved sequences are found at the C termini of HCN1 (KPRFAS$_{908}$NL in mHCN1) and HCN4 (RSKLPS$_{1199}$NL in mHCN4). To determine if Akt regulates mHCN2 by acting on S861, we made a non-phosphorylateable alanine mutation at this site. The S861A mHCN2 mutant recapitulated both the reduction in amplitude and negative shift in activation voltage dependence of the mHCN2-induced current caused by treatment of the wild-type channel with PI-103 or Akti (panel B). This result suggested that the mutation prevents Akt-mediated phosphorylation and regulation of the channel. Indeed, Akti had no effect on the S861A mHCN2 current (panel C). As indicated in panel A, S861 is located at the C terminus, close to the cAMP binding site.

We next attempted to confirm the importance of this phosphorylation site by western blotting. We immunoprecipitated GFP-mHCN2 from cell lysates and then probed western blots of the immunoprecipitated proteins with an antibody that recognizes phosphorylated Akt consensus sites (RXXS-P/T-P). Panel A of **Figure 5** (upper blot) shows that expression of a constitutively active form of Akt (m-Akt) in cells stably expressing GFP-mHCN2 slightly increased the phosphorylation of the channel protein at these sites, whereas treatment with Akti abolished the signal. The middle blot demonstrates that similar amounts of GFP-mHCN2 protein were loaded in each lane, while the bottom blot demonstrates that phosphorylation (i.e., activation) of Akt and m-Akt was high in cells under control conditions, but nearly undetectable in cells treated with Akti. Panel B compares the response to Akti treatment of transiently transfected

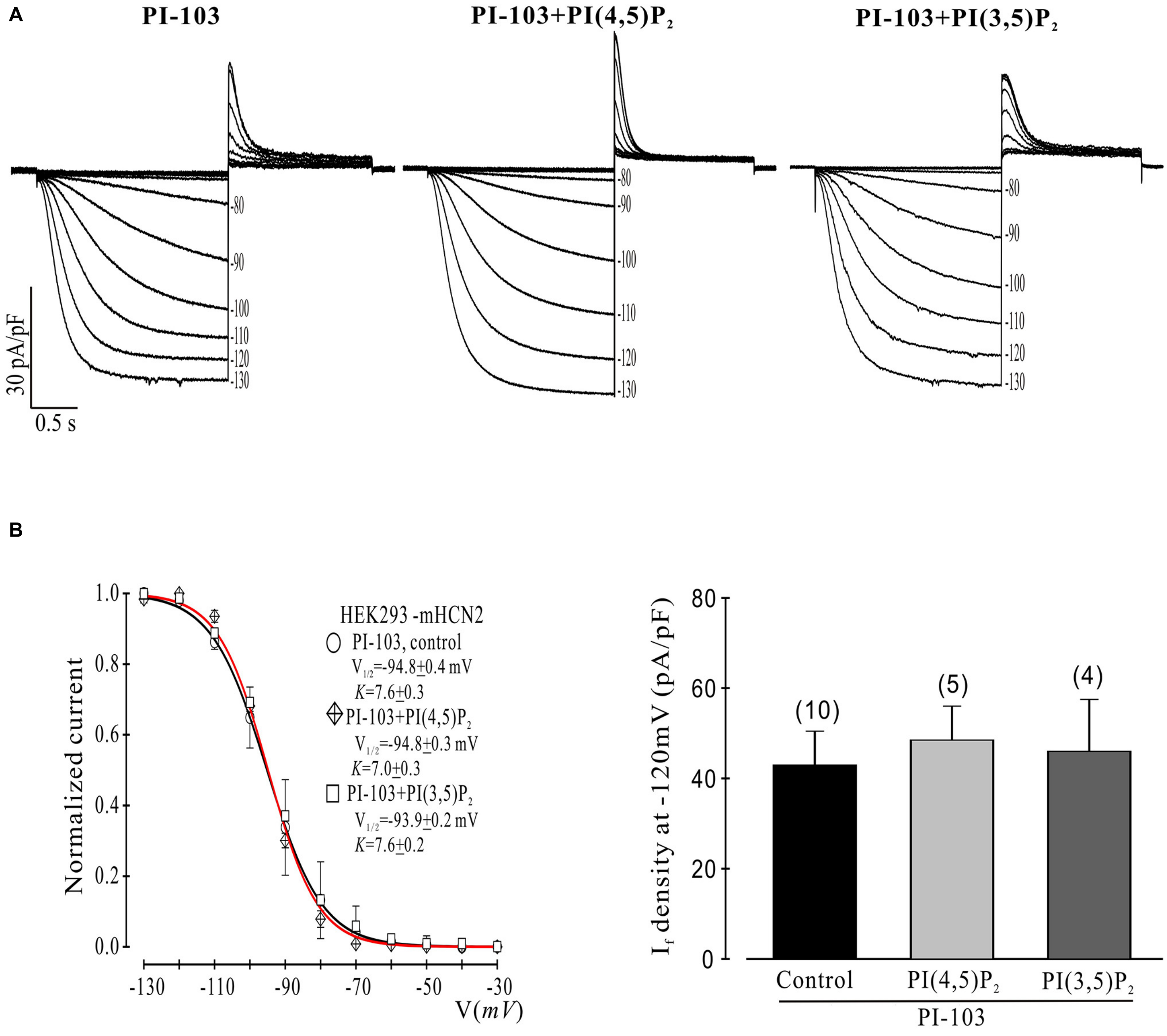

FIGURE 2 | Control phosphoinositides do not reverse PI-103 inhibition of mHCN2 current in HEK293 cells. **(A)** Original traces of PI-103-induced inhibition of mHCN2 current activation. Cells were incubated for 2 h at 37°C with 1 μM PI-103, with or without additional infusion of control phospholipid (1 μM) in the patch pipette solution. The voltage protocol for current activation is described in the text. **(B)** Activation curves from summarized data (left panel). The red curve is the fit to the PI-103 + PI(3,5)P_2 data. Summarized data show I_f density in the presence of PI-103 was not increased by control phospholipids (right panel). Numbers above the bars indicate the number of cells examined.

WT *vs.* S861A GFP-mHCN2. The upper blot shows that immunoprecipitates of cells transfected with empty vector contained a minimal level of protein containing phosphorylated Akt substrate sites, as expected. The strong signal for WT GFP-mHCN2 under control conditions was greatly reduced by Akti treatment, whereas S861A GFP-HCN2 did not appear to contain phosphorylated Akt substrate sites under either condition. The middle blot shows that the amount of channel protein was equivalent in the WT and S861A lanes, and the bottom blot shows that Akt was equally active in the WT and S861A cells and that Akti eliminated the activity of Akt. These results suggest that S861 may be the major Akt phosphorylation site in mHCN2. An alternative explanation is that mutation of S861 negatively affects Akt phosphorylation of another site.

Given the dominant effect of PI3K/Akt signaling on the mHCN2 isoform, we next decided to investigate whether Akti exerts similar effects on I_f in rabbit SN myocytes. The results are provided in **Figure 6**. The raw currents in panel A indicate little or no effect of the inhibitor on I_f. This observation was confirmed by the absence of a shift in the voltage dependence of activation

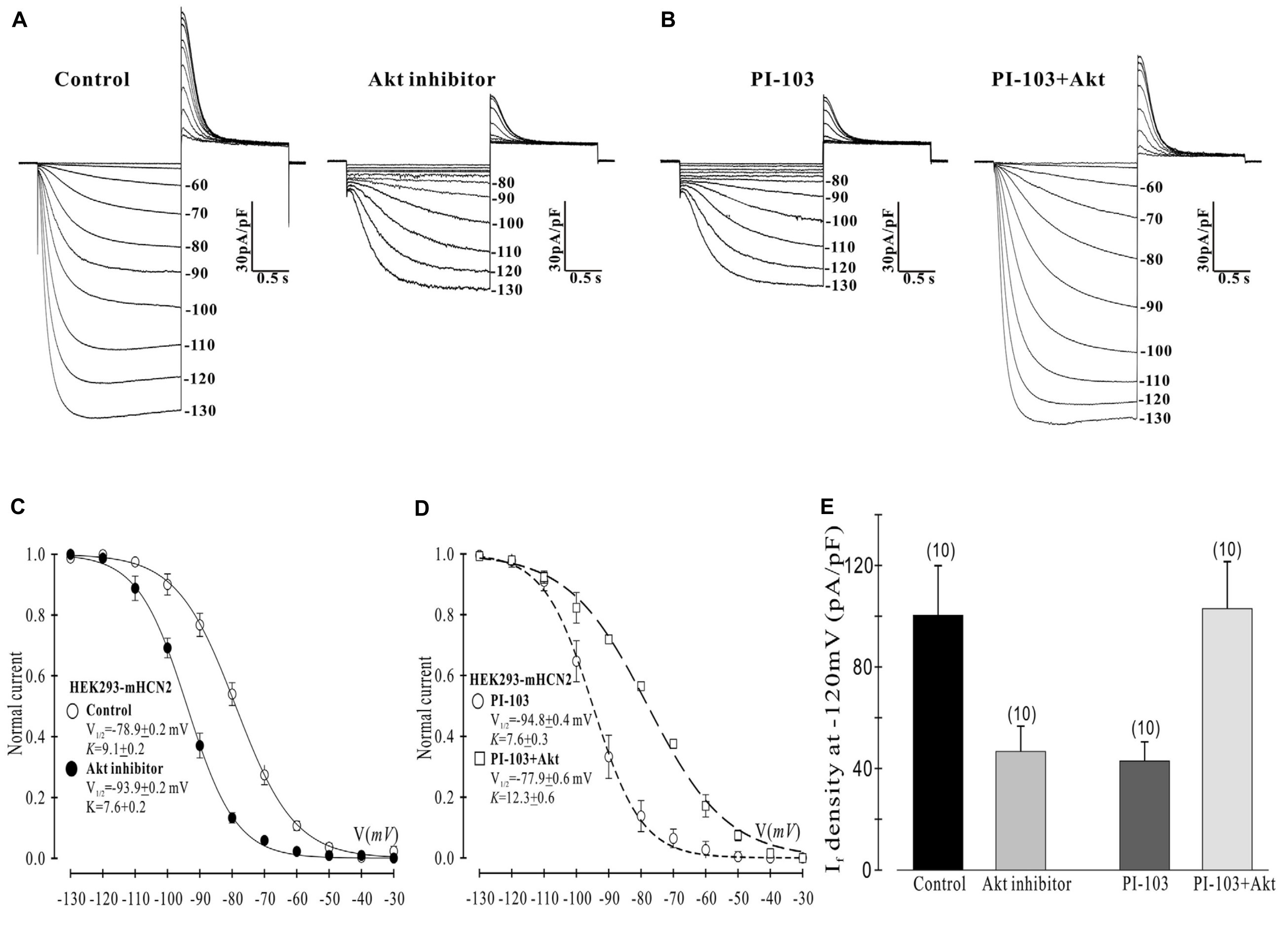

FIGURE 3 | Akt rescues the PI-103-induced inhibition of mHCN2 current in HEK293 cells. **(A,B)** Activation of mHCN2 currents. Cells were incubated for 2 h at 37°C with 10 μM Akt inhibitor (Akti) or 1 μM PI-103, or treated with PI-103 plus infusion of 20 nM active Akt1. The voltage protocol for current activation is described in the text. **(C,D)** Activation curves from summarized data. **(E)** Summarized data show a reduction of I_f density by the Akt inhibitor and rescue of the PI-103-induced reduction of mHCN2 current by Akt1. Numbers above the bars indicate the number of cells examined.

(panel B) or in the amplitude of the expressed current at −110 mV (panel C).

DISCUSSION

Although there is a clear understanding of the mechanism by which SN rate responds to changes in demand *via* the autonomic nervous system, much less is known about the determinants of basal heart rate. Basal heart rate is important, as it decreases with age, and this decrease can result in simple bradycardia as well as sick sinus syndrome (Adán and Crown, 2003). Recently, it was reported that the protein kinase AMPK may play a role in regulating basal heart rate by affecting I_f and Ca^{2+} release in the SN (Yavari et al., 2017). We reported that PI3K signaling also affects basal heart rate (Lin et al., 2019). PI3K inhibition slowed the SN rate both *in situ* and *in vitro* and shifted the activation of I_f to more negative potentials. By contrast, artificially increasing PI3K signaling by addition of PI(3,4,5)P_3 induced a positive shift in I_f. These shifts in voltage dependence were independent of and larger than those caused by autonomic agonists (Lin et al., 2019). A negative shift in the voltage dependence of I_f as well as a reduction in I_f magnitude have also been seen in mice with aging (Larson et al., 2013).

Proteins in the HCN family assemble as homotetramers or heterotetramers to form functional channels. We showed that heterologously expressed homotetramers of HCN1, HCN2 or HCN4 are differentially regulated by TKIs. The TKI genistein had no effect on HCN1, reduced the current magnitude of HCN4, and reduced the magnitude and caused a negative shift in the activation of HCN2 (Yu et al., 2004). Because TKs can activate PI3K signaling, we decided to investigate the effects of a PI3K inhibitor on HCN2 channels. Unlike HCN4 and HCN1, which are prominent in the SN, HCN2 plays a dominant role in ventricular myocytes. Similar to the results with genistein, we found that PI-103 reduced the amplitude and negatively shifted the activation of mHCN2 current. These effects were reversed by infusing PI(3,4,5)P_3 in the pipette, but not PI(3,5)P_2 or PI(4,5)$_2$. Selective reversal

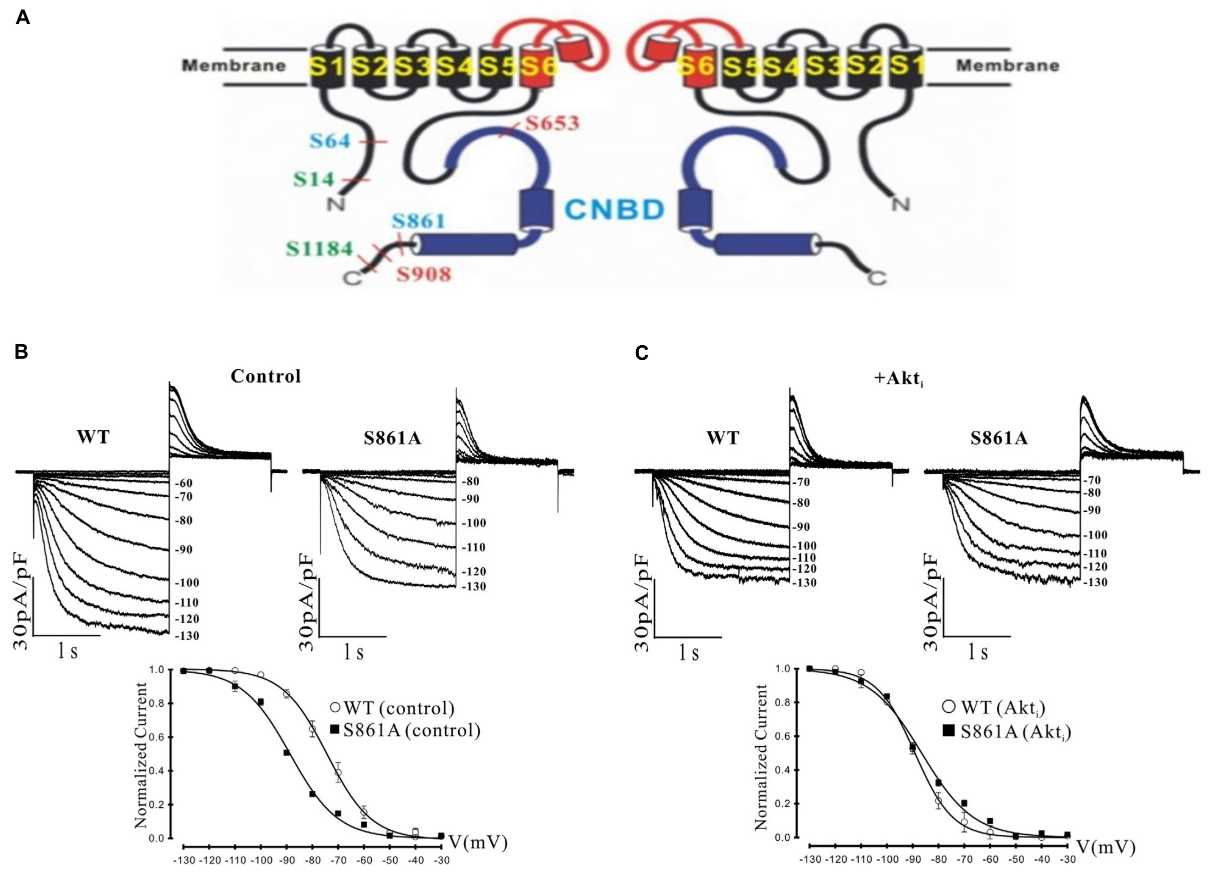

FIGURE 4 | Effect of a putative Akt phosphorylation site on mHCN2-induced current. **(A)** Potential Akt phosphorylation sites in HCN proteins. Shown are two of the four subunits that form HCN channels and the position of serines in HCN1 (red), HCN2 (blue), and HCN4 (green) located within consensus sequences for Akt phosphorylation. The pore and S6 transmembrane segments are red and the cyclic nucleotide-binding domain (CNBD) is blue. **(B,C)** Mutation of serine 861 to alanine (S861A) in mHCN2 causes an inhibition of expressed current in HEK293 cells. **(B)** Upper panels, sample traces of activation of transiently expressed WT and mutant mHCN2. Note a more negative activation threshold (–80 mV in S861A vs. –60 mV for WT) and a reduced current density at voltages (–130 mV) with maximal current activation. Lower panel, activation curves for WT and S861A mHCN2 fit with the Boltzmann equation. The $V_{1/2}$ values were -74.2 ± 0.4 mV (*n* = 10 cells, WT) and –88.6 ± 0.1 mV (*n* = 7 cells, S861A). The corresponding slope factors were 8.6 ± 0.4 mV and 9.2 ± 0.1 mV, respectively. The voltage protocol is described in the text. **(C)** Upper panels, sample traces of activation of transiently expressed WT and mutant mHCN2 in the presence of Akti (10 μM). Lower panel, activation curves for WT and S861A mHCN2 fit with the Boltzmann equation. Cells were incubated for 2 h at 37°C with Akti. The $V_{1/2}$ values were -89.1 ± 0.3 mV (*n* = 7 cells, WT with Akti) and –86.5 ± 0.7 mV (*n* = 7 cells, S861A with Akti). The corresponding slope factors were 7.4 ± 0.3 mV and 10.0 ± 0.7 mV, respectively. Note that Akti caused an inhibition of expressed WT mHCN2 and a negative shift in voltage dependence but no further inhibition of the expressed mutant current.

by PI(3,4,5)P_3 strongly suggests that the action of PI-103 is due to inhibition of PI3K. The positive effect of PI(4,5)P_2 on HCN2 currents seen under some conditions (Pian et al., 2006) thus apparently cannot compensate for the loss of Akt-induced phosphorylation of HCN2 that we believe underlies the effect of PI-103.

Several pieces of evidence indicate that Akt acts downstream of PI3K to regulate HCN2. First, Akti and PI-103 had nearly identical effects on HCN2, reducing current magnitude and shifting its activation to more negative potentials. Second, an active form of Akt reversed the actions of PI-103. Third, mutation of a putative Akt phosphorylation site in mHCN2 to alanine mimicked the effects of PI-103 or Akti on current amplitude and voltage dependence. The mHCN2 S861A current was also insensitive to Akti. Finally, WT mHCN2 expressed in cells exhibited increased phosphorylation of Akt sites when coexpressed with an activated form of the enzyme and decreased phosphorylation in the presence of Akti. By contrast, mHCN2 S861A did not seem to contain phosphorylated Akt sites.

Given the similar effects of PI-103 on mHCN2 and I_f in SN myocytes (Lin et al., 2019), we decided to investigate whether Akt also regulates I_f. We were surprised to discover that there was no observable effect of Akti on rabbit SN I_f. One possible explanation for this result is that even though HCN4 and HCN1 in the SN contain possible Akt phosphorylation sites at their C termini as discussed above, these sites do not contribute to channel regulation by PI3K. Alternatively, a kinase distinct from Akt might be responsible for phosphorylating these sites in the SN. SGK1 is one likely candidate, as it is activated downstream of PI3K, phosphorylates the same optimal peptide sequence as Akt, and is insensitive to Akti (Logie et al., 2007; Di Cristofano, 2017).

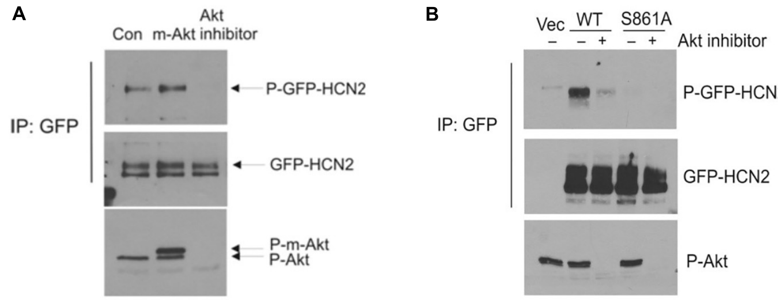

FIGURE 5 | Akt-mediated phosphorylation of GFP-mHCN2 protein. **(A)** HEK293 cells stably expressing GFP-HCN2 were transfected with vector (Con) or myristoylated Akt (m-Akt) and analyzed 2 days later or treated with 10 μM Akt inhibitor for 30 min. Cell lysates were subjected to immunoprecipitation with GFP antibody and the immunoprecipitated proteins were blotted for phospho-Ser/Thr Akt substrate sites (top) and HCN2 (middle). Cell lysates were analyzed with a phospho-Thr308 Akt antibody to assess the activation state of the enzyme (bottom). m-Akt migrates just above endogenous Akt. **(B)** Akt-mediated phosphorylation of GFP-HCN2 is abolished in the S861A mutant. HEK293 cells were transiently transfected with empty GFP vector (Vec), WT GFP-HCN2 or S861A GFP-HCN2. Two days later, the cells were treated with vehicle or 10 μM Akti for 1 h. Cell lysates were subjected to immunoprecipitation with GFP antibody, and the immunoprecipitated proteins were blotted for phospho-Ser/Thr Akt substrate sites (top) and GFP-HCN2 using HCN2 antibody (middle). The P-GFP-HCN2 signal comigrated with the upper band on the GFP-HCN2 blot. Cell lysates were analyzed with phospho-Thr308 Akt antibody to assess the activation state of the enzyme (bottom).

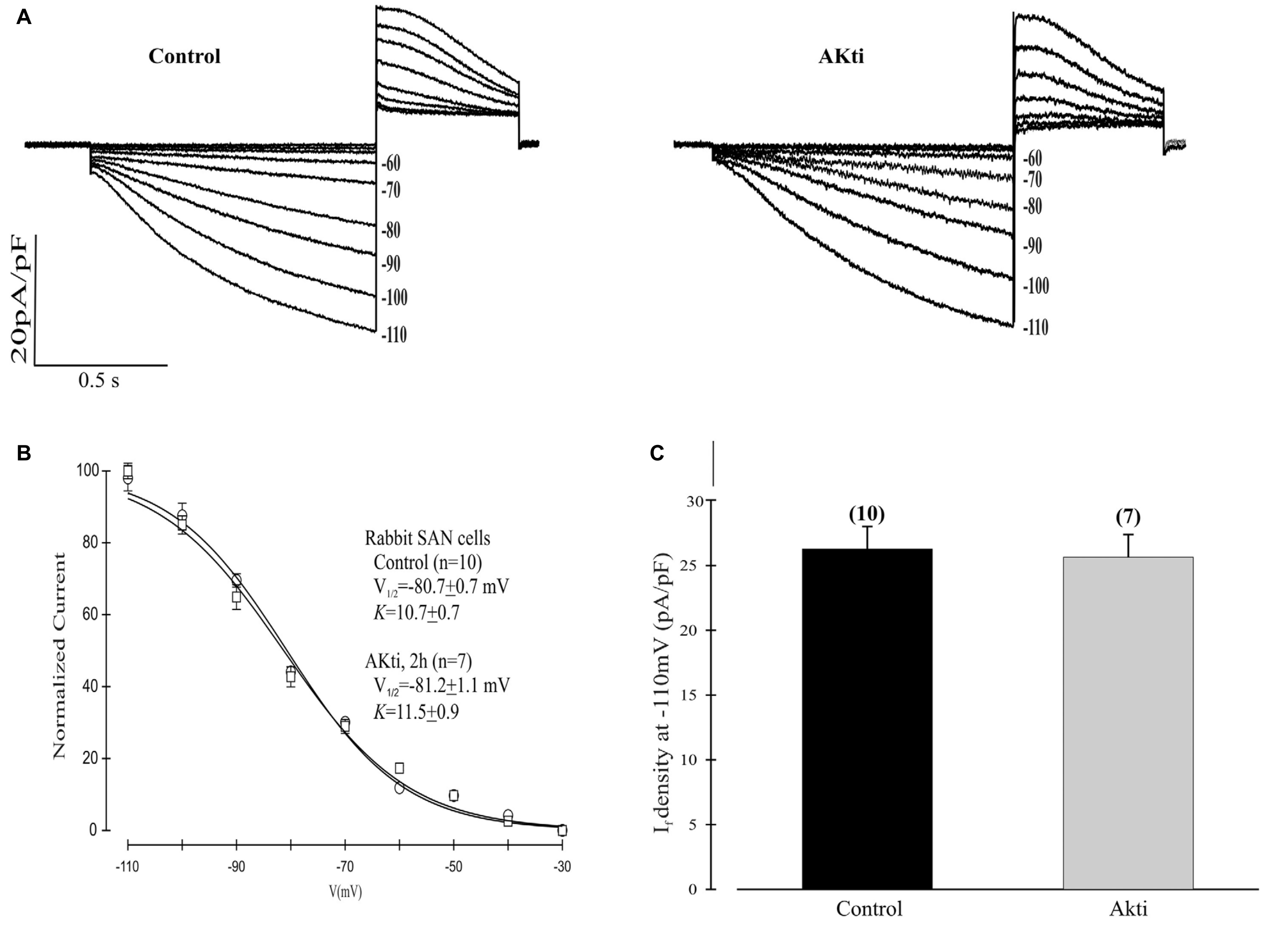

FIGURE 6 | Effect of Akti on I_f in SN cells isolated from rabbit heart. **(A)** Traces of I_f activation in control cells (left panel) or cells incubated for 2 h with 10 μM Akti at room temperature (right panel). **(B)** Boltzmann fit of 1-s isochronal activation curves for I_f shows that Akti did not shift the voltage at half-maximal activation. The $V_{1/2}$ values were -80.7 ± 0.7 mV (*n* = 10 cells, control) and –81.2 ± 1.1 mV (*n* = 7 cells, Akti). The corresponding slope factors were 10.7 ± 0.7 mV and 11.5 ± 0.9 mV, respectively. **(C)** Summary data show Akti did not affect I_f amplitude. I_f was measured at –110 mV from a holding potential of –30 mV.

Further studies using heterologous expression systems and SN myocytes are needed to elucidate how PI3K regulates HCN4, HCN1 and I_f.

CONCLUSION

In conclusion, our experiments suggest that PI3K regulates homotetrameric mHCN2 channels through Akt-dependent phosphorylation of S861. A reduction in PI3K/Akt activity causes a negative shift in the voltage dependence of activation and a decrease in current magnitude. By contrast, PI3K regulation the HCN4/HCN1 heterotetrameric channels that mediate I_f in the SN seems to be mediated by an alternative signaling pathway that does not involve Akt. Thus, consistent with previous results reporting differential effects of TKIs on HCN isoforms (Yu et al., 2004), our results suggest that regulation of HCN channels by PI3K/Akt signaling is also isoform specific.

DATA AVAILABILITY STATEMENT

The raw data supporting the conclusions of this article will be made available by the authors, without undue reservation. Requests to access the datasets should be directed to IC.

ETHICS STATEMENT

The animal study was reviewed and approved by the IACUC Stony Brook University.

AUTHOR CONTRIBUTIONS

ZL and HW designed, performed, and analyzed the patch clamp experiments. CG designed, performed, and analyzed the biochemical experiments. LB made constructs, designed, performed, and analyzed the biochemical experiments, and co-wrote the manuscript. RL conceived of the project, analyzed the data, and co-wrote the manuscript. IC conceived the project, analyzed the data, oversaw the execution of the patch clamp experiments, and co-wrote the manuscript. All authors contributed to the article and approved the submitted version.

FUNDING

This project was funded by the National Institutes of Health (DK108989 to RL and HL126774 to IC). It was also funded by a Leducq Foundation award entitled “Fighting Against Sinus Node Dysfunction and Associated Arrthymias” to IC.

REFERENCES

Adán, V., and Crown, L. A. (2003). Diagnosis and treatment of sick sinus syndrome. *Am. Fam. Physician* 67, 1725–1732.

Ballou, L. M., Lin, R. Z., and Cohen, I. S. (2015). Control of cardiac repolarization by phosphoinositide 3-kinase signaling to ion channels. *Circ. Res.* 116, 127–137. doi: 10.1161/CIRCRESAHA.116.303975

Ballou, L. M., Tian, P. Y., Lin, H. Y., Jiang, Y. P., and Lin, R. Z. (2001). Dual regulation of glycogen synthase kinase-3beta by the alpha1A-adrenergic receptor. *J. Biol. Chem.* 276, 40910–40916. doi: 10.1074/jbc.M103480200

Di Cristofano, A. (2017). SGK1: the dark side of PI3K signaling. *Curr. Top. Dev. Biol.* 123, 49–71. doi: 10.1016/bs.ctdb.2016.11.006

DiFrancesco, D. (1993). Pacemaker mechanisms in cardiac tissue. *Annu. Rev. Physiol.* 55, 455–472. doi: 10.1146/annurev.ph.55.030193.002323

Han, W., Bao, W., Wang, Z., and Nattel, S. (2002). Comparison of ion-channel subunit expression in canine cardiac Purkinje fibers and ventricular muscle. *Circ. Res.* 91, 790–797. doi: 10.1161/01.res.0000039534.18114.d9

Lakatta, E. G., Maltsev, V. A., and Vinogradova, T. M. (2010). A coupled SYSTEM of intracellular Ca^{2+} clocks and surface membrane voltage clocks controls the timekeeping mechanism of the heart’s pacemaker. *Circ. Res.* 106, 659–673. doi: 10.1161/CIRCRESAHA.109.206078

Larson, E. D., St Clair, J. R., Sumner, W. A., Bannister, R. A., and Proenza, C. (2013). Depressed pacemaker activity of sinoatrial node myocytes contributes to the age-dependent decline in maximum heart rate. *Proc. Natl. Acad. Sci. U.S.A.* 110, 18011–18016. doi: 10.1073/pnas.1308477110

Lin, R. Z., Lu, Z., Anyukhovsky, E. P., Jiang, Y. P., Wang, H. Z., Gao, J., et al. (2019). Regulation of heart rate and the pacemaker current by phosphoinositide 3-kinase signaling. *J. Gen. Physiol.* 151, 1051–1058. doi: 10.1085/jgp.201812293

Logie, L., Ruiz-Alcaraz, A. J., Keane, M., Woods, Y. L., Bain, J., Marquez, R., et al. (2007). Characterization of a protein kinase B inhibitor in vitro and in insulin-treated liver cells. *Diabetes* 56, 2218–2227. doi: 10.2337/db07-0343

Lu, Z., Wu, C. Y., Jiang, Y. P., Ballou, L. M., Clausen, C., Cohen, I. S., et al. (2012). Suppression of phosphoinositide 3-kinase signaling and alteration of multiple ion currents in drug-induced long QT syndrome. *Sci. Transl. Med.* 4:131ra50. doi: 10.1126/scitranslmed.3003623

Pian, P., Bucchi, A., Robinson, R. B., and Siegelbaum, S. A. (2006). Regulation of gating and rundown of HCN hyperpolarization-activated channels by exogenous and endogenous PIP2. *J. Gen. Physiol.* 128, 593–604. doi: 10.1085/jgp.200609648

Potapova, I., Plotnikov, A., Lu, Z., Danilo, P. Jr., Valiunas, V., Qu, J., et al. (2004). Human mesenchymal stem cells as a gene delivery system to create cardiac pacemakers. *Circ. Res.* 94, 952–959. doi: 10.1161/01.RES.0000123827.60210.72

Shi, W., Wymore, R., Yu, H., Wu, J., Wymore, R. T., Pan, Z., et al. (1999). Distribution and prevalence of hyperpolarization-activated cation channel (HCN) mRNA expression in cardiac tissues. *Circ. Res.* 85, e1–e6. doi: 10.1161/01.res.85.1.e1

Wu, J. Y., and Cohen, I. S. (1997). Tyrosine kinase inhibition reduces i(f) in rabbit sinoatrial node myocytes. *Pflugers Arch.* 434, 509–514. doi: 10.1007/s004240050430

Yavari, A., Bellahcene, M., Bucchi, A., Sirenko, S., Pinter, K., Herring, N., et al. (2017). Mammalian γ2 AMPK regulates intrinsic heart rate. *Nat. Commun.* 8:1258. doi: 10.1038/s41467-017-01342-5

Yu, H. G., Lu, Z., Pan, Z., and Cohen, I. S. (2004). Tyrosine kinase inhibition differentially regulates heterologously expressed HCN channels. *Pflugers Arch.* 447, 392–400. doi: 10.1007/s00424-003-1204-y

Conflict of Interest: The authors declare that the research was conducted in the absence of any commercial or financial relationships that could be construed as a potential conflict of interest.

HYPOTHESIS AND THEORY
published: 09 August 2021
doi: 10.3389/fcvm.2021.662410

Electrophysiological and Molecular Mechanisms of Sinoatrial Node Mechanosensitivity

Daniel Turner[1], *Chen Kang*[2], *Pietro Mesirca*[3], *Juan Hong*[2], *Matteo E. Mangoni*[3], *Alexey V. Glukhov*[1]* *and Rajan Sah*[2]*

[1] Department of Medicine, University of Wisconsin-Madison School of Medicine and Public Health, Madison, WI, United States, [2] Cardiovascular Division, Department of Internal Medicine, Washington University School of Medicine, St. Louis, MO, United States, [3] Institut de Génomique Fonctionnelle, Université de Montpellier, CNRS, INSERM, Montpellier, France

The understanding of the electrophysiological mechanisms that underlie mechanosensitivity of the sinoatrial node (SAN), the primary pacemaker of the heart, has been evolving over the past century. The heart is constantly exposed to a dynamic mechanical environment; as such, the SAN has numerous canonical and emerging mechanosensitive ion channels and signaling pathways that govern its ability to respond to both fast (within second or on beat-to-beat manner) and slow (minutes) timescales. This review summarizes the effects of mechanical loading on the SAN activity and reviews putative candidates, including fast mechanoactivated channels (Piezo, TREK, and BK) and slow mechanoresponsive ion channels [including volume-regulated chloride channels and transient receptor potential (TRP)], as well as the components of mechanochemical signal transduction, which may contribute to SAN mechanosensitivity. Furthermore, we examine the structural foundation for both mechano-electrical and mechanochemical signal transduction and discuss the role of specialized membrane nanodomains, namely, caveolae, in mechanical regulation of both membrane and calcium clock components of the so-called coupled-clock pacemaker system responsible for SAN automaticity. Finally, we emphasize how these mechanically activated changes contribute to the pathophysiology of SAN dysfunction and discuss controversial areas necessitating future investigations. Though the exact mechanisms of SAN mechanosensitivity are currently unknown, identification of such components, their impact into SAN pacemaking, and pathological remodeling may provide new therapeutic targets for the treatment of SAN dysfunction and associated rhythm abnormalities.

Keywords: automaticity, ion channel, cardiac, stretch activated, calcium, heart rate

OPEN ACCESS

Edited by:
Futoshi Toyoda,
Shiga University of Medical Science, Japan

Reviewed by:
Eilidh A. MacDonald,
University of Glasgow, United Kingdom
T. Alexander Quinn,
Dalhousie University, Canada

***Correspondence:**
Rajan Sah
rajan.sah@wustl.edu
Alexey V. Glukhov
aglukhov@medicine.wisc.edu

Specialty section:
This article was submitted to Cardiac Rhythmology, a section of the journal Frontiers in Cardiovascular Medicine

Received: *01 February 2021*
Accepted: *24 June 2021*
Published: *09 August 2021*

Citation:
Turner D, Kang C, Mesirca P, Hong J, Mangoni ME, Glukhov AV and Sah R (2021) Electrophysiological and Molecular Mechanisms of Sinoatrial Node Mechanosensitivity. Front. Cardiovasc. Med. 8:662410. doi: 10.3389/fcvm.2021.662410

INTRODUCTION

The heart is continuously experiencing a dynamic mechanical environment, both on a beat-to-beat basis (e.g., fluctuating blood pressure and exercise) and chronically (e.g., elevated venous return and high blood pressure). Alterations in intra-cardiac pressure and/or volume preload/afterload may influence cardiac performance to coordinate cardiac output with venous return and arterial blood supply, in a cardiac autonomous fashion. This process involves activation of complex mechano-electrical [i.e., mechanically induced changes in cardiac action potential (AP) morphology, frequency, and propagation] and mechanochemical (i.e., changes in various second messenger signaling that are ultimately translated into regulation of calcium handling) signal transduction feedback mechanisms that autoregulate the frequency and the force of cardiac muscle contraction (**Figure 1**). An important component of such autoregulation includes changes in heart rate controlled by the heart's primary pacemaker, the sinoatrial node (SAN). SAN response to altered hemodynamic load is described via the Bainbridge response: an increase in heart rate upon right atrial pressure/volume increase, which may help in matching cardiac output to venous return (1). SAN mechanosensitivity and associated changes in pacemaker activity have been demonstrated at multiple levels, including isolated heart (2, 3) as well as in isolated SAN cells (4), and have been linked to mechanosensitive mechanisms (5, 6) intrinsic to pacemaker cells (7). In this review, we summarize the emerging understanding of cellular and molecular mechanisms that could be involved in SAN mechanosensing and pacemaker rate attenuation. Though the exact components of mechano-electro-chemical signal transduction, specifically involved in SAN mechanosensitivity, are not currently identified, here, we overview possible candidates that might be responsible for both fast (i.e., within seconds or on beat-to-beat manner) and slow (minutes) changes in SAN automaticity in response to mechanical stress. Specifically, we focus on canonical mechanoactivated channels (Piezo, TREK, and BK), slow mechanoresponsive ion channels (including volume-regulated chloride channels (ClC), and transient receptor potential (TRP) channels), and the components of mechanochemical signal transduction, including reactive oxygen species (ROS), cyclic adenosine monophosphate (cAMP), and inositol trisphosphate (IP_3). Mechanosensitivity of these pathways has been described in either non-pacemaker cardiomyocytes (atrial or ventricular) or non-cardiac cells. Here, we show the expression profile of mechanosensitive ion channels in murine SAN (**Figure 2**) and discuss how these ion channels, as well as various mechano-chemical signaling pathways, could potentially modulate membrane and calcium clock components of the so-called coupled-clock pacemaker system (8), contributing to SAN mechanosensitivity and changing in heart rate upon alterations in intra-cardiac mechanics.

SINOATRIAL NODE ANATOMY

The SAN is a small body of specialized cardiac tissues located within the wall of the right atrium of the heart, laterally to the entrance of the superior vena cava, anatomically described by Silverman and Hollman (9). The SAN has a crescent-shaped structure positioned along the crista terminalis and running between the superior and inferior venae cavae, usually being arranged around a prominent nodal artery. The SAN is functionally insulated from the surrounding atrial myocardium, except for several critical conduction pathways (10–13). Indeed, the SAN requires anatomical (fibroblasts, adipose tissue, and blood vessels) and/or functional barriers (paucity of connexins) (13–16) to protect it from the hyperpolarizing influence of the surrounding atrium in order to function as a leading pacemaker. The presence of conduction barriers and pathways may explain how a small cluster of pacemaker cells in the SAN pacemaker complex manages to depolarize separate, widely distributed areas of the right atrium as evidenced functionally by exit points and breakthroughs (17–21). The autonomic nervous system and humoral factors can further regulate conduction through these pathways, contributing to pacemaker automaticity and ultimately determining heart rate (22–24).

MECHANOSENSITIVITY OF THE SINOATRIAL NODE

The SAN is well-positioned anatomically to sense both coronary and atrial blood pressure changes, providing a structural basis for hemodynamic regulation of heart rate via SAN mechanosensitivity. Changes in venous blood flow to the heart not only affect the volume available for atrial contraction and subsequent ventricular filling but also has an impact on the diastolic atrial dimension. Increased right atrial filling distends the atrial wall, including the SAN myocytes, which may consequently influence the pacemaker function and heart rate. This mechano-modulation of pacemaker activity was first described in 1915, when Bainbridge observed an increase in heart rate associated with right atrial distension from intravenous fluid injection in anesthetized dogs (1). While Bainbridge originally attributed this phenomenon to altering autonomic inputs, a study performed in dogs by Brooks et al. (25) determined that this positive chronotropic response was insensitive to adrenergic and cholinergic receptor blockade, and also to denervation, suggesting SAN intrinsic regulation of SAN automaticity. Conversely, in 1963, James and Nadeau demonstrated a bradycardic SAN response in dogs upon injection of fluid into the right atrium, while controlling for temperature, pH, osmolarity, oxygen, and ionic content (3). It was not until 1978, when Donald and Shepherd (2) performed controlled observations of human atrial and SAN mechanosensitivity by developing an experimental method that did not increase arterial blood pressure in humans (baroreceptor "depressor reflex"), that SAN mechanosensitivity was observed in humans. By placing subjects into a "supine" position, these researchers were able to observe an increase in heart rate concurrent with an increase in venous return to the heart. Lastly, Cooper et al. (4) determined that direct moderate stretch on isolated SAN cells, a possible consequence of increased venous pressure *in vivo*, induced elevated beating rate, confirming "for the first time, that the positive chronotropic response of the heart to stretch is, at least in part, encoded on the level of individual sinoatrial node pacemaker cells." Please refer to the review by Quinn and Kohl for a deeper examination on the history of SAN mechanosensitivity and canonical mediators (6).

While these cornerstone studies demonstrate the immediate or "fast" response of stretch on SAN automaticity, there is also growing evidence of "slow" activating channels (>1 min), ClC-2, for example (26), which can be activated by long-term pressure increases normally associated with the slow force response in the working myocardium (27). Prior to its naming,

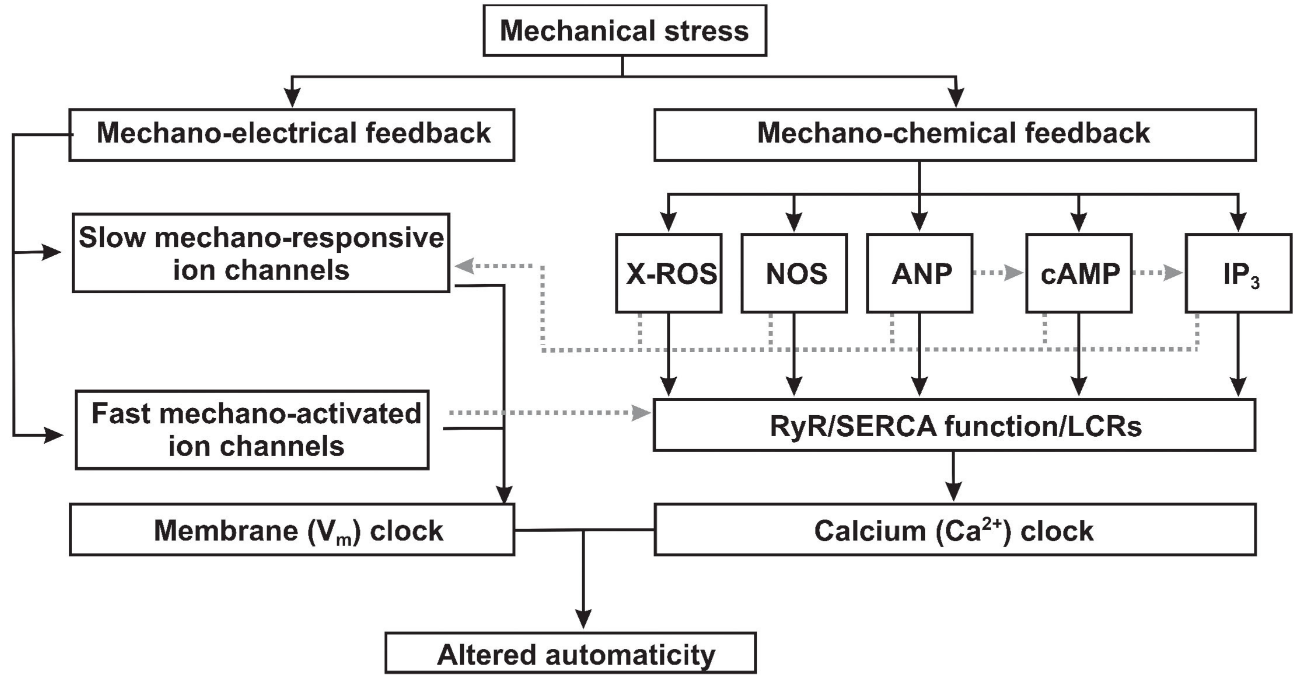

FIGURE 1 | Proposed mechanisms of mechano-electrical and mechano-chemical feedback contributions to sinoatrial node mechanosensitivity. Mechanical stress (1) triggers mechano-electrical signal transduction pathways via both slow mechano-responsive and fast mechano-activated ion channels directly changing the membrane (V$_m$) clock component of the coupled-clock pacemaker system; and (2) activates mechano-chemical feedback via various signaling factors which alters the function of the calcium (Ca^{2+}) clock component of the coupled-clock pacemaker system. ROS, reactive oxygen species; NOS, nitric oxide synthase; ANP, atrial natriuretic peptide; cAMP, cyclic adenoside monophosphate; IP$_3$, inositol triphosphate; RyR, ryanodine receptor; SERCA, sarcoplasmic reticulum Ca^{2+}-ATPase; LCRs, local calcium releases.

the slow force response was observed in feline and canine models. Gertrude et al. observed in isolated cat nodal tissue that sustained stretch accelerated beating rate and even induced spontaneous beating from quiescent nodal cells (28). From a similar group of researchers, Brooks et al. observed a similar response in anesthetized dogs (25). Using *in situ* SAN stretch, they observed a biphasic response to SAN stretch with an immediate acceleration of beating rate followed by a decrease to a rate still above pre-stretch levels (25). These gradual (over the course of minutes) and reversible changes in beating rate and cardiac contractility inherent of the slow force response may play a role in more delayed changes in SAN automaticity via slowly activating mechanosensitive channels (26, 29, 30) and various mechano-chemical signaling pathways (31–35).

ELECTROPHYSIOLOGICAL MECHANISMS OF SINOATRIAL NODE MECHANOSENSITIVITY

Overview of Sinoatrial Node Pacemaker Activity

Spontaneous beating of SAN myocytes is initiated, sustained, and regulated by a complex coupled system of cellular "clocks" that integrates ion channels and transporters on the cell membrane surface or "voltage clock," with subcellular Ca^{2+} handling machinery, also referred to as an intracellular "Ca^{2+} clock" (8, 36, 37) (**Figure 3**). The firing of SAN cells is due to diastolic depolarization, a slow depolarizing phase of the membrane potential (V$_m$), mediated by the concomitant action of both membrane and Ca^{2+} clocks. Since SAN cells lack I_{K1} current expression (41), following the minimum, or most hyperpolarized diastolic potential, potassium I_K current (I_{Ks}, and I_{Kr}) conductance decreases, allowing the inward hyperpolarization-activated current (I_f) (42, 43) and a low-threshold, voltage-gated T-type Ca^{2+} current ($I_{Ca,T}$), which contribute to the early fraction of diastolic depolarization (**Figure 3**) (44). In addition, L-type Ca$_v$1.3 Ca^{2+} channels open during diastolic depolarization to generate an inward Ca^{2+} current (45, 46) and enabling the sustained inward Na$^+$ current I_{st} (47). Local Ca^{2+} release (LCR) from the sarcoplasmic reticulum (SR) via subsarcolemmal ryanodine receptors (RyRs) generates small increments in intracellular Ca^{2+} concentration. These LCRs activate Na$^+$/Ca^{2+} exchange (NCX) to pump Ca^{2+} out of the cell in exchange for Na$^+$ ions at a ratio of 1 Ca^{2+}:3 Na$^+$, to generate an inward NCX current (I_{NCX}), and this contributes to both early and late phases of diastolic depolarization (48) and subsequent depolarization of the V$_m$ to the threshold of the next beat (**Figure 3**). The exact molecular mechanisms responsible for SR Ca^{2+} release during late diastole are not completely understood. While some studies show that such local Ca^{2+} release events

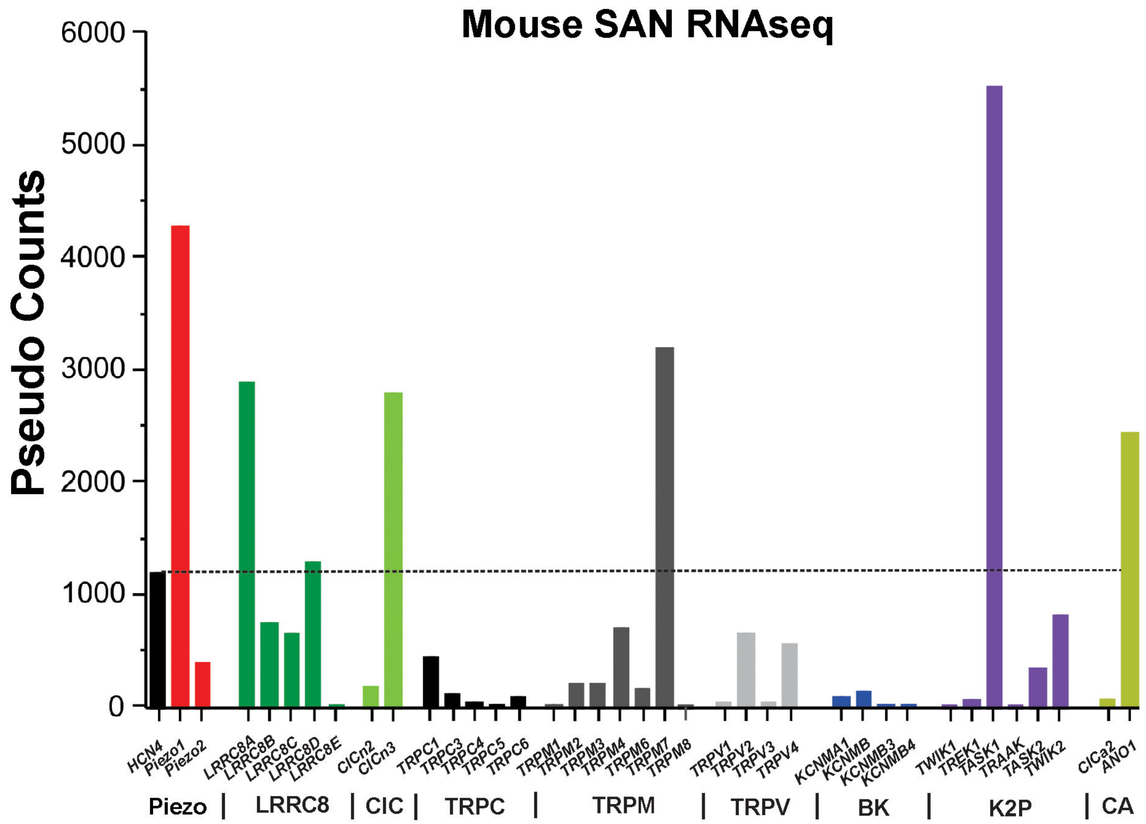

FIGURE 2 | RNAseq of mouse sinoatrial node. The graph shows the absolute values (in pseudo-counts) for mRNA expression level. Horizontal dotted line indicates HCN4 level. LRRC8, leucine-rich repeat containing 8 family chloride channels; ClC, chloride channel; TRPC/M/V, transient receptor potential cation/melastatin/vanilloid subtype ion channels; BK, Ca^{2+}-activated "big" potassium ion channels; K2P, two-pore domain potassium ion channels; CA, calcium-activated chloride ion channels; HCN4, hyperpolarization activated cyclic nucleotide gated cation channel 4.

are spontaneous, independent of transmembrane potential, and likely include stochastic opening of hyperphosphorylated RyRs (49–51), other evidence suggest that these events might be triggered by Ca^{2+} entry via low-voltage activated T-type Ca^{2+} channels (52) or $Ca_v1.3$ L-type Ca^{2+} channels (46). Particularly, recent studies indicate that $Ca_v1.3$ channel activity contributes to generation and synchronization of diastolic LCRs (46) and that $Ca_v1.3$ is necessary for the Ca^{2+} clock function during SAN firing (53). Overall, the sum of I_f, $I_{Ca,T}$, I_{NCX} and $Ca_v1.3$-mediated L-type Ca^{2+} current ($I_{Ca,L}$) contributes to diastolic depolarization required to ultimately trigger activation of cardiac $Ca_v1.2$-mediated $I_{Ca,L}$ that initiates the AP, and global Ca^{2+}-induced Ca^{2+} release. In nature, neither clock functions in the absence of the other. Abundant evidence indicates that functional interactions between the two clock components are critical for normal SAN automaticity (8, 36, 37, 46).

There has been significant interest in determining the underlying cellular and molecular mechanisms responsible for intrinsic SAN mechanosensitivity. Mechanical modulation of SAN pacemaking adds another level of complexity to SAN automaticity that has been proposed by Quinn and Kohl as the additional "mechanics-clock" (6, 7) or, more accurately, as a third coupled oscillator. The authors specifically highlighted that in case of fast, beat-to-beat changes in heart rate, the voltage and Ca^{2+} clocks do not inherently account for the rapid response of the SAN to changes in hemodynamic load and that another set of mechanisms must contribute to spontaneous diastolic depolarization of the SAN. The importance of "mechanics-clock" could be further supported by the fact that stretching of quiescent tissue frequently induces spontaneous activity. In particular, arrhythmic isolated hearts of *Prosobranch* gastropod become rhythmic when the pacemaker tissue is stretched by with internal perfusion and improve in form as pressure is increased (25). It may be more accurate to describe mechanical modulation of SAN pacemaking as an additional coupled oscillator since it could be applied to both fast and slow changes in heart rate through coupling with fast and slow mechanical oscillators, respectively.

Since ion channels are both central for the regulation of SAN automaticity and can sense mechanical stimuli via various mechanisms, they provide plausible molecular candidates for SAN mechanosensitivity. Ion channels may be grouped into two categories with respect to mechanosensitivity: (1) directly mechanoactivated (fast) and (2) indirectly mechanoresponsive (slow) (**Figure 1**). Although both categories of channels can change their open probability and other biophysical

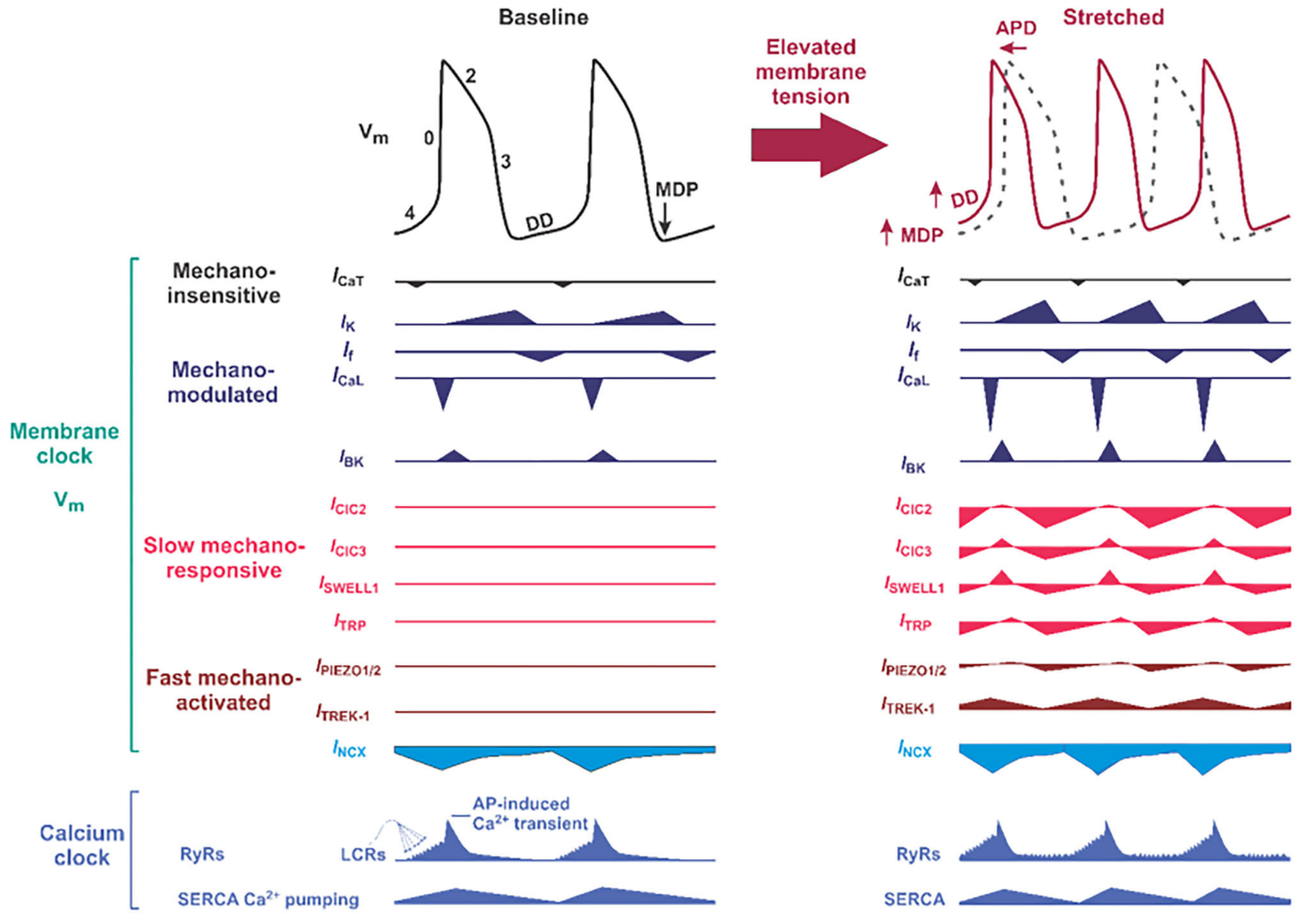

FIGURE 3 | Proposed molecular composition of the mechano-electrical signal transduction in the sinoatrial node (SAN) cell. (**Left**) Typical SAN membrane action potential (black trace) and the timing of membrane (V_m) clock and calcium (Ca^{2+}) clock components of the coupled-clock pacemaker system are shown. The phases of the action potentials are labeled including phase 4, in which diastolic depolarization (DD) that is key to automatic pacemaker activity takes place. APD, action potential duration; MDP, maximum diastolic potential; DD, diastolic depolarization; $I_{Ca,T}$ and $I_{Ca,L}$, T- and L-type voltage-dependent Ca^{2+} currents; I_{NCX}, sodium-calcium exchange current; I_K, rapid (I_{Kr}) and slow (I_{Ks}) delayed rectifier potassium currents; I_f, HCN4 “funny” current; SERCA, sarco-endoplasmic reticulum ATPase; LCRs, local Ca^{2+} releases. Below “classical” ion channels defined as mechano-modulated as indicated by various authors (38–40) which can have their normal activity altered by mechanical stress, proposed slow mechano-responsive, and fast mechano-activated ion channels are shown. ClC, chloride channels; SWELL1, swelling-activated leucine-rich repeat containing 8 (LRRC8) family chloride channels; TRP, transient receptor potential ion channels. (**Right**) Proposed changes in SAN action potential morphology (solod red trace on top of the black dotted trace for baseline condition) under mechanical stress. Below, proposed contribution of slow mechano-responsive and fast mechano-activated ion channels is shown for each ion channel.

characteristics in response to mechanical stimulation, they differ in how mechanical forces transduce these effects. Fast directly *mechanoactivated* ion channels (Piezo1-2, TREK-1, TRAAK, and BK channels) are intrinsically sensitive to mechanical forces applied to the protein or to the lipid bilayer in which the channel resides and do not require any other associated proteins or protein complexes to confer mechano-responsiveness (54, 55). Slow indirectly *mechanoresponsive* ion channels are polymodal ion channels (TRP channels, SWELL1/LRRC8, and ClC) that respond to mechanical forces in cell-type specific contexts but may not themselves be intrinsically mechanosensitive, for example, when reconstituted in a minimal lipid membrane, devoid of other cellular proteins, with some channels displaying faster activation kinetics and some slower.

RNA SEQUENCING IDENTIFIES HIGHLY EXPRESSED AND ENRICHED MECHANOSENSITIVE ION CHANNELS IN MOUSE SINOATRIAL NODE

There are a multitude of mechanosensitive and mechanoresponsive ion channels expressed in mammalian cells. However, without knowledge of the expression level of these channels in SAN, their relevance to SAN physiology is entirely speculative. To guide our discussion of the molecular mechanisms of SAN mechanosensitivity, we examined the expression levels of Piezo1-2, LRRC8a-e, TRPCs, TRPVs, TRPMs, K2P, and ClCs in a genome-wide RNA sequencing data set derived from murine SAN (**Figure 2**). Hyperpolarization-activated cyclic nucleotide-gated potassium channel 4 (HCN4) is robustly expressed and enriched in murine SAN. Remarkably, the most highly expressed mechanosensitive and mechanoresponsive ion channels (or essential components) in SAN are Piezo1 (3.6-fold greater than HCN4), LRRC8a [SWELL1/volume-regulated anion channel (VRAC), 2.4-fold greater than HCN4], ANO1 (2.04-fold greater than HCN4), and TASK-1 (4.6-fold greater than HCN4). Among TRP channels, the cells expressing TRPM7 were the most present (2.2-folds more than cells expressing HCN4), followed by cells expressing TRPM4, TRPV2, TRPV4, and TRPC1. Regarding mechanosensitive K2P channels, the number of counts for TREK-1 was lower than the number of HCN4. RNA sequencing data did not detect any cells expressing TRAAK. On the contrary, there were more counts for TASK1 than HCN4. Among ClC channels, the number of CICn3 counts was more than that for HCN4, the opposite for CICn2. Furthermore, RNA sequencing showed that the BK channel alpha subunit (KNCMA1) is lowly represented in SAN. Based on these data, we will discuss primarily those mechanosensitive/responsive ion channels that are highly expressed in SAN relative to HCN4. However, one limitation of mouse SAN is that they are the only known species to have a negative chronotropic response to sustained SAN stretch (56). Furthermore, please refer to **Table 1** as a resource for where the following ion channels have been confirmed, how they were analyzed, and their literature sources.

DIRECTLY MECHANOACTIVATED ION CHANNELS

Piezo Channels

Piezo1 and Piezo2 ion channels are bona fide mechanoactivated cation channels with established roles in the cardiovascular system (57, 72) and provide another potential mediator of SAN mechanosensitivity. These non-selective cationic channels may be activated by shear stress from nearby blood flow (laminar or turbulent) as well as membrane stretch induced by increased blood pressure, and their activation is highly sensitive to mechanical stimulus variation in frequency and duration (73). In addition, they are non-selective and are therefore permeable to Ca^{2+} and Na^{+}, in addition to K^{+}, and have a relatively low threshold for mechanoactivation (57, 74). Although there have been no studies directly examining Piezo1 in the SAN, it is expressed in cardiac tissue (54) and appears highly expressed in the murine SAN (**Figure 2**). Moreover, Piezo1 plays an important role in the regulation of vascular tone (54) and baroreceptor pressure sensing (55). Since Piezo1 channels provide a depolarizing current in response to mechanoactivation, they are good candidates for mechanically activated increases in SAN automaticity and heart rate acceleration (72). Moreover, Piezo1 channels activate rapidly (within milliseconds) and are responsive to phasic, high-frequency mechanical inputs, such as systolic contractions, but may also be modulated by more gradual mechanical inputs (75), such as increases in atrial filling pressures and could therefore govern SAN mechanosensitivity on a beat-to-beat basis and during periods of chronic stretch. Future studies with targeted genetic deletion of Piezo1 from SAN may directly test these hypotheses.

TREK-1 Channels

Cardiac cells have two-pore domain potassium currents with little time- or voltage-dependency, also known as background currents, that regulate resting membrane potential and cell excitability (76). The family of cloned mammalian background K^{+} channels includes 14 members encoded by different genes. The members were divided into six subfamilies, TWIK, TREK, TASK, TALK, THIK, and TRESK, on the basis of sequence homology and functional similarities (77). Two-pore domain potassium channels are typically insensitive to conventional K^{+} channel blockers such as 4-AP, TEA, Ba^{2+}, Cs^{+}, and glibenclamide (76), but they are sensitive to membrane stretch, changes in extracellular or intracellular pH, fatty acids, and inhalation anesthetic agents (e.g., isoflurane) and are regulated by second messenger phosphorylation (76). Structurally, these channels possess four transmembrane domains and two pore domains; each subunit contains two pore-forming domains, so two subunits can form a complete pore of the channels. In murine SAN (**Figure 2**), two subtypes of two-pore domain potassium channels are mainly expressed: stretch-activated K^{+} channel TREK-1 (78–80) and the acid-sensitive K^{+} channel TASK1 (81–83). Under basal conditions, the activity of the TREK channels is low; however, applying negative pressure to the cell membrane reversibly activates TREK-1 (84). In addition, laminar shear stress stimulates TREK-1, whereas the cell shrinkage induced by extracellular hyperosmolarity reduces the amplitude of TREK-1 (84). Indeed, it has been shown that TREK-1 mechanosensitivity is mediated directly by the lipid membrane perturbations and changes in plasma membrane tension (85). Given its expression in the SAN (**Figure 2**), it is a candidate contributor to SAN mechanosensitivity on a fast (<1 s) basis.

A number of studies on zebrafish and mice that inhibited plasma membrane trafficking of TREK-1 by inactivating the interacting proteins POPDC1 and POPDC2 revealed exercise- and age-dependent sick sinus syndrome and atrioventricular block (78, 86), suggesting a role for TREK-1 in cardiac automaticity. Similarly, transgenic overexpression of a C-terminal truncation of beta IV spectrin, which also disrupts TREK-1 plasma membrane trafficking, results in sick sinus syndrome (87). These studies provide indirect evidence of TREK-1-mediated effects on SAN automaticity. However, more direct evidence was provided by Unudurthi et al. (69). The authors determined that TREK-1 protein is indeed expressed in both murine and rabbit SAN, and TREK-1-like background currents were reduced in patch-clamped SAN cells isolated from cardiac-specific TREK-1 KO mice (αMHC-*Kcnk2*$^{f/f}$). Also, freely moving, telemetered αMHC-*Kcnk2*$^{f/f}$ mice exhibited sinus bradycardia at rest, consistent with studies by Hund et al. (87) where disrupted plasma membrane TREK-1 trafficking induced sick sinus syndrome. Paradoxically, isolated TREK-1 KO SAN cells exhibited increased rather than decreased firing rates as compared with wild-type (WT) SAN. Furthermore, exercise and treatment with

TABLE 1 | Compiled mechanosensitive ion channels discussed in the review, their known expression and detection method, and respective references.

Channel	Expression	References
Piezo1	Mouse heart homogenate (PCR), Mouse SAN (RNAseq)	(57); Present Publication
Piezo2	Mouse SAN (RNAseq)	Present Publication
LRRC8a	Mouse heart homogenate (PCR), rat and human atria (PCR, WB, IHC, IP), Mouse SAN (RNAseq)	(58, 59) Present Publication
LRRC8b-e	Mouse SAN (RNAseq)	Present Publication
ClC-2	Rat SAN (PCR), guinea pig SAN (PCR, IHC, ICC), mouse SAN (PCR, KO)	(26, 60, 61)
ClC-3	Mouse SAN (PCR), mouse atria (PCR, WB, KO), rat and human atria (PCR, WB, IHC, IP)	(59, 60, 62)
TRPC6	Rat SAN (PCR), mouse SAN (PCR, ICC)	(61, 63)
TRPM4	Mouse SAN (PCR, WB), mouse SAN (KO)	(64, 65)
TRPM7	Mouse SAN (PCR, WB, IHC, ICC, KO)	(66, 67)
TRPV1-4	Mouse SAN (RNAseq)	Present Publication
TREK-1	Rat and human SAN (PCR), mouse SAN (PCR, WB, IHC, KO), rabbit SAN (WB)	(61, 68, 69)
TASK-1	Rat and human SAN (PCR)	(61, 68)
TASK-2	Mouse, rat, and human SAN (PCR)	(60, 68)
BK	Mouse SAN (WB PCR, and IF)	(70) Present Publication
ClCa$_2$	Mouse SAN (IF and RNA seq)	(71)
ANO1	Mouse SAN (RNAseq)	Present Publication

epinephrine uncovered stress-induced sinus pauses in αMHC-*Kcnk2*$^{f/f}$ mice via unclear mechanisms, or possibly via variation in sympathetic and parasympathetic activity. Finally, intrinsic heart rates measured in telemetered αMHC-*Kcnk2*$^{f/f}$ mice with atropine and propranolol treatment exhibited no significant differences, suggesting that neurohumoral inputs are important for TREK-1-dependent regulation of SAN automaticity. These studies illustrate the incomplete understanding of TREK-1 and its contribution to SAN mechanosensitivity, which requires further investigation.

BK Channels

BK (large-conductance Ca^{2+}- and voltage-activated K^+) channels are another promising contributor to SAN mechanosensitivity and automaticity [reviewed in (88)]. These channels are characterized as having large single-channel conductance and selective inhibitors and are regulated by voltage and Ca^{2+} (70). Imlach et al. (89) determined that BK channel inhibition via paxilline caused a reduction in heart rate in isolated mouse and rat hearts but not in hearts from *Kcnma1* KO mice. This finding was confirmed at a cellular level when Lai et al. (70) demonstrated that paxilline applied directly to isolated mouse SAN cells reduced AP firing rate in WT mice but not in *Kcnma1* KO mice. Lastly, Zhao et al. (90) found that BK channels are mechanosensitive to a small degree, showing an increased activity in chick ventricular myocytes plated on stretched extracellular matrix. Given this and their expression in murine SAN (**Figure 2**), BK channels are a putative contributor to SAN mechanosensitivity. In this case, SAN membrane depolarization, increases in cytosolic Ca^{2+}, and mechanical stimulation from SAN/atrial systole all coincide to activate BK channels after the peak of the SAN AP to augment AP repolarization, re-initiation of diastolic depolarization, and heart rate acceleration (**Figure 3**). Based on this model, mechanoactivation of BK channels must be relatively rapid to contribute to SAN AP repolarization, as published data suggest; however, it remains unclear if these channels are rapidly or slowly mechanoactivated in SAN.

Mechanoresponsive Transient Receptor Channels

Putative candidates for stretch-responsive non-selective cation channels include TRP channels expressed in murine SAN: TRPC1, TRPC3, TRPM4, TRPM7, TRPV2, and TRPV4 (**Figure 2**). A number of TRP channels that we found expressed in murine SAN have been described as mechanoresponsive either directly or indirectly (29, 91). However, thus far, only TRPM4 and TRPM7 have been studied in the context of SAN function. TRPM4 is an intracellular Ca^{2+}-activated, non-selective cation channel, which is possibly indirectly mechanoresponsive (29). At negative membrane potentials, TRPM4 activation allows Na^+ influx, leading to the membrane depolarization, whereas, at the positive membrane potentials, TRPM4 allows K^+ efflux, leading to membrane repolarization (92, 93) (**Figure 3**). In rodent SAN, TRPM4 is thought to contribute to diastolic depolarization and a positive chronotropic response in response to stretch (64, 65, 94). TRPM7, an ion channel and protein kinase (chanzyme), permeable to both divalent cations, including Zn^{2+}, Mg^{2+}, and Ca^{2+}, as well as monovalent cations such as Na^+ and K^+ (95, 96), is broadly expressed. TRPM7 is highly expressed in murine SAN at the mRNA level (**Figure 2**) and generates a robust current in both SAN and atrioventricular node cells (66). Both cardiac- and SAN-targeted TRPM7 deletion impaired cardiac automaticity (67); however, the mechanism was proposed to be via regulation of *HCN4* and I_f current rather than a direct effect on diastolic depolarization via channel activity (66, 67). While it is clear that none of these TRP channels are intrinsically mechanoactivated (97, 98), it is possible that some of these channels form part of a mechanosensory system (29) and therefore may be mechanoresponsive within specific cellular contexts (99). Testing these hypotheses would require directly measuring these mechanoresponsive currents in isolated SAN, as performed by Kohl et al. (4, 100), in genetic knock-outs of each of these putative mechanoresponsive channels or using specific pharmacologic inhibitors.

Volume-Regulated Anion Channels

Another mechanoresponsive ionic current that has been implicated in the regulation of SAN automaticity is $I_{Cl,SWELL}$ or the swell-activated chloride current. This ionic current may be carried by VRAC or ClC ion channels, both of which are most commonly activated by cell swelling, which is typically achieved by applying hypotonic or hypo-osmolar solution to cells. However, in a few studies, anion or chloride conductances were demonstrated by application of mechanical forces, as described in further details below. VRACs are activated by cell swelling, ubiquitously expressed in various mammalian cell types and thought to be implicated in many physiological and pathophysiological processes, including fluid secretion, glutamate release, membrane potential regulation, and apoptosis [summarized in the review article (101)]. Although the biophysical properties of VRACs have been well-characterized in multiple cell types over the course of decades, the molecular identity of VRAC remained a mystery until the Patapoutian (58) and Jentsch (102) groups identified leucine-rich repeat containing 8a (LRRC8a, also known as SWELL1) as a required component of a heterohexameric channel complex consisting of various stoichiometries of LRRC8a, and/or LRRC8b,c,d,e. Although the function of the VRAC current has been attributed to cell volume regulation in response to relatively non-physiological osmotic gradients, the broad tissue expression pattern of LRRC8 proteins and presence of VRAC/$I_{Cl,SWELL}$ current in a multitude of cell types (103–108), including cardiac myocytes (109–113) that are rarely exposed to hypotonic swelling, suggests that the actual physiological role of VRAC and LRRC8 channels remains unknown. Indeed, experiments using magnetic dynabeads bound to monoclonal antibodies for beta1-integrins demonstrated activation of $I_{Cl,SWELL}$ in cardiac myocytes in response to mechanical force applied via magnetic fields (109, 110), supporting the notion that $I_{Cl,SWELL}$ is mechanoresponsive in cardiac cells. Therefore, given the high mRNA counts of LRRC8a (SWELL1) and associated subunits LRRC8b,c,d in murine SAN relative to HCN4 (**Figure 2**), the contribution of SWELL1-mediated $I_{Cl,SWELL}$ to pacemaker activity and response to stretch warrants further investigation.

Elegant studies by Hagiwara et al. (114) demonstrated that mechanical inflation of isolated rabbit SAN cells using positive pressure via the patch-pipette in whole-cell configuration induces an outwardly rectifying, stretch-activated anion current that is inhibited by chloride channel blockers, 4,4′-diisothiocyano-2,2′-stilbenedisulfonic acid (DIDs) and 9-anthracenecarboxylic acid (9-AC). Also, this current exhibits a shift in reversal potential consistent with a chloride conductance (115) and has a sequence of anion permeability ($I^- > NO_3^- > Br^- > Cl^- > F^-$) similar to VRAC or LRRC8 channels. $I_{Cl,SWELL}$ activates over the course of minutes (∼2 min), which implies responsiveness to tonic changes in membrane tension, as may be expected from gradual atrial stretch-associated increased venous return, but relatively unaffected by phasic changes associated with beat-to-beat changes. Based on the outwardly rectifying current–voltage relationship, and reversal potential around the Cl^- reversal potential ($E_{Cl} = -30$ mV), we speculate that inward chloride current at voltages below −30 mV may contribute to diastolic depolarization and SAN automaticity, while outward current at voltages above −30 mV may contribute to SAN AP shortening (116) (**Figure 3**). The integrated effects on automaticity and the response to stretch, however, are likely to be complex.

Similarly, Decher et al. found in guinea-pig atrial myocytes that $I_{Cl,SWELL}$ induced by osmotic swelling leads to a shortening of AP duration that was inhibited by DCPIB (a relatively selective $I_{Cl,SWELL}$ inhibitor) (117). Furthermore, Seol et al. found the $I_{Cl,SWELL}$ can be activated by axial stretch in cardiomyocytes isolated from the pulmonary vein (30, 59); and Egorov et al. determined that $I_{Cl,SWELL}$ activation in response to mechanical stretch can depolarize resting membrane potential, generate arrhythmic substrates, and confirm that it can also shorten APs (59). In isolated rabbit SAN tissue, Arai et al. also showed that application of various non-specific anion channel blockers that can block VRACs, such as DIDs, caused a reduction in the stretch-induced increase in firing rate at a high level of distension (118). On the other hand, Cooper et al. (56) reported that the application of 9-AC at 1 mM concentration had no effect on the stretch-induced increase in heart rate when a significant stretch-stimulus was applied, suggesting that $I_{Cl,SWELL}$ may not underlie the SAN response to mechanical stretch. However, application of such high concentrations of 9-AC is highly non-specific and therefore complicates the interpretation of this result. Furthermore, the use of different stretching techniques between the two studies may account for the differences observed. These studies, albeit contradictory, indicate the potential role of $I_{Cl,SWELL}$ in modulating SAN function on a slow, non-beat-to-beat basis, which may be present during periods of chronic stretch, and demonstrate the need for additional experiments. Since SWELL1 (LRRC8a) and LRRC8 subunit proteins are now known to encode $I_{Cl,SWELL}$ in numerous other cell types (103–108), future studies examining cardiac specific and SAN targeted *Swell1* KO mice, transient knockdown in isolated cells, and/or more specific small molecules such as DCPIB will provide important new insights into the contribution of $I_{Cl,SWELL}$ and VRAC in cardiac automaticity and the response to SAN stretch.

ClC Anion Channels

Other candidates for the molecular identity for $I_{Cl,SWELL}$ in SAN are the ClC ion channels. While both ClC-2 and ClC-3 have been studied in cardiac myocytes (26, 62), and ClC-3 has a high mRNA count in murine SAN (**Figure 2**), only ClC-2 has been directly studied with respect to regulating SAN automaticity. Huang et al. (26) showed that inwardly rectifying chloride current induced by osmotic swelling in isolated guinea-pig SAN pacemaker myocytes could be blocked though intracellular dialysis of anti-ClC-2 antibody, which did not affect other pacemaker currents, including I_f, $I_{Ca,L}$, and I_{Ks} and the volume-regulated outwardly rectifying Cl^- current ($I_{Cl,vol}$). Anti-ClC-2 antibody reversed the changes in SAN APs induced by osmotic swelling. The authors also showed that ClC-2 KO ($ClCN2^{-/-}$) mice demonstrate a decreased chronotropic response to acute exercise stress when compared with their age-matched $ClCN2^{+/+}$ and $ClCN2^{+/-}$ littermates. It was then concluded that targeted inactivation of ClC-2 does not alter intrinsic heart rate but prevented the positive chronotropic effect of acute exercise stress through sympathetic regulation of ClC-2 channels. While ClC-2 channels may contribute in part to cardiac $I_{Cl,SWELL}$, there have been no studies examining the signaling mechanisms underlying ClC-2 mechanoresponsivity.

ClC-3, on the other hand, has been proposed to be mechanoresponsive in osteoblasts (119) and has been shown to be expressed in cardiac myocytes, to underlie $I_{Cl,SWELL}$, and to be involved in numerous pathophysiological processes, including ischemic preconditioning, myocardial hypertrophy, and heart failure (120). However, there have yet to be any studies directly examining ClC-3 in SAN cells, and neither global nor cardiac specific ClC-3 KO mice were noted to show differences in heart rates (62).

Other Chloride Channels

Other possible contributors to SAN mechanosensitivity are calcium-activated chloride channels (CaCCs) such as anoctamin1 (ANO1) and chloride channel accessory 2 (ClCA2). Ye et al. (121) determined that ANO1 is expressed in mouse ventricular myocytes and facilitates accelerated AP repolarization. Given that ANO1 is implicated to be mechanoresponsive (121) and expressed in murine SAN (**Figure 2**), it is plausible that ANO1 may contribute similarly to shorten pacemaker potentials, as Sung et al. speculated (122). In addition, Mao et al. found that ClCA2 is highly expressed in SAN tissue and, when mutated, induces mild conduction block and ectopic pacemaker activity (71). While no study has examined ClCA2 mechanosensitivity, given its calcium-activated properties, it is likely to be affect by pressure-induced calcium transients (123). Given these findings, it is feasible that calcium-activated chloride channels could play a partial role in the response of SAN beating rate to stretch.

CAVEOLAE-MEDIATED ION CHANNEL MECHANOSENSITIVITY

Interestingly, besides ANO1 and ClCA2, all the aforementioned ion channels affected by mechanical stress have been found to associate with caveolae, which are abundantly expressed in SAN cells (5, 124, 125) and are known to mediate cellular response to mechanical stress by reserving "extra" cell membrane to buffer mechanical forces and contribute to cell volume regulation (126–128). Caveolae are small, 50- to 100-nm omega-shaped membrane invaginations of the plasma membrane enriched by sphingolipids, cholesterol, cavin proteins, and caveolin proteins. Caveolin-3 (129) is the dominant isoform in muscle cell caveolae; however, caveolin-1 has also been found in atrial myocytes (129, 130). It has been shown that caveolae compartmentalize multiple ion channels involved in SAN pacemaker activity, such as canonical contributors to the SAN AP such as HCN channels (131), L-type calcium channels, and $K_v1.5$ channels (132), as well as anion channels such as SWELL1 (LRRC8a), ClC-2, and ClC-3 (59, 103, 105, 108). Stretch-induced disruption of caveolae may participate directly or indirectly via localization of other signaling factors (133) in the activation of mechanoresponsive ion channels, including VRAC and ClC ion channels responsible for $I_{Cl,SWELL}$ (134). Specific surface membrane proteins may not only affect changes in membrane potential but also directly or indirectly regulate intracellular Ca^{2+} cycling; on the other hand, intracellular Ca^{2+} cycling proteins may also regulate V_m via Ca^{2+} modulation of surface membrane electrogenic molecules (135).

MECHANOCHEMICAL SIGNAL TRANSDUCTION

While changes in cardiac morphology are attributed to mechano-electrical signal transduction via regulating the activity of mechanosensitive ion channels, mechanochemical signal transduction could be described as a mechano-induced regulation of various second messenger signaling pathways that are ultimately translated into changes of calcium handling and ion channel activity. Here, we focus on mechano-dependent regulation of ROS, cAMP, and IP_3 signaling pathways (**Figure 4**). It should be noted that mechano-electrical and mechanochemical feedbacks are not mutually independent but rather interact in a complex and dynamic manner as described below. While mechanochemical signal transduction pathways could be involved in the regulation of various ion channels via different post-translational modifications (such as phosphorylation, nitrosylation, and oxidation), activation of mechano-electrical feedback can significantly modify intracellular ion composition affecting intracellular Ca^{2+} signaling. Below, we briefly summarize several key mechano-chemical signaling pathways that could be involved in SAN mechanosensitivity. Though the role of these pathways has not been demonstrated in SAN mechanosensitivity, it is feasible that they have an impact on mechanical heart rate modulation.

Petroff et al. (33) were the first to use confocal microscopy to monitor subcellular Ca^{2+} events in cardiomyocytes during stretch and to provide direct evidence that stretch modulates the elementary Ca^{2+} release process, the Ca^{2+} spark. Stretch-induced increases in Ca^{2+} spark frequency are a phenomenon consistently observed in myocytes (136, 137), also in response to other mechanical stimuli, such as shear stress and afterload (123). A single myocyte stretch event immediately—within milliseconds—triggers a burst of Ca^{2+} sparks, which is reversible and declines within seconds (137, 138). While in ventricular myocytes these sparks

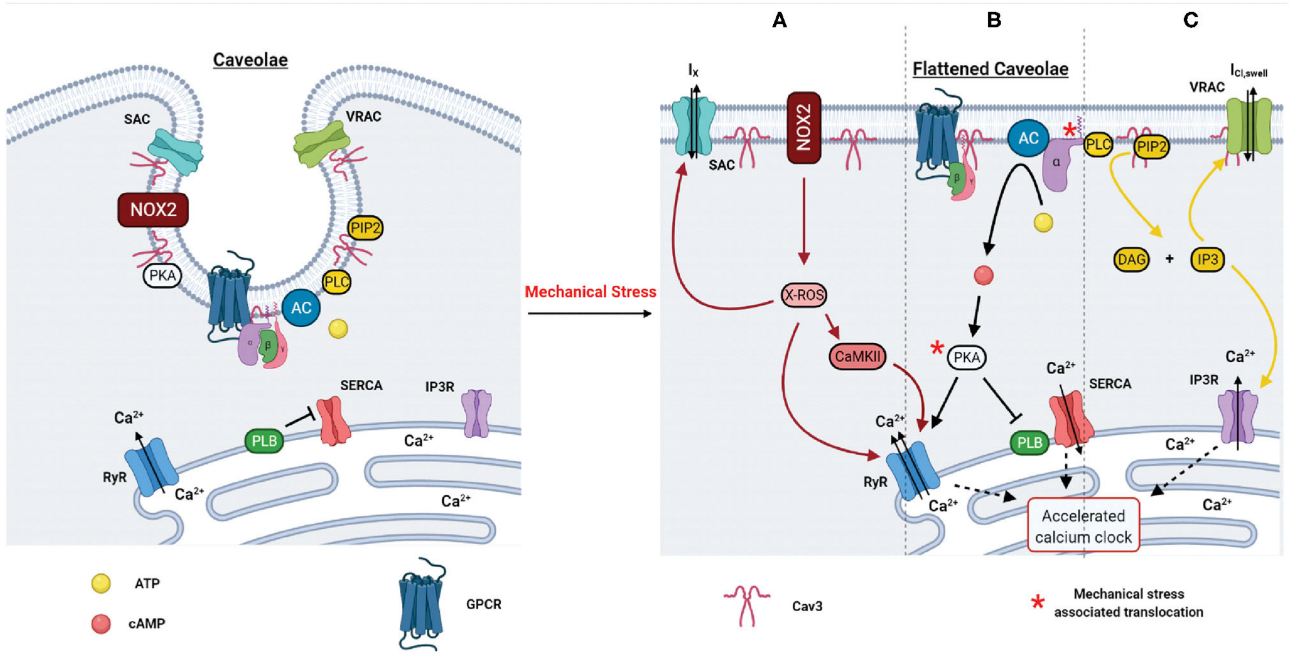

FIGURE 4 | Proposed effect of mechanical loading on caveolae-associated signaling pathways and their effect on sinoatrial node calcium clock function. Mechanical stress: **(A)** Activates X-ROS signaling via NOX2 (NAPDH oxidase 2) which stimulates CaMKII activity and upregulates RyR (ryanodine receptor) function leading to an accelerated calcium clock, as well as sensitizes SAC (stretch-activated channels) for increased activation. **(B)** Displaces the GPCR alpha subunit, activating AC (adenylyl cyclase)-mediated conversion of ATP to cAMP, which activates PKA leading to an accelerated calcium clock via RyR activation and PLB (phospholamban) inhibition of SERCA (sarcoplasmic reticulum Ca^{2+}-ATPase). **(C)** Induces PLC (phospholipase C)-mediated conversion of PIP2 to IP$_3$ (inositol triphosphate), which activates IP$_3$ receptors (IP$_3$R) and an accelerated calcium clock and also activates VRACs (volume regulated anion channels). All three pathways lead to accelerated cardiomyocyte calcium cycling, LCR (local calcium releases) rate, and increased activity of mechanosensitive channels.

are restricted in time and space, unique patterns of RyR expression and the presence of bridging RyR groups between large clusters demonstrated in the SAN cells (139–141) could lead to the generation of propagating LCR events as demonstrated in modeling studies by Stern and colleagues (141). This mechanism of stretch-induced increase in Ca^{2+} spark activity might be also present in the SAN and potentially contribute to mechanical regulation of Ca^{2+}-clock activity (**Figure 4**).

NOX2–Reactive Oxygen Species

Mechanical modulation of Ca^{2+} spark activity was linked to stretch-induced activation of ROS signaling that is also graded in a stretch-dependent manner (142). The stretch-induced NOX2-dependent ROS response sensitizes RyR to Ca^{2+} possibly through direct oxidation but may also do so indirectly via oxidation of calmodulin, displacing it from the RyR and promoting activation (143) or via RyR phosphorylation by oxidized CaMKII (144). These pathways of mechano-transduction are termed X-ROS signaling and require an intact microtubule network and functions independently of stretch-activated channels (SACs) and transsarcolemmal Ca^{2+} influx (33, 137). Furthermore, X-ROS signaling is confined to dyads (the cytosolic space between the sarcolemmal and SR membranes) (145) and has been proposed to be an important regulator of beat-to-beat adaptation to hemodynamic load in working cardiomyocytes (142). However, these pathways have not been confirmed specifically in SAN myocytes, but they are known to contain the necessary components (146).

In addition to regulation of Ca^{2+} signaling, the X-ROS pathway has also been found to be involved in the modulation of mechanoresponsive ion channels as well (147). Patch-clamp studies on stretched ventricular myocytes revealed NOX-dependent modulation of SACs (148), and this modulation may be facilitated by co-localization of NOX2 and SAC in caveolae (149, 150). Although SACs are not involved in X-ROS signaling per se, these channels may contribute to stretch-induced modulation of AP as discussed above for mechano-electrical signal transduction. Additionally, $I_{Cl,SWELL}$ activated by osmotic swelling has been found to be controlled by an angiotensin II-dependent ROS cascade that is previously implicated by integrin stretch (113). This is consistent with persistent activation of $I_{Cl,SWELL}$ and ROS present in several models of cardiac disease. Furthermore, Gradogna et al. demonstrated that LRRC8 channel subunits and their currents are differentially modulated by oxidation depending on LRRC8 channel subunit composition (151). Given that inflammation and oxidation are present in the setting of hypertension, it is possible that SAN mechanosensitivity could differ from other cardiac regions due to varying SWELL1 subunit expression (151).

Nitric Oxide Synthase

Nitric oxide synthase (NOS) also plays a discrete role facilitating cardiac stretch as Petroff et al. demonstrated that stretch increases nitric oxide (NO) production with concurrent increases in Ca^{2+} spark frequency and transient amplitudes (33). Pharmacological inhibition or genetic deletion of both neuronal NOS (nNOS) and endothelial NOS (eNOS) demonstrates that subtypes contribute to the increase of systolic Ca^{2+}, but only nNOS participated in the afterload induced Ca^{2+} sparks (152). Due to the short lifetime of NO, its effective signaling range is limited and dependent on the diffusion distance, amount produced, and the buffer capacity of the cell (33). Therefore, one possible explanation for the distinct effects of nNOS vs. eNOS-derived NO on Ca^{2+} sparks is their different subcellular localizations. While eNOS is localized at the caveolae (153, 154), nNOS is preferentially localized at the SR membrane in the vicinity of RyR, and nNOS increases RyR Ca^{2+} leak, directly by S-nitrosylation or indirectly via CaMKII (155). In addition, nNOS facilitates SERCA Ca^{2+} reuptake (155), which may compensate for the increased SR Ca^{2+} leak and reduced basal $I_{Ca,L}$ (156). In regard to the SAN, in a study by Vila-Petroff et al. using exogenous NO donors, high levels of NO induced a large increase in cGMP and a negative inotropic effect, while low levels of NO increased cAMP and caused positive inotropy via cGMP-independent activation of adenylyl cyclase (157). Furthermore, it has been shown that inhibition of NOS has a negative chronotropic effect on SAN activity and that NOS activation has an opposite effect, indicating that SAN function is somewhat dependent on NOS activity (158, 159). However, unlike X-ROS signaling, NO mechanosensitivity operates on a slower time scale of minutes rather than seconds (33), suggesting that it may play a more significant role in conditions where chronic stretch is a factor (i.e., hypertension and chamber filling pressures).

Atrial Natriuretic Peptide

Another important factor in myocyte stretch signaling is atrial natriuretic peptide (ANP) (160). Similar to X-ROS, ANP is a mechanosensitive signaling factor that is activated by a caveolae and angiotensin II-dependent pathway (161). ANP has been found to enhance reflex bradycardias (162); therefore, it is likely that ANP has a compensatory mechanosensitive role on the SAN, acting to restore it to normal function in response to elevated stretch. ANP has been found to shift midpoint activation of pacemaking I_f current toward less negative potentials (163) and thus accelerate SAN rhythm. ANP is also able to increase intracellular cGMP and cAMP levels (163), which play a crucial role in SAN automaticity via phosphorylation of the calcium clock proteins (50, 164). Indeed, ANP has been identified as a critical regulator of SAN automaticity (38, 165).

Inositol Trisphosphate

IP_3Rs are another type of SR Ca^{2+} release channels, which are activated by IP_3 through the hydrolysis of phosphatidylinositol-(4, 5)-bisphosphate by phospholipase C and thus may also contribute to the LCR generation via hypersensitization of RyRs. They are highly abundant in atrial and SAN myocytes (166–168), and recent studies demonstrated that this signaling pathway might be confined within specific microdomains, including lipid rafts and dorsal ruffles (169). Stimulation of IP_3Rs was found to accelerate spontaneous beating rate of the mouse SAN likely through regulation of Ca^{2+} spark activity and RyR function (170). In rabbit ventricular myocytes, upregulation of IP_3R-induced Ca^{2+} releases was detected and linked to enhanced spontaneous SR Ca^{2+} releases (170). It has been shown that mechanical stretch can directly activate phospholipase C with production of IP_3 (171), which may subsequently modulate SAN automaticity (**Figure 4**).

Mechanochemical Signal Transduction and Caveolae

While there are numerous mechanochemical signaling factors that may affect SAN automaticity, they are united as facilitators of cardiac mechano-transduction through their association with caveolae membrane structures (**Figure 4**) (123, 172–174). For example, NOS (173), NOX2-mediated ROS (150), and calcium dynamics (123) are all affected by the presence of caveolae, which are suspected to play an inhibitory role on these factors, which are disrupted by shear stress. Digging deeper, angiotensin II mediates activation of cAMP production (175) and X-ROS through caveolae membrane structures (176), further linking the discussed factors to these structures. The suspected regulation of these signaling factors of SAN automaticity by caveolae may explain the connection between caveolae loss and cardiac pathology (177) as chronic shear stress depletes caveolae (178), allowing these factors to activate constitutively and/or enter unusual feedback loops. For example, as shear stress increases, caveolae flatten and release NOS, which should reduce the initial mechanical stimuli and allow caveolae to reform. However, if the mechanical stimulus is prolonged, membrane caveolae density will decrease, eliminating a crucial regulator of nNOS activity. Without this negative regulation, these signaling factors can enter positive feedback loops, inducing the generation of excess ROS from sarcolemmal and mitochondrial sources that can ultimately lead to changes in myocyte electrophysiology as calcium kinetics are subsequently altered. For these reasons, it is highly plausible that SAN caveolae may regulate downstream signaling factors that are known to alter SAN automaticity and consequently heart rate.

PATHOPHYSIOLOGY

While physiological stretch provides a critical autoregulatory feedback loop to adjust SAN pacemaker rate upon hemodynamic changes, pathophysiological stretch (and physiological stretch applied to diseased myocardium) can lead to SAN dysfunction and trigger cardiac arrhythmias (6, 7, 179). It has been shown that conditions associated with atrial pressure and/or volume preload/afterload, including heart failure, atrial fibrillation, hypertension, and valvular disease, are common comorbidities linked to SAN dysfunction or sick sinus syndrome (23, 180–183). Sick sinus syndrome is manifested clinically as arrhythmias that can include sinus bradycardia, sinus pauses or arrest, sinoatrial exit block, or alternating brady- and tachyarrhythmias (184).

These manifestations can lead to chronotropic incompetence, which is an inadequate heart rate response to exercise or stress (184). Electrophysiological mechanisms that underlie SAN dysfunction in the setting of pathologically elevated atrial stretch are not completely understood and may vary for different conditions. The mechanisms could include abnormal functioning, expression, and/or regulation of the components of mechano-electrical and mechanochemical signal transduction and may be also conditioned by structural remodeling of the SAN.

Importantly, in the setting of sinus node dysfunction when SAN is not able to maintain physiologically robust rhythm, mechanical stretch can enhance automaticity in latent atrial pacemakers or provoke arrhythmogenic activity in the working myocardium to form ectopic foci and trigger atrial fibrillation (30, 185, 186). Though distribution patterns of stretch-induced atrial ectopic foci are not currently known, pulmonary veins represent the most common source of atrial fibrillation ectopy (187, 188). Mechanical stretch of pulmonary vein myocardium has been shown to promote arrhythmogenic activity from this region and may initiate atrial fibrillation (186, 189). Recently, we have demonstrated that stretch-induced activation of $I_{\text{Cl,SWELL}}$ in rat pulmonary veins leads to membrane depolarization and decreased AP amplitude, which trigger conduction discontinuities and both ectopic and reentrant activities (30, 59). We also found that downregulation of caveolin-3 protein expression and disruption of caveolae structures during chronic hypertension in spontaneously hypertensive rats significantly facilitates activation of $I_{\text{Cl,SWELL}}$ and increase the sensitivity of pulmonary vein in response to stretch to 10- to 50-fold (59). The increased sensitivity to stretch could be linked to the presence of constitutively active $I_{\text{Cl,SWELL}}$ that has been previously reported in failing (a pacing-induced congestive heart failure model) canine ventricular myocytes (111) and in human atrial myocytes obtained from patients with right atrial enlargement and/or elevated left ventricular end-diastolic pressure (112). Similar results of constitutively (i.e., without hypotonic stress) active, DIDS-sensitive $I_{\text{Cl,SWELL}}$ current was shown in cultured neonatal rat ventricular hypertrophic myocytes induced by cyclic mechanical stretch (190) and in mouse ventricular myocytes isolated from hearts subjected to 4 weeks' transverse aortic constriction (TAC) (191).

Pressure overload for 8 weeks using the TAC mouse model demonstrated a smaller basally active $I_{\text{Cl,SWELL}}$ as well as a significantly reduced hypotonic solution-induced $I_{\text{Cl,SWELL}}$ (191). Similar decreases in hypotonic $I_{\text{Cl,SWELL}}$ current without basal activation are observed in rabbit hypertrophied ventricular cells after treatment of volume and pressure overload (192) and spontaneous hypertrophic ventricular cells from caveolin-3-deficient mice (193). These may indicate that in an early adaptive stage of cardiac pressure/volume overload, $I_{\text{Cl,SWELL}}$ is basally activated by persistent mechanical stretch of the cell membrane and thus contributes to SAN tachycardia as well as facilitate atrial ectopy, as discussed earlier. However, attenuation of $I_{\text{Cl,SWELL}}$ mechanical sensitivity by long-term mechanical stretch of the plasma membrane may contribute to depressed SAN function and contribute to transformation to a non-adaptive stage. Indeed, our preliminary findings indicate that in 8-week post-myocardial infarction mouse model of heart failure, mRNA protein expression levels of ClC-2 and ClC-3 mechanosensitive chloride channels are significantly downregulated within the intercaval region of the right atrium, which correlates with a significantly enhanced cardiomyocyte membrane tension and downregulation of caveolae structures (194).

Pathological stretch can also affect mechanochemical signal transduction and contribute to stretch-mediated ectopic foci and atrial arrhythmogenesis. Stretch-induced activation of ROS systems via activation and upregulation of NADPH oxidases NOX2 and NOX4 have been linked to an increase in oxidation of RyRs and concomitant rise in spontaneous Ca^{2+} release event frequency, elevated Ca^{2+} leak, and significant increase in atrial fibrillation susceptibility (195). It should be also noted that chronic mechanical stretch may dramatically attenuate the protein expression profile of various ion channels and Ca^{2+}-handling proteins, including those involved in mechano-electrical and mechanochemical signal transductions, further contributing to SAN dysfunction and atrial arrhythmogenesis.

SUMMARY

Emerging evidence demonstrates that mechano-electrical and mechanochemical signal transduction pathways could be implicated in mechanical modulation of SAN function and thus represent an important mechanism for intrinsic regulation of cardiac rhythm. This adds another level of complexity to SAN automaticity and could be described as a "mechanics-clock" component of the pacemaker system (6, 7). Though the exact components of mechano-electro-chemical signal transduction involved in SAN mechanosensitivity are currently unknown, as summarized in the current review, these may involve a number of complex signaling feedback mechanisms that alter the function of both the voltage and calcium pacemaker clocks. As discussed, these mechanisms may interplay with each other, providing a precise attenuation of the SAN beating rate in response to various mechanical stimuli. Disruption of SAN function and regulation has been observed with multiple pathological conditions that are associated with atrial pressure/volume overload and thus may involve the remodeling of the components of the mechano-electro-chemical feedback loops in the SAN. Identification of such components, their impact into SAN pacemaking, and pathological remodeling may provide new therapeutic targets for the treatment of SAN dysfunction and associated rhythm abnormalities. Moreover, linking molecular components of mechano-electro-chemical signaling to certain cellular nanodomains and nanostructures may introduce a novel framework for therapeutic approaches for pacemaker dysfunction treatment targeted at preventing the degradation of cardiac cytoarchitecture.

AUTHOR CONTRIBUTIONS

RS and AG conceived the topic of the review and steered the general direction on what they wanted the review to cover. DT, CK, and JH examined the details of SAN mechanosensitivity and organized the literature into a concise review. PM and MM produced, analyzed, and wrote significant portions of the review related to RNAseq data. All authors allocated time and effort into writing/editing the manuscript and creating figures, small differences in effort are reflected in the author order.

FUNDING

This work was supported by NIH R01HL141214, American Heart Association 16SDG29120011, the Wisconsin Partnership Program 4140 (to AG), VA Merit Award I01BX005072, NIH R01DK106009 (RS), NIH predoctoral training grant T32GM008688 (to DT), and the *Fondation Leducq* TNE 19CV03 FANTASY (MM).

ACKNOWLEDGMENTS

The figures were generated using CorelDRAW 2018 software and BioRender.

SUPPLEMENTARY MATERIAL

The Supplementary Material for this article can be found online at: https://www.frontiersin.org/articles/10.3389/fcvm.2021.662410/full#supplementary-material

REFERENCES

1. Bainbridge FA. The influence of venous filling upon the rate of the heart. *J Physiol.* (1915) 50:65–84. doi: 10.1113/jphysiol.1915.sp001736
2. Donald DE, Shepherd JT. Reflexes from the heart and lungs: physiological curiosities or important regulatory mechanisms. *Cardiovasc Res.* (1978) 12:446–69. doi: 10.1093/cvr/12.8.449
3. James TN, Nadeau RA. Sinus bradycardia during injections directly into the sinus node artery. *Am J Physiol.* (1963) 204:9–15. doi: 10.1152/ajplegacy.1963.204.1.9
4. Cooper PJ, Lei M, Cheng LX, Kohl P. Selected contribution: axial stretch increases spontaneous pacemaker activity in rabbit isolated sinoatrial node cells. *J Appl Physiol.* (2000) 89:2099–104. doi: 10.1152/jappl.2000.89.5.2099
5. MacDonald EA, Madl J, Greiner J, Ramadan AF, Wells SM, Torrente AG, et al. Sinoatrial node structure, mechanics, electrophysiology and the chronotropic response to stretch in rabbit and mouse. *Front Physiol.* (2020) 11:809. doi: 10.3389/fphys.2020.00809
6. Quinn TA, Kohl P. Cardiac mechano-electric coupling: acute effects of mechanical stimulation on heart rate and rhythm. *Physiol Rev.* (2021) 101:37–92. doi: 10.1152/physrev.00036.2019
7. Quinn TA, Kohl P. Mechano-sensitivity of cardiac pacemaker function: pathophysiological relevance, experimental implications, and conceptual integration with other mechanisms of rhythmicity. *Prog Biophys Mol Biol.* (2012) 110:257–68. doi: 10.1016/j.pbiomolbio.2012.08.008
8. Lakatta EG, Maltsev VA, Vinogradova TM. A coupled SYSTEM of intracellular Ca2+ clocks and surface membrane voltage clocks controls the timekeeping mechanism of the heart's pacemaker. *Circ Res.* (2010) 106:659–73. doi: 10.1161/CIRCRESAHA.109.206078
9. Silverman ME, Hollman A. Discovery of the sinus node by Keith and Flack: on the centennial of their 1907 publication. *Heart.* (2007) 93:1184–7. doi: 10.1136/hrt.2006.105049
10. Boyett MR, Honjo H, Kodama I. The sinoatrial node, a heterogeneous pacemaker structure. *Cardiovasc Res.* (2000) 47:658–87. doi: 10.1016/S0008-6363(00)00135-8
11. Fedorov VV, Glukhov AV, Chang R. Conduction barriers and pathways of the sinoatrial pacemaker complex: their role in normal rhythm and atrial arrhythmias. *Am J Physiol Heart Circ Physiol.* (2012) 302:H1773–83. doi: 10.1152/ajpheart.00892.2011
12. Fedorov VV, Glukhov AV, Chang R, Kostecki G, Aferol H, Hucker WJ, et al. Optical mapping of the isolated coronary-perfused human sinus node. *J Am Coll Cardiol.* (2010) 56:1386–94. doi: 10.1016/j.jacc.2010.03.098
13. Fedorov VV, Schuessler RB, Hemphill M, Ambrosi CM, Chang R, Voloshina AS, et al. Structural and functional evidence for discrete exit pathways that connect the canine sinoatrial node and atria. *Circ Res.* (2009) 104:915–23. doi: 10.1161/CIRCRESAHA.108.193193
14. Camelliti P, Green CR, LeGrice I, Kohl P. Fibroblast network in rabbit sinoatrial node: structural and functional identification of homogeneous and heterogeneous cell coupling. *Circ Res.* (2004) 94:828–35. doi: 10.1161/01.RES.0000122382.19400.14
15. Liu J, Dobrzynski H, Yanni J, Boyett MR, Lei M. Organisation of the mouse sinoatrial node: structure and expression of HCN channels. *Cardiovasc Res.* (2007) 73:729–38. doi: 10.1016/j.cardiores.2006.11.016
16. Zicha S, Fernandez-Velasco M, Lonardo G, L'Heureux N, Nattel S. Sinus node dysfunction and hyperpolarization-activated (HCN) channel subunit remodeling in a canine heart failure model. *Cardiovasc Res.* (2005) 66:472–81. doi: 10.1016/j.cardiores.2005.02.011
17. Boineau JP, Canavan TE, Schuessler RB, Cain ME, Corr PB, Cox JL. Demonstration of a widely distributed atrial pacemaker complex in the human heart. *Circulation.* (1988) 77:1221–37. doi: 10.1161/01.CIR.77.6.1221
18. Kirchhof CJ, Bonke FI, Allessie MA, Lammers WJ. The influence of the atrial myocardium on impulse formation in the rabbit sinus node. *Pflugers Arch.* (1987) 410:198–203. doi: 10.1007/BF00581916
19. Li N, Hansen BJ, Csepe TA, Zhao J, Ignozzi AJ, Sul LV, et al. Redundant and diverse intranodal pacemakers and conduction pathways protect the human sinoatrial node from failure. *Sci Transl Med.* (2017) 9:eaam5607. doi: 10.1126/scitranslmed.aam5607
20. Li N, Kalyanasundaram A, Hansen BJ, Artiga EJ, Sharma R, Abudulwahed SH, et al. Impaired neuronal sodium channels cause intranodal conduction failure and reentrant arrhythmias in human sinoatrial node. *Nat Commun.* (2020) 11:512. doi: 10.1038/s41467-019-14039-8
21. Schuessler RB. Abnormal sinus node function in clinical arrhythmias. *J Cardiovasc Electrophysiol.* (2003) 14:215–7. doi: 10.1046/j.1540-8167.2003.02229.x
22. Glukhov AV, Fedorov VV, Anderson ME, Mohler PJ, Efimov IR. Functional anatomy of the murine sinus node: high-resolution optical mapping of ankyrin-B heterozygous mice. *Am J Physiol Heart Circ Physiol.* (2010) 299:H482–91. doi: 10.1152/ajpheart.00756.2009
23. Glukhov AV, Hage LT, Hansen BJ, Pedraza-Toscano A, Vargas-Pinto P, Hamlin RL, et al. Sinoatrial node reentry in a canine chronic left ventricular infarct model: role of intranodal fibrosis and heterogeneity of refractoriness. *Circ Arrhythm Electrophysiol.* (2013) 6:984–94. doi: 10.1161/CIRCEP.113.000404
24. Shibata N, Inada S, Mitsui K, Honjo H, Yamamoto M, Niwa R, et al. Pacemaker shift in the rabbit sinoatrial node in response to vagal nerve stimulation. *Exp Physiol.* (2001) 86:177–84. doi: 10.1113/eph8602100
25. Brooks CM, Lu HH, Lange G, Mangi R, Shaw RB, Geoly K. Effects of localized stretch of the sinoatrial node region of the dog heart. *Am J Physiol.* (1966) 211:1197–202. doi: 10.1152/ajplegacy.1966.211.5.1197
26. Huang ZM, Prasad C, Britton FC, Ye LL, Hatton WJ, Duan D. Functional role of CLC-2 chloride inward rectifier channels in cardiac sinoatrial nodal pacemaker cells. *J Mol Cell Cardiol.* (2009) 47:121–32. doi: 10.1016/j.yjmcc.2009.04.008
27. Parmley WW, Chuck L. Length-dependent changes in myocardial contractile state. *Am J Physiol.* (1973) 224:1195–9. doi: 10.1152/ajplegacy.1973.224.5.1195
28. Lange G, Lu HH, Chang A, Brooks CM. Effect of stretch on the isolated cat sinoatrial node. *Am J Physiol.* (1966) 211:1192–6. doi: 10.1152/ajplegacy.1966.211.5.1192

29. Hill-Eubanks DC, Gonzales AL, Sonkusare SK, Nelson MT. Vascular TRP channels: performing under pressure and going with the flow. *Physiology.* (2014) 29:343–60. doi: 10.1152/physiol.00009.2014
30. Seol CA, Kim WT, Ha JM, Choe H, Jang YJ, Youm JB, et al. Stretch-activated currents in cardiomyocytes isolated from rabbit pulmonary veins. *Prog Biophys Mol Biol.* (2008) 97:217–31. doi: 10.1016/j.pbiomolbio.2008.02.008
31. Caldiz CI, Garciarena CD, Dulce RA, Novaretto LP, Yeves AM, Ennis IL, et al. Mitochondrial reactive oxygen species activate the slow force response to stretch in feline myocardium. *J Physiol.* (2007) 584:895–905. doi: 10.1113/jphysiol.2007.141689
32. Neves JS, Castro-Ferreira R, Ladeiras-Lopes R, Neiva-Sousa M, Leite-Moreira AM, Almeida-Coelho J, et al. The effects of angiotensin II signaling pathway in the systolic response to acute stretch in the normal and ischemic myocardium. *Peptides.* (2013) 47:77–84. doi: 10.1016/j.peptides.2013.07.004
33. Petroff MG, Kim SH, Pepe S, Dessy C, Marban E, Balligand JL, et al. Endogenous nitric oxide mechanisms mediate the stretch dependence of Ca2+ release in cardiomyocytes. *Nat Cell Biol.* (2001) 3:867–73. doi: 10.1038/ncb1001-867
34. Reil JC, Reil GH, Kovacs A, Sequeira V, Waddingham MT, Lodi M, et al. CaMKII activity contributes to homeometric autoregulation of the heart: a novel mechanism for the Anrep effect. *J Physiol.* (2020) 598:3129–53. doi: 10.1113/JP279607
35. Todaka K, Ogino K, Gu A, Burkhoff D. Effect of ventricular stretch on contractile strength, calcium transient, and cAMP in intact canine hearts. *Am J Physiol.* (1998) 274:H990–1000. doi: 10.1152/ajpheart.1998.274.3.H990
36. Lakatta EG, DiFrancesco D. What keeps us ticking: a funny current, a calcium clock, or both? *J Mol Cell Cardiol.* (2009) 47:157–70. doi: 10.1016/j.yjmcc.2009.03.022
37. Torrente AG, Zhang R, Zaini A, Giani JF, Kang J, Lamp ST, et al. Burst pacemaker activity of the sinoatrial node in sodium-calcium exchanger knockout mice. *Proc Natl Acad Sci USA.* (2015) 112:9769–74. doi: 10.1073/pnas.1505670112
38. Fenske S, Hennis K, Rotzer RD, Brox VF, Becirovic E, Scharr A, et al. cAMP-dependent regulation of HCN4 controls the tonic entrainment process in sinoatrial node pacemaker cells. *Nat Commun.* (2020) 11:5555. doi: 10.1038/s41467-020-19304-9
39. Kraichely RE, Strege PR, Sarr MG, Kendrick ML, Farrugia G. Lysophosphatidyl choline modulates mechanosensitive L-type Ca2+ current in circular smooth muscle cells from human jejunum. *Am J Physiol Gastrointest Liver Physiol.* (2009) 296:G833–9. doi: 10.1152/ajpgi.90610.2008
40. Laitko U, Morris CE. Membrane tension accelerates rate-limiting voltage-dependent activation and slow inactivation steps in a Shaker channel. *J Gen Physiol.* (2004) 123:135–54. doi: 10.1085/jgp.200308965
41. Irisawa H, Brown HF, Giles W. Cardiac pacemaking in the sinoatrial node. *Physiol Rev.* (1993) 73:197–227. doi: 10.1152/physrev.1993.73.1.197
42. DiFrancesco D. The role of the funny current in pacemaker activity. *Circ Res.* (2010) 106:434–46. doi: 10.1161/CIRCRESAHA.109.208041
43. Severi S, Fantini M, Charawi LA, DiFrancesco D. An updated computational model of rabbit sinoatrial action potential to investigate the mechanisms of heart rate modulation. *J Physiol.* (2012) 590:4483–99. doi: 10.1113/jphysiol.2012.229435
44. Mangoni ME, Nargeot J. Genesis and regulation of the heart automaticity. *Physiol Rev.* (2008) 88:919–82. doi: 10.1152/physrev.00018.2007
45. Mangoni ME, Couette B, Bourinet E, Platzer J, Reimer D, Striessnig J, et al. Functional role of L-type Cav1.3 Ca2+ channels in cardiac pacemaker activity. *Proc Natl Acad Sci USA*. (2003) 100:5543–8. doi: 10.1073/pnas.0935295100
46. Torrente AG, Mesirca P, Neco P, Rizzetto R, Dubel S, Barrere C, et al. L-type Cav1.3 channels regulate ryanodine receptor-dependent Ca2+ release during sino-atrial node pacemaker activity. *Cardiovasc Res.* (2016) 109:451–61. doi: 10.1093/cvr/cvw006
47. Toyoda F, Mesirca P, Dubel S, Ding WG, Striessnig J, Mangoni ME, et al. CaV1.3 L-type Ca(2+) channel contributes to the heartbeat by generating a dihydropyridine-sensitive persistent Na(+) current. *Sci Rep.* (2017) 7:7869. doi: 10.1038/s41598-017-08191-8
48. Monfredi O, Maltseva LA, Spurgeon HA, Boyett MR, Lakatta EG, Maltsev VA. Beat-to-beat variation in periodicity of local calcium releases contributes to intrinsic variations of spontaneous cycle length in isolated single sinoatrial node cells. *PLoS ONE.* (2013) 8:e67247. doi: 10.1371/journal.pone.0067247
49. Vinogradova TM, Bogdanov KY, Lakatta EG. beta-Adrenergic stimulation modulates ryanodine receptor Ca(2+) release during diastolic depolarization to accelerate pacemaker activity in rabbit sinoatrial nodal cells. *Circ Res.* (2002) 90:73–9. doi: 10.1161/hh0102.102271
50. Vinogradova TM, Lyashkov AE, Zhu W, Ruknudin AM, Sirenko S, Yang D, et al. High basal protein kinase A-dependent phosphorylation drives rhythmic internal Ca2+ store oscillations and spontaneous beating of cardiac pacemaker cells. *Circ Res.* (2006) 98:505–14. doi: 10.1161/01.RES.0000204575.94040.d1
51. Vinogradova TM, Zhou YY, Maltsev V, Lyashkov A, Stern M, Lakatta EG. Rhythmic ryanodine receptor Ca2+ releases during diastolic depolarization of sinoatrial pacemaker cells do not require membrane depolarization. *Circ Res.* (2004) 94:802–9. doi: 10.1161/01.RES.0000122045.55331.0F
52. Huser J, Blatter LA, Lipsius SL. Intracellular Ca2+ release contributes to automaticity in cat atrial pacemaker cells. *J Physiol.* (2000) 524:415–22. doi: 10.1111/j.1469-7793.2000.00415.x
53. Baudot M, Torre E, Bidaud I, Louradour J, Torrente AG, Fossier L, et al. Concomitant genetic ablation of L-type Cav1.3 (alpha1D) and T-type Cav3.1 (alpha1G) Ca(2+) channels disrupts heart automaticity. *Sci Rep.* (2020) 10:18906. doi: 10.1038/s41598-020-76049-7
54. Bagriantsev SN, Gracheva EO, Gallagher PG. Piezo proteins: regulators of mechanosensation and other cellular processes. *J Biol Chem.* (2014) 289:31673–81. doi: 10.1074/jbc.R114.612697
55. Duchemin AL, Vignes H, Vermot J. Mechanically activated piezo channels modulate outflow tract valve development through the Yap1 and Klf2-Notch signaling axis. *Elife.* (2019) 8:e44706. doi: 10.7554/eLife.44706
56. Cooper PJ, Kohl P. Species- and preparation-dependence of stretch effects on sino-atrial node pacemaking. *Ann N Y Acad Sci.* (2005) 1047:324–35. doi: 10.1196/annals.1341.029
57. Coste B, Mathur J, Schmidt M, Earley TJ, Ranade S, Petrus MJ, et al. Piezo1 and Piezo2 are essential components of distinct mechanically activated cation channels. *Science.* (2010) 330:55–60. doi: 10.1126/science.1193270
58. Qiu Z, Dubin AE, Mathur J, Tu B, Reddy K, Miraglia LJ, et al. SWELL1, a plasma membrane protein, is an essential component of volume-regulated anion channel. *Cell.* (2014) 157:447–58. doi: 10.1016/j.cell.2014.03.024
59. Egorov YV, Lang D, Tyan L, Turner D, Lim E, Piro ZD, et al. Caveolae-mediated activation of mechanosensitive chloride channels in pulmonary veins triggers atrial arrhythmogenesis. *J Am Heart Assoc.* (2019) 8:e012748. doi: 10.1161/JAHA.119.012748
60. Marionneau C, Couette B, Liu J, Li H, Mangoni ME, Nargeot J, et al. Specific pattern of ionic channel gene expression associated with pacemaker activity in the mouse heart. *J Physiol*. (2005) 562(Pt 1):223–34. doi: 10.1113/jphysiol.2004.074047
61. Yanni J, Tellez JO, Maczewski M, Mackiewicz, U., Beresewicz, A., Billeter, R., et al. Changes in ion channel gene expression underlying heart failure-induced sinoatrial node dysfunction. *Circ. Heart Fail*. (2011) 4:496–508. doi: 10.1161/CIRCHEARTFAILURE.110.957647
62. Xiong D, Heyman NS, Airey J, Zhang M, Singer CA, Rawat S, et al. Cardiac-specific, inducible ClC-3 gene deletion eliminates native volume-sensitive chloride channels and produces myocardial hypertrophy in adult mice. *J Mol Cell Cardiol.* (2010) 48:211–9. doi: 10.1016/j.yjmcc.2009.07.003
63. Ju YK, Chu Y, Chaulet H, Lai D, Gervasio OL, Graham RM, et al. Store-operated Ca^{2+} influx and expression of TRPC genes in mouse sinoatrial node. *Circ Res*. (2007) 100:1605–14. doi: 10.1161/CIRCRESAHA.107.152181
64. Demion M, Bois P, Launay P, Guinamard R. TRPM4, a Ca2+-activated nonselective cation channel in mouse sino-atrial node cells. *Cardiovasc Res.* (2007) 73:531–8. doi: 10.1016/j.cardiores.2006.11.023
65. Hof T, Simard C, Rouet R, Salle L, Guinamard R. Implication of the TRPM4 nonselective cation channel in mammalian sinus rhythm. *Heart Rhythm.* (2013) 10:1683–9. doi: 10.1016/j.hrthm.2013.08.014
66. Sah R, Mesirca P, Mason X, Gibson W, Bates-Withers C, Van den Boogert M, et al. Timing of myocardial trpm7 deletion during cardiogenesis variably disrupts adult ventricular function, conduction, and repolarization. *Circulation.* (2013) 128:101–14. doi: 10.1161/CIRCULATIONAHA.112.000768

67. Sah R, Mesirca P, Van den Boogert M, Rosen J, Mably J, Mangoni ME, et al. Ion channel-kinase TRPM7 is required for maintaining cardiac automaticity. *Proc Natl Acad Sci USA*. (2013) 110:E3037–46. doi: 10.1073/pnas.1311865110
68. Brennan JA, Chen Q, Gams A, Dyavanapalli J, Mendelowitz D, Peng W, et al. Evidence of superior and inferior sinoatrial nodes in the mammalian heart. *JACC Clin Electrophysiol*. (2020) 6:1827–40. doi: 10.1016/j.jacep.2020.09.012
69. Unudurthi SD, Wu X, Qian L, Amari F, Onal B, Li N, et al. Two-Pore K+ channel TREK-1 regulates sinoatrial node membrane excitability. *J Am Heart Assoc.* (2016) 5:e002865. doi: 10.1161/JAHA.115.002865
70. Lai MH, Wu Y, Gao Z, Anderson ME, Dalziel JE, Meredith AL. BK channels regulate sinoatrial node firing rate and cardiac pacing in vivo. *Am J Physiol Heart Circ Physiol.* (2014) 307:H1327–38. doi: 10.1152/ajpheart.00354.2014
71. Mao Z, Wang Y, Peng H, He F, Zhu L, Huang H, et al. A newly identified missense mutation in CLCA2 is associated with autosomal dominant cardiac conduction block. *Gene.* (2019) 714:143990. doi: 10.1016/j.gene.2019.143990
72. Beech DJ, Kalli AC. Force sensing by piezo channels in cardiovascular health and disease. *Arterioscler Thromb Vasc Biol.* (2019) 39:2228–39. doi: 10.1161/ATVBAHA.119.313348
73. Lewis AH, Cui AF, McDonald MF, Grandl J. Transduction of repetitive mechanical stimuli by piezo1 and piezo2 ion channels. *Cell Rep.* (2017) 19:2572–85. doi: 10.1016/j.celrep.2017.05.079
74. Douguet D, Patel A, Xu A, Vanhoutte PM, Honore E. Piezo ion channels in cardiovascular mechanobiology. *Trends Pharmacol Sci.* (2019) 40:956–70. doi: 10.1016/j.tips.2019.10.002
75. Miyamoto T, Mochizuki T, Nakagomi H, Kira S, Watanabe M, Takayama Y, et al. Functional role for Piezo1 in stretch-evoked $Ca^{(2+)}$ influx and ATP release in urothelial cell cultures. *J Biol Chem.* (2014) 289:16565–75. doi: 10.1074/jbc.M113.528638
76. O'Connell AD, Morton MJ, Hunter M. Two-pore domain K+ channels-molecular sensors. *Biochim Biophys Acta.* (2002) 1566:152–61. doi: 10.1016/S0005-2736(02)00597-7
77. Enyedi P, Czirjak G. Molecular background of leak K+ currents: two-pore domain potassium channels. *Physiol Rev.* (2010) 90:559–605. doi: 10.1152/physrev.00029.2009
78. Froese A, Breher SS, Waldeyer C, Schindler RF, Nikolaev VO, Rinne S, et al. Popeye domain containing proteins are essential for stress-mediated modulation of cardiac pacemaking in mice. *J Clin Invest.* (2012) 122:1119–30. doi: 10.1172/JCI59410
79. Tan JH, Liu W, Saint DA. Trek-like potassium channels in rat cardiac ventricular myocytes are activated by intracellular ATP. *J Membr Biol.* (2002) 185:201–7. doi: 10.1007/s00232-001-0123-0
80. Xian Tao L, Dyachenko V, Zuzarte M, Putzke C, Preisig-Muller R, Isenberg G, et al. The stretch-activated potassium channel TREK-1 in rat cardiac ventricular muscle. *Cardiovasc Res.* (2006) 69:86–97. doi: 10.1016/j.cardiores.2005.08.018
81. Decher N, Wemhoner K, Rinne S, Netter MF, Zuzarte M, Aller MI, et al. Knock-out of the potassium channel TASK-1 leads to a prolonged QT interval and a disturbed QRS complex. *Cell Physiol Biochem.* (2011) 28:77–86. doi: 10.1159/000331715
82. Limberg SH, Netter MF, Rolfes C, Rinne S, Schlichthorl G, Zuzarte M, et al. TASK-1 channels may modulate action potential duration of human atrial cardiomyocytes. *Cell Physiol Biochem.* (2011) 28:613–24. doi: 10.1159/000335757
83. Putzke C, Wemhoner K, Sachse FB, Rinne S, Schlichthorl G, Li XT, et al. The acid-sensitive potassium channel TASK-1 in rat cardiac muscle. *Cardiovasc Res.* (2007) 75:59–68. doi: 10.1016/j.cardiores.2007.02.025
84. Patel AJ, Honore E, Maingret F, Lesage F, Fink M, Duprat F, et al. A mammalian two pore domain mechano-gated S-like K+ channel. *EMBO J.* (1998) 17:4283–90. doi: 10.1093/emboj/17.15.4283
85. Brohawn SG, Su Z, MacKinnon R. Mechanosensitivity is mediated directly by the lipid membrane in TRAAK and TREK1 K+ channels. *Proc Natl Acad Sci USA*. (2014) 111:3614–9. doi: 10.1073/pnas.1320768111
86. Kirchmaier BC, Poon KL, Schwerte T, Huisken J, Winkler C, Jungblut B, et al. The Popeye domain containing 2 (popdc2) gene in zebrafish is required for heart and skeletal muscle development. *Dev Biol.* (2012) 363:438–50. doi: 10.1016/j.ydbio.2012.01.015
87. Hund TJ, Snyder JS, Wu X, Glynn P, Koval OM, Onal B, et al. beta(IV)-Spectrin regulates TREK-1 membrane targeting in the heart. *Cardiovasc Res.* (2014) 102:166–75. doi: 10.1093/cvr/cvu008
88. Takahashi K, Naruse K. Stretch-activated BK channel and heart function. *Prog Biophys Mol Biol.* (2012) 110:239–44. doi: 10.1016/j.pbiomolbio.2012.08.001
89. Imlach WL, Finch SC, Miller JH, Meredith AL, Dalziel JE. A role for BK channels in heart rate regulation in rodents. *PLoS ONE.* (2010) 5:e8698. doi: 10.1371/journal.pone.0008698
90. Zhao H, Yu Y, Wu X, Liu S, Liu B, Du J, et al. A role of BK channel in regulation of Ca(2+) channel in ventricular myocytes by substrate stiffness. *Biophys J.* (2017) 112:1406–16. doi: 10.1016/j.bpj.2017.01.036
91. Inoue R, Jian Z, Kawarabayashi Y. Mechanosensitive TRP channels in cardiovascular pathophysiology. *Pharmacol Ther.* (2009) 123:371–85. doi: 10.1016/j.pharmthera.2009.05.009
92. Launay P, Fleig A, Perraud AL, Scharenberg AM, Penner R, Kinet JP. TRPM4 is a Ca2+-activated nonselective cation channel mediating cell membrane depolarization. *Cell.* (2002) 109:397–407. doi: 10.1016/S0092-8674(02)00719-5
93. Ramsey IS, Delling M, Clapham DE. An introduction to TRP channels. *Annu Rev Physiol.* (2006) 68:619–47. doi: 10.1146/annurev.physiol.68.040204.100431
94. Little SC, Mohler PJ. TRPM4 modulates sinus node diastolic depolarization. *Heart Rhythm.* (2013) 10:1690–1. doi: 10.1016/j.hrthm.2013.08.026
95. Li M, Jiang J, Yue L. Functional characterization of homo- and heteromeric channel kinases TRPM6 and TRPM7. *J Gen Physiol.* (2006) 127:525–37. doi: 10.1085/jgp.200609502
96. Runnels LW, Yue L, Clapham DE. TRP-PLIK, a bifunctional protein with kinase and ion channel activities. *Science.* (2001) 291:1043–7. doi: 10.1126/science.1058519
97. Gottlieb P, Folgering J, Maroto R, Raso A, Wood TG, Kurosky A, et al. Revisiting TRPC1 and TRPC6 mechanosensitivity. *Pflugers Arch.* (2008) 455:1097–103. doi: 10.1007/s00424-007-0359-3
98. Nikolaev YA, Cox CD, Ridone P, Rohde PR, Cordero-Morales JF, Vasquez V, et al. Mammalian TRP ion channels are insensitive to membrane stretch. *J Cell Sci.* (2019) 132:jcs238360. doi: 10.1242/jcs.238360
99. Oancea E, Wolfe JT, Clapham DE. Functional TRPM7 channels accumulate at the plasma membrane in response to fluid flow. *Circ Res.* (2006) 98:245–53. doi: 10.1161/01.RES.0000200179.29375.cc
100. Kohl P, Hunter P, Noble D. Stretch-induced changes in heart rate and rhythm: clinical observations, experiments and mathematical models. *Prog Biophys Mol Biol.* (1999) 71:91–138. doi: 10.1016/S0079-6107(98)00038-8
101. Osei-Owusu J, Yang J, Vitery MDC, Qiu Z. Molecular biology and physiology of volume-regulated anion channel (VRAC). *Curr Top Membr.* (2018) 81:177–203. doi: 10.1016/bs.ctm.2018.07.005
102. Voss FK, Ullrich F, Munch J, Lazarow K, Lutter D, Mah N, et al. Identification of LRRC8 heteromers as an essential component of the volume-regulated anion channel VRAC. *Science.* (2014) 344:634–8. doi: 10.1126/science.1252826
103. Alghanem AF, Abello J, Maurer JM, Kumar A, Ta CM, Gunasekar SK, et al. The SWELL1-LRRC8 complex regulates endothelial AKT-eNOS signaling and vascular function. *Elife.* (2021) 10:e61313. doi: 10.7554/eLife.61313
104. Kang C, Xie L, Gunasekar SK, Mishra A, Zhang Y, Pai S, et al. SWELL1 is a glucose sensor regulating beta-cell excitability and systemic glycaemia. *Nat Commun.* (2018) 9:367. doi: 10.1038/s41467-017-02664-0
105. Kumar A, Xie L, Ta CM, Hinton AO, Gunasekar SK, Minerath RA, et al. SWELL1 regulates skeletal muscle cell size, intracellular signaling, adiposity and glucose metabolism. *Elife.* (2020) 9:e58941. doi: 10.7554/eLife.58941
106. Stuhlmann T, Planells-Cases R, Jentsch TJ. LRRC8/VRAC anion channels enhance beta-cell glucose sensing and insulin secretion. *Nat Commun.* (2018) 9:1974. doi: 10.1038/s41467-018-04353-y
107. Yang J, Vitery MDC, Chen J, Osei-Owusu J, Chu J, Qiu Z. Glutamate-Releasing SWELL1 channel in astrocytes modulates synaptic transmission and promotes brain damage in stroke. *Neuron.* (2019) 102:813–27.e816. doi: 10.1016/j.neuron.2019.03.029

108. Zhang Y, Xie L, Gunasekar SK, Tong D, Mishra A, Gibson WJ, et al. SWELL1 is a regulator of adipocyte size, insulin signalling and glucose homeostasis. *Nat Cell Biol.* (2017) 19:504–17. doi: 10.1038/ncb3514
109. Browe DM, Baumgarten CM. Stretch of beta 1 integrin activates an outwardly rectifying chloride current via FAK and Src in rabbit ventricular myocytes. *J Gen Physiol.* (2003) 122:689–702. doi: 10.1085/jgp.200308899
110. Brower KJ. Insomnia, alcoholism and relapse. *Sleep Med Rev.* (2003) 7:523–39. doi: 10.1016/S1087-0792(03)90005-0
111. Clemo HF, Stambler BS, Baumgarten CM. Swelling-activated chloride current is persistently activated in ventricular myocytes from dogs with tachycardia-induced congestive heart failure. *Circ Res.* (1999) 84:157–65. doi: 10.1161/01.RES.84.2.157
112. Patel DG, Higgins RS, Baumgarten CM. Swelling-activated Cl current, ICl,SWELL, is chronically activated in diseased human atrial myocytes. *Biophys J.* (2003) 84:233a.
113. Ren Z, Raucci FJ Jr, Browe DM, Baumgarten CM. Regulation of swelling-activated Cl(-) current by angiotensin II signalling and NADPH oxidase in rabbit ventricle. *Cardiovasc Res.* (2008) 77:73–80. doi: 10.1093/cvr/cvm031
114. Hagiwara N, Masuda H, Shoda M, Irisawa H. Stretch-activated anion currents of rabbit cardiac myocytes. *J Physiol.* (1992) 456:285–302. doi: 10.1113/jphysiol.1992.sp019337
115. Hagiwara N, Irisawa H, Kasanuki H, Hosoda S. Background current in sino-atrial node cells of the rabbit heart. *J Physiol.* (1992) 448:53–72. doi: 10.1113/jphysiol.1992.sp019029
116. Kopton RA, Baillie JS, Rafferty SA, Moss R, Zgierski-Johnston CM, Prykhozhij SV, et al. Cardiac electrophysiological effects of light-activated chloride channels. *Front Physiol.* (2018) 9:1806. doi: 10.3389/fphys.2018.01806
117. Decher N, Lang HJ, Nilius B, Bruggemann A, Busch AE, Steinmeyer K. DCPIB is a novel selective blocker of I(Cl,swell) and prevents swelling-induced shortening of guinea-pig atrial action potential duration. *Br J Pharmacol.* (2001) 134:1467–79. doi: 10.1038/sj.bjp.0704413
118. Arai A, Kodama I, Toyama J. Roles of Cl- channels and Ca2+ mobilization in stretch-induced increase of SA node pacemaker activity. *Am J Physiol.* (1996) 270:H1726–35. doi: 10.1152/ajpheart.1996.270.5.H1726
119. Wang D, Wang H, Gao F, Wang K, Dong F. ClC-3 promotes osteogenic differentiation in MC3T3-E1 cell after dynamic compression. *J Cell Biochem.* (2017) 118:1606–13. doi: 10.1002/jcb.25823
120. Liang W, Huang L, Zhao D, He JZ, Sharma P, Liu J, et al. Swelling-activated Cl- currents and intracellular CLC-3 are involved in proliferation of human pulmonary artery smooth muscle cells. *J Hypertens.* (2014) 32:318–30. doi: 10.1097/HJH.0000000000000013
121. Ye Z, Wu MM, Wang CY, Li YC, Yu CJ, Gong YF, et al. Characterization of cardiac anoctamin1 Ca(2)(+)-activated chloride channels and functional role in ischemia-induced arrhythmias. *J Cell Physiol.* (2015) 230:337–46. doi: 10.1002/jcp.24709
122. Sung TS, Hwang SJ, Koh SD, Bayguinov Y, Peri LE, Blair PJ, et al. The cells and conductance mediating cholinergic neurotransmission in the murine proximal stomach. *J Physiol.* (2018) 596:1549–74. doi: 10.1113/JP275478
123. Tanaka S, Fujio Y, Nakayama H. Caveolae-specific CaMKII signaling in the regulation of voltage-dependent calcium channel and cardiac hypertrophy. *Front Physiol.* (2018) 9:1081. doi: 10.3389/fphys.2018.01081
124. Barbuti A, Terragni B, Brioschi C, DiFrancesco D. Localization of f-channels to caveolae mediates specific beta2-adrenergic receptor modulation of rate in sinoatrial myocytes. *J Mol Cell Cardiol.* (2007) 42:71–78. doi: 10.1016/j.yjmcc.2006.09.018
125. Masson-Pevet M, Gros D, Besselsen E. The caveolae in rabbit sinus node and atrium. *Cell Tissue Res.* (1980) 208:183–96. doi: 10.1007/BF00234869
126. Echarri A, Del Pozo MA. Caveolae - mechanosensitive membrane invaginations linked to actin filaments. *J Cell Sci.* (2015) 128:2747–58. doi: 10.1242/jcs.153940
127. Gilbert G, Ducret T, Savineau JP, Marthan R, Quignard JF. Caveolae are involved in mechanotransduction during pulmonary hypertension. *Am J Physiol Lung Cell Mol Physiol.* (2016) 310:L1078–87. doi: 10.1152/ajplung.00198.2015
128. Parton RG, Simons K. The multiple faces of caveolae. *Nat Rev Mol Cell Biol.* (2007) 8:185–94. doi: 10.1038/nrm2122
129. Pfleger C, Ebeling G, Blasche R, Patton M, Patel HH, Kasper M, et al. Detection of caveolin-3/caveolin-1/P2X7R complexes in mice atrial cardiomyocytes in vivo and in vitro. *Histochem Cell Biol.* (2012) 138:231–41. doi: 10.1007/s00418-012-0961-0
130. Volonte D, McTiernan CF, Drab M, Kasper M, Galbiati F. Caveolin-1 and caveolin-3 form heterooligomeric complexes in atrial cardiac myocytes that are required for doxorubicin-induced apoptosis. *Am J Physiol Heart Circ Physiol.* (2008) 294:H392–401. doi: 10.1152/ajpheart.01039.2007
131. Barbuti A, Scavone A, Mazzocchi N, Terragni B, Baruscotti M, Difrancesco D. A caveolin-binding domain in the HCN4 channels mediates functional interaction with caveolin proteins. *J Mol Cell Cardiol.* (2012) 53:187–95. doi: 10.1016/j.yjmcc.2012.05.013
132. Shibata EF, Brown TL, Washburn ZW, Bai J, Revak TJ, Butters CA. Autonomic regulation of voltage-gated cardiac ion channels. *J Cardiovasc Electrophysiol.* (2006) 17 (Suppl. 1):S34–42. doi: 10.1111/j.1540-8167.2006.00387.x
133. Ichishima K, Yamamoto S, Iwamoto T, Ehara T. alpha-Adrenoceptor-mediated depletion of phosphatidylinositol 4, 5-bisphosphate inhibits activation of volume-regulated anion channels in mouse ventricular myocytes. *Br J Pharmacol.* (2010) 161:193–206. doi: 10.1111/j.1476-5381.2010.00896.x
134. Gunasekar SK, Xie L, Sah R. SWELL signalling in adipocytes: can fat 'feel' fat? *Adipocyte.* (2019) 8:223–8. doi: 10.1080/21623945.2019.1612223
135. Kohl P, Sachs F, Franz MR. *Cardiac Mechano-Electric Coupling and Arrhythmias*. Oxford: OUP Oxford (2011).
136. Iribe G, Ward CW, Camelliti P, Bollensdorff C, Mason F, Burton RA, et al. Axial stretch of rat single ventricular cardiomyocytes causes an acute and transient increase in Ca2+ spark rate. *Circ Res.* (2009) 104:787–95. doi: 10.1161/CIRCRESAHA.108.193334
137. Prosser BL, Ward CW, Lederer WJ. X-ROS signaling: rapid mechano-chemo transduction in heart. *Science.* (2011) 333:1440–5. doi: 10.1126/science.1202768
138. Iribe G, Kohl P. Axial stretch enhances sarcoplasmic reticulum Ca2+ leak and cellular Ca2+ reuptake in guinea pig ventricular myocytes: experiments and models. *Prog Biophys Mol Biol.* (2008) 97:298–311. doi: 10.1016/j.pbiomolbio.2008.02.012
139. Lyashkov AE, Juhaszova M, Dobrzynski H, Vinogradova TM, Maltsev VA, Juhasz O, et al. Calcium cycling protein density and functional importance to automaticity of isolated sinoatrial nodal cells are independent of cell size. *Circ Res.* (2007) 100:1723–31. doi: 10.1161/CIRCRESAHA.107.153676
140. Musa H, Lei M, Honjo H, Jones SA, Dobrzynski H, Lancaster MK, et al. Heterogeneous expression of Ca(2+) handling proteins in rabbit sinoatrial node. *J Histochem Cytochem.* (2002) 50:311–24. doi: 10.1177/002215540205000303
141. Stern MD, Maltseva LA, Juhaszova M, Sollott SJ, Lakatta EG, Maltsev VA. Hierarchical clustering of ryanodine receptors enables emergence of a calcium clock in sinoatrial node cells. *J Gen Physiol.* (2014) 143:577–604. doi: 10.1085/jgp.201311123
142. Prosser BL, Khairallah RJ, Ziman AP, Ward CW, Lederer WJ. X-ROS signaling in the heart and skeletal muscle: stretch-dependent local ROS regulates [Ca(2)(+)]i. *J Mol Cell Cardiol.* (2013) 58:172–81. doi: 10.1016/j.yjmcc.2012.11.011
143. Balog EM, Norton LE, Thomas DD, Fruen BR. Role of calmodulin methionine residues in mediating productive association with cardiac ryanodine receptors. *Am J Physiol Heart Circ Physiol.* (2006) 290:H794–9. doi: 10.1152/ajpheart.00706.2005
144. Erickson JR, Joiner ML, Guan X, Kutschke W, Yang J, Oddis CV, et al. A dynamic pathway for calcium-independent activation of CaMKII by methionine oxidation. *Cell.* (2008) 133:462–74. doi: 10.1016/j.cell.2008.02.048
145. Dries E, Bito V, Lenaerts I, Antoons G, Sipido KR, Macquaide N. Selective modulation of coupled ryanodine receptors during microdomain activation of calcium/calmodulin-dependent kinase II in the dyadic cleft. *Circ Res.* (2013) 113:1242–52. doi: 10.1161/CIRCRESAHA.113.301896
146. Wu Y, Anderson ME. CaMKII in sinoatrial node physiology and dysfunction. *Front Pharmacol.* (2014) 5:48. doi: 10.3389/fphar.2014.00048

147. Dyachenko V, Husse B, Rueckschloss U, Isenberg G. Mechanical deformation of ventricular myocytes modulates both TRPC6 and Kir2.3 channels. *Cell Calcium.* (2009) 45:38–54. doi: 10.1016/j.ceca.2008.06.003

148. Dyachenko V, Rueckschloss U, Isenberg G. Modulation of cardiac mechanosensitive ion channels involves superoxide, nitric oxide and peroxynitrite. *Cell Calcium.* (2009) 45:55–64. doi: 10.1016/j.ceca.2008.06.002

149. Gervasio OL, Whitehead NP, Yeung EW, Phillips WD, Allen DG. TRPC1 binds to caveolin-3 and is regulated by Src kinase - role in Duchenne muscular dystrophy. *J Cell Sci.* (2008) 121:2246–55. doi: 10.1242/jcs.032003

150. Noel J, Wang H, Hong N, Tao JQ, Yu K, Sorokina EM, et al. PECAM-1 and caveolae form the mechanosensing complex necessary for NOX2 activation and angiogenic signaling with stopped flow in pulmonary endothelium. *Am J Physiol Lung Cell Mol Physiol.* (2013) 305:L805–18. doi: 10.1152/ajplung.00123.2013

151. Gradogna A, Gavazzo P, Boccaccio A, Pusch M. Subunit-dependent oxidative stress sensitivity of LRRC8 volume-regulated anion channels. *J Physiol.* (2017) 595:6719–33. doi: 10.1113/JP274795

152. Jian Z, Han H, Zhang T, Puglisi J, Izu LT, Shaw JA, et al. Mechanochemotransduction during cardiomyocyte contraction is mediated by localized nitric oxide signaling. *Sci Signal.* (2014) 7:ra27. doi: 10.1126/scisignal.2005046

153. Massion PB, Dessy C, Desjardins F, Pelat M, Havaux X, Belge C, et al. Cardiomyocyte-restricted overexpression of endothelial nitric oxide synthase (NOS3) attenuates beta-adrenergic stimulation and reinforces vagal inhibition of cardiac contraction. *Circulation.* (2004) 110:2666–72. doi: 10.1161/01.CIR.0000145608.80855.BC

154. Michel JB, Feron O, Sacks D, Michel T. Reciprocal regulation of endothelial nitric-oxide synthase by Ca2+-calmodulin and caveolin. *J Biol Chem.* (1997) 272:15583–86. doi: 10.1074/jbc.272.25.15583

155. Vielma AZ, Leon L, Fernandez IC, Gonzalez DR, Boric MP. Nitric oxide synthase 1 modulates basal and beta-adrenergic-stimulated contractility by rapid and reversible redox-dependent s-nitrosylation of the heart. *PLoS ONE.* (2016) 11:e0160813. doi: 10.1371/journal.pone.0160813

156. Burkard N, Rokita AG, Kaufmann SG, Hallhuber M, Wu R, Hu K, et al. Conditional neuronal nitric oxide synthase overexpression impairs myocardial contractility. *Circ Res.* (2007) 100:e32–44. doi: 10.1161/01.RES.0000259042.04576.6a

157. Vila-Petroff MG, Younes A, Egan J, Lakatta EG, Sollott SJ. Activation of distinct cAMP-dependent and cGMP-dependent pathways by nitric oxide in cardiac myocytes. *Circ Res.* (1999) 84:1020–31. doi: 10.1161/01.RES.84.9.1020

158. Chowdhary S, Harrington D, Bonser RS, Coote JH, Townend JN. Chronotropic effects of nitric oxide in the denervated human heart. *J Physiol.* (2002) 541:645–51. doi: 10.1113/jphysiol.2001.015107

159. Musialek P. Nitric oxide stimulation of cardiac pacemaking in the sino-atrial node through the activation of a novel signalling pathway: overview of in vitro and in vivo evidence for a new basic mechanism in the control of heart rate. *Przegl Lek.* (2002) 59:691–4.

160. Zhang YH, Youm JB, Earm YE. Stretch-activated non-selective cation channel: a causal link between mechanical stretch and atrial natriuretic peptide secretion. *Prog Biophys Mol Biol.* (2008) 98:1–9. doi: 10.1016/j.pbiomolbio.2008.05.005

161. Oh YB, Gao S, Lim JM, Kim HT, Park BH, Kim SH. Caveolae are essential for angiotensin II type 1 receptor-mediated ANP secretion. *Peptides.* (2011) 32:1422–30. doi: 10.1016/j.peptides.2011.06.002

162. Thomas CJ, Allen AM, McAllen RM, Woods RL. ANP potentiates nonarterial baroreflex bradycardia: evidence from sinoaortic denervation in rats. *Auton Neurosci.* (2002) 97:89–98. doi: 10.1016/S1566-0702(02)00049-8

163. Lonardo G, Cerbai E, Casini S, Giunti G, Bonacchi M, Battaglia F, et al. Atrial natriuretic peptide modulates the hyperpolarization-activated current (If) in human atrial myocytes. *Cardiovasc Res.* (2004) 63:528–36. doi: 10.1016/j.cardiores.2004.03.004

164. Li Y, Sirenko S, Riordon DR, Yang D, Spurgeon H, Lakatta EG, et al. CaMKII-dependent phosphorylation regulates basal cardiac pacemaker function via modulation of local Ca2+ releases. *Am J Physiol Heart Circ Physiol.* (2016) 311:H532–44. doi: 10.1152/ajpheart.00765.2015

165. Rose RA, Kabir MG, Backx PH. Altered heart rate and sinoatrial node function in mice lacking the cAMP regulator phosphoinositide 3-kinase-gamma. *Circ Res.* (2007) 101:1274–82. doi: 10.1161/CIRCRESAHA.107.158428

166. Ju YK, Liu J, Lee BH, Lai D, Woodcock EA, Lei M, et al. Distribution and functional role of inositol 1,4,5-trisphosphate receptors in mouse sinoatrial node. *Circ Res.* (2011) 109:848–57. doi: 10.1161/CIRCRESAHA.111.243824

167. Kapoor N, Tran A, Kang J, Zhang R, Philipson KD, Goldhaber JI. Regulation of calcium clock-mediated pacemaking by inositol-1,4,5-trisphosphate receptors in mouse sinoatrial nodal cells. *J Physiol.* (2015) 593:2649–63. doi: 10.1113/JP270082

168. Mery A, Aimond F, Menard C, Mikoshiba K, Michalak M, Puceat M. Initiation of embryonic cardiac pacemaker activity by inositol 1,4,5-trisphosphate-dependent calcium signaling. *Mol Biol Cell.* (2005) 16:2414–23. doi: 10.1091/mbc.e04-10-0883

169. Levental I, Grzybek M, Simons K. Greasing their way: lipid modifications determine protein association with membrane rafts. *Biochemistry.* (2010) 49:6305–16. doi: 10.1021/bi100882y

170. Domeier TL, Zima AV, Maxwell JT, Huke S, Mignery GA, Blatter LA. IP3 receptor-dependent Ca2+ release modulates excitation-contraction coupling in rabbit ventricular myocytes. *Am J Physiol Heart Circ Physiol.* (2008) 294:H596–604. doi: 10.1152/ajpheart.01155.2007

171. Dassouli A, Sulpice JC, Roux S, Crozatier B. Stretch-induced inositol trisphosphate and tetrakisphosphate production in rat cardiomyocytes. *J Mol Cell Cardiol.* (1993) 25:973–82. doi: 10.1006/jmcc.1993.1109

172. Forrester SJ, Booz GW, Sigmund CD, Coffman TM, Kawai T, Rizzo V, et al. Angiotensin II signal transduction: an update on mechanisms of physiology and pathophysiology. *Physiol Rev.* (2018) 98:1627–738. doi: 10.1152/physrev.00038.2017

173. Mineo C, Shaul PW. Regulation of eNOS in caveolae. *Adv Exp Med Biol.* (2012) 729:51–62. doi: 10.1007/978-1-4614-1222-9_4

174. Zhang Y, Peng F, Gao B, Ingram AJ, Krepinsky JC. Mechanical strain-induced RhoA activation requires NADPH oxidase-mediated ROS generation in caveolae. *Antioxid Redox Signal.* (2010) 13:959–73. doi: 10.1089/ars.2009.2908

175. Simo-Cheyou ER, Youreva V, Srivastava AK. cAMP attenuates angiotensin-II-induced Egr-1 expression via PKA-dependent signaling pathway in vascular smooth muscle cells. *Can J Physiol Pharmacol.* (2017) 95:928–37. doi: 10.1139/cjpp-2017-0035

176. Forrester SJ, Elliott KJ, Kawai T, Obama T, Boyer MJ, Preston KJ, et al. Caveolin-1 deletion prevents hypertensive vascular remodeling induced by angiotensin II. *Hypertension.* (2017) 69:79–86. doi: 10.1161/HYPERTENSIONAHA.116.08278

177. Fridolfsson HN, Patel HH. Caveolin and caveolae in age associated cardiovascular disease. *J Geriatr Cardiol.* (2013) 10:66–74. doi: 10.3969/j.issn.1671-5411.2013.01.011

178. Sinha B, Koster D, Ruez R, Gonnord P, Bastiani M, Abankwa D, et al. Cells respond to mechanical stress by rapid disassembly of caveolae. *Cell.* (2011) 144:402–13. doi: 10.1016/j.cell.2010.12.031

179. Peyronnet R, Nerbonne JM, Kohl P. Cardiac mechano-gated ion channels and arrhythmias. *Circ Res.* (2016) 118:311–29. doi: 10.1161/CIRCRESAHA.115.305043

180. Jensen PN, Gronroos NN, Chen LY, Folsom AR, deFilippi C, Heckbert SR, et al. Incidence of and risk factors for sick sinus syndrome in the general population. *J Am Coll Cardiol.* (2014) 64:531–8. doi: 10.1016/j.jacc.2014.03.056

181. Lou Q, Hansen BJ, Fedorenko O, Csepe TA, Kalyanasundaram A, Li N, et al. Upregulation of adenosine A1 receptors facilitates sinoatrial node dysfunction in chronic canine heart failure by exacerbating nodal conduction abnormalities revealed by novel dual-sided intramural optical mapping. *Circulation.* (2014) 130:315–24. doi: 10.1161/CIRCULATIONAHA.113.007086

182. Nakao S, Hirakawa A, Fukushima R, Kobayashi M, Machida N. The anatomical basis of bradycardia-tachycardia syndrome in elderly dogs with chronic degenerative valvular disease. *J Comp Pathol.* (2012) 146:175–82. doi: 10.1016/j.jcpa.2011.03.016

183. Sanders P, Kistler PM, Morton JB, Spence SJ, Kalman JM. Remodeling of sinus node function in patients with congestive heart failure: reduction in sinus node reserve. *Circulation.* (2004) 110:897–903. doi: 10.1161/01.CIR.0000139336.69955.AB

184. Mesirca P, Fedorov VV, Hund TJ, Torrente AG, Bidaud I, Mohler PJ, et al. Pharmacologic approach to sinoatrial node dysfunction. *Annu Rev Pharmacol Toxicol.* (2021) 61:757–78. doi: 10.1146/annurev-pharmtox-031120-115815
185. Bode F, Katchman A, Woosley RL, Franz MR. Gadolinium decreases stretch-induced vulnerability to atrial fibrillation. *Circulation.* (2000) 101:2200–5. doi: 10.1161/01.CIR.101.18.2200
186. Chang SL, Chen YC, Chen YJ, Wangcharoen W, Lee SH, Lin CI, et al. Mechanoelectrical feedback regulates the arrhythmogenic activity of pulmonary veins. *Heart.* (2007) 93:82–8. doi: 10.1136/hrt.2006.089359
187. Haissaguerre M, Jais P, Shah DC, Takahashi A, Hocini M, Quiniou G, et al. Spontaneous initiation of atrial fibrillation by ectopic beats originating in the pulmonary veins. *N Engl J Med.* (1998) 339:659–66. doi: 10.1056/NEJM199809033391003
188. Tabatabaei N, Asirvatham SJ. Supravalvular arrhythmia: identifying and ablating the substrate. *Circ Arrhythm Electrophysiol.* (2009) 2:316–26. doi: 10.1161/CIRCEP.108.847962
189. Walters TE, Lee G, Spence S, Larobina M, Atkinson V, Antippa P, et al. Acute atrial stretch results in conduction slowing and complex signals at the pulmonary vein to left atrial junction: insights into the mechanism of pulmonary vein arrhythmogenesis. *Circ Arrhythm Electrophysiol.* (2014) 7:1189–97. doi: 10.1161/CIRCEP.114.001894
190. de Jonge HW, Dekkers DH, Tilly BC, Lamers JM. Cyclic stretch and endothelin-1 mediated activation of chloride channels in cultured neonatal rat ventricular myocytes. *Clin Sci.* (2002) 103 (Suppl. 48):148S−51S. doi: 10.1042/CS103S148S
191. Yamamoto S, Kita S, Iyoda T, Yamada T, Iwamoto T. New molecular mechanisms for cardiovascular disease: cardiac hypertrophy and cell-volume regulation. *J Pharmacol Sci.* (2011) 116:343–9. doi: 10.1254/jphs.10R31FM
192. van Borren MM, Verkerk AO, Vanharanta SK, Baartscheer A, Coronel R, Ravesloot JH. Reduced swelling-activated Cl(-) current densities in hypertrophied ventricular myocytes of rabbits with heart failure. *Cardiovasc Res.* (2002) 53:869–78. doi: 10.1016/S0008-6363(01)00507-7
193. Yamamoto S, Kita S, Iyoda T, Yamada T, Ehara T, Iwamoto T. Caveolin-3 modulates the activity of the volume-regulated anion channel in mouse ventricular cells. *Biophys J.* (2011) 100:S170. doi: 10.1016/j.bpj.2010.12.1668
194. Piro ZD, Lodin R, Tyan L, Lim E, Lang D, Glukhov A. Region-specific stretch-induced disruption of caveolae decreases expression of mechanosensitive chloride channels and stimulates fibrogenesis promoting arrhythmogenic atrial ectopy in failing mice. *Biophys J.* (2019) 116:375a. doi: 10.1016/j.bpj.2018.11.2040
195. Zhang Y, Qi Y, Li JJ, He WJ, Gao XH, Zhang Y, et al. Stretch-induced sarcoplasmic reticulum calcium leak is causatively associated with atrial fibrillation in pressure-overloaded hearts. *Cardiovasc Res.* (2020) 117:1091–102. doi: 10.1093/cvr/cvaa163

Conflict of Interest: The authors declare that the research was conducted in the absence of any commercial or financial relationships that could be construed as a potential conflict of interest.

frontiers
in Physiology

REVIEW
published: 23 November 2020
doi: 10.3389/fphys.2020.590534

Small and Intermediate Calcium Activated Potassium Channels in the Heart: Role and Strategies in the Treatment of Cardiovascular Diseases

*David Weisbrod**

Independent Researcher, Tel-Aviv, Israel

Calcium-activated potassium channels are a heterogeneous family of channels that, despite their different biophysical characteristics, structures, and pharmacological signatures, play a role of transducer between the ubiquitous intracellular calcium signaling and the electric variations of the membrane. Although this family of channels was extensively described in various excitable and non-excitable tissues, an increasing amount of evidences shows their functional role in the heart. This review aims to focus on the physiological role and the contribution of the small and intermediate calcium-activated potassium channels in cardiac pathologies.

Keywords: cardiac electrophysiology, SKCa channel, arrhythmia, cardiovascular diseases, blockade and antiblockade effect, IKCa channel, atrial fibrillation, heart failure

OPEN ACCESS

Edited by:
Pietro Mesirca,
INSERM U1191 Institut de Génomique Fonctionnelle (IGF), France

Reviewed by:
Andrea Marcantoni,
University of Turin, Italy
Emilio Carbone,
University of Turin, Italy

***Correspondence:**
David Weisbrod
weisbrod.david@gmail.com

Specialty section:
This article was submitted to Cardiac Electrophysiology, a section of the journal Frontiers in Physiology

Received: *01 August 2020*
Accepted: *02 October 2020*
Published: *23 November 2020*

Citation:
Weisbrod D (2020) Small and Intermediate Calcium Activated Potassium Channels in the Heart: Role and Strategies in the Treatment of Cardiovascular Diseases. Front. Physiol. 11:590534. doi: 10.3389/fphys.2020.590534

SMALL CONDUCTANCE CALCIUM ACTIVATED POTASSIUM CHANNELS (SK1, SK2, SK3)

Characterization, Structure, and Functional Properties

First evidences of calcium-activated potassium channels were assessed under electrophysiological experiments in nerve cells from mollusks. In 1970, Meech and Strumwasser observed an increase in neuron permeability for potassium when intracellular concentrations of calcium chloride were experimentally raised (Meech and Strumwas, 1970; Adelman, 2016). In various gastropod models, the same team confirmed that increased intracellular Ca^{2+} concentrations were associated with hyperpolarization of the membrane potential, raising the hypothesis of a direct channel regulation by $[Ca^{2+}]_i$ (Meech, 1972). Interestingly, the effects were reduced in the presence of the calcium chelating agent EGTA (Meech, 1974). Similar associations between membrane potential voltages and intracellular $[Ca^{2+}]$ were reported in cat spinal motoneurones (Krnjević and Lisiewicz, 1972) and lately in T-lymphocytes (Tsien et al., 1982).

With the emergence of specific pharmacological tools such as apamin (Lazdunski, 1983) or charybdotoxin (Miller et al., 1985), it became possible to isolate several conductances and to study their electrophysiological properties. Apamin-sensitive current was quickly reported in several cell types such as neuroblastoma cells (Lazdunski, 1983), rat myocytes (Romey and Lazdunski, 1984), bullfrog sympathetic ganglion cells (Pennefather et al., 1985), hippocampal CA1 pyramidal neurons (Lancaster and Nicoll, 1987), or rat chromaffin cells (Neely and Lingle, 1992a,b). However, taking into consideration the differences in the cellular preparations or in the experimental conditions, numerous studies of this decade were heterogeneous in the biophysical parameters reported. Not only the kinetic of activation (Lancaster and Nicoll, 1987; Neely and Lingle, 1992a; Park, 1994; Xia et al., 1998) but also the single conductance experimentally estimated, ranging from 4 to 26 pS with symmetrical solutions (Blatz and Magleby, 1986; Mahaut-Smith and Schlichter, 1989; Lancaster et al., 1991; Grissmer et al., 1992, 1993; Partiseti et al., 1992), varied within the different reports, making it challenging to make a consensus. SK channels have relatively similar steady-state activation curves for Ca^{2+} (half activation reported around 300–700 nM) (Park, 1994; Kohler et al., 1996; Xia et al., 1998). This low affinity for calcium suggests a physiological activation of those channels mostly when intracellular calcium levels are elevated. In various excitable cells, those conductances were assumed to play a role either in the spike repolarization (Pennefather et al., 1985; Lancaster and Nicoll, 1987) or in the afterhyperpolarization (Blatz and Magleby, 1986).

The real and actual classification came in Kohler et al. (1996) could probe on cDNA hippocampal libraries and then clone and study the three SK-related mammalian members. Globally, those channels exhibit a high sequence homology (60%), especially within their transmembrane domains (80–90%). Pharmacologically, they differ by their drug sensitivity. KCNN1, the gene encoding the human SK1 channel (KCa2.1), is located on chromosome 19. The canonical predicted primary structure of SK1 is a 543 amino acids sequence, although other isoforms have been reported. For instance, C-terminal spliced variants derived channels have a reduced affinity for calmodulin binding, and their expressions seem to be tissue specific (Zhang et al., 2001). SK1 is moderately sensitive to apamin (IC_{50} 1–12 nM) (Wulff et al., 2007).

KCNN2 is located on chromosome 5 and encodes the SK2 (KCa2.2) channel. Two human isoforms of variable sizes have been currently reported (Willis et al., 2017). The shortest spliced variant, SK2 isoform b (SK2-hib), lacks the N-terminal region and the S1–S5 transmembrane domains (Willis et al., 2017). Thus, these channels exhibit the strongest affinity for apamin (IC_{50} 30–200 pM) or tamapin (Wulff et al., 2007).

Finally, the SK3 calcium-activated K^+ channel (KCa2.3) is encoded by KCNN3, located on chromosome 1. Although different human sliced variants have been reported (Tomita et al., 2003), including the ones in the mitochondria from ventricular cardiomyocytes (Yang et al., 2017), the longest form (731 amino acids) is considered as being the canonical one. Similarly to SK1, SK3 channels are also moderately sensitive to apamin (IC_{50} 1–20 nM). Apamin sensitivity is dependent on the presence of two residues (aspartate and asparagine), oppositely located inside the deep pore of the channels and interacting with the toxin (Ishii et al., 1997).

Structurally, those channels are, overall, similar to the well-studied K^+-voltage-dependent Kv channels. The pore-forming subunit is a tetramer formed by α-subunits. Each monomeric subunit is formed by cytoplasmic amino and carboxyl termini and by six transmembrane segments (S1–S6) (Kohler et al., 1996). The S5-P loop-S6 segments constitute the pore and potassium selectivity filter, and the S4 transmembrane domain contains two positively charged arginine amino acids. Interestingly, the number of positive charges found in the S4 TM is not sufficient to confer to the SK channels voltage dependence, a notable difference with the similar structure found in voltage-gated ion channels (Wulff et al., 2007).

The three clones contain several consensus phosphorylation target sequences, located in their cytosolic amino and carboxyl termini. The C-terminal is constituted by four alpha helices, named "helices A, B, C, and D," respectively. Although those channels do not bind directly to calcium because of the absence of the EF-hand domain, their activity is exclusively calcium-dependent (Kohler et al., 1996). In fact, SK calcium-activated potassium channels are constitutively binding calmodulin protein (CaM), which plays the role of a Ca^{2+} sensing β-subunit. Grissmer and his colleagues already raised the hypothesis of the interaction of a single calmodulin per monomer, based on the estimated Hill coefficient of the apamin-sensitive conductance that they isolated from human T-lymphocytes (Grissmer et al., 1992).

In the absence of calcium, SK channels bind CaM through their C-terminal A-D helix, whereas in the presence of calcium, regions B–C and B–D are involved in the interaction (Xia et al., 1998). These conformation changes suggest that the constitutive SK-association to calmodulin is enhanced with calcium. More recently, structural works confirmed that each CaM protein binds the C-terminal calmodulin binding domain (CaMBD) of the channel monomer through its C-lobe domain and linker, involving electrostatic interactions (Keen et al., 1999). The EF domains of the CaM C-lobe do not bind calcium, whereas the two cytoplasmic EF domains of the N-lobe are accessible and available for such interactions. In a described chemo-mechanical gating model, the Ca^{2+} binding of the CaM would allow a change of conformation of the N-lobe and its interaction to the CaMBD from another monomer. The force created would be transduced to the S6 segment, act as a lever, and drive the SK channel opening (Schumacher et al., 2001). Additionally, the N-terminal EF domains were also shown to stabilize the SK-calmodulin interaction and the channel gating (Li W. et al., 2009). Finally, experiments of targeted mutagenesis on the CaMBD of SK2 decreased the expression of the channel on the membrane of oocytes, suggesting an involvement of calmodulin in surface expression regulation, independently to calcium (Maylie et al., 2004).

Small conductance Ca^{2+} activated K^+ channels can be modulated by additional mechanisms. SK channels contain accessible Serine residues: one in the amino and four in the carboxyl-terminal regions, which can potentially be phosphorylated directly by protein kinase A (PKA) (Ren et al., 2006). Although PKA regulation seems to affect membrane recruitment, the exact consequences are still debated. In a transient expression system, rSK2 phosphorylation by PKA is associated with a reduction of the channel expression at the cell membrane (Ren et al., 2006). This regulation seems C-terminal specific, since SK trafficking is not altered when the three "major" Serine residues are replaced by non-phosphorable amino acids. On the other hand, PKA phosphorylation of the fourth carboxyl Serine is associated with a functional upregulation of SK2 in hypertrophic rat cardiomyocytes (Hamilton et al., 2020). In murine colonic myocytes, the open probability of SK channels is increased after phosphorylation by calmodulin kinase II (Kong et al., 2000).

Expression and Role in the Heart

In the Atrial and the Ventricular Myocardium

The first reports of the existence of SK channels in the heart came recently. Xu et al. (2003) showed that a low concentration of apamin or dequalinium chloride sensibly delayed the late repolarization of the action potentials (AP) recorded in mice and in human isolated atrial cells. An apamin-sensitive current was isolated and showed an inward rectification, similarly to what was described in other tissues, and a single conductance of 3 pS was estimated. Protein expression of SK2 was confirmed across several species (mice, human, cats) and was consistently higher in atrial than in ventricular biopsies.

Two years later, the same group identified SK1 and SK3 in mouse atrial and ventricular cardiomyocytes (Tuteja et al., 2005). Quantification of the mRNA levels by qRT-PCR showed a higher expression of SK1 followed by SK2 transcripts in mouse atrial compared with ventricle cardiomyocytes. The levels of SK3 were similar within the two cell types. In their experiments, the authors confirmed that the action potential recorded from atrial cells was prolonged after pharmacological blockade of SK2 by apamin. However, the effect was amplified when BAPTA-AM, a calcium chelator, was diffused onto the inside of the cytoplasm and blocked the other SK channels expressed, confirming their involvement in the atrial late repolarization (Tuteja et al., 2005). In a mouse model with null mutation of SK2 channels, atrial late repolarization was strongly delayed compared with wild-type (WT) animals (Li N. et al., 2009). Reciprocally, the atrial repolarization and the action potential duration at 90% repolarization (APD_{90}) are shortened compared to WT in mice overexpressing SK3 (Zhang et al., 2014).

In humans, SK1, 2, and 3 are expressed in atrial and ventricular cells (Xu et al., 2003; Skibsbye et al., 2014). In human atrial cells, higher transcript levels of SK2 and SK3 are observed compared with SK1. In a study that investigated the electric properties of "sinus rhythm" atrial cells isolated from the right atrial appendage of patients suffering from coronary artery or valve disorders, SK inhibition delayed the repolarization and elongated the action potential duration (APD) (Skibsbye et al., 2014). In addition, under the pacing of those cells, SK channel blockade leads to a depolarization of the resting membrane potential associated with a decrease in the AP amplitude.

The normal physiological function of the SK channels in ventricular cardiomyocytes is poorly understood and is still discussed. Pharmacological blockade of SK channels in rodents does not modify the ventricular AP and is consistent with the higher calculated IC_{50} for apamin in those cells than in atrial cells (Xu et al., 2003). Similar experiments and observations were made in canines (Bonilla et al., 2014) and humans, confirming a substantial role of these sarcolemmal conductances under physiological conditions in the ventricle (Skibsbye et al., 2014). In animal models, ventricular late repolarization is not altered in SK2 KO compared with WT mice (Li N. et al., 2009). On the other hand, it was shown that their cellular overexpression by adenovirus can shorten the rat ventricular AP (Terentyev et al., 2014).

Although SK channels were mostly thought to assemble as homotetramers, recent evidences show that SK1, SK2, and SK3 can form heterotetrameric channels through their coil–coil C-terminal domains in expression systems but also in mice or human atrial and ventricular tissues (Tuteja et al., 2010). Like their homotetrameric analogs, SK2–SK3 heterotetrameric proteins are functional channels and do play a role in atrial repolarization. Those channels lose their sensitivity for apamin, but their blockade by UCL1684 increases the "beat to beat variability" and provokes AP triangulation, in addition to the well-described delayed repolarization (Hancock et al., 2015).

SK channels can be activated by several sources of calcium—external or internal. They have been shown to colocalize with voltage-gated calcium channels in specific cellular types, such as mouse chromaffin cells (Vandael et al., 2012). Although those two channels do not physically interact, formation of microdomains, in which extracellular calcium entry activates the SK channels and regulates the firing pattern, occurs. In mouse atrial cells, SK2 colocalizes with L-type Ca^{2+} channels through α-actinin interactions, and their activation has been shown to occur essentially with external calcium. Extremely reduced SK2 currents and shortened atrial AP are observed in Cav1.3 null mice (Lu et al., 2007). In an additional mechanism, calcium can be released to the cytosol from the SR, in sparks, transients, or waves. In rat ventricular cells overexpressing SK2, enhanced or depleted SR calcium release affected the SK current recorded, independently to external calcium (Terentyev et al., 2014).

In the Conduction System

In addition to the working myocardium, SK channels are expressed in the conduction system. Pharmacological evidences demonstrated the existence of a small apamin-sensitive current in rabbit isolated sinoatrial (SAN) cells (Chen et al., 2013). Action potentials recorded in the presence of the SK blocker show a reversible decrease in the beating rate activity and an elongation of the APD associated with a delayed repolarization (Chen et al., 2013). SK1, SK2, and SK3 are detected at the transcript level, and the channel expressions can be seen by immunostaining in isolated mouse sinoatrial cells (Torrente et al., 2017). In agreement with what was observed in rabbit, the mouse SAN apamin-sensitive current reported in this work is small. However, in addition to what was previously reported, its blockade leads to a shallower pacemaker slope and a partial depolarization of the maximal diastolic potential (MDP) (Torrente et al., 2017).

SK2 channels are also expressed and functional in the atrioventricular node (AVN) (Zhang et al., 2008). ECG recordings from transgenic mice lacking SK2 show an elongation of the PR interval, whereas the opposite is seen when the channel is overexpressed (Zhang et al., 2008). At the cellular level, the spontaneous firing frequency of the AVN cells isolated from the null mutation mice are decreased compared with the same cells from WT or SK2 overexpressed animals. Interestingly, the MDP from the two types of mutant AV node cells remains unchanged.

In the Inner Organelles

On top of their role at the cellular membrane, channels can be additionally expressed at the membrane of inner organelles. In guinea pig ventricular cells, a KCa channel has been found in the mitochondria. The "mKCa" channel was purified from mitochondria membranes with standard biochemical techniques and is observed by immunostaining or by electron microscopy in the inner membrane of the mitochondria (Stowe et al., 2013). The single current recorded from purified mitochondrial channels is calcium-dependent and apamin-sensitive, similarly to the regular KCa2.2. In a model of ischemia reperfusion, Stowe et al. (2013) showed that hearts that were preconditioned with an mKCa pharmacological opener showed better LV pressure or coronary flow and a markedly reduced infarct size compared with untreated hearts. Those benefits are reduced when an $O_2{}^-$ dismutator is added together with the SK opener, suggesting a relation between those channels and the transient benefit of pathways related to the synthesis of superoxide radicals. In a longer term, however, the increased K^+ flux in the mitochondria is associated with lower mitochondrial Ca^{2+}, to a fine-tuned regulation of the mitochondrial energetic state, and decreased $O_2{}^-$ production, suggesting a protective role of those channels against cardiac injury (Stowe et al., 2013). The same group reported the existence of mitochondrial SK3 KCa isoforms in human and guinea pig ventricular cells (Yang et al., 2017). The carboxyl terminal extremity of those channels is crucial for their proper trafficking at the mitochondria membrane. The calcium from the mitochondrial matrix might activate them, resulting in the reduction of a redox state, and subsequently to cardioprotective mechanisms, similarly to other mKCa channels (Yang et al., 2017).

Implication in Cardiopathologies

Beside their normal physiological functions, small conductance potassium channels are actively involved in the mechanism of several heart diseases.

Atrial Fibrillation

Atrial fibrillation (AF), the most common cardiac disorder, is often initiated by an electric dysfunction in pulmonary vein (PV) cells. Isolated PV cells from healthy rabbits do have an intrinsic small apamin-sensitive current, which physiologically plays the role of "repolarization reserve." In the presence of apamin, the spontaneous electric activity is decreased, and the repolarization is delayed (Chen et al., 2013).

The first evidences of involvement of SK channels in atrial remodeling and AF came from experiments conducted on an isolated burst-paced atrium from rabbits (Özgen et al., 2007). This model, which simulates the pulmonary veins ectopic foci observed in AF, is associated with higher trafficking and expression of SK2 protein at the membrane of those cells and a bigger "apamin-sensitive" current. Consequently, the repolarization of the PV cells is shortened following the remodeling. ECG recorded from genetic modified mice lacking KCa2.2 channels after extrastimulation shows an AF pattern but no ventricular disorders. At the cellular level, action potential recorded from SK2 KO atrial cells shows occurrences of early afterdepolarizations (EADs) compared with WT mice atrial cells (Li N. et al., 2009). In *ex vivo* or *in vivo* WT animal models in which the atrium was acutely paced and generated induced paroxysmal AF, the duration of reversion to sinus rhythm was decreased under the infusion of SK2 blockers (Diness et al., 2010). The antiarrhythmic effect of SK blockade was associated with an elongation of the refractory period (aERP) and a termination of reentry phenomena (Diness et al., 2010; Skibsbye et al., 2011) without affecting the QT interval. Those protective effects of SK blockers on the atrium were reversible after washout, since the aERP was reduced and AF episodes were induced *de novo*. Mechanistically, the reduced SK currents would delay the repolarization of the action potentials in the atrium and the AV node, elongate the refractory period, and prevent reentrant circuits. In a canine chronic induced AFs model, hearts in which the atrium was "tachy-pached" with unipolar electrodes for 1 week underwent pathological remodeling (Qi et al., 2014). Although SK currents are bigger in the pulmonary veins compared with the left atrium in both control and paced animals, the SK open probability calculated from single channel recordings is higher in chronic AF (Qi et al., 2014). SK2 transcripts and protein expression levels were found higher in pulmonary veins but identical in diseased and healthy animals, whereas SK2.1 protein expression is specifically increased after atrial tachy-pacing (AT-P). Action potentials recorded from left atrial or PV cells have shorter duration (APD_{90}) in AF animals. Consistently, the atrial effective refractory period observed in ECG is shortened in those dogs, and the AF episodes are maintained, suggesting a direct involvement of the SK currents in the pathophysiology mechanisms of chronic AF. Finally, SK blockade elongates the AP repolarization at a cellular level and improves the AF episodes by elongating the refractoriness in ECG from AF dogs (Qi et al., 2014).

In human, however, observations are different or debated and may suggest a dynamic and chronologic pathological remodeling controlled by molecular regulations. Li et al. (2011) showed that SK2 current density is bigger in atrial cells from patients diagnosed with persistent AF (at least 6 months) than in non-AF patients. At a molecular level, CAMKII levels are increased in human AF atrial cells, associated with a left shift of the SK calcium dose-response curve and bigger currents (Fan et al., 2018). Oppositely, in atrial biopsies from chronic AF patients (more than 6 months preceding a medical surgery), the SK1, SK2, (Yu et al., 2012) or SK3 (Skibsbye et al., 2014) transcripts and protein levels are reduced compared with atrial biopsies obtained from patients with sinus rhythm. Those observations are in good agreement with the work of Ling et al. (2013), which described a negative regulation of SK3 channels in chronic AF. In fact, this group reported that the micro-RNA miRNA-499, which binds the 3′UTR of KCNN3, is upregulated in human atrial cells isolated from chronic AF patients and decreases SK3 protein expression by nearly half. A GWAS conducted in 1,335 patients showed that a common SNP variant, located in the intron between the first and the second exons of KCNN3, is positively correlated to lone AF (Ellinor et al., 2010). The apamin-sensitive current is decreased in cAF-isolated cells and could explain the attenuation of the AP elongation observed when specific SK blockers are used

(Yu et al., 2012; Skibsbye et al., 2014). Taken together, those data suggest a low involvement of the SK channels in chronic AF.

Heart Failure

Since AF and heart failure are closely related and often coexist in patients, an assumption could be that SK channels might be involved in this condition. In a canine model of recent or persistent heart failure with reduced ejection fraction (HFrEF) (1 and 4 months) with or without superimposed AF, Bonilla et al. (2014) extensively pointed out the existence of a dynamic remodeling. In paced untreated cardiomyocytes from healthy and recent heart failure (HF) animals without AF, APs are unmodified whereas those are drastically elongated four months after the HF event. Similarly, although a pharmacological blockade by apamin is ineffective in normal ventricular cells, its effects on the AP duration and the arrhythmogenicity are positively correlated to the duration of the disease (Bonilla et al., 2014).

In chronic HFrEF, the protein level of SK3—but not SK2—is strongly increased in the ventricle, whereas both proteins are overexpressed in the atrial cells. SK current density is bigger in rabbit HF ventricular cells, and an increasing gradient seems to exist between the endocardial, midmyocardial, and epicardial myocytes (Chua et al., 2011; Chang et al., 2013b). Consistently with what is shown in AF only (Qi et al., 2014), the AP of atrial cells is strongly shortened in animals with chronic HFrEF and superimposed AF. In human HFrEF patients, the same group observed an increase in the ventricular levels of SK2 and SK3 in biopsies from explanted end-stage failing hearts compared with non-HF patients (Bonilla et al., 2014). Strong beat-to-beat variability and arrhythmic patterns are visible when the HF isolated ventricular myocytes are exposed to apamin in mice, humans, and rabbits (Chang et al., 2013a; Chang and Chen, 2015). Taken together, those data suggest that SK channels are upregulated in chronic HF and are involved in the maintenance of the ventricular stability (Hsieh et al., 2013; Bonilla et al., 2014; Terentyev et al., 2014; Chang and Chen, 2015).

Cardiac Arrhythmia

Besides their role in AF, SK channels are associated with other pro- or antiarrhythmic phenomena. In telemetry recordings obtained from SK2 KO mice, AVN dysfunctions such as complete AV block with AV dissociation are visible (Zhang et al., 2008). Adenoviral overexpression of SK2 in WT rat ventricular cells is associated with an attenuation of induced afterdepolarizations (DADs) provoked by SR Ca^{2+} depletion in the presence of caffeine (Terentyev et al., 2014). On the other hand, DADs, severe bradycardia, advanced AV block, and higher incidence of sudden death occur in a murine model overexpressing SK3 (Mahida et al., 2014). In a rabbit failing heart, apamin suppresses the recurrent spontaneous ventricular fibrillation episodes (Chua et al., 2011). Mitochondrial SK channels may also be relevant therapeutic targets in the management of arrhythmia. Cardiac hypertrophy is associated with mitochondrial ROS synthesis, oxidative stress, and abnormal intracellular calcium handling. In addition to the effect on ROS levels and related cardioprotection, mSK activation reduces the frequency of ER spontaneous calcium waves and the occurrences of ventricular arrhythmia (Kim et al., 2017). The exact mechanism is unclear, but the reduced oxidation levels could improve the functional stability of ryanodine receptors (RyRs), thus preventing arrhythmic SR Ca^{2+} leakage and subsequent DADs.

Myocardial Infarction

Myocardial infarction (MI), such as heart failure, is a condition associated with an electric remodeling. Potassium currents such as the transient outward Ito, the rapid IKr, slow IKs, and a delayed rectifier are reduced (Nattel et al., 2007). In a rabbit model of chronic MI without HF, AP width and intracellular calcium transient duration are shorter in the peri-infarct zone and the remote zone compared with healthy ventricular cells, suggesting progressive remodeling (Lee et al., 2013). Isolated ventricular cells from the peri-infarct zone have a larger "apamin-sensitive" current density than cardiomyocytes from the unaffected zone, which may explain the greater elongation of the AP repolarization under SK blockade in the altered tissue. Recovery from pacing experiments shows a shortening of the AP repolarization in MI ventricle only, which is reverted with apamin. Taken together, those results suggest an extensive compensatory role of SK channels in the repolarization in a MI heart.

INTERMEDIATE CONDUCTANCE CALCIUM ACTIVATED POTASSIUM CHANNELS (SK4)

Characterization, Structure, and Biophysical Properties

The intermediate calcium activated channel SK4 (KCa 3.1) is encoded by the gene KCNN4, located on the q13.2 part of chromosome 19 in humans (Ghanshani et al., 1998). Historically, the hypothesis of a calcium-activated potassium channel was raised by Gardos (1958) when he noticed a correlation between the potassium outflow from erythrocytes and the intracellular EDTA/calcium competition. Four decades later, SK4 has been cloned (Ishii et al., 1997; Joiner et al., 1997), biophysically characterized, and formally identified in the erythrocytes (Hoffman et al., 2003). Although the main channel is a 427 amino acids protein, different mRNA transcripts have been reported (2.1, 2,5, 3.2, and 4.5 kb), suggesting different splice variants. However, no SK4 isoforms have been currently reported. SK4 is strongly expressed in non-excitable cells such as erythrocytes, lymphocytes, placenta cells, lung, prostate, bladder, or smooth muscle cells. Electrically, its single conductance varies from 12 to 42 pS (Hamill, 1981; Grygorczyk et al., 1984; Partiseti et al., 1992; Joiner et al., 1997; von Hahn et al., 2001), and the current exhibits the same inward rectification described in other SK channels. Like other SK channels, the kinetic of the deactivation of the channel is slow and calcium-independent (Berkefeld et al., 2010). However, SK4 differs by its higher affinity for intracellular Ca^{2+} (half activation at 95 nM free Ca^{2+}) (Joiner et al., 1997), compared with other SK channels (300–700 nM) (Chang and Chen, 2015). Taken together, those biochemical parameters allow

SK4 channels to play a functional role at physiological basal $[Ca^{2+}]_i$ concentrations (around 100 nM) or lower and at late phases of the action potential. Pharmacologically, SK4 is insensitive to apamin but blocked by different agents such as dequalinium chloride, clotrimazole, or, more recently, TRAM-34 and senicapoc.

Structurally, SK4 is also very close to the canonical voltage-gated potassium channels, even if it presents a low homology (40–50%) with the other SK subfamily (Ishii et al., 1997; Joiner et al., 1997). KCa3.1 is a tetrameric protein of approximately 95 Å; in length and 120 AÅ; in width. Each monomer is formed by six transmembrane domains (S1–S6) and prolonged by cytoplasmic N and C termini (**Figure 1**). S4, the voltage sensor, contains two positively charged arginines, which is not enough for voltage dependence. The hydrophobic segment (P-loop) between S5 and S6 forms the pore of SK4 and contains the GYG consensus sequence, which confers to those channels a "selectivity filter" for potassium (Joiner et al., 1997). Compared with SK2 channels, the amino and carboxyl extremities are shorter, although conserved features are observed in the C-terminal (Ishii et al., 1997). The proximal part of the C terminal, previously named Ct1, is formed by the alpha helixes HA and HB, while the Ct2 distal part contains the HC helix and a Leucin zipper domain involved in inter-unit interaction (Joiner et al., 2001). Ca^{2+} binding of SK4 is indirect since no EF hands are reported in the channel (Joiner et al., 1997; Khanna et al., 1999). Instead, and similarly to what was described in SK2 (Schumacher et al., 2001), the first 62 AA of the proximal C terminal are involved in the binding of calmodulin (Fanger et al., 1999; Khanna et al., 1999). HA and HB helixes cross while forming the calmodulin binding domain (CaMBD), a pocket parallel to the cell membrane, which preassociates with the C-Lobe of calmodulin in a calcium-independent manner. Four calmodulins interact with the channel and bind Ca^{2+} through the EF motif of their N-lobe (Schumacher et al., 2001). Mutations in calmodulin or in the CaMBD strongly decrease the IKCa current in various models, suggesting a role of calmodulin in the gating and trafficking of the channel (Fanger et al., 1999; Joiner et al., 2001). In addition, mutations in the leucin zipper also lead to drastic reduction of the current and membrane protein expression (Khanna et al., 1999), confirming a role of the distal C-terminal in the proper folding and trafficking of SK4 independently to calmodulin. Recently, Lee and MacKinnon (2018) described in depth the structure and mechanism of the human SK4 interaction and CaM using the Cryo-EM technique. The HC helix is pointing toward the cytosol and is associated with similar helixes from the other subunits in a coil-coiled structure, essential for the proper assembly and trafficking of the channel. In the absence of calcium, the CaM N-lobe is free, oriented near the bottom of the S2 subunit, and the valine amino acids from the S6 transmembrane segment of each monomer close the gate responsible for K^+ outflow. In the presence of calcium, the N-lobe of the CaM moves toward and binds the S4–S5 linker of an adjacent subunit, pulling it toward the cytosol. This movement leads to conformational changes in the S6 segments, enlargement of the gate, and opening of the channel. Ca^{2+}–CaM interactions induce cooperative conformation changes necessary for the opening of the channel (Fanger et al., 1999).

Although nucleotides or cyclic nucleotides such as cAMP do not directly bind or modulate the channel activity (Pellegrino and Pellegrini, 1998; Gerlach et al., 2000), KCa3.1 presents potential phosphorylation sites for different kinases (Joiner et al., 1997; Gerlach et al., 2000). In the distal C-terminal part of the channel, phosphorylation consensus sites such as Serine 334 for PKA or four other amino acids for PKC have been reported. Several studies pointed out the positive regulatory role of hydrolyzed ATP on SK4 (Gerlach et al., 2000; von Hahn et al., 2001; Hayashi et al., 2004). However, the downstream mechanisms or effects are debated and seem to be species dependent. In human erythrocytes (Pellegrino and Pellegrini, 1998) and rat acinar cells (Hayashi et al., 2004), cAMP-PKA increases KCa3.1 activity, whereas controverted results have been reported in oocytes (Gerlach et al., 2000; von Hahn et al., 2001). In rat glial cells or transfected cells expressing the human SK4, PKA phosphorylation was specific to the consensus site and associated with a decrease in the current (Wong and Schlichter, 2014). Surprisingly, mutagenesis studies show that ATP-dependent regulation still occurs when consensus phosphorylation sites are altered (Gerlach et al., 2001; von Hahn et al., 2001), raising the hypothesis of alternative phosphorylation sites or other kinases involved.

PKC activators reduce the opening frequency of IKCa but not its single conductance in human erythrocytes (Del Carlo et al., 2003), whereas similar regulations have not been reported in human colon T84 cell line (Devor and Frizzell, 1998). Other kinases such as the nucleoside diphosphate kinase B (NDPK-B) (Srivastava et al., 2006) or the CaMKII (Khanna et al., 1999; Gerlach et al., 2000) regulate IKCa in T-cells and could play a role in cell activation (Srivastava et al., 2006; Wulff et al., 2007). Other factors or regulators can modulate IKCa. For instance, arachidonic acid binds the pore region of the SK4 channel and strongly decreases its current (Devor and Frizzell, 1998; Hamilton et al., 2003). Temperature can affect the open probability of SK4 and the net potassium efflux in human erythroblasts (Hoffman et al., 2003). Finally, beta-blockers can fine-tune KCa3.1 activity. In human erythrocytes, where beta-receptors are absent, submillimolar concentrations of propanolol increase the calcium sensibility of SK4, whereas millimolar concentrations block the conductance (Schwarz et al., 1989).

Expression and Role in the Heart

The first reports that characterized SK4 in several tissues failed to detect a transcript in heart when 3′UTR or other cDNA sequences were used as a probe in Northern Blot experiments (Ishii et al., 1997; Joiner et al., 1997; Hoffman et al., 2003). With the emergence of high-throughput screening techniques, very detailed mapping of ionic channel expressions has been collected in atrial, ventricular working cardiomyocytes or conduction tissues (Marionneau et al., 2005; Gaborit et al., 2007). Surprisingly, while the expression of SK1-3 has been investigated, SK4 was overlooked.

First associations between KCa3.1 and the heart came in embryonic stem cells when Kleger et al. (2010) cultured mice and human (Müller et al., 2011) embryonic stem cells in the presence of the SK4 opener 1-EBIO and observed an

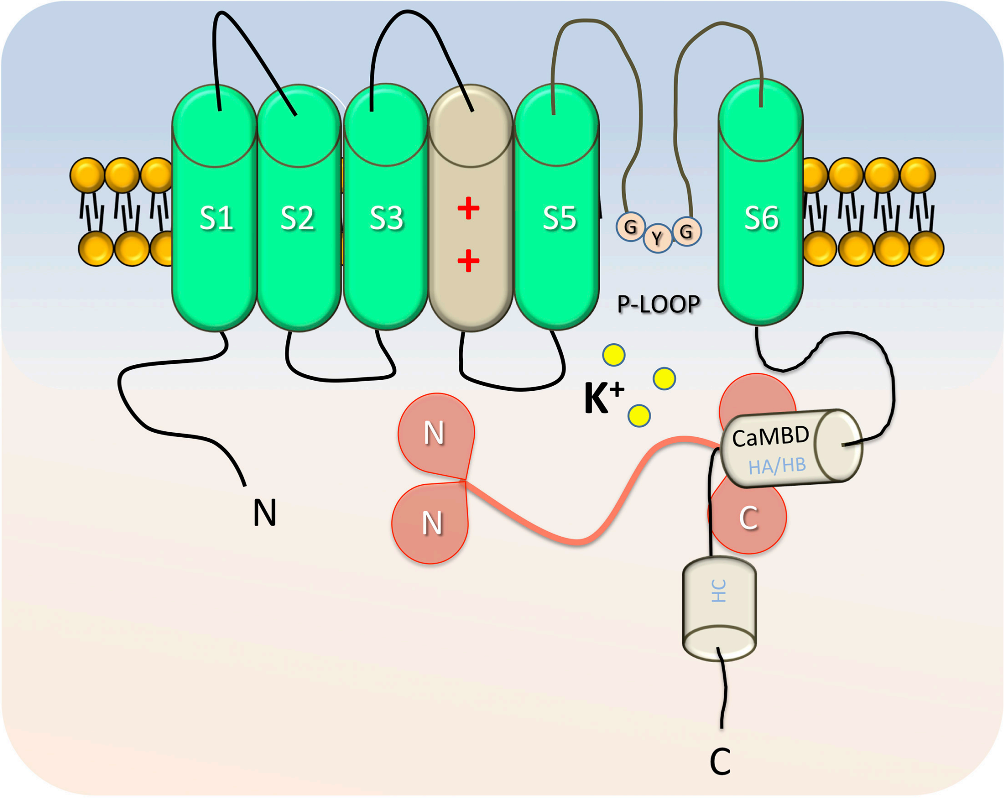

FIGURE 1 | Representative cartoon of a SK4 α-subunit in absence of calcium. Each monomer is formed by six transmembrane domains (S1–S6), which are prolonged by cytoplasmic N and C termini. S4 is the voltage sensor, with positively charged amino acids. The segment (P-loop) between S5 and S6 forms the pore of SK4 and includes the GYG "selectivity filter" for potassium. The Calmodulin binding domain (HA and HB helixes), binds Calmodulin on the C-lobes. In low $[Ca^{2+}]_i$ conditions, the N-lobes of Calmodulin are free and positioned closely to the S2-S3 intracellular segment. Helix C, toward the cytosol is involved in the assembly of the α-subunits as a functional channel.

enriched differentiation into cardiomyocytes, especially toward a pacemaker-like phenotype. In fact, typical "pacemaker signature genes" such as Tbx3, HCN4, or Cx30 were upregulated, whereas the MLC2V and Cx43 ventricular genes were downregulated. Inversely, cell culture in the presence of clotrimazole—but not apamin—or the elaboration of stable knocked down ES lines with shRNA against SK4 specifically decreased cardiogenesis. Recently, an independent group showed that rat adipocyte stem cells were effectively differentiated into pacemaker-like cells following SK4 adenoviral transduction. When those modified stem cells were injected in the heart, they generated an ectopic pacemaker after differentiation (Yang et al., 2019). An additional study focused on the dynamic gene expression in mouse AVN during development and reported a ninefold increase in SK4 transcripts (Horsthuis et al., 2009).

Taken together, those reports show a molecular involvement of KCa3.1 in cardiac and pacemaker fate through the activation of the ERK1/2 signaling pathway (Kleger et al., 2010; Yang et al., 2019). However, the channel expression itself and its role in the cardiac pacemaker mechanism were not mentioned.

First direct evidences of the protein expression of the SK4 channel in cardiomyocytes and its physiological role were assessed in cardiomyocytes derived from human embryonic stem cells (hESC-CMs) (Weisbrod et al., 2013). Young hESC-CMs beat spontaneously, mimic the features observed in the primitive heart during development, and have been used as a model to better understand the debated mechanisms underlying the pacemaker activity (Lakatta and DiFrancesco, 2009). The diastolic depolarization (DD) or "pacemaker depolarization" results from a small net inward current across the cell membrane and is the key feature of the cardiac automaticity. It occurs during the diastole, at the end of an action potential, and is responsible for triggering the next one. Different models such as the "membrane clock" involving mainly HCN and other ion channels (Brown and Difrancesco, 1980; Hagiwara et al., 1988, 1992; Mangoni et al., 2003; Stieber et al., 2004; Demion et al., 2007; Baruscotti et al., 2010; Mesirca et al., 2014), the "Ca^{2+} clock" with its spontaneous Ca^{2+} release from the SR and subsequent NCX-1 activation (Fabiato and Fabiato, 1972; Bassani et al., 1997; Bogdanov et al., 2001; Vinogradova et al., 2004; Maltsev et al., 2006; Maltsev and Lakatta, 2007; Groenke et al., 2013), or the coexistence of both could explain this mechanism (**Figure 2**) (Gao et al., 2010; Lakatta et al., 2010; Zahanich et al., 2011; Billman, 2012). Blocking the If or INCX inward conductances led to a counterintuitive reversible depolarizing drift of the MDP, suggesting a mechanistic convergence of both models to

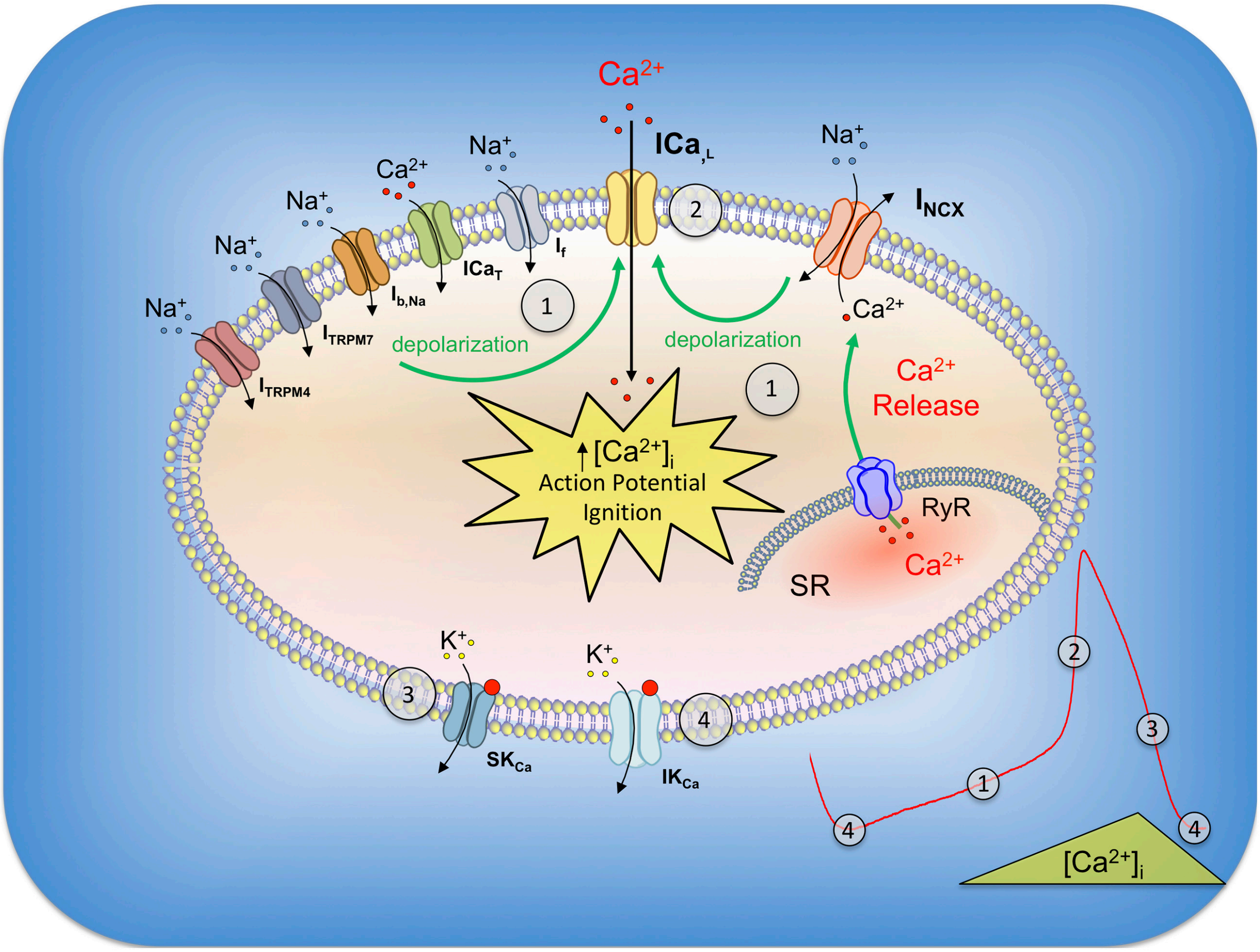

FIGURE 2 | General model of the pacemaker currents in SAN and their relation with SK and IK channels. During the late repolarization of the previous action potential, SK4 are still opened and their outward currents (4) act like a MDP driving force (4), which concurrently activates HCN channels (I_f current). The gradual depolarization recruits other conductances such as Ib, Na, ICa_T (3.1 and 3.2), ITRPM4 and ITRPM7, which, altogether in synergy, are responsible for the diastolic depolarization (1). In parallel, diastolic sarcoplasmic spontaneous calcium release through RyR receptors increases the cytoplasmic level of calcium and activates the NCX-1 exchanger in its forward mode (1). The progressive Ca^{2+} extrusion operated by NCX from early to late DD gradually reduces IKCa and allows inward currents to take over. INCX, together with the other described currents, depolarize the membrane until the threshold of activation for L-type Ca^{2+} channels (ICa,L) and AP ignition (2). During the early repolarization, high $[Ca^{2+}]$i open small SK channels (3) which contribute to this phase of the action potential. The progressive cytosolic decrease of calcium (SR reuptake and extrusion) decreases SK currents at the exception of IKCa due to SK4 higher affinity for Ca^{2+} (4). N.B. BKCa, Kv and other conductances have not been included in this cartoon for readability.

a previously undescribed blocked outward current (Weisbrod et al., 2013). RT-PCR, Western blots, immunostaining, and electrophysiological characterization of the unitary conductance isolated from membrane patches of hESC-CMs identified for the first time in human-derived cardiac pacemaker cells this current as KCa1.3, the intermediate Ca^{2+} activated-potassium channel (IKCa/SK4). Under physiological conditions, pharmacological experiments with different IKCa antagonists led to a reduction of the diastolic pacemaker slope, a depolarizing drift of the membrane resting potential, and, ultimately, a cessation of the pacing in young healthy hESC-CMs (Weisbrod et al., 2013). Interestingly, the depolarized MDP but the unaffected AP duration under SK4 blockade suggests an involvement of KCa3.1 in the late repolarization, as an outward current that dynamically balances the inward pacemaker conductances in a $[Ca^{2+}]_i$-dependent manner (Weisbrod et al., 2013, 2016). In a recent study, SK4 and HCN2 ventricular adenoviral overexpressions were sufficient to increase the *ex vivo* heart frequency recorded in a complete rate heart block rat, and transform those cells into active pacemakers (Zhao et al., 2019). After a prolonged *in vitro* maturation, hESC-CMs decrease their spontaneous firing rate and lose their intrinsic pacemaker activity, similarly to the working cardiomyocytes of the primitive heart (Satin et al., 2004; Couette et al., 2006; Bakker et al., 2010). Although SK4 is still expressed in those late-stage cells, the decrease in the beating rate associated with IKCa blockade was restricted to cells that exhibited strong pacing, suggesting an important role of SK4 in pacemaker tissue (Weisbrod et al., 2013). In a mouse adult heart, the protein expression of SK4 has been shown in atrial appendages, ventricles, and also in the sinoatrial node (Haron-Khun et al., 2017). In rats, SK4 is strongly expressed in the SAN, AVN, and ventricles, but, in a less extent, in the atria (Zhao et al., 2019). In contrast, the canine protein expression of KCa3.1 is found in the atria only, suggesting interspecies variability (Yang et al., 2020a,b). Finally, the expression of KCa3.1 has been reported in endogenous cardiac progenitor cells (Neco et al., 2012).

In biopsies from adult human hearts, although SK4 is detected at the mRNA level in right atrial and ventricular tissues, the protein is expressed only in the atrium (Weisbrod et al., 2016). In SAN cells obtained from healthy mice, a TRAM-sensitive current is pharmacologically isolated under voltage clamp configuration. The spontaneous AP frequency and the pacemaker slope are strongly reduced in a reversible manner when single SAN cells are exposed to SK4 blockers alone or together with a β-agonist (Haron-Khun et al., 2017). *In vivo* telemetric recording experiments performed on WT mice show a reduction of the heartbeats and a PR elongation at rest and during treadmill exercises when SK4 blockers are injected in IP. From a mechanistic point of view, the reduction of the heartbeat and the decrease in the spontaneous firing rate of the cardiac pacemaker cells following IKCa inhibition could be explained by the reduced driving force at the beginning of the diastole. The diminution of the outward IKCa K^+ current under SK4 blockade would impair the fine-tuning of the depolarizing currents (especially I-funny), shallow the diastolic slope, delay the time between two action potentials, and subsequently decrease the beating rate. Additionally, the depolarization of the MDP would reduce the depolarizing currents (inactivation of a subpopulation of the INa^+ plus diminution of ICa^{2+}) and the upstroke velocity (dV/dt) of the action potentials.

Taking altogether, different data show an important involvement of the intermediate calcium-activated K^+ channel in cardiac automaticity.

Implication in Cardiac Disorders and Arrhythmia

Scientific evidences supporting the involvement of an SK4 channel in cardiopathies are still limited, and the mechanisms are poorly understood.

In an acute model of myocardial infarct in rats, Saito and colleagues observed an increased expression of SK4 transcripts following the coronary ligation (Vigneault et al., 2018). Interestingly, the overexpression was higher in the animal group that underwent a reperfusion compared with those animals with permanent occlusion. While the related mechanism is not clear, SK4 channels might be involved in the vascular remodeling following MI since those are known to be associated with cell proliferation (Pena et al., 2000; Saito et al., 2002).

Catecholaminergic polymorphic ventricular tachycardia (CPVT) is a stress-induced ventricular arrhythmia associated with cytoplasmic calcium leakage due to mutations in calsequestrin 2 (CASQ2) (Postma et al., 2002; Wang et al., 2005), ryanodine receptor (RyR2) (Laitinen et al., 2001; Eldar et al., 2003), triadin (Priori et al., 2001), or calmodulin (Roux-Buisson et al., 2012). At rest, ECG is normal, although sinus bradycardia has been observed in patients (Wang et al., 2005). Under stress or exercise, the $Ca^{2+}{}_i$ overload activates NCX-1, which generates at the cellular level DADs leading to ventricle potentially fatal disorders such as ventricular premature complexes (VPCs) or non-sustained (NSVT) or sustained ventricular tachycardia (SVT) visible at ECG. In addition, CPVT is associated with SAN dysfunction caused by altered calcium homeostasis under beta-adrenergic stimulation (Makita et al., 2014; Haron-Khun et al., 2017). In cardiomyocytes derived from human induced pluripotent cells (hiPS-CMs) from CPVT2 patients carrying a CASQ2 mutation, Haron-Khun et al. (2017) showed that isoproterenol-induced DADs were neutralized in the presence of TRAM-34. Similar effects were observed in isolated SAN cells from CASQ2 KI mice expressing the same patient mutation, and a TRAM-sensitive current was isolated. Abnormal Ca^{2+} transients recorded from isolated CPVT KI mice SAN were drastically improved in the presence of the SK4 blocker. Finally, in addition to the heart rate decrease and the PR elongation, ECG arrhythmic features visible at rest and during treadmill exercises were strongly reduced or normalized when SK4 blockers were injected in IP to CPVT mice (Haron-Khun et al., 2017).

Arrhythmogenic right ventricular cardiomyopathy (ARVC) is a rare but severe cardiac condition frequently associated with mutations of proteins involved in desmosomes (Marcus et al., 2013) (Plakophilin-2, Desmoplakin, Desmoglein-2, and Desmocollin-2), structures involved in the cell–cell interactions. Ventricular cardiomyocytes progressively detach and are replaced by a fibrotic and fat tissue upon an inflammatory remodeling, leading subsequently to ventricular tachyarrhythmia and sudden death (Corrado et al., 2019). In hiPS-CMs derived from an ARVC patient carrying a mutation in the DSG2 gene coding the desmoglein-2 protein, Buljubasic et al. (2020) recently showed that protein expression of SK4 is strongly increased compared with hiPSC-CMs obtained from healthy donors. Interestingly, the transcript levels and protein expression of NDPK-B, kinase known to upregulate the IKCa current, are also increased in the lysate from ARVC cells. Consistently with this observation, the pharmacologically isolated calcium-dependent IKCa current was stronger in ARVC hiPSC cells. Quantified arrhythmic features and spontaneous pacing were higher in AP from ARVC cells compared with healthy donors (Buljubasic et al., 2020). However, intracellular addition of recombinant NDPK-D increased the IKCa current, the spontaneous beating rate, and also the frequency of arrhythmic events in the AP recorded from both healthy and ARVC cells. The reversible nature of those phenomena by exposure to protein histidine phosphatase 1 (PHP-1) points a dual regulation of SK4 in this disease. TRAM-34 perfused in ARVC hiPSC decreased the number of DADs and other arrhythmic features before depolarizing the MDP until a rapid AP cessation. Taken together, those data strengthen the pro-arrhythmic role of the SK4 upregulation through a NDPK-D-dependent mechanism and a potential approach to treat ARVC.

In addition to ventricular arrhythmia, new evidences pointed the involvement of SK4 in AF and its blockade as a potential new therapeutic strategy. In dogs, which were subjected to rapid atrial pacing for 7 h to induce AF, protein expression of SK4 expression from right and left atriums was increased compared with non-paced dogs, confirming the consistent reported proarrhythmic potential role of SK4 (Haron-Khun et al., 2017; Buljubasic et al., 2020). Infusion with 10 mg/kg TRAM-34 suppressed the AF induction in the treated group (Yang et al., 2020b). The same group confirmed the involvement of SK4 in AF and the benefit of its blockade in dogs that developed AF after acute stroke (Yang et al., 2020a). In a canine model of chronic HF, TRAM-sensitive current, SK4 transcripts, and protein expression levels are reduced compared with healthy animals (Neco et al., 2012), suggesting a pathological downregulation. The lower IKCa current density was associated with a depolarization of the cell membrane resting potential, in consistency with data observed after pharmacological blockade in previous reports (Weisbrod et al., 2013, 2016).

DISCUSSION

Since almost four decades, a better understanding of general pathophysiological mechanisms, an intensive management of patient lifestyle, and the development of new class of molecules led to a successful worldwide decline in mortality from major CV diseases such as coronary arterial diseases, stroke, MI, and ischemic cardiopathies (Mensah et al., 2017; Cheng et al., 2018). However, despite the major advances in cardiovascular pharmacology, disease registries show that the management of cardiac arrhythmia and HF did not benefit from this mortality reduction (Cheng et al., 2018).

With the aging of the worldwide population, the increased prevalence and costs related to those diseases, and the longer period of medical care, it is fundamental to improve the quality of treatment by providing alternative or additional therapeutic strategies.

Within the last 20 years, a growing number of evidences point out not only the physiological role of calcium-activated potassium channels in the heart but also their involvement in various cardiac disorders.

SK channels and IK channel (SK4) have been found in the atrial, ventricle myocardium and in conducting tissue from different species, including humans. Because of their low Ca^{2+} affinity (half activation at 300–700 nM), small-conductance Ca^{2+}-activated K^+ channels are likely to be involved in repolarization phases, where the cytosolic calcium is still elevated. This is well illustrated by the APD elongation reported especially in atrial cells when those are exposed to apamin. In the ventricle, on the other hand, small calcium-activated channels are less involved in the repolarization itself. They can enhance the cell stability by playing the function of "repolarizing reserve," especially in diseases leading to an electric remodeling such as HF or MI. In contrast, intermediate-conductance Ca^{2+}-activated K^+ channels, with their higher affinity for calcium, open at physiological $[Ca^{2+}]_i$ concentrations and are involved in the late repolarization (MDP). The fact that SK4 blockade does not elongate the APD, leads to a reduction of the diastolic slope (DD Slope) and most importantly, to a depolarization of the MDP in cardiac cells with spontaneous electric activity, strengthen its role of "fine tuner" of the well-established "pacemaker inward currents" (Weisbrod et al., 2013, 2016).

In SAN cells, SKCa and IKCa blockade leads to a reduction of the pacing. Effects on the pacemaker diastolic slope or the MDP are consistent with the SK4 blockade but seem species-dependent in the case of SK1–3.

Slowing down the heartbeat is a gold-standard approach used in modern cardiology as primary therapy and as a secondary prevention. Beta-blockers are the corner stone of this strategy in the management of acute MI, HF, AF, and other arrhythmia, since those pathologies are interconnected. After treatment initiation, up-titration to optimal dosage should occur within a short time frame ("start low, aim high") for sustainable benefits. However, in addition to the late dosage escalation or underdosing of those molecules compared with theoretical optimal treatment, the "adrenergic-escape phenomenon," in which abnormally high concentrations of catecholaminergic hormones are produced, despite the stable β-blocker treatment, drastically worsens patient survival prognostics (Coumel et al., 1984; Frankenstein et al., 2009). Although the phenomenon has been described in very few scientific papers, its prevalence, estimated in one third of chronic HF patients, is associated with a 60% increase in mortality at 3 years compared with patients without this condition (Frankenstein et al., 2009). Other bradycardic agents such as ivabradine, which selectively blocks the I-funny (If) current, have been developed and are used currently in the management of HF and chronic stable angina (Koruth et al., 2017). However, ivabradine, similarly to β-blockers, requires dosing adjustments and has limited benefits mainly due to its specific effect on the PP interval elongation. A recent study based on an animal model of CASQ2 CPVT has shown that the decrease in the sinus rhythm provoked by ivabradine was not sufficient to improve the arrhythmic features observable with telemetric ECG recordings (Bueno-Levy et al., 2020). However, the same publication showed that SK4 blockade attenuates arrhythmic features, probably due to the AVN blockade and subsequent PR segment elongation in addition to the effect on the SAN and the PP interval. Similarly, SK2 blockade is also associated with a decrease in the heart rate and a PR segment elongation (Torrente et al., 2017).

Slowing down the heart rate and increasing the refractive period are mechanistic strategies used to prevent the reentry phenomenon and arrhythmia in the atria and the ventricle.

AF is the most common diagnosed cardiac arrhythmia, with an estimated actual prevalence of 37.5 million cases worldwide and a projected increase by 60% until 2050 (Lippi et al., 2020). The task force for the management of AF in Europe estimates that 25% of middle-age adults in Europe and the United States will develop AF during their lifetime (Kirchhof et al., 2016). AF management alone represents around 2% of the healthcare expenditures in European countries. Current pharmacological management is based on oral anticoagulation therapies, β-blockers, calcium channel blockers, cardiac glycosides, and Amiodarone, if patients do not reach the optimal heart rate control (Kirchhof et al., 2016). Although there is a broad therapeutic arsenal available, control of AF is not always optimal, and recurrent episodes with new ectopic foci can develop. Catheter ablation, a second-line therapy, is considered to be more effective than a pharmacological approach for persistent AF (ATTEST Trial). However, this technique requests several surgical interventions and can be associated in some cases with severe adverse events such as atrioesophageal fistulas. AF is associated with a dynamic remodeling of the small Ca^{2+}-activated K^+ currents. Initially, those currents are increased in human atrial or acute animal models and are responsible for a shortening of the APD. Pharmacological blockade of SK channels slows down the AVN conduction, increases the refractory period, decreases the reentry, and improves the reversion time from AF episodes to sinus rhythm (Diness et al., 2010; Skibsbye et al., 2011). In human chronic AF, however, downregulation of the channels prevents such an approach. Taken together, those data point to the benefits of small KCa blockade as a potential therapeutic strategy in early AF (**Figure 3**). Although the involvement and regulation of SK4 in AF have not been studied in depth yet, a full suppression of arrhythmic features in a canine model of acute AF has been reported after IV infusion of the SK4 channel blocker (Yang et al., 2020a,b). Further studies on models or samples from AF patients could help investigate the viability of this theory, especially in cAF.

Management of ventricular arrhythmia is complex since the modulation of a specific channel can have antiarrhythmic or proarrhythmic consequences. Genetic ablation of SK2 channels leads to an extensive PR elongation, AVN dysfunction, and AV dissociation (Zhang et al., 2008). On the other hand, similar features and severe bradycardia have been described when SK3 is overexpressed (Mahida, 2014; Mahida et al., 2014). At the cellular level, pharmacological blockade of SK4 channels has been reported to improve arrhythmic features in CPVT and ARVC, two distinct ventricular disorders. *In vivo*, IP injection of the SK4 blocker reduced the occurrence of SVT, NSVT, or VPC visible at ECG in CPVT mice in addition to a negative chronotropic effect and an elongation of the PRi (Haron-Khun et al., 2017). Thus, a subtle PR segment elongation based on a mild pharmacological AVN blockade could be beneficial in the management of cardiac arrhythmia.

Heart failure management remains the last big challenge in modern cardiology since this syndrome, based on clinical manifestations, can result from extremely various pathophysiological mechanisms. HFrEF, frequently described as a "systolic HF" in older classification, is often associated with an inflammatory state, a ventricular myocardium loss (LV dilatation), and subsequent reduction of the cardiac output and ejection fraction (EF). Inversely, HFpEF or "diastolic HF" affects the ventricular stiffness and arterial compliance, and increases the LV wall thickness and filling pressure. Recently, a "mid-range" HF (HFmrEF) has been added to the actual classification for patients with mild systolic dysfunction and diastolic dysfunction (Ponikowski et al., 2016). HF, also called the "cardiovascular cancer," remains as malignant as prostate or breast cancers, with an estimated survival rate of 40–50% in 5 years following diagnosis (Mamas et al., 2017). The condition is progressive, associated with episodes of cardiac decompensation (acute exacerbations), which irreversibly worsens the myocardial function and patients' quality of life. Initial pharmacological treatment is usually based on a therapeutic triad (β-blockers, ACEi or ARBi, MRA, and diuretic for decongestion), but other molecules such as ivabradine (Swedberg et al., 2010), ARNi (McMurray et al., 2014), and very recently SGLT2i (McMurray et al., 2019) have been added to the armamentarium. Most of those molecules are used in all types of HF, although they did not constantly show a benefit besides HFrEF (Koruth et al., 2017; Solomon et al., 2019), which opens the door to additional approaches.

At a cellular level, HF is associated with an electric remodeling. Na^+ currents are increased, while Ito, IKs, and other rectifier potassium currents are reduced (Näbauer and Kääb, 1998; Nattel et al., 2007). The increased RyR Ca^{2+}-leakage, reduced SERCA activity, and INCX upregulation contribute to the altered EC coupling and reduction of the contractile function (Reuter et al., 2004; Roos et al., 2007; Ottolia et al., 2013). The gain of function of SK channels, a consequence of the higher protein expression and cytosolic Ca^{2+} leakage, could possibly be a compensatory mechanism for the loss of repolarizing currents in chronic HF. Beat to beat variability and arrhythmic features such as torsades de pointe or VPC have been described in human end-stage HFrEF and animal models when SK are blocked. In congestive HF, abnormal elongation of the human PR segment (>200 ms) is associated with higher LV end-diastolic, end-systolic volumes and higher recurrences of events (McManus et al., 2009; Husby et al., 2015) and is commonly used as a marker to evaluate the impaired exercise ability of patients (Stępniewski et al., 2017). In contrast, in end-stage HF, PRi elongation is associated with better survival prognosis in patients who underwent cardiac resynchronization therapy (Kutyifa et al., 2014). Mechanistically, a delayed conduction in the AVN could have a positively influence on ventricle filling. Overall, although modulations of calcium-activated K^+ channels could have potential positive outcomes on pacing stability or PR duration, further investigations are necessary to specify HF patient subpopulations who could positively benefit from those effects. Similarly to the remodeling seen in HF, membrane SK, mitoSK, and IK channels are upregulated in MI, especially after reperfusion. Although the mechanisms need to be elucidated, membrane IK and SK channels seem to play a role in pacing stability by counterbalancing the downregulation of other potassium currents (Lee et al., 2013). Furthermore, positive pharmacological modulation of mitochondrial SK activation decreases ROS synthesis, which improves RyR stability and reduces Ca^{2+} SR leakage and associated ventricular arrhythmia in hypertrophic hearts (Stowe et al., 2013; Kim et al., 2017; Yang et al., 2017). Finally, a preventive treatment of mSKCa reduces the infarct size in the model of ischemic perfusion (Stowe et al., 2013). Based on those cardioprotective properties, development of openers could prevent arrhythmia associated with MI.

The growing number of evidences supporting the involvement of calcium-activated potassium channels in heart diseases confirms that those players should clearly gain more consideration as potential therapeutic targets. The dual effect on the heart rhythm and the PRi associated with the blockade of KCa conductances can be beneficial in atrial or

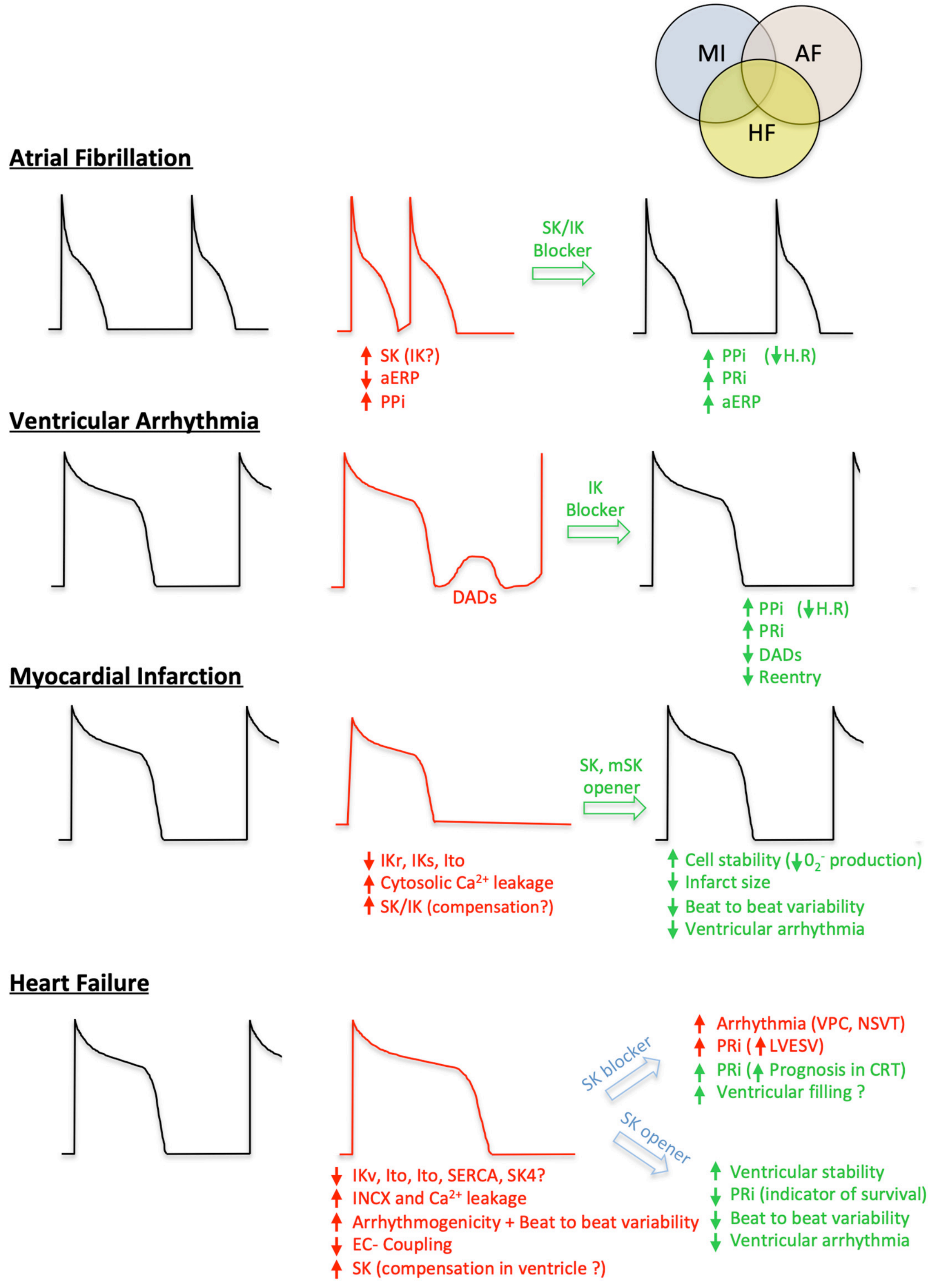

FIGURE 3 | Involvement of IK and SK in cardiovascular diseases and potential therapeutic strategies. For each condition (early stage Atrial Fibrillation, Ventricular arrhythmia, Myocardial Infarction and Heart Failure), a healthy action potential is shown (black cartoon) in comparison with the altered one (red cartoon). The different positive (green) or negative (red) effects based on ISKCa and IKCa modulations are summarized. PPi, P wave Interval; aERP, atrial effective refractory period; PRi, P-R segment; H.R, heart rate; DADs, delayed after depolarization; VPC, ventricular premature contraction; NSVT, non-sustained ventricular tachycardia; LVESV, left ventricular end-systolic volume; CRT, cardiac resynchronization therapy; IKr, rapid activating delayed rectifier potassium current; IKs, slow activating delayed rectifier potassium current; Ito, voltage-gated transient outward potassium current; INCX, sodium-calcium exchanger current.

ventricular arrhythmia but could worsen other conditions such as HF or MI. Further investigations are required to better understand mechanisms and the realism of those modulations in daily care since those pathologies are interconnected and often codiagnosed in patients.

AUTHOR CONTRIBUTIONS

DW wrote the manuscript and prepared the figures.

ACKNOWLEDGMENTS

I would like to warmly thank Dr. Pietro Mesirca (Institut de Génomique Fonctionnelle, CNRS, Montpellier) for the invitation to write this manuscript, and Dr. Yoni Lezmy (University College London) and Dr. Shiraz Haron-Khun for their feedback, suggestions, and friendship. Finally, I would like to conclude with a special homage to Daniel S. Snyder, a talented medical student and cardiology enthusiast, who did not have the chance to complete his curriculum. Your precious friendship is missed.

GLOSSARY

ACEi, inhibitors of the angiotensin converting enzyme (ACE), which prevent the formation of angiotensin II and associated vasoconstriction; AF, atrial fibrillation; AP, action potential. This is the unit pattern of the cellular electric activity; APD, action potential duration (in milliseconds). Time interval between the beginning (threshold) of an action potential and its end (hyperpolarization); $APD_{50,}$ action potential duration at 50% of the repolarization (in milliseconds); APD_{90}, action potential duration at 90% of the repolarization (in milliseconds); ARBi, inhibitors of the angiotensin II receptors. Medications used as an additional approach to prevent the vasoconstriction induced by angiotensin II; ARNi, medications used in HF, based on a combination between an angiotensin receptor inhibitor and a neprilysin inhibitor; ARVC, arrhythmogenic right ventricular cardiomyopathy; AVN (or AV node), atrioventricular node. Secondary heart pacemaker structure, responsible for a delay of the electric conduction between the SAN and the ventricles and a better blood filling; CaM, calmodulin or calcium-modulated protein. It binds Ca^{2+} and modulates ion channels properties; CaMBD, calmodulin binding domain. Structure of the ion channels that binds CaM; CAMKII, Ca^{2+}-calmodulin-dependent protein kinase II; cAMP, cyclic adenosine monophosphate; CPVT, catecholaminergic polymorphic ventricular tachycardia; DD slope (pacemaker slope), diastolic depolarization slope. Initial portion of the AP caused by the involvement of several ion channels and transporters. Those proteins lead a depolarization of the membrane (slope), until the threshold for the action potential ignition; hESC-CMs, human embryonic stem-cells derived cardiomyocytes. Cardiomyocytes differentiated from human embryonic stem cells; PP interval (PPi), interval between two successive P-waves, measured in ECG (in milliseconds). P-waves reflect the SAN activity and the PPi is used to evaluate the heart rate; PKA, cAMP-dependent protein kinase; PRi (or PR segment), interval between the P-wave and the R-wave of the QRS complex, measured in ECG (in milliseconds). It evaluates the delay of propagation of the electric activity between the SAN and the ventricular myocardium; HF, heart failure; HFpEF, heart failure with preserved ejection fraction. Mostly associated with a hypertrophic heart and a reduction of its stiffness; HFrEF, heart failure with reduced ejection fraction. Mostly associated with a reduction of the ventricular myocardium mass; If or "I-funny", depolarizing current induced by the HCN channels. Also called "pacemaker current," it plays an important role in the SAN and the AVN during the diastolic slope of the action potential; Ivabradine, selective blocker of the HCN channel; MDP, maximum diastolic potential. Value of the membrane potential at the most hyperpolarized part of the action potential (in millivolts); MI, myocardial infarction; mSKCa, mitochondrial isoform of the SKCa channel; NCX-1, sodium–calcium exchanger-1. Electrogenic antiporter (3 sodium ions for 1 calcium) strongly involved in ventricular excitation–contraction coupling and in the pacemaker mechanism; NSVT, non-sustained ventricular tachycardia. Transient VT episodes; SAN (or SA node), sinoatrial node. Structure located in the right atrium, primary cardiac pacemaker. SERCA, sarco/endoplasmic reticulum Ca^{2+}-ATPase. Pump responsible for the Ca^{2+} reuptake from the cytosol to the endoplasmic reticulum; SGLT2i, inhibitors of the sodium-glucose co-transporter-2; SR (or ER), sarcoplasmic (endoplasmic) reticulum. Organelle, which stores the cellular Ca^{2+}; ROS, reactive oxygen species; RyR, ryanodine receptors. Receptors on the SR, responsible for the intracellular Ca^{2+} release; TM, transmembrane domain; TRAM-34, 1-[(2-Chlorophenyl)diphenylmethyl]-1*H*-pyrazole. SK4 blocker; VPC, ventricular premature complexes. Arrhythmia usually ectopically induced by the Purkinje fibers; VT, ventricular tachycardia.

REFERENCES

Adelman, J. P. (2016). SK channels and calmodulin. *Channels (Austin)* 10, 1–6. doi: 10.1080/19336950.2015.1029688

Bakker, M. L., Christoffels, V. M., and Moorman, A. F. M. (2010). The cardiac pacemaker and conduction system develops from embryonic myocardium that retains its primitive phenotype. *J. Cardiovasc. Pharmacol.* 56, 6–15. doi: 10.1097/fjc.0b013e3181e775d3

Baruscotti, M., Barbuti, A., and Bucchi, A. (2010). The cardiac pacemaker current. *J. Mol. Cell. Cardiol.* 48, 55–64.

Bassani, R. A., Bassani, J. W., Lipsius, S. L., and Bers, D. M. (1997). Diastolic SR Ca efflux in atrial pacemaker cells and Ca-overloaded myocytes. *Am. J. Physiol.* 273, H886–H892.

Berkefeld, H., Fakler, B., and Schulte, U. (2010). Ca^{2+}-activated K^{+} channels: from protein complexes to function. *Physiol. Rev.* 90, 1437–1459. doi: 10.1152/physrev.00049.2009

Billman, G. E. (2012). Does the 'coupled clock' make the heart tick? *Cardiovasc. Res.* 96, 343–344. doi: 10.1093/cvr/cvs300

Blatz, A. L., and Magleby, K. L. (1986). Single apamin-blocked Ca-activated K^{+} channels of small conductance in cultured rat skeletal muscle. *Nature* 323, 718–720. doi: 10.1038/323718a0

Bogdanov, K. Y., Vinogradova, T. M., and Lakatta, E. G. (2001). Sinoatrial nodal cell ryanodine receptor and Na^{+}-Ca^{2+} exchanger: molecular partners in pacemaker regulation. *Circ. Res.* 88, 1254–1258. doi: 10.1161/hh1201.092095

Bonilla, I. M., Long, V. P. III, Vargas-Pinto, P., Wright, P., Belevych, A., Lou, Q., et al. (2014). Calcium-activated potassium current modulates ventricular repolarization in chronic heart failure. *PLoS One* 9:e108824. doi: 10.1371/journal.pone.0108824

Brown, H., and Difrancesco, D. (1980). Voltage-clamp investigations of membrane currents underlying pace-maker activity in rabbit sino-atrial node. *J. Physiol.* 308, 331–351. doi: 10.1113/jphysiol.1980.sp013474

Bueno-Levy, H., Weisbrod, D., Yadin, D., Haron-Khun, S., Peretz, A., Hochhauser, E., et al. (2020). The hyperpolarization-activated cyclic-nucleotide-gated channel blocker ivabradine does not prevent arrhythmias in catecholaminergic polymorphic ventricular tachycardia. *Front. Pharmacol.* 10:1566.

Buljubasic, F., El-Battrawy, I., Lan, H., Lomada, S. K., Chatterjee, A., Zhao, Z., et al. (2020). Nucleoside diphosphate kinase b contributes to arrhythmogenesis in human-induced pluripotent stem cell-derived cardiomyocytes from a patient with arrhythmogenic right ventricular cardiomyopathy. *J. Clin. Med.* 9:24564.

Chang, P.-C., and Chen, P.-S. (2015). SK channels and ventricular arrhythmias in heart failure. *Trends Cardiovasc. Med.* 25, 508–514. doi: 10.1016/j.tcm.2015.01.010

Chang, P.-C., Hsieh, Y.-C., Hsueh, C.-H., Weiss, J. N., Lin, S.-F., Chen, P.-S., et al. (2013a). Apamin induces early afterdepolarizations and torsades de pointes ventricular arrhythmia from failing rabbit ventricles exhibiting secondary rises in intracellular calcium. *Hear. Rhythm* 10, 1516–1524. doi: 10.1016/j.hrthm.2013.07.003

Chang, P.-C, Turker, I., Lopshire, J. C., Masroor, S., Nguyen, B.-L. L., Tao, W., et al. (2013b). Heterogeneous upregulation of apamin-sensitive potassium currents in failing human ventricles. *J. Am. Heart Assoc.* 2, 1–9.

Chen, W.-T., Chen, Y.-C., Lu, Y.-Y., Kao, Y.-H., Huang, J.-H., Lin, Y.-K., et al. (2013). Apamin modulates electrophysiological characteristics of the pulmonary vein and the Sinoatrial Node. *Eur. J. Clin. Invest.* 43, 957–963. doi: 10.1111/eci.12125

Cheng, Y. J., Imperatore, G., Geiss, L. S., Saydah, S. H., Albright, A. L., Ali, M. K., et al. (2018). Trends and disparities in cardiovascular mortality among U.S. Adults with and without self-reported diabetes, 1988-2015. *Diabetes Care* 41, 2306–2315. doi: 10.2337/dc18-0831

Chua, S.-K., Chang, P.-C., Maruyama, M., Turker, I., Shinohara, T., Shen, M. J., et al. (2011). Small-conductance calcium-activated potassium channel and recurrent ventricular fibrillation in failing rabbit ventricles. *Circ. Res.* 108, 971–979. doi: 10.1161/circresaha.110.238386

Corrado, D., van Tintelen, P. J., McKenna, W. J., Hauer, R. N. W., Anastastakis, A., Asimaki, A., et al. (2019). Arrhythmogenic right ventricular cardiomyopathy: evaluation of the current diagnostic criteria and differential diagnosis. *Eur. Heart J.* 41, 1414–1429.

Couette, B., Marger, L., Nargeot, J., and Mangoni, M. E. (2006). Physiological and pharmacological insights into the role of ionic channels in cardiac pacemaker activity. *Cardiovasc. Hematol. Disord. Drug Targets* 6, 169–190. doi: 10.2174/187152906778249572

Coumel, P., Escoubet, B., and Attuel, P. (1984). Beta-blocking therapy in atrial and ventricular tachyarrhythmias: experience with nadolol. *Am. Heart J.* 108, 1098–1108. doi: 10.1016/0002-8703(84)90589-1

Del Carlo, B., Pellegrini, M., and Pellegrino, M. (2003). Modulation of Ca^{2+}-activated K^{+} channels of human erythrocytes by endogenous protein kinase C. *Biochim. Biophys. Acta* 1612, 107–116. doi: 10.1016/s0005-2736(03)00111-1

Demion, M., Bois, P., Launay, P., and Guinamard, R. (2007). TRPM4, a Ca^{2+}-activated nonselective cation channel in mouse sino-atrial node cells. *Cardiovasc. Res.* 73, 531–538. doi: 10.1016/j.cardiores.2006.11.023

Devor, D. C., and Frizzell, R. A. (1998). Modulation of K^{+} channels by arachidonic acid in T84 cells. I. Inhibition of the Ca^{2+}-dependent K^{+} channel. *Am. J. Physiol. Physiol.* 274, C138–C148.

Diness, J. G., Sorensen, U. S., Nissen, J. D., Al-Shahib, B., Jespersen, T., Grunnet, M., et al. (2010). Inhibition of Small-Conductance Ca^{2+}-activated K^{+} channels terminates and protects against atrial fibrillation. *Circ. Arrhythmia Electrophysiol.* 3, 380–390. doi: 10.1161/circep.110.957407

Eldar, M., Pras, E., and Lahat, H. A. (2003). missense mutation in the CASQ2 gene is associated with autosomal-recessive catecholamine-induced polymorphic ventricular tachycardia. *Trends Cardiovasc. Med.* 13, 148–151. doi: 10.1016/s1050-1738(03)00025-2

Ellinor, P. T., Lunetta, K. L., Glazer, N. L., Pfeufer, A., Alonso, A., Chung, M. K., et al. (2010). Common variants in KCNN3 are associated with lone atrial fibrillation. *Nat. Genet.* 42, 240–244.

Fabiato, A., and Fabiato, F. (1972). Excitation-contraction coupling of isolated cardiac fibers with disrupted or closed sarcolemmas calcium-dependent cyclic and tonic contractions. *Circ. Res.* 31, 293–307. doi: 10.1161/01.res.31.3.293

Fan, X., Yu, Y., Lan, H., Ou, X., Yang, L., Li, T., et al. (2018). Ca^{2+}/calmodulin-dependent protein kinase II (CaMKII) increases small-conductance Ca^{2+}-activated K^{+} current in patients with chronic atrial fibrillation. *Med. Sci. Monit.* 24, 3011–3750. doi: 10.12659/msm.909684

Fanger, C. M., Ghanshani, S., Logsdon, N. J., Rauer, H., Kalman, K., Zhou, J., et al. (1999). Calmodulin mediates calcium-dependent activation of the intermediate conductance K_{Ca} channel, IKCa1. *J. Biol. Chem.* 274, 5746–5754. doi: 10.1074/jbc.274.9.5746

Frankenstein, L., Zugck, C., Schellberg, D., Nelles, M., Froehlich, H., Katus, H., et al. (2009). Prevalence and prognostic significance of adrenergic escape during chronic beta-blocker therapy in chronic heart failure. *Eur. J. Heart Fail.* 11, 178–184. doi: 10.1093/eurjhf/hfn028

Gaborit, N., Le Bouter, S., Szuts, V., Varro, A., Escande, D., Nattel, S., et al. (2007). Regional and tissue specific transcript signatures of ion channel genes in the non-diseased human heart. *J. Physiol.* 582, 675–693. doi: 10.1113/jphysiol.2006.126714

Gao, Z., Chen, B., Joiner, M.-L. A., Wu, Y., Guan, X., Koval, O. M., et al. (2010). I_f and SR Ca^{2+} release both contribute to pacemaker activity in canine sinoatrial node cells. *J. Mol. Cell. Cardiol.* 49, 33–40. doi: 10.1016/j.yjmcc.2010.03.019

Gardos, G. (1958). The role of calcium in the potassium permeability of human erythrocytes. *Acta Physiol. Hung.* 30, 653–654. doi: 10.1016/0006-3002(58)90124-0

Gerlach, A. C., Gangopadhyay, N. N., and Devor, D. C. (2000). Kinase-dependent regulation of the intermediate conductance, calcium-dependent potassium channel, hIK1. *J. Biol. Chem.* 275, 585–598. doi: 10.1074/jbc.275.1.585

Gerlach, A. C., Syme, C. A., Giltinan, L. A., Adelman, J. P., and Devor, D. C. (2001). ATP-dependent Activation of the Intermediate Conductance, Ca^{2+}-activated K^{+} Channel, hIK1, is Conferred by a C-terminal Domain. *J. Biol. Chem.* 276, 10963–10970. doi: 10.1074/jbc.m007716200

Ghanshani, S., Coleman, M., Gustavsson, P., Wu, A. C. L., Gargus, J. J., et al. (1998). Human calcium-activated potassium channel gene KCNN4 maps to chromosome 19q13.2 in the Region deleted in Diamond-Blackfan anemia. *Genomics* 51, 160–161. doi: 10.1006/geno.1998.5333

Grissmer, S., Lewis, R. S., and Cahalan, M. D. (1992). Ca^{2+}-activated K^{+} channels in human leukemic T cells. *J. Gen. Physiol.* 99, 63–84. doi: 10.1085/jgp.99.1.63

Grissmer, S., Nguyen, A. N., and Cahalan, M. D. (1993). Calcium-activated potassium channels in resting and activated human T lymphocytes. Expression levels, calcium dependence, ion selectivity, and pharmacology. *J. Gen. Physiol.* 102, 601–630. doi: 10.1085/jgp.102.4.601

Groenke, S., Larson, E. D., Alber, S., Zhang, R., Lamp, S. T., Ren, X., et al. (2013). Complete atrial-specific knockout of sodium-calcium exchange eliminates sinoatrial node pacemaker activity. *PLoS One* 8:e81633–e81633.

Grygorczyk, R., Schwarz, W., and Passow, H. (1984). Ca^{2+}-activated K^{+} channels in human red cells. Comparison of single-channel currents with ion fluxes. *Biophys. J.* 45, 693–698. doi: 10.1016/s0006-3495(84)84211-3

Hagiwara, N., Irisawa, H., and Kameyama, M. (1988). Contribution of two types of calcium currents to the pacemaker potentials of rabbit sino-atrial node cells. *J. Physiol.* 395, 233–253. doi: 10.1113/jphysiol.1988.sp016916

Hagiwara, N., Irisawa, H., Kasanuki, H., and Hosoda, S. (1992). Background current in sino-atrial node cells of the rabbit heart. *J. Physiol.* 448, 53–72. doi: 10.1113/jphysiol.1992.sp019029

Hamill, O. P. (1981). Potassium channel currents in human red blood cells. *J. Physiol. L.* 97–98.

Hamilton, K. L., Syme, C. A., and Devor, D. C. (2003). Molecular localization of the inhibitory arachidonic acid binding site to the pore of hIK1. *J. Biol. Chem.* 278, 16690–16697. doi: 10.1074/jbc.m212959200

Hamilton, S., Polina, I., Terentyeva, R., Bronk, P., Kim, T. Y., Roder, K., et al. (2020). PKA phosphorylation underlies functional recruitment of sarcolemmal SK2 channels in ventricular myocytes from hypertrophic hearts. *J. Physiol.* 598, 2847–2873. doi: 10.1113/jp277618

Hancock, J. M., Weatherall, K. L., Choisy, S. C., James, A. F., Hancox, J. C., and Marrion, N. V. (2015). Selective activation of heteromeric SK channels contributes to action potential repolarization in mouse atrial myocytes. *Hear. Rhythm* 12, 1003–1015. doi: 10.1016/j.hrthm.2015.01.027

Haron-Khun, S., Weisbrod, D., Bueno, H., Yadin, D., Behar, J., Peretz, A., et al. (2017). SK4 K^{+} channels are therapeutic targets for the treatment of cardiac arrhythmias. *EMBO Mol. Med.* 9, 415–429. doi: 10.15252/emmm.201606937

Hayashi, M., Kunii, C., Takahata, T., and Ishikawa, T. (2004). ATP-dependent regulation of SK4/IK1-like currents in rat submandibular acinar cells: possible role of cAMP-dependent protein kinase. *Am. J. Physiol. Cell Physiol.* 286, C635–C646.

Hoffman, J. F., Joiner, W., Nehrke, K., Potapova, O., Foye, K., and Wickrema, A. (2003). The hSK4 (KCNN4) isoform is the Ca^{2+}-activated K^{+} channel (Gardos channel) in human red blood cells. *Proc. Natl. Acad. Sci. U.S.A.* 100, 7366–7371. doi: 10.1073/pnas.1232342100

Horsthuis, T., Buermans, H. P. J., Brons, J. F., Verkerk, A. O., Bakker, M. L., Wakker, V., et al. (2009). Gene expression profiling of the forming atrioventricular node using a novel tbx3-based node-specific transgenic reporter. *Circ. Res.* 105, 61–69. doi: 10.1161/circresaha.108.192443

Hsieh, Y.-C., Chang, P.-C., Hsueh, C.-H., Lee, Y. S., Shen, C., Weiss, J. N., et al. (2013). Apamin-sensitive potassium current modulates action potential duration restitution and arrhythmogenesis of failing rabbit ventricles. *Circ. Arrhythm. Electrophysiol.* 6, 410–418. doi: 10.1161/circep.111.000152

Husby, M. P., Soliman, E. Z., Goldberger, J. J., Liu, K., Lloyd-Jones, D., Durazo-Arvizu, R., et al. (2015). The association between the PR interval and left ventricular measurements in the multiethnic study of atherosclerosis. *Cardiol. Res. Pract.* 2015:193698.

Ishii, T. M., Silvia, C., Hirschberg, B., Bond, C. T., Adelman, J. P., and Maylie, J. (1997). A human intermediate conductance calcium-activated potassium channel. *Proc. Natl. Acad. Sci. U.S.A.* 94, 11651L–11656L.

Joiner, W. J., Khanna, R., Schlichter, L. C., and Kaczmarek, L. K. (2001). Calmodulin regulates assembly and trafficking of SK4/IK1 Ca^{2+}-activated K^{+} channels. *J. Biol. Chem.* 276, 37980–37985.

Joiner, W. J., Wang, L. U. Y., Tang, M. D., and Kaczmarek, L. K. (1997). hSK4, a member of a novel subfamily of calcium-activated potassium channels. *Proc. Natl. Acad. Sci. U.S.A.* 94, 11013–11018. doi: 10.1073/pnas.94.20.11013

Keen, J. E., Khawaled, R., Farrens, D. L., Neelands, T., Rivard, A., Bond, C. T., et al. (1999). Domains responsible for constitutive and Ca^{2+}-dependent interactions between calmodulin and small conductance Ca^{2+}-activated potassium channels. *J. Neurosci.* 19, 8830–8838. doi: 10.1523/jneurosci.19-20-08830.1999

Khanna, R., Change, M. C., Joiner, W. J., Kaczmarek, L. K., and Schlichter, L. C. (1999). hSK4/hIK1, a calmodulin-binding K(Ca) channel in human T lymphocytes. Roles in proliferation and volume regulation. *J. Biol. Chem.* 274, 14838–14849. doi: 10.1074/jbc.274.21.14838

Kim, T. Y., Terentyeva, R., Roder, K. H. F., Li, W., Liu, M., Greener, I., et al. (2017). SK channel enhancers attenuate Ca^{2+}-dependent arrhythmia in hypertrophic hearts by regulating mito-ROS-dependent oxidation and activity of RyR. *Cardiovasc. Res.* 113, 343–353.

Kirchhof, P., Benussi, S., Kotecha, D., Ahlsson, A., Atar, D., Casadei, B., et al. (2016). 2016 ESC Guidelines for the management of atrial fibrillation developed in collaboration with EACTS. *Eur. Heart J.* 37, 2893–2962.

Kleger, A., Seufferlein, T., Malan, D., Tischendorf, M., Storch, A., Wolheim, A., et al. (2010). Modulation of calcium-activated potassium channels induces cardiogenesis of pluripotent stem cells and enrichment of pacemaker-like cells. *Circulation* 122, 1823–1836. doi: 10.1161/circulationaha.110.971721

Kohler, M., Hirschberg, B., Bond, C. T., Kinzie, J. M., Marrion, N. V., Maylie, J., et al. (1996). Small-conductance, calcium-activated potassium channels from mammalian brain. *Science* 273, 1709–1714. doi: 10.1126/science.273.5282.1709

Kong, I. D., Koh, S. D., Bayguinov, O., and Sanders, K. M. (2000). Small conductance Ca^{2+}-activated K^{+} channels are regulated by Ca^{2+}-calmodulin-dependent protein kinase II in murine colonic myocytes. *J. Physiol.* 524(Pt 2), 331–337. doi: 10.1111/j.1469-7793.2000.t01-1-00331.x

Koruth, J. S., Lala, A., Pinney, S., Reddy, V. Y., and Dukkipati, S. R. (2017). The clinical use of ivabradine. *J. Am. Coll. Cardiol.* 70, 1777L–1784L.

Krnjević, K., and Lisiewicz, A. (1972). Injections of calcium ions into spinal motoneurones. *J. Physiol.* 225, 363–390. doi: 10.1113/jphysiol.1972.sp009945

Kutyifa, V., Stockburger, M., Daubert, J. P., Holmqvist, F., Olshansky, B., Schuger, C., et al. (2014). PR interval identifies clinical response in patients with non-left bundle branch block: a multicenter automatic defibrillator implantation trial-cardiac resynchronization therapy substudy. *Circ. Arrhythm. Electrophysiol.* 7, 645–651. doi: 10.1161/circep.113.001299

Laitinen, P. J., Brown, K. M., Piippo, K., Swan, H., Devaney, J. M., Brahmbhatt, B., et al. (2001). Mutations of the cardiac ryanodine receptor (RyR2) gene in familial polymorphic ventricular tachycardia. *Circulation* 103, 485–490. doi: 10.1161/01.cir.103.4.485

Lakatta, E. G., and DiFrancesco, D. (2009). What keeps us ticking: a funny current, a calcium clock, or both? *J. Mol. Cell. Cardiol.* 47, 157–170. doi: 10.1016/j.yjmcc.2009.03.022

Lakatta, E. G., Maltsev, V. A., and Vinogradova, T. M. (2010). A coupled SYSTEM of intracellular Ca^{2+} clocks and surface membrane voltage clocks controls the timekeeping mechanism of the heart's pacemaker. *Circ. Res.* 106, 659–673. doi: 10.1161/circresaha.109.206078

Lancaster, B., and Nicoll, R. A. (1987). Properties of two calcium-activated hyperpolarizations in rat hippocampal neurones. *J. Physiol.* 389, 187–203. doi: 10.1113/jphysiol.1987.sp016653

Lancaster, B., Nicoll, R. A., and Perkel, D. J. (1991). Calcium activates two types of potassium channels in rat hippocampal neurons in culture. *J. Neurosci.* 11, 23–30. doi: 10.1523/jneurosci.11-01-00023.1991

Lazdunski, M. (1983). Apamin, a neurotoxin specific for one class of Ca^{2+}-dependent K^{+} channels. *Cell Calcium* 4, 421–428. doi: 10.1016/0143-4160(83)90018-0

Lee, C.-H., and MacKinnon, R. (2018). Activation mechanism of a human SK-calmodulin channel complex elucidated by cryo-EM structures. *Science* 360, 508–513. doi: 10.1126/science.aas9466

Lee, Y. S., Chang, P.-C., Hsueh, C.-H., Maruyama, M., Park, H. W., et al. (2013). Apamin-sensitive calcium-activated potassium currents in rabbit ventricles with chronic myocardial infarction. *J. Cardiovasc. Electrophysiol.* 24, 1144–1153.

Li, M., Li, T., Lei, M., Tan, X., Yang, Y., Liu, T., et al. (2011). [Increased small conductance calcium-activated potassium channel (SK2 channel) current in atrial myocytes of patients with persistent atrial fibrillation]. *Zhonghua Xin Xue Guan Bing Za Zhi* 39, 147–151.

Li, N., Timofeyev, V., Tuteja, D., Xu, D., Lu, L., Zhang, Q., et al. (2009). Ablation of a Ca^{2+}-activated K^{+} channel (SK2 channel) results in action potential prolongation in atrial myocytes and atrial fibrillation. *J. Physiol.* 587, 1087–1100. doi: 10.1113/jphysiol.2008.167718

Li, W., Halling, D. B., Hall, A. W., and Aldrich, R. W. (2009). EF hands at the N-lobe of calmodulin are required for both SK channel gating and stable SK-calmodulin interaction. *J. Gen. Physiol.* 134, 281–293. doi: 10.1085/jgp.200910295

Ling, T.-Y. Y., Wang, X.-L. L., Chai, Q., Lau, T.-W. W., Koestler, C. M., Park, S. J., et al. (2013). Regulation of the SK3 channel by microRNA-499 - Potential role in atrial fibrillation. *Hear. Rhythm* 10, 1001–1009. doi: 10.1016/j.hrthm.2013.03.005

Lippi, G., Sanchis-Gomar, F., and Cervellin, G. (2020). Global epidemiology of atrial fibrillation: an increasing epidemic and public health challenge. *Int. J. Stroke Off. J. Int. Stroke Soc.* 2:1747493019897870. doi: 10.1177/1747493019897870

Lu, L., Zhang, Q., Timofeyev, V., Zhang, Z., Young, J. N., Shin, H.-S., et al. (2007). Molecular coupling of a Ca^{2+}-activated K^{+} channel to L-type Ca^{2+} channels via alpha-actinin2. *Circ. Res.* 100, 112–120. doi: 10.1161/01.res.0000253095.44186.72

Mahaut-Smith, M. P., and Schlichter, L. C. (1989). Ca^{2+}-activated K^{+} channels in human B lymphocytes and rat thymocytes. *J. Physiol.* 415, 69–83. doi: 10.1113/jphysiol.1989.sp017712

Mahida, S. (2014). Expanding role of SK channels in cardiac electrophysiology. *Hear. Rhythm* 11, 1233–1238. doi: 10.1016/j.hrthm.2014.03.045

Mahida, S., Mills, R. W., Tucker, N. R., Simonson, B., Macri, V., Lemoine, M. D., et al. (2014). Overexpression of KCNN3 results in sudden cardiac death. *Cardiovasc. Res.* 101, 326–334. doi: 10.1093/cvr/cvt269

Makita, N., Yagihara, N., Crotti, L., Johnson, C. N., Beckmann, B.-M., Roh, M. S., et al. (2014). Novel calmodulin mutations associated with congenital arrhythmia susceptibility. *Circ. Cardiovasc. Genet.* 7, 466–474. doi: 10.1161/circgenetics.113.000459

Maltsev, V. A., and Lakatta, E. G. (2007). Normal heart rhythm is initiated and regulated by an intracellular calcium clock within pacemaker cells. *Heart. Lung Circ.* 16, 335–348. doi: 10.1016/j.hlc.2007.07.005

Maltsev, V. A., Vinogradova, T. M., and Lakatta, E. G. (2006). The emergence of a general theory of the initiation and strength of the heartbeat. *J. Pharmacol. Sci.* 100, 338–369. doi: 10.1254/jphs.cr0060018

Mamas, M. A., Sperrin, M., Watson, M. C., Coutts, A., Wilde, K., Burton, C., et al. (2017). Do patients have worse outcomes in heart failure than in cancer? A primary care-based cohort study with 10-year follow-up in Scotland. *Eur. J. Heart Fail.* 19, 1095–1104. doi: 10.1002/ejhf.822

Mangoni, M. E., Couette, B., Bourinet, E., Platzer, J., Reimer, D., Striessnig, J., et al. (2003). Functional role of L-type $Ca_v1.3$ Ca^{2+} channels in cardiac pacemaker activity. *Proc. Natl. Acad. Sci. U.S.A.* 100, 5543–5548.

Marcus, F. I., Edson, S., and Towbin, J. A. (2013). Genetics of arrhythmogenic right ventricular cardiomyopathy: a practical guide for physicians. *J. Am. Coll. Cardiol.* 61, 1945–1948.

Marionneau, C., Couette, B., Liu, J., Li, H., Mangoni, M. E., Nargeot, J., et al. (2005). Specific pattern of ionic channel gene expression associated with pacemaker activity in the mouse heart. *J. Physiol.* 562, 223–234. doi: 10.1113/jphysiol.2004.074047

Maylie, J., Bond, C. T., Herson, P. S., Lee, W. S., and Adelman, J. P. (2004). Small conductance Ca^{2+}-activated K^+ channels and calmodulin. *J. Physiol.* 554, 255–261. doi: 10.1113/jphysiol.2003.049072

McManus, D. D., Shah, S. J., Fabi, M. R., Rosen, A., Whooley, M. A., and Schiller, N. B. (2009). Prognostic value of left ventricular end-systolic volume index as a predictor of heart failure hospitalization in stable coronary artery disease: data from the Heart and Soul Study. *J. Am. Soc. Echocardiogr. Off. Publ. Am. Soc. Echocardiogr.* 22, 190–197. doi: 10.1016/j.echo.2008.11.005

McMurray, J. J. V., Packer, M., Desai, A. S., Gong, J., Lefkowitz, M. P., Rizkala, A. R., et al. (2014). Angiotensin–neprilysin inhibition versus enalapril in heart failure. *N. Engl. J. Med.* 371, 993–1004.

McMurray, J. J. V., Solomon, S., Inzucchi, S. E., Køber, L., Kosiborod, M. N., Martinez, F. A., et al. (2019). Dapagliflozin in patients with heart failure and reduced ejection fraction. *N. Engl. J. Med.* 381, 1995–2008.

Meech, R. W. (1972). Intracellular calcium injection causes increased potassium conductance in Aplysia nerve cells. *Comp. Biochem. Physiol. A. Comp. Physiol.* 42, 493–499. doi: 10.1016/0300-9629(72)90128-4

Meech, R. W. (1974). The sensitivity of Helix aspersa neurones to injected calcium ions. *J. Physiol.* 237, 259–277.

Meech, R. W., and Strumwas, F. (1970). Intracellular calcium injection activates potassium conductance in Aplysia nerve cells. *Federat. Proc.* 29:A834.

Mensah, G. A., Wei, G. S., Sorlie, P. D., Fine, L. J., Rosenberg, Y., Kaufmann, P. G., et al. (2017). Decline in cardiovascular mortality: possible causes and implications. *Circ. Res.* 120, 366–380. doi: 10.1161/circresaha.116.309115

Mesirca, P., Torrente, A. G., and Mangoni, M. E. (2014). T-type channels in the sino-atrial and atrioventricular pacemaker mechanism. *Pflugers Arch.* 466, 791–799. doi: 10.1007/s00424-014-1482-6

Miller, C., Moczydlowski, E., Latorre, R., and Phillips, M. (1985). Charybdotoxin, a protein inhibitor of single Ca^{2+}-activated K^+ channels from mammalian skeletal muscle. *Nature* 313, 316–318. doi: 10.1038/313316a0

Müller, M., Stockmann, M., Malan, D., Wolheim, A., Tischendorf, M., Linta, L., et al. (2011). Ca^{2+} activated K channels-new tools to induce cardiac commitment from pluripotent stem cells in mice and men. *Stem Cell Rev. Rep.* 8, 720–740. doi: 10.1007/s12015-011-9324-9

Näbauer, M., and Kääb, S. (1998). Potassium channel down-regulation in heart failure. *Cardiovasc. Res.* 37, 324–334. doi: 10.1016/s0008-6363(97)00274-5

Nattel, S., Maguy, A., Le Bouter, S., and Yeh, Y.-H. (2007). Arrhythmogenic ion-channel remodeling in the heart: heart failure, myocardial infarction, and atrial fibrillation. *Physiol. Rev.* 87, 425–456. doi: 10.1152/physrev.00014.2006

Neco, P., Torrente, A. G., Mesirca, P., Zorio, E., Liu, N., Priori, S. G., et al. (2012). Paradoxical effect of increased diastolic Ca^{2+} release and decreased sinoatrial node activity in a mouse model of catecholaminergic polymorphic ventricular tachycardia. *Circulation* 126, 392–401. doi: 10.1161/circulationaha.111.075382

Neely, A., and Lingle, C. J. (1992a). Effects of muscarine on single rat adrenal chromaffin cells. *J. Physiol.* 453, 133–166. doi: 10.1113/jphysiol.1992.sp019221

Neely, A., and Lingle, C. J. (1992b). Two components of calcium-activated potassium current in rat adrenal chromaffin cells. *J. Physiol.* 453, 97–131. doi: 10.1113/jphysiol.1992.sp019220

Ottolia, M., Torres, N., Bridge, J. H. B., Philipson, K. D., and Goldhaber, J. I. (2013). Na/Ca exchange and contraction of the heart. *J. Mol. Cell. Cardiol.* 61, 28–33. doi: 10.1016/j.yjmcc.2013.06.001

Özgen, N., Dun, W., Sosunov, E. A., Anyukhovsky, E. P., Hirose, M., Duffy, H. S., et al. (2007). Early electrical remodeling in rabbit pulmonary vein results from trafficking of intracellular SK2 channels to membrane sites. *Cardiovasc. Res.* 75, 758–769. doi: 10.1016/j.cardiores.2007.05.008

Park, Y. B. (1994). Ion selectivity and gating of small conductance Ca^{2+}-activated K^+ channels in cultured rat adrenal chromaffin cells. *J. Physiol.* 481, 555–570. doi: 10.1113/jphysiol.1994.sp020463

Partiseti, M., Choquet, D., Diu, A., and Korn, H. (1992). Differential regulation of voltage- and calcium-activated potassium channels in human B lymphocytes. *J. Immunol.* 148, 3361–3368.

Pellegrino, M., and Pellegrini, M. (1998). Modulation of Ca^{2+}-activated K^+ channels of human erythrocytes by endogenous cAMP-dependent protein kinase. *Pflugers Arch.* 436, 749–756. doi: 10.1007/s004240050698

Pena, T. L., Chen, S. H., Konieczny, S. F., and Rane, S. G. (2000). Ras/MEK/ERK Up-regulation of the fibroblast K_{Ca} channel FIK is a common mechanism for basic fibroblast growth factor and transforming growth factor-beta suppression of myogenesis. *J. Biol. Chem.* 275, 13677–13682. doi: 10.1074/jbc.275.18.13677

Pennefather, P., Lancaster, B., Adams, P. R., and Nicoll, R. A. (1985). Two distinct Ca-dependent K currents in bullfrog sympathetic ganglion cells. *Proc. Natl. Acad. Sci. U.S.A.* 82, 3040–3044. doi: 10.1073/pnas.82.9.3040

Ponikowski, P., Voors, A. A., Anker, S. D., Bueno, H., Cleland, J. G. F., Coats, A. J. S., et al. (2016). 2016 ESC Guidelines for the diagnosis and treatment of acute and chronic heart failure: The Task Force for the diagnosis and treatment of acute and chronic heart failure of the European Society of Cardiology (ESC) Developed with the special contribution of the Heart Failure Association (HFA) of the ESC. *Eur. Heart J.* 37, 2129–2200. doi: 10.1093/eurheartj/ehw128

Postma, A. V., Denjoy, I., Hoorntje, T. M., Lupoglazoff, J.-M., Da Costa, A., Sebillon, P., et al. (2002). Absence of calsequestrin 2 causes severe forms of catecholaminergic polymorphic ventricular tachycardia. *Circ. Res.* 91, e21–e26.

Priori, S. G., Napolitano, C., Tiso, N., Memmi, M., Vignati, G., Bloise, R., et al. (2001). Mutations in the cardiac ryanodine receptor gene (hRyR2) underlie catecholaminergic polymorphic ventricular tachycardia. *Circulation* 103, 196–200. doi: 10.1161/01.cir.103.2.196

Qi, X.-Y., Diness, J. G., Brundel, B. J. J. M., Zhou, X.-B., Naud, P., Wu, C.-T., et al. (2014). Role of small-conductance calcium-activated potassium channels in atrial electrophysiology and fibrillation in the dog. *Circulation* 129, 430–440. doi: 10.1161/circulationaha.113.003019

Ren, Y., Barnwell, L. F., Alexander, J. C., Lubin, F. D., Adelman, J. P., Pfaffinger, P. J., et al. (2006). Regulation of surface localization of the small conductance Ca^{2+}-activated potassium channel Sk2, through direct phosphorylation by cAMP-dependent protein kinase. *J. Biol. Chem.* 281, 11769–11779. doi: 10.1074/jbc.m513125200

Reuter, H., Han, T., Motter, C., Philipson, K. D., and Goldhaber, J. I. (2004). Mice overexpressing the cardiac sodium-calcium exchanger: defects in excitation-contraction coupling. *J. Physiol.* 554, 779–789. doi: 10.1113/jphysiol.2003.055046

Romey, G., and Lazdunski, M. (1984). The coexistence in rat muscle cells of two distinct classes of Ca^{2+}-dependent K^+ channels with different pharmacological properties and different physiological functions. *Biochem. Biophys. Res. Commun.* 118, 669–674. doi: 10.1016/0006-291x(84)91355-x

Roos, K. P., Jordan, M. C., Fishbein, M. C., Ritter, M. R., Friedlander, M., Chang, H. C., et al. (2007). Hypertrophy and heart failure in mice overexpressing the cardiac sodium-calcium exchanger. *J. Card. Fail.* 13, 318–329. doi: 10.1016/j.cardfail.2007.01.004

Roux-Buisson, N., Cacheux, M., Fourest-Lieuvin, A., Fauconnier, J., Brocard, J., Denjoy, I., et al. (2012). Absence of triadin, a protein of the calcium release complex, is responsible for cardiac arrhythmia with sudden death in human. *Hum. Mol. Genet.* 21, 2759–2767. doi: 10.1093/hmg/dds104

Saito, T., Fujiwara, Y., Fujiwara, R., Hasegawa, H., Kibira, S., Miura, H., et al. (2002). Role of augmented expression of intermediate-conductance Ca^{2+}-activated K^+ channels in postischaemic heart. *Clin. Exp. Pharmacol. Physiol.* 29, 324–329. doi: 10.1046/j.1440-1681.2002.03652.x

Satin, J., Kehat, I., Caspi, O., Huber, I., Arbel, G., Itzhaki, I., et al. (2004). Mechanism of spontaneous excitability in human embryonic stem cell derived cardiomyocytes. *J. Physiol.* 559, 479–496. doi: 10.1113/jphysiol.2004.068213

Schumacher, M. A., Rivard, A. F., Bächinger, H. P., and Adelman, J. P. (2001). Structure of the gating domain of a Ca^{2+}-activated K^+ channel complexed with Ca^{2+}/calmodulin. *Nature* 410, 1120–1124. doi: 10.1038/35074145

Schwarz, W., Keim, H., Fehlau, R., and Fuhrmann, G. F. (1989). Modulation of the Ca^{2+}- or Pb^{2+}-activated K^+-selective channels in human red cells. I. Effects of propranolol. *Biochim. Biophys. Acta* 978, 32–36. doi: 10.1016/0005-2736(89)90494-x

Skibsbye, L., Diness, J. G., Sorensen, U. S., Hansen, R. S., and Grunnet, M. (2011). The duration of pacing-induced atrial fibrillation is reduced in vivo by inhibition of small conductance Ca(2+)-activated K(+) channels. *J. Cardiovasc. Pharmacol.* 57, 672–681. doi: 10.1097/fjc.0b013e318217943d

Skibsbye, L., Poulet, C., Diness, J. G., Bentzen, B. H., Yuan, L., Kappert, U., et al. (2014). Small-conductance calcium-activated potassium (SK) channels contribute to action potential repolarization in human atria. *Cardiovasc. Res.* 103, 156–167. doi: 10.1093/cvr/cvu121

Solomon, S. D., McMurray, J. J. V., Anand, I. S., Ge, J., Lam, C. S. P., Maggioni, A. P., et al. (2019). Angiotensin–neprilysin inhibition in heart failure with preserved ejection fraction. *N. Engl. J. Med.* 381, 1609–1620.

Srivastava, S., Li, Z., Ko, K., Choudhury, P., Albaqumi, M., Johnson, A. K., et al. (2006). Histidine phosphorylation of the potassium channel KCa3.1 by nucleoside diphosphate kinase B is required for activation of KCa3.1 and CD4 T cells. *Mol. Cell* 24, 665–675. doi: 10.1016/j.molcel.2006.11.012

Stępniewski, J., Kopeć, G., Magoň, W., and Podolec, P. (2017). Atrioventricular conduction delay predicts impaired exercise capacity in patients with heart failure with reduced ejection fraction. *Med. Sci. Monit.* 23, 3989–3995. doi: 10.12659/msm.902908

Stieber, J., Hofmann, F., and Ludwig, A. (2004). Pacemaker channels and sinus node arrhythmia. *Trends Cardiovasc. Med.* 14, 23–28. doi: 10.1016/j.tcm.2003.09.006

Stowe, D. F., Gadicherla, A. K., Zhou, Y., Aldakkak, M., Cheng, Q., Kwok, W. M., et al. (2013). Protection against cardiac injury by small Ca^{2+}-sensitive K^+ channels identified in guinea pig cardiac inner mitochondrial membrane. *Biochim. Biophys. Acta Biomembr.* 1828, 427–442. doi: 10.1016/j.bbamem.2012.08.031

Swedberg, K., Komajda, M., Böhm, M., Borer, J. S., Ford, I., Dubost-Brama, A., et al. (2010). Ivabradine and outcomes in chronic heart failure (SHIFT): a randomised placebo-controlled study. *Lancet (Lond. Engl.)* 376, 875–885. doi: 10.1016/s0140-6736(10)61198-1

Terentyev, D., Rochira, J., Terentyeva, R., Roder, K., Koren, G., and Li, W. (2014). Sarcoplasmic reticulum Ca^{2+} release is both necessary and sufficient for SK channel activation in ventricular myocytes. *Am. J. Physiol. Hear. Circ. Physiol.* 306, 738–746.

Tomita, H., Shakkottai, V. G., Gutman, G. A., Sun, G., Bunney, W. E., Cahalan, M. D., et al. (2003). Novel truncated isoform of SK3 potassium channel is a potent dominant-negative regulator of SK currents: implications in schizophrenia. *Mol. Psychiatry* 8, 524–535. doi: 10.1038/sj.mp.4001271

Torrente, A. G., Zhang, R., Wang, H., Zaini, A., Kim, B., Yue, X., et al. (2017). Contribution of small conductance K^+ channels to sinoatrial node pacemaker activity: insights from atrial-specific Na^+/Ca^{2+} exchange knockout mice. *J. Physiol.* 595, 3847–3865. doi: 10.1113/jp274249

Tsien, R. Y., Pozzan, T., and Rink, T. J. (1982). T-cell mitogens cause early changes in cytoplasmic free Ca^{2+} and membrane potential in lymphocytes. *Nature* 295, 68–71. doi: 10.1038/295068a0

Tuteja, D., Rafizadeh, S., Timofeyev, V., Wang, S., Zhang, Z., Li, N., et al. (2010). Cardiac small conductance Ca^{2+}-activated K^+ channel subunits form heteromultimers via the coiled-coil domains in the C termini of the channels. *Circ. Res.* 107, 851–859. doi: 10.1161/circresaha.109.215269

Tuteja, D., Xu, D., Timofeyev, V., Lu, L., Sharma, D., Zhang, Z., et al. (2005). Differential expression of small-conductance Ca^{2+}-activated K^+ channels SK1, SK2, and SK3 in mouse atrial and ventricular myocytes. *Am. J. Physiol. Hear. Circ. Physiol.* 289, 2714–2723.

Vandael, D. H. F., Zuccotti, A., Striessnig, J., and Carbone, E. (2012). $Ca_v1.3$-driven SK channel activation regulates pacemaking and spike frequency adaptation in mouse chromaffin cells. *J. Neurosci.* 32, 16345L–16359L.

Vigneault, P., Naud, P., Qi, X., Xiao, J., Villeneuve, L., Davis, D. R., et al. (2018). Calcium-dependent potassium channels control proliferation of cardiac progenitor cells and bone marrow-derived mesenchymal stem cells. *J. Physiol.* 596, 2359–2379. doi: 10.1113/jp275388

Vinogradova, T. M., Zhou, Y.-Y., Maltsev, V., Lyashkov, A., Stern, M., and Lakatta, E. G. (2004). Rhythmic ryanodine receptor Ca^{2+} releases during diastolic depolarization of sinoatrial pacemaker cells do not require membrane depolarization. *Circ. Res.* 94, 802–809. doi: 10.1161/01.res.0000122045.55331.0f

von Hahn, T., Thiele, I., Zingaro, L., Hamm, K., Garcia-Alzamora, M., Kottgen, M., et al. (2001). Characterisation of the Rat SK4/IK1 K^+ Channel. *Cell. Physiol. Biochem.* 11, 219–230. doi: 10.1159/000051936

Wang, K., Xue, T., Tsang, S.-Y., Van Huizen, R., Wong, C. W., Lai, K. W., et al. (2005). Electrophysiological properties of pluripotent human and mouse embryonic stem cells. *Stem Cells* 23, 1526–1534. doi: 10.1634/stemcells.2004-0299

Weisbrod, D., Khun, S. H., Bueno, H., Peretz, A., and Attali, B. (2016). Mechanisms underlying the cardiac pacemaker: The role of SK4 calcium-activated potassium channels. *Acta Pharmacol. Sin.* 37, 82–97. doi: 10.1038/aps.2015.135

Weisbrod, D., Peretz, A., Ziskind, A., Menaker, N., Oz, S., Barad, L., et al. (2013). SK4 Ca^{2+} activated K^+ channel is a critical player in cardiac pacemaker derived from human embryonic stem cells. *Proc. Natl. Acad. Sci. U.S.A.* 110:783.

Willis, M., Trieb, M., Leitner, I., Wietzorrek, G., Marksteiner, J., and Knaus, H.-G. (2017). Small-conductance calcium-activated potassium type 2 channels (SK2. KCa2.2) in human brain. *Brain Struct. Funct.* 222, 973–979. doi: 10.1007/s00429-016-1258-1

Wong, R., and Schlichter, L. C. (2014). PKA reduces the rat and human KCa3.1 current, CaM binding, and Ca^{2+} signaling, which requires Ser332/334 in the CaM-binding C terminus. *J. Neurosci.* 34, 13371L–13383L.

Wulff, H., Kolski-Andreaco, A., Sankaranarayanan, A., Sabatier, J.-M., and Shakkottai, V. (2007). Modulators of small- and intermediate-conductance calcium-activated potassium channels and their therapeutic indications. *Curr. Med. Chem.* 14, 1437–1457. doi: 10.2174/092986707780831186

Xia, X.-M., Fakler, B., Rivard, A., Wayman, G., Johnson-Pais, T., Keen, J. E., et al. (1998). Mechanism of calcium gating in small-conductance calcium-activated potassium channels. *Nature* 395, 503–507. doi: 10.1038/26758

Xu, Y., Tuteja, D., Zhang, Z., Xu, D., Zhang, Y., Rodriguez, J., et al. (2003). Molecular identification and functional roles of a Ca^{2+} -activated K^+ channel in human and mouse hearts. *J. Biol. Chem.* 278, 49085–49094. doi: 10.1074/jbc.m307508200

Yang, M., Wang, Y., Xiong, X., Xie, B., Liu, J., Yin, J., et al. (2020a). SK4 calcium-activated potassium channels activated by sympathetic nerves enhances atrial fibrillation vulnerability in a canine model of acute stroke. *Heliyon* 6:e03928. doi: 10.1016/j.heliyon.2020.e03928

Yang, M., Wang, Y., Zhao, H., Yin, J., Zi, L., Wang, X., et al. (2020b). Role of intermediate-conductance calcium-activated potassium channels in atrial fibrillation in canines with rapid atrial pacing. *J. Interv. Card. Electrophysiol.* 20, 736. doi: 10.1007/s10840-020-00736-8

Yang, M., Zhao, Q., Zhao, H., Yang, A., Wang, F., Wang, X., et al. (2019). Adipose-derived stem cells overexpressing SK4 calcium-activated potassium channel generate biological pacemakers. *Int. J. Mol. Med.* 44, 2103–2112.

Yang, M. Y., Camara, A. K. S., Aldakkak, M., Kwok, W. M., and Stowe, D. F. (2017). Identity and function of a cardiac mitochondrial small conductance Ca^{2+}-activated K^+ channel splice variant. *Biochim. Biophys. Acta Bioenerg.* 1858, 442–458. doi: 10.1016/j.bbabio.2017.03.005

Yu, T., Deng, C., Wu, R., Guo, H., Zheng, S., Yu, X., et al. (2012). Decreased expression of small-conductance Ca^{2+}- activated K^+ channels SK1 and SK2 in human chronic atrial fibrillation. *Life Sci.* 90, 219–227. doi: 10.1016/j.lfs.2011.11.008

Zahanich, I., Sirenko, S. G., Maltseva, L. A., Tarasova, Y. S., Spurgeon, H. A., Boheler, K. R., et al. (2011). Rhythmic beating of stem cell-derived cardiac cells requires dynamic coupling of electrophysiology and Ca cycling. *J. Mol. Cell. Cardiol.* 50, 66–76. doi: 10.1016/j.yjmcc.2010.09.018

Zhang, B. M., Kohli, V., Adachi, R., López, J. A., Udden, M. M., and Sullivan, R. (2001). Calmodulin binding to the C-terminus of the small-conductance Ca^{2+}-activated K^+ channel hSK1 is affected by alternative splicing. *Biochemistry* 40, 3189–3195. doi: 10.1021/bi001675h

Zhang, Q., Timofeyev, V., Lu, L., Li, N., Singapuri, A., Long, M. K., et al. (2008). Functional roles of a Ca^{2+} -activated K^+ channel in atrioventricular nodes. *Circ. Res.* 102, 465–471. doi: 10.1161/circresaha.107.161778

Zhang, X. D., Timofeyev, V., Li, N., Myers, R. E., Zhang, D. M., Singapuri, A., et al. (2014). Critical roles of a small conductance Ca^{2+} -activated K^{+} channel (SK3) in the repolarization process of atrial myocytes. *Cardiovasc. Res.* 101, 317–325. doi: 10.1093/cvr/cvt262

Zhao, H., Yang, M., Wang, F., Yang, A., Zhao, Q., Wang, X., et al. (2019). Overexpression of the medium conductance calcium activated potassium channel (SK4) and the HCN2 channel to generate a biological pacemaker. *Mol. Med. Rep.* 20, 3406–3414.

Conflict of Interest: The author declares that the research was conducted in the absence of any commercial or financial relationships that could be construed as a potential conflict of interest.

frontiers in Physiology

ORIGINAL RESEARCH
published: 08 September 2021
doi: 10.3389/fphys.2021.612770

Ca^{2+} and Membrane Potential Transitions During Action Potentials Are Self-Similar to Each Other and to Variability of AP Firing Intervals Across the Broad Physiologic Range of AP Intervals During Autonomic Receptor Stimulation

Dongmei Yang[1], Christopher H. Morrell[1,2], Alexey E. Lyashkov[1], Syevda Tagirova Sirenko[1], Ihor Zahanich[1], Yael Yaniv[3], Tatiana M. Vinogradova[1], Bruce D. Ziman[1], Victor A. Maltsev[1] and Edward G. Lakatta[1]*

[1] Laboratory of Cardiovascular Science, National Institute on Aging, National Institutes of Health, Baltimore, MD, United States, [2] Department of Mathematics and Statistics, Loyola University Maryland, Baltimore, MD, United States, [3] Biomedical Engineering Faculty, Technion–Israel Institute of Technology, Haifa, Israel

Ca^{2+} and V_m transitions occurring throughout action potential (AP) cycles in sinoatrial nodal (SAN) cells are cues that (1) not only regulate activation states of molecules operating within criticality (Ca^{2+} domain) and limit-cycle (V_m domain) mechanisms of a coupled-clock system that underlies SAN cell automaticity, (2) but are also regulated by the activation states of the clock molecules they regulate. In other terms, these cues are both causes and effects of clock molecular activation (recursion). Recently, we demonstrated that Ca^{2+} and V_m transitions during AP cycles in single SAN cells isolated from mice, guinea pigs, rabbits, and humans are self-similar (obey a power law) and are also self-similar to *trans*-species AP firing intervals (APFIs) of these cells *in vitro*, to heart rate *in vivo*, and to body mass. Neurotransmitter stimulation of β-adrenergic receptor or cholinergic receptor–initiated signaling in SAN cells modulates their AP firing rate and rhythm by impacting on the degree to which SAN clocks couple to each other, creating the broad physiologic range of SAN cell mean APFIs and firing interval variabilities. Here we show that Ca^{2+} and V_m domain kinetic transitions (time to AP ignition in diastole and 90% AP recovery) occurring within given AP, the mean APFIs, and APFI variabilities within the time series of APs in 230 individual SAN cells are self-similar (obey power laws). In other terms, these long-range correlations inform on self-similar distributions of order among SAN cells across the entire broad physiologic range of SAN APFIs, regardless of whether autonomic receptors of these cells are stimulated or not and regardless of the type (adrenergic or cholinergic) of autonomic receptor stimulation. These long-range correlations among distributions of Ca^{2+} and V_m kinetic functions that regulate SAN cell clock coupling during each AP cycle in different individual, isolated SAN cells not in contact with each other. Our numerical model simulations further extended our perspectives to the molecular scale and demonstrated that many ion

OPEN ACCESS

Edited by:
Gerard J. J. Boink,
University of Amsterdam, Netherlands

Reviewed by:
Matteo Elia Mangoni,
Centre National de la Recherche Scientifique (CNRS), France
Zhilin Qu,
University of California, Los Angeles, United States

***Correspondence:**
Edward G. Lakatta
lakattae@grc.nia.nih.gov

Specialty section:
This article was submitted to Cardiac Electrophysiology, a section of the journal Frontiers in Physiology

Received: 30 September 2020
Accepted: 02 June 2021
Published: 08 September 2021

Citation:
Yang D, Morrell CH, Lyashkov AE, Tagirova Sirenko S, Zahanich I, Yaniv Y, Vinogradova TM, Ziman BD, Maltsev VA and Lakatta EG (2021) Ca^{2+} and Membrane Potential Transitions During Action Potentials Are Self-Similar to Each Other and to Variability of AP Firing Intervals Across the Broad Physiologic Range of AP Intervals During Autonomic Receptor Stimulation. Front. Physiol. 12:612770. doi: 10.3389/fphys.2021.612770

currents also behave self-similar across autonomic states. Thus, to ensure rapid flexibility of AP firing rates in response to different types and degrees of autonomic input, nature "did not reinvent molecular wheels within the coupled-clock system of pacemaker cells," but differentially engaged or scaled the kinetics of gears that regulate the rate and rhythm at which the "wheels spin" in a given autonomic input context.

Keywords: single sinoatrial nodal pacemaker cells, local diastolic Ca^{2+} releases, diastolic depolarization, autonomic receptor stimulation, self-similarity of Ca^{2+} and membrane potential during action potentials, action potential, firing interval variability

INTRODUCTION

The heart is a central player within a hierarchical system of clocks operating within the autonomic neurovisceral axis that creates and synchronizes rhythmic functions ranging from milliseconds to days and beyond (Shivkumar et al., 2016; Lakatta, 2021). The heart's beating rate and rhythm are regulated by autonomic input to sinoatrial nodal (SAN) pacemaker cells that modulates functions within a coupled-clock system intrinsic to SAN cells (Lakatta et al., 2010).

What Is the Coupled-Clock System Within Pacemaker Cells and How Do Clocks Couple to Each Other?

The SAN cell coupled-clock system comprised a calcium "clock," the sarcoplasmic reticulum (SR), which continuously oscillates Ca^{2+} via a criticality mechanism (Nivala et al., 2012) and phase-like transitions (Maltsev et al., 2011); the Ca^{2+} clock is continuously but variably coupled to a "membrane clock," an ensemble of surface membrane ion channels that generates current oscillations via a limit-cycle mechanism (Weiss and Qu, 2020). The criticality mechanisms, in turn, are governed by power law and self-similarity across wide scales (Bak, 1999). The "biochemical engine" of the coupled-clock system is a constitutively active, Ca^{2+} calmodulin-dependent adenylyl cyclase (AC) that generates cyclic AMP (cAMP), leading to modulation of cAMP-gated ion channels, exchange protein directly activated by cAMP (EPAC) signaling, and protein kinase A (PKA) and Calcium/calmodulin-dependent protein kinase II (CaMKII)-dependent kinase activities, mechanisms that regulate intracellular Ca^{2+} levels, Ca^{2+} dynamics and membrane potential within SAN cells (Lakatta et al., 2003, 2006, 2008, 2010; Maltsev and Lakatta, 2008; Yaniv et al., 2015). Variable rates and rhythms at which SAN cells fire action potentials (APs) are controlled by the kinetics of subcellular and cell-wide transitions in $[Ca^{2+}]$ gradients and the membrane potential (V_m), and the extent to which V_m and Ca^{2+} become coupled during AP cycles in any given epoch. For more details, see **Supplementary Discussion**.

The well-known variability of AP firing intervals (APFIs) of isolated SAN cells *in vitro*, of SAN tissue *ex vivo*, or of heartbeat intervals *in vivo* (Monfredi et al., 2014; Yaniv et al., 2014a) indicates that coupled-clock system Ca^{2+} and V_m functions during AP cycles never achieve a true steady state from one AP to the next.

These time-dependent Ca^{2+} and V_m domain transitions during APs are cues, which not only regulate activation states of clock molecules, but are also regulated by the activation status of the very molecules they regulate. In other terms, changes in these cues cause changes in clock molecule activation that feed back to change the characteristics of activation cues. This recursive dynamic imparts robustness to SAN cell automaticity (Maltsev and Lakatta, 2009; Lyashkov et al., 2018). The variability in the degree to which Ca^{2+} and membrane clock molecules couple to each other throughout AP cycles is due to transitions (changes) that occur in Ca^{2+} and V_m domain cues throughout AP cycles (Monfredi et al., 2013; Yaniv et al., 2014b).

Spontaneous transitions in subcellular Ca^{2+} and V_m domains that emerge during the spontaneous diastolic depolarization (DD) phase of an AP cycle have been conceptualized as the AP "ignition phase" (Lyashkov et al., 2018). The ignition process in the Ca^{2+} domain is linked to the emergence of local spontaneous, diastolic oscillatory RyR activation, which generates local Ca^{2+} releases (LCRs) that self-organize to form Ca^{2+} wavelets that propagate locally (Bogdanov et al., 2001; Vinogradova et al., 2004). Ca^{2+}-dependent activation of the surface membrane electrogenic Na^+/Ca^{2+} exchanger generates inward current that accelerates diastolic V_m depolarization and couples the clocks. The time at which the rate of this feed-forward crosstalk acutely accelerates to 0.15 V/s marks the onset of the coupled-clock ignition process (Lyashkov et al., 2018).

Following ignition onset, the extent to which the Ca^{2+} and V_m clock become coupled continues to increase throughout the diastolic period as LCRs and Ca^{2+} wavelets emerge at remote areas across the cell and continue to self-organize in time throughout the cellular space, creating an explosive ensemble Ca^{2+} signal that progressively depolarizes the cell membrane; i.e., clock coupling progressively increases. This Ca^{2+}-induced change in V_m increases in clock-coupling cues the activation of low-voltage activated Ca^{2+} channels ($Ca_v1.3$ and $Ca_v3.1$), resulting in Ca^{2+} influx that contributes to the

---

Abbreviations: AP, action potential; APD_{90}, action potential duration from AP overshoot to 90% repolarization; APFI, AP firing interval; APFIV, variability of AP firing intervals; TTIO, time from the previous AP overshoot to the ignition onset when dV/dt = 0.15 (V/S); CaTFI, firing internal of AP-induced Ca^{2+} transient; CaT_{90}, 90% decay time of AP-induced Ca^{2+} transient; LCR, local Ca^{2+} releases; SR, sarcoplasmic reticulum; SD, standard deviation; CV, coefficient of variation; PC, principal component; I_{CaL}, high voltage-activated, L-type Ca^{2+} current; I_f, hyperpolarization-activated funny current; I_{KACh}, acetylcholine-activated K^+ current; I_{Kr}, K^+ current exhibiting strong inward rectification; I_{NCX}, Na^+-Ca^{2+} exchanger (NCX) current; βARs, β-adrenergic receptor stimulation; CRs, cholinergic receptor stimulation; CCh, carbachol; ISO, isoproterenol; HR, heart rate; SAN, sinoatrial node.

further organization of the ensemble LCR Ca^{2+} signal via feed-forward electrochemical (Ca^{2+}–V_m–Ca^{2+}) signaling, when the diastolic V_m enters a range that cues the activation of L-type Ca^{2+} channels ($Ca_v1.2$). The ignition phase of the coupled-Ca^{2+} and V_m domain subcellular kinetic transitions culminates in the generation of cell-wide events; a marked transition in the rate of V_m depolarization, due to the activation of $Ca_v1.2$, results in the rapid AP upstroke and Ca^{2+} influx, which, via Ca^{2+}-induced Ca^{2+} release from the SR via RyRs, generates an AP-induced cytosolic Ca^{2+} transient (CaT). In other terms, spontaneous, cell-wide Ca^{2+} signals and APs in SAN cells emerge from spatiotemporal self-organization of spontaneous subcellular Ca^{2+} oscillations (the criticality mechanism) (Nivala et al., 2012). SERCA2a pumping Ca^{2+} into SR and K^+ channel repolarization of V_m return the Ca^{2+} and V_m domain cues toward their diastolic levels at which LCRs again begin to emerge, creating the ignition phase of the next AP cycle.

Self-Organized Criticality

Spatiotemporal self-organization across geometric scales (subcellular to cell-wide) is a manifestation of criticality that has been observed in excitable cells throughout nature (Stožer et al., 2019) including cultured astrocytes (Jung et al., 1998), immature oocytes (Lopez et al., 2012), and mouse cardiac ventricular myocytes (Nivala et al., 2012). Self-similar, scale-free distributions of parameters across wide scales that obey power law behavior (are ln–ln linear) are an indication of their self-ordered criticality (Bak, 1999).

It has recently been discovered that coupling of subcellular Ca^{2+} signals (cues) generated by the Ca^{2+} clock within isolated SAN cells to the cell surface membrane proteins during APs to elicit a change in V_m manifests long-range power law correlations (are self-similar) across species (Sirenko et al., 2021). Specifically, Ca^{2+} and V_m domain kinetic transitions (cues) during AP cycles in single SAN cells isolated from mice, guinea pigs, rabbits, and humans are self-similar to each other during APS and self-similar to *trans*-species APFIs of these cells *in vitro*, to heart rate *in vivo*, and to body mass (Sirenko et al., 2021).

Neurotransmitter stimulation of β-adrenergic receptor stimulation (βAR) or cholinergic receptor (CR)–initiated signaling modulates the AP firing rate and rhythm of SAN cells by impacting on coupled-clock protein functions, modulating the degree to which criticality (Ca^{2+} domain) and limit-cycle (V_m domain) mechanisms couple to each other during AP cycles (Maltsev and Lakatta, 2009; Lakatta et al., 2010). APFIs in rabbit SAN cells during autonomic stimulation vary over a fourfold range, from approximately 200 ms during βARs up to approximately 800 ms during CR stimulation (CRs) (Vinogradova et al., 2002; Lyashkov et al., 2009).

We hypothesized that transitions in V_m and Ca^{2+} domain cues during the diastolic AP ignition (Lyashkov et al., 2018) and recovery phases (**Figure 1**) of APs are (1) not only self-similar to each other in cells without autonomic receptor stimulation (control cells), but are self-similar to V_m and Ca^{2+} cues in other cells during CRs and during βARs and (2) that Ca^{2+} and V_m cues during APs are self-similar to APFI variabilities (and therefore self-similar to mean APFIs) regardless of the presence or absence or type of autonomic receptor stimulation. In other terms, we hypothesized that Ca^{2+} and V_m domain clock-coupling cues occurring during all APs are self-similar to each other, i.e., manifest long-range correlations in all isolated SAN cells within populations of cells that differ with respect to autonomic input, and that these Ca^{2+} and V_m cues during APs are also self-similar to the rate and rhythm of AP firing across the entire range of APFIs created by these cues in all isolated SAN cells.

To test these hypotheses, we studied a large population (n = 230) of single rabbit SAN cells to which we applied CRs [carbachol (CCh)] to one subset of cells, βARs [isoproterenol (ISO)] to another subset, and no autonomic receptor stimulation to a third subset of cells. This created three populations of SAN cells having APFIs distributed across the entire physiologic range. We measured intracellular Ca^{2+} or membrane potential in these cells to (1) characterize the times to ignition onset and times to 90% recovery of V_m and Ca^{2+} parameters during APs in AP time series and (2) to determine the correlations of these V_m and Ca^{2+} kinetic parameters to each other during APs, to APFI variability (APFIV; and therefore to mean APFIs). Thus, the data set to be analyzed consisted of 12 different kinetic parameters in each cell population (control, CCh, and ISO); six parameter means, three each in the Ca^{2+} and V_m domains; and six parameter variabilities (SDs) around the means. To determine the degree of self-similarity among V_m and Ca^{2+} domain parameters, we constructed density distribution plots and applied correlation, power law, and principal component (PC) analyses to Ca^{2+} and V_m domain data sets separately and to the combined Ca^{2+} and V_m data sets. We further extended our perspectives from cell population and single-cell levels downward to the molecular scale by performing numerical modeling simulation and analyzing variabilities of ion currents and Ca^{2+} with respect to APFI to determine whether these ion currents and Ca^{2+} also obeyed a power law across autonomic states.

MATERIALS AND METHODS

The study was performed in accordance with the Guide for the Care and Use of Laboratory Animals published by the National Institutes of Health (NIH publication 85–23, revised 1996). The experimental protocols have been approved by the Animal Care and Use Committee of the NIH (protocol #457-LCS-2024). Materials and methods briefly presented here are detailed in **Supplementary Material**.

Isolation of Single Rabbit SAN Cells

Single, spindle-shaped, spontaneously beating SAN cells were isolated from the hearts of New Zealand rabbits (Charles River Laboratories, Wilmington, MA, United States) as described previously (Vinogradova et al., 2000).

Spontaneous APs Recordings

Time series of spontaneous APs were recorded in subsets of freshly isolated SAN cells using the perforated patch-clamp technique with Axopatch 200B patch-clamp amplifier (Axon

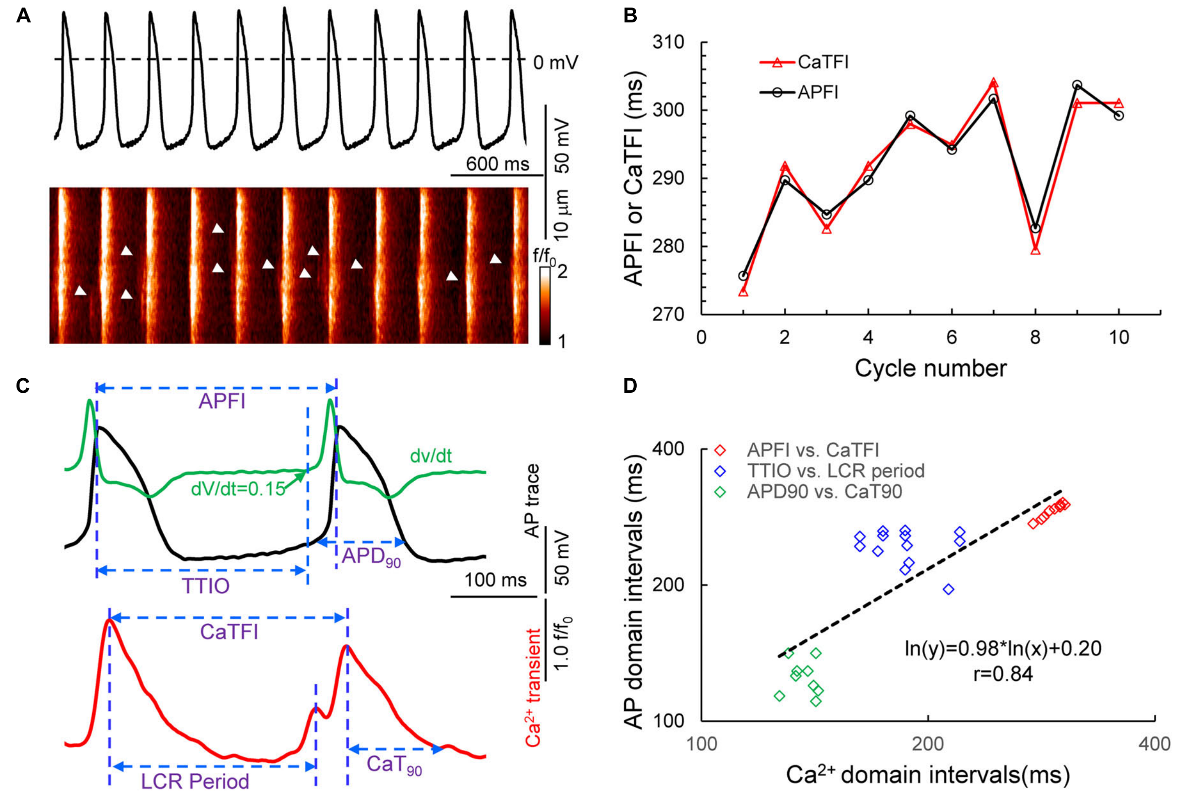

FIGURE 1 | Simultaneous recording of AP and Ca^{2+} in a 10 beat time series of APs **(A)** and the measured APFI and CaTFI (firing internal of AP-induced Ca^{2+} transient) **(B)**; the definition of parameters measured in V_m and Ca^{2+} domains **(C)** and the self-similarity of the V_m and Ca^{2+} parameters during APs to each other and to the APFI **(D)**.

Instruments) (Bogdanov et al., 2001) at 34°C ± 0.5°C. AP parameters (**Figure 1**) measured via a customized program (Lyashkov et al., 2018) were APFI, APD_{90}, and the time to ignition onset (TTIO) measured by the time at which diastolic membrane potential dV/dt accelerates to 0.15 V/s (**Figure 1**), which reflects the onset of the ignition phase of the AP cycle (Lyashkov et al., 2018).

Ca^{2+} Measurements

In another subset of SAN cells, AP-induced global CaTs and spontaneous LCRs (**Figure 1**) were measured at 34°C ± 0.5°C with a confocal microscope (Zeiss LSM510, Germany) in the line-scan mode (Vinogradova et al., 2004; Yang et al., 2012). The interval between the peaks of two adjacent AP-induced CaTs (**Figure 1**) is defined as CaT firing interval, which is highly correlated with the APFI, as demonstrated by simultaneous recordings of V_m and Ca^{2+} in a separate subset of cells (**Figure 1**). The LCR period is defined as the time from the peak of the prior AP-induced CaT to an LCR peak in diastole (**Figure 1**); the time to 90% decay of the CaT was defined as CaT_{90}.

Numerical Modeling

We performed numerical simulations using a modified Maltsev–Lakatta model that features the coupled-clock mechanism (Maltsev and Lakatta, 2009). The computer code for the original model is freely available and can be downloaded and run in CellML format[1] using the Cellular Open Resource software developed by Alan Garny at Oxford University in the United Kingdom (Garny et al., 2009) (for recent development of this software)[2]. The original model could not be directly used for APFIV simulations because it is a system of first-order differential equations that is deterministic and showing no APFIV in limit-cycle oscillatory regime of AP steady firing. Thus, we modified the model to generate variability of AP waveforms by supplementing total membrane current (I_{tot}) with an additional randomly fluctuating current around its zero-mean value, known as perturbation current or I_{per} [as previously implemented by Henggui Zhang (Monfredi et al., 2014)]. Furthermore, we also performed an additional set of simulations with I_{per} added to Ca^{2+} release flux to mimic the effect of stochastic LCRs (Bogdanov et al., 2006; Monfredi et al., 2013). Using the resultant stochastic dynamical system of SAN cell, we simulated fluctuating APFI, ion currents, and Ca^{2+} dynamics for three conditions: (i) basal AP firing, (ii) during βARs with ISO (100 nM), and (iii) during CRs with CCh

---

[1] http://models.cellml.org/workspace/maltsev_2009

[2] http://www.opencor.ws/

(100 nM). The effects of autonomic modulation (conditions ii and iii) were modeled as previously described (Maltsev and Lakatta, 2010), except modulation of I_{CaL} current by CCh that was modeled as described by Zaza et al. (1996). All model equations and parameters are provided in the **Supplementary Material**.

Experimental Design and Statistics

Supplementary Figure 1 illustrates schematic of the experimental design to assess long-range correlations of V_m and Ca^{2+} parameters during APs and APFI intervals in cells within and among populations of cells that differed with respect to autonomic input. V_m and Ca^{2+} parameter intervals (milliseconds) are presented as mean ± SD. APFIV within a time series is taken as standard deviation (SD) about the mean or as the coefficient of variation (CV) (the ratio of SD to the mean).

Analyses of V_m and Ca^{2+} parameter interval distributions measured in AP time-series in different cells determined the association among pairs of variables using Pearson's correlations for both average and individual data (Howell, 2002). In cells in which Ca^{2+} was measured, the mean interval between AP-induced CaTs was usually longer than the mean APFI in cells in which APs were recorded (due to slight buffering effects of the fluorescent Ca^{2+} probe). To allow all the variables to be combined into a single analysis, we matched on the APFI variable Z scores in control, ISO, or CCh populations by "matchit" function in R (Ho et al., 2011).

Density estimates of within-cell standard deviations and means of parameters of cells within each autonomic state population are presented as non-parametric kernel estimates of probability density functions, scaled so that the total area under each curve is unity (Silverman, 1986).

In order to determine whether distributions of parameter means and SDs are self-similar, i.e., obeyed a power law suggesting fractal-like behavior, we constructed ln–ln plots of distributions of the AP and Ca^{2+} function means and SDs measured across the broad range of apparent steady states in the absence of, or the presence of, βARs or CRs (Kucera et al., 2000; Yaniv et al., 2013).

The relationships among all distributions of all parameters (means and SDs) were also assessed in principal component analyses (Johnson and Wichern, 2008).

In a few cells in which experimentally measured parameter interval distributions measured in the V_m and Ca^{2+} domains in the same cell and for numerical simulation of ion currents and Ca^{2+} prior to and during autonomic receptor stimulation Poincaré indices were employed to define long-range correlations among variables, a Poincaré plot graphs a parameter (n), in an AP time series on the x axis versus the same parameter of the succeeding AP (n + 1) on the y axis; i.e., one takes a sequence of parameters and plots each one against the following parameter (Huikuri et al., 2000).

When statistical inference was performed, $p < 0.05$ was considered statistically significant.

RESULTS

Assessment of Self-Similarity of Ca^{2+} and V_m Kinetic Interval Parameters to Each Other During APs and to APFIV

Figure 1A illustrates a time series of APs in a SAN cell during which Ca^{2+} and V_m were simultaneously measured in the absence of autonomic receptor stimulation. Kinetic transitions in Ca^{2+} and V_m parameters as illustrated in **Figure 1B** were assessed during each AP. **Figures 1C,D** shows that V_m and Ca^{2+} parameters during AP time series are self-similar to each other and are also self-similar to the APFIs ($r = 0.844$ in this cell).

Figure 2 illustrates the time series of AP intervals in **Figure 1A** plotted as phase-plane diagrams in which V_m is depicted as a function of Ca^{2+} throughout each cycle. The times at which various channels are activated throughout the V_m/Ca loop are indicated. The times of ignition and 90% recovery are also indicated. The point resolution is 3.072 ms, and the point spread indicates the rates at which the electrochemical signal changes during each cycle. The dashed line in the figure marks the border between the disordered and ordered molecular activation. The arrows indicate the direction of the electrochemical signal emergence.

A Poincaré plot (scatter graph) constructed from consecutive data points in a time series (**Figure 3A**) is a convenient tool that provides information on correlations (self-similarity) of data across the time series. The x axis defines the parameter (n) occurrence in milliseconds, and the y axis defines the parameter occurrence at (n + 1). The Poincaré plot in **Figure 3A** depicts the data of the time series of the cell in **Figure 1**. Note that although the means vary over a threefold range, all six parameter means (the Ca^{2+} and V_m interval parameters measured during APs and APFIs) in the absence of autonomic receptor stimulation are described by a line of identity, indicating their self-similarity across the AP time series. Quantitative analysis of short- and long-term variability in a given time series of observations entails fitting an ellipse to each cloud of data points within the Poincaré plot (**Figure 3B**): The length of a line describing the slope of the long axis of each ellipse is referred to as SD2 of the data points (c.f. Figure inset); the length of the line describing the slope of the short axis, which is perpendicular in direction to the long axis line, is referred to as SD1. Note in **Figure 3C** that the SD1 is self-similar to SD2 across the fourfold range of Ca^{2+} and V_m parameters. The center point of each ellipse, i.e., the intersection of SD1 and SD2, is the average interval between events (AP intervals or other parameters measured in the time series) within the time series. SD1/SD2 (Figure inset) informs on non-linear trends (unequal lengths of SD1 and SD2) across intervals within each ellipse.

Figure 4 illustrates combined Poincaré plots of TTIO, APD_{90}, during APs and APFIs in time series of APs of two representative cells: one cell in control and during CRs by CCh and the other cell in control and during βARs stimulation by ISO.

Although the range of absolute values of kinetic interval parameters of cells depicted in the Poincaré plot in **Figure 4B** vary by 20-fold, all points (n = 5,673) are self-similar, i.e., fit by

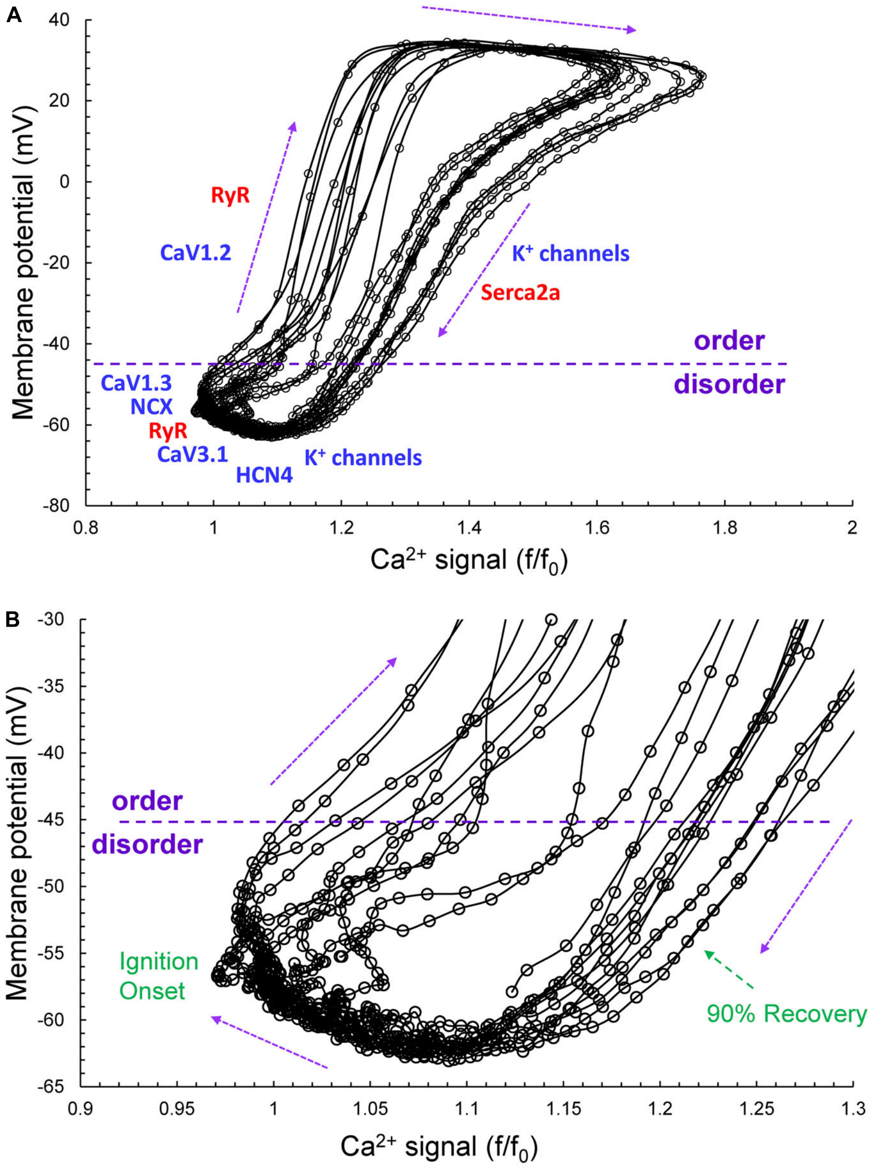

FIGURE 2 | (A) The time series of AP intervals in **Figure 1A** plotted as phase-plane diagrams in which V_m is depicted as a function of Ca^{2+} throughout each cycle. The times at which various channels are activated throughout the V_m/Ca phase-plane loop are indicated. The times of ignition and 90% recovery are also indicated **(B)**. The point resolution is 3.072 ms, and the spread indicates the rates at which the electrochemical signal changes during each cycle. The dashed line in the figure marks the border between the disordered and ordered molecular activation. The arrows indicate the direction of the electrochemical signal emergence.

a single line ($r = 0.992$) with a slope of unity, passing nearly through the origin.

Supplementary Table 1 lists the SD1s, SD2s, SD1/SD2, the means of the TTIO and APD_{90} intervals, and APFIs depicted in **Figure 4B**. Note also that the SD1s, SD2s, and SD1/SD2 of TTIO, APD_{90}, and APFIs progressively increase from ISO to control and markedly increase from control to CCh, creating degrees of non-linearity across the combined control, ISO, and CCh states, which is also reflected in the mean APFIs across the three states (**Supplementary Table 1**). The V_m transitions during APs across different autonomic states are self-similar to APFIs across these states (**Figure 5A**). **Figure 5B** shows the self-similarity of parameter means of SD1s of V_m parameters to their SD2s across autonomic states, indicating self-similarity of short-term (e.g., beat to beat) and long-term (e.g., rhythm across more than two beats) variabilities across autonomic states within the time series. **Figure 5C** shows the self-similarity of all parameter means depicted in **Figures 4**, **5A,B** to their SDs across autonomic states.

The data in **Figures 4**, **5** demonstrate that over the entire range of physiologic APFIs from 192.7 ms in ISO to 305.5 ms in control, and to 910.3 ms in CCh, variabilities of TTIO and APD_{90} measured during APs are self-similar to each other and are also self-similar to the variability of APFIs within the time series, and therefore self-similar to the mean APFI of the time series.

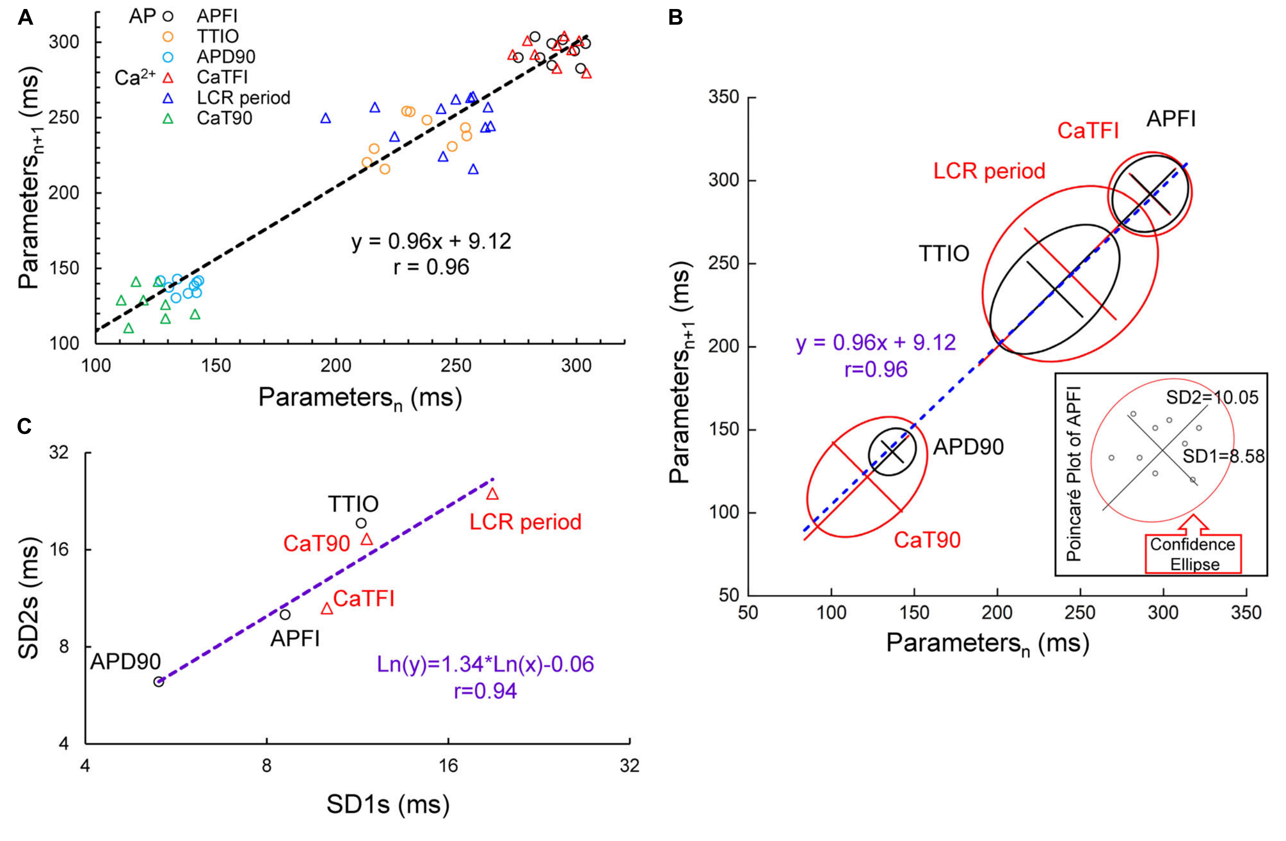

FIGURE 3 | Poincaré plots **(A)** and fitting of the Poincaré plot ellipse clouds **(B)**, the relation of SD2s to SD1s **(C)** of the six parameters from simultaneously recorded during the 10 beats time series from **Figure 1**.

Self-similarity among V_m variables in the cells in **Figure 4** across autonomic states in control and during ISO and CCh in **Figures 2**, **3A** can also easily be ascertained from the shapes of their population density distributions (**Figure 6**). Note that in the cell superfused with CCh, the distributions of TTIO, APD_{90}, and APFIs (**Figures 6A–C**) are broader than in control or during ISO. Note also that the distributions of kinetic transitions during APs and APFI become more synchronized from CCh to ISO (**Figure 6A–C**). In other terms, the degree to which V_m and Ca^{2+} parameters are synchronized during APs increases from CCh to control to ISO, similar to the AP firing variabilities and mean APFIs.

Self-Similarity of Ca^{2+} and V_m Parameter Means to Each Other During APs and to APFI Variabilities and Mean APFIs Across Autonomic States in Different Cells

We next determined whether the self-similarity (long-range correlations) of Ca^{2+} to V_m parameters measured within the same cells as depicted in **Figures 1–6** extends to populations of different cells within and among different autonomic states. To accomplish this, we applied CRs (CCh) to one subset of cells, βAR stimulation (ISO) to another subset, and no autonomic receptor stimulation to a third subset of cells. This created populations of SAN cells having APFIs distributed across the entire physiologic range.

Table 1 lists descriptive statistics (means and SDs) of the variabilities and means of Ca^{2+} and V_m kinetic parameter intervals measured in different cells within and among populations of cells that differ with respect to autonomic input. The mean SD of V_m and Ca^{2+} domain parameters listed in **Table 1A** gives the average time-series variability of each parameter among cells within each of the three cell populations (control, ISO, or CCh). The standard deviation of the SDs (SDSD) in **Table 1A** tells us how variable the SDs of each parameter are among cells within each cell population. The means of each parameter measured within a time series (**Table 1B**) tell us the average level of the parameter among cells within each of the three populations, and the SD of the means tells us the variability of the mean parameter levels among cells within each cell population.

Figure 7A illustrates the distributions of SDs of parameters within Ca^{2+} and V_m domains during APs and of APFIs in cells listed in **Table 1A** of each of the three populations of cells that differed in autonomic state: control cells (n = 78), cells during superfusion with ISO (n = 27), and in cells superfused with CCh (n = 10). The self-similarity (long-range correlations) of the mean SDs of Ca^{2+} to V_m parameter transitions during ignition and recovery phases of APs across the wide range of APFIs induced

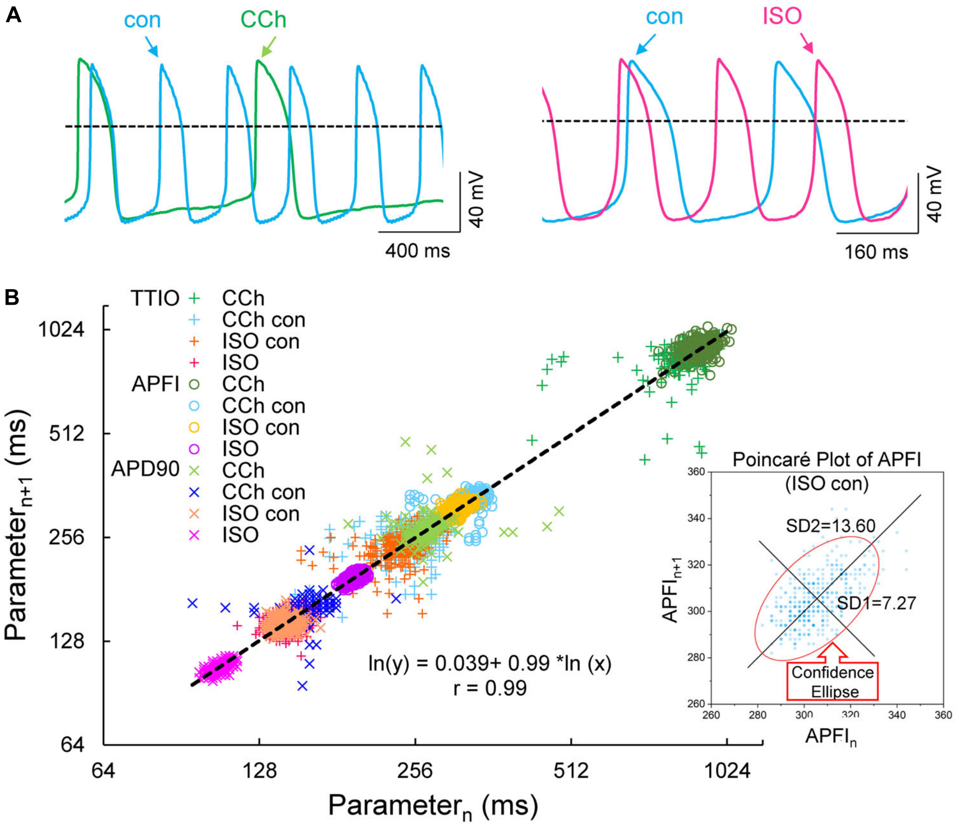

FIGURE 4 | Self-control AP recordings in two cells during CCh or ISO **(A)**, Poincaré plots of the three measured V_m domain parameters in three autonomic states: CCh, control (two cells), and ISO (**B**, number of beats in each time series was 197, 397, 397, and 900, respectively, in carbachol, carbachol control, isoproterenol control, and isoproterenol). The inset shows an example of ellipse fitting.

by the type of autonomic receptor stimulation, or lack thereof, is evident in the self-similarity of their mean SD distribution shapes (**Figure 7A**).

The distribution of the means listed in **Table 1B** is illustrated in **Figure 7B**. Note that the shapes of the distributions are self-similar to each other across the three different autonomic states. Note also that the shapes of the distribution of the means of a given parameter in **Figure 7B** are similar to the distribution of that parameter's SDs in **Figure 7A** (because the interval distribution means stem from the distributions of their SDs). In other terms, the variability in the times at which parameters occur within a time series (their parameter SDs) determines what the mean interval of events in the time series will be.

Also note in **Figure 7** that compared to cells not superfused with an autonomic receptor agonist (control cells) and those superfused with ISO, the shapes of the distributions of cells superfused with CCh are broad, indicating marked variability among CCh cells within the parameter distributions of both interval means and interval SDs.

Figure 8A illustrates the self-similarity of V_m parameter means and SDs to Ca^{2+} means and SDs across autonomic states. Heatmaps of the long-range correlations among V_m and Ca^{2+} parameter means are shown in **Supplementary Figure 3**. The long-range correlations (self-similarity) between the means of the means and means of SDs given in **Table 1** is shown in **Figure 8B**.

Self-Similarity of Ca^{2+} and V_m Parameters Among All Individual Cells Within and Among the Three Autonomic States

Two-by-two correlations of V_m and Ca^{2+} parameter means and SDs of all 230 cells that comprised the three different cell populations in **Figure 7** and **Table 1** are highly significant (**Table 2**).

Figure 9 shows ln–ln plots of the distributions of means and SDs of Ca^{2+} and V_m parameters of all cells across the three autonomic states. The piecewise linear fit of the data in each panel is largely driven by the data from cells superfused with CCh that manifested broad interval distributions and high mean APFIs in **Figures 4–7**. **Figure 8C** shows that the means and SDs of V_m parameters measured during APs in individual cells ($n = 115$) are self-similar to Ca^{2+} means and SDs measured during AP in other individual cells ($n = 115$) across the three autonomic states.

Although, as noted above, the V_m and Ca^{2+} parameters within and among cells during CCh superfusion were more broadly distributed than those during control or during ISO, the

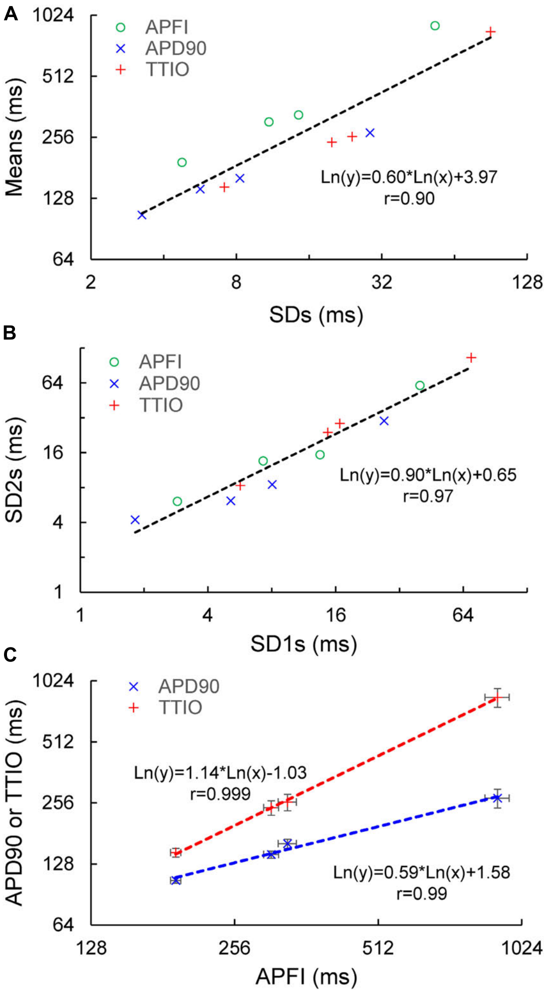

FIGURE 5 | Correlation between mean and SD of the three V_m parameters **(A)**, correlation of Poincaré ellipse fitting SD1 and SD2 **(B)**, and the self-similarity of APD90 and TTIO to APFI **(C)** across the three autonomic states, the same as in **Figure 4**.

correlations between V_m and Ca^{2+} parameters among all cells within the CCh superfused population of cells were extremely strong for most parameters (**Supplementary Figure 3**). Weaker but still significant correlations between times to 90% recovery and other variables are observed in CCh superfused cells (likely because times to 90% are the most difficult parameters in the data set to measure accurately).

Figure 8D shows that V_m and Ca^{2+} parameters measured during APs are self-similar to APFI means and SDs across the three autonomic states.

Correlation of Ca^{2+} and V_m Domain Parameter Means in Individual Cells to Their SDs Within and Across Autonomic States

The relationship between mean AP firing rate and its SD is known to be non-linear (Monfredi et al., 2014). Whereas the relationships of all Ca^{2+} and V_m parameter means relative to their corresponding SDs measured in the combined set of data derived from different populations of cells in control or during ISO or CCh superfusion are non-linear (**Figures 10A–C**), the ln–ln plots of these combined data (**Figure 10D–F**) are linear, indicating their self-similarity across all 230 cells that differed by autonomic state.

Principal Component Analyses

Next, we employed principal component analyses to determine whether the self-similarity of parametric measures within the entire data set of variables could be summarized by a smaller set of principal components that contain most of the information in all the variables. PCs are linear combinations of the original variables, and each PC is statistically independent of the others: the first PC explains as much of the total variability in the data as possible, the second PC as much of the remaining variability, and so on. Highly self-similar parameters within the complete data set are explained by the sum of the first few PCs.

In a PC analysis of SDs of the six variables (three in the V_m domain and three in the Ca^{2+} domain), the first three PCs explained 91.4% of the total variation within the entire SD data set (**Supplementary Table 2** and **Figure 11A**). Similarly, in a PC analysis of the means of all six measured variables means (three in the V_m domain and three in the Ca^{2+} domain) in a PC analysis, the first two PCs explained 92.8% of the variability in the data set of all six means (**Supplementary Table 2** and **Figure 11B**). Finally, in a PC analysis of all 12 variables (six means and six SDs), the first three PCs explained 88% of the variability within the total (means plus SDs) data set (**Supplementary Table 2** and **Figure 11C**).

Because a smaller set of PCs can explain a substantial proportion of the total variability in each set of V_m or Ca^{2+} domain means, SDs, and means and SDs, means that these distributions of V_m and Ca^{2+} parameters measured during an AP and APFIs in control cells and different cells superfused with ISO or CCh are each self-similar to each other. In other terms, Ca^{2+} and V_m domain functions operative within the SAN cells coupled-clock system manifest self-similar scale-free characteristics, i.e., kinetic fractals of each other, across the entire physiologic range of APFIs.

Numerical Model Simulations of APFIV, Major Ion Currents, and Ca^{2+}

Variability of V_m and Ca^{2+} parameters measured experimentally in cells within and across autonomic states is linked to the respective variabilities of clock molecular availability to respond to V_m and Ca^{2+} cues (**Figure 2**) that cannot be directly measured experimentally during AP firing. To gain further insight into the variability of these biophysical mechanisms, we performed numerical modeling simulations. The APFIV was generated by SAN cell model described as a stochastic dynamical system, i.e., a dynamical system [deterministic Maltsev–Lakatta model (Maltsev and Lakatta, 2009)] subjected to the effects of noise current, I_{per} (see section "Materials and Methods" and **Supplementary Material** for details). I_{per} amplitude was tuned

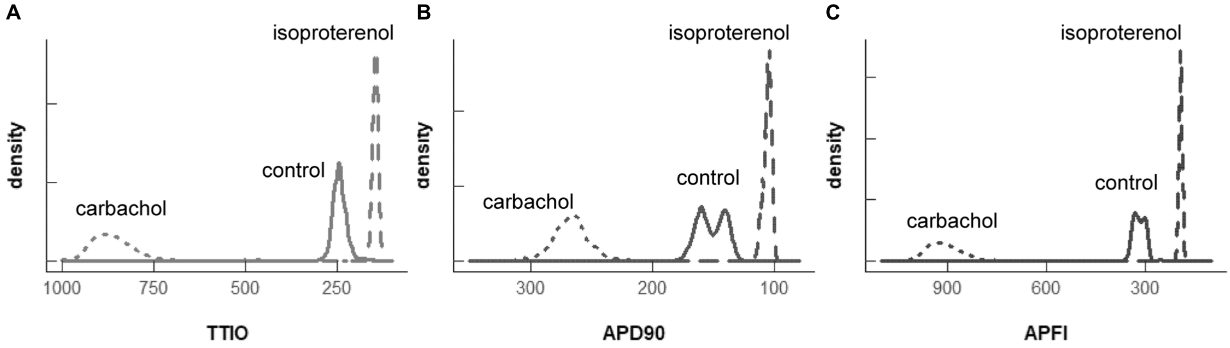

FIGURE 6 | Density distributions of the self-control V_m parameters, TTIO **(A)**, APD90 **(B)** and APFI **(C)**, measured in the same cell as in **Figures 4**, **5** (two control cells are combined). The density distributions are presented as non-parametric kernel estimates of probability density functions (Silverman, 1986), scaled so that the total area within each curve is unity.

for the model APFIV to match that measured experimentally under respective experimental conditions. We investigated two scenarios of noise generation: when I_{per} was added to I_{tot} or when I_{per} was added to Ca^{2+} release flux current in each of the three autonomic states: (i) basal AP firing, (ii) ISO 100 nM, and (iii) CCh (100 nM). Variability of six major currents was simulated and analyzed: I_f, I_{NCX}, I_{Kr}, I_{CaL}, I_{CaT}, and I_{KACh}. Variability of [Ca] under cell membrane was also simulated during the three autonomic states. For all items, we measured variability of their peak amplitudes and amplitudes at −40 mV during DD.

TABLE 1 | (A) Mean of SDs and SD of SDs of AP and Ca^{2+} domain intervals among individual cells in each of the three steady state populations that differ with respect to autonomic receptor stimulation; **(B)** Mean ± SD of means of AP and Ca^{2+} domain interval in each cell population **(A)**.

(A) Mean SD ± SD of SDs (ms, individual cells within each population)			
AP recordings	**ISO (*n* = 27)**	**Control (*n* = 78)**	**CCh (*n* = 10)**
APFI, SD	8.43 ± 1.90	13.30 ± 5.18	99.08 ± 57.28
TTIO, SD	13.14 ± 4.54	23.72 ± 13.33	132.78 ± 88.24
APD_{90}, SD	4.52 ± 1.91	9.23 ± 4.56	78.40 ± 58.07
Ca^{2+} recordings	**ISO (*n* = 27)**	**Control (*n* = 78)**	**CCh (*n* = 10)**
CaTFI, SD	17.52 ± 14.30	16.23 ± 11.24	86.08 ± 54.28
CaT_{90}, SD	17.31 ± 12.34	13.17 ± 7.81	30.79 ± 13.35
LCR period, SD	38.11 ± 24.77	40.34 ± 23.90	153.31 ± 93.59
(B) Mean ± SD of Means (ms)			
AP recordings	**ISO (*n* = 27)**	**Control (*n* = 78)**	**CCh (*n* = 10)**
APFI, mean	244.87 ± 22.13	321.57 ± 63.08	786.45 ± 374.35
TTIO, mean	188.01 ± 18.69	239.45 ± 60.45	690.44 ± 334.27
APD_{90}, mean	123.55 ± 14.06	169.06 ± 35.37	249.72 ± 81.38
Ca^{2+} recordings	**ISO (*n* = 27)**	**Control (*n* = 78)**	**CCh (*n* = 10)**
CaTFI, mean	357.80 ± 64.94	390.64 ± 83.37	872.84 ± 284.33
CaT_{90}, mean	160.76 ± 43.49	174.73 ± 42.73	289.94 ± 70.24
LCR period, mean	302.92 ± 55.65	342.68 ± 72.87	734.92 ± 191.01

CaTFI, firing internal of AP-induced Ca^{2+} transient.

Model simulation results are presented in **Figure 12**, with their numerical values given in **Supplementary Tables 6, 7**. Regardless of the type of noise generation (via Ca^{2+} or I_{tot}), it affected the variability of ion currents and Ca^{2+} the same way, and the predicted variabilities for many parameters differed substantially from that of APFI:

(1) I_f variability was substantial: in the basal state and in ISO I_f variability was similar to or larger than APFIV; the variability of I_f decreased in CCh.
(2) I_{NCX} variability was also substantial: at −40 mV, it was substantially larger than that of APFIV (except in CCh when I_{per} was added to I_{tot}); variability of I_{NCX} peak amplitude (negative, during AP upstroke) was similar to that of APFI in the basal state and ISO, but became reduced in CCh.
(3) I_{Kr} variability was substantially less than APFIV under all conditions.
(4) I_{CaT} variability was the largest among ion currents, being similar to that of I_{NCX}, in CCh when I_{per} was added to Ca^{2+} release.
(5) Peak I_{CaL} variability was always less than that of APFIV; at −40 mV, it was greater in ISO than in basal state and CCh.
(6) Variability of Ca^{2+} release flux in the basal state and ISO at −40 mV was greater than or similar to APFIV; in CCh, variability of Ca^{2+} release flux was less than that of APFI.

Some components exhibited power law behavior over a wide range of APFI over all conditions tested (**Figure 13**).

We next determined whether self-similarity across autonomic states observed for experimental data during the ignition phase is also applied to simulated ion currents or Ca^{2+} data during this time of the cycle, i.e., at −40 mV. To this end, we applied the statistical tests utilized for experimental data to simulated data (for the scenario when I_{per} was added to I_{tot}).

Simulated ion currents and Ca^{2+} amplitudes during AP ignition (−40 mV) across the three autonomic states are self-similar to each other, strongly correlated to each other, as were experimentally measured parameters (**Table 2**). These

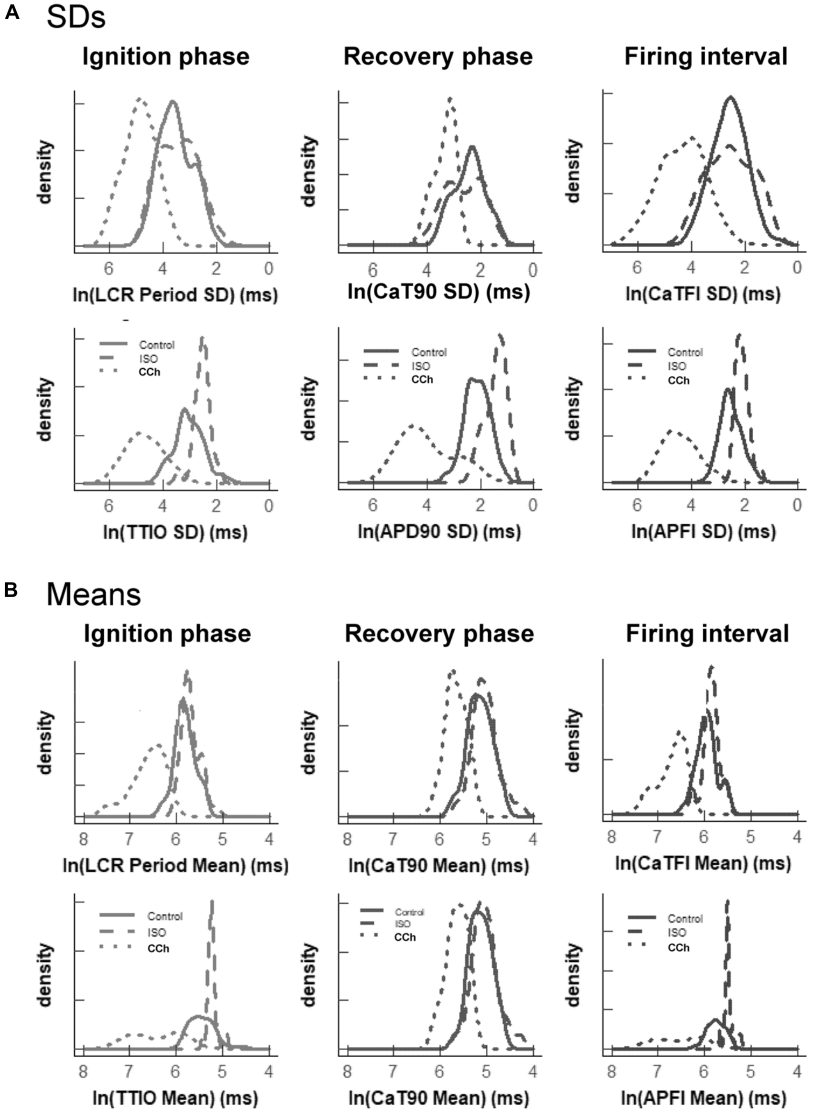

FIGURE 7 | Density distributions of selected parameter means **(B)** and SDs **(A)** of M and Ca^{2+} clock functions measured in different cells prior to and during autonomic receptor stimulation across the three groups of mean APFI steady states in **Table 1**. The density distributions are presented as non-parametric kernel estimates of probability density functions (Silverman, 1986), scaled so that the total area within each curve is unity. Both the mean and variability about the mean are concordant with each other across the three experimental groups in control and shift concordantly in response to autonomic receptor stimulation in all cells measured.

two-by-two correlations of all the simulated components are listed in **Supplementary Table 3**. Selected examples of these correlations are shown in **Figure 14**. As I_{NCX} is fully determined by V_m and Ca^{2+}, at a fixed voltage (−40 mV) it is fully determined by only Ca^{2+}. That is why we have 100% correlation of I_{NCX} and Ca^{2+}. I_{CaT} strongly correlated with Ca^{2+} variations, because the stronger Ca^{2+} signal is linked to the higher DD rate and hence stronger (time-dependent) activation of I_{CaT}. Surprisingly, I_{KACh} amplitude was also highly correlated with Ca variations.

Variations in I_f and I_{Kr} at −40 mV did not depend on variations of Ca^{2+}, but their mean values strongly depended on Ca^{2+} across the autonomic states. I_f activation and I_{Kr} deactivation are early DD mechanisms and do not seem to interplay with Ca^{2+} at the ignition onset at −40 mV in a given cycle.

Figure 15A illustrates the Poincaré plots of many simulated parameters (APFI and TTIO; I_{NCX}, I_{CaT}, I_{Kr}, [Ca], I_{CaL}, I_{KACh}, and I_f, all at −40 mV). Although the ranges of absolute values of these simulated parameters substantially vary, all simulated parameters are self-similar, i.e., fit by a single line (r = 0.998) with a slope of unity, resembling Poincaré relationship of experimentally measured AP parameters (**Figures 1**, **4**).

Figure 15B illustrates ln–ln plots of the relationships of the means of simulated components to their SDs. Note that this relationship follows power law behavior just as did

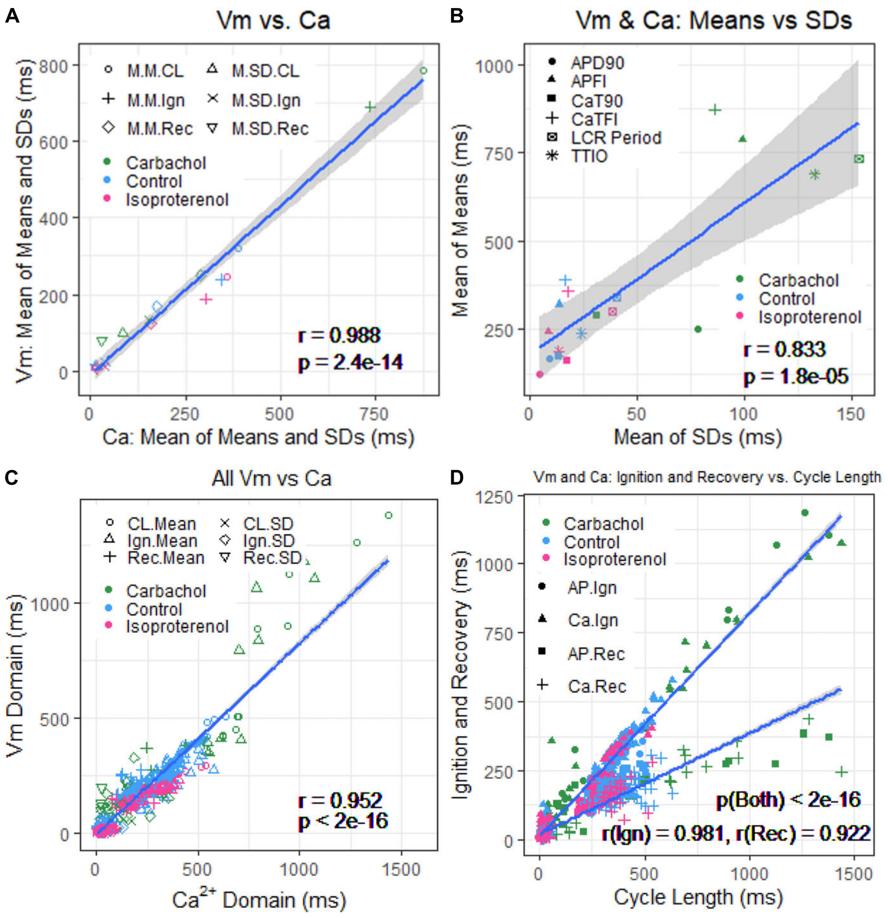

FIGURE 8 | (A) Plot of mean of means and SDs of V_m versus Ca^{2+} from **Table 1**. **(B)** Mean of means in **Table 1** versus mean of the SDs in **Table 1**. **(C)** Means and SDs of V_m parameters versus means and SDs of corresponding Ca^{2+} parameters for all 230 cells. **(D)** Means and SDs of ignition and recovery versus means and SDs of cycle length for all 230 cells (In panel **(A)**, M.M = mean of means; M.SD = mean of SDs; CL = cycle length; Ign = Ignition; Rec = recovery).

the relationship of experimentally measured means for AP parameters versus their SDs (**Figure 10**).

Finally, in PC analyses of the simulated parameters in **Figure 15B**, the first two PCs accounted for 94% of the variation in the eight variables (**Supplementary Figure 4**).

DISCUSSION

We measured membrane potential and Ca^{2+} times to onsets of AP ignition during diastole and times to 90% recovery during APs and APFIs in three populations of single, isolated rabbit SAN cells that differed with respect to autonomic input: those in which CRs were stimulated by CCh, those in which βARs were stimulated with ISO, and in untreated (control) cells. Absolute values of times to AP ignition onsets and to 90% recovery intervals in Ca^{2+} and V_m domains during APs and APFIs differed within and among individual cells in cell populations and different autonomic states and differed markedly among cells of the three populations of cells with differential autonomic receptor stimulation. Our novel finding is that although differing markedly in absolute values, Ca^{2+} and V_m parameters were self-similar to each other during APs and self-similar to APFIs, not only within and among different cells within each of the three populations of cells studied, but remarkably, among all cells, regardless of the autonomic receptor stimulation profile. Thus, Ca^{2+} and V_m domain kinetic transitions (intervals) during APs, individual APFI, and mean APFIs within AP time series manifest long-range correlations (self-similar scale-free correlations, i.e., obey power law) across the entire broad range of APFIs, regardless of whether autonomic receptors of these cells are stimulated and regardless of the type of autonomic receptor stimulation.

The degree to which molecular activation states within each clock and between clocks are synchronized during APs determines when the next AP will occur, i.e., the APFIV and mean APFIs within a cell and across the entire population of single SAN cells studied: the higher the degree of order (self-organized activation of clock molecules), the more ordered and less variable the aggregate of kinetic functions, the least variability of APFIs, and the shorter the mean APFI; *vice versa*, the lower the degree of order among clock molecular activation states,

TABLE 2 | Correlation matrices of V_m or Ca^{2+} parameters measured in different cells within three different autonomic states (summary data listed in **Table 1**).

			Action potential (V_m) (n = 115)						**Ca^{2+} (n = 115)**					
			Means			**SDs**			**Means**			**SDs**		
			APFI	**TTIO**	**APD90**	**APFI**	**TTIO**	**APD90**	**CaTFI**	**CaT90**	**LCR period**	**CaTFI**	**CaT90**	**LCR period**
Action potential (V_m)	Means	APFI: r	1											
		APFI: p												
		TTIO: r	0.9817	1										
		TTIO: p	2.7E-83											
		APD90: r	0.8550	0.7879	1									
		APD90: p	5.3E-34	1.5E-25										
	SDs	APFI: r	0.8947	0.8954	0.6540	1								
		APFI: p	2.3E-41	1.6E-41	2.2E-15									
		TTIO: r	0.9139	0.8777	0.7132	0.9284	1							
		TTIO: p	4.7E-46	6.8E-38	3.8E-19	2.2E-50								
		APD90: r	0.8164	0.7868	0.6705	0.7742	0.8414	1						
		APD90: p	1.8E-28	3.2E-25	4.4E-16	5.5E-24	1.0E-31							
Ca^{2+}	Means	CaTFI: r	0.9573	0.9373	0.8307	0.8408	0.8702	0.8375	1					
		CaTFI: p	9.9E-63	1.4E-53	1.6E-30	6.8E-32	1.6E-36	3.6E-31						
		CaT90: r	0.6574	0.6797	0.5982	0.5532	0.4897	0.5245	0.7017	1				
		CaT90: p	1.3E-15	6.7E-17	1.7E-12	1.4E-10	2.8E-08	2.1E-09	2.4E-18					
		LCR period: r	0.9380	0.9162	0.8342	0.8257	0.8442	0.8137	0.9792	0.6962	1			
		LCR period: p	7.7E-54	1.1E-46	5.5E-31	7.2E-30	2.2E-32	3.7E-28	3.7E-80	5.8E-18				
	SDs	CaTFI: r	0.6349	0.6170	0.5236	0.7077	0.6678	0.6416	0.7064	0.4362	0.7200	1		
		CaTFI: p	4.3E-14	3.4E-13	2.7E-09	1.9E-18	6.5E-16	2.5E-14	2.3E-18	1.4E-06	2.6E-19			
		CaT90: r	0.3194	0.3367	0.2951	0.3146	0.2598	0.3078	0.4448	0.5409	0.4531	0.6040	1	
		CaT90: p	0.0006	0.0003	0.0015	0.0007	0.0055	0.0010	8.0E-07	6.2E-10	4.7E-07	2.3E-12		
		LCR period: r	0.7174	0.7321	0.6283	0.6234	0.5874	0.6696	0.7665	0.6262	0.7282	0.6704	0.4619	1
		LCR period: p	1.9E-19	1.5E-20	5.6E-14	1.0E-13	5.2E-12	4.4E-16	1.8E-23	7.2E-14	2.9E-20	4.6E-16	2.6E-07	

the lower the aggregate synchronization among clock molecular functions, the greater the variability of APFIs, and the longer the mean AP cycle interval.

Self-similar or fractal-like beating rate variability among cardiac cells in culture has been previously identified in a number of studies but only when cells were confluent or electrically connected to each other. This behavior has been attributed to influences of tonic or phasic resetting of membrane potential or to mechanical factors via cell-to-cell connections (Clay and DeHaan, 1979; Jongsma et al., 1983; Kucera et al., 2000). Our novel observation is self-similarity of V_m and Ca^{2+} domain intervals during APs and APFIs across diverse populations of single SAN cells that were not physically connected to each other.

Thus, self-similar distributions of order that have been demonstrated to occur in other instances throughout nature (Bak, 1999) also exist within SAN cell coupled-clock system functions. We interpret this power law behavior of SAN cell functions to result from concordant gradations of self-organized order (synchronization) of clock molecular activation across the entire physiologic range of APFIs.

Clock Molecular Activation Cues

Voltage, time, Ca^{2+}, cAMP signaling, and PKA and CaMKII-dependent clock protein phosphorylation are the cues that regulate the activation kinetics of molecules that control pacemaker functions in single SAN cells (**Supplementary Figure 2**; Lakatta et al., 2003, 2006, 2008, 2010; Maltsev and Lakatta, 2008; Yaniv et al., 2015). Some coupled-clock system proteins are activated by Ca^{2+}, e.g., SERCA2; others by V_m and cAMP binding, e.g., HCN channels (DiFrancesco and Tortora, 1991) and other cyclic nucleotide-regulated channels; or by Ca^{2+} and V_m, e.g., NCX, or by phosphorylation and Ca^{2+}, e.g., phospholamban and ryanodine receptors and AC type 8, whereas the activation states of still other coupled-clock system proteins are modulated by V_m, Ca^{2+}, and phosphorylation, e.g., L-type and some K^+ channels.

Both voltage and Ca^{2+} activation cues oscillate in amplitude throughout each AP cycle and command rapid responses from clock molecules. The degree to which activation status of molecules of a given species is synchronized at any given time following the prior AP determines the ensemble response of that molecular species to its activation cues. It is well documented that following a synchronizing event, e.g., the occurrence of an AP, activation states of molecules underlie AP cycle transition through variably inactivated states, altering the availability to respond to a subsequent activation cue. Our new concept of synchronization of functional cues is based on the idea that the coupled-clock system inheres (inevitably) some degree of disorder that stems from its key constituent proteins operating (stochastically switching) intrinsically within

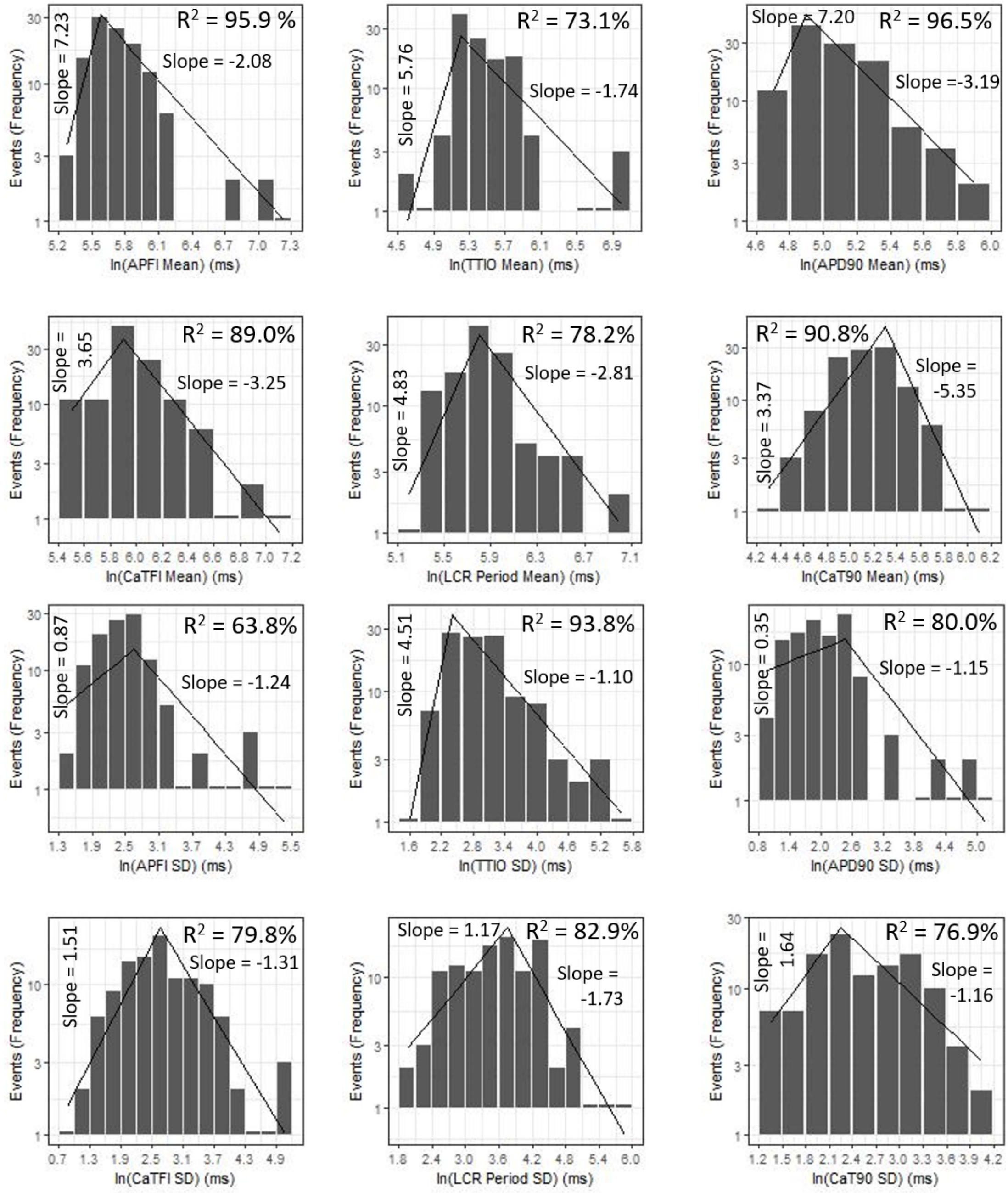

FIGURE 9 | Distributions of SDs and means over all groups illustrating self-similarity (fractal-like behavior). The regression lines are fit as a single piecewise linear model with a join point at the center of the interval with the highest frequency.

their conformational flexibilities and heterogeneity. The balance of order/disorder is linked to molecule interactions (i.e., effectiveness of their respective cues) that allow them to operate cooperatively as an ensemble or system with various degrees of synchronization (i.e., order) that is reflected in respective variability of the output function of the system, i.e., APFIV in our case.

Thus, we interpret the experimentally measured concordant behavior of surface membrane and Ca^{2+} regulatory functions during AP cycles across the entire physiologic range of AP cycles to reflect a concordance in the degrees of activation of molecules that drive these regulatory functions. Importantly, Ca^{2+} and V_m cues not only regulate the synchronization clock of molecular activation states but are also regulated by the degree of synchronized activation of molecules determined by these cues (recursion). Because membrane and Ca^{2+} clocks become coupled in the context of the electrochemical signal that waxes and wanes to cause the AP cycle, the extent of self-organized

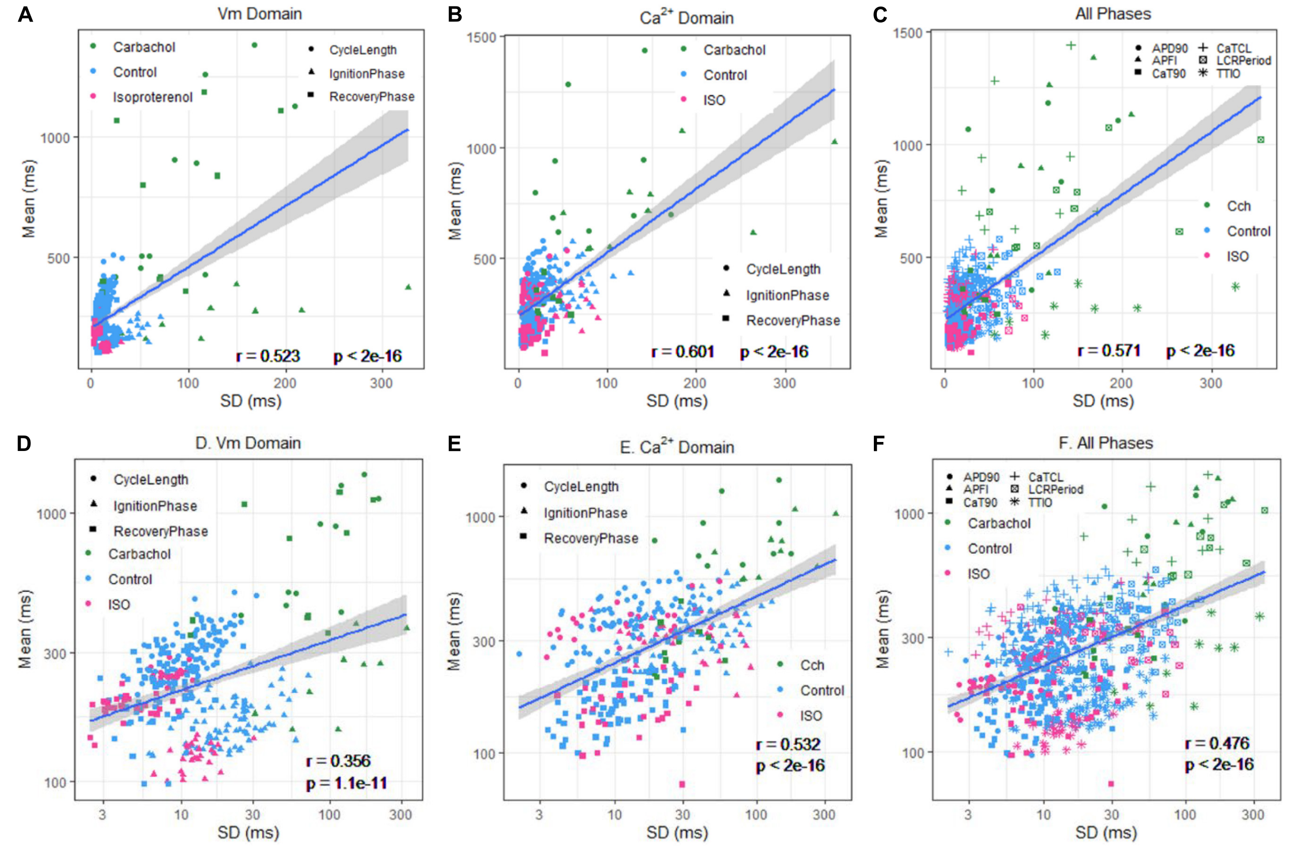

FIGURE 10 | Means versus SDs for all cells on a linear scale for **(A)** V_m, **(B)** Ca^{2+}, and **(C)** V_m and Ca^{2+}, and using a logarithmic scale for **(D)** V_m, **(E)** Ca, and **(F)** V_m and Ca^{2+}.

molecular activation within each clock indirectly affects self-organization of molecular activation of the other clock operating within the coupled-clock system. And because scaling of mean APFIs among all cells is self-similar to APFIV among cells, AP firing variability and mean APFI are determinants of the Ca^{2+} and V_m cues that determine kinetic intervals during an AP: a recursive, feed-forward process.

Mean APFI and APFIV Are Not Only Regulated by but Also Regulate the Degree to Which Clock Molecular Functions Are Synchronized

Changes in Ca^{2+} and V_m cues during an AP determine not only the characteristics of that AP but also when the next AP will occur and the mean APFI within an AP time series.

A prolongation of the mean APFIs, itself, contributes to the concurrent increase in the APFIV at a long mean APFI: because an increase in mean APFI reduces net Ca^{2+} influx and indirectly reduces Ca^{2+}/CaMKII-AC–dependent phosphorylation of Ca^{2+} cycling proteins, reducing the SR Ca^{2+} cycling kinetics and increasing the variability of LCR periods.

Characteristics of the AP that are determined by availability of M clock molecules to respond to a change in membrane potential both directly and indirectly entrain the Ca^{2+} and M clock activation: as the mean AP interval shortens, less time elapses between APs, and therefore at shorter intervals, less time is required than at longer intervals for molecules to retain (remember) the synchronizing influences imparted by the preceding AP. This causes the relationship of mean APFI to APFIV of isolated SAN cells to be non-linear (**Figure 5** and **Supplementary Figure 2**), as originally demonstrated by Zaza and Lombardi (2001) and later by Monfredi et al. (2014). Conversely, as time following a prior AP increases, the effectiveness of the Ca^{2+} activation cue, itself, wanes because the cell Ca^{2+} level and SR Ca^{2+} load become reduced because of time-dependent Ca^{2+} efflux from the cell. We may speculate therefore that during long AP cycles, fewer molecules of some molecular species are available to respond to Ca^{2+} activation cues.

Gradations of self-organized molecular activation within and between clocks regulate the APFI rhythm, i.e., the APFIV. In other terms, the average APFI, kinetics of the AP, AP-triggered Ca^{2+}-transient, LCR periods and DD kinetics, and beat-to-beat variability of these parameters measured in the present study are readouts of the relative extents to which of clock molecules become activated and the degree to which the clocks are coupled. When the degree to which Ca^{2+} and M clocks kinetics are

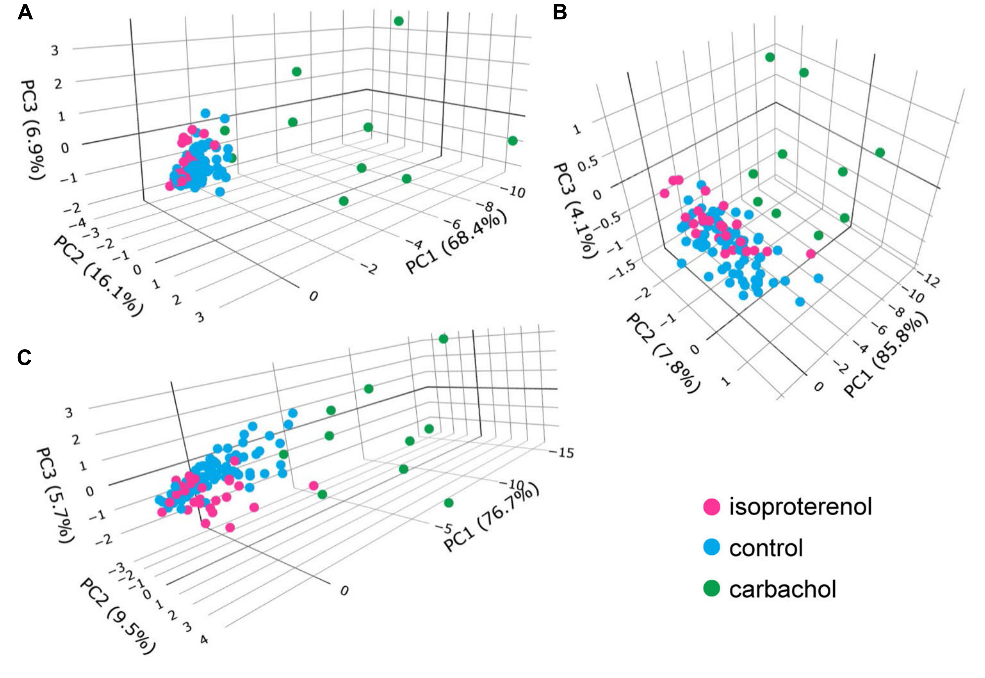

FIGURE 11 | Plots of principal components: **(A)** SDs only, **(B)** means only, **(C)** means and SDs.

coupled or synchronized is low, the AP firing rate is slow, and APFIV is high, e.g., during CRs. Conversely, when the degree of coupling or synchronization of the Ca^{2+} and V_m kinetics of the two clocks is high, e.g., during βAR stimulation, AP firing is rapid, and APFIV is low.

So, What Factors Affect the Degree of Synchronization of Clock Molecules?

Concordant degrees of self-similar synchronization of M and Ca^{2+} clock kinetic functions reflect concordant gradations of activation states of specific molecules that govern these functions and how these cues change throughout an AP cycle.

AP Firing Rate and Rhythm Synchronization of Clock Molecules

The AP that emerges from the diastolic ignition events is, itself, the most potent integrator or synchronizer, not only of surface membrane electrogenic molecules, but also of Ca^{2+} clock functions: a synchronized global cytosolic CaT that ensues following synchronous activation of voltage-dependent L-type Ca^{2+} channels is created by synchronized Ca^{2+}-induced, Ca^{2+} release from SR via ryanodine receptor activation (Song et al., 1998; Wang et al., 2001; Lakatta, 2004; Zhou et al., 2009).

The efficacy of V_m and Ca^{2+} activation cues that oscillate as electrochemical signal that underlies the V_m change during AP cycle varies with the AP cycle interval or period: shorter periods (i.e., faster AP firing rates or shorter APFIs) are more effective than longer periods (i.e., slower AP firing rates or longer APFIs), because during very long AP cycles, Ca^{2+} activation states of some molecules become more unsynchronized. At very short times following a large voltage oscillation (i.e., an AP), many molecules of a given molecular species in relatively inactivated state may not optimally respond to activation cues (e.g., impaired excitability/non-excitability). As the time following a prior activation increases, although a subpopulation of molecules of given species may regain full ability to respond to activation cues, substantial variability in the activation status of other molecules of that species still may exist, limiting the number of molecules that can respond to (be recruited by) an activation cue. Our results provide novel clues to the cellular basis for the observation that an AP occurrence, itself, influences the range of APFIs that immediately follow it (Nolasco and Dahlen, 1968). The AP, itself, indirectly affects all Ca^{2+} clock functions because it regulates net cell Ca^{2+} balance. Functions of M clock molecules that underlie the generation of an AP indirectly regulate the availability for SR Ca^{2+} cycling by modulation of the level of cell Ca^{2+}, the SR "oscillatory substrate." Thus, M clock functions also indirectly regulate LCR periods and sizes via their impact on the "steady state" intracellular Ca^{2+} level. When the average interval between APs becomes prolonged, a reduction net Ca^{2+} influx into efflux from the cell (Lakatta, 2004) reduces the cytosolic $[Ca^{2+}]$, the rate of Ca^{2+} pumping into SR, and the SR Ca^{2+} load. These reductions, in turn, prolong the average time from the prior AP occurrence for spontaneous local diastolic ryanodine receptor activation to occur within SAN cell local microdomains; the randomness of spontaneous local diastolic ryanodine receptor activation occurring within these microdomains also increases, broadening the distribution of LCR periods and shifting these to longer times at a long AP cycle (**Figure 4**).

Thus, the degree of variability in activation states of M and Ca^{2+} clock molecules that emerges over time following their

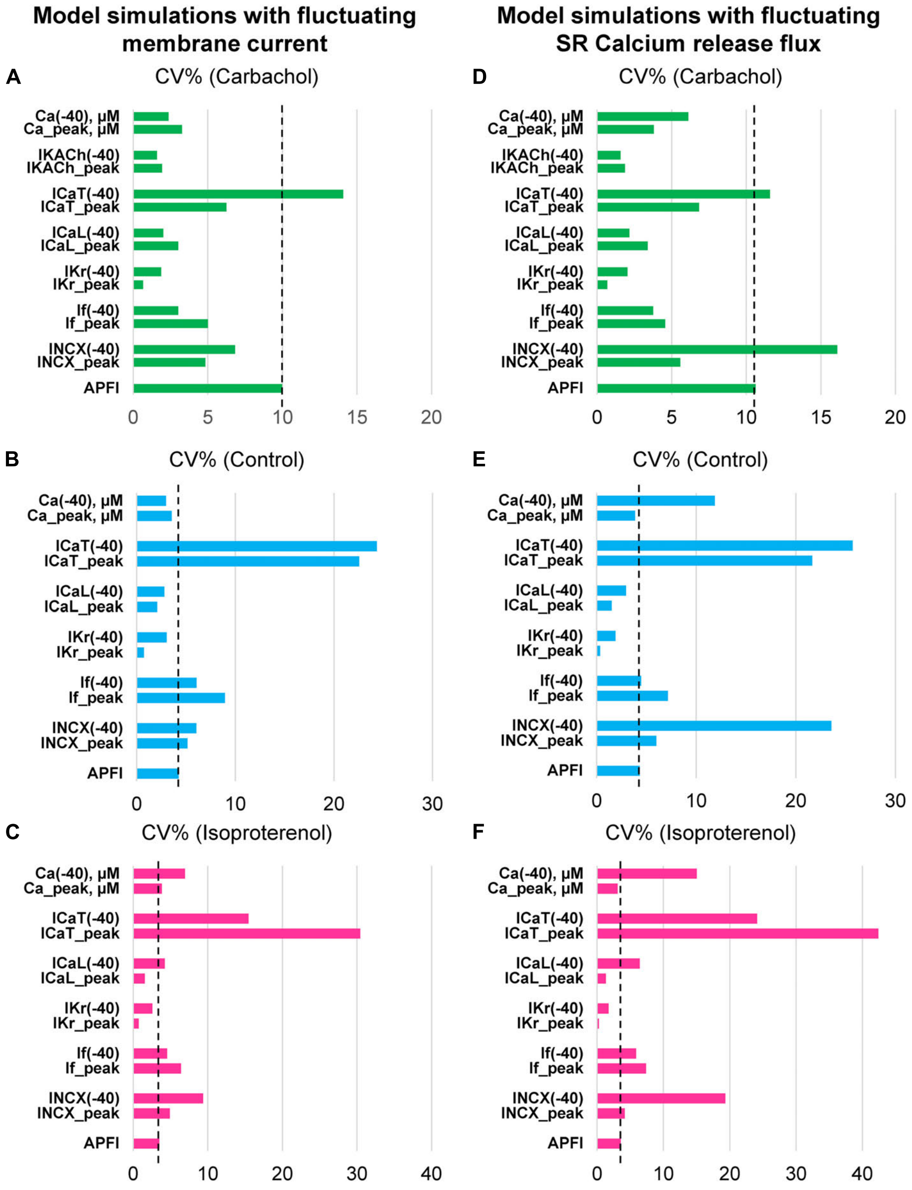

FIGURE 12 | Results of analysis of coefficient of variation (CV) of major ion currents I_f, I_{Kr}, I_{CaL}, I_{CaT}, I_{KACh}, and Ca^{2+} simulated by Maltsev–Lakatta coupled-clock model with noise current (I_{per}) added to either total current I_{tot} **(A–C)** or Ca release flux **(D–F)**.

synchronization by the prior AP is implicated in the cycle length dependence of variability of Ca^{2+} and M clock functions measured here (**Table 1** and **Figures 3–5**). Heartbeat variability *in vivo* and APFIV of isolated SAN cells *in vitro* indicate that neither autonomic input to SAN cells, nor functions intrinsic to the SAN cell coupled-clock system, respectively, achieve a steady state from one beat to the next.

Ca^{2+}-Dependent Synchronization of Clock Molecules

The local $[Ca^{2+}]$, itself, also serves as a powerful synchronizer of clock molecular function: ordered/disordered Ca^{2+} regulation has been recently reported for ryanodine receptor–mediated Ca^{2+} releases (Maltsev et al., 2019).

Studies in permeabilized SAN cells, in which Ca^{2+} clock function is preserved, but M clock function is abolished, and therefore APs cannot occur and do not influence LCR periodicity, clearly demonstrate that in a fixed, physiologic, free $[Ca^{2+}]$, LCR occurrences are random when the free $[Ca^{2+}]$ is low and that LCR periodicity emerges as the free $[Ca^{2+}]$ in the system is increased due in part to an increase in the Ca^{2+} charge of the SR capacitor (Sirenko et al., 2013). The intracellular concentration of the oscillatory substrate, Ca^{2+}, itself is regulated, in part, by the SAN cell transmembrane Na^+ gradient and membrane potential (Sirenko et al., 2013, 2016).

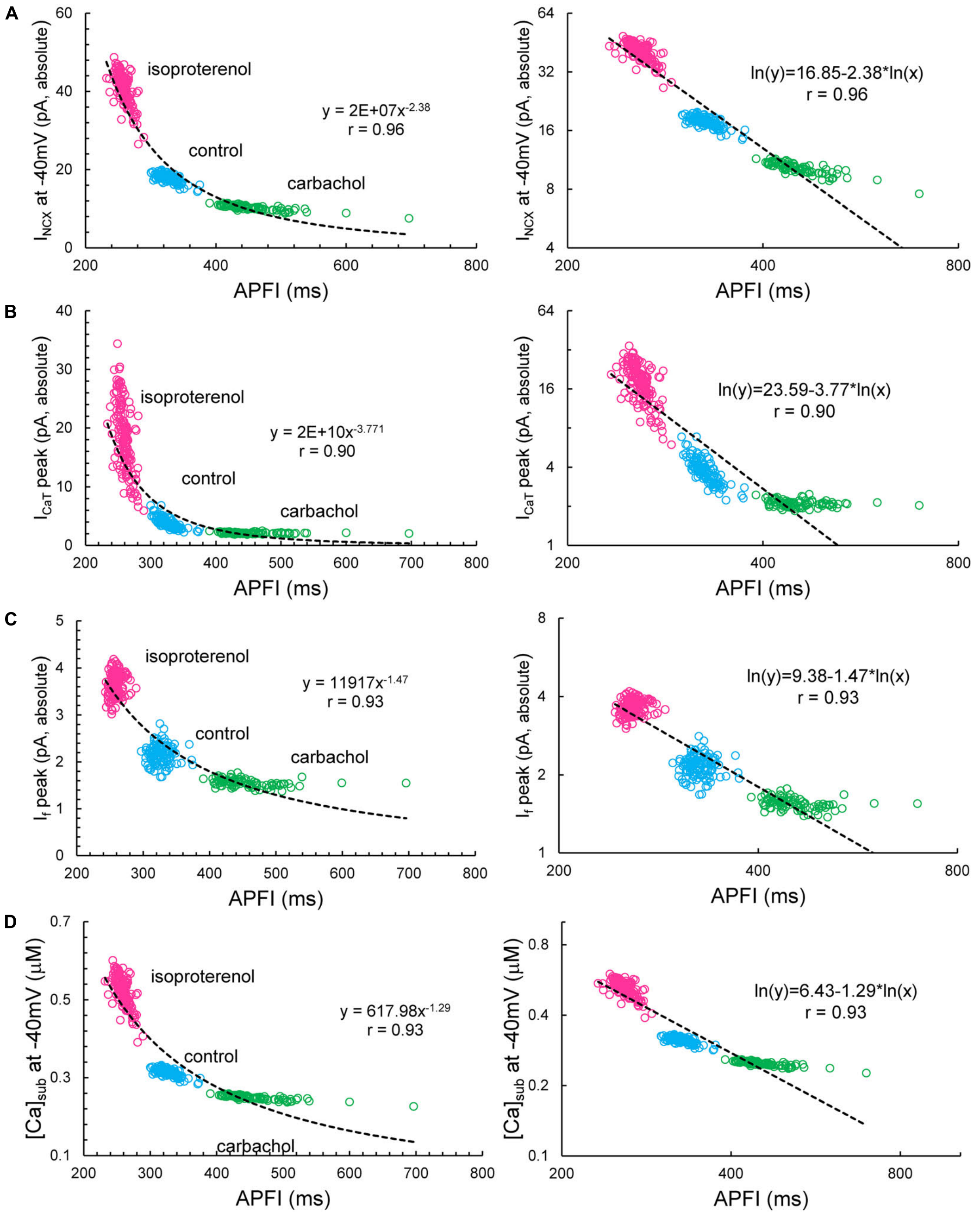

FIGURE 13 | I_{NCX} **(A)**, I_{CaT} **(B)**, I_f **(C)**, and $[Ca]_{sub}$ **(D)** exhibited power law behavior (a linear dependence in the ln–ln plot here) over a wide range of APFI over all conditions tested. Noise (I_{per}) was added to I_{tot} in Maltsev–Lakatta coupled-clock model. Similar dependencies were found when I_{per} was added to Ca release flux (not shown).

cAMP Activation or Phosphorylation of Clock Proteins Modulates the Synchronization of and Response to Activation Cues

Autonomic receptor stimulation modulates both the activation cues and responses of clock molecules to these cues. The impact of autonomic receptor signaling on the effectiveness of clock coupling occurs over several AP cycles and is reflected in time-dependent transitions in the AP firing rate and rhythm. The kinetics and stoichiometry of increases in PKA activity in response to gradations in βAR stimulation predict the kinetics and stoichiometry of concurrent time-dependent increases in AP firing rate (Yaniv et al., 2014b). Prior studies (Lyashkov et al., 2009; Yang et al., 2012) have demonstrated that gradations in the

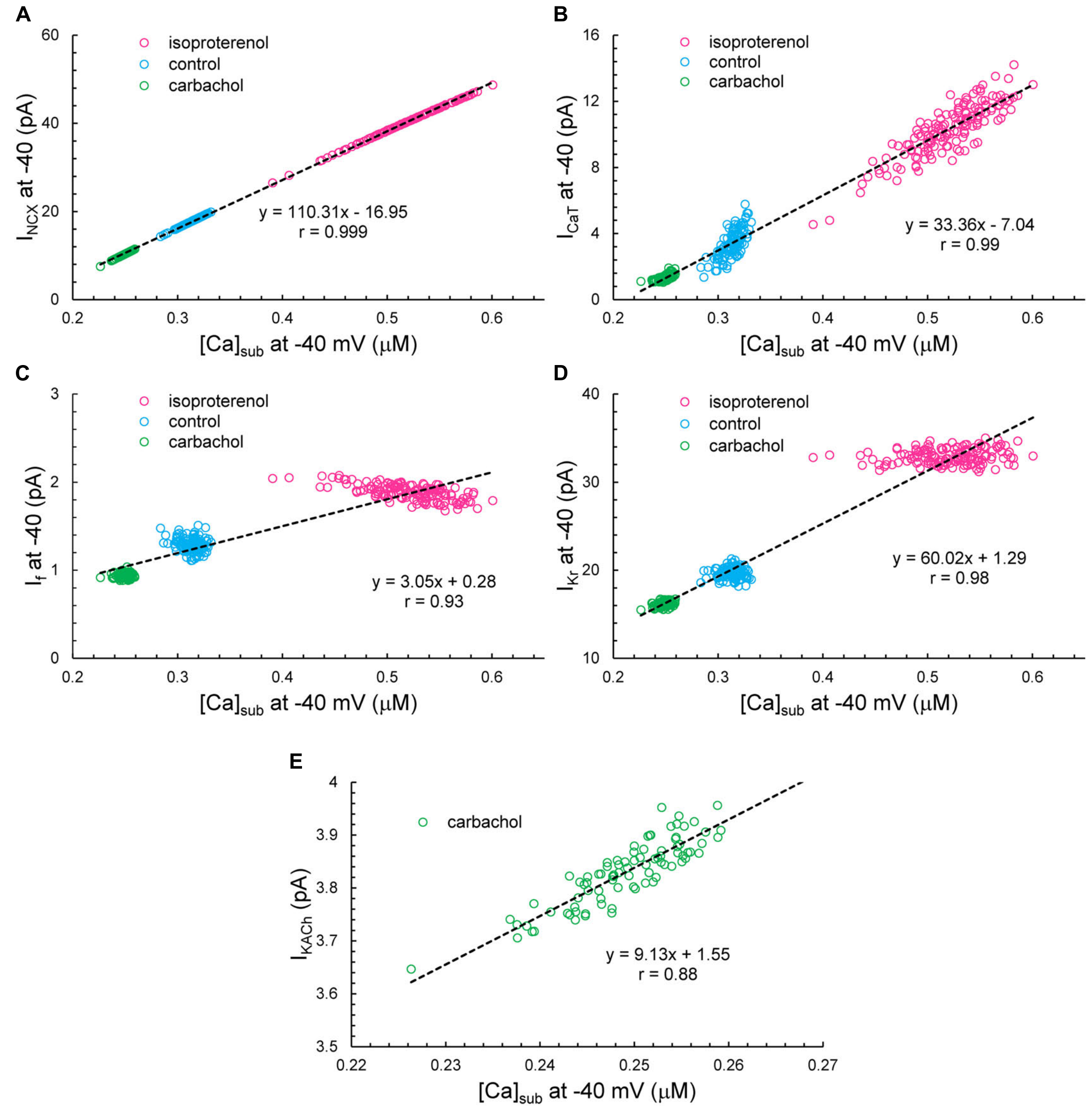

FIGURE 14 | The correlation between I_{NCX} **(A)**, I_{CaT} **(B)**, I_f **(C)**, I_{Kr} **(D)**, or I_{KACh} **(E)** versus $[Ca]_{Sub}$ at –40 mV. Note that I_{KACh} presents only during CCh.

phosphorylation status of phospholamban at Ser^{16} across the three autonomic state mean APFIs of cell populations in the present study (**Supplementary Figure 3**) strikingly resemble gradations of the means of APFIs and APFIVs observed across these autonomic states measured in the present study (**Table 1**).

The extent to which clock molecules respond to Ca^{2+} or V_m activation cues during an AP is modulated by βAR- or CR-dependent phosphorylation of many of the same proteins that drive SAN cell automaticity in the absence of autonomic receptor activation. These βARs or CRs impact on the memory of the extent to which clock molecule activation had been synchronized during the prior AP. βAR or CR modulation has two facets: (1) a direct effect, due to cAMP or phosphorylation-dependent activation of clock proteins and (2) an indirect effect by altering the APFI, which alters the cell Ca^{2+} activation cues that are directly modulated by autonomic receptor stimulation. Specifically, βARs and CRs, respectively, not only reduce or increase mean APFI, but also, respectively, shift variability within distributions of Ca^{2+} and V_m functions in the same direction (Sirenko et al., 2016) as the shift in mean APFI.

Numerical Modeling

Because we experimentally measured characteristics of APs in populations of single cells that differed by autonomic input status, we were able to glean insights not only into APFIV in an "average" cell, but also into populations of cells isolated from SAN tissue. Embracing SAN function at the cell population level resonates with recent studies of SAN function at the tissue level (Bychkov et al., 2020; Fenske et al., 2020) that have revealed a novel understanding of the SAN impulse as an emergent property created by

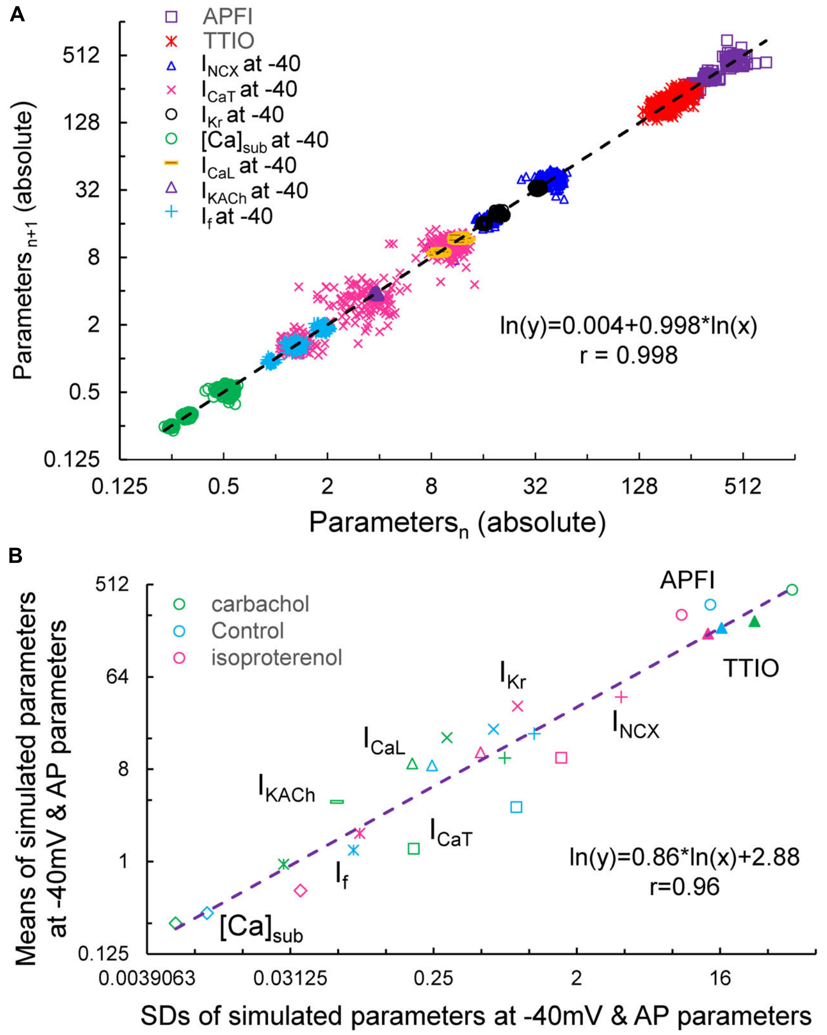

FIGURE 15 | Poincaré plots of the simulated I_{NCX}, I_{CaT}, I_{CaL}, I_{Kr}, I_{KACh}, I_f, and $[Ca]_{Sub}$ at –40 mV, APFI and TTIO from one model cell during ISO, CCh or at basal condition in ln–ln plot **(A)**, and the correlation between the means and SDs of these parameters **(B)**. Note that I_{KACh} only presents during carbachol.

a collective of variable interactions among heterogeneous cell populations within the SAN tissue. On the other end, APFIV *per se* also emerges at smaller, subcellular scales, due to variability in the functions of individual molecules, such as ion channels, transporters, and pumps, individually and in complex cooperation with each other. These molecular functions cannot be measured directly in our single-cell experiments. Thus, we employed numerical modeling to extend our perspectives from cell populations and single-cell levels downward to the molecular scale. Such broader consideration of variability makes sense when we approach pacemaker function as a multiscale phenomenon (Qu et al., 2011) featuring free scale and fractal-like characteristics (Weiss and Qu, 2020). Considering the SAN cell as a stochastic dynamic system, we examined variability of major ion currents and submembrane $[Ca^{2+}]$ during different autonomic states that created a broad range of APFIs, which were measured experimentally.

Our simulations indicate that the APFIV of some ion currents and submembrane Ca^{2+} can be close to that of the APFI itself, but also can be substantially lower or higher than the APFIV, depending on the presence or absence of autonomic receptor stimulation, and the time during the AP cycle (**Figure 12**): components such as I_f, I_{NCX}, I_{CaT}, and Ca^{2+} exhibit substantial cycle to cycle variability, whereas I_{CaL}, I_{KACh}, and I_{Kr} show less or moderate variability. This behavior reflects complex non-linear recursive interactions of V_m and Ca^{2+} that couple the clocks that drive the system (Lyashkov et al., 2018) and as such cannot be directly and definitively interpreted in cause-effect terms. Nevertheless, our simulations confirmed ion channel behavior that could have been envisioned. For example, independent of the nature of the noise added (to I_{tot} or to Ca^{2+} release flux): components contributing to DD (I_f, I_{NCX}, and I_{CaT}) exhibit a larger cycle to cycle variability, whereas components contributing to generation of all-or-none AP characteristics exhibit less variability (peak I_{CaL} and I_{Kr}). This result is in accord with the idea of order/disorder transitions during AP cycle (**Figure 2**, order/disorder dash line), i.e., the DD manifests disorder and transition to order, and hence, a larger variability, and then following the AP upstroke, the AP itself manifests order and hence less variability.

However, our simulations also provided some unexpected, interesting results: I_{NCX} and submembrane Ca^{2+} amplitudes during DD followed a power law relationship over a wide range of APFI under all conditions tested, indicating that self-similar scale-free or fractal-like behavior is operative within the coupled-clock mechanism via I_{NCX} (**Figure 13**). There is also likely to be a secondary effect of I_{NCX} amplitude itself on DD acceleration in a recursive fashion. Indeed, an increase in I_{NCX} is expected to accelerate DD but, at the same time, is further accelerated by the very same acceleration it imparts to the ignition mechanism (i.e., diastolic I_{CaL} and Ca^{2+}-induced Ca^{2+} release). This self-acceleration ignition mechanism results in the power law behavior predicted by the model.

Peak I_f also followed a power function over a broad range of APFIs, albeit in a noisy manner manifesting some extremely long APFIs in CCh. The current that fluctuated most with respect to variabilities in APFI turned out to be I_{CaT}, the peak amplitude of which also reflects DD dynamics. When DD is rapidly accelerating (as it does at shorter cycles), I_{CaT} peak quickly activates and achieves a higher peak amplitude, and *vice versa*, when DD is slower at longer APFIs, I_{CaT} becomes inactivated over time without achieving a peak. In log–log plots, this forms a straight line for almost the entire range of APFIs (power law behavior), except extremely long APFIs when variations in (already) slow DD dynamics have almost no effect on I_{CaT} peak. Thus, simulations of biophysical components within the pacemaker cell system exhibited a power law behavior over a wide range of APFIs that encompasses the broad range of APFIs measured experimentally.

Observation of model simulations through analytic lenses applied to experimental data indicated that (as was the case for the experiment data) the simulated variables are self-similar to each other across a broad range of APFIs within the three autonomic states (**Figure 15**, **Supplementary Figure 4**, and **Supplementary Table 3**).

Model Limitation

Our I_{CaL} model was adopted from the Kurata model (Kurata et al., 2002), and although it does include Ca^{2+}-dependent inactivation mechanism, it lacks I_{CaL} facilitation described in 2000 by Mangoni et al. (2000). Also, our numerical model of I_f lacks dynamic regulation by cAMP (DiFrancesco, 1999), Ca^{2+} activated K^+ channels and store-operated channels that may potentially contribute to APFIV.

DATA AVAILABILITY STATEMENT

The original contributions presented in the study are included in the article/**Supplementary Material**, further inquiries can be directed to the corresponding author/s.

ETHICS STATEMENT

The animal study was reviewed and approved by the Animal Care and Use Committee of the National Institutes of Health (protocol #457-LCS-2024).

AUTHOR CONTRIBUTIONS

EL and VM designed the project. DY, AL, IZ, YY, TV, and BZ performed the experiments and analyzed the results. DY, CM, and ST did the statistical analyses. DY and VM performed the numerical simulation. DY and EL wrote the manuscript with the support from YY and VM. All authors contributed to the article and approved the submitted version.

FUNDING

This work was supported partially by the Intramural Research Program of the NIH, National Institute on Aging, and by the ISF [No. 330/19].

ACKNOWLEDGMENTS

The authors wish to acknowledge the assistance of Dr. Jia-Hua Qu for assistance with the PC analysis illustrations, and sincerely appreciate Loretta Lakatta, Robert Monticone, Tracy Oppel, and Ruth Sadler for their editorial assistance. This manuscript has been released as a pre-print at bioRxiv (https://www.biorxiv.org/content/10.1101/2020.09.01.277756v2) (Yang et al., 2020).

SUPPLEMENTARY MATERIAL

The Supplementary Material for this article can be found online at: https://www.frontiersin.org/articles/10.3389/fphys.2021.612770/full#supplementary-material

REFERENCES

Bak, P. (1999). *How Nature Works: The Science of Self-Organized Criticality*. New York, NY: Springer-Verlag.

Bogdanov, K. Y., Maltsev, V. A., Vinogradova, T. M., Lyashkov, A. E., Spurgeon, H. A., Stern, M. D., et al. (2006). Membrane potential fluctuations resulting from submembrane Ca2+ releases in rabbit sinoatrial nodal cells impart an exponential phase to the late diastolic depolarization that controls their chronotropic state. *Circ. Res.* 99, 979–987. doi: 10.1161/01.RES.0000247933.66532.0b

Bogdanov, K. Y., Vinogradova, T. M., and Lakatta, E. G. (2001). Sinoatrial nodal cell ryanodine receptor and Na+-Ca2+ exchanger: molecular partners in pacemaker regulation. *Circ. Res.* 88, 1254–1258. doi: 10.1161/hh1201.092095

Bychkov, R., Juhaszova, M., Tsutsui, K., Coletta, C., Stern, M. D., Maltsev, V. A., et al. (2020). Synchronized cardiac impulses emerge from multi-scale, heterogeneous local calcium signals within and among cells of heart pacemaker tissue. *JACC Clin. Electrophysiol.* 6, 907–931. doi: 10.1016/j.jacep.2020.06.022

Clay, J. R., and DeHaan, R. L. (1979). Fluctuations in interbeat interval in rhythmic heart-cell clusters. Role of membrane voltage noise. *Biophys. J.* 28, 377–389. doi: 10.1016/S0006-3495(79)85187-5

DiFrancesco, D. (1999). Dual allosteric modulation of pacemaker (f) channels by cAMP and voltage in rabbit SA node. *J. Physiol. Pharmacol.* 515, 367–376. doi: 10.1111/j.1469-7793.1999.367ac.x

DiFrancesco, D., and Tortora, P. (1991). Direct activation of cardiac pacemaker channels by intracellular cyclic AMP. *Nature* 351, 145–147. doi: 10.1038/351145a0

Fenske, S., Hennis, K., Rotzer, R., Brox, V. F., Becirovic, E., Scharr, A., et al. (2020). cAMP-dependent regulation of HCN4 controls the tonic entrainment process in sinoatrial node pacemaker cells. *Nat. Commun.* 11:5555. doi: 10.1038/s41467-020-19304-9

Garny, A., Noble, D., Hunter, P. J., and Kohl, P. (2009). CELLULAR OPEN RESOURCE (COR): current status and future directions. *Philos. Trans. A Math. Phys. Eng. Sci.* 367, 1885–1905. doi: 10.1098/rsta.2008.0289

Ho, D., Imai, K., King, G., and Stuart, E. (2011). MatchIt: nonparametric preprocessing for parametric causal inference. *J. Stat. Softw.* 42, 1–28.

Howell, D. C. (2002). *Statistical Methods for Psychology*, 5th Edn. Duxbury, MA: Thomson Learning.

Huikuri, H. V., Makikallio, T. H., Peng, C. K., Goldberger, A. L., Hintze, U., and Moller, M. (2000). Fractal correlation properties of R-R interval dynamics and mortality in patients with depressed left ventricular function after an acute myocardial infarction. *Circulation* 101, 47–53. doi: 10.1161/01.cir.101.1.47

Johnson, R. A., and Wichern, D. W. (2008). *Applied Multivariate Statistical Analysis*, 6th Edn. Upper Saddle River, NJ: Pearson.

Jongsma, H. J., Tsjernina, L., and de Bruijne, J. (1983). The establishment of regular beating in populations of pacemaker heart cells. A study with tissue-cultured rat heart cells. *J. Mol. Cell. Cardiol.* 15, 123–133. doi: 10.1016/0022-2828(83)90288-2

Jung, P., Cornell-Bell, A., Madden, K. S., and Moss, F. (1998). Noise-induced spiral waves in astrocyte syncytia show evidence of self-organized criticality. *J. Neurophysiol.* 79, 1098–1102. doi: 10.1152/jn.1998.79.2.1098

Kucera, J. P., Heuschkel, M. O., Renaud, P., and Rohr, S. (2000). Power-law behavior of beat-rate variability in monolayer cultures of neonatal rat ventricular myocytes. *Circ. Res.* 86, 1140–1145. doi: 10.1161/01.res.86.11.1140

Kurata, Y., Hisatome, I., Imanishi, S., and Shibamoto, T. (2002). Dynamical description of sinoatrial node pacemaking: improved mathematical model for primary pacemaker cell. *Am. J. Physiol.* 283, H2074–H2101.

Lakatta, E. G. (2004). Beyond Bowditch: the convergence of cardiac chronotropy and inotropy. *Cell Calcium* 35, 629–642. doi: 10.1016/j.ceca.2004.01.017

Lakatta, E. G. (2021). Heartbeat music. *Heart Rhythm* 18, 811–812. doi: 10.1016/j.hrthm.2021.01.011

Lakatta, E. G., Maltsev, V. A., Bogdanov, K. Y., Stern, M. D., and Vinogradova, T. M. (2003). Cyclic variation of intracellular calcium: a critical factor for cardiac pacemaker cell dominance. *Circ. Res.* 92, e45–e50.

Lakatta, E. G., Maltsev, V. A., and Vinogradova, T. M. (2010). A coupled SYSTEM of intracellular Ca2+ clocks and surface membrane voltage clocks controls the timekeeping mechanism of the heart's pacemaker. *Circ. Res.* 106, 659–673. doi: 10.1161/CIRCRESAHA.109.206078

Lakatta, E. G., Vinogradova, T., Lyashkov, A., Sirenko, S., Zhu, W., Ruknudin, A., et al. (2006). The integration of spontaneous intracellular Ca2+ cycling and surface membrane ion channel activation entrains normal automaticity in cells of the heart's pacemaker. *Ann. N. Y. Acad. Sci.* 1080, 178–206. doi: 10.1196/annals.1380.016

Lakatta, E. G., Vinogradova, T. M., and Maltsev, V. A. (2008). The missing link in the mystery of normal automaticity of cardiac pacemaker cells. *Ann. N. Y. Acad. Sci.* 1123, 41–57. doi: 10.1196/annals.1420.006

Lopez, L., Piegari, E., Sigaut, L., and Dawson, S. P. (2012). Intracellular calcium signals display an avalanche-like behavior over multiple lengthscales. *Front. Physiol.* 3:350. doi: 10.3389/fphys.2012.00350

Lyashkov, A. E., Behar, J., Lakatta, E. G., Yaniv, Y., and Maltsev, V. A. (2018). Positive feedback mechanisms among local Ca Releases, NCX, and ICaL ignite pacemaker action potentials. *Biophys. J.* 114, 1176–1189. doi: 10.1016/j.bpj.2017.12.043

Lyashkov, A. E., Vinogradova, T. M., Zahanich, I., Li, Y., Younes, A., Nuss, H. B., et al. (2009). Cholinergic receptor signaling modulates spontaneous firing of sinoatrial nodal cells via integrated effects on PKA-dependent Ca2+ cycling and IKACh. *Am. J. Physiol. Heart Circ. Physiol.* 297, H949–H959. doi: 10.1152/ajpheart.01340.2008

Maltsev, A. V., Maltsev, V. A., Mikheev, M., Maltseva, L. A., Sirenko, S. G., Lakatta, E. G., et al. (2011). Synchronization of stochastic Ca2+ release units creates a rhythmic Ca2+ clock in cardiac pacemaker cells. *Biophys. J.* 100, 271–283. doi: 10.1016/j.bpj.2010.11.081

Maltsev, A. V., Stern, M. D., and Maltsev, V. A. (2019). Mechanisms of calcium leak from cardiac sarcoplasmic reticulum revealed by statistical mechanics. *Biophys. J.* 116, 2212–2223. doi: 10.1016/j.bpj.2019.04.031

Maltsev, V. A., and Lakatta, E. G. (2008). Dynamic interactions of an intracellular Ca2+ clock and membrane ion channel clock underlie robust initiation and regulation of cardiac pacemaker function. *Cardiovasc. Res.* 77, 274–284. doi: 10.1093/cvr/cvm058

Maltsev, V. A., and Lakatta, E. G. (2009). Synergism of coupled subsarcolemmal Ca2+ clocks and sarcolemmal voltage clocks confers robust and flexible pacemaker function in a novel pacemaker cell model. *Am. J. Physiol. Heart Circ. Physiol.* 296, H594–H615. doi: 10.1152/ajpheart.01118.2008

Maltsev, V. A., and Lakatta, E. G. (2010). A novel quantitative explanation for the autonomic modulation of cardiac pacemaker cell automaticity via a dynamic system of sarcolemmal and intracellular proteins. *Am. J. Physiol. Heart Circ. Physiol.* 298, H2010–H2023. doi: 10.1152/ajpheart.00783.2009

Mangoni, M. E., Fontanaud, P., Noble, P. J., Noble, D., Benkemoun, H., Nargeot, J., et al. (2000). Facilitation of the L-type calcium current in rabbit sino-atrial cells: effect on cardiac automaticity. *Cardiovasc. Res.* 48, 375–376. doi: 10.1016/s0008-6363(00)00182-6

Monfredi, O., Lyashkov, A. E., Johnsen, A. B., Inada, S., Schneider, H., Wang, R., et al. (2014). Biophysical characterization of the underappreciated and important relationship between heart rate variability and heart rate. *Hypertension* 64, 1334–1343. doi: 10.1161/HYPERTENSIONAHA.114.03782

Monfredi, O., Maltseva, L. A., Spurgeon, H. A., Boyett, M. R., Lakatta, E. G., and Maltsev, V. A. (2013). Beat-to-beat variation in periodicity of local calcium releases contributes to intrinsic variations of spontaneous cycle length in isolated single sinoatrial node cells. *PLoS One* 8:e67247. doi: 10.1371/journal.pone.0067247

Nivala, M., Ko, C. Y., Nivala, M., Weiss, J. N., and Qu, Z. (2012). Criticality in intracellular calcium signaling in cardiac myocytes. *Biophys. J.* 102, 2433–2442. doi: 10.1016/j.bpj.2012.05.001

Nolasco, J. B., and Dahlen, R. W. (1968). A graphic method for the study of alternation in cardiac action potentials. *J. Appl. Physiol.* 25, 191–196. doi: 10.1152/jappl.1968.25.2.191

Qu, Z., Garfinkel, A., Weiss, J. N., and Nivala, M. (2011). Multi-scale modeling in biology: how to bridge the gaps between scales? *Prog. Biophys. Mol. Biol.* 107, 21–31. doi: 10.1016/j.pbiomolbio.2011.06.004

Shivkumar, K., Ajijola, O. A., Anand, I., Armour, J. A., Chen, P. S., Esler, M., et al. (2016). Clinical neurocardiology defining the value of neuroscience-based cardiovascular therapeutics. *J. Physiol.* 594, 3911–3954. doi: 10.1113/JP271870

Silverman, B. W. (1986). *Density Estimation for Statistics and Data Analysis.* London: Chapman & Hall/CRC.

Sirenko, S., Maltsev, V. A., Yaniv, Y., Bychkov, R., Yaeger, D., Vinogradova, T. M., et al. (2016). Electrochemical Na+ and Ca2+ Gradients drive coupled-clock regulation of automaticity of isolated rabbit sinoatrial nodal pacemaker cells. *Am. J. Physiol. Heart Circ. Physiol.* 311, H251–H267. doi: 10.1152/ajpheart.00667.2015

Sirenko, S., Yang, D., Li, Y., Lyashkov, A. E., Lukyanenko, Y. O., Lakatta, E. G., et al. (2013). Ca2+-dependent phosphorylation of Ca2+ cycling proteins generates robust rhythmic local Ca2+ releases in cardiac pacemaker cells. *Sci. Signal.* 6:ra6. doi: 10.1126/scisignal.2003391

Sirenko, S. T., Tsutsui, T., Tarasov, K. V., Yang, D., Wirth, A. N., Maltsev, V. A., et al. (2021). Self-similar synchronization of calcium and membrane potential transitions during action potential cycles predict heart rate across species. *JACC Clin. Electrophysiol.* doi: 10.1016/j.jacep.2021.02.016 [Epub ahead of print].

Song, L. S., Sham, J. S., Stern, M. D., Lakatta, E. G., and Cheng, H. (1998). Direct measurement of SR release flux by tracking 'Ca2+ spikes' in rat cardiac myocytes. *J. Physiol.* 512(Pt 3), 677–691. doi: 10.1111/j.1469-7793.1998.677bd.x

Stožer, A., Markovic, R., Dolensek, J., Perc, M., Marhl, M., Rupnik, M. S., et al. (2019). Heterogeneity and delayed activation as hallmarks of self-organization and criticality in excitable tissue. *Front. Physiol.* 10:869. doi: 10.3389/fphys.2019.00869

Vinogradova, T. M., Bogdanov, K. Y., and Lakatta, E. G. (2002). beta-Adrenergic stimulation modulates ryanodine receptor Ca2+ release during diastolic depolarization to accelerate pacemaker activity in rabbit sinoatrial nodal cells. *Circ. Res.* 90, 73–79. doi: 10.1161/hh0102.102271

Vinogradova, T. M., Bogdanov, K. Y., Yang, D., Kuschel, M., Cheng, H., and Xiao, R. P. (2000). Sinoatrial node pacemaker activity requires Ca2+/calmodulin-dependent protein Kinase II activation. *Circ. Res.* 87, 760–767. doi: 10.1161/01.res.87.9.760

Vinogradova, T. M., Zhou, Y. Y., Maltsev, V., Lyashkov, A., Stern, M., and Lakatta, E. G. (2004). Rhythmic ryanodine receptor Ca2+ releases during diastolic depolarization of sinoatrial pacemaker cells do not require membrane depolarization. *Circ. Res.* 94, 802–809. doi: 10.1161/01.RES.0000122045.55331.0F

Wang, S. Q., Song, L. S., Lakatta, E. G., and Cheng, H. (2001). Ca2+ signalling between single L-type Ca2+ channels and ryanodine receptors in heart cells. *Nature* 410, 592–596. doi: 10.1038/35069083

Weiss, J. N., and Qu, Z. (2020). The sinus node: still mysterious after all these years. *JACC Clin. Electrophysiol.* 6, 1841–1843.

Yang, D., Lyashkov, A. E., Li, Y., Ziman, B. D., and Lakatta, E. G. (2012). RGS2 overexpression or Gi inhibition rescues the impaired PKA signaling and slow AP firing of cultured adult rabbit pacemaker cells. *J. Mol. Cell. Cardiol.* 53, 687–694. doi: 10.1016/j.yjmcc.2012.08.007

Yang, D., Morrell, C. H., Lyashkov, A. E., Tagirova, S., Zahanich, I., Yaniv, Y., et al. (2020). Ca^{2+} and membrane potential transitions during action potentials are self-similar to each other and to variability of ap firing intervals across the broad physiologic range of AP intervals during autonomic receptor stimulation. *bioRxiv* [Preprint]. doi: 10.1101/2020.09.01.277756

Yaniv, Y., Ahmet, I., Liu, J., Lyashkov, A. E., Guiriba, T. R., Okamoto, Y., et al. (2014a). Synchronization of sinoatrial node pacemaker cell clocks and its autonomic modulation impart complexity to heart beating intervals. *Heart Rhythm* 11, 1210–1219. doi: 10.1016/j.hrthm.2014.03.049

Yaniv, Y., Ganesan, A., Yang, D., Ziman, B. D., Lyashkov, A. E., Levchenko, A., et al. (2015). Real-time relationship between PKA biochemical signal network dynamics and increased action potential firing rate in heart pacemaker cells: kinetics of PKA activation in heart pacemaker cells. *J. Mol. Cell. Cardiol.* 86, 168–178. doi: 10.1016/j.yjmcc.2015.07.024

Yaniv, Y., Lyashkov, A. E., and Lakatta, E. G. (2013). The fractal-like complexity of heart rate variability beyond neurotransmitters and autonomic receptors: signaling intrinsic to sinoatrial node pacemaker cells. *Cardiovasc. Pharm. Open Access.* 2:111.

Yaniv, Y., Lyashkov, A. E., Sirenko, S., Okamoto, Y., Guiriba, T. R., Ziman, B. D., et al. (2014b). Stochasticity intrinsic to coupled-clock mechanisms underlies beat-to-beat variability of spontaneous action potential firing in sinoatrial node pacemaker cells. *J. Mol. Cell Cardiol.* 77, 1–10. doi: 10.1016/j.yjmcc.2014.09.008

Zaza, A., and Lombardi, F. (2001). Autonomic indexes based on the analysis of heart rate variability: a view from the sinus node. *Cardiovasc. Res.* 50, 434–442. doi: 10.1016/s0008-6363(01)00240-1

Zaza, A., Robinson, R. B., and Difrancesco, D. (1996). Basal responses of the L-type Ca2+ and hyperpolarization-activated currents to autonomic agonists in the rabbit sino-atrial node. *J. Physiol. Pharmacol.* 491, 347–355. doi: 10.1113/jphysiol.1996.sp021220

Zhou, P., Zhao, Y. T., Guo, Y. B., Xu, S. M., Bai, S. H., Lakatta, E. G., et al. (2009). Beta-adrenergic signaling accelerates and synchronizes cardiac ryanodine receptor response to a single L-type Ca2+ channel. *Proc. Natl. Acad. Sci. U.S.A.* 106, 18028–18033. doi: 10.1073/pnas.0906560106

Conflict of Interest: The authors declare that the research was conducted in the absence of any commercial or financial relationships that could be construed as a potential conflict of interest.

frontiers in Physiology

ORIGINAL RESEARCH
published: 20 November 2020
doi: 10.3389/fphys.2020.547577

Mechanistic Insights Into the Reduced Pacemaking Rate of the Rabbit Sinoatrial Node During Postnatal Development: A Simulation Study

Azzah M. Alghamdi*[1,2], *Craig P. Testrow*[1], *Dominic G. Whittaker*[3], *Mark R. Boyett*[4], *Jules. C. Hancox*[1,5] and *Henggui Zhang*[1,6,7]*

[1] Biological Physics Group, School of Physics and Astronomy, The University of Manchester, Manchester, United Kingdom, [2] Department of Physics, Faculty of Science, University of Jeddah, Jeddah, Saudi Arabia, [3] Department of Mathematics, University of Nottingham, Nottingham, United Kingdom, [4] Department of Biomedical Sciences, Faculty of Health and Medical Sciences, University of Copenhagen, Copenhagen, Denmark, [5] School of Physiology, Pharmacology and Neuroscience, and Cardiovascular Research Laboratories, School of Medical Sciences, University of Bristol, Bristol, United Kingdom, [6] Peng Cheng Laboratory, Shenzhen, China, [7] Key Laboratory of Medical Electrophysiology of Ministry of Education and Medical Electrophysiological Key Laboratory of Sichuan Province, Institute of Cardiovascular Research, Southwest Medical University, Luzhou, China

Edited by:
Futoshi Toyoda,
Shiga University of Medical Science,
Japan

Reviewed by:
Yael Yaniv,
Technion Israel Institute
of Technology, Israel
Wayne Rodney Giles,
University of Calgary, Canada

****Correspondence:***
Henggui Zhang
henggui.zhang@manchester.ac.uk

Specialty section:
This article was submitted to
Cardiac Electrophysiology,
a section of the journal
Frontiers in Physiology

Received: *31 March 2020*
Accepted: *29 October 2020*
Published: *20 November 2020*

Citation:
Alghamdi AM, Testrow CP,
Whittaker DG, Boyett MR, Hancox JC
and Zhang H (2020) Mechanistic
Insights Into the Reduced
Pacemaking Rate of the Rabbit
Sinoatrial Node During Postnatal
Development: A Simulation Study.
Front. Physiol. 11:547577.
doi: 10.3389/fphys.2020.547577

Marked age- and development- related differences have been observed in morphology and characteristics of action potentials (AP) of neonatal and adult sinoatrial node (SAN) cells. These may be attributable to a different set of ion channel interactions between the different ages. However, the underlying mechanism(s) have yet to be elucidated. The objective of this study was to determine the mechanisms underlying different spontaneous APs and heart rate between neonatal and adult SAN cells of the rabbit heart by biophysical modeling approaches. A mathematical model of neonatal rabbit SAN cells was developed by modifying the current densities and/or kinetics of ion channels and transporters in an adult cell model based on available experimental data obtained from neonatal SAN cells. The single cell models were then incorporated into a multi-cellular, two-dimensional model of the intact SAN-atrium to investigate the functional impact of altered ion channels during maturation on pacemaking electrical activities and their conduction at the tissue level. Effects of the neurotransmitter acetylcholine on the pacemaking activities in neonatal cells were also investigated and compared to those in the adult. Our results showed: (1) the differences in ion channel properties between neonatal and adult SAN cells are able to account for differences in their APs and the heart rate, providing mechanistic insight into understanding the reduced pacemaking rate of the rabbit sinoatrial node during postnatal development; (2) in the 2D model of the intact SAN-atria, it was shown that cellular changes during postnatal development impaired pacemaking activity through increasing the activation time and reducing the conduction velocity across the SAN; (3) the neonatal SAN model, with its faster beating rates, showed a greater sensitivity to parasympathetic modulation in response to acetylcholine than did the adult model. These results provide novel insights into the understanding of the cellular mechanisms underlying the differences in the cardiac pacemaking activities of the neonatal and adult SAN.

Keywords: postnatal development, sinoatrial node, sodium current, funny current, calcium current, pacemaking action potentials, ion channel mechanisms

INTRODUCTION

In many species maturation leads to a decrease in the heart rate (HR) (Larson et al., 2013). The HR of mammals including humans, rabbits, rats, and dogs (Dobrzynski et al., 2007; Yanni et al., 2010), decreases with age development; in humans, the heart rate range is between approximately 100–150 beats/min in the neonate (Myrnerts Höök et al., 2018), and 60–100 beats/min in the adult (Your heart rate-British Heart Foundation, 2019).

In normal conditions, the HR is determined by the primary pacemaker of the heart, the sinoatrial node (SAN), which possesses intrinsic pacemaking activity (Boyett et al., 2000; Satoh, 2003; Dobrzynski et al., 2007). Spontaneous APs of sinoatrial nodal pacemaker cells are produced by ion channels and ion transporters, as well as by the intracellular Ca^{2+} dynamics in SAN myocytes (Dobrzynski et al., 2007). It has been shown that significant developmental changes in the expression and function of ion channels and other cellular elements may be responsible for a postnatal alteration in the spontaneous activity of the transmembrane potential in single cells isolated from rabbit SAN (Yang et al., 2006; Dobrzynski et al., 2007). As compared with neonatal SAN cells, spontaneous APs in adult SAN cells show a reduction in spontaneous beating rate, increases in action potential duration (APD) and the intrinsic cycle length (CL), and an increasingly negative maximal diastolic potential (MDP) (Roberts et al., 2012; Larson et al., 2013).

A number of studies have investigated the ionic basis of automaticity in the adult SAN and the age-dependent factors responsible for the changes in the intrinsic heart rate (Jose and Collison, 1970; Toda, 1980; Campbell et al., 1992; Opthof, 2000; Baruscotti and Robinson, 2007). However, there have been far fewer studies on the basis of automaticity of the neonate or immature node cells until recently (Yang et al., 2006; Baruscotti and Robinson, 2007; Yang et al., 2002; Baruscotti et al., 1996; Baruscotti et al., 2001; Accili et al., 1997). The mechanism(s) that underlie the different pacemaking activities between the neonatal and the adult SAN are unclear, though a number of recent studies have stated categorically that the ionic basis of automaticity in neonate mammalian cells is distinct from that in the adult (Baruscotti and Robinson, 2007; Jones et al., 2007; Larson et al., 2013).

Prior studies on the developing SAN in rabbits have revealed that the sodium current, I_{Na} (Baruscotti et al., 1996, 2001), and pacemaker current, I_f (Accili et al., 1997; Yang et al., 2006), are associated with a developmental maturation-dependent decrease of SAN automaticity, as the two currents have been shown to be greater in the neonate than in the adult. In contrast, the opposite was observed for L-type Ca^{2+} current, $I_{Ca,L}$ (Jones et al., 2007; Protas et al., 2017), as the contribution from this current to the automaticity increased in the central cells of adult SAN in rabbits compared with that in the neonate. This may reflect species differences (Adachi and Shibata, 2013).

Although experimental information regarding developmental maturation-dependent changes in potassium and other transmembrane currents within the sinoatrial node is lacking, there are experimental data that have considered molecular markers of other relevant parameters and highlighted the key differences between neonates and adults, including an increase in the fibroblast content of the node and a lack of expression of connexins (Jones et al., 2004; Baruscotti and Robinson, 2007), each of which may produce alterations to the electrophysiological properties of the cardiac tissues.

It is unclear whether these differences could account for the different pacemaking activities between the neonatal and adult SAN. Computer-based modeling approaches have proved to be powerful tools to gain a further understanding of the behavior and complexity of electrical, mechanical, structural, and genetic mechanisms of the pacemaker activities in healthy animals (Fabbri et al., 2015), and during the development of arrhythmia (Fabbri et al., 2017). They have also offered a means to predict quantitatively the functional roles of altered molecular dynamics and ionic channels in a systematic way that is otherwise difficult to achieve in an experimental setting at the level of ion channels, cells and tissues (Roberts et al., 2012). These models have usually been constructed and validated against experimental data, and so these approaches are considered reliable (Wilders, 2007).

This study was undertaken to provide a framework in which to analyze the ionic mechanisms underlying the changes in cardiac pacemaking action potentials at the single cell level during the developmental maturation of the rabbit SAN. We have combined different experimental findings from voltage clamp experiments with those on gene expression of the ion-channel currents. Through simulations, we first investigated how changes in the expression and function of different ion channels can contribute to the alteration of the spontaneous AP waveform of the SAN cells and therefore slow spontaneous rate at the single-cell level of the adult heart. This was done by simulating the integral effect of remodeled ion channels on the pacemaking rate and AP characteristics, which were validated by comparing the simulation results to prior experimental data. Then, further mechanistic analysis was conducted to investigate the functional role of individual ion channel changes in producing the pacemaking differences between the neonate and the adult. These analyses elucidated the primary ion channel that is responsible for the pacemaking difference between the neonatal and the adult pacemakers, adding new mechanistic insight into the understanding of neonatal and adult pacemakers to previous experimental studies. In addition, we have updated a 2D model of the intact SAN and surrounding atrial tissue to determine the functional impact of development-dependent changes in electrical coupling through connexins on the initiation and conduction of SAN APs, and their conduction into the atrium.

MATERIALS AND METHODS

A framework for investigating the underlying mechanism of fast heart rhythm in the neonate rabbit SA node cells arising from ion channel remodeling was developed by updating: (1) the electrophysiologically detailed central and peripheral SAN cell models developed by Zhang et al. (2000) at the single cell level; (2) a 2D anatomical model of the intact SAN-atrium tissue developed by Butters et al. (2010; Bai et al., 2017), which incorporated tissue geometry for SAN and the right atrium (RA), including the crista terminalis (CT) (Dobrzynski et al., 2005). These models represented the adult rabbit. Therefore, based on the literature review of the ion channel properties of neonate heart as summarized in **Table 1**, both models were modified at the single cell and tissue level for two age groups: neonate and adult. In simulations, we did not include postnatal development changes in the intracellular Ca^{2+} handling because the experimental data of Allah et al. (2011) showed no significant change of Ca^{2+} uptake and Ca^{2+} release proteins, as determined by RyR and SERCA2a expression levels, between the neonatal and adult SAN.

Model Development at the Single-Cell Level

The single-cell models developed by Zhang et al. (2000), as based on experimental data from isolated rabbit SAN preparations, were used as basal models. In brief, the model described the membrane potential of rabbit SAN cells using Hodgkin-Huxley formulations of ionic currents (see Eq. 1) at body temperature (37°C). The model consisted of 39 coupled ordinary differential equations (ODEs) to describe voltage-gated ion-channel currents, exchanger currents, and an ionic pump (see Eq. 2) for central (cell capacitance of 20 pF) and peripheral (cell capacitance of 65 pF) SAN cells.

$$\frac{dV_m}{dt} = -\frac{1}{C_m} I_{tot} \quad (1)$$

$$I_{tot} = (I_{Na} + I_{Ca,T} + I_{Ca,L} + I_{Kr} + I_{Ks} + I_{to} + I_{sus} + I_f + I_b + I_{NaK} + I_{NaCa}) \quad (2)$$

In order to model the AP of the SAN cell of neonatal rabbits, the conductances and kinetics of some ionic channels responsible

TABLE 1 | Summary of differences in current densities and kinetic parameters of ion channels between newborn and adult central SAN cells from multiple species.

Ion channel	Current density (pA/pF)		Midpoint potential for the activation curve (mV)		Midpoint potential for the inactivation curve (mV)		Change in relative abundance of mRNAs for ion channel in central SAN	Species	References
	Neonate	Adult	Neonate	Adult	Neonate	Adult			
I_{Na}	68.51 ± 16.0	9.00 ± 0.3	−38 ± 2.2	−37.50 ± 0.9	−89.70 ± 0.7	−93.42 ± 1.9	–	Canine	Protas et al. (2010)
	180.55 ± 16.0	0.00 ± 0.0	−33.9 + 0.7	−23.21 ± 0.8	−63.51 ± 1.0	−61.75 ± 1.1	–	Rabbit	Baruscotti et al. (1996)
	–	–	–		–	–	↑ +64%	Rabbit	Allah et al. (2011)
I_f	–	–	−68.5 ± 4.0	−63.20 ± 0.6	–	–	–	Rabbit	Yang et al. (2006)
	0.24 ± 1.5	0.15 ± 0.1	–	–	–	–	–	Rabbit	Accili et al. (1997)
	17.23 ± 6.2	9.60 ± 1.0	−82.9 ± 5.2	−84.13 ± 2.9	–	–	–	Canine	Protas et al. (2010)
	–	–	−104.7 ± 3.1	−110.66 ± 3.2	–		–	Mouse	Larson et al. (2013)
	–		–		–		HCN2↑ +31% HCN4↑ +24%	Rat	Huang et al. (2016)
$I_{Ca,L}$	17.61 ± 2.5	12.31 ± 1.4	−17.33 ± 1.4	−22.00 ± 0.8	−33.41 ± 1.4	−28.31 ± 1.7	–	Rabbit	Protas et al. (2017)
	–	–	–	–	–	–	↑ +42%	Rabbit	Allah et al. (2011)
	9.02 ± 3.1	4.60 ± 2.6	–	–	–	–	–	Mouse	Larson et al. (2013)
$I_{Ca,T}$	4.55 ± 0.0	4.52 ± 0.0	−33.00 ± 2.2	−35.11 ± 2.0	−65.00 ± 2.1	−65.09 ± 2.4	–	Rabbit	Protas et al. (2017)
	9.10 ± 2.6	6.36 ± 2.7	–		–	–	–	Mouse	Larson et al. (2013)
I_{Kr}	–		–		–		↑ +36%	Rabbit	Allah et al. (2011)
I_{Ks}	–		–		–		↑ +27%	Rabbit	
I_{NaCa}	–		–		–		↑ +66%	Rabbit	
$I_{K,ACh}$	–		–		–		↑ +60%	Rabbit	
Cx43	–		–		–		↑ +60%	Guinea-pig	Jones et al. (2007)

Available data regarding relative abundance of mRNAs that code for some ion channels between neonatal and adult cells are also shown.

for cellular depolarization and repolarization were adjusted, based on a comprehensive literature review of experiment data on some ion-channel currents, such as, $I_{Ca,L}$ and I_f, and gene expression levels of ion channels, such as I_{Ks}, I_{Kr} and I_{NaCa}, on the neonatal rabbit SAN (see **Table 1**).

The contribution of all or individual remodeled ion channels to the genesis of different pacemaking action potentials between neonatal and adult SAN cells were investigated by integral (inclusive) and exclusive methods. Using the inclusive method, the effect of all experimentally observed changes in different ion channels on the APs was simulated, and results were compared with (validated against) experimental data of the pacemaking rate and the characteristics of APs obtained from experimental studies (Baruscotti et al., 1996; Allah et al., 2011). This method helps to answer whether these changes in ion channels are sufficient to account for the observed differences in pacemaking activity between the neonatal and adult SAN cells. **Tables 2**, **3** summarize experimental data on the two groups' current densities and conductances of SAN cells. With the exclusive method, only changes in the selected ion channel were considered in each simulation to investigate the relative role of the remodeled channel in affecting pacemaking activity. Using the exclusive method, the major contributor(s) to the greater heart rate of the neonate SAN cells was determined. In all simulations, the models were solved numerically with a time step of 0.01 ms, which is sufficiently small for stable numerical solutions.

Modeling I_{Na} in the Neonatal Rabbit SAN

The sodium-channel current, I_{Na}, is considered to be the main ion channel responsible for the upstroke phase of the APs in non-pacemaking cells (Dobrzynski et al., 2007). However, it is not detected in the central cells of the adult rabbit SAN (Zhang et al., 2000; Dobrzynski et al., 2007). In contrast, according to Baruscotti et al. (1996), voltage clamp measurements from neonatal SAN cells revealed the presence of sodium-channel current. This ion-channel current decreased gradually to disappear 40 days after birth. Of further interest is the difference of I_{Na} between the neonate and young rabbit SAN cells (Baruscotti et al., 1996). In particular, as compared to the neonate there is ~76% reduction in the sodium channel current density in the young, which ultimately reduced to zero, together with a rightward shift of the activation curve (midpoint changed by 7 mV in the young) and little or no alteration of the inactivation curve (see **Table 1**). Consistent with this, quantitative PCR analysis of the mRNA of neonatal and adult SAN rabbit cells showed a relatively greater abundance of the isoforms Nav1.1 and Nav1.5 in the neonatal rabbit SAN cells, which significantly decreased during postnatal development (Allah et al., 2011). It is not yet clear if/how such a decreased I_{Na} helps to explain the slowing of the heart rate with postnatal development.

TABLE 2 | Implemented conductances of different ionic currents in the neonate and adult central SAN cell models based on experimental data as listed in **Table 1.**

Ion current	Conductance		
	Neonate	Adult	Ratio (neonate/adult)
g_{Na}	0.5350×10^{-6} µS	0	∞
$g_{Ca,L}$	0.841×10^{-2} µS	0.58×10^{-2} µS	1.45
$g_{K,r}$	10.839×10^{-4} µS	7.97×10^{-4} µS	1.34
$g_{K,s}$	6.57×10^{-4} µS	5.18×10^{-4} µS	1.27
$g_{f,Na}$	9.5725×10^{-4} µS	5.47×10^{-4} µS	1.75
$g_{f,K}$	9.5725×10^{-4} µS	5.47×10^{-4} µS	1.75
K_{NaCa}	0.4482×10^{-5} nA	0.27×10^{-5} nA	1.66

TABLE 3 | Current densities in the neonate and adult central SAN cell models.

Ion current	Current density, pA/pF		
	Neonate (simulation)	Neonate (experimental)	Adult
I_{Na}	179.56	180.5 ± 16	0.0
$I_{Ca,L}$	17.58	17.6 ± 2.5	12.23
I_f	17.45	17.2 ± 6.2	3.36
I_{Ks}	0.84	–	0.66
I_{Kr}	1.07	–	0.97
I_{NaCa}	0.22	–	0.13

To model the postnatal development of the sodium-channel current in rabbit SAN, maturation-dependent I_{Na} equations were developed based on experimental data from both newborn and young rabbit SAN cells. In the developed model, data on the steady-state activation and inactivation curves for neonate and young rabbit SAN cells reported in Baruscotti et al. (1996) were implemented, taking into account of the shift in the steady-state activation midpoints (as shown in **Figures 1A,B**). As these experimental data were obtained at room temperature (20–22°C) while the model was developed at body temperature at 37°C, therefore, a Q_{10} of 1.7 correction of the current density was considered accounting for the temperature difference (Lindblad et al., 1996; Zhang et al., 2000). The maximal channel conductance of the sodium current ($g_{Na,max}$) was determined by reproducing the experimental data for the I–V relationship (Baruscotti et al., 1996). The developed equations and use of their parameters were validated by the model's ability to reproduce voltage-clamp data for the I_{Na} channel, using the same voltage-clamp protocol as used in the experiments. In brief, I_{Na} was recorded from a holding potential of −65 mV by applying a series of testing potentials that each lasted 10 ms and were varied between −60 mV and +45 mV in 5 mV increments (see **Figure 1C**). As shown in **Table 2**, changes in parameters of the age-related I_{Na} equations were incorporated into the Zhang et al.'s (2000) SAN model. **Figure 1D** shows the simulated I–V currents for both neonate and young rabbits (black and red lines respectively), which are compared with experimental values (the square points) reported for both neonate and adult rabbits. Simulation data were consistent with the experimental data in showing a peak current density of the neonate I–V curve greater than that of the young, similar to experimental data as shown in **Table 2**. In sensitivity analysis, a systematic change in the conductance of I_{Na} was implemented to investigate the role of Ina on the pacemaking CL (see **Supplementary Figure S1A** for details).

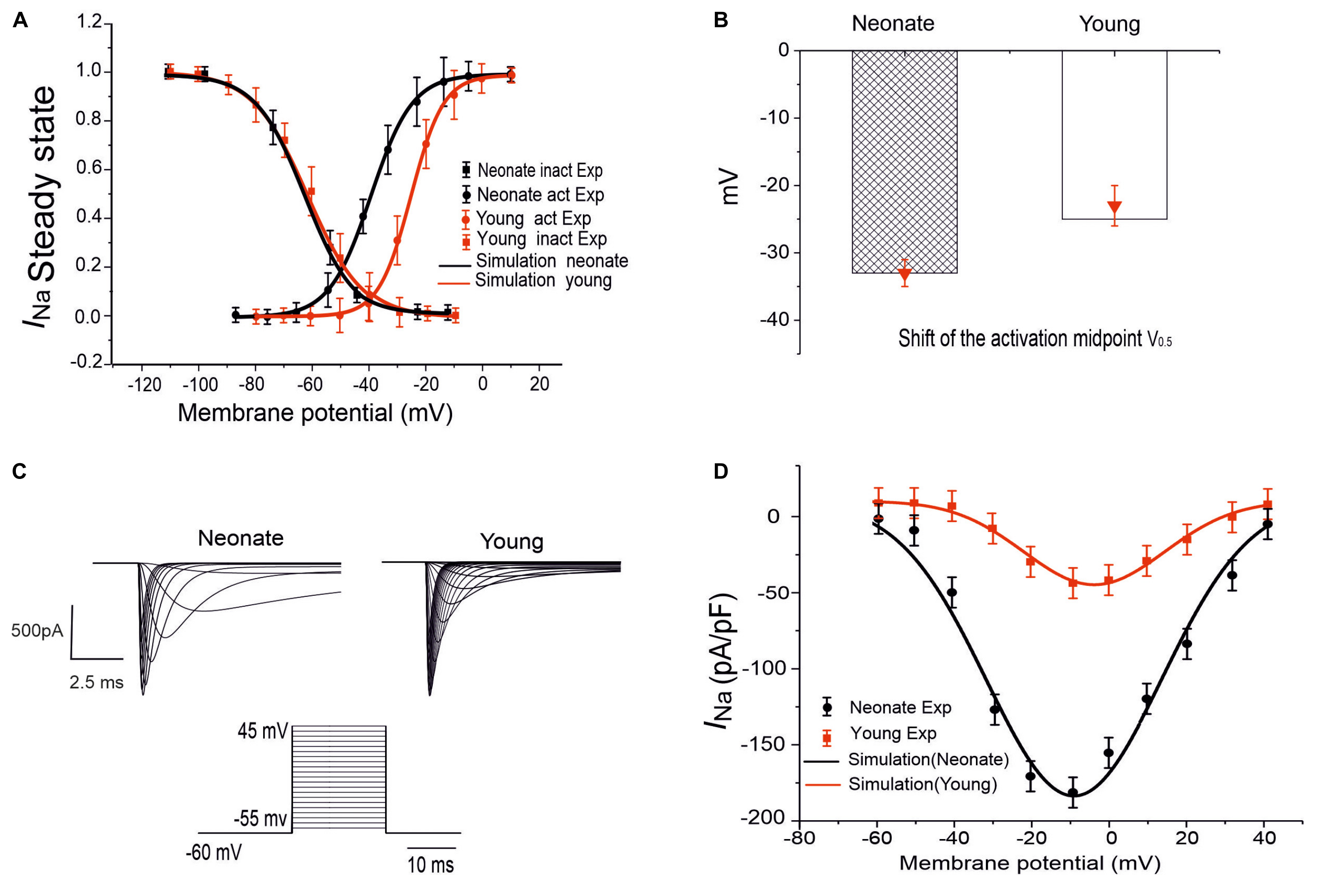

FIGURE 1 | I_{Na} simulation and validation. **(A)** Steady-state activation and inactivation curves of the I_{Na} in two groups: neonate (black line) and adult (red line), which are compared with experimental data by Baruscotti et al. (1996). **(B)** Midpoint of the activation curve ($V_{0.5}$) for neonatal and adult. **(C)** Simulated traces of I_{Na} for neonate and young SAN cells under the voltage-clamp protocol as shown by the inset. **(D)** Simulated I–V relationship and its validation against experimental data by Baruscotti et al. (1996).

Modeling I_f

The hyperpolarization activated current, I_f, is well known as a pacemaking current due to its significant contribution to the pacemaking potential during the phase 4 of the AP of SAN cells (DiFrancesco, 1993; Baruscotti et al., 2005). This ionic channel is permeable to Na^+ and K^+ ion fluxes, and comprised of HCN1, HCN2, and HCN4 isoforms, which have been found to be the most abundant isoforms among other subunits (Brioschi et al., 2009). Postnatal changes of this ion channel in rabbit SAN cells were identified experimentally by Accili et al. (1997) and Yang et al. (2006). According to Accili et al. (1997), SAN development affects I_f by decreasing the current density and altering the slope factor of the activation curve of the channel, though without changing the midpoint of the activation curve. The decreased I_f is assumed to result from the change to the cAMP during development. In agreement with this, voltage clamp data recorded by Yang et al. (2006) suggested a smaller I_f in adult SAN cells (12-week-old group) as compared to neonatal SAN cells (2 weeks old) in the rabbit heart. The smaller I_f in the adult group was also associated with a negative shift of the voltage-dependent activation relationship (**Table 1**). Moreover, quantitative PCR measurements on the mRNA of the HCN subunit confirmed a 69% reduction in HCN4 expression in adult SAN cells compared with the numbers in neonates (Allah et al., 2011). Similar age-induced remodeling of SAN I_f during development was also observed in changes of HCN expression in other species, including rats (Huang et al., 2016), mice (Larson et al., 2013), and canines (Protas et al., 2010). These results indicate that the change in I_f with age may be an important contributor to the declined SAN function and therefore the decreased HR. However, this has not yet been shown explicitly.

The role of the remodeled I_f on the pacemaking APs of SAN cells was assessed by incorporation of the development maturation-dependent I_f equations into the Zhang et al.'s (2000) model. These maturation-dependent I_f equations were developed based on experimental data from Accili et al. (1997) and Yang et al. (2006), and were validated by their ability to reproduce these experimental data. Results are shown in **Figure 2** for neonatal and adult I_f, taking into account the maturation-related negative shift of the midpoint of the activation curve by 7 mV as suggested by Yang et al. (2006) (see **Figures 2A,B**), as well as an increase in the maximal conductances of g_f (e.g., $g_{f,Na}$, $g_{f,K}$) by 70%. The time constant for the activation of I_f in neonates was similar to that of adults in the Zhang et al. (2000) model.

The simulated current traces for the I_f current in both neonate and adult SAN cells were obtained under the following voltage-clamp protocols: the I_f current was recorded from a holding potential of −35 mV by applying a series of testing potentials lasting for 600 ms and were varied between −45 mV and −105 mV in 10 mV increments at 36°C, as shown in **Figure 2C**. The resultant I–V curve (**Figure 2D**) showed reasonable agreement between the simulation and experimental data obtained for both neonatal and adult cells. The peak current–voltage relationships for I_f from the central SAN cell model in neonates (black line) and adults (red line) are shown in **Figure 2D**, and these were validated against experimental data reported by Honjo et al. (1996) and Protas et al. (2010). In sensitivity analysis, a systematic change in the conductance for I_f was implemented to investigate the effect of changed I_f on the pacemaking CL (see **Supplementary Figure S1B** for details).

Calcium Currents and Remodeling

In the SAN cells, two types of Ca^{2+} current are present: L-Type and T-Type, which are activated at relatively high and low voltages, respectively (Verheijck et al., 1998). The contributions made by the two currents to the pacemaking AP of the rabbit SAN cells have been investigated previously (Dobrzynski et al., 2007). The L-type calcium current was found to be a major contributor to the phase 0 (upstroke) of the APs, either alone in the central cells of adult rabbits' SAN or in combination with the I_{Na} current in peripheral SAN cells, in addition to its contribution to the late diastolic depolarization phase of the adult rabbit SAN cells spontaneous AP (Zaza et al., 1996; Verheijck et al., 1999; Mangoni et al., 2003; Baruscotti and Robinson, 2007). A comparative analysis of the postnatal changes of Ca^{2+} ion currents $I_{Ca,T}$ and $I_{Ca,L}$ in central cells of the rabbit SAN was carried out by Protas et al. (2017). It was shown that there were no developmental changes in recorded $I_{Ca,T}$ densities, suggesting that, although it contributes to the automaticity of rabbit SAN cells, $I_{Ca,T}$ is not a critical determinant of age-dependent changes of the SAN pacemaking.

There is experimental evidence for the reduction of $I_{Ca,L}$ with postnatal development (Protas et al., 2017); in particular, a 42% reduction in the current density of $I_{Ca,L}$ has been seen in adults as compared to neonates. However, this was accompanied by a rightward shift of the inactivation curve (midpoint changed by 5 mV in adults), and a leftward shift of the activation curve (midpoint changed by 5 mV in adults), leading to an increase

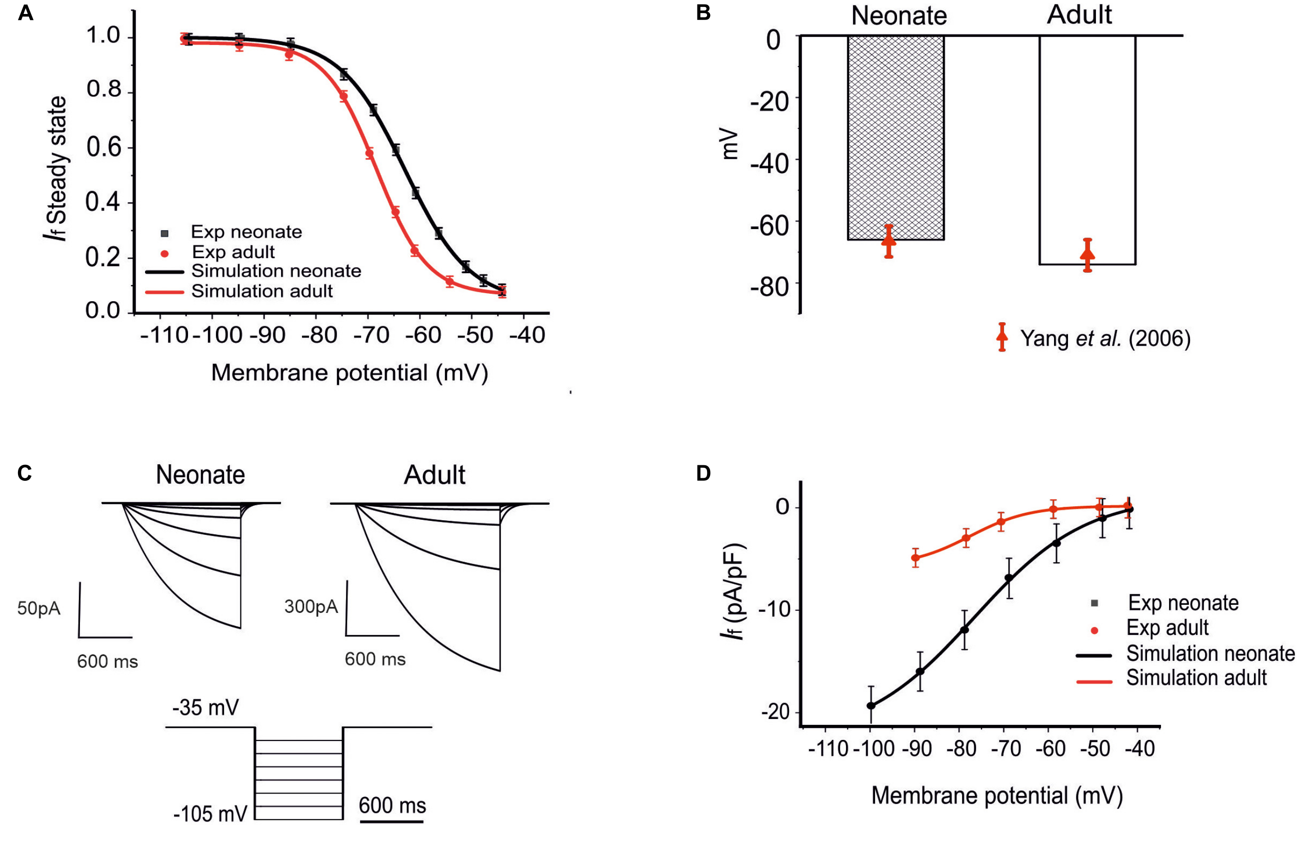

FIGURE 2 | Model of I_f and its comparison to experimental data. **(A)** The steady-state activation curves for the I_f for two age groups: neonates (black line) and adults (red line). **(B)** Shift of the midpoint of the activation relation. **(C)** Simulated time traces of I_f in both neonate and adult SAN cells under the voltage-clamp protocols as shown at the bottom. **(D)** Simulated I–V relationship. Results are validated against experimental data reported by Honjo et al. (1996); Yang et al. (2006), and Protas et al. (2010) .

in the window current (the overlap between the activation and inactivation steady-state curves). The increased window current in the adult would suggest a greater contribution of this current to pacemaking in the adult as compared to the neonate. Additional support for this hypothesis comes from the findings of Jones et al. (2007), who observed a progressive loss of Cav1.2 with age in guinea-pig SAN. Moreover, molecular identification of the ion channels at the protein level showed an association between heartbeat decline and decrease in $I_{Ca,L}$ transcript by 58% in developing SAN rabbit cells (Allah et al., 2011).

To investigate if/how $I_{Ca,L}$ influences age-dependent changes SAN activity development, a model for neonatal $I_{Ca,L}$ was developed, based on the above-mentioned experimental data reported by Protas et al. (2017). **Figures 3A,B** illustrates the simulated steady-state activation and inactivation curves for neonates (black lines) and adults (red lines). The I–V relationship was computed from the model using a voltage clamp protocol with 10 mV incrementing steps between −60 mV and 60 mV of 300 ms duration (see **Figure 3C**), at a temperature of 36°C. The established I–V relationship curve for the $I_{Ca,L}$ of neonate and adult rabbit SAN is illustrated in **Figure 3D**. The magnitude of the neonate (black line) peak current density, 17.30 pA/pF, was considerably larger than the peak current density in adults of 12.32 pA/pF (see **Table 3**). This result was comparable with values recorded experimentally (Protas et al., 2017). In sensitive analysis, a systematic change in the conductance of $I_{Ca,L}$ was implemented to study the effect of altered I_{CaL} in modulating CL (see **Supplementary Figure S1C** for details).

I_{NaCa} and Remodeling

NCX is believed to be functionally important for pacemaking activity through the release of Ca^{2+} from the SR during late diastole and the consequent activation of the inward Na^{+}–Ca^{2+} exchange current, I_{NaCa} (Satoh, 2003). In the SAN, it was observed that the expression of NCX1 for both mRNA and protein levels was more abundant in the neonate than the adult (Allah et al., 2011). In addition, the expression of NCX1 protein was different between the neonate and the adult. This decrease in NCX1 mRNA abundance suggests a possible contribution to the decrease in the heart rate during postnatal development (Allah et al., 2011). Consistent with this, several previous studies have observed a similar postnatal decrease in NCX1 in rabbit ventricles, (Artman, 1992; Artman et al., 1995; Chen et al., 1995; Dan et al., 2007), rabbit whole hearts (Artman, 1992) and human ventricles (Qu et al., 2000). In our model, the I_{NaCa} of the rabbit SAN cells was considered to be greater in neonates compared to adults; therefore, based on Allah et al. (2011), the magnitude of the I_{NaCa} current density was adjusted by multiplying the maximal value of the scaling factor for I_{NaCa} by a ratio of 1.66, as summarized in **Tables 1**, **2**.

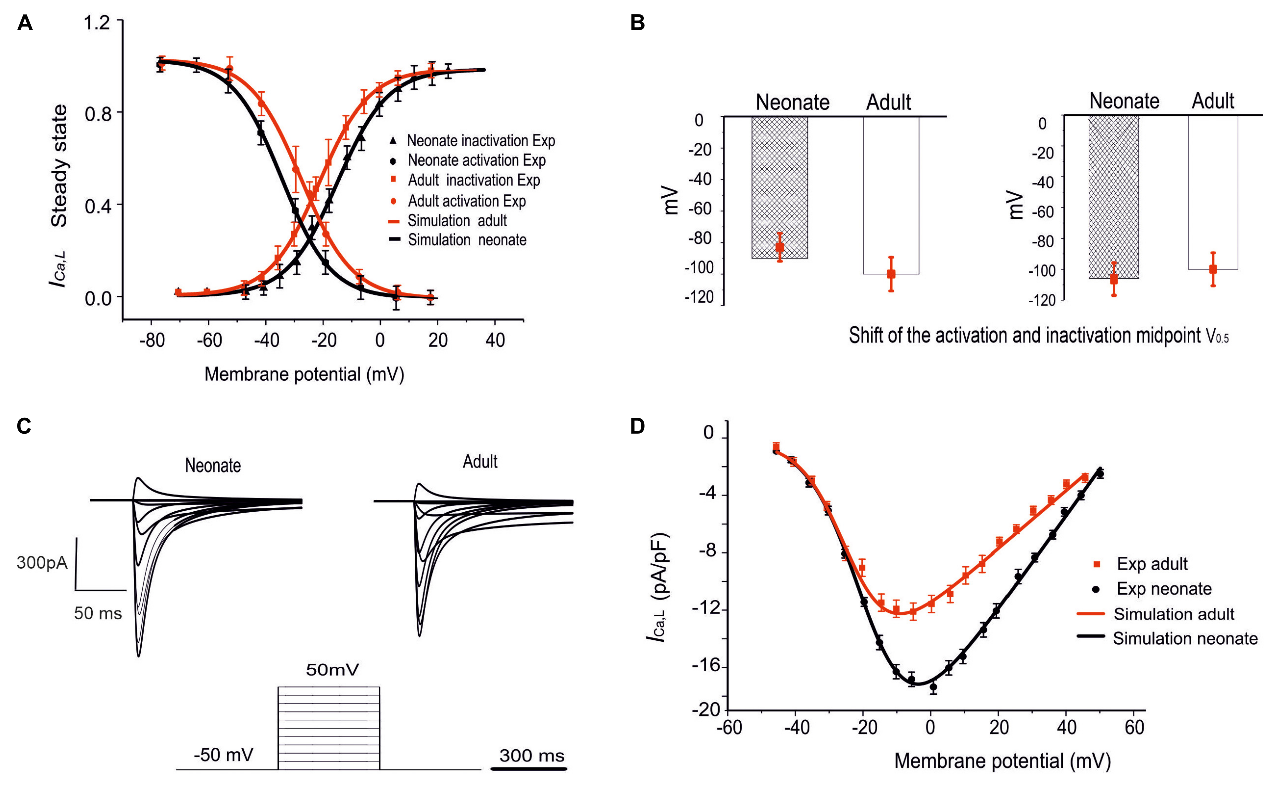

FIGURE 3 | Simulation of $I_{Ca,L}$ and its validation. **(A)** The fitted steady-state activation and inactivation curves of the $I_{Ca,L}$ in two age groups: neonates (black line) and adults (red line). **(B)** The bar chart shows the shifted midpoints of activation and inactivation curves. **(C)** The simulated time traces of $I_{Ca,L}$ in both neonate and adult SAN cells with the voltage-clamp protocols as shown at the bottom of the diagram. **(D)** Simulated I–V relationship. Results validated against experimental data reported by Protas et al. (2017).

Modeling of the Rapid/Slow Delayed Rectifier K$^+$ Currents: I_{Kr}/I_{Ks}

There are two components of the delayed rectifier potassium current in rabbit SAN cells: rapidly activating current (I_{Kr}) and slowly activating current (I_{Ks}). These outward currents are crucial for the repolarization phase of the APs in the SAN. For the neonate condition, limited voltage-clamp experiments for the two currents have been reported in the literature. However, the postnatal developmental changes in the expression of the two ion channels have been characterized by using quantitative PCR, *in situ* hybridization and immunohistochemistry for neonatal (2–7 days of age) and adult (∼6 months of age) New Zealand White rabbits (Allah et al., 2011). The results showed that the mRNA expression of ERG (responsible for I_{Kr}) and both KvLQT1 and minK (responsible for I_{Ks}) were more abundant in the SAN compared to the left ventricle for both neonate and adult cases. It was also found that there was a postnatal reduction in mRNAs associated with delayed rectifier K$^+$ channels by 36% for the ERG and 27% for the KvLQT1 in the SAN. Therefore, for the purposes of our simulation, the ratios of the I_{Kr} and I_{Ks} maximal conductances of neonate to adult were adjusted by multiplying these ratios by 1.36 and 1.27 as factors in the conductance in the neonatal SAN model, respectively (see **Tables 1**, **2**).

Acetylcholine-Activated Potassium Current: $I_{K,ACh}$

Acetylcholine (ACh) is a neurotransmitter which has a chronotropic effect opposite to that of (nor)adrenaline. It is released from the vagal nerve terminals in the SAN, leading to a negative chronotropic effect which appears as a significant reduction in the HR. The effects of ACh on the HR and CL in both age groups for SAN cells in rabbits were simulated by using a formulation of the ACh-activated potassium current, $I_{K,ACh}$, given by Zhang et al. (2002):

$$I_{K,ACh} = g_{K,ACh^*}\left(\frac{[K]_e}{10+[K]_e}\right)^{*}((V_m - E_K)/(1 \\ +\exp[V_m - E_K - 140)F/2.5RT])) \tag{3}$$

in which $g_{K,ACh}$ is the conductance; $I_{K,ACh}$ is the ionic current; F and R are the Faraday and universal gas constants, respectively; $[K]_e$ is the extracellular concentration of K$^+$; V_m is the membrane potential; and E_K is the reversal potential for K$^+$.

The conductance $g_{K,ACh}$ is given by:

$$g_{K,ACh} = g_{K,ACh\ max} {*} jk {*} \frac{[ACh]^{nK,ACh}}{K^{\ nK,ACh}_{\ 0.5,K,ACh} + [ACh]^{nK,ACh}} \tag{4}$$

where *j, k* refer to the inactivation variables (fast and slow, respectively); $g_{K,ACh\ max}$ is the maximum value of $g_{K,ACh}$; $n_{\ K,ACh}$ is the Hill coefficient; $K_{0\cdot 5,K,ACh}$ is the concentration of ACh that produces a half-maximal activation; and $\left[ACh\right]$ is the molar concentration of ACh.

The voltage-dependent inactivation variables *j* and *k* are ODEs of the form given in the following equations:

$$\frac{dj}{dt} = \alpha_j\ \left(j-1\right) - \ \beta_j\, j \tag{5}$$

$$\frac{dk}{dt} = \alpha_k\ \left(1-k\right) - \ \beta_k\, k \tag{6}$$

In these equations, α_j, β_j ,α_k, and β_k are rate constants. The constants α_k and α_j represent voltage-independent constants given by 3.7 s^{-1} and 73.1 s^{-1}, respectively. However, the voltage-dependent constants β_j , and β_k are given by:

$$\beta_j = \frac{120}{1+\exp(-(v_m\ + 50)/15)} \tag{7}$$

$$\beta_k = \frac{5.82}{1+\exp(-(v_m\ + 50)/15)} \tag{8}$$

The equation that describes the change of time dependence of the membrane potential is as follows:

$$\frac{dV_m}{dt} = -\ \frac{I_{tot} + I_{K,ACh}}{C_m} \tag{9}$$

in which I_{tot} is the net magnitude of the various ionic currents.

The incorporation of ACh into our model incorporated two additional effects on ionic currents: a shift in the activation curve for the funny current, I_f, and the fractional block of $I_{Ca,L}$, the L-type Ca^{2+} channel (Zhang et al., 2002).

Acetylcholine causes a shift in the activation curve (mV) of the funny current I_f to a more negative potential as follows:

$$S = S_{max^*}\ \frac{[ACh]^{nf}}{K^{nf}_{0.5,f}\ \ +\ \ [ACh]^{nf}} \tag{10}$$

In this equation, $S_{\ max}$ refers to the maximum shift of the I_f activation curve; $K_{\ 0.5,\mathrm{f}}$ is the ACh concentration that produces a half-maximal shift in the funny current activation curve; and nf is the Hill coefficient. This was factored into the model by subtracting *s* from the exponent in the Boltzmann equation for the steady-state gating variables of the funny current.

The activated ACh also leads to a partial depression of $I_{Ca,L}$, which is given by a dimensionless quantity:

$$b = b_{\ max}{\ }^{*}\ \frac{[ACh]}{K_{0.5,Ca} +\ \ [ACh]} \tag{11}$$

where $b_{\ max}$ is the maximum fractional block of $I_{Ca,L}$, and $\mathrm{K}_{0.5,Ca}$ is the concentration of ACh that produces a half-maximal block of $I_{Ca,L}$. This depression can be included in the model by multiplying the $I_{Ca,L}$ ionic current by $(1 - b)$.

For the neonatal condition, it was found in patch clamp experiments that the neonatal SAN cells exhibited particular sensitivity to autonomic stimulation compared with adult SAN cells. Accili et al. (1997) examined the activation curves of the I_f in neonate and adult rabbit cells. It was shown that cells in both groups exhibited similar shifts in the I_f activation in response to maximal concentrations of acetylcholine. Therefore, it was suggested that the greater heart rate and the greater sensitivity of the SAN to ACh was partly the result of the greater magnitude of the hyperpolarization-activated current (I_f). Another study (Allah et al., 2011), which measured changes in the mRNA expression of Kir3.1 that is responsible for $I_{K,ACh}$, found that the relative abundance of mRNAs for Kir3.1 in the SAN was greater (60%) than in the right atrium and left ventricles in the neonates, but not in the adults. In order to model the effect of ACh, the dose dependency of ACh-affected ion channels, including $I_{K,ACh}$, $I_{Ca,L}$, and I_f, were considered and incorporated into our newly developed neonate (central and peripheral) SAN models, while taking into consideration the fact that $g_{K,ACh}$ is greater in neonates (60%) by incorporating this percentage as a factor in $g_{K,ACh}$.

Tissue Model for AP Propagations

In order to investigate the consequences of postnatal changes in different ion-channel properties on the propagation and conduction of excitation waves in the intact SAN-atrium, the 2D anatomical model of the intact SAN-atrium tissue described in previous study (Butters et al., 2010) was implemented. This model considered the heterogeneities of the AP characteristics and the anisotropy of the tissue, including distinct regions of the SAN-atrium, central and peripheral cells of the SAN, which were simulated by Zhang et al. (2000) models. For right atrial cell APs, due to lack of a complete set of experimental data for developing a neonatal model, the model of Aslanidi et al. (2009) for the adult atrial cell was used for both neonatal and adult conditions. The geometry of the 2D model was extracted using histological and immunohistochemistry-imaging data from anatomical models of rabbit SAN cells (Verheijck et al., 1998). The geometry represented the whole intact SAN-atrium meshing from the endo-cardiac surface with a high spatial resolution of 0.04mm to form a Cartesian grid which was divided into 385 × 250 nodes (Dobrzynski et al., 2005; Butters et al., 2010).

In the SAN-atrium tissue model, intercellular electrical coupling *via* connexin between cells is modeled by the diffusive interactions of membrane potentials, which generates the propagation of excitation waves. In the tissue model, such a diffusive interaction of membrane potentials is modeled by a diffusion coefficient (D). Since our model represents an intact SAN-atrial tissue is anisotropic, the 2D model took into consideration of regional differences in the intercellular electrical coupling by using a spatially dependent diffusion coefficient, which determines the conduction velocity of excitation propagation within the SAN-atrium tissue. Anisotropic conduction of the excitation waves due to cardiac fiber orientations was modeled by implementing different values of D in the longitudinal and transverse directions of the tissue fiber as used in our previous studies (see **Supplementary Figure S2A** and Eq. 12) (Dobrzynski et al., 2005; Butters et al., 2010).

$$D(x) = D_C + D_P \;.\left(\frac{1}{1+\mathrm{e}^{-0.5(x-x1)}} + \frac{1}{1+\mathrm{e}^{0.5(x-x2)}}\right) \quad (12)$$

where x is the horizontal coordinate through the 2D slice, $x1$ and $x2$ approximately correspond to the positions of the SAN boundaries within the tissue, and D_C and D_P are the diffusion coefficients of central and peripheral SAN cells, respectively. The regional differences in cell-membrane capacitance (C_m) in the SAN-atrium tissue were based on the study of Zhang et al. (2000) model (**Supplementary Figure S2B**). The spatial distributions of current densities for different ion channels were correlated with the cell membrane capacitance (C_m), which increased gradually from the center to the periphery of the SAN (Zhang et al., 2007).

The 2D model used the monodomain equation to simulate the propagation of the AP and describe the transmembrane potential changes with time. The equation was solved using the finite partial differential equation (PDE) solver with a time step of 0.01 ms and space step of 0.04 mm, which gave accurate numerical solutions (Dobrzynski et al., 2005; Butters et al., 2010).

To investigate the functional impact of postnatal development in the intact SAN-atrium at the tissue level, the 2D model for the SAN-atrium at the tissue level was used to simulate both the neonatal and adult conditions. In the instance of the neonate, the electrophysiology of the cells in the 2D model was adjusted in the same way as for the single-cell level. In addition, changes to intercellular coupling that arose from the connexin remodeling were considered, as explained in the following section. Further, the pacemaking activity of the AP propagation, activation time and conduction velocity were analyzed, as presented in the results section.

Remodeling of Connexins

Connexins play a critical role in intercellular electrical coupling between the cells through the movement of ion channels and intracellular exchange via the gap junction, as explained above (Boyett et al., 2006). In the SAN tissue, Dobrzynski et al. (2007) found that Cx43 was present in the peripheral cells of adult rabbits. Another study measured the relative abundance of each Cx43, Cx40, and Cx45 in different tissues including the SAN, right atrium and left ventricle of the rabbit heart, from birth to adulthood. These measurements showed that the Cx45 protein was distributed similarly in the different tissues but at decreased levels in the adult; only 45% of that found in adult compared to neonates (Allah et al., 2011). This observation was corroborated by the study of Jones et al. (2004) in guinea-pig SAN for different age groups, which revealed a substantial rearrangement of Cx43 and a 60% decrease in its expression level in adults compared with neonates (see **Supplementary Figure S2C**). Therefore, in this simulation, the connexin remodeling was achieved by adjustment of the diffusion coefficient value of D within the 2D tissue model (see **Supplementary Figure S2C**).

RESULTS

Effects of Ion-Channel Remodeling at the Single Cell Level

Development-related remodeling of the different ion channels (I_{Na}, $I_{Ca,L}$, I_f, I_{Kr}, I_{Ks} and I_{NaCa}) was incorporated into the adult single-cell model of the central SAN developed by Zhang et al.

(2000). **Figure 4** illustrates the simulated APs and time course of age-remodeled ionic channel currents for the neonatal condition, which were superimposed on those from the adult condition, for the central SAN model. The simulation results showed that the neonatal model reproduces the characteristic AP shapes of neonatal cells as compared with the adult equivalent.

In general, the neonatal APs had faster spontaneous rates, shorter APD and greater amplitudes than those of the adult. The computed CL (the time interval between two successive pacemaking APs) for the neonatal SAN was 277 ms in the neonate and 327 ms in the adult, which showed an 18% prolongation of CL with developmental maturation. The computed maximal upstroke velocity of AP (dV/dt_{max}) was 11.9 V/s in the neonate, which was reduced to 2.7 V/s in the adult condition. The greater dV/dt_{max} in the neonatal SAN cells can be attributed to the presence of the I_{Na}. The action potential peak amplitude, PA,

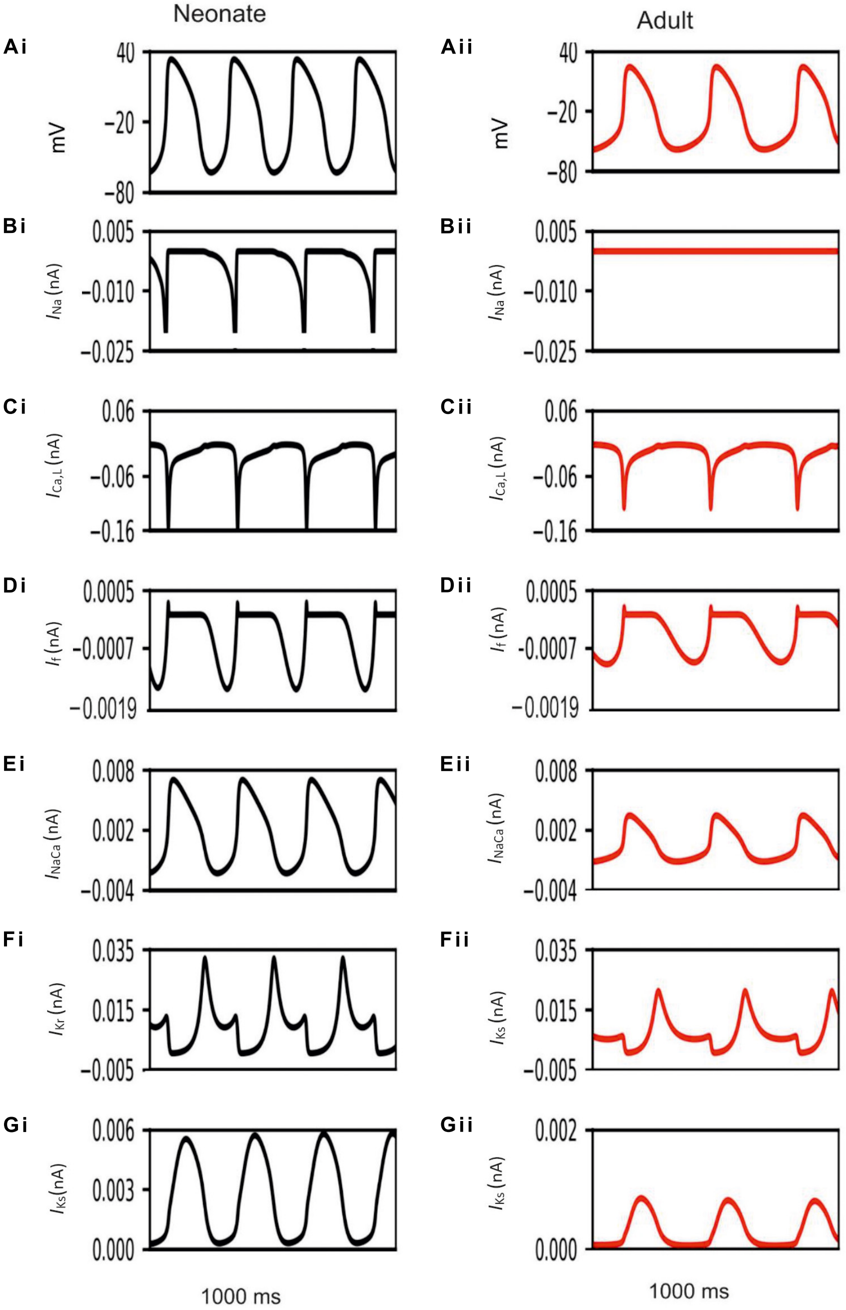

FIGURE 4 | Simulated central SAN action potentials in the neonate (black lines) and adult (red lines) **(Ai,Aii)** and underlying ionic currents I_{Na}, $I_{Ca,L}$, I_f, I_{NaCa}, I_{Kr} and I_{Ks} **(Bi–Gii)**.

TABLE 4 | AP characteristics of neonatal and adult central SAN cell model.

	References	PA (mV)	CL (ms)	MDP (mV)	dV/dt_{max} (V/s)
Neonate	Experiment (Baruscotti et al., 1996)	40.22 ± 8	280	−59.2 ± 2.2	14 ± 4.5
	Experiment (Allah et al., 2011)	–	246 ± 50	−53.5 ± 2.2	–
	Simulation (our model)	32.22	277	−63	11.99
Adult	Simulation (Zhang et al., 2000)	21.2	327	−57.31	2.76

of the neonate was greater than that of the adult (32 mV compared with 21 mV) in the central SAN model. These simulation results are consistent with experimental observations, as summarized in **Table 4**.

Our simulation showed a reduction of spontaneous AP rate with development, with the measured pacemaking rate of 217 min^{-1} in neonates and 170 min^{-1} in adults (**Figure 5**). The simulation results were in agreement with the experimental observations, which showed that the heartbeat of the rabbit SAN was around 200 ± 50 min^{-1} for neonates, but then reduced by 21.6% in the adult (Allah et al., 2011). The bar charts in **Figure 5** show a comparison of the AP characteristics of the neonatal and adult central SAN from simulations, which quantitatively matched experimental data, validating the model development and showing that the experimentally observed changes in ion channels are sufficient to account for the differences in spontaneous action potentials between the neonatal and the adult SAN cells.

As most available experimental data were acquired from the central SAN cells of neonatal rabbits, data on the peripheral SAN cells were lacking. In simulations, the same modification to ion channels as was implemented in the neonatal central cells was assumed to be applicable to the peripheral model. The resultant APs and the underlying ion channel currents are illustrated in **Supplementary Figure S3**.

Simulation results showed that the morphology of the neonatal APs of peripheral SAN cells was similar to that of the adult, but with some changed characteristics. The simulated CL in the neonate was smaller than that in the adult: 156 ms compared with 175 ms, indicating 12% reduction in the pacemaking rate by the development. Such heart rate reduction was attributable to the integral actions of altered I_{Na}, $I_{Ca,L}$, and I_f. The measured peak amplitude of the AP in the neonatal condition was greater than that in the adult condition, changing from 31 mV to 23 mV. The reduced AP amplitude by development can be explained by the reduced $I_{Ca,L}$. In addition, the peripheral cell model considered I_{Na}, but with a greater conductance and changes in the kinetics in neonates as compared with adults. The remodeled I_{Na} also contributed to the decreased maximal upstroke velocity of APs with developmental maturation. Furthermore, the computed MDP was more negative in the neonatal model than in the adult model, which helped to produce greater I_{Na}, $I_{Ca,L}$, I_f and I_{NaCa} during the diastolic phase that help to accelerate the pacemaker depolarization. The development-related remodeling of I_{Ks}, I_{Kr} and NCX had only small effects on the peripheral AP characteristics, which is discussed in the following section. Characteristics of simulated APs for both peripheral neonatal and adult SAN models are summarized in **Supplementary Table S1** and **Supplementary Figure S4**.

Functional Role of Individual Remodeling of Ion Channels in the Neonate Condition

The central and peripheral cell models were used to investigate the individual roles of each remodeled ion channel in modulating the SAN cell APs, in order to identify the major contributor to the fast neonatal AP rate. This was done by the exclusive method (each individual remodeled ion channel action was considered in turn), with results being compared to those from the inclusive method (i.e., all remodeled ion channel currents were considered in turn) for the neonate case. Results are shown in **Figures 6A,B** and summarized in **Table 5**. It was shown that changes of I_f, I_{CaL}, I_{Na} and NCX contributed to a decrease in CL, however, changes in I_{Kr} and I_{Ks} contributed to an increase in CL of the neonatal cell model, in both of the central and peripheral cell models.

Further analysis was conducted to evaluate possible functional roles of the age-dependent differences of I_{Na} on spontaneous APs, the results are shown in **Figures 7Ai,Aii** for the central and **Supplementary Figures S5Ai,Aii** for the peripheral SAN cells. In simulations, when the shift of the activation midpoint was considered alone (the AP and time course of the I_{Na} represented by green lines compared with the adult red lines), there was a marked reduction in neonatal CL in both central (by 99 ms) and peripheral (by 29 ms) cells compared with CL in the adult. When a reduced I_{Na} magnitude was considered alone (the AP and time course of I_{Na} are represented by blue lines compared with the adult red lines), the recorded CL was reduced by 72 ms in the center and 9 ms in the periphery compared with CL values in the adult. When both developmental effects on I_{Na} were considered (the AP and time course of the I_{Na} are represented by black lines compared with the adult red lines), the resultant APs were found to be faster than both of the previous changes, with an increase in the diastolic depolarization (phase 0), and a smaller CL by 123 ms in the center and 30 ms in the periphery compared to CL in the adult condition. Thus, a combined effect of the shifted activation curve and reduced current density of I_{Na} in neonatal SAN cells played a crucial role in influencing AP rate.

Figures 7Bi,Bii and **Supplementary Figures S5Bi,Bii** show the effect of age-related change of $I_{Ca,L}$ alone on the pacemaking APs for central and peripheral cell models. In simulations, the shift in the activation and inactivation midpoints alone reduced the CL by 20 ms in the center and 15 ms in the peripheral model as compared with the adult (represented by green lines compared with the adult red lines). When the current density of $I_{Ca,L}$ was increased (i.e., by modifying the conductance), a decrease in the CL by 12 ms was observed in the center, but

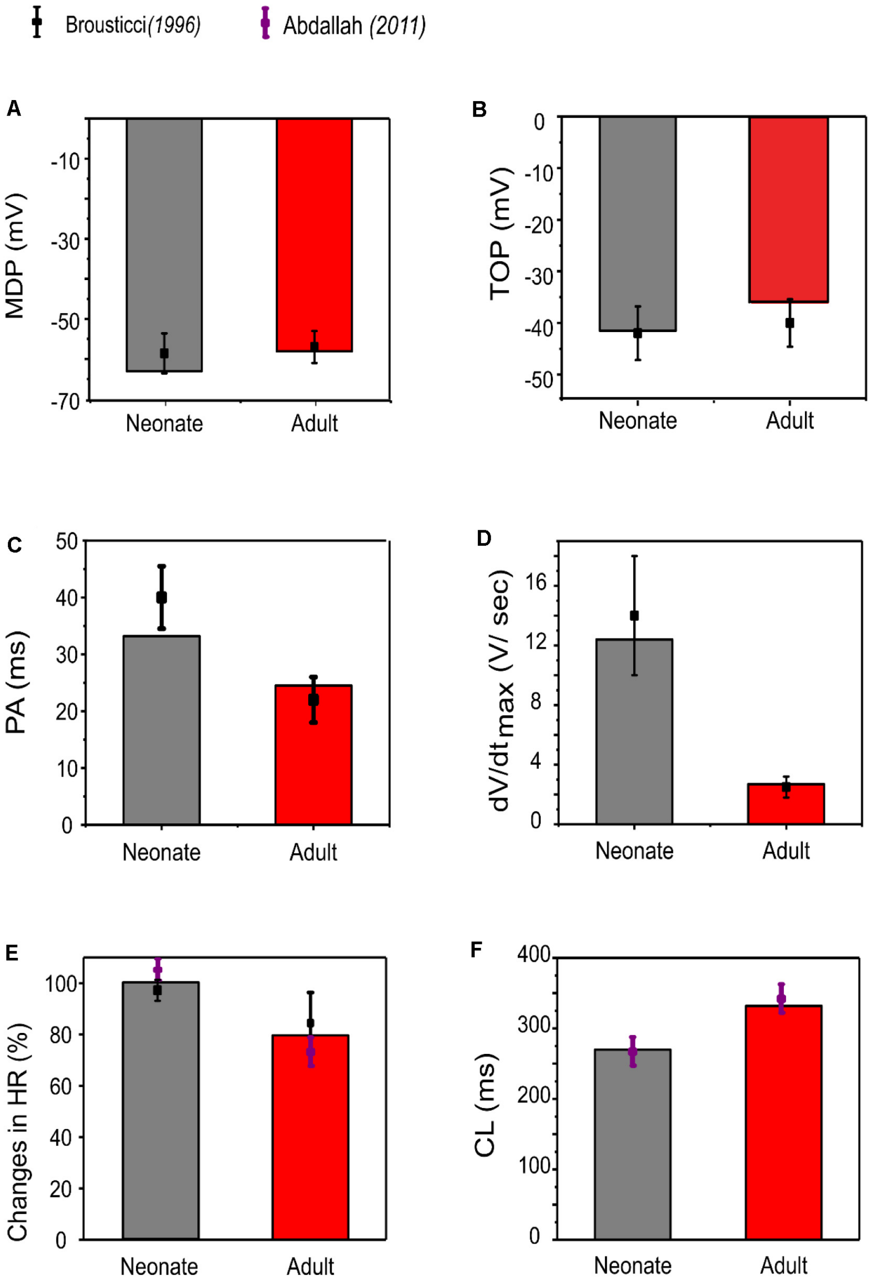

FIGURE 5 | Bar chart comparison of the main AP characteristics of central SAN. **(A)** MDP, **(B)** TOP, **(C)** PA, **(D)** dV/dt_{max}, **(E)** HR, and **(F)** CL in neonate (gray) and adult (red) rabbits. All characteristics were compared against experimental values from Baruscotti et al. (1996).

an increase of the CL by 20 ms in the peripheral model were observed (represented by blue lines) as compared to the adult APs (represented by red lines), which was due to the regional different contribution of $I_{Ca,L}$ (Zhang et al., 2000). When the shift in activation/inactivation curves and $I_{Ca,L}$ densities were considered together, the resultant APs were faster (represented by black lines) (CL being reduced by 24 ms in the center and by 5 ms in the periphery) with a decreased diastolic depolarization phase. This demonstrates that the opposite shift of the steady-state activation and inactivation curves is an important contributor as compared with the current density changes in modulating the pacemaking rate. It was also noted that the PA was greater in the neonate than in the adult by 7 mV in the center and 8 mV in the periphery, indicative of the contribution of the $I_{Ca,L}$ current to the diastolic depolarization phase (phase 0) and the plateau phase (phase 2).

Figures 7Ci,Cii and **Supplementary Figures S5Ci,Cii** elucidate the modulatory effect of the I_f current on spontaneous APs in the neonatal SAN. A shift of the steady-state activation curve by −7 mV reduced the CL by 5 ms in the center and 2 ms

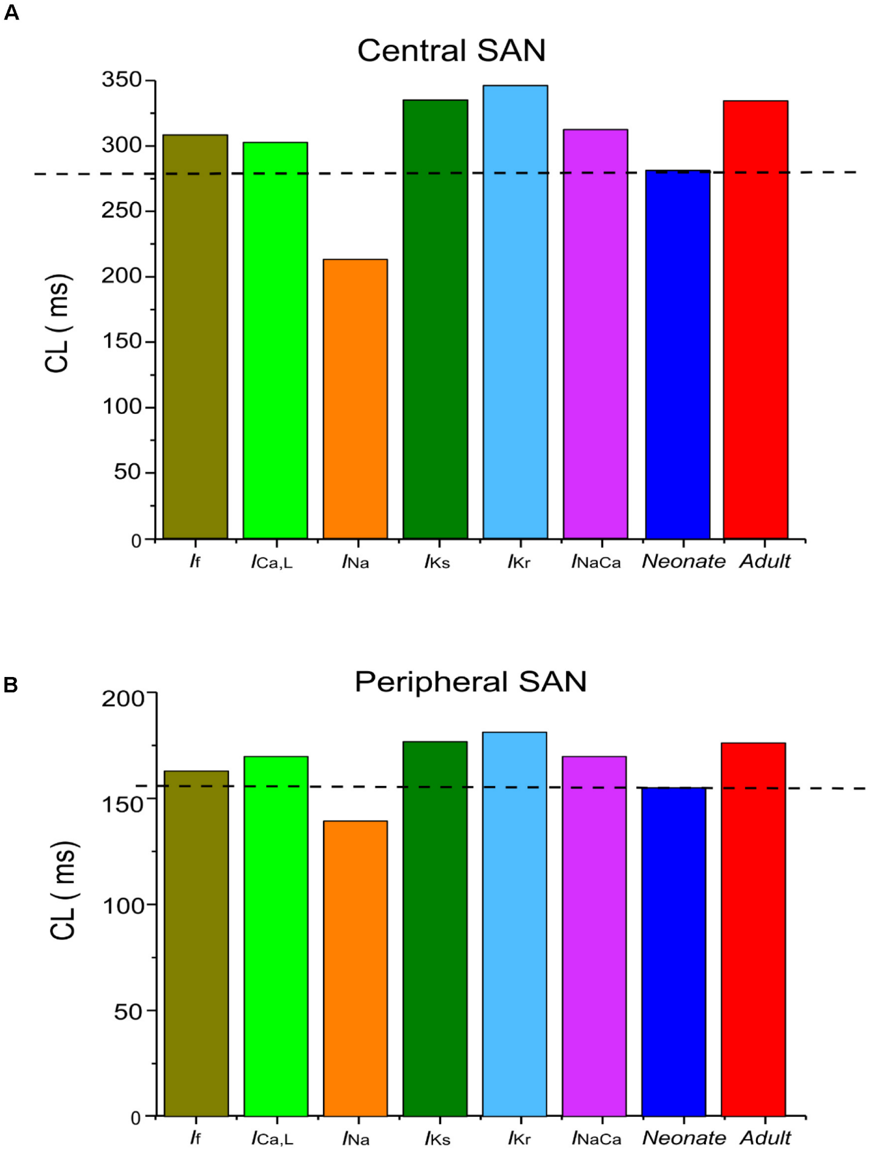

FIGURE 6 | Computed CL from **(A)** central and **(B)** peripheral SAN-cell models, when age-related change to each of the remodeled ionic-channel currents was considered alone.

in the periphery (represented by green lines compared with the adult red lines). An increase in I_f density alone produced a notable decrease in CL: by 16 ms in the center and by 12 ms in the periphery (represented by blue lines). A combined action of the shifted activation curve and increased current density of I_f produced a CL reduction by 21 ms in the center and 16 ms in the peripheral cell models (represented by blue lines).

Figures 7Di,Dii,Ei,Eii,Fi,Fii illustrate the effects of remodeled I_{Kr}, I_{Ks} and I_{NaCa} on pacemaking APs of the central cell model, while their effects on the APs of the peripheral cell model are shown in **Supplementary Figures S5Di,Dii,Ei,Eii,Fi,Fii**. An increase of the I_{Ks} by 27% as seen in the neonate did not lead to a significant change in the CL or the APs' morphology. When I_{Kr} was increased by 36%, there was a CL increase by 10 ms in the center, and by 2 ms in the periphery. An increase of the I_{NaCa} alone decreased the CL by 17 ms in the central model and caused a small change (5 ms) in the peripheral model. The overall ion channel remodeling effect on the computed CL is summarized in **Table 5**.

Figure 8 shows overlaid APs in neonatal and adult conditions, together with APs simulated from the adult model with consideration of postnatal development-related changes in I_{Na}, I_{CaL}, I_f, I_{NaCa}, I_{Kr} and I_{Ks} individually. It was shown that the observed changes in the MDP, AP, ADP between the neonatal and the adult cell models were generated by the integral actions of the considered ion channel and exchanger currents that are responsible for the maturation development of the

TABLE 5 | Effect of individual age-related remodeled ionic-channel currents on the CL of central and peripheral SAN-cell models.

	Center		Periphery	
	CL (ms)	Change in CL compared with adult (ms)	CL (ms)	Change in CL compared with adult (ms)
I_f	306	−21	159	−16
$I_{Ca,L}$	303	−24	170	−5
I_{Na}	204	−123	145	−30
I_{Ks}	327	0	175	0
I_{Kr}	337	+10	177	+2
I_{NaCa}	310	−17	170	−5
Neonate	277	−50	156.23	−18.77
Adult	327	0	175	0

pacemaking cycle length (CL). It was shown that when the postnatal development change in I_{Kr} or I_{Ks} alone was considered, a hyperpolarized maximal diastolic potential was seen, leading to an increase in CL as compared to the adult model, with the effect being more obviously seen in the increased I_{Kr} case than in the increased I_{Ks} case.

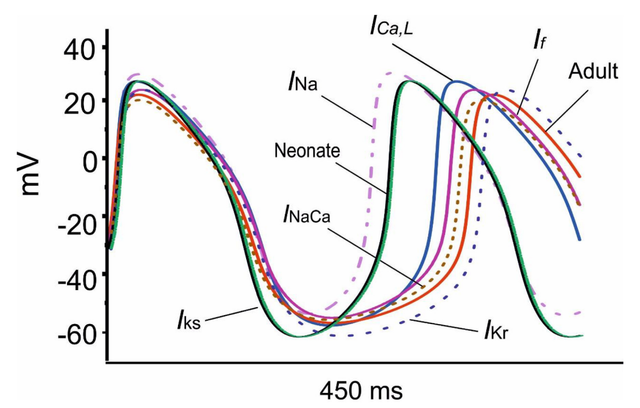

FIGURE 8 | Effect of an individual ion channel remodeling of maturation on modulation of the membrane action potential during the diastolic depolarization phase of SAN cells.

Effects of ACh on SAN Cell Activity

It is not known whether the negative chronotropic action of ACh is similar between adult and neonatal rabbit SAN cells.

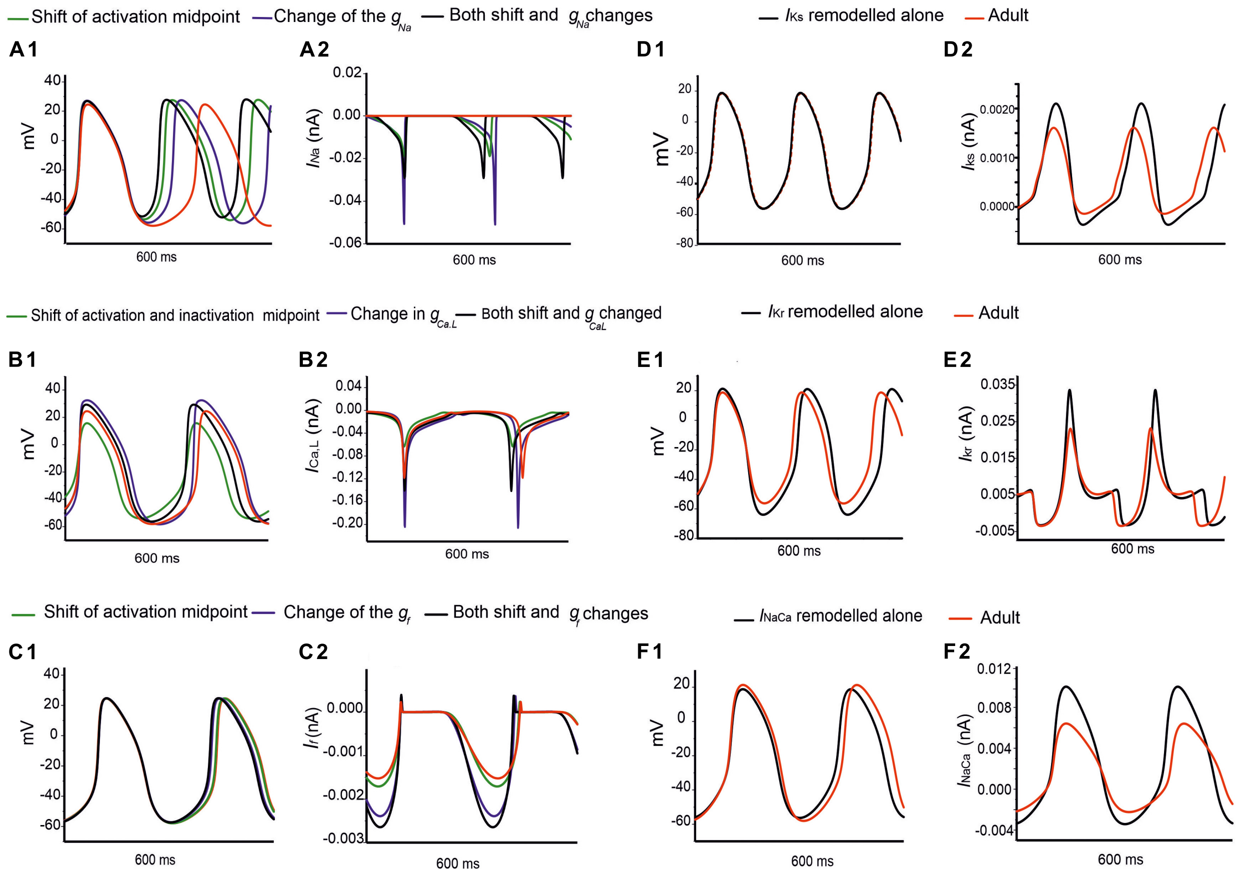

FIGURE 7 | Simulations of the effects of individual remodeled ion channels on modulation of pacemaking APs in the central SAN-cell model. Corresponding action potentials and underlying ionic currents are shown for **(Ai,Aii)** I_{Na}, **(Bi,Bii)** $I_{Ca,L}$, **(Ci,Cii)** I_f, **(Di,Dii)** I_{Kr}, **(Ei,Eii)** I_{Ks} and **(Fi,Fii)** I_{NaCa}.

Simulations were conducted to address this question, in which actions of ACh on APs were simulated at a physiological concentration of (5×10^{-8} M) for the neonate and adult conditions. Results are shown in **Figure 9**.

In the adult condition, ACh slowed down the pacemaking APs: the measured CL increased from 327 ms to 430 ms (by 30.4%) for the central cells, and from 175 ms to 219 ms (by 23%) for the peripheral cells (**Figures 9Ai,Aii**). It reduced the PA (from 23.8 mV to 18.38 mV, a decrease of 21.11% in the central cells; from 24.4 mV to 21.5 mV, a decrease of 10.6% in the peripheral cells). It also reduced the APD_{50} (by 13.33% in the center and by 11.9% in the periphery). It hyperpolarized the MDP, which changed from −57 mV to −61 mV in the center and from −80.88 mV to −81.4 mV in the periphery. This resultant negative chronotropic effect of ACh on the APs was attributed to the combination of the activation of $I_{K,ACh}$, partial depression of $I_{Ca,L}$ and the I_f activation shift.

Acetylcholine had a greater effect on modulating simulated APs in the neonatal than in the adult SAN cell models, which is consistent with previous experimental observations (Atkins and Marvin, 1989; Zhang et al., 2002). The changes in the CL under the influence of ACh were markedly greater in the neonatal condition: see the bar-chart comparison on the computed CL under WT and ACh effects for both cases in the central and peripheral cells in **Figures 9Ei,Eii**. This demonstrates that the negative chronotropic effects of ACh were grater in both the center and the peripheral cells of the neonatal models than in the adult ones. The PA changed from 32.5 mV to 14.5 mV (by 55.38%) in the central cells and from 30 mV to 28 mV (by around 13%) in the peripheral cells. There was a reduction in the APD_{50} values by 23.4% in the center and 13% in the periphery. The simulated MDP values for the APs were hyperpolarized from −62.8 mV to −64.6 mV in the center and from −82.04 mV to −83.53 mV in the periphery in the neonate. These changes were 2.8% and 1.8% for the central and peripheral cell models in the neonate condition. All these values are summarized in **Table 6**.

The dose-dependent effects of ACh on pacemaking APs in developing SAN were also investigated. **Figure 10** illustrates the results obtained from the central and peripheral cell models for both age groups under three different "physiological" ACh concentrations. Increase of the ACh concentration resulted in a monotonic increase of CL of the APs for both cell types, with greater effects in the neonate condition. At an ACh concentration of 7.0×10^{-8} M (**Figures 10Ci,Cii**), pacemaking was still occurred in the adult central SAN cells (though with a prolonged CL compared with the control condition) but became quiescent in the neonatal condition. The results for the peripheral cells showed less sensitivity to ACh at a concentration of 7.0×10^{-8} M compared with the central model, although the neonate was more affected than the adult. **Figures 10Di,Dii** summarizes the simulated dose-dependent effect of ACh on the CL recorded in both conditions. The concentration-response relation of the CL shifted leftward with developmental maturation, indicating an amplified effect of ACh on SAN cells in neonates.

Figure 11 shows the effects of various ACh concentrations on the primary AP characteristics of the neonate cell models (black symbols) compared with the adult cell models (red symbols). **Figures 11Ai,Aii** shows the changes in AP amplitude; **Figures 11Bi,Bii** shows the changes in APD_{50}; and **Figures 11Ci,Cii** shows the changes in MDP. For both age groups, all these changes in AP characteristics illustrate that the central cell shows more sensitivity to ACh than the peripheral cell.

AP Conduction in the Two-Dimensional Tissue Slice Model During SAN Development

Figures 12A,B shows snapshots of the initiation and conduction patterns of pacemaking APs in the 2D SAN-atrium model for both neonate and adult conditions at different time-points after impulse initiation. In both age groups, the AP propagation displayed a similar conduction sequence, but with a shorter conduction time and thus a greater conduction velocity in the neonate with respect to the adult. In both cases, the AP propagation first started slowly in the center of the SAN. Once initiated, it propagated preferentially from the center toward the periphery of the SAN, and then parallel to the crista terminalis (CT) before entering rapidly into the atrium in a direction toward the atrial septum. The AP conduction was blocked in the block zone, which was encircled by excitation waves from the superior and inferior tissues that surrounded the zone. Such simulated activation and conduction patterns are consistent with experimental observations (Dobrzynski et al., 2005).

The isochrones of the activation timing sequence of the SAN-atrium tissue for both conditions are shown in **Figures 13A,B**. The computed time taken to activate the whole tissue was less in the neonate (55–65 ms) than in the adult (75–95 ms). In association with this, the computed pacemaking CL showed an age-dependent increase, which changed from 290 ms in the neonate to 376 ms in adult tissue, equivalent to a decrease in the heart rate from 207 min^{-1} to 160 min^{-1} in the neonate and adult tissue respectively. This maturation development change in HR was qualitatively close to that observed experimentally from the intact SAN-atrial tissue of guinea pigs (**Figure 13C**) (Jones et al., 2004; Bai et al., 2017). The measured conduction velocity (CV) was also reduced by developmental maturation in the 2D SAN-atrium model (**Figure 13D**).

The Effect of ACh on Two-Dimensional SAN-Atrial Tissue

The single cell simulations showed higher sensitivity of neonatal SAN cells to ACh as compared to the adult, which has also been observed experimentally (Atkins and Marvin, 1989; Yang et al., 2006). Further simulations were conducted to evaluate the functional consequence of ACh on AP conduction in the 2D model of intact SAN-atrium in neonatal and adult conditions.

As at the single cell level, our simulation results implied that when the ACh concentration value was above 8×10^{-8} M in neonatal condition, the AP of the central model was suppressed.

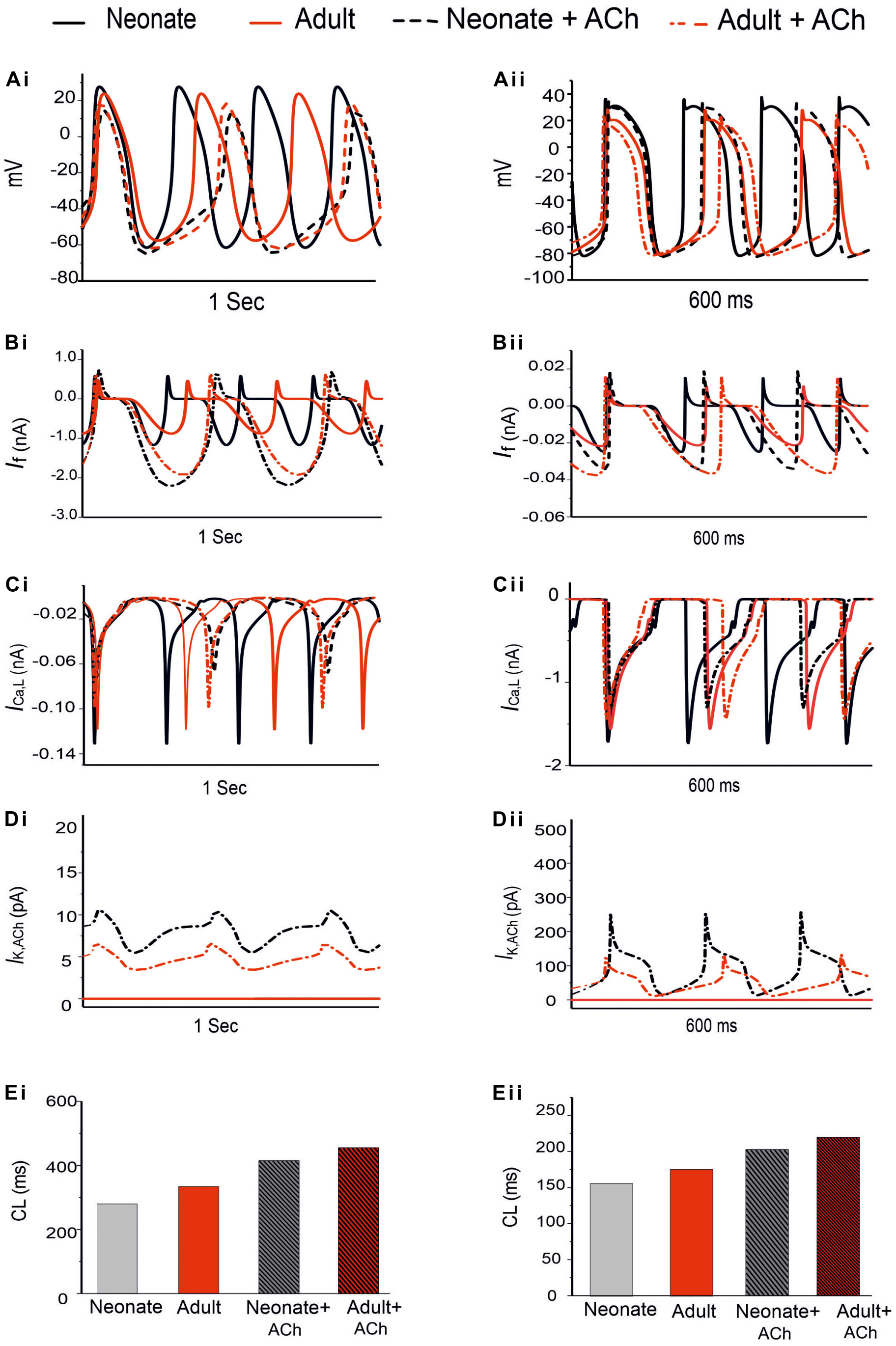

FIGURE 9 | Effect of ACh on the SAN pacemaking APs. Both neonate and adult conditions are shown for the central **(Ai)** and the peripheral SAN cells **(Aii)**; ACh concentration for both conditions was [ACh] = 5 × 10^{-8} M. **(Bi,Bii)** Time course of I_f current. **(Ci,Cii)** Time course of the $I_{Ca,L}$ current. **(Di,Dii)** Time course of $I_{K,Ach}$ current. **(Ei,Eii)** Bar-chart comparison on the computed CL under WT and ACh effects for both cases in the central and peripheral cells.

Therefore, in the 2D model simulations, two physiological values for ACh (3 × 10^{-8} M, 8 × 10^{-8} M) were used.

Supplementary Figure S6 provides snapshots of the AP initiation and conduction sequences in the 2D model for both neonate and adult conditions. With application of ACh ([ACh] = 3 × 10^{-8} M), in both cases, the wave propagation pattern is similar to that seen in the control condition, but with a slower conduction velocity and pacemaking rates (the measured CL changed from 290 ms to 454 ms (by 30%) in the neonate; and changed from 366 ms to 411 ms (by 12.3%) in the adult tissue). The greater effect of the ACh in the neonate as compared with the adult in the tissue

TABLE 6 | The negative chronotropic effect of ACh is shown on the pacemaking APs in central and peripheral rabbit SAN cells, at a physiological concentration of 5 × 10^{-8} M for the neonate and adult conditions.

		Neonate			Adult		
		No ACh	ACh 5 × 10^{-8} M	Change %	No ACh	ACh 5 × 10^{-8} M	Change %
Center	MDP (mV)	−62.08	−64.6	↑2.8	−57	−61	↓7
	PA (mV)	32.5	14.5	↓55.38	23.8	18.38	↓21.11
	CL (ms)	277	403	↑47	327	430	↑30.0
Periphery	MDP (mV)	−82.04	−83.53	↓1.8	−80.88	−81.0	↓2.4
	PA (mV)	30	28	↓13	24.4	21.5	↓10.6
	CL (ms)	156	202.37	↑27	175	219	↑ 23.0

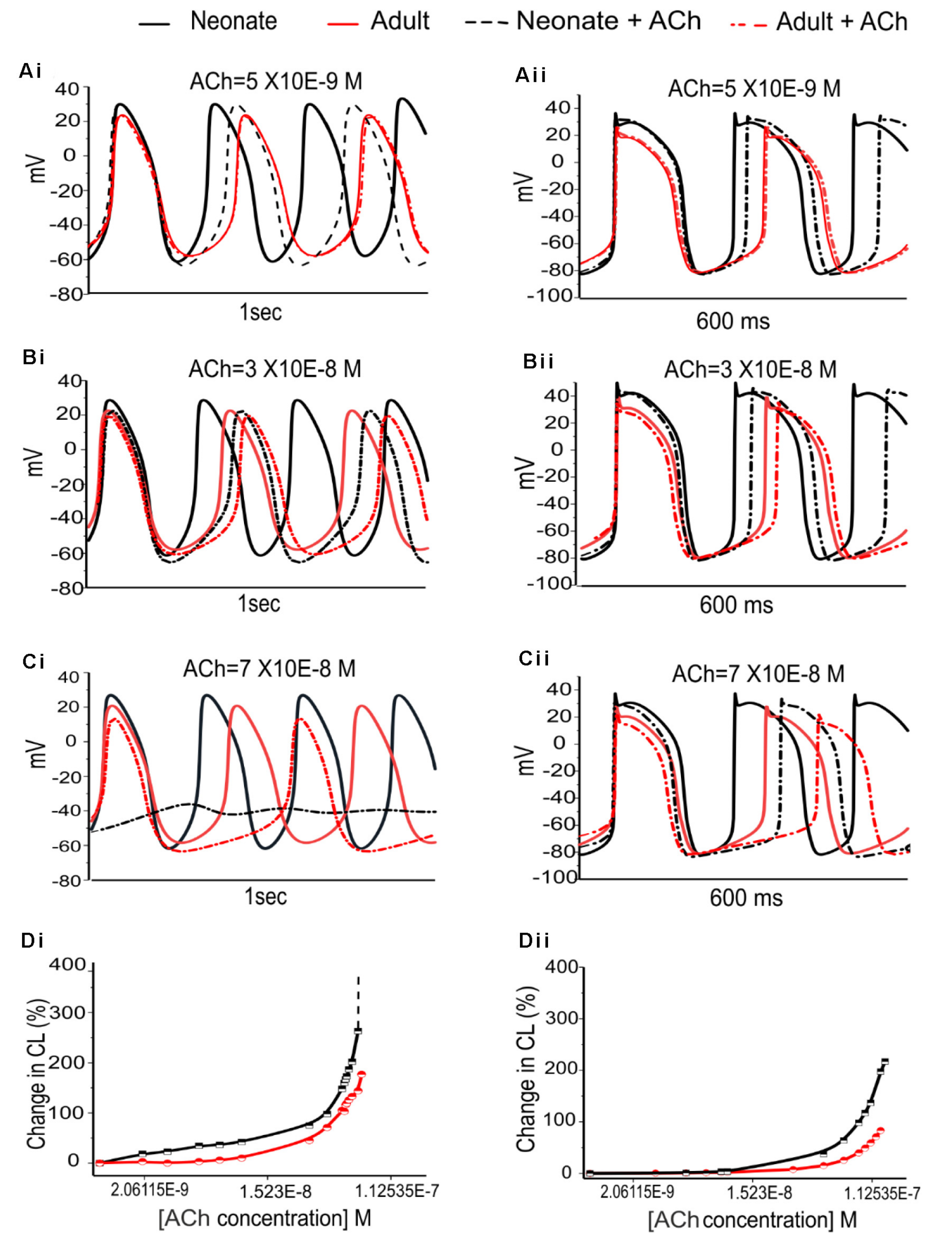

FIGURE 10 | Dose-dependent effects of ACh on spontaneous APs of the SANs for the neonate and adult. **(Ai,Aii)**: At [ACh] = 5 × 10^{-9} M. **(Bi,Bii)**: At [ACh] = 3 × 10^{-8} M. **(Ci,Cii)**: At [ACh] = 7 × 10^{-8} M. **(Di,Dii)**: Dose-dependent effects of ACh on pacemaking CL for the central and peripheral SAN cells, respectively. The black line represents the neonate condition and the red line represents the adult condition.

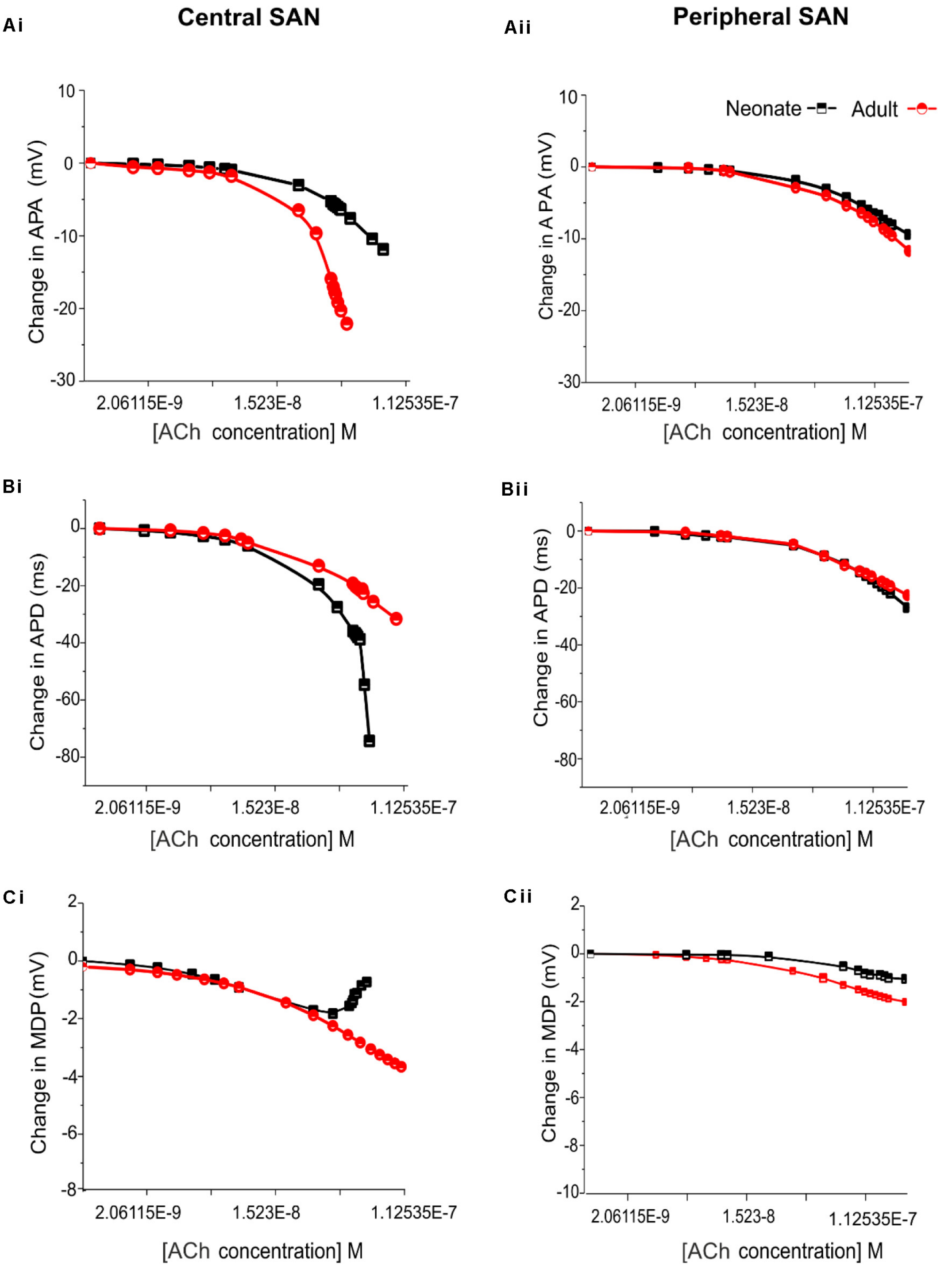

FIGURE 11 | Concentration-dependent effects of ACh on the AP characteristics of rabbit central and peripheral SAN cells for neonate (black squares) and adult (red circles) conditions. **(Ai,Aii)**: Action potential peak amplitude (PA). **(Bi,Bii)**: Action potential duration (APD_{50}). **(Ci,Cii)**: Maximal diastolic potential (MDP).

simulations was consistent with the simulation results at the single-cell level.

When ACh concentration was increased as shown in **Supplementary Figure S7**, with [ACh] = 8×10^{-8} M, there was a further reduction in the wave propagation velocity within the SAN and atrium tissue, but a more marked increase in the computed pacemaker CL (by 49%). The resulting decreased conduction velocity and increased CL have been observed experimentally for the adult rabbit SAN (Rana et al., 2010). Interestingly, ACh caused a shift of the leading pacemaker

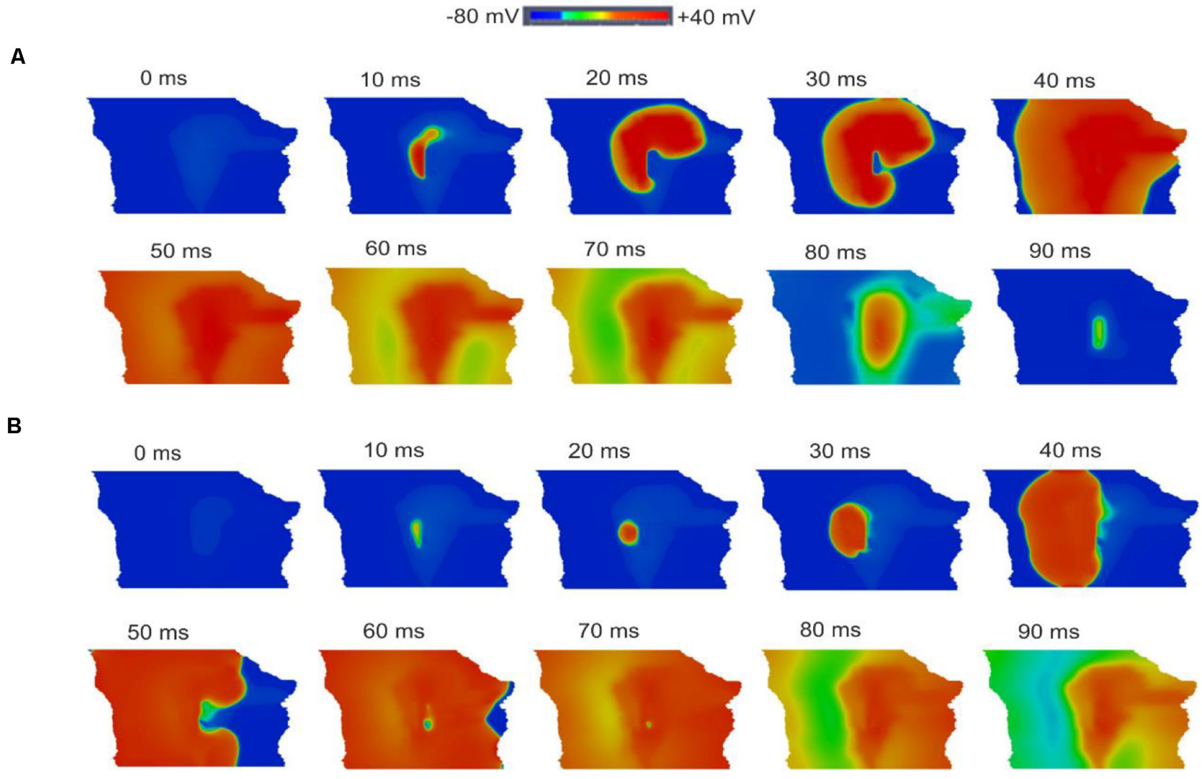

FIGURE 12 | Snapshots of AP initiation and conduction patterns in the 2D model of intact SAN-atrial tissue in the neonate **(A)** and adult **(B)** conditions.

site to the peripheral region in the neonatal condition. As the new leading pacemaker was far from the original location, the conduction pathway was altered, leading to differences in the activation timing and conduction velocity in the neonate tissue between the control and ACh conditions (for details see **Table 7**). The simulated pacemaking shift in response to ACh was consistent with previous experimental observations, in which the leading pacemaker was shifted in response to vagal nerve stimulation (Spear et al., 1979; Shibata et al., 2001; Zhang, 2011).

Quantitative analyses were also performed to investigate the effect of postnatal development effect on AP activation timing and the AP conduction velocity in the intact SAN-atrial tissue model. **Figure 14A** plots the measured activation timings from the representative cells across the middle of the 2D neonate tissue for control (black curve) and ACh = 8×10^{-8} M conditions (blue line), which were compared with those obtained from the adult tissue in control (red curve) and ACh = 8×10^{-8} M conditions (green line). In the adult, the activation timings across the tissue increased. With ACh, the activation time for the neonate was reduced in the direction toward the atrial septum (blue line) due to the shift of leading pacemaking site. The corresponding average conduction velocity across the tissue is shown in **Figure 14B**. The conduction velocity under control for the neonate condition was found to be greater than that for the adult: approximately 0.30 m/s in the neonate and 0.26 m/s in the adult along the CT. This age-dependent reduction in the CV is in accordance with the increased activation time in the direction toward the CT during developmental maturation. Application of higher ACh concentrations may lead to a further reduced conduction velocity and increased CL and may even impair the SAN to drive the atrial muscle, leading to a “SAN conduction exit block.” Both developmental maturation changes of the activation time and conduction velocity seen in simulations seen in **Figures 14C,D** were reasonably comparable with the experimental observations from guinea-pig SAN tissue (Jones et al., 2004).

DISCUSSION

In this study, we have modified the rabbit SAN model developed by Zhang et al. (2000) to simulate the APs of the neonatal SAN based on available experimental data from immature rabbit cells for some major underlying ionic channel currents (details are reported in **Tables 1–3**). The developed model successfully reproduces the morphology of neonatal SAN APs with their characteristics quantitatively matching experimental data, validating the cell model development (Baruscotti et al., 1996). Using the inclusive method, we showed that the implemented changes in ion channels (as listed in **Tables 1–3**) due to postnatal development are sufficient to account for the observed changes in pacemaking action potentials between the neonatal and the adult SAN cells. This may have important implications for the diagnosis and

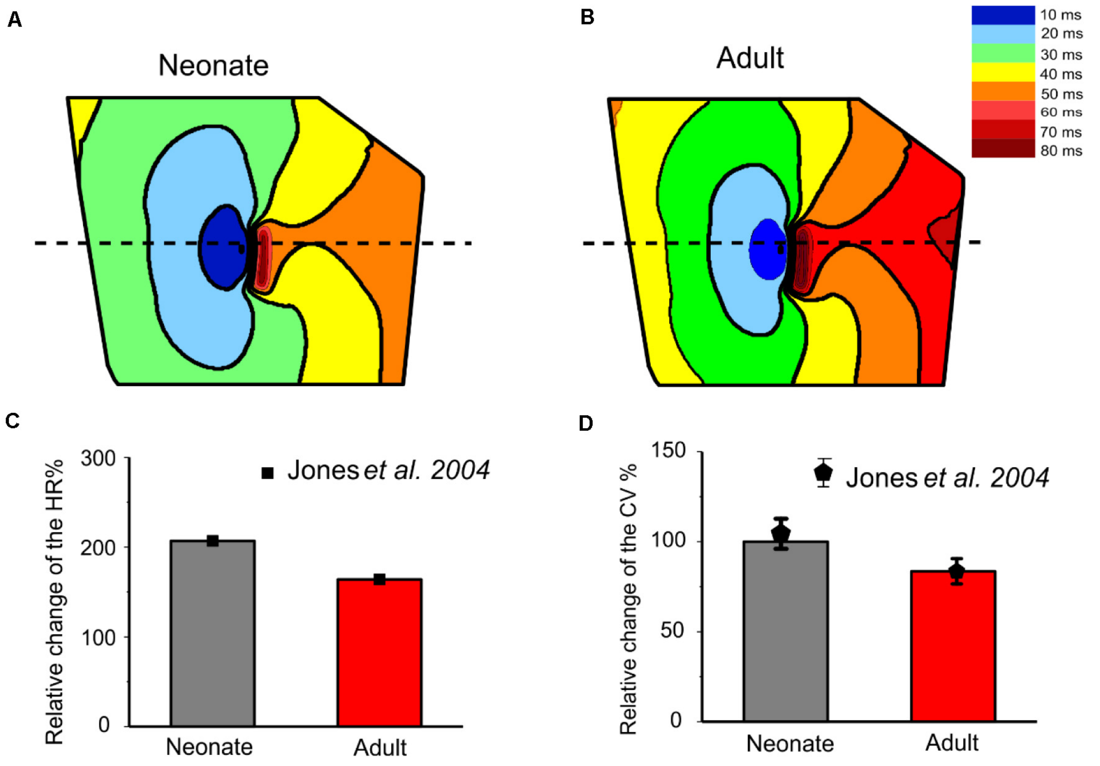

FIGURE 13 | Isochrones of the activation map in 2D rabbit intact SAN-atrial models for both neonatal **(A)** and adult **(B)** conditions. The activation timing in the model was recorded every 10 ms, as illustrated with various colors, which changed from blue at 0 ms to dark red at 80 ms. The bar chart **(C)** shows the reduction of HR and **(D)** the conduction velocity (CV) with developmental maturation in the 2D SAN-atrium, compared with experimental values from Jones et al. (2004).

TABLE 7 | Simulated CL and averaged CV in control and ACh for both neonate and adult central SAN cell models.

	Cycle length (ms)	Conduction velocity along the SAN (m/s)	HR (b/m)	Reduction of the HR under ACh (%)	HR (b/m) (Jones et al., 2004)
Neonate	290.7	0.30	206.0	0.0	250.0 ± 60.0
Neonate + ACh (3×10^{-8} M)	377.21	–	159.1	22.8	–
Neonate + ACh (8×10^{-8} M)	569.00	0.18	105.4	49.0	–
Adult	366.21	0.26	163.0	0.0	160.0 ± 20.06
Adult + ACh (3×10^{-8} M)	411.32	–	150.0	8.0	–
Adult + ACh (8×10^{-8} M)	536.1	0.21	111.9	31.13	–

treatment of cardiac rhythm disorders in the immature and adult individuals. Using the "exclusive" method, we further analyzed the functional role of individual post-developmental ion-channel remodeling on the APs, by which the major contributor to the fast pacemaking rhythm of the neonate hearts was elucidated. The functional impact of age-related ion-channel remodeling on AP propagation in a 2D model of the intact rabbit SAN-atrium tissue were also investigated. Effects of ACh on pacemaking APs and their conduction were also investigated to elucidate the mechanisms that underlie the post-developmental difference of vagal tone modulation on cardiac pacemaking activities.

The major findings of this study are: (1) at the single cell level, neonatal mathematical models produced higher frequency APs in both the central and peripheral SAN cells with a higher upstroke phase as compared to adult APs. These differences may be attributable to the ion channel remodeling of I_{Na} and I_f in the developing SAN. The resultant APs at neonatal age showed greater peak amplitude values and smaller APD values, which can be attributed to the post-developmental changes of $I_{Ca,L}$ and I_{NaCa}; (2) at the tissue level, the post-neonatal changes in cellular APs are reflected by a decrease in the pacemaking rate and AP conduction velocity across the SAN-atrium; (3) acetylcholine had a greater effect on modulating AP pacemaking and conduction

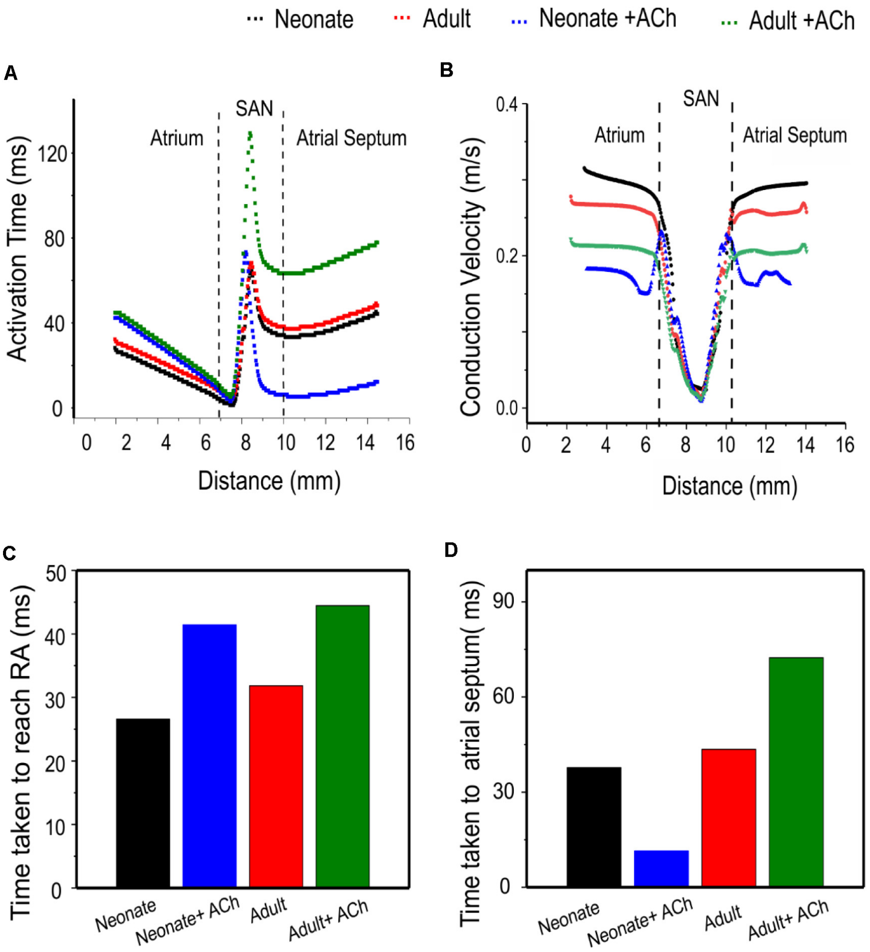

FIGURE 14 | Postnatal development effects on AP conduction across the tissue in the 2D intact SAN-atrium slice. **(A)** Activation time profile and **(B)** conduction velocity of the neonate (black line) as compared with those in the adult (red line) under the effect of WT and ACh at a concentration of [ACh] = 8 × 10^{-8} M on the neonate (blue line) and adult (green line). **(C,D)** Bar charts showing the increase in time taken for APs to reach the RA, and the relative change of the conduction velocity with maturation development.

in the neonate compared to the adult. A high concentration of ACh in the neonate not only slowed down AP propagation, but also compromised the ability of the SAN to pace and drive the atrium. It could also produce a leading pacemaking site shift to the periphery. These findings together increase understanding of the ion channel mechanisms underlying the different pacemaking activity between the neonatal and the adult SAN cells and their response to acetylcholine, which may be of relevance to understand factors responsible for risk of cardiac arrest (e.g., the "cot death syndrome") in new-born babies during sleep when the vagal tone is more active.

Role of Postnatal Ion-Channel Remodeling on Pacemaking Activity

At the cellular level, our simulation results reproduced the development-dependent changes in pacemaking APs and their characteristics, such as the pacemaking rates, between neonatal and adult SAN as observed experimentally (Baruscotti et al., 1996). Further analyses of the role of each individual remodeled ion channel of I_{Na}, $I_{Ca,L}$, I_f, I_{Kr}, I_{Ks} and I_{NaCa} by the "exclusive method" elucidated the contribution of each of these channels to the faster pacemaking Aps observed in the neonatal group compared with the adult group.

Role of I_{Na}

Our simulation results suggested that (i) the presence of I_{Na} in the neonate central cells is the one of the major factors responsible for their faster pacemaking activity (i.e., short CL) than that in the adult. This finding is consistent with a previous study (Baruscotti et al., 1996), showing that I_{Na} was present in rabbit central SAN cells at birth, but fully disappeared by the 40th postnatal day. In the earlier experimental study, the functional role of the current was assessed by applying a Na^+ channel blocker, TTX, at a concentration of 3 μM and measuring the spontaneous activity of the APs in both the neonatal and adult cells in the SAN. It was found that TTX modified the action potential parameters of the neonatal cells, including a reduction of the upstroke velocity, a decrease in the diastolic depolarization slope from 0.035 to 0.015 V/s, and the consequent slowing down of the pacemaking rate by 60%. However, in the adult cells from the central SAN, I_{Na} was absent and application of TTX did not show changes in their APs; (ii) the marked developmental maturation change in the I_{Na} channel properties also contributes to the faster pacemaking APs in the central neonate SAN cells. In the neonatal SAN cells, a noticeable window I_{Na} current, resulting from the overlap between activation and inactivation curves of the current, provides a depolarizing current in the diastolic phase, accelerating pacemaking APs in neonates. However, with development, the position of the activation curve shifts in the positive direction while the inactivation curve remains, resulting in a reduced overlap of the two curves and hence the window current slowing down the depolarization.

Role of $I_{Ca,L}$ and $I_{Ca,T}$

Our simulation results showed that the age-related modulation of $I_{Ca,L}$ has a secondary contribution to the faster pacemaking rate of the neonate. The greater $I_{Ca,L}$ density in the neonate and the modulation of $I_{Ca,L}$ kinetics with maturation development (activation curve shifted to the left, steady-state inactivation curve shifted to the right) also play an important role in the high peak value of the APs in the neonate. However, in the adult, although the current density of the $I_{Ca,L}$ in the central cells was found to be smaller than in the neonate, the opposite shift in activation and inactivation curves during the developmental course resulted in a greater window current in the adult, providing more depolarizing Ca^{2+} current during the depolarization phase of the AP in the adult (Protas et al., 2017), which slowed down the repolarization phase, forming the secondary cause of the fast HR in neonates. Despite the fact that there were recorded changes to the HR between the neonate and adult SAN cells, the absence of developmental changes in $I_{Ca,T}$ may indicate that this current does not make a major contribution to the different ion currents regulating the APs in central rabbit SAN during development. However, this can vary among different species, as cellular electrophysiology experiments on mice in different age groups showed an age-dependent decline of the heart rate accompanied by a significant decrease of $I_{Ca,T}$ conductance densities in adult SAN currents (Larson et al., 2013).

Role of I_f

The present study also demonstrated an association between the age-dependent difference in current density and the modulation of the I_f activation curve in SAN cells, causing a slowing of pacemaking rate during postnatal development. Previous studies demonstrated that the pacemaker current, I_f, exhibited an developmental maturation decrease in current density which was assumed to result from a reduction in baseline cAMP levels in the SA node, suggesting that the combined action between the I_f channels and the reduced number of cAMP molecules are the main cause of the shift in the activation curve toward hyperpolarization in the adult group, leaving fewer I_f channels available to initiate diastolic depolarization, a key determinant of the heart rate decrease of the SA node (Accili et al., 1997; Yang et al., 2006).

Role of Other Channel Currents

Based on the measurement of gene-expression levels, the great abundance of I_{Kr}, I_{Ks} and I_{NaCa} in the neonatal SAN is of relatively small consequence for developmental maturation differences in pacemaking (Vinogradova et al., 2000). In addition, the mechanism of the Na^+/Ca^{2+} exchange merits study as it is intimately associated with other components of Ca^{2+} homeostasis, such as sarcoplasmic reticular Ca^{2+} stores and release mechanisms, both of which change with postnatal development in other cardiac regions, but not in neonatal SAN (Kaplan et al., 2007). The contribution of the delayed rectifier K^+ currents and Na^+/Ca^{2+} exchange current to SAN pacemaking in adults has been previously studied (Tibbits et al., 2002; Janowski et al., 2006; Kaplan et al., 2007), but the role of developmental changes in K^+ currents in the sinus node remains unexplored (Irisawa et al., 1993; Vinogradova et al., 2000).

Postnatal Effect on AP Conduction in SAN-Atrial Tissue

At the tissue level, our results show that the combined effect of ion-channel remodeling and the reduced intercellular electrical coupling alters the conduction properties of the APs across the tissue, thereby impairing the function of the SAN with maturation development. The simulation results on the increased conduction time and reduced conduction velocity in the adult tissue are consistent with experimental observations of changed conduction velocity and time taken for the APs to travel toward the RA from guinea pigs (Jones et al., 2004), which demonstrated a link between the progressive increase in the area of SAN tissue lacking the Cx43 protein and the decrease in the intrinsic HR A previous study of intact SAN-atria in guinea pigs during their lifespan (Jones et al., 2004). Without considering the connexin remodeling, ionic-channel remodeling alone resulted in multiple leading pacemaking sites (**Supplementary Figure S8**), which implied a functional role of connexin remodeling with developmental maturation to ensure a normal pacemaking AP initiation and conduction in the intact SAN-atrium tissue. According to a number of experimental studies (Woods et al., 1976; Yanni et al., 2010; Bai et al., 2017), the electrotonic interaction between the SAN and the atrium affects the pacemaking APs of the SAN cells, leading to a depression in the pacemaking APs. Thus, the magnitude of the CL at the tissue level is greater than that of the isolated single SAN cells.

Effects of Acetylcholine on the SAN During Developmental Maturation

The chronotropic responsiveness of developing sinoatrial myocytes to acetylcholine (ACh) has been studied (Atkins and Marvin, 1989; Accili et al., 1997). This study elucidated possible mechanisms underlying the increased responsiveness of the neonate SAN cells to ACh. Our simulation results show that the large current density of $I_{K,ACh}$ in the neonate SAN cells plays a major role in this responsiveness, together with greater densities of I_f and $I_{Ca,L}$, which play an important secondary contribution to this significant effect of ACh in neonate SAN cells. At both cellular and 2D-tissue levels, a more suppressive effect of ACh on the neonate pacemaking rate in SAN has been observed with increased ACh concentrations, which is comparable with experimental observation (Atkins and Marvin, 1989). Above a critical concentration ($>8 \times 10^{-8}$ M), ACh not only slows down the pacemaking rate in SAN cells, but also shifts the leading pacemaking site from the SAN to the periphery (**Supplementary Figure S8**). In comparison, in the adult tissue, previous studies have demonstrated that the leading pacemaker can be shifted within the SAN in response to vagal nerve stimulation (Spear et al., 1979; Shibata et al., 2001; Zhang, 2011). These studies revealed that the application of specific concentrations of ACh (above 15×10^{-8} M) may trigger a leading pacemaker site shift alongside the CT, usually toward the superior vena cava but occasionally toward the interior vena cava. The observed notable increase in the activation timing and decrease in the AP conduction velocity underlies possible conduction failure from the SAN to the atrium, providing a potential mechanistic insight into bradycardia-related dysfunction under conditions of high vagal tone.

Limitations of the Study

This study was based on mathematical models of the APs of adult rabbit SAN cells, which inherited some limitations that have been described previously in the literature (Zhang et al., 2000; Bai et al., 2017). The model developed for the neonatal SAN cells was based on data from various sources. Specifically, the formulations and the current densities of I_{Na}, $I_{Ca,L}$ and I_f were based on voltage-clamp data from newborn rabbit SAN cells, while data on I_{Kr}, I_{Ks}, $I_{K,ACh}$ and I_{NaCa} were based on data from messenger RNA gene expression or protein levels, as no experimental data on their kinetic or current densities in the SAN cell is available. In model development, we assumed there is a correlation between the gene expression or protein level for certain ion channel subunits and their current densities. However, such correlation may be non-linear and is still unclear. Remodeling of connexin Cx43 was based on data from guinea-pig SAN tissue. Though it is necessary to make clear these limitations, it is an accepted practice in computational modeling to use data from other species when there is a lack of data from the target species (Bai et al., 2017). In addition, our simulations were based on extant data only on ion-channel remodeling, but other factors such as remodeling in Ca^{2+} handling (Allah et al., 2011), ionic homeostasis and energy metabolism, or changes in the phosphorylation levels have not been considered due to lack of available data or because extant mRNA data showed no significant changes (Allah et al., 2011). Such factors may also be of significance in modulation of postnatal pacemaking APs. In addition, the simulation of maturation-related changes in I_{Kr} and I_{Ks} was based on the quantitative PCR data from neonatal and adult rabbits (Allah et al., 2011) as there are no direct experimental electrophysiology data that we can use to modify the model. Such data were used to scale conductance, rather than kinetic properties such as the activation and deactivation time constants. Our results (**Figure 8**) though showed that the postnatal development change in I_{Kr} and I_{Ks} hyperpolarized the maximal diastolic potential, but they slowed down, rather than accelerated the pacemaking APs as compared to the adult model. Interpretation of the results on the role of postnatal development related changes in I_{Kr} and I_{Ks} in modulating neonatal pacemaking APs needs to be cautious and requires further improvement when more voltage-clamp data become available. However, it is notable that the simulated neonatal pacemaking APs matched well prior experimental data from newborn rabbit SAN cells (Baruscotti et al., 1996; Allah et al., 2011), which validates the model development and justifies the use of parameters for the mathematical model of neonatal rabbit SAN cells.

In simulation of the effects of acetylcholine, it would be valuable also to study the effect of acetylcholine in the presence and absence of adrenergic tone. In the present study, we considered the acetylcholine action only, a computational approach to investigate how ACh alone modulates pacemaking action potentials of isolated SAN cells in neonatal and adult conditions. This is a conventional approach that has been used to investigate the effect of ACh on modulating cardiac pacemaker activity in previous studies by us and others in various conditions, such as sick sinus syndrome and atrial arrhythmogenesis (Butters et al., 2010; Muñoz et al., 2011; Bai et al., 2017). However, this approach presupposes the absence of concomitant adrenergic tone. Further work is warranted to determine the consequences of different levels of sympatho-vagal balance.

The 2D anatomical tissue model considered the anisotropic and electrical heterogeneity of the SAN-atrial tissue, providing valuable insights into the age-related effect on the AP initiation and conduction pathway in the SAN and surrounding tissue. However, further 3D anatomical models that considered tissue anisotropy, heterogeneity and spatial structure might be more useful to investigate the initiation and conduction of APs in control or ACh conditions (e.g., the phenomenon of leading pacemaking site shift). Moreover, the tissue geometry used in the neonatal case here was similar to that in the adult. It has been reported that during the growth of the rabbit, the heart weight and cell diameter increases for the central and peripheral SAN and/or atrial tissue, suggesting that the AP conduction distance may increase with development (Baruscotti et al., 1996; Allah et al., 2011). Further research is therefore required to determine the tissue geometry in neonate rabbit intact SAN-atrial tissue. In addition, in the tissue model we did not consider possible postnatal changes in atrial electrophysiology and used a cell model of the adult rabbit atrial cell due to the lack of experimental data. This limitation demands further improvement when more experimental data become available.

CONCLUSION

This simulation study is of significance for three reasons. First, it provides an updated computational model for neonatal rabbit

SAN cells. The model has been well validated and can be further used to study the key mechanism responsible for the fast heart rate in neonatal hearts, which may have value for the understanding and treatment of cardiac rhythm disorders in the immature, adult, and aged individuals. Second, the results of the study help understand the dramatic differences in the initiation and conduction of APs at the cellular and tissue levels between neonates and adults. Third, ionic mechanisms responsible for the high sensitivity of neonatal SAN cells to acetylcholine were elucidated. The observation of an amplified effect of ACh in the neonates leading to possible sinus arrest or conduction exit block may be of relevance to cardiac dysfunction in the very young, under situations of high vagal tone.

DATA AVAILABILITY STATEMENT

The original contributions presented in the study are included in the article/**Supplementary Material**, further inquiries can be directed to the corresponding author.

AUTHOR CONTRIBUTIONS

HZ conceived and designed the study, developed the model, analyzed and interpreted the data, and supervised and wrote the manuscript. AA developed the model, performed the experiments, collected the data, analyzed and interpreted the data, and wrote the manuscript. CT analyzed the data, and edited the manuscript. DW analyzed the data, and edited the manuscript. MB developed the model, analyzed the data, and edited the manuscript. JH developed the model, analyzed and interpreted the data, and wrote the manuscript. All authors contributed to the article and approved the submitted version.

FUNDING

This work was funded by, King Abdul-Aziz University KAU, Jeddah, Saudi Arabia; University of Jeddah, Jeddah, Saudi Arabia, and supported by a scholarship from the Saudi Cultural Bureau, London, United Kingdom, and by grants from EPSRC (United Kingdom) (EP/J00958X/1 and EP/I029826/1), United Kingdom.

SUPPLEMENTARY MATERIAL

The Supplementary Material for this article can be found online at: https://www.frontiersin.org/articles/10.3389/fphys.2020.547577/full#supplementary-material

Supplementary Figure 1 | Sensitivity analyses of the change of the CL as a function of the conductance for I_{Na} **(A)**, $I_{Ca,L}$ **(B)**, and I_f **(C)**.

Supplementary Figure 2 | The gradient distribution in **(A)** cell capacitance (C_m) and **(B)** diffusion (D) in both longitudinal and transverse directions of the 2D tissue slice. Figure adapted from Bai et al. (2017). The decline of the Cx43 protein expression in the SAN of rat represented as percentage during developmental maturation **(C)** (Jones et al., 2004).

Supplementary Figure 3 | Simulated peripheral SAN action potentials in the neonate (black lines) as compared with the adult (red lines) **(Ai,Aii)** and their underlying time courses of ionic channel currents I_{Na}, $I_{Ca,L}$, I_f, I_{NaCa}, I_{Kr}, and I_{Ks} **(Bi–Gii)**.

Supplementary Figure 4 | Bar chart comparison of the main AP characteristic of peripheral SAN cells: MDP **(A)**, TOP **(B)**, PA **(C)**, dV/dt_{max} **(D)**, reduction of HR **(E)**, and CL **(F)** in the neonate (gray) corresponding to the adult (red).

Supplementary Figure 5 | Simulated individual effects of ion-channel remodeling on central SAN action potentials in the adult and the underlying ionic currents **(Ai,Aii)** I_{Na}, **(Bi,Bii)** $I_{Ca,L}$, **(Ci,Cii)** I_f, **(Di,Dii)** I_{Kr}, **(Ei,Eii)** I_{Ks} and **(Fi,Fii)** I_{NaCa}.

Supplementary Figure 6 | ACh effect at a concentration of 3×10^{-8} M on the propagation of the SAN and surrounding area of the neonate **(A)** and adult **(B)** rabbit 2D tissue. Snapshots of the activation pattern at various timings are shown.

Supplementary Figure 7 | ACh effect at a concentration of 8×10^{-8} M on the propagation of the SAN and surrounding area of the neonate **(A)** and adult **(B)** rabbit 2D tissue. Snapshots of the activation pattern at various times are shown.

Supplementary Figure 8 | Multi-leading pacemaking sites resulting from ion-channel remodeling in the absence of connexin remodeling. Snapshots of the activation pattern at various timings are shown.

Supplementary Table 1 | AP characteristics of the neonate and adult peripheral SA node cell models.

REFERENCES

Accili, E. A., Robinson, R. B., and DiFrancesco, D. (1997). Properties and modulation of If in newborn versus adult cardiac SA node. *Am. J. Physiol. Circ. Physiol.* 272, H1549–H1552.

Adachi, T., and Shibata, S. (2013). The mechanism of increased postnatal heart rate and sinoatrial node pacemaker activity in mice. *J. Physiol. Sci.* 63, 133–146. doi: 10.1007/s12576-012-0248-1

Allah, E. A., Tellez, J. O., Yanni, J., Nelson, T., Monfredi, O., Boyett, M. R., et al. (2011). Changes in the expression of ion channels, connexins and Ca2+-handling proteins in the sino-atrial node during postnatal development. *Exp. Physiol.* 96, 426–438. doi: 10.1113/expphysiol.2010.055780

Artman, M. (1992). Sarcolemmal Na(+)-Ca2+ exchange activity and exchanger immunoreactivity in developing rabbit hearts. *Am. J. Physiol. Circ. Physiol.* 263, H1506–H1513.

Artman, M., Ichikawa, H., Avkiran, M., and Coetzee, W. A. (1995). Na+/Ca2+ exchange current density in cardiac myocytes from rabbits and guinea pigs during postnatal development. *Am. J. Physiol.* 268(4 Pt 2), H1714–H1722.

Aslanidi, O. V., Boyett, M. R., Dobrzynski, H., Li, J., and Zhang, H. (2009). Mechanisms of transition from normal to reentrant electrical activity in a model of rabbit atrial tissue: interaction of tissue heterogeneity and anisotropy. *Biophys. J.* 96, 798–817. doi: 10.1016/j.bpj.2008.09.057

Atkins, D. L., and Marvin, W. J. (1989). Chronotropic responsiveness of developing sinoatrial and ventricular rat myocytes to autonomic agonists following adrenergic and cholinergic innervation in vitro. *Circ. Res.* 64, 1051–1062. doi: 10.1161/01.res.64.6.1051

Bai, X., Wang, K., Yuan, Y., Li, Q., Dobrzynski, H., and Boyett, M. R. (2017). Mechanism underlying impaired cardiac pacemaking rhythm during ischemia: a simulation study. *Chaos* 27:093934. doi: 10.1063/1.5002664

Baruscotti, M., Bucchi, A., and DiFrancesco, D. (2005). Physiology and pharmacology of the cardiac pacemaker ("funny") current. *Pharmacol. Ther.* 107, 59–79. doi: 10.1016/j.pharmthera.2005.01.005

Baruscotti, M., DiFrancesco, D., and Robinson, R. B. (1996). A TTX-sensitive inward sodium current contributes to spontaneous activity in newborn rabbit sino-atrial node cells. *J. Physiol.* 492(Pt 1), 21–30. doi: 10.1113/jphysiol.1996.sp021285

Baruscotti, M., Difrancesco, D., Robinson, R. B., and Generali, B. (2001). Single-channel properties of the sinoatrial node Na + current in the newborn rabbit. *Pflügers Archiv.* 442, 192–196. doi: 10.1007/s004240100527

Baruscotti, M., and Robinson, R. B. (2007). Electrophysiology and pacemaker function of the developing sinoatrial node. *Am. J. Physiol. Hear. Circ. Physiol.* 293, 2613–2623.

Boyett, M. R., Honjo, H., and Kodama, I. (2000). The sinoatrial node, a heterogeneous pacemaker structure. *Cardiovasc. Res.* 47, 658–687. doi: 10.1016/s0008-6363(00)00135-8

Boyett, M. R., Inada, S., Yoo, S., Li, J., Liu, J., Tellez, J., et al. (2006). Connexins in the sinoatrial and atrioventricular nodes. *Cardiovasc. Gap Junct. Adv. Cardiol.* 42, 175–197. doi: 10.1159/000092569

Brioschi, C., Micheloni, S., Tellez, J. O., Pisoni, G., Longhi, R., Moroni, P., et al. (2009). Distribution of the pacemaker HCN4 channel mRNA and protein in the rabbit sinoatrial node. *J. Mol. Cell Cardiol.* 47, 221–227. doi: 10.1016/j.yjmcc.2009.04.009

Butters, T. D., Aslanidi, O. V., Inada, S., Boyett, M. R., Hancox, J. C., Lei, M., et al. (2010). Mechanistic links between Na+ channel (SCN5A) mutations and impaired cardiac pacemaking in sick sinus syndrome. *Circ. Res.* 107, 126–137. doi: 10.1161/circresaha.110.219949

Campbell, D. L., Rasmusson, R. L., and Strauss, H. C. (1992). Ionic current mechanisms generating vertebrate primary cardiac pacemaker activity at the single cell level: an integrative view. *Annu. Rev. Physiol.* 54, 279–302. doi: 10.1146/annurev.ph.54.030192.001431

Chen, F., Mottino, G., Klitzner, T. S., Philipson, K. D., and Frank, J. S. (1995). Distribution of the Na+/Ca2+ exchange protein in developing rabbit myocytes. *Am. J. Physiol. Physiol.* 268, C1126–C1132.

Dan, P., Lin, E., Huang, J., Biln, P., and Tibbits, G. F. (2007). Three-dimensional distribution of cardiac Na+-Ca2+ exchanger and ryanodine receptor during development. *Biophys. J.* 93, 2504–2518. doi: 10.1529/biophysj.107.104943

DiFrancesco, D. (1993). Pacemaker mechanisms in cardiac tissue. *Annu. Rev. Physiol.* 55, 455–472. doi: 10.1146/annurev.ph.55.030193.002323

Dobrzynski, H., Boyett, M. R., and Anderson, R. H. (2007). New insights into pacemaker activity: promoting understanding of sick sinus syndrome. *Circulation* 115, 1921–1932. doi: 10.1161/circulationaha.106.616011

Dobrzynski, H., Li, J., Tellez, J., Greener, I. D., Nikolski, V. P., Wright, S. E., et al. (2005). Computer three-dimensional reconstruction of the sinoatrial node. *Circulation* 111, 846–854. doi: 10.1161/01.cir.0000152100.04087.db

Fabbri, A., Fantini, M., Wilders, R., and Severi, S. (2015). "A novel computational model of the human sinoatrial action potential," in *Proceedings of the 2015 Computing in Cardiology Conference (CinC)*, Nice.

Fabbri, A., Fantini, M., Wilders, R., and Severi, S. (2017). Computational analysis of the human sinus node action potential: model development and effects of mutations. *J. Physiol.* 595, 2365–2396. doi: 10.1113/jp273259

Honjo, H., Boyett, M. R., Kodama, I., and Toyama, J. (1996). Correlation between electrical activity and the size of rabbit sino-atrial node cells. *J. Physiol.* 496(Pt 3), 795–808. doi: 10.1113/jphysiol.1996.sp021728

Huang, X., Yang, P., Yang, Z., Zhang, H., and Ma, A. (2016). Age-associated expression of HCN channel isoforms in rat sinoatrial node. *Exp. Biol. Med.* 241:331. doi: 10.1177/1535370215603515

Irisawa, H., Brown, H. F., and Giles, W. (1993). Cardiac pacemaking in the sinoatrial node. *Physiol. Rev.* 73, 197–227. doi: 10.1152/physrev.1993.73.1.197

Janowski, E., Cleemann, L., Sasse, P., and Morad, M. (2006). Diversity of Ca2+ signaling in developing cardiac cells. *Ann. N.Y. Acad. Sci.* 1080, 154–164. doi: 10.1196/annals.1380.014

Jones, S. A., Boyett, M. R., and Lancaster, M. K. (2007). Declining into failure: the age-dependent loss of the L-type calcium channel within the sinoatrial node. *Circulation* 115, 1183–1190. doi: 10.1161/circulationaha.106.663070

Jones, S. A., Lancaster, M. K., and Boyett, M. R. (2004). Ageing-related changes of connexins and conduction within the sinoatrial node. *J. Physiol.* 560, 429–437. doi: 10.1113/jphysiol.2004.072108

Jose, A. D., and Collison, D. (1970). The normal range and determinants of the intrinsic heart rate in man. *Cardiovasc. Res.* 4, 160–167. doi: 10.1093/cvr/4.2.160

Kaplan, P., Jurkovicova, D., Babusikova, E., Hudecova, S., Racay, P., Sirova, M., et al. (2007). Effect of aging on the expression of intracellular Ca2+ transport proteins in a rat heart. *Mol. Cell Biochem.* 301, 219–226. doi: 10.1007/s11010-007-9414-9

Larson, E. D., St Clair, J. R., Sumner, W. A., Bannister, R. A., and Proenza, C. (2013). Depressed pacemaker activity of sinoatrial node myocytes contributes to the age-dependent decline in maximum heart rate. *Proc. Natl. Acad. Sci. U.S.A.* 110, 18011–18016. doi: 10.1073/pnas.1308477110

Lindblad, D. S., Murphey, C. R., Clark, J. W., and Giles, W. R. (1996). A model of the action potential and underlying membrane currents in a rabbit atrial cell. *Am. J. Physiol. Hear. Circ. Physiol.* 271, 40–44.

Mangoni, M. E., Couette, B., Bourinet, E., Platzer, J., Reimer, D., Striessnig, J., et al. (2003). Functional role of L-type Cav1.3 Ca channels in cardiac pacemaker activity. *Proc. Natl. Acad. Sci. U.S.A.* 100, 5543–5548. doi: 10.1073/pnas.0935295100

Muñoz, M. A., Kaur, J., and Vigmond, E. J. (2011). Onset of atrial arrhythmias elicited by autonomic modulation of rabbit sinoatrial node activity: a modeling study. *Am. J. Physiol. Heart Circ. Physiol.* 301, H1974–H1983. doi: 10.1152/ajpheart.00059.2011

Myrnerts Höök, S., Pejovic, N. J., Marrone, G., Tylleskär, T., and Alfvén, T. (2018). Accurate and fast neonatal heart rate assessment with a smartphone-based application – a manikin study. *Acta Paediatr.* 107, 1548–1554. doi: 10.1111/apa.14350

Opthof, T. (2000). The normal range and determinants of the intrinsic heart rate in man. *Cardiovasc. Res.* 45, 177–184. doi: 10.1016/s0008-6363(99)00322-3

Protas, L., Oren, R. V., Clancy, C. E., and Robinson, R. B. (2010). Age-dependent changes in Na current magnitude and TTX-sensitivity in the canine sinoatrial node. *J. Mol. Cell Cardiol.* 48, 172–180. doi: 10.1016/j.yjmcc.2009.07.028

Protas, L. E. V., Difrancesco, D., Robinson, R. B., Difrancesco, D., and Rob, R. B. (2017). L-type but not T-type calcium current changes during postnatal development in rabbit sinoatrial node. *Am. J. Physiol. Hear. Circ. Physiol.* 10032, 1252–1259.

Qu, Y., Ghatpande, A., El-Sherif, N., and Boutjdir, M. (2000). Gene expression of Na+/Ca2+ exchanger during development in human heart. *Cardiovasc. Res.* 45, 866–873. doi: 10.1016/s0008-6363(99)00402-2

Rana, O. R., Schauerte, P., Kluttig, R., Schröder, J. W., Koenen, R. R., Weber, C., et al. (2010). Acetylcholine as an age-dependent non-neuronal source in the heart. *Auton. Neurosci.* 156, 82–89. doi: 10.1016/j.autneu.2010.04.011

Roberts, B. N., Yang, P.-C., Behrens, S. B., Moreno, J. D., and Clancy, C. E. (2012). Computational approaches to understand cardiac electrophysiology and arrhythmias. *Am. J. Physiol. Heart Circ. Physiol.* 303, H766–H783.

Satoh, H. (2003). Sino-atrial nodal cells of mammalian hearts: ionic currents and gene expression of pacemaker ionic channels. *J. Smooth Musc. Res.* 39, 175–193. doi: 10.1540/jsmr.39.175

Shibata, N., Inada, S., Mitsui, K., Honjo, H., Yamamoto, M., Niwa, R., et al. (2001). Pacemaker shift in the rabbit sinoatrial node in response to vagal nerve stimulation. *Exp. Physiol.* 86, 177–184. doi: 10.1113/eph8602100

Spear, J. F., Kronhaus, K. D., Moore, E. N., and Kline, R. P. (1979). The effect of brief vagal stimulation on the isolated rabbit sinus node. *Circ. Res.* 44, 75–88. doi: 10.1161/01.res.44.1.75

Tibbits, G. F., Xu, L., and Sedarat, F. (2002). Ontogeny of excitation-contraction coupling in the mammalian heart. *Comp. Biochem. Physiol. A Mol. Integr. Physiol.* 132, 691–698. doi: 10.1016/s1095-6433(02)00128-9

Toda, N. (1980). Age-related changes in the transmembrane potential of isolated rabbit sino-atrial nodes and atria. *Cardiovasc. Res.* 14, 58–63. doi: 10.1093/cvr/14.1.58

Verheijck, E., Van Ginneken, A. C. G., Wilders, R., and Bouman, L. N. (1999). Contribution of L-type Ca^{2+} current to electrical activity in sinoatrial nodal myocytes of rabbits. *Am. J. Physiol.* 276(3 Pt 2), H1064–H1077.

Verheijck, E. E., Wessels, A., van Ginneken, A. C., Bourier, J., Markman, M. W., Vermeulen, J. L., et al. (1998). Distribution of atrial and nodal cells within the rabbit sinoatrial node: models of sinoatrial transition. *Circulation* 97, 1623–1631. doi: 10.1161/01.cir.97.16.1623

Vinogradova, T. M., Zhou, Y. Y., Bogdanov, K. Y., Yang, D., Kuschel, M., Cheng, H., et al. (2000). Sinoatrial node pacemaker activity requires Ca(2+)/calmodulin-dependent protein kinase II activation. *Circ. Res.* 87, 760–767. doi: 10.1161/01.res.87.9.760

Wilders, R. (2007). Computer modelling of the sinoatrial node. *Med. Biol. Eng. Comput.* 45, 189–207. doi: 10.1007/s11517-006-0127-0

Woods, W. T., Urthaler, F., James, T. N., and Lin, S.-F. (1976). Spontaneous action potentials of cells in the canine sinus node. *Circ. Res.* 39, 76–82. doi: 10.1161/01.res.39.1.76

Yang, Z.-F., Li, C.-Z., Li, Q., Wang, X.-J., and Liu, Y.-M. (2002). The sinus node itself also plays a role in heart rate slowing down during postnatal development. *Sheng Li Xue Bao* 54, 282–286.

Yang, Z. F., Sun, Y., Li, C. Z., Wang, H. W., Wang, X. J., Zheng, Y. Q., et al. (2006). Reduced sinoatrial cAMP content plays a role in postnatal heart rate slowing in the rabbit. *Clin. Exp. Pharmacol. Physiol.* 33, 757–762. doi: 10.1111/j.1440-1681.2006.04437.x

Yanni, J., Tellez, J. O., Sutyagin, P. V., Boyett, M. R., and Dobrzynski, H. (2010). Structural remodelling of the sinoatrial node in obese old rats. *J. Mol. Cell Cardiol.* 48, 653–662. doi: 10.1016/j.yjmcc.2009.08.023

Your heart rate-British Heart Foundation (2019). *Your Heart Rate - British Heart Foundation*. Available online at: https://www.bhf.org.uk/informationsupport/how-a-healthy-heart-works/your-heart-rate

Zaza, A., Robinson, R. B., and DiFrancesco, D. (1996). Basal responses of the L-type Ca2+ and hyperpolarization- activated currents to autonomic agonists in the rabbit sino- atrial node. *J. Physiol.* 491, 347–355. doi: 10.1113/jphysiol.1996.sp021220

Zhang, H., Holden, A. V., Kodama, I., Honjo, H., Lei, M., Varghese, T., et al. (2000). Mathematical models of action potentials in the periphery and center of the rabbit sinoatrial node. *Am. J. Physiol. Hear. Circ. Physiol.* 279, H397–H421.

Zhang, H., Holden, A. V., Nobel, D., and Boyett, M. R. (2002). Analysis of the chronotropic effect of acetylcholine on sinoatrial node cells. *J. Cardiovasc. Electrophysiol.* 13, 465–474. doi: 10.1046/j.1540-8167.2002.00465.x

Zhang, H., Zhao, Y., Lei, M., Dobrzynski, H., Liu, J. H., Holden, A. V., et al. (2007). Computational evaluation of the roles of Na + current, *i* Na, and cell death in cardiac pacemaking and driving. *Am. J. Physiol. Circ. Physiol.* 292, H165–H174.

Zhang, X. (2011). *Simulation of Cardiac Pacemaker Dysfunction Arising from Genetic Mutations*. Ph. D thesis, The University of Manchester Manchester.

Conflict of Interest: The authors declare that the research was conducted in the absence of any commercial or financial relationships that could be construed as a potential conflict of interest.

The reviewer WG declared a past co-authorship with one of the authors HZ to the handling editor.

frontiers
in Physiology

ORIGINAL RESEARCH
published: 03 December 2020
doi: 10.3389/fphys.2020.546508

Cardiac Pacemaker Dysfunction Arising From Different Studies of Ion Channel Remodeling in the Aging Rat Heart

Aaazh M. Alghamdi[1,2], Mark R. Boyett[3], Jules C. Hancox[1,4] and Henggui Zhang[1,5,6]*

[1] Biological Physics Group, Department of Physics and Astronomy, The University of Manchester, Manchester, United Kingdom, [2] Department of Physics, Faculty of Science, University of Jeddah, Jeddah, Saudi Arabia, [3] Department of Biomedical Sciences, Faculty of Health and Medical Sciences, University of Copenhagen, Copenhagen, Denmark, [4] School of Physiology, Pharmacology and Neuroscience, and Cardiovascular Research Laboratories, Faculty of Life Sciences, University of Bristol, Bristol, United Kingdom, [5] Peng Cheng Laboratory, Shenzhen, China, [6] Key Laboratory of Medical Electrophysiology of Ministry of Education and Medical Electrophysiological Key Laboratory of Sichuan Province, Institute of Cardiovascular Research, Southwest Medical University, Luzhou, China

Edited by:
Joseph L. Greenstein,
Johns Hopkins University,
United States

Reviewed by:
Yukiko Himeno,
Ritsumeikan University, Japan
Jichao Zhao,
The University of Auckland,
New Zealand
Thomas Hund,
The Ohio State University,
United States

***Correspondence:**
Henggui Zhang
henggui.zhang@manchester.ac.uk

Specialty section:
This article was submitted to Computational Physiology and Medicine, a section of the journal Frontiers in Physiology

Received: *28 March 2020*
Accepted: *13 November 2020*
Published: *03 December 2020*

Citation:
Alghamdi AM, Boyett MR, Hancox JC and Zhang H (2020) Cardiac Pacemaker Dysfunction Arising From Different Studies of Ion Channel Remodeling in the Aging Rat Heart. Front. Physiol. 11:546508. doi: 10.3389/fphys.2020.546508

The function of the sinoatrial node (SAN), the pacemaker of the heart, declines with age, resulting in increased incidence of sinoatrial node dysfunction (SND) in older adults. The present study assesses potential ionic mechanisms underlying age associated SND. Two group studies have identified complex and various changes in some of membrane ion channels in aged rat SAN, the first group (Aging Study-1) indicates a considerable changes of gene expression with up-regulation of mRNA in ion channels of Cav1.2, Cav1.3 and KvLQT1, Kv4.2, and the Ca^{2+} handling proteins of SERCA2a, and down-regulation of Cav3.1, NCX, and HCN1 and the Ca^{2+}-clock proteins of RYR2. The second group (Aging Study-2) suggests a different pattern of changes, including down regulation of Cav1.2, Cav1.3 and HCN4, and RYR2, and an increase of NCX and SERCA densities and proteins. Although both data sets shared a similar finding for some specific ion channels, such as down regulation of HCN4, NCX, and RYR2, there are contradictory changes for some other membrane ion channels, such as either up-regulation or down-regulation of Cav1.2, NCX and SERCA2a in aged rat SAN. The present study aims to test a hypothesis that age-related SND may arise from different ionic and molecular remodeling patterns. To test this hypothesis, a mathematical model of the electrical action potential of rat SAN myocytes was modified to simulate the functional impact of age-induced changes on membrane ion channels and intracellular Ca^{2+} handling as observed in Aging Study-1 and Aging Study-2. The role and relative importance of each individually remodeled ion channels and Ca^{2+}-handling in the two datasets were evaluated. It was shown that the age-induced changes in ion channels and Ca^{2+}-handling, based on either Aging Study-1 or Aging Study-2, produced similar bradycardic effects as manifested by a marked reduction in the heart rate (HR) that matched experimental observations. Further analysis showed that although the SND arose from an integrated action of all remodeling of ion channels and Ca^{2+}-handling in both studies, it was the change to I_{CaL} that played the most important influence.

Keywords: aging, SA node, ion channel remodeling, I_{CaL}, sick sinus syndrome (brady-arrhythmia)

INTRODUCTION

The sinoatrial node (SAN) is the primary pacemaker of the heart. It is situated in the superior right atrium and produces a sequence of auto-rhythmic electrical activities that control the heartbeat (Baruscotti and Robinson, 2007). Dysfunction of the sinoatrial node (SND) associated with "sick sinus syndrome" (SSS) manifests as pathological bradycardia or systolic pauses (Haqqani and Kalman, 2007), producing inadequate blood supply to satisfy the demands of the body. This condition leads to symptoms such as dizziness and syncope (Haqqani and Kalman, 2007), though the initial stages of SND may be latent and asymptomatic (Choudhury et al., 2015).

Various physiological and pathological mechanisms (intrinsic, extrinsic or a combination of the two) are responsible for SND (Semelka et al., 2013). Among them is the failure of a specific part of the SAN to achieve impulse generation (Fenske et al., 2013), or the impulse conduction from the SAN to the surrounding atrial muscle, due to genetic mutations (Butters et al., 2010; Choudhury et al., 2018) or ischemic conditions (Bai et al., 2017). Increased fibrosis and degenerative changes in physiological properties of the SAN may also cause SND (Baruscotti and Robinson, 2007; Zhang et al., 2007; Choudhury et al., 2015).

Sinoatrial node dysfunction is also associated with aging (Tohno et al., 2014; Alghamdi et al., 2018). Whilst it can occur at any age, the occurrence of SND significantly increases with age (Härtel and Talvensaari, 1975). In a retrospective research study of 277 participants with compromised bradycardia, 51% of the cases were attributed to extrinsic causes (such as adverse drug reactions, imbalance of electrolytes or acute myocardial infarction, etc.), and 49% were attributable to either intrinsic or idiopathic (Sodeck et al., 2007) conditions, such as cardiac ischemia, gene mutations, excessive training and particularly aging (Semelka et al., 2013; Choudhury et al., 2015). More than 600,000 pacemaker implants are performed worldwide each year (Lamas et al., 2000; Wood and Ellenbogen, 2002; Bai et al., 2017), of which older adults account for the largest percentage.

Experimental data from animal models (Alings and Bouman, 1993; Satoh et al., 2005; Jones et al., 2007; Moghtadaei et al., 2016; Du et al., 2017) and human studies (Opthof, 1994; Dobrev, 2009) have demonstrated an association between SND and aging. It has been shown that during the aging process, changes occur to SAN function, manifested by increased pacemaking cycle length (CL) (*i.e.*, slower heart rate) and reduced conduction of action potentials [*i.e.*, an increased sinoatrial node-atrium conduction time (SACT)]. Both of these contribute to the reduced aerobic capacity of older adults, leading to an increased incidence of abnormal pacemaking and atrial arrhythmia (Sharpe et al., 2017). Further investigations have also revealed that such aging-associated SND is related to changes in the cellular electrical properties of the SAN (see **Supplementary Table 1** in the Appendix) (Congxin Huang et al., 2006; Zhang et al., 2007; Hao et al., 2011; Larson et al., 2013; Tohno et al., 2014; Huang et al., 2015; Moghtadaei et al., 2016; Du et al., 2017) in a similar way to aging-induced cellular changes in atrial and ventricular cells (Congxin Huang et al., 2006) and intercellular electrical coupling (Jones et al., 2004). A list of aging-related changes in mRNA/proteins of ion channels, Ca^{2+} handling, intercellular coupling and tissue fibrosis population of the SAN for different species is given in **Supplementary Table 1** in the Appendix.

Complex and variable patterns of changes to ion channels and calcium-handling proteins have been observed in aging-induced SND rat models (Tellez et al., 2011; Hatch, 2012; Huang et al., 2016). In their study, Tellez et al. (2011) (Aging Study-1) found that aging-SND was associated with a considerable changes of gene expression in the SAN, including: an increase in the relative abundance of mRNA for many ion channels [e.g., Nav1.5, Navβ1 and Cav1.2, Cav1.3 and KvLQT1, Kv4.2 (which are responsible for I_{Ks} and I_{to})] in addition to an increase of the Ca^{2+} handling proteins, SERCA2a, that responsible for Ca^{2+}-uptake process. The study also showed, a decrease in some other ion channels (e.g., in Cav3.1, NCX, and HCN1) and in the Ca^{2+} clock (RYR2) gene expressions of the SAN during aging. This implied changes of them during aging, though there is no explicit link between mRNA levels and channel activity (Brioschi et al., 2009). However, other studies (Aging Study-2) showed conflicting data, suggesting a trend of down-regulation of some ion channels (e.g., decreases of Cav1.2, HCN4, and RyR2 densities and proteins, and an increase of NCX and SERCA densities and proteins) in aged SAN cells (Hatch, 2012; Huang et al., 2016).

The ionic mechanisms that underlie the aging associated SND are as yet unclear. It is possible that SND is associated with different "patterns" of ionic and molecular remodeling mechanisms, including up-regulation or down-regulation of particular ion channels as identified in previous studies (Tellez et al., 2011; Hatch, 2012; Huang et al., 2016). The aims of the present study were to:

1. determine whether the age-induced changes in ion channels as identified in Aging Study-1 and Aging Study-2 were sufficient to account for the observed SND;
2. investigate the relative roles of particular remodeled ion channels on modulation of the characteristics of pacemaking APs, including the cycle length (CL), action potential duration (APD_{50}), peak amplitude (PA), maximal upstroke velocity (dV/dt_{max}), and maximal diastolic potential (MDP); and
3. address the question of how differently remodeled $I_{Ca,L}$ could lead to SND.

MATERIALS AND METHODS

Mathematical Models of Single SAN Cells

The consequence of aging-induced electrophysiological changes in ion channel currents in rat SAN cells was investigated using the model developed by Tao et al. (2011) for rat pacemaking APs. The model was based on modifications of rabbit SAN models (Zhang et al., 2000; Kurata et al., 2002) by incorporating experimental data for major ion channels obtained from rat SAN cells by Satoh (2003a,b) and Shinagawa et al. (2000). The data included aging-induced remodeling in key currents – $I_{Ca,L}$, I_{Ks},

I_{Kr}, and I_f – which were modeled by incorporation into classical Hodgkin-Huxley formulations.

In the Tao et al. model, the membrane potential V_m is dependent on a set of voltage-gated ion-channel currents, exchanger currents, and ionic pump currents, in the form of the following equations (1) and (2):

$$\frac{dV_m}{dt} = -\frac{1}{C_m} I_{tot} \tag{1}$$

$$\begin{aligned} I_{tot} = (&I_{Ca,T} + I_{Ca,L} + I_{Kr} + I_{Ks} + I_{st} + I_{sus} + \\ &I_{to} + I_{K,ACh} + I_f + I_{b,Na} + I_{NaCa} + I_{NaK}) \end{aligned} \tag{2}$$

where C_m is the cell capacitance (set at 32pF); I_f the hyperpolarization-activated current; $I_{Ca,L}$ and $I_{Ca,T}$ the inward L-type and T-type Ca^{2+} currents; I_{Kr} and I_{Ks} the rapid and slow delayed rectifier K^+ currents; I_{to} the Ca^{2+}-independent transient outward K^+ current; I_{st} the sustained inward current (carried by Na^+); I_{sus} the sustained component of 4-AP sensitive current; $I_{K,ACh}$ the muscarinic K^+ channel current; I_{NaK} the Na^+-K^+ pump current; I_{NaCa} the Na^+-Ca^{2+} exchanger current; and $I_{b,Na}$ the background inward Na^+ current. Details of the equations and parameters of the model are documented in Tao et al. (2011).

We obtained the source code of this mathematical model *via* a request to the author. The original model was developed with neural-myocyte coupling and the modulation of pacemaking by nitric oxide and cyclic GMP in response to brief sympathetic stimulations observed in hypertension. As the present study was focused on studying the effects of aging on the morphology and characteristics of the pacemaking APs, therefore the neural-myocyte coupling was removed from the model, resulting in the simulated cycle length of the pacemaking APs at 230 ms, which is slightly different to that of the original model at 257 ms, but is still within the experimental range value of the rat SAN in Shinagawa et al. (2000). Numerically, the Hodgkin-Huxley equations for the rat SAN cell model were solved with a time step of 0.01 ms, which was sufficiently small to ensure a stable numerical solution.

Aging SAN Model

To simulate the functional impact of aging-induced changes of membrane ion channels and intracellular Ca^{2+}-handling on cardiac pacemaking activity, experimental data from two independent groups of studies on aging rat SAN cells, as identified by Tellez et al. (2011) (denoted Aging Study-1); and Hatch (2012) and Huang et al. (2016) (collectively denoted Aging Study-2) for adult and older adult rat SAN were incorporated into the model Tao et al. (2011). As some of the experimental data were derived from mRNA gene expression or protein levels, their incorporation was carried out with an assumption on that there is a correlation between the gene expression or protein levels and certain ion channel current densities as we did in our previous studies (Hao et al., 2011; Choudhury et al., 2018). Both datasets were obtained from SAN cells isolated from the right atrium of Wistar Hannover rats with ages of ≥25 or ≥24 months (equivalent to about a 70-year-old human) (Tellez et al., 2011; Hatch, 2012). In both studies, cellular APs and ECGs were recorded. These data showed reductions in heart rates in the older adult rat SAN preparations by 18 (Tellez et al., 2011) and 11% (Hatch, 2012), respectively, as compared with adult preparations. Such a change in heart rate is associated with changes in cellular ion channels, as summarized in **Supplementary Table 2** (see Appendix).

Changes of different ion channels in the aging condition as shown in **Supplementary Table 2** were incorporated into the Tao et al. model through modifying the maximal channel conductance value of a particular ion channel equation. To simulate the effects of the aging-induced changes of the expression for RyR and SERCA, we modified the Tao et al. model which includes the Ca^{2+} handling equations from the Zhang et al. (2000) and Kurata et al. (2002) models of the rabbit SA node cells, by changing the flux of the Ca^{2+} release from the SR (J_{rel}) and Ca^{2+} uptake by the SERCA (P_{up}) based on scaling factors as listed in **Supplementary Table 2**. The equations for the SR Ca^{2+} release and SERCA Ca^{2+} uptake are as follows:

$$J_{up} = P_{up} \times \frac{\left[{C_a}^{2+}\right]_i}{\left[{C_a}^{2+}\right]_i + K_{up}} \tag{3}$$

$$J_{rel} = P_{rel} \times \left(\left[{C_a}^{2+}\right]_{rel} - \left[{C_a}^{2+}\right]_{sub}\right) \times \frac{\left[{C_a}^{2+}\right]_{sub}^2}{\left[{C_a}^{2+}\right]_{sub}^2 + {K_{rel}}^2} \tag{4}$$

In simulations, AP characteristics including CL (and hence HR), maximal diastolic potential (MDP), peak amplitude (PA) and action potential duration (APD_{50}) were computed in adult and older adult conditions, which were compared with the relevant experimental data (Hatch, 2012; Huang et al., 2016) for validation. In order to elucidate the primary factor(s) responsible for the slower heart rate in the older adult cells, the relative impact of different remodeled ionic channels on CL were analyzed *via* two distinct methods: the inclusive, and the exclusive. With the inclusive method, all changes in the remodeled ion channels and Ca^{2+}-handling due to aging were considered for the older adult condition. With the exclusive method, only a specific remodeled ion channel or subsets of all the remodeled ion channels were considered for the older adult condition, while the rest of the aging-induced changes were not included in the models. Details of ion channels considered in each case are described in the following sections.

RESULTS

Effects of Ion-Channel Remodeling on Pacemaking APs

Figure 1 shows the simulated effects of aging on the pacemaking AP of rat SAN cells based on the experimental data set of Aging Study-1 (left panels) and Aging Study-2 (right panels). Both aging datasets produced a similar consequence of aging-related bradycardia, *i.e.*, a slower pacemaking rate in the older adult compared with the adult condition, although there are dramatic differences in the underlying remodeling of membrane ion channels and the Ca^{2+}-handling (see **Supplementary Table 2** in the Appendix). With the use of Aging Study-1 data (Tellez et al., 2011), the CL was increased from 230 ms in the control condition to 310 ms in the older adult condition, implying a 19% decrease in pacemaking rate (HR). Similarly, using the Aging Study-2 data, an increase of the CL from 230 to 265 ms was observed, corresponding to ∼12.9% decrease in HR. Such simulated effects of aging on slowing the cardiac pacemaking APs are in agreement with those observed experimentally (Hatch, 2012; Huang et al., 2016).

Although simulations using both experimental data (Tellez et al., 2011) sets showed similar effects on the reduction of the pacemaking rate, each of which produced different changes in the characteristics of the simulated APs. In the case of Aging Study-1, the simulated pacemaking APs in the older adult condition (**Figure 1Ai**) presented a more hyperpolarized maximum diastolic potential (MDP) (by −12.8 mV), a greater dV/dt_{max} (by 60%), PA (by 20%), and APD_{50} (by 14%). These changes in AP characteristics were attributable to changes in the underlying ion-channel currents and Ca^{2+}-handling, which were manifested as a decreased I_f (**Figure 1Bi**), increased $I_{Ca,L}$ (**Figure 1Ci**), decreased I_{NaCa} (**Figure 1Di**), as well as an increased I_{NaK} (**Figure 1Ei**) and Ca^{2+}-uptake (**Figure 1Fi**), but a decreased Ca^{2+} release (**Figure 1Gi**).

However, in the case of Aging Study-2, the simulated pacemaking APs (**Figure 1Aii**) presented an elevated maximum diastolic potential value (by + 9.3 mV), decreased dV/dt_{max} (by 64%) and PA (by 70%), as well as an abbreviated APD_{50} (by 17%). These changes were attributable to decreased I_f (**Figure 1Bii**) and I_{CaL} (**Figure 1Cii**), increased I_{NaCa} (**Figure 1Dii**) and Ca^{2+} uptake (**Figure 1Fii**), but decreased Ca^{2+} release (**Figure 1Gii**). The decrease in PA was attributable to the reduction of I_{CaL}.

Simulations of the aging effect on the pacemaking APs and their characteristics were validated by quantitatively comparing the simulation data to experimental data when possible. Results are shown in **Figure 2** and summarized in **Supplementary Table 3** in the Appendix. In the case of Aging Study-1, simulations showed about 80 ms increase in CL, leading to a 19% reduction in HR. This is quantitatively consistent with the study of Tellez et al. (2011), who observed about 30% increase in CL that corresponded to an 18% reduction in HR. We also observed increases in APD_{50} and maximal dV/dt_{max} in simulations, that were quantitatively consistent with the results of Tellez et al. (2011).

In Aging Study-2, our simulations showed that aging caused an increased CL by 35 ms, which corresponded to a reduction in HR of about 12.9%. This was also comparable with data from Hatch (2012), who observed a CL increase of 40% in CL; corresponding to a 30% decrease in HR. It was also comparable with the data from Huang et al. (2016), which showed an increase of the CL from 193 to 235 ms (the intrinsic HR changed from 310 to 255 bpm) with aging, corresponding to 17.7% reduction of the intrinsic HR. We also observed decreases in APD_{50}, dV/dt_{max} and the amplitude of action potentials. However, there are no experimental data available for quantitative comparison with these values.

Relative Role of Individual (or a Subset of) Remodeled Ion Channel(s) in Aging Bradycardia

Simulation results using the data sets from Aging Study- 1 and 2 produced similar bradycardic effects that both qualitatively and quantitatively matched to their experimental observations (although limited experimental observations for Aging Study-2 were available), despite of marked differences in their underlying remodeled ion channels and Ca^{2+}-handling were observed. In order to elucidate the primary factor(s) that contributed to aging bradycardia, effects and their relative roles of individual, or a subset of, remodeled ion channels and Ca^{2+}-handling on pacemaking APs were simulated and analyzed using the exclusive method. Through this method, only some specific aging-induced change(s) were considered, while other remodeling factors were omitted.

After analysis of the differences and similarities in the aging-induced remodeling patterns between Aging Study- 1 and 2, three different cases were analyzed, as shown below.

Case 1: Effects of Remodeled I_f and RyR2

Both group aging studies showed a down-regulation of HCN channels in mRNA for aging study-1 and in protein expression for aging study-2. For RyR Ca^{2+} release channels, also, presented a reduction of in mRNA expression in aging study-1, in protein expression and expression density of aging-2. Therefore, in Case 1, simulations were conducted to evaluate the effects of a reduced I_f by 16% in Aging Study-1 [this value was based on the mRNA expression data in Tellez et al. (2011) study], and 30% in Aging Study-2 [this value was based on the data of Huang et al. (2016) study], and RyR Ca^{2+} release from the sarcoplasmic reticulum (SR), by 80% in Aging Study-1 [this value was obtained from the mRNA expression data in Tellez et al. (2011) study], and 24% in Aging Study-2 [this value was based on the protein expression density data in Hatch (2012) study], on the pacemaking APs. Results in **Figure 3** show the computed APs for the control (adult) and for the older adult conditions based on Aging Study-1 [left panels (Ai)] and Aging Study-2 [right panels (Aii)]. During the time course of APs, the time traces of I_f and Ca^{2+} release flux from the SR are also shown in panels (Bi) and (Bii), and (Ci) and (Cii), for the adult and older adult conditions, respectively.

With both data sets, reduced I_f and Ca^{2+} release from the SR had a limited effect on slowing down pacemaking rate. With a combined action of reduced I_f and Ca^{2+} release, the HR was reduced with the dataset from Aging Study-1, but unchanged with the dataset from Aging Study-2.

Simulation results from both datasets suggested a limited role of combined action of remodeled I_f and Ca^{2+} release in the bradycardia. Further analysis was conducted to analyze the individual role of a wide-range reduction of I_f or SR Ca^{2+} release. When I_f reduction alone was considered from 16% (Aging Study-1) to 30% (Aging Study-2), there was no noticeable change in spontaneous APs (data not shown). This result was in agreement

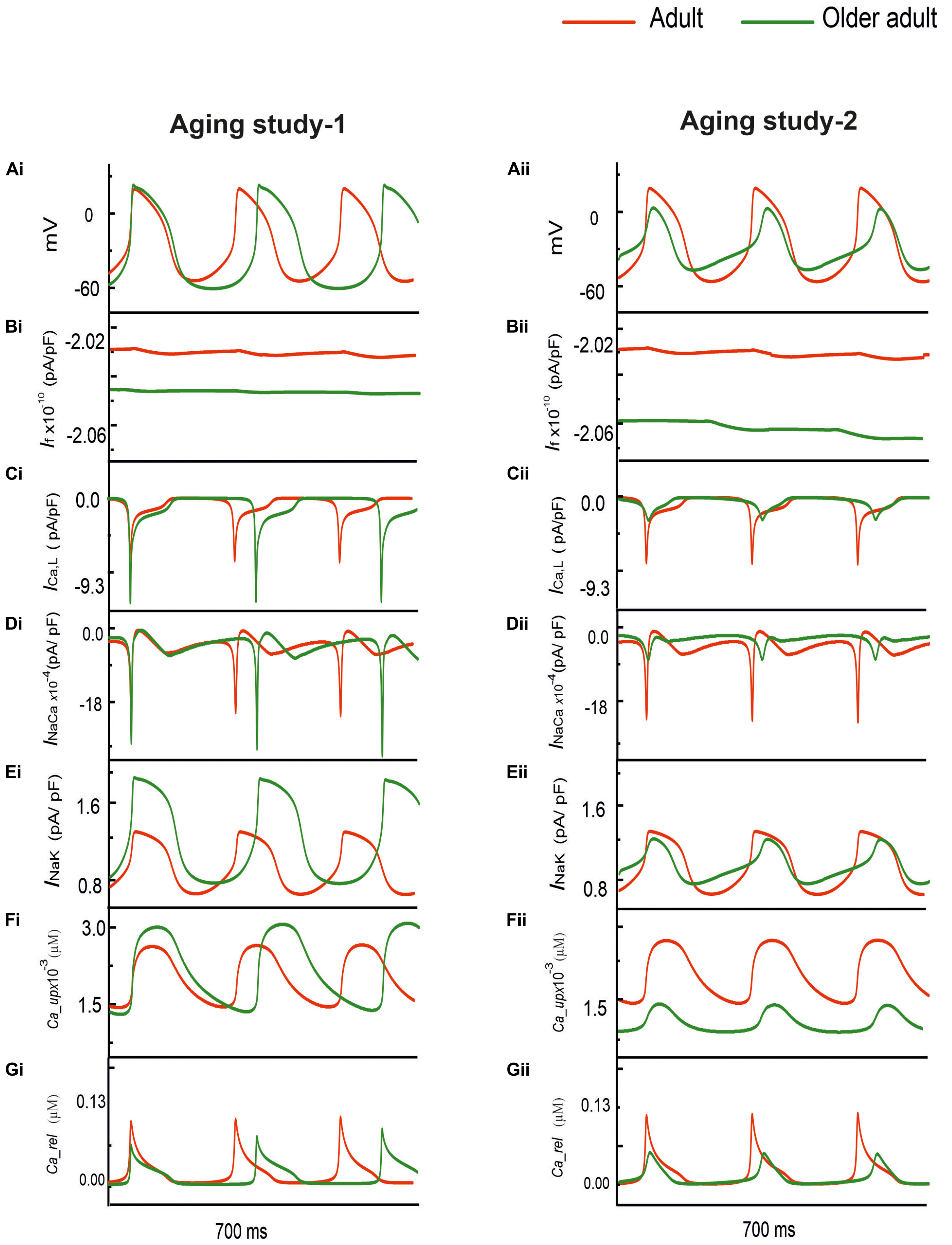

FIGURE 1 | (Ai,Aii) Action potentials computed from rat SAN myocyte model in adult (red) and older adult (green) conditions using the Aging Study-1 **(left panels)** and Aging Study-2 **(right panels)** datasets. Simulations were conducted by using the rat SAN cell model developed by Tao et al. (2011). **(Bi–Gi,Bii–Gii)** Underlying ionic channel currents and Ca^{2+}-handling during APs: I_f, I_{CaL}, I_{NaCa}, I_{NaK}, Ca^{2+} uptake and Ca^{2+} release.

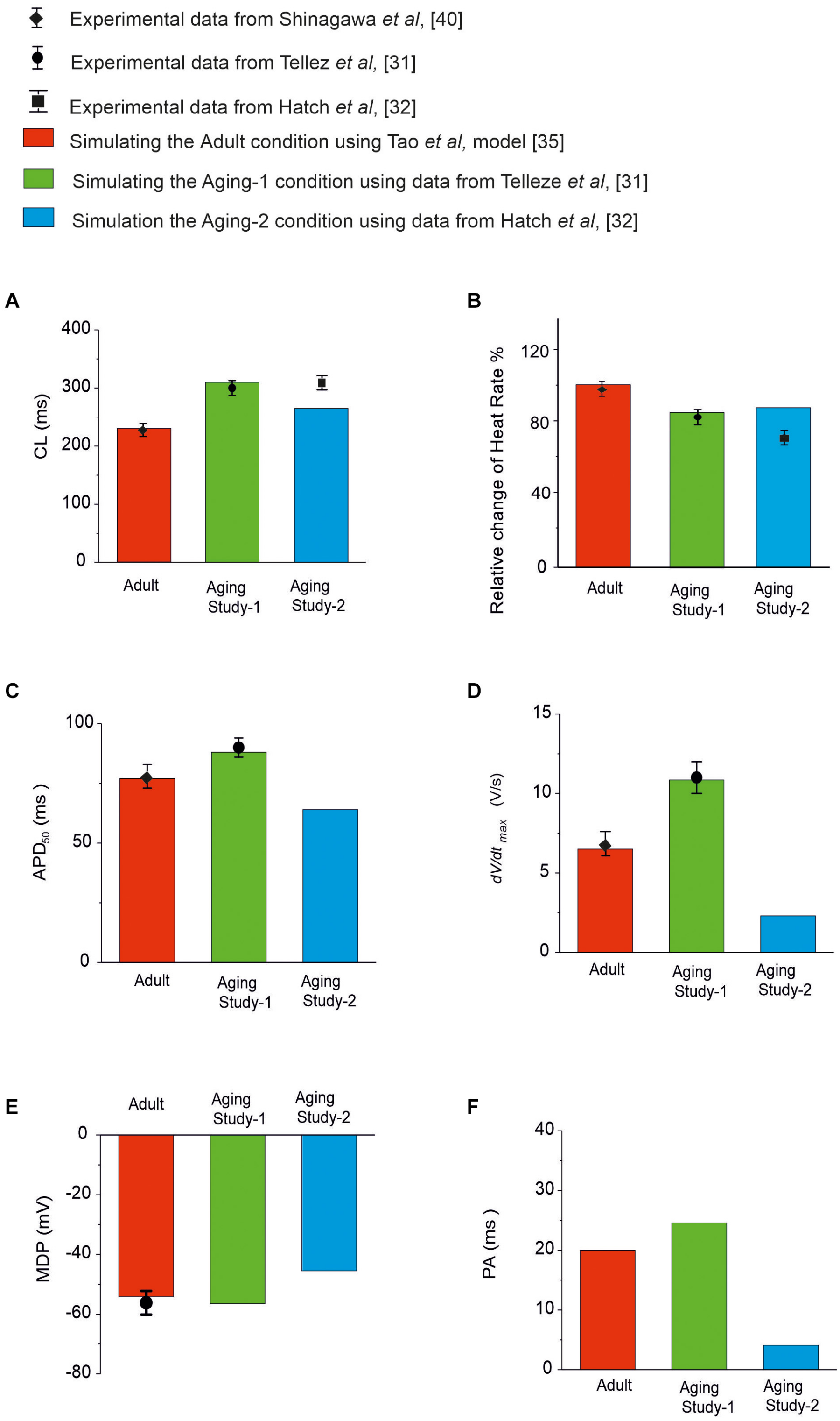

FIGURE 2 | Quantitative comparison between experimental and simulation data of the functional effects of aging on the pacemaking APs and their characteristics. **(A)** CL; **(B)** HR; **(C)** APD_{50}; **(D)** dV/dt_{max}; **(E)** MDP; and **(F)** PA. Data for adult is shown in red, and from Aging Study-1 and -2 in green and blue, respectively. Experimental data with error bars, where available, are from Tellez et al. (2011); Hatch (2012), Huang et al. (2016), and Shinagawa et al. (2000), which were all from rat SAN cells.

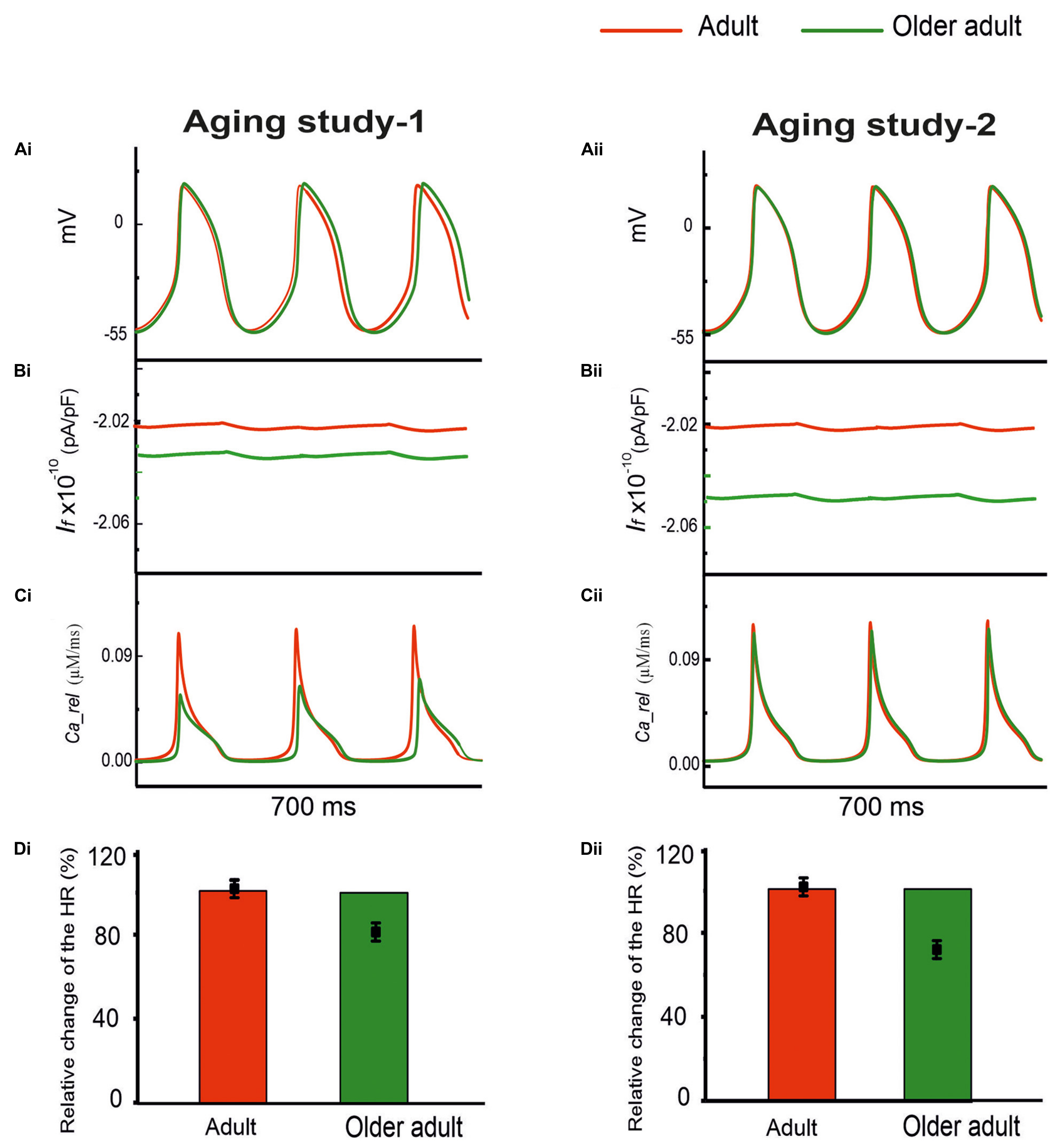

FIGURE 3 | Simulated role of reduced I_f and Ca^{2+} release from the SR in aging bradycardia. Changes in other ion-channel currents as reported by Tellez et al. (2011) in Aging Study-1 (right panels) and by Hatch (2012) and Huang et al. (2016) in Aging Study-2 (left panels) were omitted. **(Ai,Aii)** APs. **(Bi,Bii)** Ionic current profiles for I_f, and **(Ci,Cii)** for Ca^{2+} release, for adult (red) and older adult (green) conditions. **(Di,Dii)**: Bar charts showing the simulated age-dependent relative change in HR for this case; data-points with error bars show the experimental HR reduction due to aging.

with the results of Bers (2001), who observed that I_f played only a minor role in primary and central SAN cells, though a critical role in peripheral SAN cells.

When a reduced SR Ca^{2+} release alone was considered, either by 80% (Aging Study-1) or by 24% (Aging Study-2), there was a small increase in the measured CL. With an 80% reduction in the RyR2 alone, as suggested by Aging Study-1, CL was increased by 2.45%, while with a 24% reduction in the RyR2 alone as seen in Aging Study-2, no noticeable change in the CL was observed (data not shown).

To test whether or not the simulated consequences of RyR2 reduction by 80% (Aging Study-1), and 24% (Aging Study-2) are model-dependent, the Maltsev and Lakatta (2009) model for the rabbit SAN cells was also used. Results are shown in

Supplementary Figure 1. It was found that a 24% reduction of the RyR2 had little effect on reducing the pacemaking rate, while 80% reduction of RyR2 produced a small, but notable change of the APs, manifested by an increased CL (by 5.2%), elevated MDP and less steep DD phase, leading to an increased time taken to producing the successive peacemaking APs. The simulation results using the Maltsev and Lakatta (2009) model for the rabbit SAN cells matched the findings using the Tao et al. model for the rat SAN cells in showing that the aging-induced change in RyR made a limited contribution to aging-associated modulation of SAN spontaneous APs.

The time traces of Ca^{2+} release flux during the APs are shown in panels (Ci) and (Cii) for the adult (red) and older adult (green) conditions (with a combined action of reduced I_f and Ca^{2+} release). Panels (Di) and (Dii) compare the simulation and experimental results of relative changes in HR when the age-induced remodeling of I_f and RyR2 alone were considered.

Case 2: Effects of Remodeled $I_{Ca,L}$, I_{NaCa}, and SERCA2a

Both the experimental datasets showed changes to $I_{Ca,L}$, I_{NaCa} and Ca^{2+} uptake from the SR with aging, but with conflicting findings. In Aging Study-1, up-regulation of $I_{Ca,L}$ and Ca^{2+} uptake, but down-regulation of I_{NaCa}, were observed; whilst in Aging Study-2, down-regulation in $I_{Ca,L}$ and Ca^{2+} uptake, but an up-regulation of I_{NaCa}, were shown.

In order to investigate the role of this conflicting subset of aging-induced remodeling shown by the two sets of data, further simulations were conducted by incorporating the altered $I_{Ca,L}$, I_{NaCa} and Ca^{2+} uptake into the model to investigate their contribution to the aging bradycardia.

Results are shown in **Figure 4** for the computed APs (Ai and Aii) in the adult and older adult conditions, as well as the underlying time courses of $I_{Ca,L}$ (Bi, Bii), I_{NaCa} (Ci, Cii), and Ca^{2+}-uptake (Di, Dii) based on data of Aging Study-1 (left panels) and -2 (right panels). **Figure 4Ai** shows the simulated pacemaking APs based on data from Aging Study-1, with considerations only of an increase of $I_{Ca,L}$ by 25%, Ca^{2+} uptake by 15%, and a decrease in I_{NaCa} by 6% for the older adult condition [data based on the mRNA expression data in Tellez et al. (2011) study]. As compared with the adult condition, the computed CL increased by 23.4% (*i.e.*, a decrease in HR of 11%), and this was accompanied by changes in other AP characteristics, including an increase in PA of 17.5% and in APD_{50} of 23.4%. In this case, the observed changes in CL and AP characteristics were comparable with those obtained when all remodeled factors were considered, as well as close to experimental observations (Tellez et al., 2011). The results seem to suggest that the aging-induced up-regulations of $I_{Ca,L}$ and Ca^{2+}-uptake, and down-regulation of I_{NaCa}, are sufficient to account for the aging bradycardia seen experimentally in Aging Study-1.

Figure 4Aii shows simulated APs based on data from Aging Study-2 with a consideration of a decrease of $I_{Ca,L}$ by 50%, Ca^{2+}-uptake by 29%, and an increase of I_{NaCa} by 42% [data based on the protein expression density data in Hatch study (Hatch, 2012) as shown in **Supplementary Table 2**]. As compared with the APs in the adult condition, the implemented changes also reproduced bradycardia, resulting in a 9% increase in CL (i.e., a 7% HR decrease), which was accompanied by other changes in AP characteristics. These included an elevated MDP by 6 mV, a reduction of PA by 55% and an APD_{50} shortening by 14%. Those observed changes in APs were also close to the experimental observations of Hatch (2012), which implied that the subset of remodeled $I_{Ca,L}$, I_{NaCa}, and Ca^{2+} uptake, as seen in Aging Study-2, were also sufficient to produce the aging-related bradycardia.

The use of this subset of data from either Aging Study-1 or Aging Study-2 produced bradycardia, though there are clear differences between the two. In Aging Study-1, bradycardia was associated with an increased $I_{Ca,L}$ (**Figure 4Bi**) and SR Ca^{2+} uptake (**Figure 4Ci**), and a decreased I_{NaCa} (**Figure 4Di**). In contrast, in Aging Study-2 it was associated with a decreased $I_{Ca,L}$ (**Figure 4Bii**) and decreased SR Ca^{2+} uptake (**Figure 4Cii**), and an increased I_{NaCa} (**Figure 4Dii**). Quantitatively, the computed HR reductions in the older adult condition were close to the experimental data of Tellez et al. (2011) and Hatch (2012) for Aging Study-1 (**Figure 4Ei**) and Aging Study-2 (**Figure 4Eii**), respectively.

Figure 5 shows the results when aging-related remodeling of I_{CaL} in a range based on the study of Tellez et al. (2011) and Hatch (2012) was considered. In Aging Study-1 (**Figure 5Ai**), the 25% up-regulated $I_{Ca,L}$ increased the peak amplitude of the AP from 20 to 25 mV and prolonged the APD_{50} from 77.06 to 95.11 ms, which slowed down the time course for repolarization and consequently led to a slowing down in the pacemaking as seen in aging bradycardia when all remodeled ion channels were considered in Aging Study-1. It also produced a more hyperpolarized maximal diastolic membrane potential, which led to an increased voltage difference between the maximal diastolic membrane potential, MDP, and the take-off potential (TOP), at which a line from the MDP along the diastolic depolarization time course intersects with a vertical line drawn from the AP overshoot. This contributed to increased time taken to generate a successive action potential, though the depolarization I_{NaCa} current during the diastolic depolarization (DD) phase was increased. Overall, this led to an increased time interval between two successive APs (i.e., CL), leading to a slowed heart rate (see **Table 1**). **Figure 5B** shows how both increase and decrease of the $I_{Ca,L}$ through changing the gCaL can affect the measured CL leading to increase the pacemaking.

In Aging Study-2 (**Figure 5Aii**), a decreased $I_{Ca,L}$ also produced bradycardia. In this case, the decreased $I_{Ca,L}$ was associated with a decreased AP peak amplitude from 20 to 6.61 mV and abbreviated APD_{50} from 77.06 to 57.77 ms. Both accelerated the repolarization process but produced an incomplete repolarization as a consequence of reduced AP amplitude and abbreviated APD_{50}. Consequently, an elevated MDP was produced, leading to a reduced depolarization current in the DD phase (such as I_{NaCa}), which slowed down the time course between the MDP and the take-off potential, leading to an increased time interval between two successive pacemaking APs, resulting in bradycardia that was also comparable to the case when all remodeled ion channels were considered in Aging Study-2. **Figure 5B** shows how either an increase or a decreased

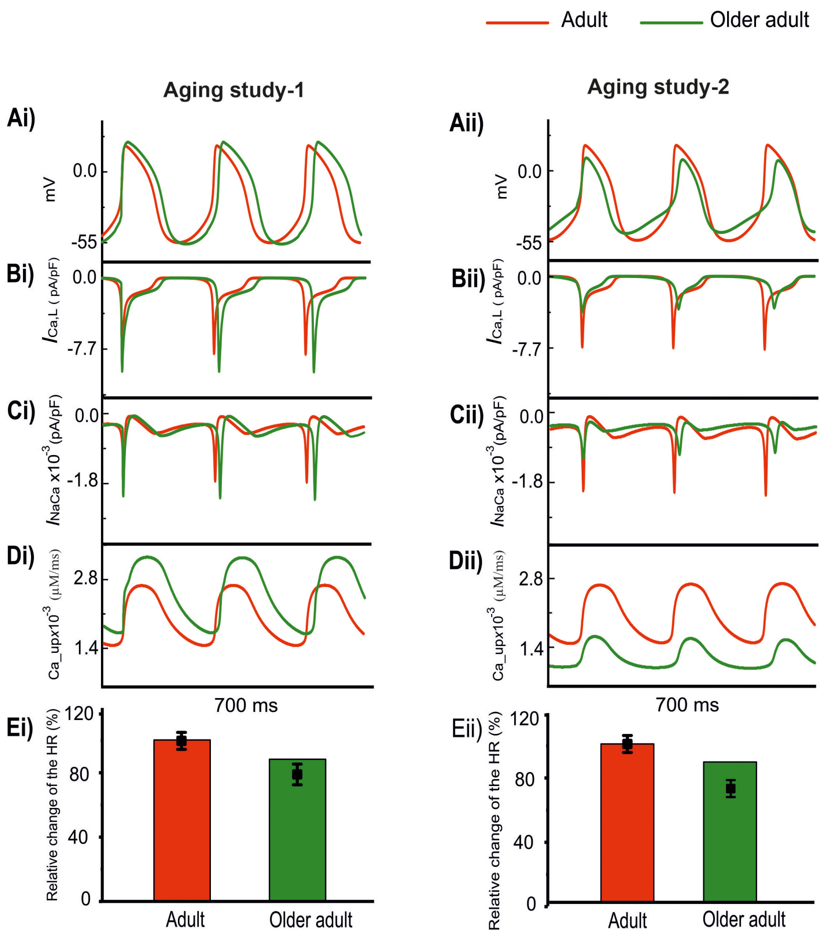

FIGURE 4 | Effect of remodeled $I_{Ca,L}$, I_{NaCa}, and Ca^{2+} uptake on pacemaking APs (red: adult; green: older adult). Other ion channel changes, as seen by Tellez et al. (2011) in Aging Study-1 **(right panels)**, and by Hatch (2012) in Aging Study-2 **(left panels)**, were omitted in simulations. **(Ai,Aii)** APs. **(Bi,Bii)** $I_{Ca,L}$. **(Ci,Cii)** I_{NaCa}. **(Di,Dii)** Ca^{2+} uptake. **(Ei,Eii)** Relative HR and its reduction. Data-points with error bars show the experimental data.

$I_{Ca,L}$ through changing g_{CaL} modulates the measured CL leading to bradycardiac pacemaking.

In Aging Study-1, when the age-related increase in SERCA2a (by 15%), or the decrease in NCX (by 6%) alone was considered, negligible effects in modulating the pacemaking APs was observed. Similarly, in Aging Study-2, when a decrease in SERCA2a (by 29%) or an increase in NCX (by 42%) alone was considered, their effect on the pacemaking APs was also limited.

These simulations implied that based on experimental data of Aging Study- 1 and 2 the altered $I_{Ca,L}$ produced notable effects on the modulation of the pacemaking AP profiles and rates, leading to bradycardia, though through different actions of either up-regulation or down-regulation of it.

Case 3: Effect of Remodeled I_{Kr}, I_{Ks}, I_{to}, I_{NaK}, and $I_{Ca,T}$ (Specific for Dataset 1)

Aging Study-1 also found changes in other ion channels, including I_{Kr}, I_{Ks}, I_{to}, I_{Nak}, and $I_{Ca,T}$, which were absent in Aging Study-2. Further simulations were conducted to investigate the effects of such a subset of remodeled ion channels on aging bradycardia. In simulations, we considered the integral action of changes to I_{Kr} (by a 6% reduction), I_{Ks} (by a 25% increase), I_{to} (by a 60% increase), I_{NaK} (by a 50% increase), and $I_{Ca,T}$ (by a 12% decrease).

Simulation results of APs for the adult and older adult conditions are shown in **Figure 6A**. In this case, the remodeled ion channels produced a 9.13% increase in CL (i.e., a 6.9% decrease in HR). It also produced changes in other AP characteristics, including a more hyperpolarized MDP (by −3 mV), and a prolonged APD_{50} (by 26 ms).

Panels B–F in **Figure 6** show the time traces of the relevant ion-channel currents for I_{Kr}, I_{Ks}, I_{to}, $I_{Ca,T}$, and I_{NaK} in the adult and older adult conditions. It was shown that during APs, the decreased of the peak amplitude might be attributable to the change in I_{to} and I_{Ks}; the more hyperpolarized MDP might be attributable to the increased I_{NaK}; the prolonged APD_{50} was attributable to the decreased I_{Kr}; and the decreased DD phase was partially attributable to the integral action of the decreased I_{Kr} and $I_{Ca,T}$. The

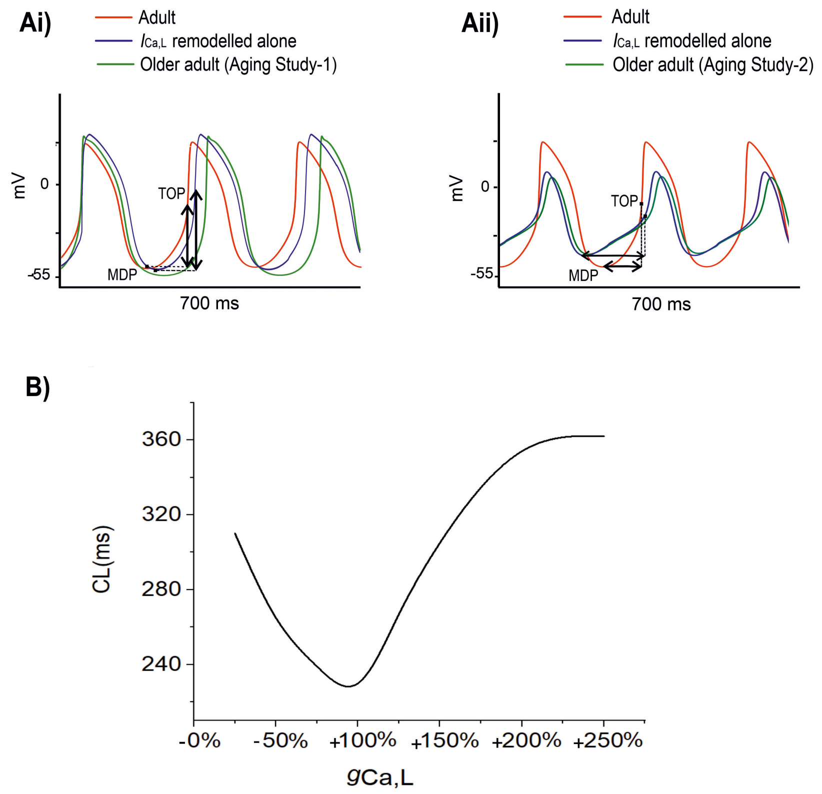

FIGURE 5 | (A) Simulated APs when the age-related remodeling of $I_{Ca,L}$ alone (blue) was considered [other ion channel and Ca^{2+} handling changes, as seen by Tellez et al. (2011) in Aging Study-1 (right panels), and by Hatch (2012) in Aging Study-2 (left panels), were ignored]. The obtained APs were compared with those of adult (red) and those with all ion channel and Ca^{2+} handling remodeling were considered (green). **(B)** Relationship between CL and increase (positive direction) or decrease (negative direction) in g_{CaL}. It demonstrates that CL increases with either an increased or a decreased g_{CaL} compared to the reference value of 100%. MDP: the maximal diastolic membrane potential. TOP, the take-off potential at which a line drawn from the MDP along the diastolic depolarization time course intersects with a vertical line drawn from the AP overshoot.

TABLE 1 | Quantitative analysis of the role of age-related remodeling of $I_{Ca,L}$ alone in bradycardia as compared to the case when all remodeling were considered.

APS characteristics	Adult	Aging study 1		Aging study 2	
		+25% $I_{Ca,L}$ remodeled alone	All ion-channel remodeling	−50% $I_{Ca,L}$ remodeled alone	All ion-channel remodeling
dV/dt_{max} (V/s)	6.50	7.22	10.85	3.20	2.31
MDP (mV)	−54.01	−55.02	−56.84	−47.00	−45.70
PA (mV)	20.00	25.00	24.58	6.61	9.5
APD_{50} (ms)	77.06	95.11	88.00	57.77	64.00
CL (ms)	230.00	267.50	310.44	260.00	265.22

prolonged APD_{50} slowed down the repolarization phase and, together with the slowed DD depolarization phase and the increased time interval required for membrane potential to reach the take-off potential from the MDP, resulted in a slowed HR.

The individual roles of each remodeled I_{Ks}, I_{to}, I_{NaK}, and $I_{Ca,T}$ ion channels were also simulated, generating a 1.3, 1.7, 6.7, and 5.6% change in CL, respectively, as shown in **Figure 6G**. The simulation showed that the remodeled I_{NaK} and $I_{Ca,T}$ currents alone made notable contributions to an increased CL, in which the remodeled I_{Kr} current was responsible for the increase in APD_{50}, slowing the repolarization phase of the APs.

DISCUSSION

The main findings of this study are the following:

(1) heart-rate reduction in aged rat sinoatrial myocytes can be sufficiently accounted for by the age-induced ionic-current and Ca^{2+}-handling remodeling of $I_{Ca,L}$, I_f, I_{NaCa}, SERCA2a, and RyR;

(2) whilst all remodeled channels and Ca^{2+}-handling contribute to the heart-rate reduction in the older adult, the remodeled $I_{Ca,L}$ plays the most significant role; and

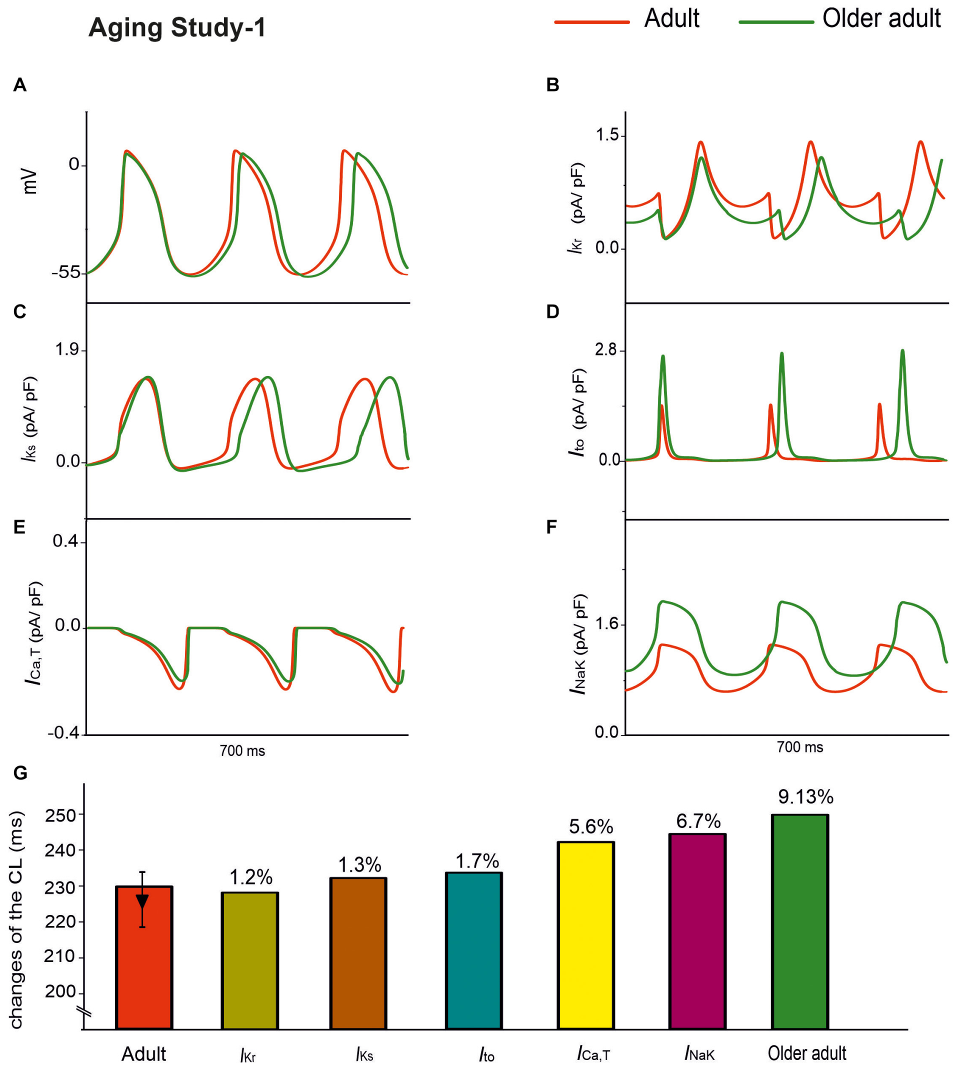

FIGURE 6 | APs for the adult and older adult conditions with the subset of changes to the ion-channel currents involved in Aging Study-1, namely I_{Kr}, I_{Ks}, I_{to}, $I_{Ca,T}$, and I_{NaK} **(A)**. Panels **(B–F)** show the time traces for the relevant ion-channel currents, namely I_{Kr}, I_{Ks}, I_{to}, $I_{Ca,T}$ and I_{NaK} in the adult and older adult conditions. **(G)** Illustrates the role of the individual remodeled ionic channels on CL values.

(3) remodeled $I_{Ca,L}$, either up-regulated or down-regulated by aging, leads to a similar bradycardia effect.

Mechanism Underlying Age-Related SAN Dysfunction

Possible mechanism(s) underlying the age-related SAN dysfunction were investigated by both the inclusive and exclusive methods in simulations. With the inclusive method, when all remodeling of ion channels and Ca^{2+} handling identified in Aging Study-1 (Tellez et al., 2011) and Aging Study-2 (Hatch, 2012; Huang et al., 2016) were considered, a similar bradycardic effect was produced, which was manifested by a slower pacemaking rate of APs in the older adult as compared with the adult rat SAN cell. This observation suggested that the identified age-related changes in ion channels ($I_{Ca,L}$, I_f, I_{NaCa}) and Ca^{2+}-handling (SERCA2a and RyR) in both studies were adequately responsible for the experimentally observed age-related changes in APs, which were consistent to the experimental data of the two studies. Note that, though a similar bradycardic effect was produced, changes in some other AP characteristics, such as the maximal upstroke velocity (dV/dt_{max}), AP amplitude and duration (APD_{50}), were different between the two cases of simulations. While the computed dV/dt_{max} and APD_{50} in the older adult condition were increased in the case of Aging Study-1, they were decreased in the case of Aging Study-2.

Role of I_f and Ca^{2+} RyR Release

The relative roles of aging-remodeled I_f and Ca^{2+}-RyR release in bradycardia was investigated by using the exclusive method. When down-regulations of I_f and Ca^{2+} RyR release were considered for the older adult condition as seen in both Aging Studies 1 and 2, no apparent effect was observed on modulating the APs. This suggested a limited role of remodeled I_f and Ca^{2+} RyR release in generating the age-related bradycardic effect.

A limited role of I_f in aging bradycardia in slowing down the pacemaking APs as seen in the present study is consistent with the experimental observation of Shinagawa et al. (2000), who reported that I_f activated at a very negative threshold, −90 mV, and is little activated under the normal AP threshold range (−70 to −50 mV). As the Tao et al. model was developed for the primary pacemaking cells of the rat SAN, which has a MDP at around −55 mV, at which the activated I_f is small, and therefore contributes only slightly to the pacemaking APs of the rat SAN cells. Considering the regional differences in cellular electrophysiological properties of SAN between central and peripheral regions, including the MDP and ion channel current densities as seen in the rabbit heart (Zhang et al., 2000), it is expected that the aging-induced I_f remodeling may have a greater effect in modulating the pacemaking APs in peripheral cells as compared to the results seen in the present study using the Tao et al. model for the central SAN cells. Unfortunately, a lack of rat SAN experimental data in this regard precluded investigation of this possibility in this study. The issue certainly warrants future investigation when experimental data on the regional differences in cellular electrophysiological properties of the rat SAN become available.

In both data sets of Aging Studies 1 and 2, substantial down-regulation of RYR2 in the SAN during the aging process was observed, which was believed to be responsible for a reduced heart rate in the aged rat (Tellez et al., 2011). However, in our simulations, a reduction of SR Ca^{2+} release in the range from 30 to 80% as observed in the two experimental studies showed only limited effects in slowing down the heart rate. A complete block of Ca^{2+} release from the SR only produced a 3.5% increase in CL. This finding was in agreement with previous experimental observations, which showed that the effect of SR Ca^{2+} release on pacemaker activity in adult rat central SAN cells was small due to the poor development of SR in these cells (Tao et al., 2011).

There has been an ongoing debate as to the leading mechanism responsible for the pacemaking activity in the SAN (Lakatta and DiFrancesco, 2009). One theory is the role of the membrane clock, in which I_f plays an important role (DiFrancesco, 1993; Accili et al., 2002). The other is that the Ca^{2+} clock plays an important role, by which SR pumping kinetics are thought to regulate spontaneous beating in rabbit SAN (Maltsev and Lakatta, 2009). The rate of SR replenishment defines the cycle length of each natural beat. Its occurrence is based on the cytosolic Ca^{2+} availability and SERCA2a activity due to RYR2 release flux and Cav1.2 influx, as described by Vinogradova et al. (2000). Even though the SR's role in initiating an AP is debatable and may be species dependent (DiFrancesco, 1993; Accili et al., 2002; Lakatta and DiFrancesco, 2009; Maltsev and Lakatta, 2009; Li et al., 2013), there are distinct changes in SR proteins that are clearly related to aging.

Role of $I_{Ca,L}$, I_{NaCa} and SR Ca^{2+} Uptake

There are contradictory changes in $I_{Ca,L}$, I_{NaCa} and Ca^{2+} uptake from the SR between the two group datasets of the aging studies. In order to understand their relative contribution(s) to the age-related bradycardia, the exclusive method was used to investigate the collective effect of the three factors as well as their individual role. It was shown that whilst this subset of remodeling factors collectively are attributable to the bradycardic effect, it was the remodeling of $I_{Ca,L}$ that played a primary role. In both datasets, when a down-regulation or up-regulation of I_{CaL} alone was considered, a dramatic bradycardic effect was observed, which was comparable to the case when all ion channel and Ca^{2+} handling remodeling were considered. An increase in the pacemaking CL with a decrease of the channel conductance of I_{CaL} has been shown before by Kurata et al. in the rabbit SAN cell model (Kurata et al., 2002). In the present study, we expanded their observation by showing that not only the decrease, but also the increase of I_{CaL} can cause slowing down in the pacemaking APs as manifested by an increase in the CL.

Our results highlight the importance of the remodeled $I_{Ca,L}$ to generate aging-related bradycardia (see **Figure 7**). This is consistent with a previous study, which showed that I_{CaL} was a critical pacemaking current in adult rat SAN, as demonstrated by spontaneous beating being halted by Ca^{2+} antagonists (Hatch, 2012). In simulations, we also observed a complete $I_{Ca,L}$ block abolished the pacemaker activity (data not shown), which is consistent with the experimental observation. When remodeling in SERCA2a (by 29%) or NCX alone was considered, limited effects on pacemaking APs were observed as seen in previous studies (Katz and Miledi, 1968; Szentesi et al., 2004). Collectively, our simulation results implied that the remodeled $I_{Ca,L}$ has the most significant influence on slowing down of the pacemaking rates in the older adult rat SAN myocytes.

Role of Remodeled I_K, I_{to}, I_{Ks}, I_{NaK}, and $I_{Ca,T}$

The role of each individual remodeled ion channel of I_{Kr}, I_{to}, I_{Ks}, I_{NaK}, and $I_{Ca,T}$, as seen in Aging Study-1, was also investigated. The functional effect of these remodeled ion channels prolonged the time course of APs, leading to a reduced pacemaking rate, some of which was associated with a secondary action. For example, the reduction in I_{Kr} prolonged the APD_{50}, therefore slowing down the repolarization phase of the APs. In the adult rat SAN model, I_{Kr} is considered to be another important pacemaking current. It has been observed that during diastole, I_{Kr} is slowly deactivated and the decreased outward current enables self-activated depolarization. Therefore, in combination with other currents, remodeling of this current might play a secondary role in reducing the HR of the aged SAN (Talano et al., 1978; Hagiwara et al., 1988; Zhou and Lipsius, 1994; Lei et al., 2002; Tellez et al., 2011). Decreased spontaneous activity and sinus arrest were observed in rat SAN cells when I_{Kr} was completely blocked by E-4031 (Mitsuiye et al., 2000).

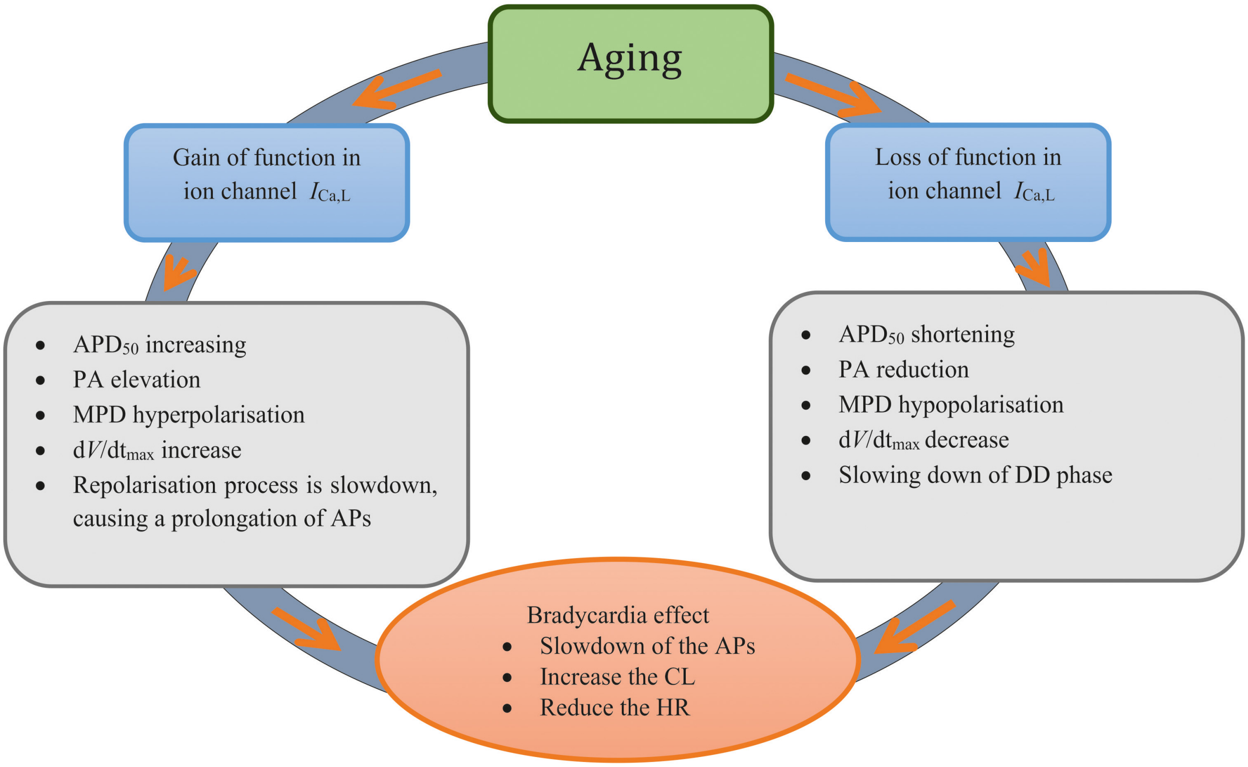

FIGURE 7 | Diagrammatic representation to summarize the two 'ways' of remodeled $I_{Ca,L}$ Investigated in this study and the mechanisms associated with each process.

Are Their Multiple Causes of Aging-Dependent Sinus Node Dysfunction?

The differences between Aging Study-1 and Aging Study-2 could be the result of mRNA changes not reflecting changes in protein or erroneous protein measurement. Alternatively, the differences between the two studies could reflect different remodeling patterns to age-dependent sinus node dysfunction. The literature on age-dependent sinus node dysfunction is conflicting with different studies reporting different changes (Lamas et al., 2000; Hao et al., 2011; Moghtadaei et al., 2016). Once again the differences could be the result of shortcomings in the methodologies used, but they could be genuine. Genuine differences could be the result of the use of different species in different studies. There are other possible reasons. A clue comes from the study of Moghtadaei et al. (2016) which shows that in aged mice the sinus node dysfunction depends on the frailty of the mouse. Therefore, it is possible that in the aged animal the nature of sinus node dysfunction depends on co-morbidities. For example, in a study of age-dependent sinus node dysfunction in the rat, we noted that the old male rats were obese (Yanni et al., 2010). We have independently shown that obesity in the rat causes molecular remodeling of ion channels and sinus node dysfunction (Linscheid et al., 2019; Webb et al., 2017, 2018). Therefore, the differences between studies could be the result of co-morbities which vary in different studies. In summary, it is not proven but it is feasible that there are multiple causes of sinus node dysfunction in the old animal. This computer modeling study shows that it is at least feasible that the ion channel remodeling in Aging Study-1 and Aging Study-2 causes sinus node dysfunction. There is now a need for further experimental studies of age-dependent sinus node dysfunction taking into account species, strain, gender, age, frailty and co-morbidities – any or all of these may affect sinus node function.

LIMITATIONS OF THE STUDY

The rat SAN model used in our simulations had certain inherent limitations, as described previously (Tao et al., 2011). Our simulation incorporated age-induced changes in ion channels and intracellular Ca^{2+} handling from two independent studies into the rat SAN model (Jones et al., 2004; Tellez et al., 2011; Hatch, 2012). The data were derived from mRNA gene expression or protein levels whenever experimental data on their kinetic or current densities in the SAN cell were unavailable. Mathematical modeling of the cardiac action potential ideally should be based on electrophysiological (usually patch clamp) recording of ionic currents obtained under physiological conditions. However, when such data are incomplete or absent, measurements of ion channel protein levels can be used as they may be used as a rough measure of ion channel density. Implicit assumptions of this approach are a direct relationship between expression levels of transcript levels or membrane proteins and the measured macroscopic channel conductance, and that relative change of expression levels may reflect changes in the macroscopic channel conductance. Whilst, such assumptions have limitations because a direct correlation between the gene expression or protein levels for certain ion channel subunits and their current densities cannot be guaranteed, this is a secondary approach in cases where direct current measurement data are missing. For example, with such an assumption, data on the expression of ion channels in the human SAN obtained by the quantitative polymerase chain reaction method, especially the ratio of the expression level between the SAN and human atrial cells have been successfully used to develop a computer model for the human SAN from the human atrial cell model (Yanni et al., 2010). Moreover, this approach has also been used effectively in additional modeling studies (Hao et al., 2011; Choudhury et al., 2018), and some computer modeling of action potentials (Chandler et al., 2009; Benoist et al., 2011; Abd Allah et al., 2012; Temple et al., 2016; D'Souza et al., 2020) have been done based on the RT-qPCR measurement of ion channel mRNA levels that often reflect protein levels (Tellez et al., 2006; D'Souza et al., 2014, 2015). In the present study, we followed the same approach as implemented by these prior studies (Yanni et al., 2010; Hao et al., 2011; Choudhury et al., 2018) and successfully reproduced the bradycardia effect in the model of Aging Study -1 which is comparable to experimental data, validating again the use of this approach.

Our results have shown that the aging-induced remodeling in I_{CaL} plays an important contribution to the aging bradycardia. It is known that L-type Ca^{2+} channels are multi-subunit complexes formed by different isoforms, including Cav1.2 and Cav1.3, which have different kinetics that influence their contribution to SAN pacemaking (Zuccotti et al., 2011). It would therefore be informative to further analyze their relative contributions to aging-associated bradycardia. However, due to a lack of available voltage clamp data on the activation, inactivation and channel kinetics of the two distinct I_{CaL} components from the rat SAN cells, it was possible in the model to consider only a general form of I_{CaL}, without differentiating effects on the two specific isoforms. The relative roles of the two I_{CaL} components in the aging bradycardia warrants further investigation in future, when suitable experimental data become available.

Finally, the results of this study were determined at the single-cell level. Consequently, other factors associated with aging, such as remodeling the electrical coupling between cells via the gap junction (Huang et al., 2015), or connexin, and the possible incidence of fibrosis (Baruscotti and Robinson, 2007; Semelka et al., 2013), might also play a specific role in production of the bradycardia effect that is more pronounced at the tissue level. Nevertheless, without considering age-induced changes in the connexins and fibrosis, such changes in various ionic channel conductances can nevertheless increase CL and reduce HR in a manner that is quantitatively comparable with experimental data.

CONCLUSION

In this study, the mechanism underlying the age-related SAN dysfunction in a commonly used model species was elucidated. Our results suggest that while it is an integral action of all remodeled ion channels and Ca^{2+} handling, the remodeled $I_{Ca,L}$, either via a gain or loss of function, contributes primarily to age-related bradycardia. Although further work is required to establish the extent to which these findings also apply to the human SAN, aging-related bradycardia appears able to be linked to different remodeling of $I_{Ca,L}$, which may ultimately have utility for clinical treatment strategies.

DATA AVAILABILITY STATEMENT

The original contributions presented in the study are included in the article/**Supplementary Material**, further inquiries can be directed to the corresponding author/s.

AUTHOR CONTRIBUTIONS

HZ conceived the study and contributed to data analysis and interpretation, supervision, and manuscript writing. AA conducted experiments, collected the data, and contributed to data analysis and interpretation and manuscript writing. JH contributed to data analysis and interpretation and manuscript writing. MB contributed to data analysis and interpretation and manuscript writing. All authors contributed to the article and approved the submitted version.

FUNDING

This work was funded by King Abdul-Aziz University KAU, Jeddah, Saudi Arabia; University of Jeddah, Jeddah, Kingdom Saudi Arabia, and supported by a scholarship from the Saudi Cultural Bureau, London, United Kingdom, and by grants from EPSRC (United Kingdom) (EP/J00958X/1 and EP/I029826/1).

SUPPLEMENTARY MATERIAL

The Supplementary Material for this article can be found online at: https://www.frontiersin.org/articles/10.3389/fphys.2020.546508/full#supplementary-material

REFERENCES

Abd Allah, E. S. H., Tellez, J. O., Aslanidi, O. V., Zhang, H., Dobrzynski, H., and Boyett, M. R. (2012). Postnatal development of transmural gradients in expression of ion channels and Ca2+-handling proteins in the ventricle. *J. Mol. Cell. Cardiol.* 53, 145–155. doi: 10.1016/j.yjmcc.2012.04.004

Accili, E. A., Proenza, C., Baruscotti, M., and DiFrancesco, D. (2002). From Funny Current to HCN channels: 20 years of excitation. *Physiology* 17, 32–37. doi: 10.1152/physiologyonline.2002.17.1.32

Alghamdi, A. M., Testrow, C. P., Whittaker, D. G., and Zhang, H. (2018). The mechanism underlying heart rate and pacemaking activity decline in developing sinoatrial node of the rabbit heart. *Comp. Cardiol.* 45, 1–4.

Alings, A. M. W., and Bouman, L. N. (1993). Electrophysiology of the aging rabbit and cat sinoatrial node a comparative study. *Eur. Heart J.* 14, 1278–1288. doi: 10.1093/eurheartj/14.9.1278

Bai, X., Wang, K., Yuan, Y., Li, Q., Dobrzynski, H., and Boyett, M. R. (2017). Mechanism underlying impaired cardiac pacemaking rhythm during ischemia: a simulation study. *Chaos* 27:093934. doi: 10.1063/1.5002664

Baruscotti, M., and Robinson, R. B. (2007). Electrophysiology and pacemaker function of the developing sinoatrial node. *Am. J. Physiol. Hear. Circ. Physiol.* 293, 2613–2623.

Benoist, D., Stones, R., Drinkhill, M., Bernus, O., and White, E. (2011). Arrhythmogenic substrate in hearts of rats with monocrotaline-induced pulmonary hypertension and right ventricular hypertrophy. *Am. J. Physiol. Heart Circ. Physiol.* 300, H2230–H2237.

Bers, D. M. (2001). *Excitation-Contraction Coupling and Cardiac Contractile Force [Internet]. cited 4 Jul 2018]. (Developments in Cardiovascular Medicine; vol. 237)*. Dordrecht: Springer.

Brioschi, C., Micheloni, S., Tellez, J. O., Pisoni, G., Longhi, R., Moroni, P., et al. (2009). Distribution of the pacemaker HCN4 channel mRNA and protein in the rabbit sinoatrial node. *J. Mol. Cell Cardiol.* 47, 221–227. doi: 10.1016/j.yjmcc.2009.04.009

Butters, T. D., Aslanidi, O. V., Inada, S., Boyett, M. R., Hancox, J. C., Lei, M., et al. (2010). Mechanistic links between Na^+ channel (SCN5A) mutations and impaired cardiac pacemaking in sick sinus syndrome. *Circ. Res.* 107, 126–137. doi: 10.1161/circresaha.110.219949

Chandler, N. J., Greener, I. D., Tellez, J. O., Inada, S., Musa, H., Molenaar, P., et al. (2009). Molecular architecture of the human sinus node - insights into the function of the cardiac pacemaker. *Circulation* 119, 1562–1575. doi: 10.1161/circulationaha.108.804369

Choudhury, M., Black, N., Alghamdi, A., Souza, A. D., Wang, R., Yanni, J., et al. (2018). TBX18 overexpression enhances pacemaker function in a rat subsidiary atrial pacemaker model of sick sinus syndrome. *J. Physiol.* 596, 6141–6155. doi: 10.1113/jp276508

Choudhury, M., Boyett, M. R., and Morris, G. M. (2015). Biology of the sinus node and its disease. *Arrhythmia Physiol. Rev.* 4, 28–34.

Congxin Huang, M. D., Wenmao Ding, M. D., Lan Li, M. D., and Dongdong Zhao, M. C. (2006). Differences in the aging-associated trends of the monophasic action potential duration and effective refractory period of the right and left atria of the rat. *Circ. J.* 70, 352–357. doi: 10.1253/circj.70.352

DiFrancesco, D. (1993). Pacemaker mechanisms in cardiac tissue. *Annu. Rev. Physiol.* 55, 455–472. doi: 10.1146/annurev.ph.55.030193.002323

Dobrev, D. (2009). Ion channel portrait of the human sinus node: useful for a better understanding of sinus node function and dysfunction in humans? *Circulation* 119, 1556–1558. doi: 10.1161/circulationaha.108.836866

D'Souza, A., Bucchi, A., Johnsen, A. B., Logantha, S. J., Monfredi, O., Yanni, J., et al. (2014). Exercise training reduces resting heart rate via downregulation of the funny channel HCN4. *Nat. Commun.* 5:3775.

D'Souza, A., Wang, Y., Johnsen, A. B., Olieslagers, S., Ni, H., Cox, C., et al. (2020). *(Full Paper Under Revision). Circadian Control of Heart Rate Occus via an Intrinsic Sinus Node Clock and the Pacemaker Channel. Heart Rhythm*, submitted.

D'Souza, A., Wegner, S., Johnsen, A. B., Gill, E., Cox, C., Dobrzynski, H., et al. (2015). Circadian control of heart rate. *Circ. Res.* 117, A430–A430.

Du, J., Deng, S., Pu, D., Liu, Y., Xiao, J., and She, Q. (2017). Age-dependent down-regulation of hyperpolarization-activated cyclic nucleotide-gated channel 4 causes deterioration of canine sinoatrial node function. *Acta Biochim. Biophys. Sin.* 49, 400–408. doi: 10.1093/abbs/gmx026

Fenske, S., Krause, S. C., Hassan, S. I. H., Becirovic, E., Auer, F., Bernard, R., et al. (2013). Sick sinus syndrome in HCN1-Deficient mice. *Circulation* 128, 2585–2594. doi: 10.1161/circulationaha.113.003712

Hagiwara, N., Irisawa, H., and Kameyama, M. (1988). Contribution of two types of calcium currents to the pacemaker potentials of rabbit sino-atrial node cells. *J. Physiol.* 395, 233–253. doi: 10.1113/jphysiol.1988.sp016916

Hao, X., Zhang, Y., Zhang, X., Nirmalan, M., Davies, L., Konstantinou, D., et al. (2011). TGF-β1-mediated fibrosis and ion channel remodeling are key mechanisms in producing the sinus node dysfunction associated with SCN5A deficiency and aging. *Circ. Arrhythmia Electrophysiol.* 4, 397–406. doi: 10.1161/circep.110.960807

Haqqani, H. M., and Kalman, J. M. (2007). Aging and sinoatrial node dysfunction: musings on the not-so-funny side. *Circulation* 115, 1178–1179. doi: 10.1161/circulationaha.106.685248

Härtel, G., and Talvensaari, T. (1975). Treatment of sinoatrial syndrome with permanent cardiac pacing in 90 patients. *Acta Med. Scand.* 198, 341–347. doi: 10.1111/j.0954-6820.1975.tb19555.x

Hatch, F. S. (2012). *Age-associated Changes to Calcium Handling Proteins Across the Whole Heart*. Ph.D. thesis, University of Hull, Hull.

Huang, X., Du, Y., Yang, P., Lin, S., Xi, Y., Yang, Z., et al. (2015). Age-dependent alterations of voltage-gated Na + channel isoforms in rat sinoatrial node. *Mech. Aging Dev.* 152, 80–90. doi: 10.1016/j.mad.2015.10.003

Huang, X., Yang, P., Yang, Z., Zhang, H., and Ma, A. (2016). Age-associated expression of HCN channel isoforms in rat sinoatrial node. *Exp. Biol. Med.* 241, 331–339. doi: 10.1177/1535370215603515

Jones, S. A., Boyett, M. R., and Lancaster, M. K. (2007). Declining into failure: the age- dependent loss of the L-type calcium channel within the sinoatrial node. *Circulation* 115, 1183–1190. doi: 10.1161/circulationaha.106.663070

Jones, S. A., Lancaster, M. K., and Boyett, M. R. (2004). Aging-related changes of connexins and conduction within the sinoatrial node. *J. Physiol.* 560, 429–437. doi: 10.1113/jphysiol.2004.072108

Katz, B., and Miledi, R. (1968). The role of calcium in neuromuscular facilitation. *J. Physiol.* 195, 481–492. doi: 10.1113/jphysiol.1968.sp008469

Kurata, Y., Hisatome, I., Imanishi, S., and Shibamoto, T. (2002). Dynamical description of sinoatrial node pacemaking: improved mathematical model for primary pacemaker cell. *Physiol. Hear. Circ. Physiol.* 283, H2074–H2101.

Lakatta, E. G., and DiFrancesco, D. (2009). What keeps us ticking: a funny current, a calcium clock, or both? *J. Mol. Cell Cardiol.* 47, 157–170. doi: 10.1016/j.yjmcc.2009.03.022

Lamas, G. A., Lee, K., Sweeney, M., Leon, A., Yee, R., Ellenbogen, K., et al. (2000). The Mode Selection Trial (MOST) in sinus node dysfunction: design, rationale, and baseline characteristics of the first 1000 patients. *Am. Heart J.* 140, 541–551. doi: 10.1067/mhj.2000.109652

Larson, E. D., St Clair, J. R., Sumner, W. A., Bannister, R. A., and Proenza, C. (2013). Depressed pacemaker activity of sinoatrial node myocytes contributes to the age-dependent decline in maximum heart rate. *Proc. Natl. Acad. Sci. U.S.A.* 10, 18011–18016. doi: 10.1073/pnas.1308477110

Lei, M., Cooper, P. J., Camelliti, P., and Kohl, P. (2002). Role of the 293b-sensitive, slowly activating delayed rectifier potassium current, IKs, in pacemaker activity of rabbit isolated sino-atrial node cells. *Cardiovasc. Res.* 53, 68–79. doi: 10.1016/s0008-6363(01)00459-x

Li, P., Lines, G. T., Maleckar, M. M., and Tveito, A. (2013). Mathematical models of cardiac pacemaking function. *Front. Phys.* 1:20. doi: 10.3389/fphy.2013.00020

Linscheid, N., Logantha, S., Poulsen, P. C., Zhang, S., Schrolkamp, M., Egerod, K. L., et al. (2019). Quantitative proteomics and single-nucleus transcriptomics of the sinus node elucidates the foundation of cardiac pacemaking. *Nat. Commun.* 10:2889.

Maltsev, V. A., and Lakatta, E. G. (2009). Synergism of coupled subsarcolemmal Ca^{2+} clocks and sarcolemmal voltage clocks confers robust and flexible pacemaker function in a novel pacemaker cell model. *Am. J. Physiol. Circ. Physiol.* 296, H594–H615.

Mitsuiye, T., Shinagawa, Y., and Noma, A. (2000). Sustained inward current during pacemaker depolarization in mammalian sinoatrial node cells. *Am. Hear. Assoc. Inc. Circ.* 87, 88–91. doi: 10.1161/01.res.87.2.88

Moghtadaei, M., Jansen, H. J., Mackasey, M., Rafferty, S. A., Bogachev, O., Sapp, J. L., et al. (2016). The impacts of age and frailty on heart rate and sinoatrial node function. *J. Physiol.* 594, 7105–7126. doi: 10.1113/jp272979

Opthof, T. (1994). Gap junctions in the sinoatrial node: immunohistochemical localization and correlation with activation pattern. *J. Cardio Electrophys.* 5, 138–143. doi: 10.1111/j.1540-8167.1994.tb01153.x

Satoh, H. (2003a). Sino-atrial nodal cells of mammalian hearts: ionic currents and gene expression of pacemaker ionic channels. *J Smooth Muscle Res.* 39, 175–193.

Satoh, H. (2003b). Elecropharmacology of taurine on the hyperpolarization activated inward current and the sustained inward current in spontaneously beating rat sino-atrial nodal cells. *J. Pharmacol. Sci.* 91, 229–238. doi: 10.1254/jphs.91.229

Satoh, H., Tohno, S., Azuma, C., Minami, T., Ohishi, T., Hayashi, M., et al. (2005). Age-related attenuation in the elements in monkey sino-atrial node. *Biol. Trace Elem. Res.* 107, 43–52.

Semelka, M., Gera, J., and Usman, S. (2013). Sick sinus syndrome: a review. *Am. Fam. Phys.* 87, 691–696.

Sharpe, E. J., Larson, E. D., and Proenza, C. (2017). Cyclic AMP reverses the effects of aging on pacemaker activity and I_f in sinoatrial node myocytes. *J. Gen. Physiol.* 149, 237–247. doi: 10.1085/jgp.201611674

Shinagawa, Y., Satoh, H., and Noma, A. (2000). The sustained inward current and inward rectifier K^+ current in pacemaker cells dissociated from rat sinoatrial node. *J. Physiol.* 523(Pt 3), 593–605. doi: 10.1111/j.1469-7793.2000.t01-2-00593.x

Sodeck, G. H., Domanovits, H., Meron, G., Rauscha, F., Losert, H., and Thalmann, M. (2007). Compromising bradycardia: management in the emergency department. *Resuscitation* 73, 96–102. doi: 10.1016/j.resuscitation.2006.08.006

Szentesi, P., Pignier, C., Egger, M., Kranias, E. G., and Niggli, E. (2004). Sarcoplasmic reticulum Ca^{2+} refilling controls recovery from Ca^{2+} -induced Ca^{2+} release refractoriness in heart muscle. *Circ. Res.* 95, 807–813.

Talano, J. V., Euler, D., Randall, W. C., Eshaghy, B., Loeb, H. S., and Gunnar, R. M. (1978). Sinus node dysfunction. *Am. J. Med.* 64, 773–781.

Tao, T., Paterson, D. J., and Smith, N. P. (2011). A model of cellular cardiac-neural coupling that captures the sympathetic control of sinoatrial node excitability in normotensive and hypertensive rats. *Biophys. J.* 101, 594–602. doi: 10.1016/j.bpj.2011.05.069

Tellez, J. O., Dobrzynski, H., Greener, I. D., Graham, G. M., Laing, E., Honjo, H., et al. (2006). Differential expression of ion channel transcripts in atrial muscle and sinoatrial node in rabbit. *Circ. Res.* 99, 1384–1393. doi: 10.1161/01.res.0000251717.98379.69

Tellez, J. O., Maczewski, M., Yanni, J., Sutyagin, P., Mackiewicz, U., Atkinson, A., et al. (2011). Aging-dependent remodelling of ion channel and Ca^{2+} clock genes underlying sino-atrial node pacemaking. *Exp. Physiol.* 96, 1163–1178. doi: 10.1113/expphysiol.2011.057752

Temple, I. T., Logantha, S. J. R. J., Absi, M., Zhang, Y., Pervolaraki, E., Yanni, J., et al. (2016). Atrioventricular node dysfunction and ion channel transcriptome in pulmonary hypertension. *Circ. Arrhythmia Electrophysiol.* 9:e003432.

Tohno, Y., Tohno, S., Viwatpinyo, K., Minami, T., Chaisuksunt, V., Mahakkanukrauh, P., et al. (2014). Age-related changes of elements in the human sinoatrial nodes. *OA Anat.* 2:21.

Vinogradova, T. M., Zhou, Y. Y., Bogdanov, K. Y., Yang, D., Kuschel, M., Cheng, H., et al. (2000). Sinoatrial node pacemaker activity requires Ca(2+)/calmodulin-dependent protein kinase II activation. *Circ. Res.* 87, 760–767. doi: 10.1161/01.res.87.9.760

Webb, K., Absi, M., Logantha, S. J., Zaborska, K., Gurney, A., Heagerty, A., et al. (2017). Obesity increases the propensity for atrial arrhythmias. *Eur. Heart J.* 37:86343.

Webb, K., Logantha, S. J., Absi, M., Cartwright, E., Zhang, H., Monfredi, O., et al. (2018). Obesity causes cardiac ion channel remodelling and increases the propensity for atrial arrhythmias. *Eur. Heart J.* 39:5702. doi: 10.1093/eurheartj/ehy566.P5702

Wood, M. A., and Ellenbogen, K. A. (2002). Cardiology patient pages, cardiac pacemakers from the patient's perspective. *Circulation* 105, 2136–2138.

Yanni, J., Tellez, J. O., Sutyagin, P. V., Boyett, M. R., and Dobrzynski, H. (2010). Structural remodelling of the sinoatrial node in obese old rats. *J. Mol. Cell. Cardiol.* 48, 653–662. doi: 10.1016/j.yjmcc.2009.08.023

Zhang, H., Holden, A. V., Kodama, I., Honjo, H., Lei, M., Varghese, T., et al. (2000). Mathematical models of action potentials in the periphery and center of the rabbit sinoatrial node. *Am. J. Physiol. Hear. Circ. Physiol.* 279, H397–H421.

Zhang, H., Zhao, Y., Lei, M., Dobrzynski, H., Liu, J. H., and Holden, A. V. (2007). Computational evaluation of the roles of Na + current, iNa, and cell death in cardiac pacemaking and driving. *Am. J. Physiol. Circ. Physiol.* 292, H165–H174.

Zhou, Z., and Lipsius, S. L. (1994). T-type calcium current in latent pacemaker cells isolated from cat right atrium. *J. Mol. Cell Cardiol.* 26, 1211–1219. doi: 10.1006/jmcc.1994.1139

Zuccotti, A., Clementi, S., Reinbothe, T., Torrente, A., Vandael, D. H., and Pirone, A. (2011). Structural and functional differences between L-type calcium channels: crucial issues for future selective targeting. *Trends Pharmacol. Sci.* 32, 366–375. doi: 10.1016/j.tips.2011.02.012

Conflict of Interest: The authors declare that the research was conducted in the absence of any commercial or financial relationships that could be construed as a potential conflict of interest.

frontiers in Physiology

ORIGINAL RESEARCH
published: 22 October 2019
doi: 10.3389/fphys.2019.01314

Proarrhythmia in the p.Met207Val PITX2c-Linked Familial Atrial Fibrillation-Insights From Modeling

Jieyun Bai[1]*, *Yaosheng Lu*[1], *Andy Lo*[2], *Jichao Zhao*[2]* *and Henggui Zhang*[3,4]*

[1] *Department of Electronic Engineering, College of Information Science and Technology, Jinan University, Guangzhou, China,* [2] *Auckland Bioengineering Institute, The University of Auckland, Auckland, New Zealand,* [3] *Biological Physics Group, School of Physics & Astronomy, University of Manchester, Manchester, United Kingdom,* [4] *Pilot National Laboratory for Marine Science and Technology, Qingdao, China*

Functional analysis has shown that the p.Met207Val mutation was linked to atrial fibrillation and caused an increase in transactivation activity of PITX2c, which caused changes in mRNA synthesis related to ionic channels and intercellular electrical coupling. We assumed that these changes were quantitatively translated to the functional level. This study aimed to investigate the potential impact of the PITX2c p.Met207Val mutation on atrial electrical activity through multiscale computational models. The well-known Courtemanche-Ramirez-Nattel (CRN) model of human atrial cell action potentials (APs) was modified to incorporate experimental data on the expected p.Met207Val mutation-induced changes in ionic channel currents (I_{NaL}, I_{Ks}, and I_{Kr}) and intercellular electrical coupling. The cell models for wild-type (WT), heterozygous (Mutant/Wild type, MT/WT), and homozygous (Mutant, MT) PITX2c cases were incorporated into homogeneous multicellular 1D and 2D tissue models. Effects of this mutation-induced remodeling were quantified as changes in AP profile, AP duration (APD) restitution, conduction velocity (CV) restitution and wavelength (WL). Temporal and spatial vulnerabilities of atrial tissue to the genesis of reentry were computed. Dynamic behaviors of re-entrant excitation waves (Life span, tip trajectory and dominant frequency) in a homogeneous 2D tissue model were characterized. Our results suggest that the PITX2c p.Met207Val mutation abbreviated atrial APD and flattened APD restitution curves. It reduced atrial CV and WL that facilitated the conduction of high rate atrial excitation waves. It increased the tissue's temporal vulnerability by increasing the vulnerable window for initiating reentry and increased the tissue spatial vulnerability by reducing the substrate size necessary to sustain reentry. In the 2D models, the mutation also stabilized and accelerated re-entrant excitation waves, leading to rapid and sustained reentry. In conclusion, electrical and structural remodeling arising from the PITX2c p.Met207Val mutation may increase atrial susceptibility to arrhythmia due to shortened APD, reduced CV and increased tissue vulnerability, which, in combination, facilitate initiation and maintenance of re-entrant excitation waves.

Keywords: atrial fibrillation, PITX2c, modeling and simulation, human atrial action potential model, electrical and structural remodeling, gene regulation, transcription factors, single nucleotide polymorphism

Edited by:
Futoshi Toyoda,
Shiga University of Medical Science, Japan

Reviewed by:
Kunichika Tsumoto,
Kanazawa Medical University, Japan
Georges Christé,
Institut National de la Santé et de la Recherche Médicale (INSERM), France

***Correspondence:**
Jieyun Bai
bai_jieyun@126.com
Jichao Zhao
j.zhao@auckland.ac.nz
Henggui Zhang
henggui.zhang@manchester.ac.uk

Specialty section:
This article was submitted to Computational Physiology and Medicine,
a section of the journal Frontiers in Physiology

Received: *26 June 2019*
Accepted: *30 September 2019*
Published: *22 October 2019*

Citation:
Bai J, Lu Y, Lo A, Zhao J and Zhang H (2019) Proarrhythmia in the p.Met207Val PITX2c-Linked Familial Atrial Fibrillation-Insights From Modeling. Front. Physiol. 10:1314. doi: 10.3389/fphys.2019.01314

INTRODUCTION

The most common arrhythmia atrial fibrillation (AF) increases with age and is associated with adverse events (such as heart failure, stroke, hypertension and diabetes) (Heijman et al., 2018). These cardiac disorders are thought to promote AF which is characterized by uncoordinated patterns of atrial electrical activation and a fast and irregular heartbeat (Hansen et al., 2015). Whilst the precise mechanisms underlying AF are complex and poorly understood, AF-induced ionic remodeling and structural cardiac diseases are major factors in initiating and sustaining AF (Grandi et al., 2011; Colman et al., 2013; Koivumäki et al., 2014). However, genome-wide association studies suggested genetic variation contributes to AF susceptibility, with >100 AF-associated loci reported to date (Nielsen et al., 2018), including the atrial-selective transcription factor PITX2 (paired like homeodomain-2) that regulates membrane effector genes associated with AF (Gudbjartsson et al., 2007; Chinchilla et al., 2011; Kirchhof et al., 2011; Qiu et al., 2014; Tao et al., 2014; Lozano-Velasco et al., 2015; Pérez-Hernández et al., 2015; Bai et al., 2018; Mechakra et al., 2019). In these studies, Mechakra et al. (2019) identified a non-synonymous mutation c.619A>G (p.Met207Val, rs138163892) of PITX2. Functional analysis of the transactivation activity of wild-type and variant PITX2c revealed a gain-of-function of PITX2c (the PITX2 c isoform), leading to an increase in the mRNA level of KCNH2 (the α subunit of I_{Kr}), KCNQ1 (the α subunit of I_{Ks}), SCN1B (the β1 subunit of sodium channels that modulates I_{NaL}), GJA5 (Cx40), and GJA1 (Cx43) (Mechakra et al., 2019).

I_{Kr}, I_{Ks}, and I_{NaL} regulate late repolarization of action potentials (APs), and Cx40 and Cx43 mediate intercellular electrical coupling via gap junctions (Dhillon et al., 2014). Ionic remodeling due to changes in potassium currents (Caballero et al., 2010; González de la Fuente et al., 2012; Pérez-Hernández et al., 2015) and I_{NaL} (Sossalla et al., 2010), and structural remodeling arising from abnormalities in Cx40 and Cx43 (Polontchouk et al., 2001; Nao et al., 2003; Wetzel et al., 2005) have been found in chronic AF patients. In a previous experimental study, it has been shown that overexpression of PITX2c (a gain-of-function) increased I_{Ks} density and decreased I_{CaL}density in atrial myocytes from chronic AF patients (Pérez-Hernández et al., 2015). These changes could contribute to the long-term stabilization of the arrhythmia by shortening the AP duration (APD) (González de la Fuente et al., 2012). By contrast, whilst the gain-of-function arising from the p.Met207Val mutation has been suggested to increase susceptibility to familial AF (Mechakra et al., 2019), this link remains to be demonstrated directly.

The mechanisms by which ionic and structural remodeling induced by the PITX2c p.Met207Val mutation promotes and perpetuates AF have not yet been elucidated. Complex electrical wave dynamics observed during AF is determined by AP morphology, APD, conduction velocity (CV) restitution, wavelength (WL), vulnerable window (VW) for unidirectional conduction block, and the minimal substrate size required to induce re-entry (Bai et al., 2016b; Ni et al., 2017; Whittaker et al., 2017, 2018a,b). Therefore, utilizing a multi-scale computational model of the human atria based on experimental data on the PITX2c p.Met207Val mutation, we simulated electrical activity to quantify its potential impact at the cellular, 1D fiber tissue and 2D sheet tissue levels.

METHODS

Human Atrial Action Potential Model

The Courtemanche-Ramirez-Nattel (CRN) model (Courtemanche et al., 1998) of the human atrial AP was chosen to investigate the proarrhythmic effects of the PITX2c p.Met207Val mutation, because this model was suggested to study spatiotemporal characteristics of atrial fibrillation at the tissue and organ levels (Seemann et al., 2006; Kharche et al., 2012). The original CRN model was modified to reflect the observed kinetic properties of the I_{NaL} current (**Figure 1A**) that was based on the work of Grandi et al. (2011), who developed it using experimental data from human atrial myocardium (Sossalla et al., 2010). This I_{NaL} model is given by:

$$I_{NaL} = G_{NaL} \times m^3 \times h \times (V_m - E_{Na}) \tag{1}$$

$$\frac{dh}{dt} = \frac{h_\infty - h}{\tau_h} \tag{2}$$

$$h_\infty = \frac{1.0}{1.0 + \exp\left(\left(V_m + 91\right)/6.1\right)} \tag{3}$$

$$\tau_h = 600\ ms \tag{4}$$

$$\frac{dm}{dt} = \frac{m_\infty - m}{\tau_m} \tag{5}$$

$$m_\infty = \frac{\alpha_m}{\alpha_m + \beta_m} \tag{6}$$

$$\tau_m = \frac{1}{\alpha_m + \beta_m} \tag{7}$$

$$\alpha_m = \frac{0.32\,(V_m + 47.13)}{1.0 - \exp\left(-0.1\,(V_m + 47.13)\right)} \tag{8}$$

$$\beta_m = 0.08 \exp\left(-V_m/11\right) \tag{9}$$

where G_{NaL} (0.0025 nS/pF) is the maximal conductance, m and h are two gate variables for I_{NaL}, V_m is the membrane potential, and E_{Na} is the sodium equilibrium potential. m_∞ and h_∞ denote steady-state activation and steady-state inactivation, respectively. τ_m/τ_h is the time constant for m_∞/h_∞.

Abbreviations: 1D and 2D, one- and two-dimensional model; AF, Atrial fibrillation; AP, Action potential; APD, Action potential duration; APDR, APD restitution; APD_{50}, APD values at 50% repolarization; APD_{90}, APD values at 90% repolarization; APA, AP amplitude; BCL, Basic cycle length; CV, Conduction velocity; CVR, CV restitution; CRN model, Courtemanche–Ramirez–Nattel model of electrical action potential of human atrial cells; D, Diffusion coefficient; DI, Diastolic interval; dV/dt_{max}, Maximum depolarization rate; ERP, Effective refractory period; Grandi model, Grandi model of electrical action potential of human atrial cells; I_{CaL}, L-type calcium current; I_{NaL}, Late sodium current; I_{Ks}, The slow delayed rectifier potassium current; I_{Kr}, The rapid delayed rectifier potassium current; MT, Mutant PITX2c; MT/WT, Mutant/Wild type PITX2c; PITX2, Paired like homeodomain-2; PITX2c, PITX2 c isoform; RMP, Resting membrane potential; VW, Vulnerable window; WL, Wavelength; WT, Wild-type PITX2c.

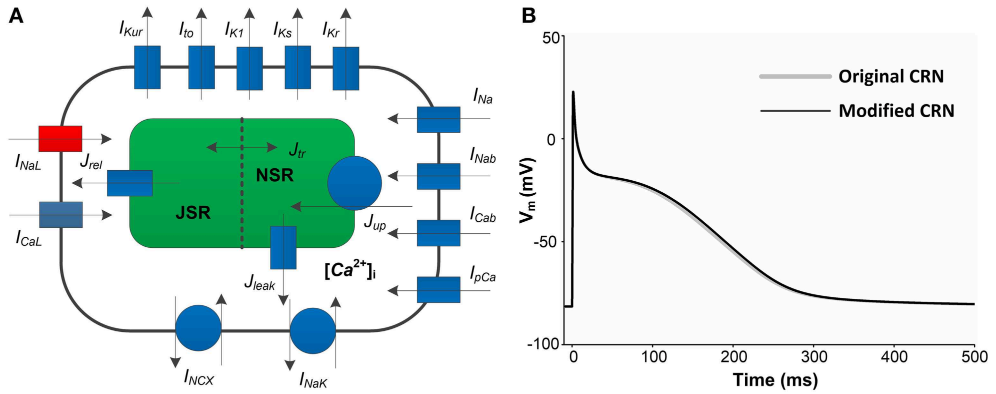

FIGURE 1 | A schematic overview of human atrial myocyte model and its corresponding action potentials (APs). **(A)** The original myocyte model (Original CRN) was improved to include the I_{NaL} model (marked in red). **(B)** APs obtained from the Original CRN model and the Modified CRN model.

Thus, the modified CRN model is described as

$$\frac{dV_m}{dt} = -\frac{I_{ion} + I_{stim}}{C_m} \quad (10)$$

$$I_{ion} = I_{Na} + I_{NaL} + I_{CaL} + I_{Nab} + I_{Cab} + I_{pCa} + I_{to} + I_{Kr} + I_{Ks} + I_{Kur} + I_{NCX} + I_{NaK} \quad (11)$$

where I_{ion} is the sum of all ionic currents, I_{stim} (with a duration of 0.5 ms and a strength of −80 pA/pF) is the external stimulus current and C_m (100 pF) is the total membrane capacitance. Compared with the original CRN model, the amplitude, duration, and shape of the AP obtained from the modified CRN model had no significant changes (**Figure 1B**). All the equations, parameter values and initial conditions necessary to carry out the single cell simulations in this study can be found in the **Supplementary Table 1**.

The modified CRN model was used to investigate the characteristics of APs. These AP features included resting membrane potential (RMP), AP amplitude (APA), the maximum depolarization rate (dV/dt_{max}), AP duration at 50% repolarization (APD-$_{50}$), AP duration at 90% repolarization (APD-$_{90}$) and APD restitution (APDR). APDR was measured by using the standard dynamic method. The human atrial myocyte was firstly paced at a basic cycle length (BCL) of 1,000 ms for 700 beats to achieve steady-state APD$_{90}$s and then the BCL was progressively reduced by 5 to 50 ms. APDR curves were generated by plotting APD$_{90}$ vs. diastolic interval (DI) which was computed as BCL minus APD$_{90}$.

Modeling Electrical and Structural Remodeling Due to the PITX2c p.Met207Val Mutation

To obtain human atrial myocyte models that reproduced the experimentally observed changes in the mRNA levels corresponding to key proteins under wild-type (WT), heterozygous (Mutant/Wild type PITX2c, MT/WT) and homozygous (Mutant PITX2c, MT) conditions (Mechakra et al., 2019), we assumed that these changes in mRNA expression are quantitatively reflected at the final functional level of ion channels and connexins. Therefore, we changed the maximal conductances of I_{NaL}, I_{Ks} and I_{Kr} to account for ionic remodeling due to the PITX2c p.Met207Val mutation, and altered the diffusion coefficient (D) to simulate the effects of changed intercellular electrical coupling via gap junctions (Cx43 and Cx40). According to the work of Kanagaratnam et al. (2002), the Cx43/[Cx40+Cx43] ratio is associated with intercellular electrical coupling and conduction velocity (CV), such that, as the proportion of Cx40 signal increased (and that for Cx43 decreased), the CV decreased. Therefore, the Cx43/[Cx40+Cx43] ratio was used to change the parameter D. In our study, two different cases (i.e., MT/WT and MT) were considered for PITX2c p.Met207Val mutation-induced changes in I_{NaL}, I_{Ks}, I_{Kr}, and D (**Table 1**).

TABLE 1 | The PITX2c p.Met207Val mutation-induced changes (%) in structural and electrical components.

	Wild-type (WT)	Heterozygous expression (MT/WT)	Homozygous expression (MT)
I_{NaL}(%)	100	190	**170**
I_{Ks}(%)	100	100	**180**
I_{Kr}(%)	100	260	**360**
D (%)	100	80	**76**

The reduction rate of the diffusive coefficient was determined by the Cx43/[Cx43+Cx40] ratio. Under the WT condition, the Cx43: Cx40 ratio is 1:1, so the Cx43/[Cx43+Cx40] ratio is 0.5 and D (%) is set to be 100%. According to experimental data on mRNA levels of Cx43 and Cx40, D (%) is set to be 80% and 76%, respectively, under MT/WT and MT conditions. Bold values represent parameters and characteristics under the p.Met207Val PITX2c mutation condition.

Multicellular Atrial Tissue Models

These developed human atrial myocyte models were incorporated into 1D and 2D multicellular atrial tissue models with the modification to D for representing structural remodeling. These multicellular models were described by the following partial differential equation

$$C_m \frac{\partial V_m}{\partial t} = -I_{ion} + \nabla D \nabla V_m \quad (12)$$

where D is a tensor describing the conductivity of the tissue and ∇ is a gradient or Laplacian operator. In one dimension, $D = 0.031$ mm^2/ms; in two dimensions, $D_{ij} = 0.031$ mm^2/ms for $i = j$, and $D_{ij} = 0.0$ mm^2/ms for $i \neq j$. The surface to volume ratio is 1 and C_m is 100 pF. These values, in the WT case, which can lead to a planar wave with a CV of 0.269 mm/ms. Time (t) and space (x) steps were set to be 0.005 ms and 0.1 mm, respectively.

In the present study, we designed three idealized geometries (a 1D cable model with 375 nodes, a 2D sheet model with 375×375 nodes and a homogeneous 2D tissue model with 750 × 750 nodes). In these models, the 1D cable was used to generate CV restitution (CVR) curves, and to measure CV, WL, and VW. CVR was measured by using the standard dynamic method. The 1D cable was paced at a BCL of 1,000 ms for 50 beats to achieve steady-state AP wavefronts and then the BCL was progressively reduced by 50 ms. CVR curves were constructed by plotting CV against BCL. WL was computed as the product of CV and effective refractory period (ERP). ERP and VW were calculated by using the extra stimulus method. Propagating AP wavefronts were evoked by an S1 stimulus at a BCL of 1,000 ms for 50 beats and then a test S2 stimulus applied during the refractory tail of the 50th AP wave after a time delay (S1-S2 time interval). The maximal S1-S2 interval to fail to excite AP waves (bidirectional block) was defined as ERP in atrial tissues. The time window between the maximal S1-S2 interval for bidirectional block and the minimal S1-S2 interval for bidirectional conduction was defined as VW to induce unidirectional conduction block.

In addition to the temporal vulnerability of atrial tissues quantified by VW, the spatial vulnerability was evaluated in the homogeneous 2D tissue model with 750 × 750 nodes using an S1-S2 protocol. A planar wave evoked by an S1 stimulus propagated from the left side to the right side. Once this wave had passed over the first half of the domain, an S2 stimulus was applied to a center region with the same width (1.0 mm) and different lengths. The minimal substrate size was defined as the minimal size of the S2 stimulus necessary to form and sustain reentry.

To further investigate the temporal-spatial characteristics of electrical waves due to the PITX2c p.Met207Val mutation, we used the standard S1-S2 protocol to induce spiral waves in the homogeneous 2D tissue model with 375 × 375 nodes. A planar S1 stimulus was applied to the left boundary to initiate a planar wave. During the VW, a rectangular S2 stimulus was applied to the top left quarter of the domain to initiate a spiral wave. The life span of the spiral wave was measured as the time duration from initiation to dissipation. The tip meander path was traced with the method of Fenton and Karma (Fenton and Karma, 1998). Dominant frequencies of action potential (AP) profiles obtained from the central point of the domain were computed using the Fast Fourier Transform technique (Bai et al., 2016a, 2017a,b).

RESULTS

Effects of the PITX2c p.Met207Val Mutation on the Human Atrial Action Potential

Based on the experimental study of Mechakra et al. (2019), simulations of the functional impact of an increased transactivation activity of PITX2c due to the p.Met207Val mutation on Cx43, Cx40, I_{NaL}, I_{Ks}, and I_{Kr} were conducted to investigate how they contribute to atrial electrical and structural abnormalities. **Figure 2A** shows the relative changes caused by the gain-of-function mutation p.Met207Val (MT) include an increase in I_{NaL}(1.7-fold), I_{Ks} (1.8-fold), and I_{Kr} (3.6-fold) and a reduction in the Cx43/[Cx40+Cx43] ratio (0.76-fold).

This ionic remodeling (I_{NaL}, I_{Ks}, and I_{Kr}) arising from the PITX2c p.Met207Val mutation abbreviated human atrial APD$_{90}$ as shown in **Figure 2B.** The measured APD$_{90}$ was 260.62 ms for the WT condition, which was shortened to 197.58 ms for the MT/WT condition and to 170.14 ms under the MT condition. APA, dV/dt$_{\text{max}}$ and RMP under the MT condition showed no significant changes as compared to the WT condition. The most obvious change of AP due to the electrical remodeling induced by the mutation was the APD shortening.

The APD shortening in the MT/WT and MT conditions was also rate-dependent as shown in **Figure 2C**. Across a range of DIs, the measured APD$_{90}$s under MT/WT and MT conditions were smaller compared to the WT condition. APD restitution curves plotted by APD$_{90}$ vs. DI were downshifted and flattened by the PITX2c p.Met207Val mutation. The computed maximal slope (0.41) for the WT condition was reduced to 0.20 and 0.18 under MT/WT and MT conditions, respectively (**Figure 2D**). APD shortening and flattened APD restitution curve implied that the PITX2c p.Met207Val mutation enabled human atrial cells to support electrical activity to persist at high rates.

Effects of the PITX2c p.Met207Val Mutation on Electrical Conduction at the 1D Tissue Level

In addition to ionic remodeling, structural remodeling associated with reduced intercellular coupling due to the PITX2c p.Met207Val mutation was incorporated into atrial tissue models. Using a 1D cable model, we computed CVR and WL under the WT, WT/MT, and MT conditions (**Figure 3**). At a BCL of 1,000 ms, the measured CV was decreased from 0.269 mm/ms for the WT condition to 0.237 and 0.230 mm/ms, under the WT/MT and MT conditions, respectively. The PITX2c p.Met207Val mutation downshifted CVR curves (**Figure 3A**) and facilitated electrical conduction at higher rates compared to the WT condition. The computed maximum rate of an electrical wave was increased from 194 beats/min for the WT condition to 220 and 238 beats/min, under MT/WT and MT conditions, respectively. WL abbreviation was also observed under mutant conditions (**Figure 3B**). The measured WL at a BCL of 1,000 ms was 82.72, 64.11, and 57.73 mm, for WT, MT/WT and MT conditions, respectively. Changes in CV and WL implied that the PITX2c p.Met207Val mutation allowed electrical waves to maintain in smaller tissue sizes that could occur under the WT condition.

Effects of the PITX2c p.Met207Val Mutation on Temporal and Spatial Vulnerabilities of Atrial Tissue

The PITX2c p.Met207Val mutation led to an increase in the atrial tissue's temporal vulnerability to unidirectional conduction block indexed by VW as shown in **Figure 4**. Under the WT

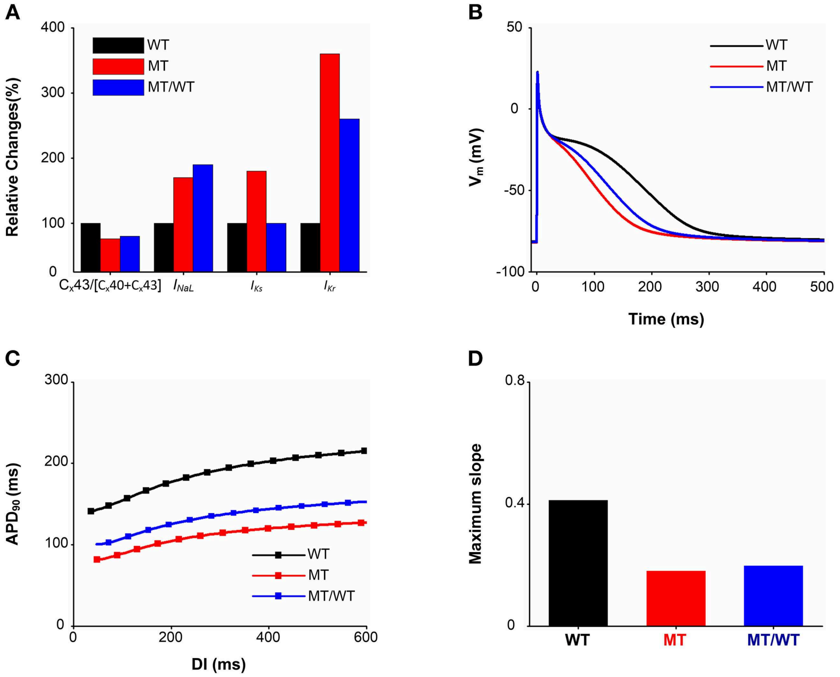

FIGURE 2 | Effects of the p.Met207Val PITX2c mutation on atrial electrophysiological properties at the cellular and subcellular levels. There are three conditions (Wild type: WT, homozygous p.Met207Val mutation: MT and heterozygous p.Met207Val mutation: MT/WT). **(A)** Relative changes (%) in the Cx43/[Cx40+Cx43] ratio, I_{NaL}, I_{Ks}, and I_{Kr}. **(B)** AP profiles. **(C)** APD restitution curves. **(D)** Measured maximum slopes of APD restitution curves.

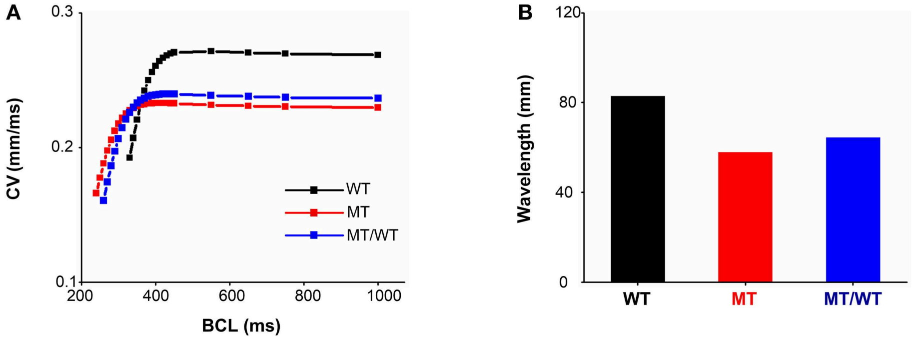

FIGURE 3 | Effects of the p.Met207Val PITX2c mutation on electrical conduction at the one-dimensional tissue level. **(A)** Conduction velocity (CV) restitution curves for WT, MT, and MT/WT conditions, respectively. **(B)** Measured wavelengths at a basic cycle length (BCL) of 1,000 ms in the three cases.

condition, the maximal S1-S2 interval for the generation of bidirectional conduction block was 307.5 ms and the minimal S1-S2 interval to induce bidirectional conduction was 316.5 ms. When S1-S2 time interval (e.g., 308.0 ms) was between 307.5 and 316.5 ms, unidirectional conduction block was induced (**Figure 4A**, top panel). The PITX2c p.Met207Val mutation decreased the S1-S2 time intervals, for bidirectional conduction block and bidirectional conduction, respectively (**Figure 4A**, middle and bottom panels). However, the width of VW was increased by the mutation (**Figure 4B**). The measured VW for the WT condition was 9.0 ms, which was increased to 9.5 ms for MT/WT and MT conditions.

The PITX2c p.Met207Val mutation caused an increase in the atrial tissue's spatial vulnerability to spiral wave formation. As shown in **Figure 5A** (top panel), under the WT condition, a planar wave was initiated by an S1 stimulus (time = 10 ms) and an S2 stimulus (time = 380 ms) with the minimal substrate size of 54 mm could result in sustaining reentry (time = 630 ms). The minimal substrate size was significantly decreased by the mutation from 54 to 47 and 36 mm, under MT/WT and MT conditions, respectively (**Figure 5B**).

Changes in VW and the minimal substrate size implied that the PITX2c p.Met207Val mutation may increase the likelihood of reentry formation.

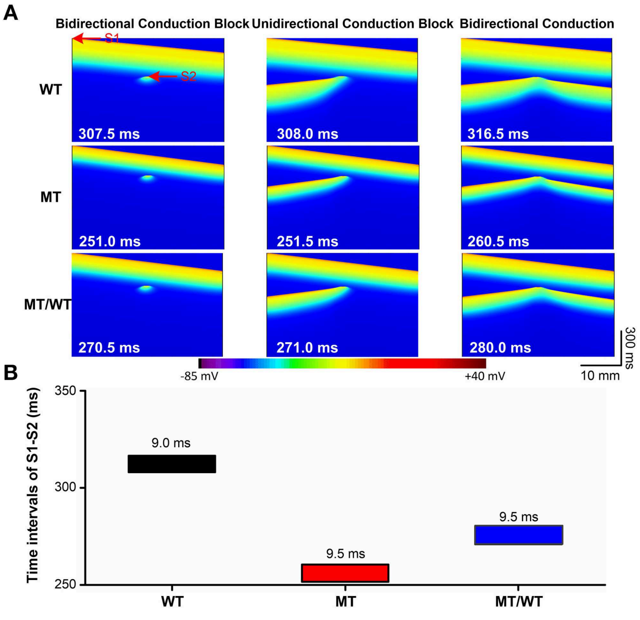

FIGURE 4 | Effects of the p.Met207Val PITX2c mutation on the temporal vulnerability of atrial tissue in the 1D cable model with 375 nodes. **(A)** Electrical waves at different S1-S2 intervals, illustrating bidirectional conduction block (left), unidirectional conduction block (middle) and bidirectional conduction (right) for WT, MT, and MT/WT conditions, respectively. **(B)** Vulnerable windows of atrial tissue vulnerability to unidirectional conduction block under WT, MT, and MT/WT conditions, respectively.

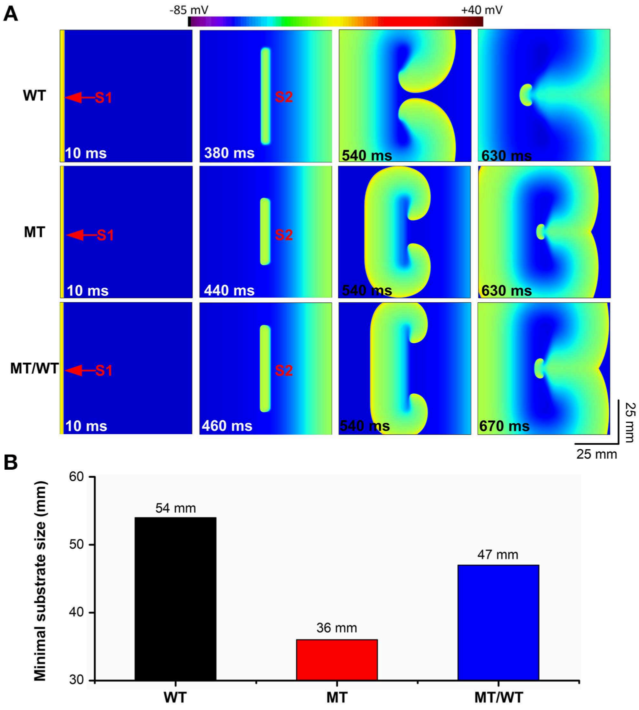

FIGURE 5 | Effects of the p.Met207Val PITX2c mutation on the spatial vulnerability of atrial tissue in the 2D tissue model with 750 × 750 nodes. **(A)** Electrical waves following an S2 stimulus at different time intervals, illustrating the minimal substrate size required to induce a pair of re-entrant circuits under WT, MT, and MT/WT conditions, respectively. **(B)** Minimal substrate sizes of atrial tissue vulnerability to the genesis of re-entrant excitation waves under WT, MT, and MT/WT conditions, respectively.

Effects of the PITX2c p.Met207Val Mutation on Spiral Wave Re-entry

To further examine whether the PITX2c p.Met207Val mutation promotes and perpetuates familial AF, its effects on the temporal-spatial dynamics of spiral waves were investigated. **Figure 6A** shows that the mutation led to the slow propagation of planar waves (time = 50 ms) and facilitated stable rotation (time = 4,000 ms) compared with the WT condition. The life span of the spiral wave was <2,000, >5,000 and >5,000 ms, under WT, MT/WT, and MT conditions, respectively. The meander area of the re-entrant wave trajectory under the MT condition was smaller than in the WT condition (**Figure 6B**). And the dominant oscillatory frequency of the membrane potential oscillations (**Figure 6C**) obtained from the marked point (**Figure 6A**, left panel) was increased from <4.0 Hz for the WT condition to 5.4 and 10.0 Hz, under the MT/WT and MT conditions, respectively (**Figure 6D**). Changes in life span, trajectory and dominant frequency of spiral waves implied that the PITX2c p.Met207Val mutation may increase the likelihood of familial AF (see **Supplementary Videos 1–3** for details).

A quantitative summary of the proarrhythmic effects of the PITX2c p.Met207Val mutation on human atrial electrical activity is listed in **Table 2**.

Action Potential Simulations With an Alternative Human Atrial Cell Model

To avoid model dependence of simulation results, we performed AP simulations using the Grandi et al. (Grand) model (Grandi et al., 2011). The abbreviated APD (**Figures 7A,B**) and the flattened APD restitution curve (**Figure 7C**) under the MT condition were observed. This mutation-induced changes in AP obtained from the Grandi model was qualitatively similar to that from the modified CRN model. APA, dV/dt$_{max}$ and RMP under the MT condition showed no significant changes as compared to the WT condition (**Table 3**). In addition, the maximal slope of the APD restitution curve was reduced from 20.70 under the WT condition to 5.90 and 4.16, under MT/WT and MT conditions, respectively (**Figure 7D**).

DISCUSSION

Main Findings

To our knowledge, this is the first study to investigate mechanisms underlying the generation and maintenance of re-entrant arrhythmias arising from the PITX2c p.Met207Val mutation (Mechakra et al., 2019). Our major findings are as follows: (1) This mutation-induced electrical remodeling abbreviated APD and flattened APDR curves. (2) The combined effects of electrical and structural remodeling due to the PITX2c p.Met207Val mutation slowed CV and shortened WL. (3) It increased atrial tissue vulnerability to initiation and maintenance of reentry by decreasing the substrate size to induce the figure-of-eight reentry and by increasing VW for unidirectional

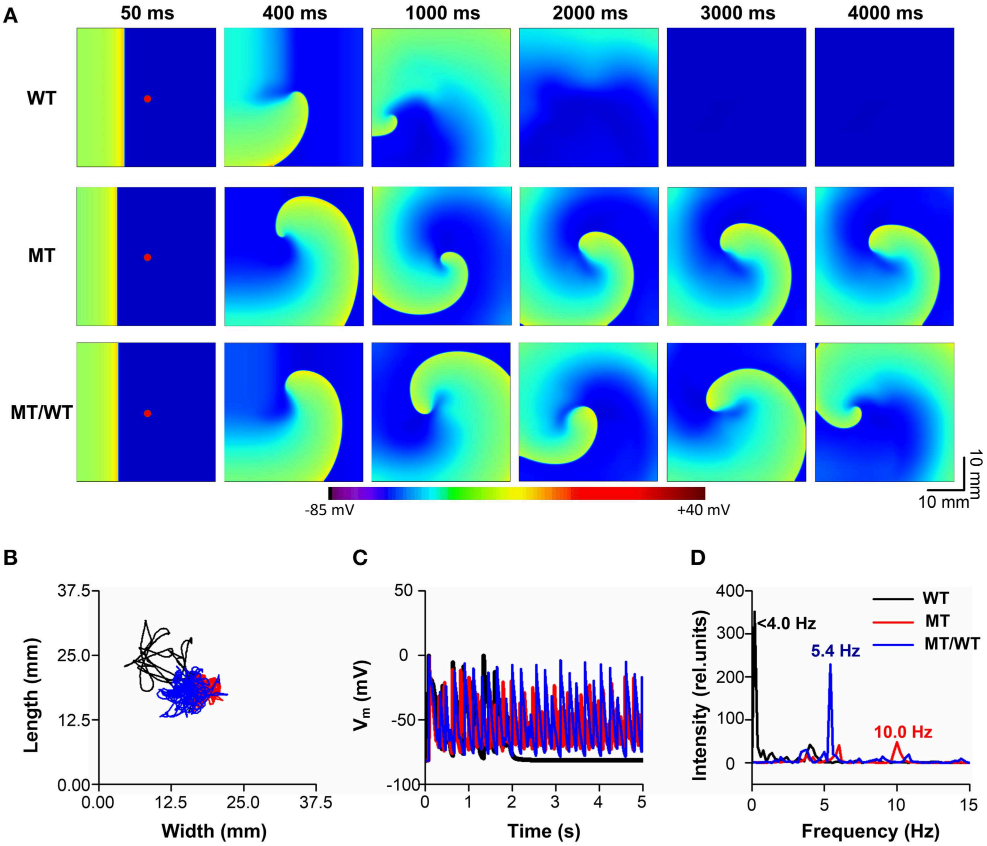

FIGURE 6 | Effects of the p.Met207Val PITX2c mutation on the maintenance of spiral waves in the 2D sheet model with 375 × 375 nodes. **(A)** Snapshots of electrical waves, for WT, MT, and MT/WT conditions, at time = 50, 400, 1,000, 2,000, 3,000, and 4,000 ms. **(B)** Tip trajectories of re-entrant waves under WT, MT, and MT/WT conditions. **(C)** Membrane potential traces of localized electrical excitations (marked with red points in **(A)**. **(D)** Dominant frequencies under WT, MT, and MT/WT conditions.

conduction block. (4) It allowed electrical waves to maintain in smaller tissue sizes at higher rates. Consequently, these findings demonstrate that the PITX2c p.Met207Val mutation may increase the likelihood of familial AF due to increased atrial tissue's temporal and spatial vulnerabilities, which facilitate genesis and maintenance of re-entrant excitation waves.

Mechanisms of Familial Atrial Fibrillation Due to the PITX2c p.Met207Val Mutation

The increase of PITX2c expression or PITX2c activity has been linked to AF, as seen in the left atrium (Gore-Panter et al., 2014) and right atrial myocytes (Pérez-Hernández et al., 2015) from AF patients. In the case of the PITX2c p.Met207Val mutation, this variant was identified in 1 of 60 French patients with early-onset AF and its transactivation activity was increased 3.1-fold (Mechakra et al., 2019). In turn, this gain-of-function caused electrical and structural remodeling by modulating the mRNA levels corresponding to key proteins in AF (Mechakra et al., 2019). Although the causal link between atrial remodeling and the increased risk of AF has been demonstrated in previous modeling studies (Grandi et al., 2011; Colman et al., 2013; Koivumäki et al., 2014), the mechanisms underlying familial AF associated with the PITX2c p.Met207Val mutation were not addressed directly.

In the present study, the genesis of AF in patients with the PITX2c p.Met207Val mutation may be attributable to APD shortening due to electrical remodeling and slow conduction resulted from structural remodeling. Electrical remodeling in our models included up-regulation in I_{NaL}, I_{Ks}, and I_{Kr}. Although upregulated I_{NaL} led to APD prolongation (Sossalla et al., 2010), the increase in I_{Ks} and I_{Kr} was found to play an important role in APD shortening (Kanaporis et al., 2019), resulting in an abbreviated WL of excitation waves that facilitated the initiation and maintenance of re-entry. Structural remodeling was modeled by decreasing the diffusion coefficient to simulate the reduced Cx43/(Cx43+Cx40) ratio. The reduction in the Cx43/(Cx43+Cx40) ratio caused slow conduction (Kanagaratnam et al., 2002; Beauchamp et al., 2006), leading to WL shortening and excitation waves at higher rates. The combined impact of electrical and structural remodeling on initiation and maintenance of atrial fibrillation can be characterized by atrial tissue's vulnerabilities to re-entry.

Effects of the PITX2c p.Met207Val mutation on the temporal and spatial vulnerabilities of atrial tissue contributed to the increased susceptibility to familial AF. According to the leading circle concept (Allessie et al., 1977), functional re-entry pathways during AF naturally assume a path length equal to the minimum circuit size for re-entry, quantified mathematically as the wavelength (or product of refractoriness and conduction velocity) (Wiener, 1946). The wavelength is therefore expected to indicate average functional re-entry circuit size. Since the maintenance of AF depends on the presence of a number of simultaneous reentering waves, and the minimum size of a reentrant wave is related to the wavelength, the wavelength should be an important determinant of the occurrence of AF. The spatial vulnerability of the atrial tissue (or the minimum length of the functional pathway necessary to sustain re-entry) was measured reciprocally by the minimal substrates to sustain re-entry (Kharche et al., 2012). In our modeling study, the formation of the induced reentrant excitation wave was dependent on the spatial size of the premature stimulus. We therefore measured the minimal size of the premature stimulus that enabled the formation of re-entry, as this is correlated with the wavelength of excitation (Kharche et al., 2012), and measures the minimal size of atrial substrate necessary to sustain re-entry. In our simulations, the PITX2c p.Met207Val mutation increased the spatial vulnerability of atrial tissue by decreasing the substrate size and WL due to abbreviated ERP and reduced CV. On the

TABLE 2 | A quantitative summary of the proarrhythmic effects of the PITX2c p.Met207Val mutation on human atrial electrical activity.

Model	Quantity	WT	MT/WT	MT
Cell	RMP (mV)	−81.49	−81.84	**−81.98**
	APA (mV)	104.23	104.39	**104.46**
	dV/dt_{max} (mV/ms)	199.92	199.26	**199.07**
	APD_{50} (ms)	123.36	77.61	**61.26**
	APD_{90} (ms)	260.62	197.58	**170.14**
	APD restitution slope	0.41	0.20	**0.18**
1D	CV (mm/ms)	0.269	0.237	**0.230**
	ERP (ms)	307.5	270.5	**251.0**
	WL (mm)	82.72	64.11	**57.73**
	Maximum rate (beats/min)	194	220	238
	VW (ms)	8.5	9.0	**9.0**
2D	Life span (ms)	<2,000	>5,000	**>5,000**
	Dominant frequency (Hz)	<4.0	5.4	**10.0**
	Minimal substrate size (mm)	54	47	**36**
	Tip meander area (cm^2)	2.904	1.198	**0.469**

Bold values represent parameters and characteristics under the p.Met207Val PITX2c mutation condition.

TABLE 3 | Quantitative characteristics of action potentials obtained from the Grandi model.

Quantity	WT	MT/WT	MT
RMP (mV)	−73.37	−73.50	**−73.58**
APA (mV)	99.19	99.62	**99.83**
dV/dt_{max} (mV/ms)	205.42	207.53	**208.56**
APD_{50} (ms)	136.04	127.44	**122.04**
APD_{90} (ms)	400.46	351.61	**325.97**

Bold values represent parameters and characteristics under the p.Met207Val PITX2c mutation condition.

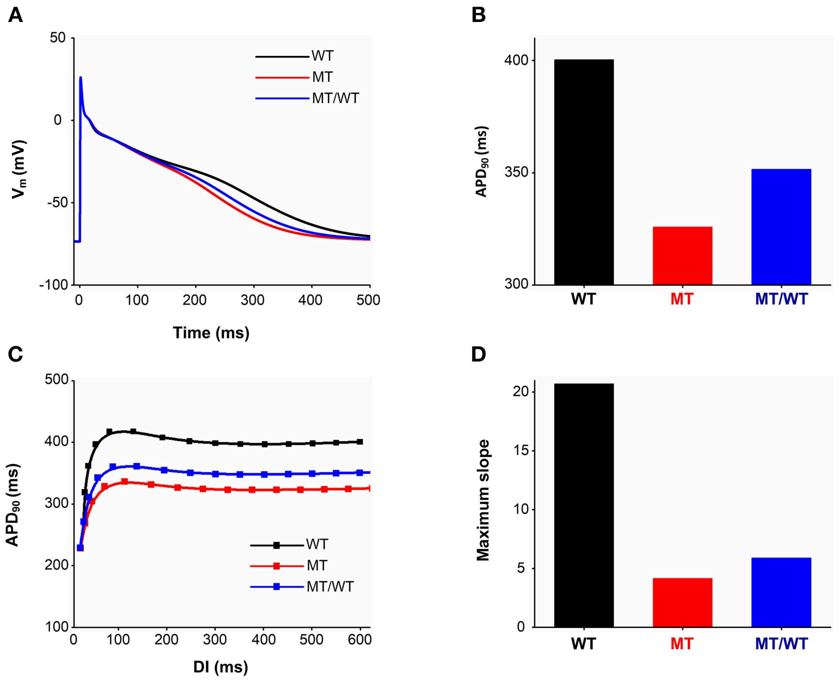

FIGURE 7 | Effects of the p.Met207Val PITX2c mutation on action potential shape and action potential duration (APD) obtained from the Grandi model. AP profiles **(A)**, APDs **(B)**, APD restitution curves **(C)**, and measured maximum slopes **(D)** of APD restitution curves, for WT, MT, and MT/WT conditions, respectively.

other hand, the temporal vulnerability of atrial tissue is measured as VW during which unidirectional conduction block and re-entry can be induced by a test stimulus (Zhang et al., 2008; Kharche et al., 2012). In this study, the VW was significantly increased for atrial tissue incorporating remodeling due to the PITX2c p.Met207Val mutation. Consequently, the increase of temporal and spatial vulnerabilities of atrial tissues may explain why the PITX2c p.Met207Val mutation promotes initiation of re-entry.

In addition to AF initiation, the PITX2c p.Met207Val mutation promoted the maintenance of reentry by flattening the APD restitution curves. Steady-state APD is the principal determinant of the slope of the APD restitution curve. A recent study suggested factors that prolong the action potential would be expected to steepen the restitution curve (Shattock et al., 2017). In the present study, changes in I_{Ks} and I_{Kr} contribute to APD shortening and thereby flattened APD restitution curves. APD restitution has been proposed as a mechanistic determinant of the stability of re-entrant arrhythmia (Kharche et al., 2012; Shattock et al., 2017). In the case of the PITX2c p.Met207Val mutation, the maximum slope of the APD restitution curve was reduced. This led to a gradual decrease in APD alternans toward a steady state level and thereby a stable spiral wave at the tissue level. The stable spiral wave was characterized by decreased tip meander area and prolonged life span.

Therefore, the gain-of-function of the PITX2c p.Met207Val mutation promoted AF initiation and maintenance by abbreviating APD and slowing conduction.

Relevance to Previous Studies

Dysfunction of PITX2c predisposes to AF associated with both decreased (Wang et al., 2010; Chinchilla et al., 2011; Kirchhof et al., 2011; Kolek et al., 2014; Scridon et al., 2014; Tao et al., 2014; Aguirre et al., 2015; Lozano-Velasco et al., 2015, 2017; Herraiz-Martínez et al., 2018) and increased (Gore-Panter et al., 2014; Pérez-Hernández et al., 2015) expression (or activity) of PITX2c, and both loss- (Yang et al., 2013; Yuan et al., 2013; Zhou et al., 2013; Qiu et al., 2014; Wang et al., 2014; Wei et al., 2014) and gain-of-function of PITX2c mutations (Mechakra et al., 2019). Gain-of-function of PITX2c has previously been implicated in a marked shortening of the atrial APD and refractoriness (Pérez-Hernández et al., 2015). Overexpressed PITX2c increased the transcription of KCNQ1 and KCNE1 genes encoding I_{Ks}, and decreased I_{CaL} density through the atrial natriuretic peptide in human right atrial myocytes from chronic AF patients (Pérez-Hernández et al., 2015). Significantly, previous studies have reported that the I_{CaL} decrease (Van Wagoner et al., 1999) and the I_{Ks} increase (Voigt et al., 2010) critically contribute to the APD shortening (González de la Fuente et al., 2012). Recently, there has been increasing awareness of APD shortening due to malfunction of PITX2c in AF genesis (Kirchhof et al., 2011; Bai et al., 2018). Our data indicate that, in the case of the gain-of-function mutation p.Met207Val, the increase in $I_{Ks}$and I_{Kr}not only abbreviates APD, but also increases vulnerabilities of the atrial tissue to the initiation and maintenance of re-entry. Therefore, our study adds to the growing weight of evidence implicating gain-of-function of PITX2c in increased susceptibility to AF.

Limitations

In this study, we used both CRN and Grandi models to simulate the AP of human atrial myocytes. Although these models were developed based on experimental data on human atrial myocytes and validated by their ability to reproduce APs and calcium transients, there were several limitations discussed elsewhere (Wilhelms et al., 2013; Voigt et al., 2014; Sutanto et al., 2018). Here, the limitations special to the present study are summarized. Firstly, the diffusion coefficient (D) was set to be 0.031 mm^2/ms to make the tissue model fulfill the stability criterion ($D\frac{t}{x^2} < 0.5$) (Clayton and Panfilov, 2008; Kharche et al., 2012). Although the measured CV (∼27 cm/s) is very close to realistic CVs (slow, 30 to 40 cm/s; normal 60 to 75 cm/s; and fast, 150 to 200 cm/s) (Gong et al., 2007), it is less than the human atrial CV under the normal condition (Kanagaratnam et al., 2002). Secondly, the potential impact of this mutation was evaluated under the following assumptions: (1) The PITX2c p.Met207Val mutation-induced functional changes in the proteins would be proportional to their mRNAs changes, and (2) These pro-arrhythmogenic effects would appear in human atrial cells as seen in HL1 cells. Further investigations should be conducted when more functional changes due to the PITX2c p.Met207Val mutation. Finally, the intrinsic heterogeneity, realistic geometry of the human atria and fiber orientation were not considered in this study, but these factors can influence the conduction of AP and may contribute to the genesis of spiral waves. The roles of these factors in AF were investigated in previous studies (Colman et al., 2013; Hansen et al., 2016; Zhao et al., 2017) and should not influence our conclusions. In fact, omitting these factors is useful to understand the mechanisms underlying reentrant arrhythmias arising from the PITX2c p.Met207Val mutation, in that changes in APD and spiral waves can be attributed with confidence to the implemented modifications to electrical components.

CONCLUSIONS

In this study, our findings add to the increasing weight of evidence implicating gain-of-function of PITX2c in increased susceptibility to the genesis and maintenance of familial AF, and further highlight the impact of electrical and structural remodeling in response to the PITX2c p.Met207Val mutation. In both heterozygous and homozygous forms of this mutation led to APD shortening due to ionic remodeling and slow conduction due to structural remodeling, which together increased tissue vulnerability to arrhythmogenesis. Therefore, we concluded that APD shortening and slow conduction may increase atrial susceptibility to atrial fibrillation arising from the PITX2c p.Met207Val mutation.

DATA AVAILABILITY STATEMENT

All datasets generated for this study are included in the manuscript/**Supplementary Files**.

AUTHOR CONTRIBUTIONS

JB, JZ, and HZ conceived and designed this work. JB conducted the experiments. JB, YL, AL, and HZ drafted the manuscript, interpreted the data, reviewed, revised, and approved the final version of this manuscript.

FUNDING

This work was supported by the National Natural Science Foundation of China (No. 61901192) (JB) and the Science and Technology Planning Project of Guangdong Province (No. 2015B020214004 and No. 2015B020233010) (YL).

SUPPLEMENTARY MATERIAL

The Supplementary Material for this article can be found online at: https://www.frontiersin.org/articles/10.3389/fphys.2019.01314/full#supplementary-material

Supplementary Video 1 | Electrical waves under the WT condition.

Supplementary Video 2 | Electrical waves under the WT/MT condition.

Supplementary Video 3 | Electrical waves under the MT condition.

REFERENCES

Aguirre, L., Alonso, M., Badía-Careaga, C., Rollán, I., Arias, C., Fernández-Miñán, A., et al. (2015). Long-range regulatory interactions at the 4q25 atrial fibrillation risk locus involve PITX2c and ENPEP. *BMC Biol.* 13, 26–26. doi: 10.1186/s12915-015-0138-0

Allessie, M. A., Bonke, F. I., and Schopman, F. J. (1977). Circus movement in rabbit atrial muscle as a mechanism of tachycardia. III. The "leading circle" concept: a new model of circus movement in cardiac tissue without the involvement of an anatomical obstacle. *Circ. Res.* 41, 9–18. doi: 10.1161/01.RES.41.1.9

Bai, J., Gladding, P. A., Stiles, M. K., Fedorov, V. V., and Zhao, J. (2018). Ionic and cellular mechanisms underlying TBX5/PITX2 insufficiency-induced atrial fibrillation: insights from mathematical models of human atrial cells. *Sci. Rep.* 8:15642. doi: 10.1038/s41598-018-33958-y

Bai, J., Wang, K., Li, Q., Yuan, Y., and Zhang, H. (2016a). Pro-arrhythmogenic effects of CACNA1C G1911R mutation in human ventricular tachycardia: insights from cardiac multi-scale models. *Sci. Rep.* 6:31262. doi: 10.1038/srep31262

Bai, J., Wang, K., Liu, Y., Li, Y., Liang, C., Luo, G., et al. (2017a). Computational cardiac modeling reveals mechanisms of ventricular arrhythmogenesis in long QT syndrome type 8: CACNA1C R858H mutation linked to ventricular fibrillation. *Front. Physiol.* 8:771. doi: 10.3389/fphys.2017.00771

Bai, J., Wang, K., and Zhang, H. (2016b). Potential pathogenesis discovery of arrhythmia based on cardiac electrophysiological models: research progress. *Progr. Biochem. Biophys.* 43, 128–140. doi: 10.16476/j.pibb.2015.0302

Bai, J., Yin, R., Wang, K., and Zhang, H. (2017b). Mechanisms underlying the emergence of post-acidosis arrhythmia at the tissue level: a theoretical study. *Front. Physiol.* 8:195. doi: 10.3389/fphys.2017.00195

Beauchamp, P., Yamada, K. A., Baertschi, A. J., Green, K., Kanter, E. M., Saffitz, J. E., et al. (2006). Relative contributions of connexins 40 and 43 to atrial impulse propagation in synthetic strands of neonatal and fetal murine cardiomyocytes. *Circ. Res.* 99, 1216–1224. doi: 10.1161/01.RES.0000250607.34498.b4

Caballero, R., de la Fuente, M. G., Gómez, R., Barana, A., Amorós, I., Dolz-Gaitón, P., et al. (2010). In humans, chronic atrial fibrillation decreases the transient outward current and ultrarapid component of the delayed rectifier current differentially on each atria and increases the slow component of the delayed rectifier current in both. *J. Am. Coll. Cardiol.* 55, 2346–2354. doi: 10.1016/j.jacc.2010.02.028

Chinchilla, A., Daimi, H., Lozano-Velasco, E., Dominguez, J. N., Caballero, R., Delpón, E., et al. (2011). PITX2 insufficiency leads to atrial electrical and structural remodeling linked to arrhythmogenesis. *Circ. Cardiovasc. Genet.* 4, 269–279. doi: 10.1161/CIRCGENETICS.110.958116

Clayton, R., and Panfilov, A. (2008). A guide to modelling cardiac electrical activity in anatomically detailed ventricles. *Progr. Biophys. Mol. Biol.* 96, 19–43. doi: 10.1016/j.pbiomolbio.2007.07.004

Colman, M. A., Aslanidi, O. V., Kharche, S., Boyett, M. R., Garratt, C., Hancox, J. C., et al. (2013). Pro-arrhythmogenic effects of atrial fibrillation-induced electrical remodelling: insights from the three-dimensional virtual human atria. *J. Physiol.* 591, 4249–4272. doi: 10.1113/jphysiol.2013.254987

Courtemanche, M., Ramirez, R. J., and Nattel, S. (1998). Ionic mechanisms underlying human atrial action potential properties: insights from a mathematical model. *Am. J. Physiol. Heart Circ. Physiol.* 275, H301–H321. doi: 10.1152/ajpheart.1998.275.1.H301

Dhillon, P. S., Chowdhury, R. A., Patel, P. M., Jabr, R., Momin, A. U., Vecht, J., et al. (2014). Relationship between connexin expression and gap junction resistivity in human atrial myocardium. *Circ. Arrhythm. Electrophysiol.* 7, 321–329. doi: 10.1161/CIRCEP.113.000606

Fenton, F., and Karma, A. (1998). Vortex dynamics in three-dimensional continuous myocardium with fiber rotation: filament instability and fibrillation. *Chaos* 8, 20–47. doi: 10.1063/1.166311

Gong, Y., Xie, F., Stein, K. M., Garfinkel, A., Culianu, C. A., Lerman, B. B., et al. (2007). Mechanism underlying initiation of paroxysmal atrial flutter/atrial fibrillation by ectopic foci. *Circulation* 115, 2094–2102. doi: 10.1161/CIRCULATIONAHA.106.656504

González de la Fuente, M., Barana, A., Gomez, R., Amoros, I., Dolz-Gaiton, P., Sacristan, S., et al. (2012). Chronic atrial fibrillation up-regulates β1-adrenoceptors affecting repolarizing currents and action potential duration. *Cardiovasc. Res.* 97, 379–388. doi: 10.1093/cvr/cvs313

Gore-Panter, S. R., Hsu, J., Hanna, P., Gillinov, A. M., Pettersson, G., Newton, D. W., et al. (2014). Atrial Fibrillation associated chromosome 4q25 variants are not associated with PITX2c expression in human adult left atrial appendages. *PLoS ONE* 9:e86245. doi: 10.1371/journal.pone.0086245

Grandi, E., Pandit, S. V., Voigt, N., Workman, A. J., Dobrev, D., Jalife, J., et al. (2011). Human atrial action potential and Ca^{2+} model: sinus rhythm and chronic atrial fibrillation. *Circ. Res.* 109, 1055–1066. doi: 10.1161/CIRCRESAHA.111.253955

Gudbjartsson, D. F., Arnar, D. O., Helgadottir, A., Gretarsdottir, S., Holm, H., Sigurdsson, A., et al. (2007). Variants conferring risk of atrial fibrillation on chromosome 4q25. *Nature* 448, 353–357. doi: 10.1038/nature06007

Hansen, B. J., Csepe, T. A., Zhao, J., Ignozzi, A. J., Hummel, J. D., and Fedorov, V. V. (2016). Maintenance of atrial fibrillation. *Circ. Arrhythm. Electrophysiol.* 9:e004398. doi: 10.1161/CIRCEP.116.004398

Hansen, B. J., Zhao, J., Csepe, T. A., Moore, B. T., Li, N., Jayne, L. A., et al. (2015). Atrial fibrillation driven by micro-anatomic intramural re-entry revealed by simultaneous sub-epicardial and sub-endocardial optical mapping in explanted human hearts. *Eur. Heart J.* 36, 2390–2401. doi: 10.1093/eurheartj/ehv233

Heijman, J., Guichard, J.-B., Dobrev, D., and Nattel, S. (2018). Translational challenges in atrial fibrillation. *Circ. Res.* 122, 752–773. doi: 10.1161/CIRCRESAHA.117.311081

Herraiz-Martínez, A., Llach, A., Tarifa, C., Gandía, J., Jiménez-Sabado, V., Lozano-Velasco, E., et al. (2018). The 4q25 variant rs13143308T links risk of atrial fibrillation to defective calcium homoeostasis. *Cardiovasc. Res.* 115, 578–589. doi: 10.1093/cvr/cvy215

Kanagaratnam, P., Rothery, S., Patel, P., Severs, N. J., and Peters, N. S. (2002). Relative expression of immunolocalized connexins 40 and 43 correlates with human atrial conduction properties. *J. Am. Coll. Cardiol.* 39, 116–123. doi: 10.1016/S0735-1097(01)01710-7

Kanaporis, G., Kalik, Z. M., and Blatter, L. A. (2019). Action potential shortening rescues atrial calcium alternans. *J. Physiol.* 597, 723–740. doi: 10.1113/JP277188

Kharche, S., Adeniran, I., Stott, J., Law, P., Boyett, M. R., Hancox, J. C., et al. (2012). Pro-arrhythmogenic effects of the S140G KCNQ1 mutation in human atrial fibrillation–insights from modelling. *J. Physiol.* 590, 4501–4514. doi: 10.1113/jphysiol.2012.229146

Kirchhof, P., Kahr, P. C., Kaese, S., Piccini, I., Vokshi, I., Scheld, H.-H., et al. (2011). PITX2c is expressed in the adult left atrium, and reducing Pitx2c expression promotes atrial fibrillation inducibility and complex changes in gene expression. *Circ. Cardiovasc. Genet.* 4, 123–133. doi: 10.1161/CIRCGENETICS.110.958058

Koivumäki, J. T., Seemann, G., Maleckar, M. M., and Tavi, P. (2014). *In silico* screening of the key cellular remodeling targets in chronic atrial fibrillation. *PLoS Comput. Biol.* 10:e1003620. doi: 10.1371/journal.pcbi.1003620

Kolek, M. J., Parvez, B., Muhammad, R., Shoemaker, M. B., Blair, M. A., Stubblefield, T., et al. (2014). A common variant on chromosome 4q25 is associated with prolonged PR interval in subjects with and without atrial fibrillation. *Am. J. Cardiol.* 113, 309–313. doi: 10.1016/j.amjcard.2013.08.045

Lozano-Velasco, E., Hernandez-Torres, F., Daimi, H., Serra, S. A., Herraiz, A., Hove-Madsen, L., et al. (2015). Pitx2 impairs calcium handling in a dose-dependent manner by modulating Wnt signalling. *Cardiovasc. Res.* 109, 55–66. doi: 10.1093/cvr/cvv207

Lozano-Velasco, E., Wangensteen, R., Quesada, A., Garcia-Padilla, C., Osorio, J. A., Ruiz-Torres, M. D., et al. (2017). Hyperthyroidism, but not hypertension, impairs PITX2 expression leading to Wnt-microRNA-ion channel remodeling. *PLoS ONE* 12:e0188473. doi: 10.1371/journal.pone.0188473

Mechakra, A., Footz, T., Walter, M., Aránega, A., Hernández-Torres, F., Morel, E., et al. (2019). A novel PITX2c gain-of-function mutation, p. Met207Val, in patients with familial atrial fibrillation. *Am. J. Cardiol.* 123, 787–793. doi: 10.1016/j.amjcard.2018.11.047

Nao, T., Ohkusa, T., Hisamatsu, Y., Inoue, N., Matsumoto, T., Yamada, J., et al. (2003). Comparison of expression of connexin in right atrial myocardium in patients with chronic atrial fibrillation versus those in sinus rhythm. *Am. J. Cardiol.* 91, 678–683. doi: 10.1016/S0002-9149(02)03403-3

Ni, H., Adeniran, I., and Zhang, H. (2017). *In-silico* investigations of the functional impact of KCNA5 mutations on atrial mechanical dynamics. *J. Mol. Cell. Cardiol.* 111, 86–95. doi: 10.1016/j.yjmcc.2017.08.005

Nielsen, J. B., Thorolfsdottir, R. B., Fritsche, L. G., Zhou, W., Skov, M. W., Graham, S. E., et al. (2018). Genome-wide association study of 1 million people identifies 111 loci for atrial fibrillation. *bioRxiv* 2018:242149. doi: 10.1101/242149

Pérez-Hernández, M., Matamoros, M., Barana, A., Amorós, I., Gómez, R., Núñez, M., et al. (2015). Pitx2c increases in atrial myocytes from chronic atrial fibrillation patients enhancing I Ks and decreasing I Ca, L. *Cardiovasc. Res.* 109, 431–441. doi: 10.1093/cvr/cvv280

Polontchouk, L., Haefliger, J.-A., Ebelt, B., Schaefer, T., Stuhlmann, D., Mehlhorn, U., et al. (2001). Effects of chronic atrial fibrillation on gap junction distribution in human and rat atria. *J. Am. Coll. Cardiol.* 38, 883–891. doi: 10.1016/S0735-1097(01)01443-7

Qiu, X.-B., Xu, Y.-J., Li, R.-G., Xu, L., Liu, X., Fang, W.-Y., et al. (2014). PITX2C loss-of-function mutations responsible for idiopathic atrial fibrillation. *Clinics* 69, 15–22. doi: 10.6061/clinics/2014(01)03

Scridon, A., Fouilloux-Meugnier, E., Loizon, E., Rome, S., Julien, C., Barrès, C., et al. (2014). Long-standing arterial hypertension is associated with Pitx2 down-regulation in a rat model of spontaneous atrial tachyarrhythmias. *Europace* 17, 160–165. doi: 10.1093/europace/euu139

Seemann, G., Höper, C., Sachse, F. B., Dössel, O., Holden, A. V., and Zhang, H. (2006). Heterogeneous three-dimensional anatomical and electrophysiological model of human atria. *Philos. Transac. R. Soc. A Math. Phys. Eng. Sci.* 364, 1465–1481. doi: 10.1098/rsta.2006.1781

Shattock, M. J., Park, K. C., Yang, H.-Y., Lee, A. W., Niederer, S., MacLeod, K. T., et al. (2017). Restitution slope is principally determined by steady-state action potential duration. *Cardiovasc. Res.* 113, 817–828. doi: 10.1093/cvr/cvx063

Sossalla, S., Kallmeyer, B., Wagner, S., Mazur, M., Maurer, U., Toischer, K., et al. (2010). Altered Na^+ currents in atrial fibrillation: effects of ranolazine on arrhythmias and contractility in human atrial myocardium. *J. Am. Coll. Cardiol.* 55, 2330–2342. doi: 10.1016/j.jacc.2009.12.055

Sutanto, H., van Sloun, B., Schönleitner, P., van Zandvoort, M. A. M. J., Antoons, G., and Heijman, J. (2018). The subcellular distribution of ryanodine receptors and L-type Ca^{2+} channels modulates Ca^{2+}-transient properties and spontaneous Ca^{2+}-release events in atrial cardiomyocytes. *Front. Physiol.* 9:1108. doi: 10.3389/fphys.2018.01108

Tao, Y., Zhang, M., Li, L., Bai, Y., Zhou, Y., Moon, A. M., et al. (2014). Pitx2, an atrial fibrillation predisposition gene, directly regulates ion transport and intercalated disc genes. *Circ. Cardiovasc. Genet.* 7, 23–32. doi: 10.1161/CIRCGENETICS.113.000259

Van Wagoner, D. R., Pond, A. L., Lamorgese, M., Rossie, S. S., McCarthy, P. M., and Nerbonne, J. M. (1999). Atrial L-type Ca^{2+} currents and human atrial fibrillation. *Circ. Res.* 85, 428–436. doi: 10.1161/01.RES.85.5.428

Voigt, N., Heijman, J., Wang, Q., Chiang, D. Y., Li, N., Karck, M., et al. (2014). Cellular and molecular mechanisms of atrial arrhythmogenesis in patients with paroxysmal atrial fibrillation. *Circulation* 129, 145–156. doi: 10.1161/CIRCULATIONAHA.113.006641

Voigt, N., Trausch, A., Knaut, M., Matschke, K., Varr,ó, A., Van Wagoner, D. R., et al. (2010). Left-to-right atrial inward rectifier potassium current gradients in patients with paroxysmal versus chronic atrial fibrillation. *Circ. Arrhythm. Electrophysiol.* 3, 472–480. doi: 10.1161/CIRCEP.110.954636

Wang, J., Klysik, E., Sood, S., Johnson, R. L., Wehrens, X. H., and Martin, J. F. (2010). Pitx2 prevents susceptibility to atrial arrhythmias by inhibiting left-sided pacemaker specification. *Proc. Natl. Acad. Sci. U.S.A.* 107, 9753–9758. doi: 10.1073/pnas.0912585107

Wang, J., Zhang, D.-F., Sun, Y.-M., and Yang, Y.-Q. (2014). A novel PITX2c loss-of-function mutation associated with familial atrial fibrillation. *Eur. J. Med. Genet.* 57, 25–31. doi: 10.1016/j.ejmg.2013.11.004

Wei, D., Gong, X.-H., Qiu, G., Wang, J., and Yang, Y.-Q. (2014). Novel PITX2c loss-of-function mutations associated with complex congenital heart disease. *Int. J. Mol. Med.* 33, 1201–1208. doi: 10.3892/ijmm.2014.1689

Wetzel, U., Boldt, A., Lauschke, J., Weigl, J., Schirdewahn, P., Dorszewski, A., et al. (2005). Expression of connexins 40 and 43 in human left atrium in atrial fibrillation of different aetiologies. *Heart* 91, 166–170. doi: 10.1136/hrt.2003.024216

Whittaker, D., Colman, M. A., Ni, H., Hancox, J., and Zhang, H. (2018a). Human atrial arrhythmogenesis and sinus bradycardia in KCNQ1-linked short QT syndrome: insights from computational modelling. *Front. Physiol.* 9:1402. doi: 10.3389/fphys.2018.01402

Whittaker, D. G., Hancox, J., and Zhang, H. (2018b). *In silico* assessment of pharmacotherapy for human atrial patho-electrophysiology associated with hERG-linked short QT syndrome. *Front. Physiol.* 9:1888. doi: 10.3389/fphys.2018.01888

Whittaker, D. G., Ni, H., El Harchi, A., Hancox, J. C., and Zhang, H. (2017). Atrial arrhythmogenicity of KCNJ2 mutations in short QT syndrome: insights from virtual human atria. *PLoS Comput. Biol.* 13:e1005593. doi: 10.1371/journal.pcbi.1005593

Wiener, N. (1946). The mathematical formulation of the problem of conduction of impulses in a network of connected excitable elements, specifically in cardiac muscle. *Arch. Inst. Cardiol. Mex.* 16, 1–61.

Wilhelms, M., Hettmann, H., Maleckar, M., Koivumäki, J., Dössel, O., and Seemann, G. (2013). Benchmarking electrophysiological models of human atrial myocytes. *Front. Physiol.* 3:487. doi: 10.3389/fphys.2012.00487

Yang, Y.-Q., Xu, Y.-J., Li, R.-G., Qu, X.-K., Fang, W.-Y., and Liu, X. (2013). Prevalence and spectrum of PITX2c mutations associated with familial atrial fibrillation. *Int. J. Cardiol.* 168, 2873–2876. doi: 10.1016/j.ijcard.2013.03.141

Yuan, F., Zhao, L., Wang, J., Zhang, W., Li, X., Qiu, X.-B., et al. (2013). PITX2c loss-of-function mutations responsible for congenital atrial septal defects. *Int. J. Med. Sci.* 10, 1422–1429. doi: 10.7150/ijms.6809

Zhang, H., Kharche, S., Holden, A. V., and Hancox, J. C. (2008). Repolarisation and vulnerability to re-entry in the human heart with short QT syndrome arising from KCNQ1 mutation—A simulation study. *Progr. Biophys. Mol. Biol.* 96, 112–131. doi: 10.1016/j.pbiomolbio.2007.07.020

Zhao, J., Hansen, B. J., Wang, Y., Csepe, T. A., Sul, L. V., Tang, A., et al. (2017). Three dimensional integrated functional, structural, and computational mapping to define the structural fingerprints of heart specific atrial fibrillation drivers in human heart *ex vivo*. *J. Am. Heart Assoc.* 6:e005922. doi: 10.1161/JAHA.117.005922

Zhou, Y. M., Zheng, P. X., Yang, Y. Q., Ge, Z. M., and Kang, W. Q. (2013). A novel PITX2c loss-of-function mutation underlies lone atrial fibrillation. *Int. J. Mol. Med.* 32, 827–834. doi: 10.3892/ijmm.2013.1463

Conflict of Interest: The authors declare that the research was conducted in the absence of any commercial or financial relationships that could be construed as a potential conflict of interest.

frontiers in Physiology

ORIGINAL RESEARCH
published: 19 August 2021
doi: 10.3389/fphys.2021.582037

The Functional Role of Hyperpolarization Activated Current (I_f) on Cardiac Pacemaking in Human vs. in the Rabbit Sinoatrial Node: A Simulation and Theoretical Study

Xiangyun Bai[1,2,3], *Kuanquan Wang*[3], *Mark R. Boyett*[4], *Jules C. Hancox*[1,5] and *Henggui Zhang*[1,6,7]*

[1] *Biological Physics Group, Department of Physics and Astronomy, The University of Manchester, Manchester, United Kingdom,* [2] *School of Computer Science and Technology, Xi'an University of Posts and Telecommunications, Xi'an, China,* [3] *School of Computer Science and Technology, Harbin Institute of Technology, Harbin, China,* [4] *Department of Biomedical Sciences, Faculty of Health and Medical Sciences, University of Copenhagen, København, Denmark,* [5] *School of Physiology, Pharmacology and Neuroscience, Biomedical Sciences Building, University Walk, Bristol, United Kingdom,* [6] *Peng Cheng Laboratory, Shenzhen, China,* [7] *Key Laboratory of Medical Electrophysiology of Ministry of Education, Medical Electrophysiological Key Laboratory of Sichuan, Institute of Cardiovascular Research, Southwest Medical University, Luzhou, China*

OPEN ACCESS

Edited by:
Gerard J. J. Boink,
University of Amsterdam, Netherlands

Reviewed by:
Thomas Hund,
The Ohio State University,
United States
Victor A. Maltsev,
National Institute on Aging (NIH),
United States

***Correspondence:**
Henggui Zhang
henggui.zhang@manchester.ac.uk

Specialty section:
This article was submitted to Computational Physiology and Medicine,
a section of the journal Frontiers in Physiology

Received: *10 July 2020*
Accepted: *23 July 2021*
Published: *19 August 2021*

Citation:
Bai X, Wang K, Boyett MR, Hancox JC and Zhang H (2021) The Functional Role of Hyperpolarization Activated Current (I_f) on Cardiac Pacemaking in Human vs. in the Rabbit Sinoatrial Node: A Simulation and Theoretical Study. Front. Physiol. 12:582037. doi: 10.3389/fphys.2021.582037

The cardiac hyperpolarization-activated "funny" current (I_f), which contributes to sinoatrial node (SAN) pacemaking, has a more negative half-maximal activation voltage and smaller fully-activated macroscopic conductance in human than in rabbit SAN cells. The consequences of these differences for the relative roles of I_f in the two species, and for their responses to the specific bradycardic agent ivabradine at clinical doses have not been systematically explored. This study aims to address these issues, through incorporating rabbit and human I_f formulations developed by Fabbri et al. into the Severi et al. model of rabbit SAN cells. A theory was developed to correlate the effect of I_f reduction with the total inward depolarising current (I_{total}) during diastolic depolarization. Replacing the rabbit I_f formulation with the human one increased the pacemaking cycle length (CL) from 355 to 1,139 ms. With up to 20% I_f reduction (a level close to the inhibition of I_f by ivabradine at clinical concentrations), a modest increase (~5%) in the pacemaking CL was observed with the rabbit I_f formulation; however, the effect was doubled (~12.4%) for the human I_f formulation, even though the latter has smaller I_f density. When the action of acetylcholine (ACh, 0.1 nM) was considered, a 20% I_f reduction markedly increased the pacemaking CL by 37.5% (~27.3% reduction in the pacing rate), which is similar to the ivabradine effect at clinical concentrations. Theoretical analysis showed that the resultant increase of the pacemaking CL is inversely proportional to the magnitude of I_{total} during diastolic depolarization phase: a smaller I_f in the model resulted in a smaller I_{total} amplitude, resulting in a slower pacemaking rate; and the same reduction in I_f resulted in a more significant change of CL in the cell model with a smaller I_{total}. This explained the mechanism by which a low dose of ivabradine slows pacemaking rate more in humans than in the rabbit. Similar results were seen in the Fabbri et al. model of human SAN cells, suggesting our observations are model-independent. Collectively, the results of study explain why low dose ivabradine at clinically relevant concentrations acts as an effective bradycardic agent in modulating human SAN pacemaking.

Keywords: human and rabbit sinoatrial node, funny current, bradycardic agent (ivabradine), electrophysiological simulation, theoretical analysis

INTRODUCTION

The pacemaker activity of sinoatrial node (SAN) cells in the mammalian heart arises from the integrated action of multiple sarcolemmal ionic channel currents and the interaction between the intracellular calcium handling and sarcolemmal electrogenic processes (Irisawa et al., 1993; Mangoni and Nargeot, 2008; Lakatta et al., 2010). The hyperpolarization-activated "funny" current, I_f, present in the SAN and other regions of the cardiac conduction system (Boyett, 2009; Difrancesco, 2010), is produced by the hyperpolarization-activated cyclic nucleotide gated (HCN) channel isoforms (of which there are four: HCN1-4), each of which is comprised of six transmembrane domains with four subunits combining to produce functional tetrameric channels, as occurs for voltage-gated potassium channels (Bois et al., 2007; Difrancesco, 2010). Previous studies of the rabbit SAN have shown that although HCN isoforms 1, 2, and 4 are all expressed in the heart, HCN4 is the most abundant in the SAN and the I_f density within SAN sub-regions correlates strongly with HCN4 expression levels (Thollon et al., 2007; Brioschi et al., 2009). The unique features of HCN channels lie in the fact that they are activated not on depolarization but on hyperpolarization of cell membrane potential (to voltages negative to ~ -40 to ~ -50 mV) (Hagiwara and Irisawa, 1989; Accili et al., 1997; Baruscotti et al., 2005) and are permeable to both Na^+ and K^+ ions, with an approximate reversal potential of −30 mV (Van Ginneken and Giles, 1991; Verkerk et al., 2009a). Upon hyperpolarization, HCN channels generate an inward current over the pacemaking potential range which, together with the current generated by other electrogenic processes of the intracellular calcium handling (i.e., the Ca^{2+} clock), contributes to the genesis of intrinsic pacemaker activity of the SAN (Lakatta and Difrancesco, 2009). HCN channels are also modulated by adrenergic agonists *via* cAMP (Bucchi et al., 2003; Craven and Zagotta, 2006).

I_f channels are also present in the human SAN. It has been shown that HCN4 is strongly expressed in the human SAN, with the measured mRNA level of other isoforms accounting for <16% (with HCN3 being negligible, accounting for only 0.5%) of the total mRNA measurement (Chandler et al., 2009). Though the HCN expression in the human SAN is similar to that in the rabbit, properties and kinetics of I_f are clearly different. It has been shown the fully-activated I_f conductance in the human is about 3–4 times smaller than that in the rabbit (Verkerk et al., 2007a). Additionally, I_f in human SAN cells has a more negative half-maximal activation voltage, and a greater time constant of deactivation/activation process which is also negatively shifted (Verkerk et al., 2007a). With such a marked species differences in I_f conductance and kinetics between the rabbit and human, a question arises as to whether a smaller I_f in the human SAN cells plays the same important role in regulating cardiac pacemaking activity as in the rabbit SAN?

Although I_f in human SAN cells is much smaller than those in other mammals, it may play a comparable role to that in the rabbit in modulating cardiac pacemaking. In their study, (Verkerk et al., 2007b) observed about a 26% increase in pacemaking cycle length in human SAN cells on complete block of I_f by using 2 mM Cs^+, which is close to that seen in the rabbit (Verkerk and Wilders, 2010; Fabbri et al., 2017). Pharmacological targeting of I_f by ivabradine has also shown the clinical value of I_f in controlling the heart rate in patients who need heart rate control in conditions of coronary artery disease (CAD) (Tardif et al., 2005; Camici et al., 2016; Niccoli et al., 2017) and heart failure (HF) (Bohm et al., 2015; Yancy et al., 2016). In both conditions, slowing down the heart rate by ivabradine increases the diastolic interval, thereby reducing the metabolic load on the working myocardium; this reduces the risks of ischemia of the heart leading to reduced risk of sudden death (Niccoli et al., 2017).

Although inhibition of I_f by ivabradine provides an efficient pharmacological control of heart rate in the clinic, it is still unclear how the clinical concentration range of ivabradine [about 20–140 nM (Choi et al., 2013; Jiang et al., 2013); blocking I_f < 20% (Bois et al., 1996; Bucchi et al., 2002)] can produce a significant effect in reducing human heart rate. In pre-clinical animal model studies, ivabradine has been reported to inhibit I_f in SAN cells with a half-maximal inhibitory concentration of 1.5–2.8 μM (Bois et al., 1996; Bucchi et al., 2002), and recombinant HCN4 channels with an IC_{50} values between 0.5 and 2.0 μM (Bucchi et al., 2002, 2006, 2013). In rabbit SAN cells, 1 μM ivabradine has been observed to reduce the pacemaking rate by 12.3% (Thollon et al., 1994), whilst about 16.2 and 23.8% of heart rate reduction at 3 μM have been seen (Thollon et al., 1994; Bucchi et al., 2007).

When ivabradine was administered intravenously (0.2 mg kg^{-1}) to patients with normal baseline electrophysiology, mean heart rate reductions of 12.9 and 14.1 beats min^{-1} (at 0.5 and 1 h respectively following administration) were observed (Camm and Lau, 2003). The drug is usually administered orally, however, and after repeated oral dosing at 5 mg, mean maximal plasma (C_{max}) levels of 11–16 ng ml^{-1} (23.5–34.1 nM) have been measured, whilst for repeated dosing at 10 mg, mean C_{max} levels of 29–42 ng ml^{-1} (61.8–89.6 nM) have been seen (Choi et al., 2013; Jiang et al., 2013).

Repeated dosing with a high ivabradine concentration of 20 mg has been associated with a C_{max} of 137 nM (Jiang et al., 2013). On the basis of the pre-clinically observed concentration-dependence for I_f inhibition, comparatively low levels of I_f block might be expected at such plasma levels (Thollon et al., 1994; Bucchi et al., 2007). However, clinical concentrations of ivabradine produce about 18–20% reduction in human heart rate (Camm and Lau, 2003; Doesch et al., 2007).

Previous animal model studies (Difrancesco, 1991, 2010) have found that inhibition of I_f by ivabradine slowed down the spontaneous firing rate of the rabbit SAN cell in a use-dependent manner (Bois et al., 1996), and about 15% reduction of the pacemaking rate was observed at a concentration of 3 μM, which produced about 60% I_f reduction at membrane potential of −92 mV, and about 41% I_f reduction at physiologically relevant membrane potentials (∼60 mV) (Yaniv et al., 2012). Numerically, in a recent in silico exploration of the role of I_f in SAN pacemaking using a rabbit SAN model, the effect of ivabradine was simulated through implementing a 66% reduction of I_f (mimicking an experimentally reported effect of 3 μM ivabradine), leading to a 22% reduction in spontaneous rate (Severi et al., 2012). However, due to the non-linear concentration-dependent action of ivabradine on I_f, it is hard (if not impossible) to derive the effect of a low concentration of ivabradine from that of a high concentration on modulating cardiac pacemaking rate. To date, therefore, the effect of blocking I_f at the level of I_f reduction at clinical plasma levels of ivabradine (<20%) on pacemaking rate of the rabbit SAN has not been elucidated, as is how such concentration can produce a marked effect on the human SAN, in which I_f is much smaller than that in the rabbit SAN. Most importantly, it is unclear either how clinical concentrations of ivabradine affect cardiac pacemaking activity *in vivo* as compared to those predicted by single cell experiments *in vitro*, in which vagal tone modulation of cardiac pacemaking is missing. The aim of the present study was therefore to investigate through simulations and theoretical analysis the effect of I_f reduction over a wide range of values on cardiac pacemaking activity in the presence and absence of vagal tone modulation of cardiac pacemaking activity by acetylcholine.

METHODS

SAN Cell Model and I_f Formulations

In this study, the contemporary model of rabbit SAN cells developed by Severi et al. (2012) was used as a basal model. The model was chosen as it represents the most updated progress in the model development of rabbit SAN cells, in particular it incorporates an updated I_f formulation based on recently available experimental data (Altomare et al., 2003; Barbuti et al., 2007). The basal model code was downloadable from cellML at the following URL: https://models.physiomeproject.org/e/139; and the source codes used for this study are available on request to: henggui.zhang@manchester.ac.uk. In brief, the dynamics of the membrane action potential the SAN cell were modeled as:

$$\frac{dV}{dt} = -\frac{i_{total}}{C_m} \tag{1}$$

$$i_{total} = I_{CaL} + I_{CaT} + I_{Kr} + I_{Ks} + I_{sus} + I_{to} + I_{NaK} + I_{NaCa} + I_{Na} + I_f$$

Where V is the membrane potential, C_m the membrane capacitance, t the time, I_{total} the total membrane current generated by potassium (I_{Kr}, I_{Ks}, I_{sus}, I_{to}), calcium (I_{CaL}, I_{CaT}), sodium (I_{Na}), Na^+-K^+ pump (I_{NaK}), Na^+-Ca^{2+} exchanger (I_{NaCa}), and funny (I_f) channels. More details of the basal model are documented in the study of Severi et al. (2012).

Previous experimental studies have shown some distinctive differences in the maximal macroscopic conductance, the steady-state activation curve and the time constant of the channel activation of I_f between the rabbit and the human SAN cells (Difrancesco et al., 1989; Altomare et al., 2003; Barbuti et al., 2007; Verkerk et al., 2007b). In order to take into consideration the reported species difference in I_f properties, in our simulations we implemented two different sets of I_f formulations, one is the original model formulations developed by Severi et al. (2012) (rabbit-like formulation), and the other is Fabbri et al. formulation (Fabbri et al., 2017) based on the human I_f data (Verkerk et al., 2007b) (human-like formulation), which takes the form:

$$I_f = I_{f,Na} + I_{f,K}$$

$$I_{f,Na} = g_{f,Na} \cdot y \cdot (V - E_{Na})$$

$$I_{f,K} = g_{f,K} \cdot y \cdot (V - E_K)$$

$$\tau_y = \frac{1}{(0.36 \cdot (V + 148.8)/(e^{0.066 \cdot (V+148.8)} - 1) + 0.1 \cdot (V + 87.3)/(1 - e^{-0.21 \cdot (V+87.3)})} - 0.054$$

$$y_\infty = 0.01329 + 0.99921/(1 + e^{(V+97.134)/8.1752}), \quad \text{if V} < -80\text{mV}$$

$$y_\infty = 0.0002501 \cdot e^{(-V/12.861)}, \text{if V} \geq -80\text{mV}$$

$$\frac{dy}{dt} = \frac{y_\infty - y}{\tau_y}$$

where $I_{f,Na}$ and $I_{f,K}$ are Na^+ and K^+ components of I_f, $g_{f,Na}$ (0.00268 μS) and $g_{f,K}$ (0.00159 μS) conductance of $I_{f,Na}$ and $I_{f,K}$. E_{Na} and E_K the equilibrium potential for Na^+ and K^+. y_∞ is the steady state activation variable, τ_y the time constant of activation variable (y).

To determine and validate the parameters in the equations of human-like and rabbit-like I_f formulations, the equations for the steady-state activation curves (**Figure 1A**), and the equation for the activation time constant (**Figure 1B**) were fitted to experimental data obtained from human and rabbit SAN cells respectively (Difrancesco et al., 1989; Altomare et al., 2003; Barbuti et al., 2007; Verkerk et al., 2007b). The developed I_f formulations were validated by their ability to reproduce experimental I-V relationship data (**Figure 1C**) obtained by running a series of voltage-clamp commands (**Figure 1D**) for both the human-like and rabbit-like formulations. **Figure 1** shows clearly that I_f in the human SAN has a more negative half-maximal activation voltage (**Figure 1A**), a greater activation time constant (i.e., slower activation process (**Figure 1B**) and a smaller current density (**Figure 1C**) than that in the rabbit SAN.

Simulating the Effects of I_f Blockade

It has been shown that ivabradine blocks I_f without affecting channel kinetics, with block leading to a constant level of I_f reduction after a period of transition (Bucchi et al., 2002, 2013). Therefore, in this study, we implemented a pore-block theory (Yuan et al., 2015) to simulate the steady-state effect of I_f blocking by ivabradine over a wide concentration range by reducing its conductance by a factor k ($k \in (0,1)$, mimicking 0–100% (Bucchi et al., 2013) of I_f reduction. With varying levels of I_f inhibition, by the pore-block theory the I_f conductance became:

$$\begin{cases} g'_{fNa} = (1-k)\cdot g_{fNa} \\ g_{fK} = (1-k)\cdot g_{fK} \end{cases}$$

Simulating the Effect of Acetylcholine (ACh)

In vivo, ACh released from vagal activity slows down the spontaneous pacing rate of the SAN mainly by inhibiting I_f and I_{CaL} (Boyett et al., 1995), and activating acetylcholine-dependent K^+ current (I_{KACh}) (Voigt et al., 2014). Vagal activity may also play a significant role in slowing down the pacing rate when ivabradine blocks I_f. To test the combined action of ivabradine and ACh, we simulated the ACh effect on SAN spontaneous APs, based on the formulations of Severi et al. (2012) for I_f and I_{CaL} inhibition, as well as I_{KACh} activation. In simulations, the values of $g_{K,ACh}$ used were the same as those used in the Severi et al. (2012) and Fabbri et al. models (Fabbri et al., 2017) for the human-like model (Severi model with human-like I_f) ((Fabbri et al., 2017) and the rabbit-like model (i.e., the Fabbri et al. model with rabbit-like I_f; see details in the **Supplementary Material**) (Severi et al., 2012). Effects of ACh on pacemaking APs were qualitatively analyzed and compared with the implementation of rabbit-like and human-like I_f formulation, as well as I_f blocking. Details of the I_{KACh} formulation were listed in the **Supplementary Material**.

Study of Model-Dependence

In order to test the model-dependence of results, simulations were also conducted in the Fabbri et al. model of the human SAN cell (Fabbri et al., 2017), the source code of which was downloadable from cellML at the following URL: https://models.physiomeproject.org/e/568?searchterm=human++si. In this case, the Fabbri et al. model with the human-like I_f formulation was taken as the basal model, which was then modified by replacing the I_f formulation by the rabbit-like one.

Although simulated action potentials from the original Fabbri et al. (2017) model closely match experiment data of AP properties and calcium transient of human SAN cells, some modification was necessary as most of the ionic currents in the model (except I_f, I_{Kr}, and I_{Ks}) were based on rabbit SAN cell model, densities of which were modified by automatic optimization to match simulated action potential characteristics to experimental data. Such automatic optimization of model parameters may deviate from physiological relevance, resulting in some limitations. For example, a full block of I_{CaT} in the model abolished the pacemaking action potential. Though there are no direct experimental data from human SAN cells to validate the simulation result, data from rabbit sinoatrial node (Hagiwara et al., 1988; Takeda et al., 2004) and human patients (Madle et al., 2001) suggested a more modest change in the pacemaking cycle length when I_{CaT} was blocked. Therefore, we updated the model to address some of the limitations. Details about model updating and validations are presented in **Supplementary Figure 1**. Using the updated model, simulations in the Serveri et al. model were repeated in the Fabbri et al. model, and results are included in the **Supplementary Material** to support the major conclusion of the study.

Numerical Scheme

A fourth-order Runge-Kutta-Merson numerical integration method was used to solve the ordinary differential equations of the model. The time step was 5×10^{-6} s, which gives a stable solution of the equations and maintains the accuracy of the computation of membrane current and potential. In simulations, action potentials after the 20th one were recorded for analysis. For solving the Severi et al. model with the human I_f formulation, a set of initial values were used, which were taken from the recorded state variables when the model reached its steady state (see details about the initial values for solving the model in the **Supplementary Material**). This allows the secondary effect of different I_f formulations to other channel variables of the models to be considered in the simulations.

Theoretical Analysis

Theoretical analysis of the effect of I_f block on altered cardiac pacemaking cycle length (CL) was conducted following a similar approach as implemented in previous studies (Rocchetti et al., 2000; Zaza and Lombardi, 2001; Monfredi et al., 2014; Winter and Shattock, 2016; Zaza, 2016).

Figure 2 shows a schematic illustration of a cycle of action potentials of SAN cells. During the time course of the action potential, the voltage difference between the MDP and the voltage at the beginning of AP upstroke (V_{up}) (ΔV_m) can

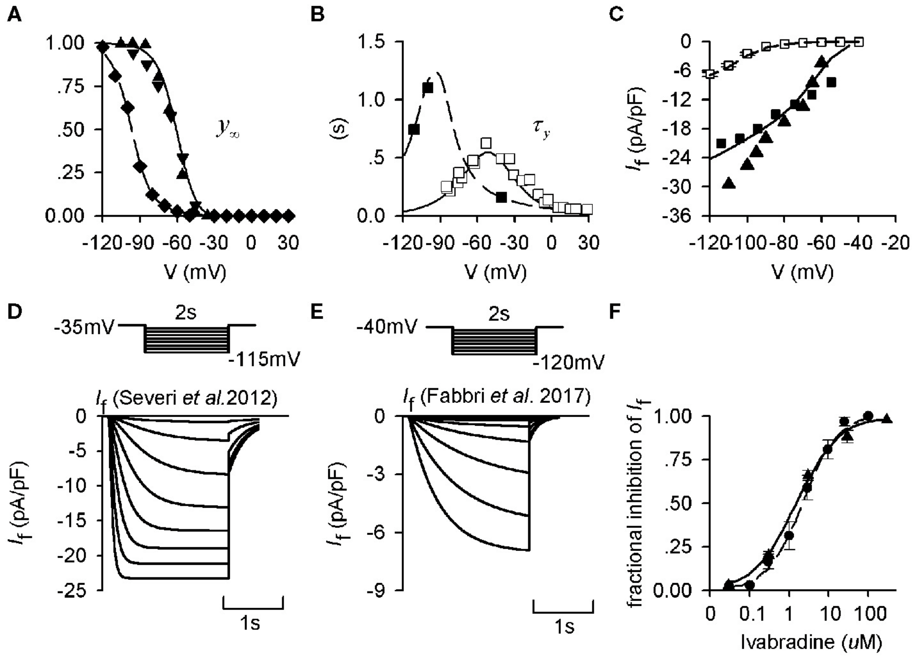

FIGURE 1 | Kinetics of I_f from experimental and mathematical modeling data. **(A)** Steady-state activation curves in rabbit and human and SAN cells, which were used to fit I_f formulations for the Severi et al. (2012) rabbit (solid lines) and the modified Fabbri et al. (2017) human (dashed lines) models. Experimental data from Altomare et al. (2003) (▲), Barbuti et al. (2007) (▼), and Verkerk et al. (2007b) (♦) are also shown. **(B)** Corresponding activation time constant of I_f for human and rabbit SAN cells. Experimental data from Difrancesco et al. (1989) (☐) and Verkerk et al. (2007b) (■) are also shown. **(C)** Computed *I-V* relationship for the human- (dashed line) and rabbit-like (solid line) models, which are compared with experimental data from the study of Verkerk et al. (2007b) (☐) for the human SAN cells, Zaza et al. (1996) (■) and Goethals et al. (1993) (▲) for the rabbit SAN cells. **(D,E)** Voltage-clamp protocol and simulated time traces of I_f during voltage-clamp for the rabbit and human I_f model. **(F)** Dose-dependent effect of ivabradine on I_f in rabbit SAN cells. Experimental data of Bois et al. (1996) (•) and Bucchi et al. (2002) (▲) were based to develop the concentration-response curves as shown by the solid line and dashed line respectively.

be discretized as many small steps by ΔV_i, each taking a time period DI_i to complete. Here dV_i/dt represents the local diastolic depolarization rate (DDR). During the diastolic depolarization phase, with small time interval (dt), $|dV_i/dt|$ can be approximately considered as a constant and denoted by $|dV/dt|$. And the total diastolic interval (DI) can be expressed as:

$$\mathrm{DI} = \sum \mathrm{DI}_i = \sum \frac{\Delta \mathrm{V}_i}{|\mathrm{dV}_i/\mathrm{d}t|} = \frac{\sum \Delta \mathrm{V}_i}{|\mathrm{dV}/\mathrm{d}t|} = \frac{\Delta \mathrm{V}_m}{|\mathrm{dV}/\mathrm{d}t|} \quad (2)$$

Considering Equation (2), the pacemaking cycle length (CL) can be denoted as:

$$\mathrm{CL} = \mathrm{APD} + \mathrm{DI} = \mathrm{APD} + \frac{\Delta \mathrm{V}_m}{|\mathrm{dV}/\mathrm{d}t|} = \mathrm{APD} + \frac{\mathrm{C}_m \Delta \mathrm{V}_m}{|I_{total}|}$$

Where I_{total} denotes total membrane currents during the diastolic depolarization phase.

In response to I_f block, a new total ion channel current during the diastolic depolarization phase I'_{total} is generated, which takes the form

$$I'_{total} = I_{total} - \Delta I$$

ΔI is the change of I_{total} caused by I_f reduction. This produces a new pacing cycle length (CL′), which can be represented as:

$$\mathrm{CL}' = \mathrm{APD}' + \frac{C_m \Delta \mathrm{V}_m}{|I'_{total}|} = \mathrm{APD} + \frac{C_m \Delta \mathrm{V}_m}{|I_{total} - \Delta I|}$$

where APD' is the new action potential duration in response to I_f blockade. As a small I_f block in response to a low dose of ivabradine mainly affects the diastolic depolarization phase and has little or no impact on the AP duration and the MDP, APD′ is approximately equal to APD. Therefore, the increased cycle length (ΔCL) can be represented as

$$\begin{aligned}\Delta \mathrm{CL} &= \mathrm{CL}' - \mathrm{CL} = \mathrm{C}_m \Delta \mathrm{V}_m \left(\frac{1}{|I_{total} - \Delta I|} - \frac{1}{|I_{total}|}\right) \\ &= \mathrm{C}_m \Delta \mathrm{V}_m \frac{|\Delta I|}{|I_{total}| \cdot |I_{total} - \Delta I|}\end{aligned}$$

Then the relative change of the pacing cycle length is:

$$\frac{\Delta \mathrm{CL}}{\mathrm{CL}} = \frac{\mathrm{C}_m \Delta \mathrm{V}_m}{(\mathrm{APD} + \frac{\mathrm{C}_m \Delta \mathrm{V}_m}{|I_{total}|})} \cdot \frac{1}{|I_{total}|} \cdot \frac{|\Delta I|}{|I_{total} - \Delta I|}$$

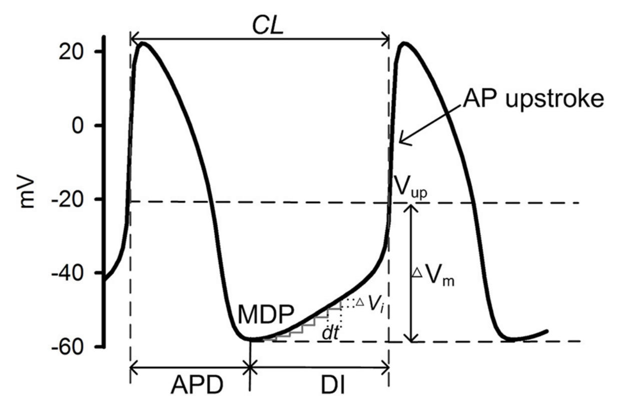

FIGURE 2 | Schematic illustration of a cycle of SAN cell action potentials. During one cycle, the time interval between two consecutive action potentials measures the intrinsic pacemaking CL, which can be considered as a sum of the AP duration (APD) and the diastolic interval (DI) which starts from the maximum diastolic potential (MDP) to the beginning of AP upstroke [V_{up} (Fabbri et al., 2017)]. ΔV_m denotes the voltage difference between the MPD and the V_{up}. During the DI, multiple time intervals (d*t*) were needed for the membrane potential to transit from the MDP to the V_{up}, during each of which a ΔV_i is generated.

By denoting p as I_f current block potency ($p = |\Delta I/I_f|$), and x as the proportion of I_f to I_{total} during the diastolic phase ($x = |I_f/I_{total}|$), then we have:

$$\frac{\Delta \mathrm{CL}}{\mathrm{CL}} = \frac{C_m \Delta V_m}{(\mathrm{APD} + \frac{C_m \Delta V_m}{|I_{total}|})} \cdot \frac{1}{|I_{total}|} \cdot \frac{|\Delta I/I_f|}{|I_{total}/I_f - \Delta I/I_f|}$$
$$= \frac{p}{(\frac{\mathrm{APD}}{C_m \Delta V_m}|I_{total}| + 1)} \cdot \frac{1}{|\frac{1}{x} - p|}$$

By setting

$$C_1 = \frac{\mathrm{APD}}{C_m \Delta V_m}$$

where C_1 ($C_1 > 0$) can be considered as a constant during the diastolic depolarization phase with a fixed level of I_f reduction (i.e., p is fixed), which has no significant effect on the difference between MDP and the V_{up} (i.e., ΔV_m), then we have:

$$\frac{\Delta \mathrm{CL}}{\mathrm{CL}} = \frac{p}{(C_1 |I_{total}| + 1)} \cdot \frac{1}{|\frac{1}{x} - p|} \propto C_2 \cdot \frac{1}{|I_{total}|} \cdot \frac{1}{|\frac{1}{x} - p|} \quad (3)$$

Where C_2 also can be seen as a constant related to C_1 and p, also with a fixed level of I_f reduction.

With I_f block, the resultant relative change of the CL predicted by Equation (3) is inversely proportional to the amplitude of I_{total} during the diastolic depolarization phase, which determines the intrinsic CL of the pacemaking action potential. It is also related to the level of I_f reduction and the ratio between I_f and I_{total}. With a small level of I_f block, the resultant relative change of CL is greater for a smaller I_{total} (i.e., greater when the CL is larger or the heart rate is lower).

RESULTS

Simulation Results

Figure 3 shows the simulated action potentials from the Severi et al. model with rabbit (**Figures 3Ai–Fi**) and human (**Figures 3Aii–Fii**) I_f formulations. In the figure, action potentials (**Figures 3Ai,Aii**) are shown together with membrane currents during the genesis of action potentials, including I_{CaL} (**Figures 3Bi,Bii**), I_f (**Figures 3Ci,Cii**), I_{Na} (**Figures 3Di,Dii**), I_{CaT} (**Figures 3Ei,Eii**), I_{NaCa} (**Figures 3Fi,Fii**), I_{Kr} (**Figures 3Gi,Gii**), I_{Ks} (**Figures 3Hi,Hii**), I_{to} (**Figures 3Ii,Iii**), and I_{NaK} (**Figures 3Ji,Jii**). By replacing the rabbit I_f formulation with the human I_f formulation, the pacemaking activity was slowed down, with a pacemaking CL that increased from 355 ms to 1,139 ms, which was associated with a slight increase in I_{Na} and I_{CaT} at the late period of the diastolic depolarization phase (DDP) (with no noticeable difference at the initial period of the DDP), and a slight decrease in I_{Kr}, I_{Ks}, I_{to}, and I_{NaK} during the DDP. Such a small increase in the above-mentioned inward currents and a decrease in the outward currents, though contributory factors, are not the major determinants of the prolonged diastolic depolarization phase. The slowing down in the pacemaking activity of the human-like formulation model is mainly attributable to the smaller I_f, I_{CaL}, and I_{NaCa} during the diastolic depolarization phase.

In **Figure 3**, effects of reducing I_f by 20% on the pacemaking activity of the two models are also shown.

Reduction of I_f by 20% produced an increase of the CL in the rabbit-like I_f formulation model by about 4.6% (**Figure 3K**). This is in agreement with experimental data from isolated rabbit SAN cells, which showed that a low level of I_f block by ivabradine [$<0.5\,\mu$M, a concentration not affecting SAN I_{CaL} which only slightly decreased by $18.12 \pm 0.66\%$ at 10 μM (Bois et al., 1996)] produced only a slight slowing down of the pacemaking rate, while >50% I_f blockade by 3 μM ivabradine (see **Figure 1F**) only reduced the spontaneous pacing rate by 11–17.7% (Bucchi et al., 2007; Yaniv et al., 2012).

However, in the human-like I_f formulation model, I_f reduction by 20% produced a more than 2-fold increase in the pacemaking CL by 12.4% (i.e., equivalent to about 11.1% reduction in the heart rate) as compared to the rabbit-like model (**Figure 3K**). The pacing rate reduction though was slightly less than the effect of intravenous administration of ivabradine by 0.2 $\mathrm{mg \cdot kg^{-1}}$ (~23.5–34.1 nM of mean maximal ivabradine plasma levels) produced a reduction of heart rate by 18–20% (i.e., mean heart rate reductions of 12.9 and 14.1 beats min^{-1}; Camm and Lau, 2003; Jiang et al., 2013), but close to experimental data of the pacing rate reduction when I_f was blocked by 3 μM ivabradine in rabbit SAN (Bucchi et al., 2007; Yaniv et al., 2012). This illustrates that the small human-like I_f has a greater effect on slowing down the pacing rate than the rabbit-like one when I_f is inhibited by ivabradine.

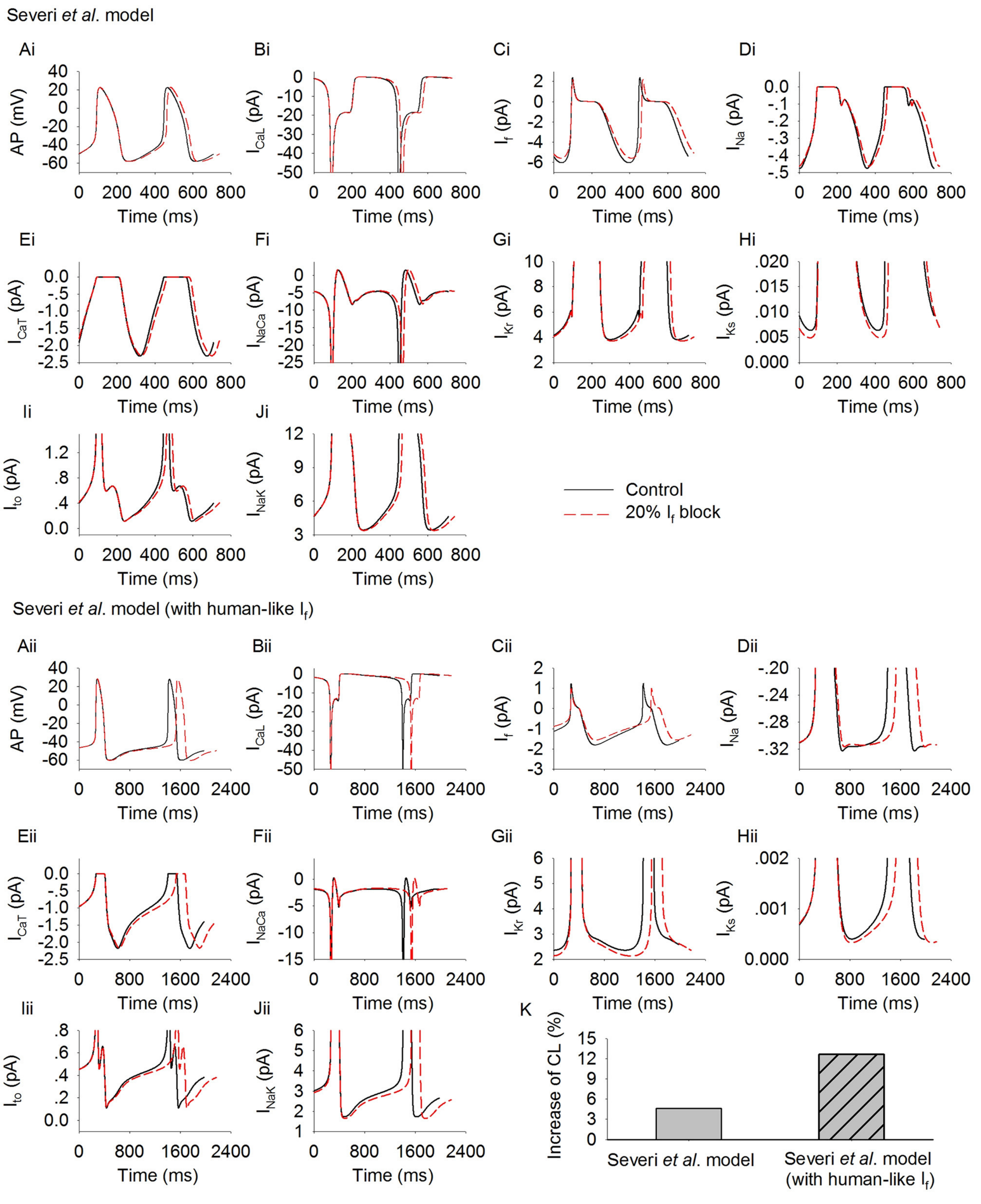

FIGURE 3 | Simulated spontaneous action potentials and underlying currents by the Severi et al. model with rabbit I_f **(Ai–Fi)** and human I_f **(Aii–Fii)** formulations. Effects of blocking I_f by 20% on action potentials and underlying ionic currents (dotted lines) are also shown and superimposed with those in control condition (solid lines). **(Ai,Aii)**: action potentials; **(Bi,Bii)**: I_{CaL}; **(Ci,Cii)**: I_f; **(Di,Dii)**: I_{Na}; **(Ei,Eii)**: I_{CaT}; **(Fi,Fii)**: I_{NaCa}; **(Gi,Gii)**: I_{Kr}; **(Hi,Hii)**: I_{Ks}; **(Ii,Iii)**: I_{to}; **(K)** increase of pacing CL.

The results above suggested that the increased CL induced by 20% I_f reduction is proportional to the intrinsic cycle length of the model, i.e., the greater the intrinsic CL (e.g., the model with human-like I_f formulation) the greater the increase of the CL. This observation was model-independent as shown in **Supplementary Figure 3**, in which Fabbri et al. model of the human SAN was implemented by using rabbit-like and human-like I_f formulations. In the basal condition (Fabbri et al. model with human-like I_f formulation), the CL was 810 ms, which was increased by 44 ms with 20% I_f reduction (i.e., 5.5%). When the rabbit-like I_f formulation was used, the pacemaking rate was increased due to a larger I_f, resulting a CL of 355 ms. With 20% I_f reduction, the CL was increased by 18 ms (i.e., 4.7%), which was smaller than that when the human-like I_f formulation was used.

As shown in **Figures 3Ci,Cii**, a 20% reduction in the channel conductance did not necessarily produce 20% reduction in I_f amplitude during the time course of action potential, due to the dependence of I_f on membrane voltage. To further investigate this, we computed the average I_f during the diastolic phase before and after 20% reduction in its channel conductance. Results are shown in **Supplementary Figure 2**. It was found that 20% reduction in the channel conductance produced a similar decrease in the avarage I_f in the rabbit-like (by 0.34 pA) and the human-like model (by 0.22 pA), but the relative change was greater in the latter model because of its smaller I_f in the control condition. Such difference in the relative change of I_f may also be one of the important reasons for the more pronounced prolongation of the diastolic phase in model with human I_f formulation. Note that in both models (rabbit-like and human-like models), the relative change of I_f was smaller than 20% though the channel conductance was reduced by 20%, due to the voltage-dependence of the channel's activation.

Further simulations were carried out to analyze possible effects of the cross talk between the membrane clock (I_f) and Ca^{2+} clock on modulating pacemaking action potentials in response to I_f reduction. **Figure 4** shows results for the rabbit-like (**Figures 4Ai–Ei**) and human-like (**Figures 4Aii–Eii**) I_f formulation models. Blocking I_f by 20% decreased intracellular (cytoplasmic) Ca^{2+} transients ($[Ca^{2+}]_i$, **Figures 4Bi,Bii**), the intracellular subspace Ca^{2+} concentration ($[Ca^{2+}]_{sub}$, **Figures 4Ci,Cii**) and the Ca^{2+} content in the network SR ($[Ca^{2+}]_{nsr}$, **Figures 4Ei,Eii**). The diastolic level of $[Ca^{2+}]_{sub}$ was reduced by 2.9 and 5% in the rabbit-like and human-like I_f formulation model respectively, the decreased $[Ca]_{sub}$ during the diastolic depolarization phase of the action potential (**Figures 4Ci,Cii**) leads to a decreased I_{NaCa} (**Figures 3Fi,Fii**) and I_{CaL} (**Figures 3Bi,Bii**), especially during the later phase of diastolic depolarization, which prolonged the later phase of the diastolic depolarization in the human-like I_f formulation model (**Figure 4Aii**). There was a negligible change in I_{Na} (**Figures 3Di,Dii**) and I_{CaT} (**Figures 3Ei,Eii**) during the diastolic phase. Taken together with the observation of changes in I_{NaCa} (**Figure 3F**), our simulation results imply that the slowing down of the spontaneous action potentials in response to a low level of I_f block (< 20%) may be mainly attributable to I_f reduction (i.e., membrane clock), with some contribution from a crosstalk between the membrane clock and Ca^{2+} clock in the later diastolic depolarization phase.

Effects were also investigated of how a systematic change in I_f density affects spontaneous pacemaker activity. Results are shown in **Figure 5**, in which the computed CL (**Figure 5A**) and its increase (**Figure 5B**) with I_f being blocked from 0 to 100% with 1% increment for the rabbit-like (closed circles) and human-like I_f formulations (open circles). It was shown that over the range 0–80%, I_f block produced a greater CL increase with the human-like formulation than in the rabbit-like model. With a low level of I_f reduction, a linear relationship between the CL increase and I_f block was seen (**Figure 5B**). However, the relationship changed to an exponential one (**Figure 5B**) when a high level of I_f block was implemented. With about 66% I_f reduction, the CL was increased by about 26% (reduced pacemaking rate by 21%) in the rabbit-like model, which is consistent with experimental data (Thollon et al., 1994; Bucchi et al., 2007), but by about 42% in the human I_f formulation. A low level of I_f reduction (<20%) resulted in a negligible change in the MDP (<-0.3 mV in both models) in both rabbit-like and human-like I_f formulation models, and 100% I_f reduction hyperpolarised MDP by only 3.2 mV in the latter model (**Figure 5C**). Corresponding changes in APD_{90} (**Figure 5D**) and the voltage at the beginning of AP upstroke (**Figure 5E**) were also shown (also see **Supplementary Table 1**). While a high level of I_f reduction hyperpolarized the MDP, it had modest secondary effect on APD_{90} (mainly prolonging the late repolarization phase which may be due to the decreased I_{Kr} and I_{NaK} as shown in **Supplementary Figures 4Gi,Ji**, and there was no significant change in the fundamental morphology of the action potential as shown in **Supplementary Figure 4Ai**) and AP upstroke potential in the rabbit-like model.

Changes of the membrane currents and ion concentrations with a systematic change in I_f density in the two models were also investigated (**Supplementary Figures 3, 4**). During the diastolic depolarization phase of the action potentials, $[Ca]_{sub}$ decreased as I_f density gradually decreased (**Supplementary Figures 3Ci,Cii**), further leading to a slower activation of the I_{CaL} (**Supplementary Figures 4Bi,Bii**) and a decrease in I_{NaCa} (**Supplementary Figures 4Fi,Fii**) during this phase. Reduction *of* I_{NaCa} decreased $[Na]_i$ (**Supplementary Figures 3Fi,Fii**), leading to a reduction in I_{NaK} (**Supplementary Figures 4Ji,Jii**) which further exacerbated the reduction of $[Na]_i$. The outward currents (I_{Kr}, I_{Ks}, I_{to}, I_{NaK}) also showed a gradual decrease with a decreased I_f density during the diastolic depolarization phase (**Supplementary Figures 4Gi–Ji,Gii–Jii**).

The simulated action potentials from the two models showed some differences when I_f was fully blocked (**Figure 5A**), with the rabbit-like model failing to generate spontaneous action potentials. Such differences may be attributable to the use of different sets of initial values recorded from their steady state variables as there was no other changes in model equations or parameters, except for the use of rabbit-like I_f or human-like I_f formulations. In order to determine potential

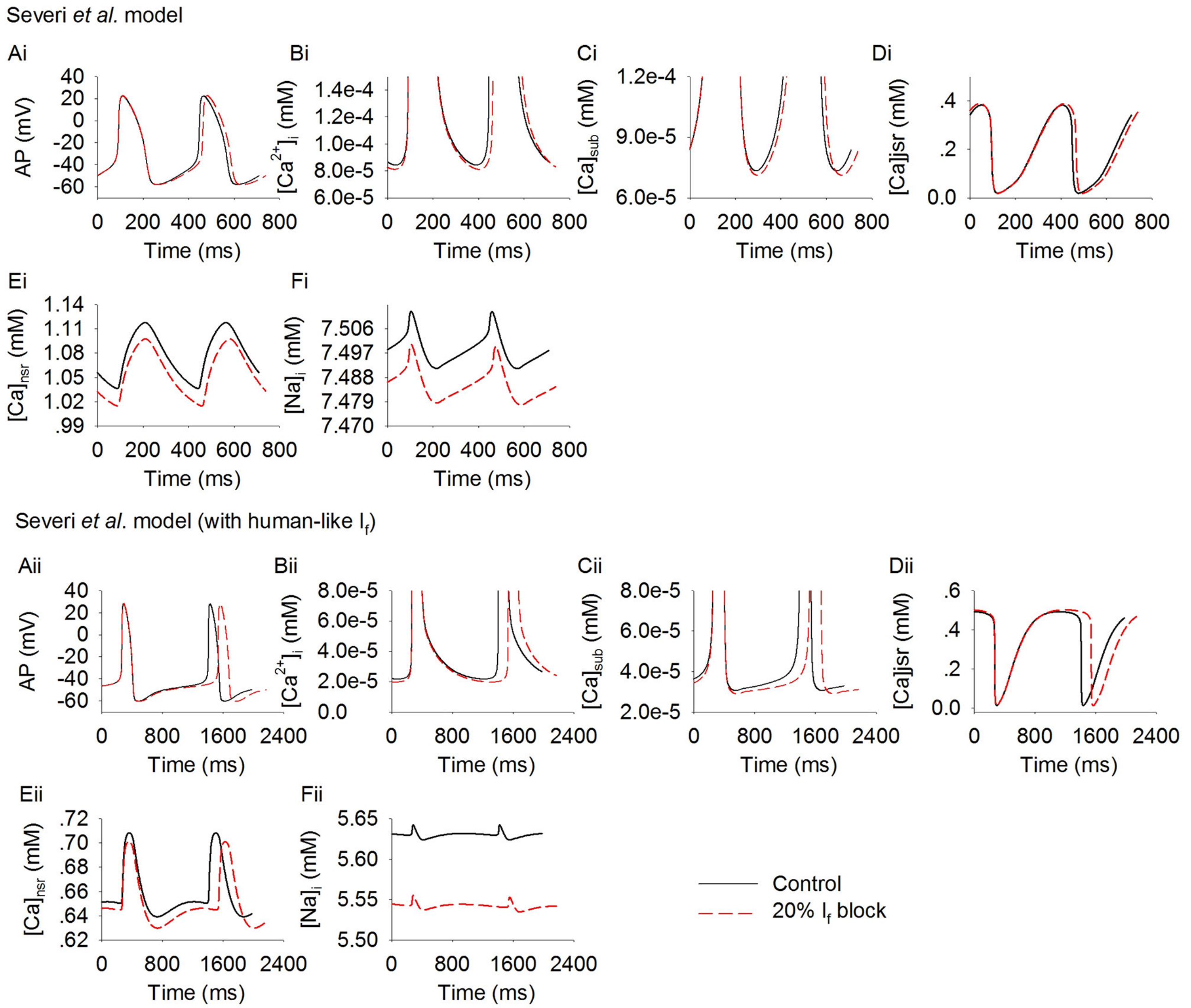

FIGURE 4 | Effect of I_f block on the Ca^{2+} transient in rabbit-like **(Ai–Ei)** and human-like **(Aii–Eii)** SAN cell models. **(Ai,Aii)**: the action potentials; **(Bi,Bii)**: Ca^{2+} transient in the myoplasmic space; **(Ci,Cii)**: Ca^{2+} transient in the myoplasmic sub-space; **(Di,Dii)**: Ca^{2+} transients in the junctional SR; **(Ei,Eii)**: Ca^{2+} transient in the network SR space; **(Fi,Fii)**: intracellular Na^+ concentration. Simulation results in control (solid line) are superimposed on those of I_f blocking (dotted lines).

factors contributing to such differences or contributing to the pacemaking action potentials in the two models, further analyses on membrane currents and the intracellular Ca^{2+} transients between control and 99% reduction of I_f were conducted. Results are shown in **Supplementary Figures 3, 4**. It was shown that in both models, in addition to I_f, I_{CaT}, I_{NaCa}, and I_{Na} contributed to the diastolic depolarization. With a high level of I_f reduction (99%), there was a significant decrease in $[Ca]_{sub}$ during the diastolic depolarization phase (**Supplementary Figure 3Ci**), causing a significant reduction in I_{NaCa} (**Supplementary Figure 4Fi**). Consequently, the spontaneous membrane depolarization was not able to reach the I_{CaL} activation potential, terminating the action potentials in the rabbit-like model.

In the human-like model, a reduction of $[Ca]_{sub}$ was also observed with a high level of I_f reduction, resulting in a decreased I_{NaCa}. However I_{NaCa} was sufficient to maintain the spontaneous depolarization to generate a full action potential.

The focus of this study was on the action of a modest extent (i.e., $<20\%$) of I_f bock, mimicking the clinical use of ivabradine, rather than on the action of a large percentage of I_f block. With $<50\%$ I_f block, the increase in CL was about $<30\%$, which is reasonably close to the experimental data observed in rabbit SAN cells when I_f is blocked by use of Cs^+ (Nikmaram et al., 1997), validating the physiological relevance of the results obtained.

Further simulations were conducted to investigate the combined action of I_f reduction by ivabradine and actions of ACh (Boyett et al., 1995), mimicking the autonomic regulation

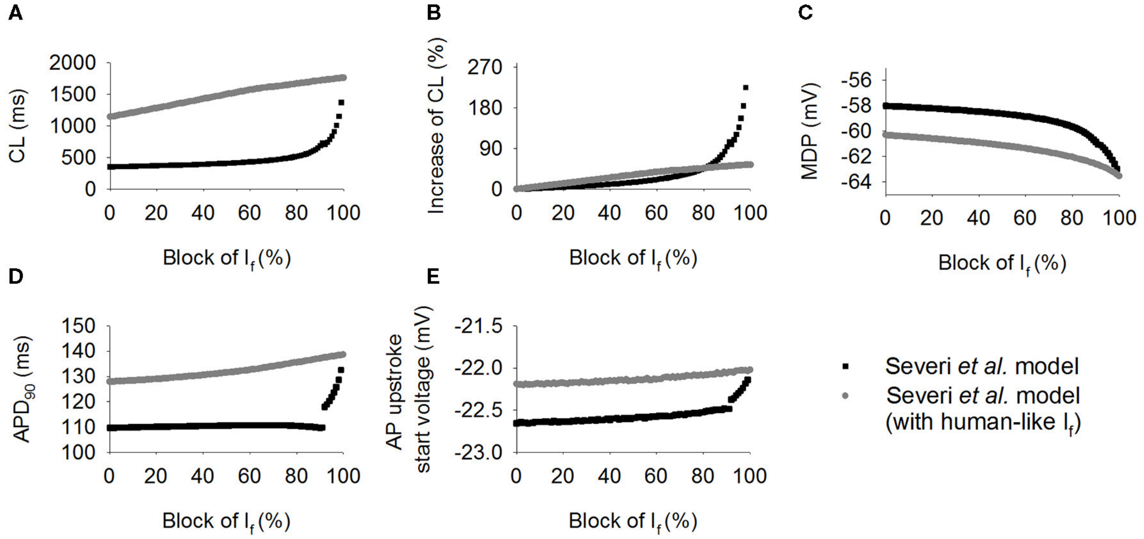

FIGURE 5 | Simulated effect of I_f block on the CL increase. **(A,B)** Pacing cycle length and the relative percentage changes of CL when I_f blocked from 0 to 100% with 1% increment in the human-like (open circle) and rabbit-like (closed circle) SAN cell models; **(C,D)** the maximum diastolic potential (MDP) and action potential duration at 90% of repolarization (APD_{90}); **(E)** change of the beginning of action potential upstroke voltage, which was calculated as the diastolic depolarization rate reached about 50% of its maximum value. I_f block produced greater effect in the human-like (gray circle) and rabbit-like (black square) SAN cell models.

of cardiac pacemaking *in vivo*. In simulations, acetylcholine-dependent inhibition of I_f and I_{CaL}, and activation of K^+ current ($I_{K,ACh}$) (Voigt et al., 2014) were considered. Results are shown in **Figure 6**, in which computed time courses of APs in control (with both rabbit-like and human-like I_f formulations), I_f reduction alone (by 20%) and I_f reduction together with actions of 0.1 nM ACh were compared (**Figures 6A,B**). It was shown that ACh augmented the effect of I_f reduction on the increase of CL in the model with both the rabbit-like and human-like I_f formulations. With the action of 0.1 nM ACh, 20% of I_f block increased the CL by 37.5% (about 27.3% reduction the pacing rate) (**Figure 6C**) in the model with human-like I_f formulation, which is remarkably greater than that of 10.1% (about 9.1% reduction in the pacing rat) in the model with the rabbit-like I_f formulation. This observation held true when different ACh concentrations were considered (**Figure 6D**). These results illustrate that the combined action of I_{KACh} and I_f reduction further slowed down the pacemaking AP due to a reduced total depolarization current during diastolic depolarization phase, resulting in a greater CL prolongation. It suggested that the clinical observed effect of low ivabradine on reducing pacing rate may partially result from the action of ACh due to active vagal tone *in vivo*. Similar observations were also seen in the Fabbri et al. model as shown in **Supplementary Figure 4**, in which ACh augmented more the effect of I_f reduction on pacemaking rate in the model with human-like I_f formulation than that with rabbit-like I_f formulation. Results from the Fabbri et al. model were similar, as shown in **Supplementary Figure 5**.

Theoretical Analysis Validation

The simulation results presented above showed that I_f block produced a greater impact on slowing down the pacemaking rate with the human-like I_f formulation than that in the rabbit-like cell model in both the Severi et al. and Fabbri et al. model (see **Supplementary Material**). This is paradoxical as the I_f density over the pacemaker range with the human-like formulation is much smaller than that in the rabbit-like model, and one would expect a smaller I_f contribution to the spontaneous action potentials (therefore a smaller CL increase with I_f block). However, such a paradoxical effect of I_f reduction on the increase of CL as observed in the two models matched the theoretical prediction shown in the Method section (Equation 2), which showed an inverse relationship between an increased CL and the amplitude of total ionic membrane currents during the diastolic depolarization phase. With the theoretical prediction, a greater CL increase in the human-like I_f formulation SAN cell model can be attributed to a smaller I_{total} during the diastolic depolarization phase.

To test the theoretical prediction, further analyses were conducted to compute the averaged I_{total} amplitude during the DDP. Results from the Severi et al. model are shown in **Figure 7** for control and 20% I_f reduction for action potentials (**Figures 7Ai,Aii**), the time course of I_{total} (**Figures 7Bi,Bii**) and the averaged amplitude of I_{total} (**Figure 7C**) during the DDP. It was found that during the time course of diastolic depolarization, the averaged I_{total} amplitude in the cell model with the human I_f formulations was much smaller (<30%) than that in the rabbit-like model, which produced a slower pacemaking rate (i.e., longer CL) and greater CL increase in response to 20% I_f reduction, matching the theoretical prediction. The changes in currents and Ca^{2+} ion concentration associated with the change in I_{total} (**Figures 7Bi,Bii**) are shown in **Figures 3**, **4**. A similar

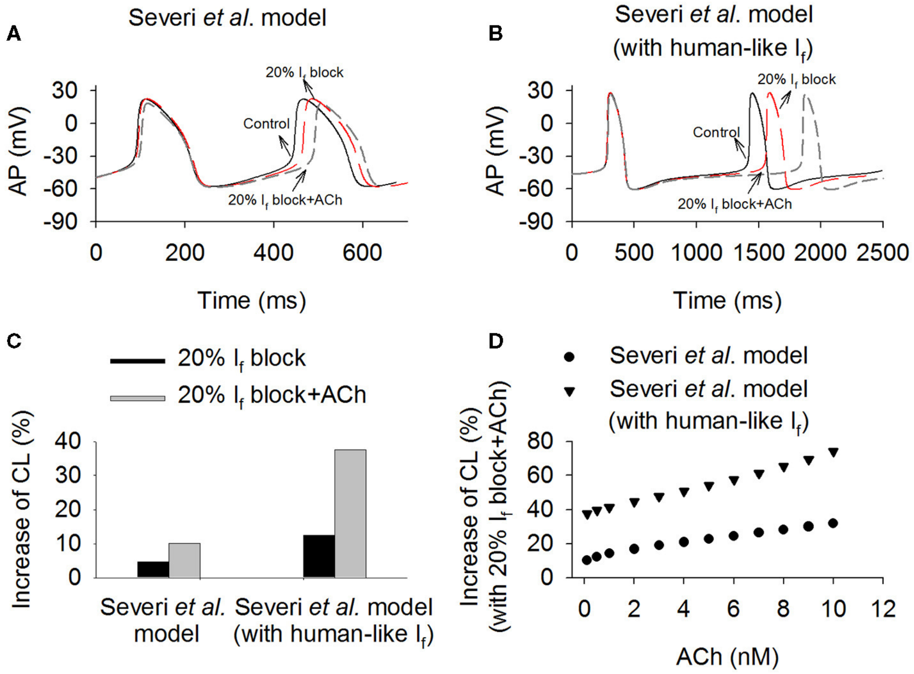

FIGURE 6 | Effects of combined action of ACh and 20% I_f reduction on sponteneous action potentials in the Severi et al. model with the rabbit-like and human-like I_f formulations. **(A,B)** Time courses of action potentials in control, I_f reduction and combined effect of I_f reduction and ACh (0.1 nM). **(C)** The increase of pacemaking CL in the conditions of 20% I_f block alone and combined action with ACh (0.1 nM). **(D)** Combined effect of variant concentrations of ACh (from 0.1 to 10 nM) and 20% I_f block on pacemaking CL in the rabbit-like and human-like I_f formulations models.

observation was also seen in the Fabbri et al. model as shown in **Supplementary Figure 6C**.

In theoretical analysis it was shown that the relative increase of CL was also influenced by a factor of $\frac{1}{|1/x-p|}$, which was related to the ratio of I_f to I_{total} (x) and I_f block potency (p). In simulations, we further computed the values of $\frac{1}{|1/x-p|}$ and $\frac{1}{|I_{total}|}\cdot\frac{1}{|1/x-p|}$ for control and I_f reduction cases. Results from the Severi et al. model are shown in **Figure 8**, in which the time courses of $\frac{1}{|1/x-0.2|}$ (**Figures 8Ai,Aii**) and $\frac{1}{|I_{total}|}\cdot\frac{1}{|1/x-0.2|}$ (**Figures 8Bi,Bii**) were plotted for the control (black) and 20% I_f reduction ($p = 0.2$) for the rabbit-like (left panels) and human-like (the right panels) models. The computed $\frac{1}{|1/x-0.2|}$ (acting as a piecewise function) was set to $\frac{1}{1\times10^{-3}}$ when $|1/x - 0.2|$ was smaller than 1×10^{-3} to avoid the value close to positive infinity. It was shown that in both models with a small I_f block the difference in the computed value of $\frac{1}{|1/x-p|}$ between control (solid line) and 20% I_f reduction (dotted line) was very small during diastolic depolarization phase, and also small when the value was normalized against I_{total} ($\frac{1}{|I_{total}|}\cdot\frac{1}{|1/x-0.2|}$). This provides support for the notion that the relative increase of CL was mainly determined by the amplitude of I_{total} during the diastolic depolarisation phase in response to I_f block.

Note that during the last period of diastolic depolarisation phase (i.e., during time period of 310–387 ms as shown in the figure for the rabbit-like model and 890–1,331 ms for the human-like model), the difference in the computed values of $\frac{1}{|1/x-0.2|}$ and $\frac{1}{|I_{total}|}\cdot\frac{1}{|1/x-0.2|}$ became more noticeable. This may be attributable to the different timings by which the upstroke of pacemaking actions potentials occurred between control and I_f reduction conditions. Note that the value of $\frac{1}{|1/x-0.2|}$ was also greater in the human-like model than that in the rabbit, which amplified the contribution of $\frac{1}{|I_{total}|}$ toward a relative increase of CL. Results from the Fabbri et al. model were similar, as shown in **Supplementary Figure 7**.

A marked difference in the $V_{1/2}$ of the steady-state activation relationship (y_∞) of I_f between the rabbit and the human SAN cells has been observed (Difrancesco et al., 1989; Altomare et al., 2003; Barbuti et al., 2007; Verkerk et al., 2007b). In this study, we used $V_{1/2}$ of −52.5 and −97.1 mV for the rabbit-like and the human-like I_f formulation respectively. In order to systematically determine a possible role of varying $V_{1/2}$ in modulating I_f amplitude, and thus the I_{total} and the effect of I_f reduction on the increase of CL, we changed $V_{1/2}$ of y_∞ in the human-like I_f formulation in a border range from −50 to−70 mV. Results from the Serveri et al. model are shown in **Figure 9** for the pacemaking CL (**Figure 9A**), the averaged I_{total} during diastolic depolarization phase (**Figure 8B**), and increase of CL (**Figure 9C**) with 20% I_f block. Shifting the $V_{1/2}$ from−50 mV (about rabbit $V_{1/2}$) to −70 mV (about human $V_{1/2}$), the I_{total} was decreased (**Figure 9B**), which were correlated with an increased CL (**Figure 9A**) as well as an increased effect of I_f reduction on CL (**Figure 9C**). These results supported our theoretical analysis on that a smaller I_f in the model resulted in a smaller I_{total}

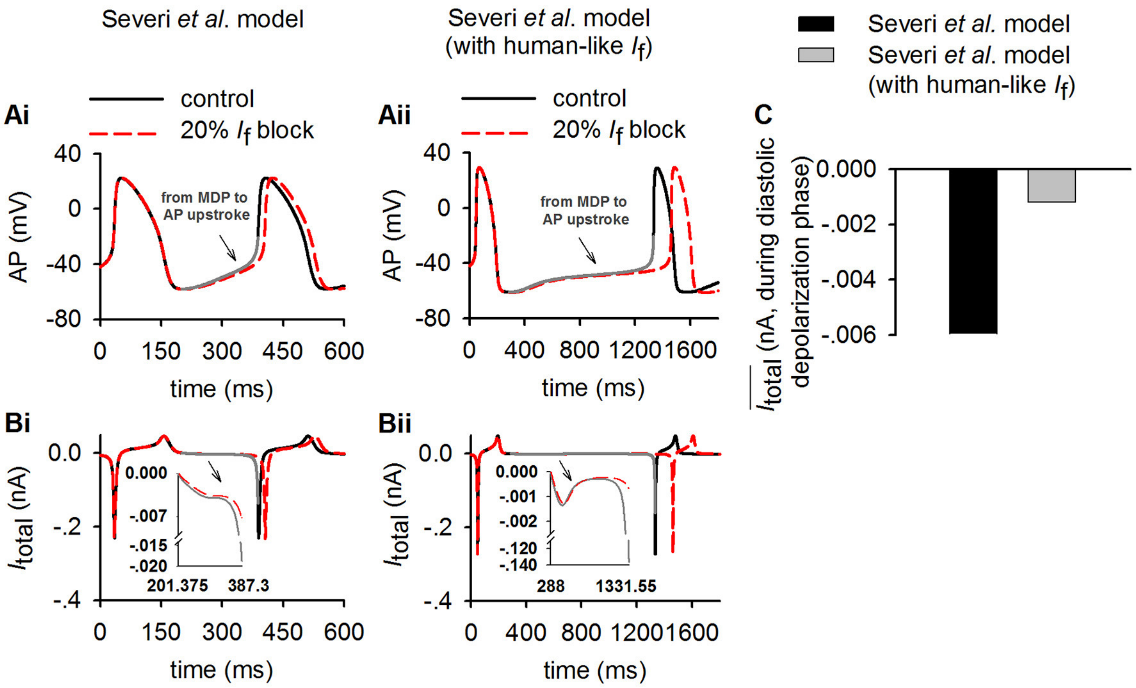

FIGURE 7 | Simulation of the inverse relationship of I_{total} and the increasing of CL in control (solid lines) and 20% I_f reduction (dotted lines) to validate theoretical analysis result (Equation 2) in method section ($p = 0.2$, modeling 20% I_f reduction). **(Ai,Aii)** Time course of action potentials for rabbit-like and human-like SAN cell models respectively (gray lines represents diastolic depolarization voltage changes from the MDP to the voltage at the beginning of AP upstroke in control condition); **(Bi,Bii)** time courses of I_{total} (gray lines represents diastolic depolarization voltage changes from the MDP to the voltage at the beginning of AP upstroke in control condition). **(C)** Averaged value of I_{total} amplitude during the diastolic depolarization phase for the rabbit-like (black) and human-like (gray) SAN cell models. In each case, the integral interval was set to the time interval between the MDP and beginning of the upstroke membrane potential (V_{up}).

amplitude, resulting in a slower pacemaking rate; and as such the same reduction in I_f resulted in a more significant change of CL in the cell model with a smaller I_{total}. Similar results were also observed using the Fabbri et al. model as shown in **Supplementary Figure 8**.

DISCUSSION

This study was conducted to determine the mechanism by which a low level of I_f block by clinical drug (ivabradine) concentration is able to reduce the heart rate of patients by about 18–20%. In a previous study, Verkerk and Wilders found that though I_f has a small magnitude in the human SA node cells, it has an equally important role as in the rabbit (Verkerk and Wilders, 2010). In another study, Maltsev and Lakatta argued that I_f provides a relatively modest contribution to spontaneous beating rate regulation of human and rabbit sinoatrial node cells, and its major role in human SAN cells is to prevent excessive hyperpolarization during AP repolarization, thus representing an anti-bradycardic mechanism, rather than a primary rate regulatory mechanism (Maltsev and Lakatta, 2010). Though these previous studies addressed how a smaller I_f can produce the same effect in humans with respect to rabbit (Verkerk and Wilders, 2010; Fabbri et al., 2017) on complete I_f block, however, the question on how <20% I_f block produces a marked heart rate reduction in humans in *vivo* had remained unclear. This is due to the nonlinear relationship between the extent of I_f block and heart rate reduction (see **Figure 5**); effects of partial I_f block cannot be predicted with certainty from the complete block data already in the literature.

The principal contributions of the work are insights into how a small extent of I_f block (<20%; as may occur during clinical use of ivabradine) produces a marked heart rate reduction in human SAN, greater than that predicted by single cell experiments in the rabbit though the latter has a greater I_f density. Our principal findings are: (i) blocking I_f by 20% resulted in only about a 4.6 % increase in the CL in the rabbit-like SAN cell model, but about 12.4% in the cell model with human I_f formulation. This finding suggests that I_f block has a greater effect with the human-like SAN cell I_f formulation than with rabbit-like I_f formulation, despite the fact that the former has a smaller I_f current density over diastolic potentials, based on which one might expect a smaller contribution of I_f to pacemaking; (ii) there is a cross-talk between the membrane clock and Ca^{2+} clock with 20% I_f block in the later phase of the diastolic depolarization of the action potential; (iii) a theoretical analysis matching the simulation data has been produced, providing a numerical formalism explaining the relationship between I_f block effects and its contribution to total current during diastolic phase. In this study, both numerical simulations and theoretical analysis here have attributed the paradoxical effect of I_f reduction (i.e., a greater effect in SAN cells with smaller I_f current density

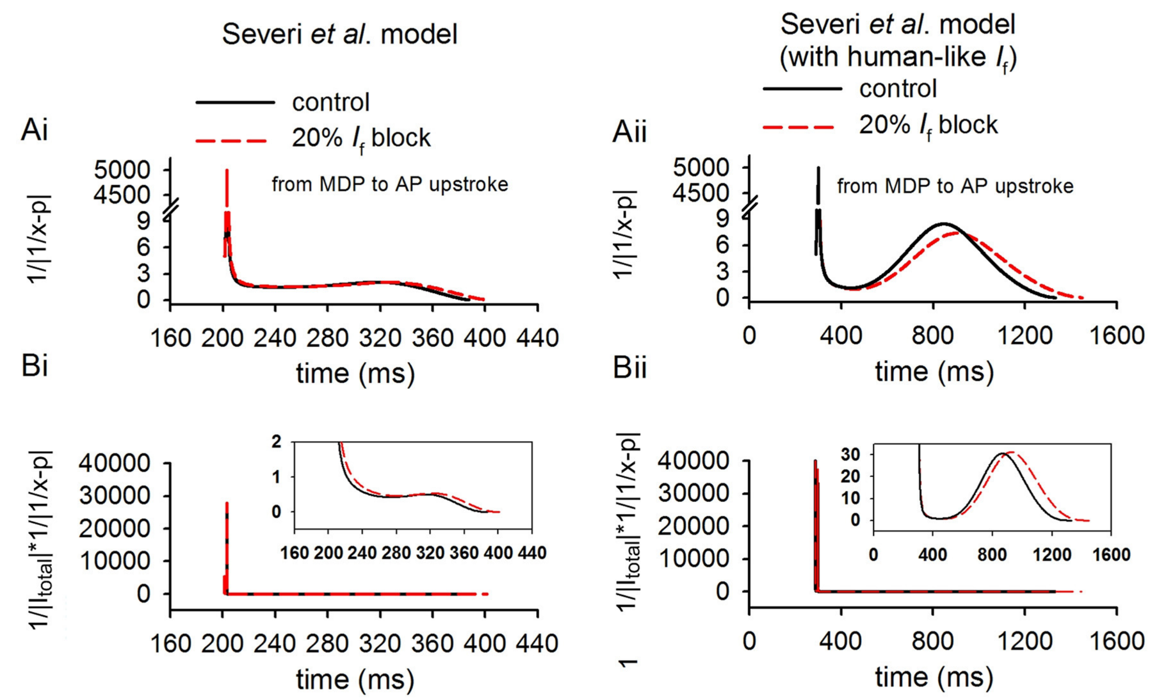

FIGURE 8 | Computed values of $\frac{1}{|1/x-p|}$ and $\frac{1}{|I_{total}|}\cdot\frac{1}{|1/x-p|}$ to validate theoretical analysis result (Equation 2) in method section ($p = 0.2$, modeling 20% I_f reduction). The highlighted lines shown in this figure are during the diastolic depolarization phase of the action potentials of control (solid lines) and 20% I_f reduction (dotted lines) cases for the rabbit-like **(Ai,Bi)** and human-like **(Aii,Bii)** SAN cell models.

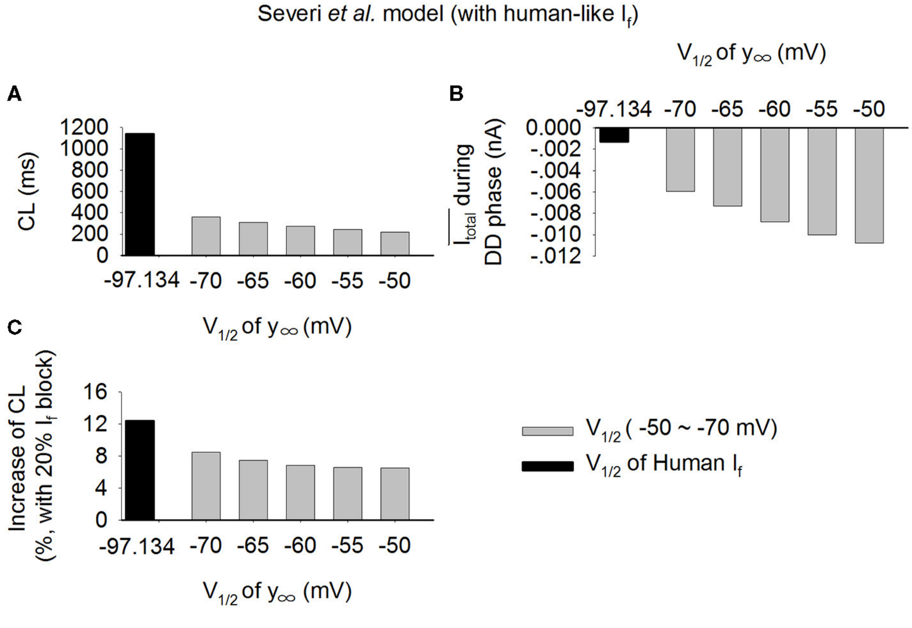

FIGURE 9 | (A–C) Effect of varied half-activation voltage ($V_{1/2}$) of the steady state activation variable (y_∞) on pacemaking CL in the Serveri et al. model with human-like I_f formulation. $V_{1/2}$ changed from −50 to −70 mV, covering the experimental data range for rabbit (−50 mV) and human (−97.1 mV) SAN cells.

and therefore a slower heart rate) to an inverse relationship between the relative increase of CL and the amplitude of the total current during the diastolic depolarization phase in response to I_f block; and (iv) significantly, vagal tone activity *via* ACh augments the effects of ivabradine on heart rate reduction, providing a possible mechanism(s) by which the clinical concentrations can have larger effects *in vivo* than those predicted by single cell experiments *in vitro*. It has been shown that combined action of ACh (0.1 nM) and 20% I_f reduction markedly increase the pacemaking CL by 37.5%, close to the clinical effect of ivabradine when human-like I_f formulation was used, which is significantly greater than that of 10.1% when the rabbit-like I_f formulation was used. These findings were also observed in the Fabbri et al. model.

The results of the present study demonstrate and explain why a smaller human I_f has a greater effect on prolonging the diastolic depolarization phase when it is partially blocked, using both mathematical theoretical analysis and computer simulation, which is clearly distinct from the previous studies (Verkerk and Wilders, 2010; Fabbri et al., 2017). Collectively, they add mechanistic insight into the understanding of how a low dose of clinical use of ivabradine ($<$137 nM) can effectively slow down the human heart rate by about 18–20% (Camm and Lau, 2003; Joannides et al., 2006; Doesch et al., 2007; Jiang et al., 2013), which contrasts with a negligible effect predicted by experimental studies in the rabbit ($<$4% at 10 min after administration of ivabradine; Thollon et al., 2007).

Role of I_f in Generating Cardiac Pacemaking Activity

I_f channels encoded by HCN genes are richly expressed in cardiac conduction systems including the primary pacemaker, the SAN (Altomare et al., 2003; Ravagli et al., 2016). Previous studies from animal models have suggested an important role of I_f in the SAN (Difrancesco and Noble, 2012; Baruscotti et al., 2016; Kozasa et al., 2018). It has been shown that a complete block of I_f by Cs^+ (2 mM) slowed down the pacemaking rate by 30% in the rabbit SAN cells (Denyer and Brown, 1990), a 17.6% reduction of pacemaking rate also seen when blocking of I_f with 0.5 mmol/L Cs^+ (Liu et al., 2008). In transgenic mice, knocking down HCN4 produced bradycardiac effects as well as atrioventricular node conduction block (Herrmann et al., 2007; Hoesl et al., 2008; Baruscotti et al., 2011). All of this evidence demonstrates that I_f, together with the more recently identified Ca^{2+} clock [arising from the coupling between the intracellular Ca^{2+} cycling and electrogenesis of membrane currents (e.g., I_{NaCa}) (Maltsev and Lakatta, 2008; Lakatta and Difrancesco, 2009)], provide a major driving force for generating the spontaneous depolarization during the diastolic phase that leads to intrinsic pacemaker activity.

I_f is also present in human SAN cells (Verkerk et al., 2009b; Li et al., 2015) and contributes to pacemaking. It has been shown that loss-of-function of HCN channel mutations is associated with sick sinus syndrome, which manifests with symptoms of bradycardia and conduction block (Schweizer et al., 2014; Verkerk and Wilders, 2014, 2015). However, the functional role of I_f in generating pacemaking action potentials of human SAN is less well-characterized as compared to that from small mammals. Limited data have shown that I_f in the human SAN cells has a smaller current density, more negative depolarised membrane potential of half maximal activation and slower activation rate as compared to the rabbit (Verkerk et al., 2007a,b, 2009b). All of these suggested a smaller I_f current during the diastolic depolarization phase, which may result in a slower heart rate. Indeed this is the case as shown in the present simulation study. In the Severi et al. model (Severi et al., 2012) with the rabbit-like I_f formulation, the measured pacemaking cycle length was 354.8 ms. However, when the rabbit-like I_f formulation was replaced by the human one, the pacemaking rate was slowed down and the pacemaking cycle length increased to 1,139.4 ms, greater than the intrinsic pacemaking cycle length of native human SAN cells [about 828 ± 21 ms (Verkerk et al., 2007b)]. Note that in the model, such a significant increase of the pacemaking CL from the one of rabbit SAN cells to the one close to human SAN cells was mainly attributable to a small I_f, as no change or negligible secondary changes of other ion channels were implemented. This suggests that I_f exerts a strong influence on pacemaker rhythm. Note that there is a marked difference in the pacemaking CL between the human-like model (1,139.4 ms) and native human SAN cells [about 828 ± 21 ms (Verkerk et al., 2007b)], which may be due to possible species differences in the properties of other membrane currents (Fabbri et al., 2017) and Ca^{2+} clock (Tsutsui et al., 2018). With the increase of I_f blocking, the pacemaking CL increased non-linearly in the model with either rabbit-like or human-like I_f formulations.

In simulations, the action of 100% I_f block abolished the pacemaking in the model with rabbit-like I_f formulations. This may over emphasize the role of I_f in the rabbit SAN pacemaking and is non-physiological. However, the focus of this study is on the action of small I_f block (i.e., $<$20%), mimicking the use of effect of ivabradine in practice, rather than on the action of large percentage of I_f block. With $<$50% I_f block, the increase in CL is about $<$30%, which is reasonably close to the experimental data observed in rabbit SAN cells when I_f is blocked by use of Cs^+ (Nikmaram et al., 1997).

Mechanism for the Action of Low Dose Ivabradine on Human SAN

Our theoretical and numerical simulation results have shown that a low level of I_f block, mimicking the clinical concentrations of ivabradine, produced a more marked effect in reducing the heart rate of the human-like I_f formulation SAN cell model than the rabbit-like I_f formulation SAN cell model. When the action of ACh (0.1 nM) was considered, there was a further reduction of sponteneous pacing rate (reduced upto by 27.3%), which is close to the effect of ivabradine at clinical concentration. Results from the Fabbri et al. model were similar, showing that these observations are model-independent. All these results suggest that a combined action of I_f reduction by ivabradine at clinical concentrations and ACh are attributable to the heart rate reduction as seen clinically (Camm and Lau, 2003; Doesch et al., 2007).

It is possible that ivabradine regulates the heart rate by a cross-talk between the membrane clock and Ca^{2+} clock *via* the electrogenic Na^+-Ca^{2+} exchangers (Yaniv et al., 2013). While the direct action of ivabradine on the intracellular Ca^{2+} handling is unclear, our simulation results showed that a 20% I_f reduction produced secondary modulations of other ionic currents (e.g., I_{NaCa}) and the intracellular Ca^{2+} handling, suggesting there is a cross-talk between the membrane clock and Ca^{2+} clock in the late phase of the diastolic depolarization of the action potential (**Figures 4Bii–Eii**). All these illustrated that ivabradine affected the heart rate at clinical concentrations mainly through regulating membrane clock and Ca^{2+} clock, and combining with the action of ACh.

Limitations of the Study

Possible limitations of the Severi et al. model of the rabbit SAN cells have been well-discussed and documented (Severi et al., 2012). For example, as highlighted by Verkerk and Wilders (2014), the reversal potential of I_f in the Severi et al. model (−4.39 mV) was more positive than that experimentally reported (about −30 mV) (Difrancesco et al., 1986; Van Ginneken and Giles, 1991; Verkerk et al., 2009a), which is a limitation of the Severi et al. model, and therefore also of studies employing this model. However, we did not modify the I_f equation of the Severi et al. model for the following reasons: (1) the simulated I-V relationship data shown in (**Figure 1C**) lie within the range of experimental data, and I_f is very small when the voltage is more positive than −40 mV; (2) when the voltage is more positive than −30 mV, the activation of I_{CaL} is dominant, which contributes mainly to the upstroke phase (non-diastolic depolarization phase) of the action potential. Therefore, even if the reversal potential of I_f is changed from −30 mV to −4.39 mV, it has negligible effect on the diastolic depolarization of spontaneous action potentials. Moreover, in simulations in which the rabbit-like I_f was replaced by the human-like formulations in the Severi et al. model, the reversal potential of I_f used was −27.5 mV, close to the experimentally determined value of -22.1 ± 2.4 mV (Verkerk et al., 2007b).

Another potential limitation of the present study relates to modification of the Severi et al. model to incorporate the human I_f formulation developed by Fabbri et al. based on experimental data from human SAN cells. Due to lack of experimental data from human SAN cells, equations and parameters for other ion channels and transporters in the Severi et al. model were not updated. Note that experimental data on the Ca^{2+} clock of the human SAN became available recently (Tsutsui et al., 2018), which are not incorporated in the model yet. This may explain why the computed CL of the human-like SAN cell is greater than that of natural human SAN cells, and consequently the smaller effect of I_f blocking on the reduction of the heart rate the clinical data. In addition, the action of low dose ivabradine was simulated by considering its action on blocking I_f only, and did not incorporate its possible actions on I_{Kr} as seen in some experimental studies on ventricular cells/tissue at low dose (Melgari et al., 2015) or high doses (Lees-Miller et al., 2015). However, the present study deliberately focused on the difference in direct effects of ivabradine on I_f in the SAN cells between species (I_f in the rabbit SAN and in the human-like SAN). Whilst it is necessary to point out these potential limitations, nevertheless, the simulation data strongly supported the mechanism demonstrated by the theoretical analysis in showing the inverse correlation between I_{total} during the diastolic depolarization phase and the relative increase of the CL. Therefore, these limitations do not alter our major conclusion on the role of I_f block in modulating cardiac pacemaking activities in the human SAN by low concentrations of ivabradine.

CONCLUSION

An inverse correlation between the relative increase of CL and the amplitude of the total ion channel current during the diastolic depolarization phase has been observed. Both theoretical analysis and simulations have shown that a low level of I_f block (<20%) can produce a more marked reduction of in the pacemaking rate of the human-like SAN cell model than the rabbit-like one due to its smaller I_{total} during the diastolic depolarization phase. This was particularly the case when ACh actions were considered, which amplified the pacemaking cycle length prolongation. This study thus provides a mechanistic explanation into how a low level of I_f block by the clinical concentrations of ivabradine can effectively reduce the heart rate in humans but produce a small or negligible effect in the rabbit.

DATA AVAILABILITY STATEMENT

The original contributions presented in the study are included in the article/**Supplementary Material**, further inquiries can be directed to the corresponding author/s.

CODE AVAILABILITY STATEMENT

The code for the models employed is available on request to Henggui Zhang at henggui.zhang@manchester.ac.uk.

AUTHOR CONTRIBUTIONS

HZ and JH conceived the study. XB conducted simulation and data analysis. HZ and MB contributed to theoretical analysis. XB, KW, MB, JH, and HZ wrote the paper. All authors contributed to the article and approved the submitted version.

FUNDING

This work was supported by grants from the British Heart Foundation FS/14/5/30533, EPSRC (UK) (EP/J00958X/1; EP/I029826/1), Shenzhen Science and Technology Innovation Committee (JCYJ20151029173639477; JSGG20160229125049615), and Scientific research plan projects of Shaanxi Education Department (20JK0917). JH received a University of Bristol Research Fellowship.

ACKNOWLEDGMENTS

We are grateful to Dr. Severi's group for providing us the source code of the Severi et al. model.

SUPPLEMENTARY MATERIAL

The Supplementary Material for this article can be found online at: https://www.frontiersin.org/articles/10.3389/fphys.2021.582037/full#supplementary-material

REFERENCES

Accili, E. A., Robinson, R. B., and Difrancesco, D. (1997). Properties and modulation of I_f in newborn versus adult cardiac SA node. *Am. J. Physiol.* 272, H1549–H1552. doi: 10.1152/ajpheart.1997.272.3.H1549

Altomare, C., Terragni, B., Brioschi, C., Milanesi, R., Pagliuca, C., Viscomi, C., et al. (2003). Heteromeric HCN1-HCN4 channels: a comparison with native pacemaker channels from the rabbit sinoatrial node. *J. Physiol.* 549, 347–359. doi: 10.1113/jphysiol.2002.027698

Barbuti, A., Baruscotti, M., and Difrancesco, D. (2007). The pacemaker current: from basics to the clinics. *J. Cardiovasc. Electrophysiol.* 18, 342–347. doi: 10.1111/j.1540-8167.2006.00736.x

Baruscotti, M., Bianco, E., Bucchi, A., and Difrancesco, D. (2016). Current understanding of the pathophysiological mechanisms responsible for inappropriate sinus tachycardia: role of the I_f "funny" current. *J. Interv. Card Electrophysiol.* 46, 19–28. doi: 10.1007/s10840-015-0097-y

Baruscotti, M., Bucchi, A., and Difrancesco, D. (2005). Physiology and pharmacology of the cardiac pacemaker ("funny") current. *Pharmacol. Ther.* 107, 59–79. doi: 10.1016/j.pharmthera.2005.01.005

Baruscotti, M., Bucchi, A., Viscomi, C., Mandelli, G., Consalez, G., Gnecchi-Rusconi, T., et al. (2011). Deep bradycardia and heart block caused by inducible cardiac-specific knockout of the pacemaker channel gene *Hcn4*. *Proc. Natl. Acad. Sci. U. S. A.* 108, 1705–1710. doi: 10.1073/pnas.1010122108

Bohm, M., Robertson, M., Ford, I., Borer, J. S., Komajda, M., Kindermann, I., et al. (2015). Influence of cardiovascular and noncardiovascular co-morbidities on outcomes and treatment effect of heart rate reduction with ivabradine in stable heart failure (from the SHIFT trial). *Am. J. Cardiol.* 116, 1890–1897. doi: 10.1016/j.amjcard.2015.09.029

Bois, P., Bescond, J., Renaudon, B., and Lenfant, J. (1996). Mode of action of bradycardic agent, S 16257, on ionic currents of rabbit sinoatrial node cells. *Br. J. Pharmacol.* 118, 1051–1057. doi: 10.1111/j.1476-5381.1996.tb15505.x

Bois, P., Guinamard, R., Chemaly, A. E., Faivre, J. F., and Bescond, J. (2007). Molecular regulation and pharmacology of pacemaker channels. *Curr. Pharm. Des.* 13, 2338–2349. doi: 10.2174/138161207781368729

Boyett, M. R. (2009). "And the beat goes on." The cardiac conduction system: the wiring system of the heart. *Exp. Physiol.* 94, 1035–1049. doi: 10.1113/expphysiol.2009.046920

Boyett, M. R., Kodama, I., Honjo, H., Arai, A., Suzuki, R., and Toyama, J. (1995). Ionic basis of the chronotropic effect of acetylcholine on the rabbit sinoatrial node. *Cardiovasc. Res.* 29, 867–878. doi: 10.1016/S0008-6363(96)88625-1

Brioschi, C., Micheloni, S., Tellez, J. O., Pisoni, G., Longhi, R., Moroni, P., et al. (2009). Distribution of the pacemaker HCN4 channel mRNA and protein in the rabbit sinoatrial node. *J. Mol. Cell Cardiol.* 47, 221–227. doi: 10.1016/j.yjmcc.2009.04.009

Bucchi, A., Baruscotti, M., and Difrancesco, D. (2002). Current-dependent block of rabbit sino-atrial node I_f channels by ivabradine. *J. Gen. Physiol.* 120, 1–13. doi: 10.1085/jgp.20028593

Bucchi, A., Baruscotti, M., Nardini, M., Barbuti, A., Micheloni, S., Bolognesi, M., et al. (2013). Identification of the molecular site of ivabradine binding to HCN4 channels. *PLoS ONE* 8:e53132. doi: 10.1371/journal.pone.0053132

Bucchi, A., Baruscotti, M., Robinson, R. B., and Difrancesco, D. (2003). I_f-dependent modulation of pacemaker rate mediated by cAMP in the presence of ryanodine in rabbit sino-atrial node cells. *J. Mol. Cell Cardiol.* 35, 905–913. doi: 10.1016/S0022-2828(03)00150-0

Bucchi, A., Baruscotti, M., Robinson, R. B., and Difrancesco, D. (2007). Modulation of rate by autonomic agonists in SAN cells involves changes in diastolic depolarization and the pacemaker current. *J. Mol. Cell Cardiol.* 43, 39–48. doi: 10.1016/j.yjmcc.2007.04.017

Bucchi, A., Tognati, A., Milanesi, R., Baruscotti, M., and Difrancesco, D. (2006). Properties of ivabradine-induced block of HCN1 and HCN4 pacemaker channels. *J. Physiol.* 572, 335–346. doi: 10.1113/jphysiol.2005.100776

Camici, P. G., Gloekler, S., Levy, B. I., Skalidis, E., Tagliamonte, E., Vardas, P., et al. (2016). Ivabradine in chronic stable angina: effects by and beyond heart rate reduction. *Int. J. Cardiol.* 215, 1–6. doi: 10.1016/j.ijcard.2016.04.001

Camm, A. J., and Lau, C. P. (2003). Electrophysiological effects of a single intravenous administration of ivabradine (S 16257) in adult patients with normal baseline electrophysiology. *Drugs R D* 4, 83–89. doi: 10.2165/00126839-200304020-00001

Chandler, N. J., Greener, I. D., Tellez, J. O., Inada, S., Musa, H., Molenaar, P., et al. (2009). Molecular architecture of the human sinus node: insights into the function of the cardiac pacemaker. *Circulation* 119, 1562–1575. doi: 10.1161/CIRCULATIONAHA.108.804369

Choi, H. Y., Noh, Y. H., Cho, S. H., Ghim, J. L., Choe, S., Kim, U. J., et al. (2013). Evaluation of pharmacokinetic and pharmacodynamic profiles and tolerability after single (2.5, 5, or 10 mg) and repeated (2.5, 5, or 10 mg bid for 4.5 days) oral administration of ivabradine in healthy male Korean volunteers. *Clin. Ther.* 35, 819–835. doi: 10.1016/j.clinthera.2013.04.012

Craven, K. B., and Zagotta, W. N. (2006). CNG and HCN channels: two peas, one pod. *Annu. Rev. Physiol.* 68, 375–401. doi: 10.1146/annurev.physiol.68.040104.134728

Denyer, J. C., and Brown, H. F. (1990). Pacemaking in rabbit isolated sino-atrial node cells during Cs$^+$ block of the hyperpolarization-activated current i_f. *J. Physiol.* 429, 401–409. doi: 10.1113/jphysiol.1990.sp018264

Difrancesco, D. (1991). The contribution of the "pacemaker" current (if) to generation of spontaneous activity in rabbit sino-atrial node myocytes. *J. Physiol.* 434, 23–40. doi: 10.1113/jphysiol.1991.sp018457

Difrancesco, D. (2010). The role of the funny current in pacemaker activity. *Circ. Res.* 106, 434–446. doi: 10.1161/CIRCRESAHA.109.208041

Difrancesco, D., Ducouret, P., and Robinson, R. B. (1989). Muscarinic modulation of cardiac rate at low acetylcholine concentrations. *Science* 243, 669–671. doi: 10.1126/science.2916119

Difrancesco, D., Ferroni, A., Mazzanti, M., and Tromba, C. (1986). Properties of the hyperpolarizing-activated current (i_f) in cells isolated from the rabbit sino-atrial node. *J. Physiol.* 377, 61–88. doi: 10.1113/jphysiol.1986.sp016177

Difrancesco, D., and Noble, D. (2012). The funny current has a major pacemaking role in the sinus node. *Heart Rhythm* 9, 299–301. doi: 10.1016/j.hrthm.2011.09.021

Doesch, A. O., Celik, S., Ehlermann, P., Frankenstein, L., Zehelein, J., Koch, A., et al. (2007). Heart rate reduction after heart transplantation with beta-blocker versus the selective I_f channel antagonist ivabradine. *Transplantation* 84, 988–996. doi: 10.1097/01.tp.0000285265.86954.80

Fabbri, A., Fantini, M., Wilders, R., and Severi, S. (2017). Computational analysis of the human sinus node action potential: model development and effects of mutations. *J. Physiol.* 595, 2365–2396. doi: 10.1113/JP273259

Goethals, M., Raes, A., and Van Bogaert, P. P. (1993). Use-dependent block of the pacemaker current I(f) in rabbit sinoatrial node cells by zatebradine (UL-FS 49). On the mode of action of sinus node inhibitors. *Circulation* 88, 2389–2401. doi: 10.1161/01.CIR.88.5.2389

Hagiwara, N., and Irisawa, H. (1989). Modulation by intracellular Ca^{2+} of the hyperpolarization-activated inward current in rabbit single sino-atrial node cells. *J. Physiol.* 409, 121–141. doi: 10.1113/jphysiol.1989.sp017488

Hagiwara, N., Irisawa, H., and Kameyama, M. (1988). Contribution of two types of calcium currents to the pacemaker potentials of rabbit sino-atrial node cells. *J. Physiol.* 395, 233–253. doi: 10.1113/jphysiol.1988.sp016916

Herrmann, S., Stieber, J., Stockl, G., Hofmann, F., and Ludwig, A. (2007). HCN4 provides a "depolarization reserve" and is not required for heart rate acceleration in mice. *EMBO J.* 26, 4423–4432. doi: 10.1038/sj.emboj.7601868

Hoesl, E., Stieber, J., Herrmann, S., Feil, S., Tybl, E., Hofmann, F., et al. (2008). Tamoxifen-inducible gene deletion in the cardiac conduction system. *J. Mol. Cell Cardiol.* 45, 62–69. doi: 10.1016/j.yjmcc.2008.04.008

Irisawa, H., Brown, H. F., and Giles, W. (1993). Cardiac pacemaking in the sinoatrial node. *Physiol. Rev.* 73, 197–227. doi: 10.1152/physrev.1993.73.1.197

Jiang, J., Tian, L., Huang, Y., Li, Y., and Xu, L. (2013). Pharmacokinetic and safety profile of ivabradine in healthy Chinese men: a phase I, randomized, open-label, increasing single- and multiple-dose study. *Clin. Ther.* 35, 1933–1945. doi: 10.1016/j.clinthera.2013.10.007

Joannides, R., Moore, N., Iacob, M., Compagnon, P., Lerebours, G., Menard, J. F., et al. (2006). Comparative effects of ivabradine, a selective heart rate-lowering agent, and propranolol on systemic and cardiac haemodynamics at rest and during exercise. *Br. J. Clin. Pharmacol.* 61, 127–137. doi: 10.1111/j.1365-2125.2005.02544.x

Kozasa, Y., Nakashima, N., Ito, M., Ishikawa, T., Kimoto, H., Ushijima, K., et al. (2018). HCN4 pacemaker channels attenuate the parasympathetic response and stabilize the spontaneous firing of the sinoatrial node. *J. Physiol.* 596, 809–825. doi: 10.1113/JP275303

Lakatta, E. G., and Difrancesco, D. (2009). What keeps us ticking: a funny current, a calcium clock, or both? *J. Mol. Cell Cardiol.* 47, 157–170. doi: 10.1016/j.yjmcc.2009.03.022

Lakatta, E. G., Maltsev, V. A., and Vinogradova, T. M. (2010). A coupled SYSTEM of intracellular Ca^{2+} clocks and surface membrane voltage clocks controls the timekeeping mechanism of the heart's pacemaker. *Circ. Res.* 106, 659–673. doi: 10.1161/CIRCRESAHA.109.206078

Lees-Miller, J. P., Guo, J., Wang, Y., Perissinotti, L. L., Noskov, S. Y., and Duff, H. J. (2015). Ivabradine prolongs phase 3 of cardiac repolarization and blocks the hERG1 (KCNH2) current over a concentration-range overlapping with that required to block HCN4. *J. Mol. Cell Cardiol.* 85, 71–78. doi: 10.1016/j.yjmcc.2015.05.009

Li, N., Csepe, T. A., Hansen, B. J., Dobrzynski, H., Higgins, R. S., Kilic, A., et al. (2015). Molecular mapping of sinoatrial node HCN channel expression in the human heart. *Circ. Arrhythm Electrophysiol.* 8, 1219–1227. doi: 10.1161/CIRCEP.115.003070

Liu, J., Noble, P. J., Xiao, G., Abdelrahman, M., Dobrzynski, H., Boyett, M. R., et al. (2008). Role of pacemaking current in cardiac nodes: insights from a comparative study of sinoatrial node and atrioventricular node. *Prog. Biophys. Mol. Biol.* 96, 294–304. doi: 10.1016/j.pbiomolbio.2007.07.009

Madle, A., Linhartova, K., and Koza, J. (2001). Effects of the T-type calcium channel blockade with oral mibefradil on the electrophysiologic properties of the human heart. *Med. Sci. Monit.* 7, 74–77.

Maltsev, V. A., and Lakatta, E. G. (2008). Dynamic interactions of an intracellular Ca^{2+} clock and membrane ion channel clock underlie robust initiation and regulation of cardiac pacemaker function. *Cardiovasc. Res.* 77, 274–284. doi: 10.1093/cvr/cvm058

Maltsev, V. A., and Lakatta, E. G. (2010). Funny current provides a relatively modest contribution to spontaneous beating rate regulation of human and rabbit sinoatrial node cells. *J. Mol. Cell Cardiol.* 48, 804–806. doi: 10.1016/j.yjmcc.2009.12.009

Mangoni, M. E., and Nargeot, J. (2008). Genesis and regulation of the heart automaticity. *Physiol. Rev.* 88, 919–982. doi: 10.1152/physrev.00018.2007

Melgari, D., Brack, K. E., Zhang, C., Zhang, Y., El Harchi, A., Mitcheson, J. S., et al. (2015). hERG potassium channel blockade by the HCN channel inhibitor bradycardic agent ivabradine. *J. Am. Heart Assoc.* 4:1813. doi: 10.1161/JAHA.115.001813

Monfredi, O., Lyashkov, A. E., Johnsen, A. B., Inada, S., Schneider, H., Wang, R., et al. (2014). Biophysical characterization of the underappreciated and important relationship between heart rate variability and heart rate. *Hypertension* 64, 1334–1343. doi: 10.1161/HYPERTENSIONAHA.114.03782

Niccoli, G., Borovac, J. A., Vetrugno, V., Camici, P. G., and Crea, F. (2017). Ivabradine in acute coronary syndromes: protection beyond heart rate lowering. *Int. J. Cardiol.* 236, 107–112. doi: 10.1016/j.ijcard.2017.02.046

Nikmaram, M. R., Boyett, M. R., Kodama, I., Suzuki, R., and Honjo, H. (1997). Variation in effects of Cs^+, UL-FS-49, and ZD-7288 within sinoatrial node. *Am. J. Physiol.* 272, H2782–H2792. doi: 10.1152/ajpheart.1997.272.6.H2782

Ravagli, E., Bucchi, A., Bartolucci, C., Paina, M., Baruscotti, M., Difrancesco, D., et al. (2016). Cell-specific Dynamic Clamp analysis of the role of funny I_f current in cardiac pacemaking. *Prog. Biophys. Mol. Biol.* 120, 50–66. doi: 10.1016/j.pbiomolbio.2015.12.004

Rocchetti, M., Malfatto, G., Lombardi, F., and Zaza, A. (2000). Role of the input/output relation of sinoatrial myocytes in cholinergic modulation of heart rate variability. *J. Cardiovasc. Electrophysiol.* 11, 522–530. doi: 10.1111/j.1540-8167.2000.tb00005.x

Schweizer, P. A., Schroter, J., Greiner, S., Haas, J., Yampolsky, P., Mereles, D., et al. (2014). The symptom complex of familial sinus node dysfunction and myocardial noncompaction is associated with mutations in the HCN4 channel. *J. Am. Coll. Cardiol.* 64, 757–767. doi: 10.1016/j.jacc.2014.06.1155

Severi, S., Fantini, M., Charawi, L. A., and Difrancesco, D. (2012). An updated computational model of rabbit sinoatrial action potential to investigate the mechanisms of heart rate modulation. *J. Physiol.* 590, 4483–4499. doi: 10.1113/jphysiol.2012.229435

Takeda, K., Yamagishi, R., Masumiya, H., Tanaka, H., and Shigenobu, K. (2004). Effect of cilnidipine on L- and T-type calcium currents in guinea pig ventricle and action potential in rabbit sinoatrial node. *J. Pharmacol. Sci.* 95, 398–401. doi: 10.1254/jphs.SCJ04001X

Tardif, J. C., Ford, I., Tendera, M., Bourassa, M. G., Fox, K., and Investigators, I. (2005). Efficacy of ivabradine, a new selective I_f inhibitor, compared with atenolol in patients with chronic stable angina. *Eur. Heart J.* 26, 2529–2536. doi: 10.1093/eurheartj/ehi586

Thollon, C., Bedut, S., Villeneuve, N., Coge, F., Piffard, L., Guillaumin, J. P., et al. (2007). Use-dependent inhibition of hHCN4 by ivabradine and relationship with reduction in pacemaker activity. *Br. J. Pharmacol.* 150, 37–46. doi: 10.1038/sj.bjp.0706940

Thollon, C., Cambarrat, C., Vian, J., Prost, J. F., Peglion, J. L., and Vilaine, J. P. (1994). Electrophysiological effects of S 16257, a novel sino-atrial node modulator, on rabbit and guinea-pig cardiac preparations: comparison with UL-FS 49. *Br. J. Pharmacol.* 112, 37–42. doi: 10.1111/j.1476-5381.1994.tb13025.x

Tsutsui, K., Monfredi, O. J., Sirenko-Tagirova, S. G., Maltseva, L. A., Bychkov, R., Kim, M. S., et al. (2018). A coupled-clock system drives the automaticity of human sinoatrial nodal pacemaker cells. *Sci. Signal* 11:aap7608. doi: 10.1126/scisignal.aap7608

Van Ginneken, A. C., and Giles, W. (1991). Voltage clamp measurements of the hyperpolarization-activated inward current I(f) in single cells from rabbit sino-atrial node. *J. Physiol.* 434, 57–83. doi: 10.1113/jphysiol.1991.sp018459

Verkerk, A. O., Den Ruijter, H. M., Bourier, J., Boukens, B. J., Brouwer, I. A., Wilders, R., et al. (2009a). Dietary fish oil reduces pacemaker current and heart rate in rabbit. *Heart Rhythm.* 6, 1485–1492. doi: 10.1016/j.hrthm.2009.07.024

Verkerk, A. O., Van Borren, M. M., Peters, R. J., Broekhuis, E., Lam, K. Y., Coronel, R., et al. (2007a). Single cells isolated from human sinoatrial node: action potentials and numerical reconstruction of pacemaker current. *Conf. Proc. IEEE Eng. Med. Biol. Soc.* 2007, 904–907. doi: 10.1109/IEMBS.2007.4352437

Verkerk, A. O., Van Ginneken, A. C., and Wilders, R. (2009b). Pacemaker activity of the human sinoatrial node: role of the hyperpolarization-activated current, I_f. *Int. J. Cardiol.* 132, 318–336. doi: 10.1016/j.ijcard.2008.12.196

Verkerk, A. O., and Wilders, R. (2010). Relative importance of funny current in human versus rabbit sinoatrial node. *J. Mol. Cell Cardiol.* 48, 799–801. doi: 10.1016/j.yjmcc.2009.09.020

Verkerk, A. O., and Wilders, R. (2014). Pacemaker activity of the human sinoatrial node: effects of HCN4 mutations on the hyperpolarization-activated current. *Europace* 16, 384–395. doi: 10.1093/europace/eut348

Verkerk, A. O., and Wilders, R. (2015). Pacemaker activity of the human sinoatrial node: an update on the effects of mutations in HCN4 on the hyperpolarization-activated current. *Int. J. Mol. Sci.* 16, 3071–3094. doi: 10.3390/ijms16023071

Verkerk, A. O., Wilders, R., Van Borren, M. M. G. J., Peters, R. J. G., Broekhuis, E., Lam, K., et al. (2007b). Pacemaker current (I_f) in the human sinoatrial node. *Eur. Heart J.* 28, 2472–2478. doi: 10.1093/eurheartj/ehm339

Voigt, N., Abu-Taha, I., Heijman, J., and Dobrev, D. (2014). Constitutive activity of the acetylcholine-activated potassium current $I_{K,ACh}$ in cardiomyocytes. *Adv. Pharmacol.* 70, 393–409. doi: 10.1016/B978-0-12-417197-8.00013-4

Winter, J., and Shattock, M. J. (2016). Geometrical considerations in cardiac electrophysiology and arrhythmogenesis. *Europace* 18, 320–331. doi: 10.1093/europace/euv307

Yancy, C. W., Jessup, M., Bozkurt, B., Butler, J., Casey, D. E. Jr., Colvin, M. M., et al. (2016). 2016 ACC/AHA/HFSA focused update on new pharmacological therapy for heart failure: an update of the 2013 ACCF/AHA guideline for the management of heart failure: a report of the American College of Cardiology/American Heart Association Task Force on Clinical Practice Guidelines and the Heart Failure Society of America. *J. Am. Coll. Cardiol.* 68, 1476–1488. doi: 10.1016/j.jacc.2016.05.011

Yaniv, Y., Maltsev, V. A., Ziman, B. D., Spurgeon, H. A., and Lakatta, E. G. (2012). The "funny" current (I_f) inhibition by ivabradine at membrane potentials encompassing spontaneous depolarization in pacemaker cells. *Molecules* 17, 8241–8254. doi: 10.3390/molecules17078241

Yaniv, Y., Sirenko, S., Ziman, B. D., Spurgeon, H. A., Maltsev, V. A., and Lakatta, E. G. (2013). New evidence for coupled clock regulation of the normal automaticity of sinoatrial nodal pacemaker cells: bradycardic effects of ivabradine are linked to suppression of intracellular Ca^{2+} cycling. *J. Mol. Cell Cardiol.* 62, 80–89. doi: 10.1016/j.yjmcc.2013.04.026

Yuan, Y., Bai, X., Luo, C., Wang, K., and Zhang, H. (2015). The virtual heart as a platform for screening drug cardiotoxicity. *Br. J. Pharmacol.* 172, 5531–5547. doi: 10.1111/bph.12996

Zaza, A. (2016). Electrophysiology meets geometry. *Europace* 18:317. doi: 10.1093/europace/euv378

Zaza, A., and Lombardi, F. (2001). Autonomic indexes based on the analysis of heart rate variability: a view from the sinus node. *Cardiovasc. Res.* 50, 434–442. doi: 10.1016/S0008-6363(01)00240-1

Zaza, A., Robinson, R. B., and Difrancesco, D. (1996). Basal responses of the L-type Ca^{2+} and hyperpolarization-activated currents to autonomic agonists in the rabbit sino-atrial node. *J. Physiol.* 491, 347–355. doi: 10.1113/jphysiol.1996.sp021220

Conflict of Interest: The authors declare that the research was conducted in the absence of any commercial or financial relationships that could be construed as a potential conflict of interest.

frontiers
in Physiology

REVIEW
published: 16 July 2021
doi: 10.3389/fphys.2021.712666

Transcriptional and Epigenetic Landscape of Cardiac Pacemaker Cells: Insights Into Cellular Specialization in the Sinoatrial Node

Ravi Mandla, Catherine Jung and Vasanth Vedantham*

Division of Cardiology, Department of Medicine and Cardiovascular Research Institute, University of California, San Francisco, San Francisco, CA, United States

Cardiac pacemaker cells differentiate and functionally specialize early in embryonic development through activation of critical gene regulatory networks. In general, cellular specification and differentiation require that combinations of cell type-specific transcriptional regulators activate expression of key effector genes by binding to DNA regulatory elements including enhancers and promoters. However, because genomic DNA is tightly packaged by histones that must be covalently modified in order to render DNA regulatory elements and promoters accessible for transcription, the process of development and differentiation is intimately connected to the epigenetic regulation of chromatin accessibility. Although the difficulty of obtaining sufficient quantities of pure populations of pacemaker cells has limited progress in this field, the advent of low-input genomic technologies has the potential to catalyze a rapid growth of knowledge in this important area. The goal of this review is to outline the key transcriptional networks that control pacemaker cell development, with particular attention to our emerging understanding of how chromatin accessibility is modified and regulated during pacemaker cell differentiation. In addition, we will discuss the relevance of these findings to adult sinus node function, sinus node diseases, and origins of genetic variation in heart rhythm. Lastly, we will outline the current challenges facing this field and promising directions for future investigation.

Keywords: sinoatrial node, cardiac pacemaker cell, transcriptional regulation, enhancer, ATAC-seq and chromatin accessibility, heart rate, sinus node dysfunction

Edited by:
Alicia D'Souza,
University of Manchester,
United Kingdom

Reviewed by:
Bastiaan J. Boukens,
University of Amsterdam, Netherlands
Nikhil Munshi,
University of Texas Southwestern
Medical Center, United States

Correspondence:
Vasanth Vedantham
vasanth.vedantham@ucsf.edu

Specialty section:
This article was submitted to
Cardiac Electrophysiology,
a section of the journal
Frontiers in Physiology

Received: *20 May 2021*
Accepted: *23 June 2021*
Published: *16 July 2021*

Citation:
Mandla R, Jung C and Vedantham V (2021) Transcriptional and Epigenetic Landscape of Cardiac Pacemaker Cells: Insights Into Cellular Specialization in the Sinoatrial Node. Front. Physiol. 12:712666. doi: 10.3389/fphys.2021.712666

CARDIAC PACEMAKER CELLS ARE SPECIALIZED CARDIOMYOCYTES WITH A DISTINCT GENE EXPRESSION PROGRAM

Pacemaker cells comprise a small population of specialized cardiomyocytes within the sinoatrial node (SAN) that spontaneously fire to trigger each heartbeat. Although pacemaker cells are contractile and have sarcomeres, they possess striking phenotypic differences from atrial cardiomyocytes, including smaller cell size with elongated morphology, cellular protrusions, and

---

Abbreviations: ATAC-seq, assay for transposase accessible chromatin; SAN, sinoatrial node.

robust electrical automaticity with weak intercellular electrotonic coupling (**Figure 1**). In the context of the SAN, these cellular specializations allow pacemaker cells to perform their primary function – dynamic impulse generation at rates that ensure cardiac output meets metabolic need.

Over the past several decades, a prevailing model for the cellular basis of pacemaker cell function has emerged in which mutual entrainment of a membrane clock (driven by hyperpolarization-activated cation current) and a calcium clock (driven by spontaneous sub-sarcolemmal calcium release) confers robust automatic firing (Lakatta et al., 2010). In parallel, investigations at the tissue level have shown that the SAN has a distributed architecture that spans the region from the superior vena cava-right atrium junction to the inferior vena cava, bounded by the crista terminalis and the interatrial septum (Boyett et al., 2000). Nodal tissue consists of a fibrous matrix in which centrally located pacemaker cells are poorly electrotonically coupled with the atrial myocardium while pacemaker cells at the SAN periphery, where impulse transmission occurs, are more robustly coupled to the atrium (Joyner and van Capelle, 1986; De Maziere et al., 1992; Nikolaidou et al., 2012). This architecture allows for source-sink matching between the SAN and atrium without compromising automaticity.

Depending on neurohormonal state and electrolyte concentration, the nodal impulse can arise from different locations within the intercaval groove, generating an electrical wavefront that ultimately exits the SAN through species-specific pathways (Nikolaidou et al., 2012). Aligned with this conceptual framework, recent evidence has demonstrated the existence of discrete nodal structures within the SAN region that control heart rate under different conditions, with a superior SAN (located at the superior vena cava-RA junction) containing the dominant pacemaker at rapid heart rates and an inferior SAN (located near the inferior vena cava) operating at lower rates (Brennan et al., 2020). Finally, the atrioventricular node, which can function as a subsidiary pacemaker, also contains pacemaker-like cells that exhibit automaticity and hyperpolarization-activated cation current.

Remarkably, despite the anatomical and physiological complexity in heart rate regulation, both the cellular physiology of pacemaker cells and the tissue architecture in the SAN are broadly similar among diverse mammalian species despite dramatic variation in body mass and heart rate, suggesting that the determinants of cardiac automaticity constitute a robust and deeply evolutionarily conserved morphogenetic and cellular program (Bleeker et al., 1980; Opthof et al., 1985). In keeping with this notion, many of the specific molecular components required for pacemaker cell automaticity in the SAN have been identified and are present in pacemaker cells isolated from widely divergent vertebrate species (fish, mouse, and human), including hyperpolarization-activated, cyclic-nucleotide gated ion channels (Hcn4, Hcn1) and lower conductance gap junctions (connexin-45, connexin 30.2) (Blaschke et al., 2007; Tessadori et al., 2012). Conversely, high-conductance gap junctions such as connexin-43 and connexin-40, as well as channels associated with rapid conduction (NaV1.5) and hyperpolarized resting potential (Kir2.1), are present at much lower levels in pacemaker cells than in atrial cardiomyocytes (Mommersteeg et al., 2007b). More recently, genome wide expression profiles using RNA sequencing on mouse and human SAN have identified numerous common transcripts that are differentially expressed between SAN and non-SAN cardiomyocytes in both species, indicative of a shared transcriptional program that underlies the phenotypic similarities among mammalian pacemaker cells in different species (**Figure 1**; Vedantham et al., 2015; Goodyer et al., 2019; van Eif et al., 2019).

It is thus clear that (1) the problem of generating a robust mechanism for heart rate regulation was solved early in vertebrate evolution through the differentiation, proliferation, and architectural assembly of a specialized subtype of cardiomyocyte at the venous pole of the heart; and (2) pacemaker cells become functionally specialized by executing a conserved gene expression program with increased transcription of genes responsible for spontaneous firing and autonomic connectivity, and decreased transcription of genes associated with force generation and rapid conduction.

By connecting cellular specialization at the phenotypic level to cell type-specific gene expression programs, this unified model for the origin of vertebrate heart rhythm raises several important questions that will be the focus of the present article. First, what are the upstream regulators that allow pacemaker cells to specialize and differentiate during heart development? Second, how do these regulators turn on the SAN gene program and how is this program maintained? Third, what is the relevance of these regulatory pathways to human genetic variation and human disease? Historically, our ability to address these questions has been limited by the lack of genetic tools to mark and track pacemaker cells in model systems, as well as the difficulty of isolating sufficient quantities of purified pacemaker cells for molecular analysis. Therefore, in the present work, we will also touch on technological breakthroughs in the past decade that have allowed us to define gene expression and chromatin dynamics in pacemaker cells with unprecedented genomic resolution.

A DISTINCT SET OF TRANSCRIPTION FACTORS IS ENRICHED IN PACEMAKER CELLS AND IS REQUIRED TO ESTABLISH A SPECIALIZED GENE PROGRAM

In general, tissue-specific gene expression is accomplished through cell-type specific transcription factors (TFs) that bind combinatorially and often synergistically to *cis*-acting genomic DNA sequences known as enhancers that can be located far from their target genes (more on this below). These binding events, in turn, permit the formation of transcriptional complexes between TF-bound enhancers and basal promoters of target genes to activate expression. The specific complement of activated transcriptional regulators available to bind genomic DNA has been termed the "nuclear regulatory environment." The

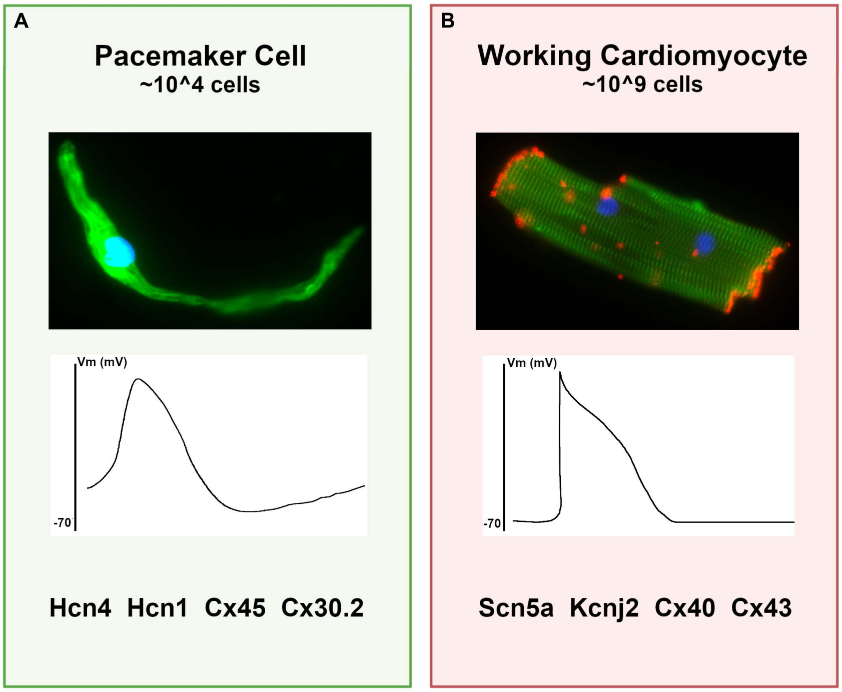

FIGURE 1 | Differences between pacemaker cells and working cardiomyocytes. **(A)** Characteristics of typical pacemaker cells: (top panel) micrograph of an isolated pacemaker cell taken from an adult *Hcn4-GFP* mouse demonstrates an elongated spindle-like morphology; (middle panel) a typical pacemaker cell action potential with elevated resting membrane potential and diastolic depolarization; (bottom panel), a list of key functional proteins enriched in pacemaker cells. **(B)** For comparison, typical ventricular cardiomyocyte characteristics are shown, including (top panel) a micrograph of an adult mouse ventricular cardiomyocyte stained for alpha-actinin (green) to demonstrate sarcomeres and connexin-43 (red) to demonstrate gap junctions; (middle panel) a typical working cardiomyocyte is quiescent with a negative resting potential, rapid upstroke, and plateau phase; (bottom panel) key functional genes expressed in working cardiomyocytes that are reduced in pacemaker cells.

nuclear regulatory environment in a given cell, in combination with the distribution of available enhancers, determines which genes are expressed.

Pacemaker cells express a set of transcriptional regulators that are absent in atrial cardiomyocytes: Tbx3, Tbx18, Shox2, and Isl1 (Hoogaars et al., 2004; Christoffels et al., 2006; Blaschke et al., 2007; Sun et al., 2007; Weinberger et al., 2012). These factors could therefore function as cell-intrinsic regulators that directly activate gene expression of pacemaker cell-specific genes and/or repress expression of the atrial gene program. Conversely, there are transcriptional regulators that are present in atrial cardiomyocytes that are excluded from pacemaker cells, including Nkx2.5 and Pitx2c, that may be important for activating atrial genes and repressing pacemaker cell genes (Christoffels et al., 2006; Mommersteeg et al., 2007b). Over the past 15 years, several rigorous *in vivo* global and conditional loss of function studies have been carried out in animal models with each of these factors, leading to a general model for transcriptional control summarized in this section.

Repression of the Atrial Gene Program in Pacemaker Cells

Several pacemaker cell-enriched transcription factors directly repress expression of atrial-enriched genes in the SAN. By blocking differentiation toward a working cardiomyocyte cell fate, this inhibition is hypothesized to permit differentiation along the path to pacemaker cells.

Tbx3, a T-box transcription factor whose expression within the SAN is conserved across several species, is the most well-characterized factor to play this role. Tbx3 binds to the regulatory elements that control expression of working myocardial genes such as *Nppa* and *Gja5*, possibly competing with Tbx5 (an activating T-box factor) to inhibit their expression and thereby inhibit chamber differentiation within the SAN (Hoogaars et al., 2004). Mice lacking Tbx3 demonstrate ectopic expression of atrial genes within the SAN with SAN hypoplasia, and exhibit embryonic lethality, whereas conditional deletion of Tbx3 within the adult SAN also results in ectopic atrial gene expression in the SAN and sinus arrhythmias (Hoogaars et al., 2007). Underscoring its primary role as a repressor, transgenic misexpression of *Tbx3* within atrial myocardium can repress the atrial gene program and even result in some ectopic arrhythmogenic foci, but it does not directly activate expression of pacemaker cell genes ectopically.

Analogous to Tbx3, Tbx18 also appears to function as a repressor of atrial genes such as Gja5 (Wiese et al., 2009; Kapoor et al., 2011). However, as the central sinus node fails to form in the Tbx18$^{-/-}$ mouse, additional specific targets of Tbx18 within the SAN have not been defined using loss of function models (Christoffels et al., 2006). In a large animal model, Tbx18 can reprogram ventricular myocardium to exhibit automaticity and transiently pace the heart, although the transcriptional mechanisms underlying this effect have not been determined (Kapoor et al., 2011, 2013).

The homeodomain transcription factor Shox2 also restricts atrial gene expression within pacemaker cells to promote SAN development. Complete loss of Shox2 causes embryonic lethality with hypoplasia of the sinus venosus, reduced embryonic heart rate, and ectopic expression of atrial genes in the SAN domain (Blaschke et al., 2007; Espinoza-Lewis et al., 2009). Recent findings have suggested a competitive mechanism whereby Shox2 directly represses Nkx2.5 expression in pacemaker cells and occupies sites normally bound by Nkx2.5 in atrial myocardium to repress atrial gene expression, thereby maintaining indirectly the expression of genes such as Hcn4, Tbx3, and Isl1 within the SAN (Ye et al., 2015). In myocardium at the interface between the SAN and the atrium, where Shox2 and Nkx2.5 are both expressed at higher levels, this competition may produce an intermediate cellular phenotype that facilitates electrophysiological source-sink matching between the SAN interior and the atrium (Li et al., 2019).

Repression of Pacemaker Cell Program in Atrial Cardiomyocytes

Within the working myocardium, the cardiac TF Nkx2.5 may act to repress expression of pacemaker cell genes. For example, conditional deletion of Nkx2.5 in ventricular myocardium results in upregulation of Hcn1, a gene normally restricted to pacemaker cells (Pashmforoush et al., 2004). Further supporting such a role, Nkx2.5 is among the few core cardiac TFs that is downregulated in pacemaker cells and their embryonic precursors in the sinus venosus (Christoffels et al., 2006). Transgenic misexpression of Nkx2.5 in pacemaker cells leads to repression of both Hcn4 and Tbx3, key components of the pacemaker cell-specific gene regulatory network (Espinoza-Lewis et al., 2011).

The homeodomain transcription factor Pitx2c is expressed throughout the left atrial and pulmonary vein myocardium, where it is largely responsible for encoding left sided identity within the atrium (Liu et al., 2002; Mommersteeg et al., 2007a). Accordingly, Pitx2c$^{-/-}$ mice can develop right atrial isomerism and form a secondary SAN in the left atrium that is normally repressed by the presence of Pitx2c (Mommersteeg et al., 2007b). Importantly, the Pitx2 locus harbors genomic variation that contributes to inherited susceptibility to atrial fibrillation, an arrhythmia that is triggered by focal firing from the region of the pulmonary venous myocardium and left-sided SAN remnant (Roselli et al., 2018; Zhang et al., 2019).

Activation of Specialized Gene Expression Programs in Pacemaker Cells and Atrial Myocardium

One of the major remaining unknowns in pacemaker cell transcriptional regulation is how pacemaker cell-specific gene expression is activated in the SAN. Data from avians and zebrafish have suggested that pacemaker cell progenitors arise from mesodermal cells located at the periphery of the embryonic heart fields in response to a Wnt signal (Bressan et al., 2013; Ren et al., 2019), and subsequently adopt their unique phenotype and transcriptional program as they become integrated with the atrial myocardium in a dynamic cellular process that occurs after heart looping (Bressan et al., 2018; Thomas et al., 2021).

Once committed, pacemaker cells express the broad cardiac transcription factors Gata4, Gata6, Mef2C, and Tbx5 at relatively high levels during development, similar to atrial cardiomyocytes (Vedantham et al., 2015; van Eif et al., 2019). These factors cooperatively activate the cardiac gene expression program, and their binding sites are overrepresented near both atrial cardiomyocyte and pacemaker cell genes (Galang et al., 2020; van Eif et al., 2020). Accordingly, depletion of any of these factors profoundly affects SAN development, heart rhythm, and heart development more broadly (Molkentin et al., 1997; Bruneau et al., 2001; Moskowitz et al., 2007; Kuratomi et al., 2009). Thus, although these factors are undoubtedly relevant to directing pacemaker cell-specific genes to the SAN, they do not fully account for the cell type-specificity of expression seen in pacemaker cells. One possibility is that within pacemaker cells, the repressive TFs Tbx3 and Shox2 bind to loci important for working myocardium and thereby cause Mef2C, Gata4, and Tbx5 to redistribute occupancy to pacemaker cell-specific loci where they activate transcription. This mechanism would not necessarily require any additional pacemaker cell-specific factors to explain pacemaker cell-specific gene expression.

More recently, the LIM homeodomain TF Isl1 has emerged as a potential activator of pacemaker cell-specific gene expression that could explain how pacemaker cells differentiate along a transcriptional path that is distinct from the atrial cardiomyocyte program. Although Isl1 is expressed broadly in cardiac progenitor cells of the second heart field, its expression becomes restricted to the SAN and its precursors by mid-development onward (Cai et al., 2003; Sun et al., 2007). Conditional deletion of Isl1 within the SAN results in dysregulated gene expression with major downregulation of pacemaker cell-specific genes and some upregulation of atrial genes (Liang et al., 2015). Moreover, these Isl1 SAN-conditional loss of function embryos exhibit sinus bradycardia and SAN hypoplasia, confirming a critical role for this factor in function and morphogenesis of the SAN. Analysis of promoter-adjacent regions of SAN genes downregulated after deletion of Isl1 demonstrated enrichment of Isl1 binding sites, a finding that raises the likelihood of an activating role for Isl1 in pacemaker cell-specific gene expression (Vedantham et al., 2015).

REGULATORY BASIS FOR CELLULAR SPECIALIZATION: ROLE OF GENOME ARCHITECTURE AND CHROMATIN ACCESSIBILITY

While the genetic models discussed in the previous section have provided insight into the factors that likely activate and repress cell-type specific gene expression patterns in pacemaker cells, the mechanisms that connect these factors to their target genes have not been elucidated. To a great extent, this knowledge gap has resulted from the inability to identify specific genomic loci (enhancers) where combinations of pacemaker cell and other TFs bind directly and regulate transcription of specific genes. In the absence of such direct binding information, the connection between TFs and their targets cannot be definitively established, and a common logic to combinatorial activation of pacemaker cell gene expression cannot be defined. Thus, identifying enhancers that exhibit pacemaker cell-specific activity would add another crucial piece to this complex puzzle. Before reviewing recent experiments that have tackled this problem, this section briefly outlines our current model for how enhancers and promoters interact with each other in the context of the nucleus, and the experimental methods that can be used to identify enhancers.

Organization of Genomic DNA in the Nucleus Facilitates Transcription

In mammalian cells, chromosomes each have distinct territories within the nucleus, and within each territory, transcriptionally inactive genomic loci are sequestered at the nuclear periphery, while actively transcribed regions are positioned in the interior of the nucleus (**Figure 2A**; van Steensel and Belmont, 2017). These transcriptionally active chromatin regions are organized into topologically associated domains (TADs), which can range in length from kilobases to megabases and can contain one or many genes along with non-coding regions that contain enhancers (**Figure 2B**; Dixon et al., 2016). TADs are formed when the multifunctional cohesin protein complex is recruited by chromatin-bound CCCTC-binding factor (CTCF). Cohesin then extrudes chromatin through the center of its ring-like structure to form a loop. Loop extrusion occurs until Cohesin encounters CTCF bound in the inverted orientation, thereby fixing the boundaries of the TAD along the genome and defining the regions for potential interaction. Importantly, during the process of loop extrusion, distant chromatin elements along the TAD are brought into close proximity, permitting contact of TF-bound enhancers with target promoters, and thereby initiating transcription (**Figure 2B**; Hanssen et al., 2017). Genomic regions such as enhancers and promoters within a TAD can interact whereas interactions across TAD boundaries rarely occur.

In order for DNA binding TFs to access enhancers, histone proteins undergo covalent modifications at specific sites that relax their otherwise tight association with genomic DNA, which then assumes an "open chromatin" conformation (**Figure 2C**; Boland et al., 2014). These histone modifications are regulated by specific classes of enzymes, and in some cases, by a group of TFs known as "pioneer factors" that can bind to their sites in nucleosomal DNA in a "closed configuration" and recruit factors that result in opening of chromatin and binding of larger transcriptional complexes (Larson et al., 2021). In this manner, enhancers can "read out" the nuclear regulatory environment to determine whether a specific gene should be transcribed. Thus, in order to understand how transcription factors regulate their target genes in differentiated cell types, comparing the chromatin landscape among closely related cell types can uncover the specific set of enhancers that activate tissue-specific gene expression.

Experimental Approaches to Epigenetic Profiling: Relevance to Pacemaker Cells

Because chromatin at transcriptionally active enhancers must be accessible to DNA binding factors, the Assay for Transposase Accessible Chromatin with Sequencing (ATAC-seq) offers a conceptually straightforward method to identify regulatory elements genome-wide. In this technique, a bacterial Tn5 transposase is used to insert oligonucleotide tags into regions of accessible chromatin (locations where histones are in the relaxed or open conformation). Sequencing these regions in a given cell type allows for high-resolution determination of regions of genome accessibility. ATAC-seq datasets can be compared among closely related cell types to identify loci of differential accessibility that might contain tissue-specific enhancers (**Figure 2D**; Buenrostro et al., 2013). ATAC-seq can be performed successfully on tens of thousands of cells and more recently, single cell ATAC-seq methodologies are available (Buenrostro et al., 2015), making this a practical tool for use with cardiac pacemaker cells directly isolated from SAN tissue.

Several factors complicate the interpretation of ATAC-seq data: First, differentially accessible genome regions are not always transcriptionally active enhancers; Second, a single enhancer can have more than one gene target; Third, because most TADs contain multiple genes, it is not always clear how to assign a putative enhancer to one or more specific gene targets within its TAD. One possible experimental approach to address these problem is to define contact frequencies among distant genomic loci through chromosome conformation capture and its variants (Sati and Cavalli, 2017). By covalently crosslinking genomic DNA and then sequencing crosslinked fragments, libraries can be generated in which sequences include fragments from an enhancer and the distant promoter it regulates since these will be in close spatial proximity during active transcription. With enough library complexity and sequencing depth, a genome-wide proximity map at tens of kilobase resolution can be readily generated to define mutually interacting regions within each TAD (**Figure 2E**). Variants of this approach, including promoter-capture Hi-C, can enrich libraries for promoter-containing fragments, thereby compiling a high-fidelity list of promoter - enhancer interactions in a given cell type (Mifsud et al., 2015; Schoenfelder et al., 2015; Montefiori et al., 2018).

Unfortunately, the limiting number of pacemaker cells (∼10,000 per heart) presents an insurmountable barrier for chromosome conformation capture, which ordinarily requires 10–20 million cells. In the future, scalable *in vitro* strategies to differentiate pacemaker cells from induced pluripotent stem cells may provide enough material, or, alternatively, lower input chromosome conformation techniques may be become available. Until then, connecting putative enhancers in pacemaker cells with target genes will require experimental validation using *in vivo* models.

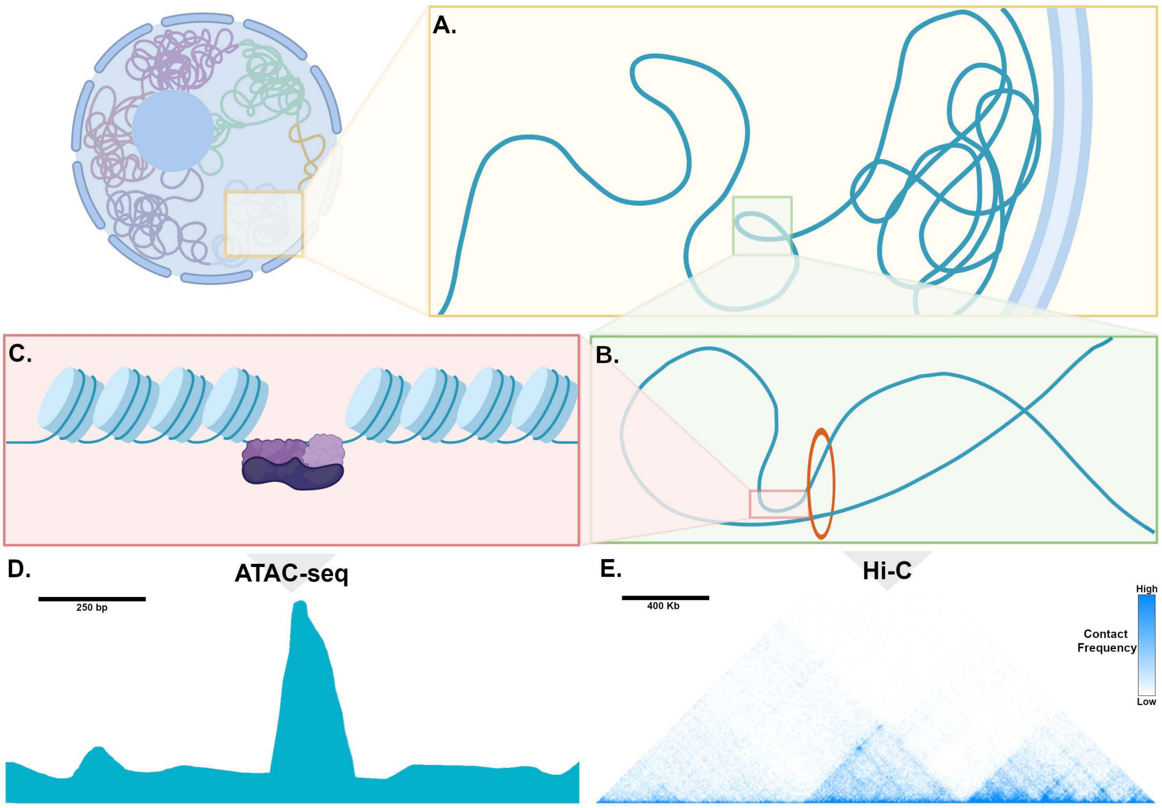

FIGURE 2 | Genome organization, chromatin, and mechanisms of transcription. **(A)** Within the nucleus, chromosomes occupy distinct territories and within a given territory, compacted, non-transcribed DNA is clustered into lamina-associated domains (LADs) adjacent to the nuclear periphery. DNA that is actively transcribed is located in the interior of the nucleus, where is it organized into topologically associated domains (TADs). **(B)** Enhancers and promoters are brought into proximity through loop extrusion by the ring-like Cohesion complex bound to *Ctcf* (red circle). **(C)** Chromatin is tightly wound around histone complexes. At sites of active enhancers, histone proteins are modified, allowing access of transcription factors (purple) to bind to DNA. **(D)** An example of processed ATAC-seq data aligned with the cartoon in **(C)**, expressed as a graph of read count versus genomic location, showing a "peak" or region of open chromatin, where histones are modified to make DNA accessible to a transposase. **(E)** An example of processed Hi-C data expressed as a heatmap, where the horizontal axis reflects genomic location. Pixel color represents the number of read counts, corresponding to the extent of contact frequency in *cis* between two regions of genomic DNA positioned along a chromosome. Topologically associated domains, visualized as discrete triangular shaped structures on the heatmap, are defined by regions that are permissive for long-range contacts.

CHROMATIN ACCESSIBILITY PROFILING OF PACEMAKER CELLS CONNECTS TRANSCRIPTION FACTORS TO THEIR TARGET GENES

Recently, several ATAC-seq data sets derived from pacemaker cells in mouse and human model systems have provided important new information about regulatory networks in pacemaker cells. Using the Hcn4-GFP transgenic mouse, both (Fernandez-Perez et al., 2019) and (Galang et al., 2020) used ATAC-seq to profile accessible chromatin regions in pacemaker cells (Fernandez-Perez et al., 2019; Galang et al., 2020). Fernandez Perez et al. compared these results to accessibility profiles of murine embryonic fibroblasts reprogrammed into induced pacemaker-like cells, while Galang et al. compared them to accessibility profiles from right atrial cardiomyocytes, a closely related cell type to pacemaker cells. In a parallel study, van Eif et al. (2020) used ATAC-seq to identify pacemaker-specific accessible chromatin regions in human cells. By implementing a recently described protocol for deriving pacemaker-like cells from induced pluripotent stem cells, van Eif et al. compared accessible chromatin regions between induced pacemaker-like cells (SANLPC) and induced ventricular-like cardiomyocytes (VLCM). As detailed below, these three datasets exhibited a remarkable congruence and have thereby provided novel insights into a deeply conserved *cis*-regulatory architecture in pacemaker cells (**Figure 3A**).

Motif Enrichment Analysis and *in vivo* Transgenic Assays Demonstrate a Deeply Conserved Regulatory Code in Pacemaker Cells

Because regions of accessible chromatin are bound by tissue-specific transcription factors, binding sites for lineage-determining TFs should be overrepresented in chromatin regions that are differentially accessible between closely related

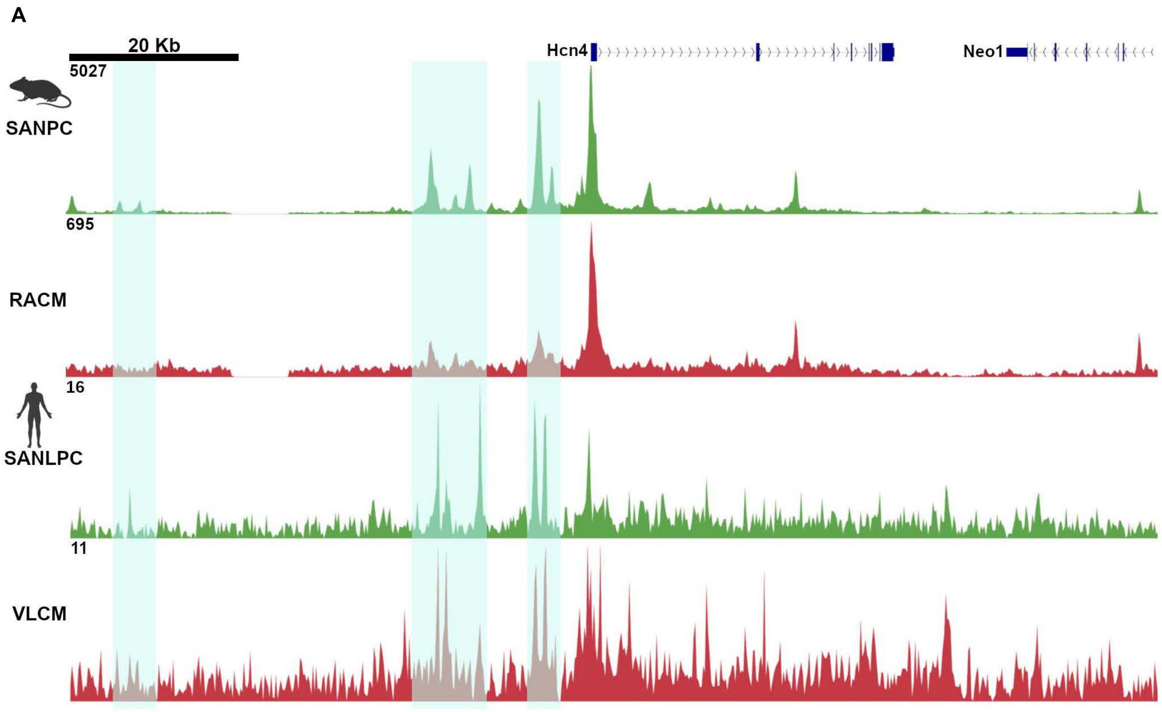

B

Type	Transcription Factor	Motif	Mouse P-value	Human P-value
Mef2	**Mef2c**,Mef2a, Mef2d,Mef2b		10^{-26}	10^{-42}
Gata	Gata3,Gata6, **Gata4**		10^{-14}	10^{-75}
TALE	Tgif2,**Meis1**, Tgif1		10^{-10}	10^{-93}
T-Box	**Tbx5**,Tbx20, Tbx3		10^{-4}	10^{-80}
Lim	Lhx3,**Isl1**,Lhx1		10^{-5}	10^{-65}

FIGURE 3 | Pacemaker cell-specific chromatin accessibility profiles are deeply conserved. **(A)** Alignment of ATAC-seq data at the *Hcn4* genomic locus from mouse neonatal pacemaker cells with human induced pacemaker-like cells demonstrate regions of open chromatin that are present in both species, highlighted in cyan. **(B)** Motif enrichment analysis of differentially accessible regions between SAN and non-SAN myocytes demonstrated that enrichment of similar transcription factor motifs are present in mouse and human pacemaker cells, suggesting a conserved mammalian pacemaker cell transcriptional program. SANLPC, sinoatrial node pacemaker cells; RACM, right atrial cardiomyocytes; SANLPC, sinoatrial node-like pacemaker cells; VLCM, ventricular-like cardiomyocytes.

cell types. Accordingly, both Galang et al. and van Eif et al. looked at DNA binding motifs enriched in differentially accessible regions as compared to background sequences using an unbiased search algorithm. The results revealed a striking convergence in the motifs in both sets of differentially accessible regions. Unsurprisingly, known cardiomyocyte transcription factor motifs including Gata and T-box motifs were overrepresented. More strikingly, differentially accessible regions from both data sets, drawn from very different types of samples (mouse primary pacemaker cells versus human iPSC-derived SANLPC), showed overrepresentation of Isl1 TF binding motifs, as well as binding motifs for Meis1, a TALE-class homeodomain factor not previously studied in the context of SAN gene expression (**Figure 3B**). Similar findings were observed in the data set from Fernandez-Perez et al. (2019). The finding of overrepresentation of Isl1 motifs among the differentially accessible peaks in pacemaker cells, in particular, provides strong evidence that Isl1 is a transcriptional activator in pacemaker cells and that, together with interacting partners, is likely to be a key player in activating the genes that endow pacemaker cells with their unique phenotypes.

To test whether differentially accessible ATAC-seq peaks were sufficient to function as regulatory elements *in vivo*, both Galang et al. and van Eif et al. cloned selected differentially accessible ATAC-seq peaks they identified and tested them using enhancer-reporter transgenesis in mice and in zebrafish. In Galang et al., 17 differentially accessible peaks were selected and tested using EnSERT, a locus-specific transgenesis assay, or using an *hsp68LacZ* reporter relying on random insertion. Of these, 4 ATAC-seq peaks directed reporter activity to the SAN primordium in mouse embryos; notably, these peaks were located within TADs that encompassed *Hcn4*, *Rgs6*, *Ptgfr*, and *Isl1*, all of which are differentially expressed in pacemaker cells. The enhancer at the *Isl1* locus, in particular, exhibited remarkable specificity for pacemaker cells in the developing and postnatal heart, suggesting that it functions within the pacemaker cell lineage from a very early developmental stage onward.

In a similar vein, van Eif et al. tested 8 human differentially accessible ATAC-seq peaks located within TADs encompassing SHOX2, ISL1, and TBX3, and identified several with expression in the heart and sinus venosus in zebrafish, of which 3 had activity in the sinus venosus region of mice (2 at the SHOX2 locus and one at the TBX3 locus). Notably, the human region syntenic to the Isl1 enhancer identified in mouse pacemaker cells by Galang et al. was also strongly differentially accessible in the human ATAC-seq data from van Eif et al. providing a convincing example of cross-species conservation of genomic regulatory architecture. Indeed, both studies found that enhancer function was conserved across species to a remarkable extent – human sequences were active in mouse and fish, and mouse sequences were active in fish – often with the expected tissue-specific expression pattern. The fact that the nuclear regulatory environment in zebrafish pacemaker cells can "read out" both human and mouse DNA to achieve tissue-specific expression indicates that the regulatory kernel involving Isl1, Shox2, and other pacemaker cell TFs is an ancient vertebrate regulatory module that has been conserved over hundreds of millions of years.

Enhancer Knockouts Demonstrate Required Roles for Enhancers in Gene Regulation, Development, and Function

To test the functional relevance of these enhancers, both Galang et al. and van Eif et al. deleted regulatory sequences from the

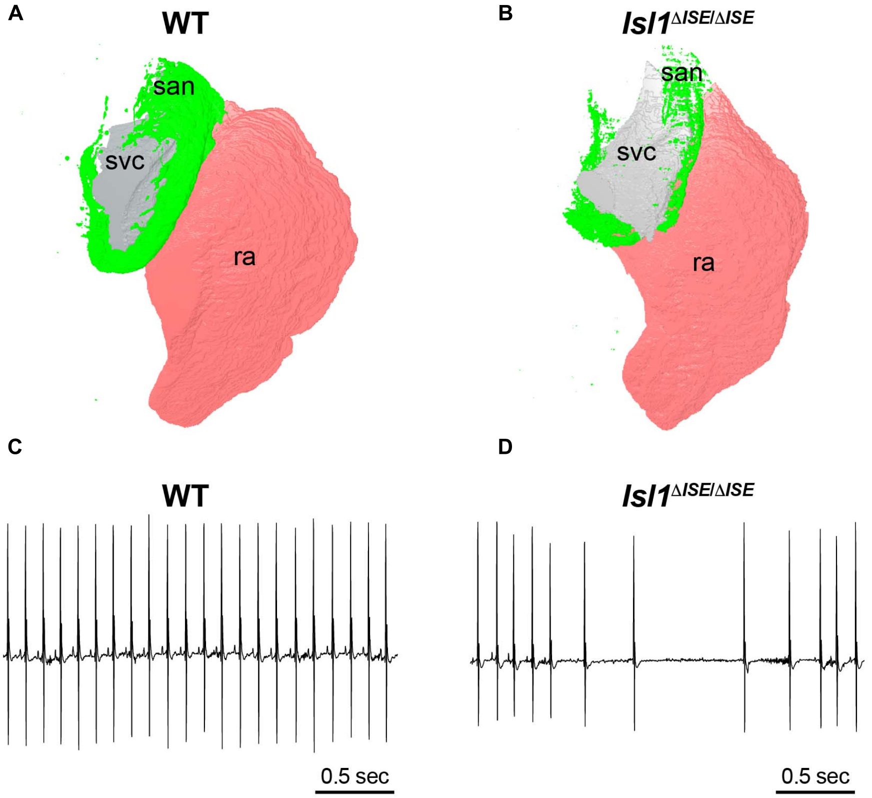

FIGURE 4 | Sinoatrial node hypoplasia and dysfunction after deletion of a key pacemaker cell-specific enhancer. **(A)** Three-dimensional reconstruction of light sheet fluorescence image of *Hcn4* + sinoatrial node (san, green), right atrium (pink, ra) and superior vena cava (gray, svc) from a WT control adult heart (left) in comparison to **(B)** a heart obtained from a littermate lacking both copies of an SAN-specific enhancer (ISE) for the transcription factor *Isl1*. Hearts were stained in whole mount with Hcn4 antibody and san, ra, and svc were manually segmented. Note the markedly reduced size of the Hcn4 + SAN in the *Isl1*$^{\Delta\ ISE/\Delta\ ISE}$ heart.
(C) Electrocardiograms recorded from a WT control adult mouse (left) and **(D)** an *Isl1*$^{\Delta\ ISE/\Delta\ ISE}$ littermate demonstrate an example of sinus arrhythmias in animals lacking the Isl1 enhancer.

genome of mice to test whether target gene expression and SAN development are affected. In Galang et al., a 2.7-Kb segment at the Isl1 locus (hereafter, *Isl1*-Locus SAN Enhancer, or *ISE*) was deleted using CRISPR-Cas9. Homozygous *Isl1*$^{\Delta ISE/\Delta ISE}$ mice were born in Mendelian ratios and were viable and fertile with no major cardiac structural abnormality by echocardiography. However, detailed molecular and histological studies showed that Isl1 protein and mRNA expression were reduced specifically in *Isl1*$^{\Delta ISE/\Delta ISE}$ pacemaker cells, with a corresponding hypoplasia of the SAN and reduced pacemaker cell number (**Figures 4A,B**). Furthermore, heart rhythm monitoring revealed a slower heart rate in the mutant mice, as well as episodes of sinus arrhythmia and bradycardia, indicative of abnormal SAN function (**Figures 4C,D**). Taken together, these findings support a model in which *ISE* supports *Isl1* transcription during SAN morphogenesis to ensure that the SAN achieves its normal size and cellularity, allowing for normal SAN function.

van Eif et al. deleted larger genomic regions within the SHOX2 and TBX3 TADs that contained differentially accessible ATAC-seq peaks. Examination of knockout embryos from a 250-kb deletion mouse line at the *Shox2* locus showed loss of Shox2 expression in the SAN, with dysregulation of Shox2 target genes, hypoplasia of the SAN, and embryonic lethality presumed due to bradycardia. In a parallel experiment, a 280-kb putative regulatory region containing differentially accessible ATAC peaks was also deleted from the Tbx3 locus. Homozygous mutant mice had absent Tbx3 expression in the SAN and exhibited perinatal lethality, while heterozygous mice survived to adulthood and exhibited prolonged SAN recovery times with programmed stimulation, indicating an important role for this enhancer in regulating SAN electrophysiology.

Building a Model for Transcriptional Regulation in Pacemaker Cells Based on Loss of Function Studies and Epigenetic Profiling

By combining data from conditional loss of function studies for critical TFs, available ChIP-seq datasets for these factors, and the insights gleaned from the recent epigenetic profiling studies, a working model for transcriptional regulation in pacemaker cells can be constructed (**Figure 5**). Based on loss of function studies, Shox2 and Isl1 act upstream of Tbx3, which downregulates the atrial gene program. Shox2 also represses Nkx2.5 and its target genes. As noted above, within SAN pacemaker cell-specific ATAC-seq peaks, Isl1 binding motifs are enriched, suggesting it acts primarily as an activator of the SAN gene program. Outside of the SAN, Nkx-2.5 and Pitx2c repress the differentiation of additional pacemaker cells, further localizing the primary pacemaker of the heart specifically to the SAN. Overlapping ChIP-seq data for Gata4, Mef2c, and Tbx5 with SAN-specific ATAC-seq peaks confirms the binding of these TFs to putative SAN enhancers as well as more broadly to cardiac enhancers (Galang et al., 2020). *In vivo* studies have also demonstrated Mef2's upstream role in regulating both SAN and non-SAN genes, similar to Tbx5 and Gata4 (Vedantham et al., 2013). Remaining questions include the identities of factors that may cooperate with Isl1 to regulate transcription in pacemaker cells. Since Isl1 is broadly expressed in other non-cardiac tissues, it is unlikely that Isl1 alone is sufficient to activate the pacemaker cell gene program. Candidate genes include Shox2 and Meis1, whose motifs are overrepresented near Isl1 sites in pacemaker cell-specific enhancers, as well as core cardiac TFs such as Tbx5, Gata4, Mef2, and others. In the coming years, as low-input ChIP-seq methodologies such as CUT&TAG are deployed more broadly, answers to these questions will be forthcoming.

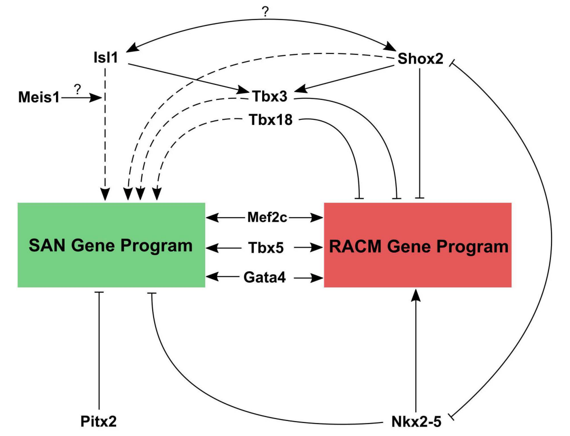

FIGURE 5 | Working model for transcriptional regulation in pacemaker cells. Transcriptional control of the SAN gene program and right atrial cardiomyocyte gene program are contrasted. Both tissues require the cardiac factors Mef2, Gata4, and Tbx5 to active cardiac gene expression. However, reciprocal repression of SAN genes by Nkx2.5 and atrial genes by Tbx3, Tbx18, and Shox2, along with activation of SAN genes by Isl1 (with possible interacting partners) allows for cell type specific gene expression patterns. Question marks indicate a hypothesized interaction that has not been tested yet. Solid lines represent direct promotion/inhibition and dashed lines represent either direct or indirect promotion/inhibition.

RELATIONSHIP OF GENE REGULATION IN PACEMAKER CELLS TO HUMAN VARIATION AND DISEASE

Ultimately, a major goal of dissecting regulatory networks in pacemaker cells is to gain a better understanding of the pathophysiology of sinus node dysfunction and, more generally, to provide insight into the genetic underpinnings of variation in human heart rhythm. A number of previous studies have related genetic variation in heart rhythm parameters to regions of non-coding DNA that were subsequently found to contain enhancer that regulate expression of nearby genes (Christophersen et al., 2017; Roselli et al., 2018). Indeed, genome wide association studies (GWAS) have identified numerous single nucleotide polymorphisms (SNPs) in non-coding DNA that confer susceptibility to atrial fibrillation. Most notably, the chromosome 4q25 genomic locus, which exhibits the highest association with atrial fibrillation, contains enhancers that control expression of the homeodomain transcriptional factor Pitx2, a key regulator of left atrial identity and pulmonary venous

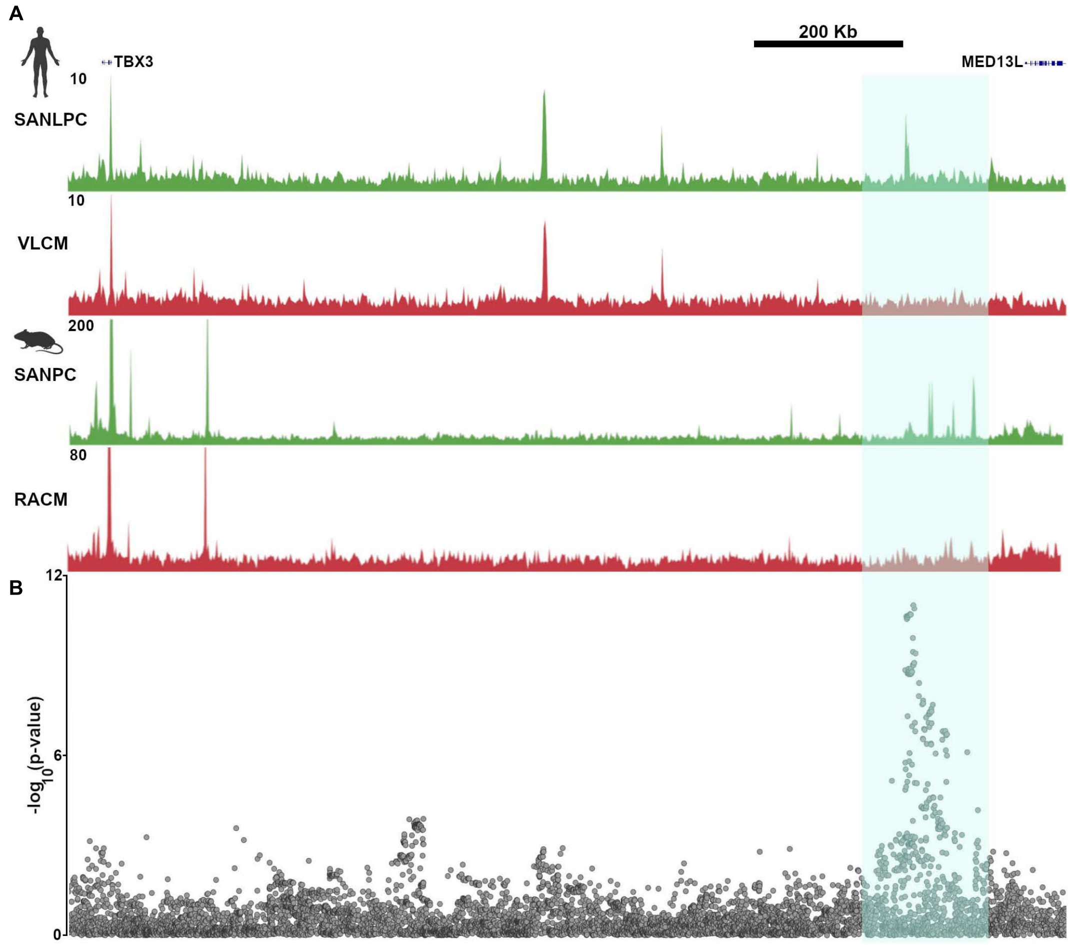

FIGURE 6 | Common genetic variants in pacemaker cell enhancers affect sinoatrial node function in human populations. **(A)** Aligned SAN ATAC-seq data from human iPSC-derived pacemaker-like cells (SANLPC) and ventricular like cells (VLCM) with syntenic genomic region from mouse sinoatrial node pacemaker cells (SANPC) and right atrial cardiomyocytes (RACM) demonstrate differentially accessible chromatin regions shared by both sets of pacemaker cells (highlighted in cyan). **(B)** shows alignment of a resting heart rate GWAS at the TBX3 locus, with highly significant associations seen in the region with differentially accessible ATAC-seq peaks, underscoring the relevance of SAN enhancers to human sinoatrial node function. GWAS results were downloaded from http://www.nealelab.is/uk-biobank/.

myocardium that also inhibits growth of the left-sided SAN node primordium (Roselli et al., 2018).

In keeping with these findings, GWAS that have been performed using resting heart rate or heart rate recovery after exercise have found numerous "hotspots" in non-coding regions of the genome that were presumed to have regulatory function (Kilpeläinen, 2016; Ramirez et al., 2018). One such region is closest to the gene MED13L, but also lies within a TAD that encompasses TBX3. SNPs in this region display strong associations with heart rate recovery after exercise. Not surprisingly, the GWAS hot spot overlaps all of the *TBX3* enhancers that were identified and validated in van Eif et al. (2020), providing a conclusive demonstration of the relevance of epigenetic profiling to human heart rhythm (**Figure 6**). In the absence of the ATAC-seq data derived from pacemaker cells and the subsequent confirmatory studies, the association of a gene desert near MED13L with heart rate recovery would remain merely speculative.

Galang et al. worked from the presumption that ATAC-seq peaks were more likely than other regions of the genome to harbor heart rate-associated SNPs, prompting them to perform a new association study on UK Biobank participants, limiting the analysis to SNPs occurring within 500 bp on either side of the human genomic regions syntenic to mouse pacemaker cell ATAC-seq peaks. The results of this analysis demonstrated many associations between heart rate and SNPs occurring near ATAC-seq peaks that are close to established genes that regulate heart rate. Furthermore, by focusing the association study on a subset of SNPs, and hence reducing the number of hypotheses tested, the uncorrected p value threshold needed to establish a significant association was reduced. Thus, by focusing only on differentially accessible peaks that are open in pacemaker cells, Galang et al. (2020) uncovered a significant association between heart rate and SNPs in the vicinity of the Isl1 SAN enhancer described above. Although the effect size was small, alongside the rest of the association study, this finding establishes that enhancers are important genomic loci for determination of sinus node function, and that epigenetic profiling techniques such as ATAC-seq have the potential to illuminate the genetic basis for variation in heart rhythm at the population level.

OUTSTANDING QUESTIONS AND FUTURE DIRECTIONS

The data summarized in this article have brought us closer than ever before to a detailed understanding of how pacemaker cells acquire their unique phenotypes during development, and to connecting the genetic determinants of pacemaker cell biology to vertebrate evolution and human physiology. Nevertheless, critical knowledge gaps remain.

First, while ATAC-seq data establish the genomic locations of the regulatory elements important for pacemaker cell-specific gene expression and indicate some of the transcription factors that are likely to bind to them, further work is needed to establish the precise timing and location of transcription factor binding events onto these enhancers. For example, which enhancers are specifically bound by Isl1 and what are its binding partners? What are the pioneer factors that open chromatin to allow for execution of the pacemaker cell gene expression program and what are the signaling pathways that activate these factors during sinus node development? Are these same pathways required for maintenance of pacemaker cell identify in the adult heart? How is epigenetic and transcriptional control related to age-related SAN dysfunction? Answers to these questions will fill in the missing pieces in our model for transcriptional control in pacemaker cells and will point the way toward translational strategies that could reverse SAN failure or even regenerate pacemaker cells.

A second area that will require further exploration is the connection between human genetic variation and SAN disease. As discussed, genome-wide and more limited association studies have demonstrated convincingly that a significant portion of human variation in SAN behavior is attributable to genetic differences at enhancer loci that regulate expression levels of critical SAN genes. A remaining challenge will be to take these analyses a step further by exploring whether variation in human non-coding regions is associated with the development of age-related or premature-onset sinus node dysfunction, atrial arrhythmias, and need for pacemaker implant. Defining the nature of these associations and the regulatory pathways involved could lead to new targets for interventions to prevent or treat SAN disease and other atrial arrhythmias.

Historically, research on these aspects of pacemaker cell and SAN biology has been challenging because of the difficulty of isolating pacemaker cells in large numbers, the lack of a suitable *in vitro* system to model pacemaker cells, and the limited access to human primary pacemaker cells. Fortunately, new tools and approaches are rapidly becoming available to surmount these technical hurdles. First, the development of human iPSC-based *in vitro* differentiation protocols, as highlighted in the study by van Eif et al., allows for the possibility of exploring the functions of *cis*-regulatory elements and transcriptional regulators in a more realistic human context without the limits imposed by low cell numbers. Thus, techniques such as ChIP-seq and Hi-C will eventually be used to create detailed, functionally annotated genomic maps of pacemaker cells. These datasets can then be integrated with data emerging from increasingly large cohorts of genotyped patients, including those with whole-genome sequencing alongside clinical data, to provide us with a detailed high-resolution model for how the epigenome and transcriptional biology connect with disease.

Alongside these technical innovations, the development of single cell genomic profiling technologies, including scRNA-seq and scATAC-seq, will circumvent the need to purify primary pacemaker cells for molecular analysis. Furthermore, data using these techniques can now be integrated across different platforms, allowing for more powerful *in silico* examination of cellular subtypes and cellular differentiation. Used in combination with new technologies that can isolate individual nuclei from differentiated tissues, these techniques will be invaluable as individual genes and pathways are explored in loss- and gain-of-function animal models and in small samples derived from human tissue. Taken together, the combination of recent technical and scientific advances leaves the field poised for rapid progress in the next several years.

CONCLUSION

Over the last several decades, an integrated model for the electrophysiological basis of pacemaker cell automaticity and SAN physiology has taken shape, but a detailed understanding of the underlying gene regulatory networks has remained elusive. Recent advances in developmental biology, chromatin biology, bioinformatics, and human genetics have now revealed that several key transcriptional regulators and genomic loci are critical for pacemaker cell development, SAN formation, and SAN function, and have clarified their relevance to human variation. Work in the coming years will translate these findings to an improved understanding of SAN disease, novel targets for therapeutics, and possibly SAN regeneration.

AUTHOR CONTRIBUTIONS

RM and VV wrote the manuscript and prepared the figures. CJ prepared the figures, performed the imaging and image processing, and edited the text for intellectual content. All authors contributed to the article and approved the submitted version.

FUNDING

VV was supported by a grant from the National Institutes of Health (DP2-HL152425).

ACKNOWLEDGMENTS

The figures were created with Biorender.com. 3D image reconstructions were created using the Nikon Imaging Center at UCSF.

REFERENCES

Blaschke, R. J., Hahurij, N. D., Kuijper, S., Just, S., Wisse, L. J., Deissler, K., et al. (2007). Targeted mutation reveals essential functions of the homeodomain transcription factor Shox2 in sinoatrial and pacemaking development. *Circulation* 115, 1830–1838. doi: 10.1161/circulationaha.106.637819

Bleeker, W. K., Mackaay, A. J., Masson-Pevet, M., Bouman, L. N., and Becker, A. E. (1980). Functional and morphological organization of the rabbit sinus node. *Circ. Res.* 46, 11–22. doi: 10.1161/01.res.46.1.11

Boland, M. J., Nazor, K. L., and Loring, J. F. (2014). Epigenetic regulation of pluripotency and differentiation. *Circ. Res.* 115, 311–324. doi: 10.1161/circresaha.115.301517

Boyett, M. R., Honjo, H., and Kodama, I. (2000). The sinoatrial node, a heterogeneous pacemaker structure. *Cardiovasc. Res.* 47, 658–687. doi: 10.1016/s0008-6363(00)00135-8

Brennan, J. A., Chen, Q., Gams, A., Dyavanapalli, J., Mendelowitz, D., Peng, W., et al. (2020). Evidence of superior and inferior sinoatrial nodes in the mammalian heart. *JACC Clin. Electrophysiol.* 6, 1827–1840. doi: 10.1016/j.jacep.2020.09.012

Bressan, M., Henley, T., Louie, J. D., Liu, G., Christodoulou, D., Bai, X., et al. (2018). Dynamic cellular integration drives functional assembly of the heart's pacemaker complex. *Cell Rep.* 23, 2283–2291. doi: 10.1016/j.celrep.2018.04.075

Bressan, M., Liu, G., and Mikawa, T. (2013). Early mesodermal cues assign avian cardiac pacemaker fate potential in a tertiary heart field. *Science* 340, 744–748. doi: 10.1126/science.1232877

Bruneau, B. G., Nemer, G., Schmitt, J. P., Charron, F., Robitaille, L., Caron, S., et al. (2001). A murine model of Holt-Oram syndrome defines roles of the T-box transcription factor Tbx5 in cardiogenesis and disease. *Cell* 106, 709–721. doi: 10.1016/s0092-8674(01)00493-7

Buenrostro, J. D., Giresi, P. G., Zaba, L. C., Chang, H. Y., and Greenleaf, W. J. (2013). Transposition of native chromatin for fast and sensitive epigenomic profiling of open chromatin, DNA-binding proteins and nucleosome position. *Nat. Methods* 10, 1213–1218. doi: 10.1038/nmeth.2688

Buenrostro, J. D., Wu, B., Litzenburger, U. M., Ruff, D., Gonzales, M. L., Snyder, M. P., et al. (2015). Single-cell chromatin accessibility reveals principles of regulatory variation. *Nature* 523, 486–490. doi: 10.1038/nature14590

Cai, C. L., Liang, X., Shi, Y., Chu, P. H., Pfaff, S. L., Chen, J., et al. (2003). Isl1 identifies a cardiac progenitor population that proliferates prior to differentiation and contributes a majority of cells to the heart. *Dev. Cell* 5, 877–889. doi: 10.1016/s1534-5807(03)00363-0

Christoffels, V. M., Mommersteeg, M. T. M., Trowe, M. O., Prall, O. W. J., De Gier-De Vries, C., Soufan, A. T., et al. (2006b). Formation of the venous pole of the heart from an Nkx2-5-negative precursor population requires Tbx18. *Circ. Res.* 98, 1555–1563. doi: 10.1161/01.res.0000227571.84189.65

Christophersen, I. E., Rienstra, M., Roselli, C., Yin, X., Geelhoed, B., Barnard, J., et al. (2017). Large-scale analyses of common and rare variants identify 12 new loci associated with atrial fibrillation. *Nat. Genet.* 49, 946–952.

De Maziere, A. M., van Ginneken, A. C., Wilders, R., Jongsma, H. J., and Bouman, L. N. (1992). Spatial and functional relationship between myocytes and fibroblasts in the rabbit sinoatrial node. *J. Mol. Cell Cardiol.* 24, 567–578. doi: 10.1016/0022-2828(92)91041-3

Dixon, J. R., Gorkin, D. U., and Ren, B. (2016). Chromatin domains: the unit of chromosome organization. *Mol. Cell* 62, 668–680. doi: 10.1016/j.molcel.2016.05.018

Espinoza-Lewis, R. A., Liu, H., Sun, C., Chen, C., Jiao, K., and Chen, Y. (2011). Ectopic expression of Nkx2.5 suppresses the formation of the sinoatrial node in mice. *Dev. Biol* 356, 359–369. doi: 10.1016/j.ydbio.2011.05.663

Espinoza-Lewis, R. A., Yu, L., He, F., Liu, H., Tang, R., Shi, J., et al. (2009). Shox2 is essential for the differentiation of cardiac pacemaker cells by repressing Nkx2-5. *Dev. Biol.* 327, 376–385. doi: 10.1016/j.ydbio.2008.12.028

Fernandez-Perez, A., Sathe, A. A., Bhakta, M., Leggett, K., Xing, C., and Munshi, N. V. (2019). Hand2 selectively reorganizes chromatin accessibility to induce pacemaker-like transcriptional reprogramming. *Cell Rep.* 27, 2354–2369e7.

Galang, G., Mandla, R., Ruan, H., Jung, C., Sinha, T., Stone, N. R., et al. (2020). ATAC-seq Reveals an Isl1 enhancer that regulates sinoatrial node development and function. *Circ. Res.* 127, 1502–1518. doi: 10.1161/circresaha.120.317145

Goodyer, W. R., Beyersdorf, B. M., Paik, D. T., Tian, L., Li, G., Buikema, J. W., et al. (2019). Transcriptomic profiling of the developing cardiac conduction system at single-cell resolution. *Circ. Res.* 125, 379–397. doi: 10.1161/circresaha.118.314578

Hanssen, L. L. P., Kassouf, M. T., Oudelaar, A. M., Biggs, D., Preece, C., Downes, D. J., et al. (2017). Tissue-specific CTCF-cohesin-mediated chromatin architecture delimits enhancer interactions and function in vivo. *Nat. Cell Biol.* 19, 952–961. doi: 10.1038/ncb3573

Hoogaars, W. M., Engel, A., Brons, J. F., Verkerk, A. O., de Lange, F. J., Wong, L. Y., et al. (2007). Tbx3 controls the sinoatrial node gene program and imposes pacemaker function on the atria. *Genes Dev.* 21, 1098–1112. doi: 10.1101/gad.416007

Hoogaars, W. M., Tessari, A., Moorman, A. F., de Boer, P. A., Hagoort, J., Soufan, A. T., et al. (2004). The transcriptional repressor Tbx3 delineates the developing central conduction system of the heart. *Cardiovasc. Res.* 62, 489–499. doi: 10.1016/j.cardiores.2004.01.030

Joyner, R. W., and van Capelle, F. J. (1986). Propagation through electrically coupled cells. How a small SA node drives a large atrium. *Biophys. J.* 50, 1157–1164. doi: 10.1016/s0006-3495(86)83559-7

Kapoor, N., Galang, G., Marban, E., and Cho, H. C. (2011). Transcriptional suppression of connexin43 by TBX18 undermines cell-cell electrical coupling in postnatal cardiomyocytes. *J. Biol. Chem.* 286, 14073–14079. doi: 10.1074/jbc.m110.185298

Kapoor, N., Liang, W., Marban, E., and Cho, H. C. (2013). Direct conversion of quiescent cardiomyocytes to pacemaker cells by expression of Tbx18. *Nat. Biotechnol.* 31, 54–62. doi: 10.1038/nbt.2465

Kilpeläinen, T. O. (2016). Genome-wide association studies and resting heart rate. *J. Electrocardiol.* 49, 860–863. doi: 10.1016/j.jelectrocard.2016.07.022

Kuratomi, S., Ohmori, Y., Ito, M., Shimazaki, K., Muramatsu, S., Mizukami, H., et al. (2009). The cardiac pacemaker-specific channel Hcn4 is a direct transcriptional target of MEF2. *Cardiovasc. Res.* 83, 682–687. doi: 10.1093/cvr/cvp171

Lakatta, E. G., Maltsev, V. A., and Vinogradova, T. M. (2010). A coupled SYSTEM of intracellular Ca2+ clocks and surface membrane voltage clocks controls the timekeeping mechanism of the heart's pacemaker. *Circ. Res.* 106, 659–673. doi: 10.1161/circresaha.109.206078

Larson, E. D., Marsh, A. J., and Harrison, M. M. (2021). Pioneering the developmental frontier. *Mol. Cell* 81, 1640–1650. doi: 10.1016/j.molcel.2021.02.020

Li, H., Li, D., Wang, Y., Huang, Z., Xu, J., Yang, T., et al. (2019). Nkx2-5 defines a subpopulation of pacemaker cells and is essential for the physiological function of the sinoatrial node in mice. *Dev.* 146:dev178145.

Liang, X., Zhang, Q., Cattaneo, P., Zhuang, S., Gong, X., Spann, N. J., et al. (2015). Transcription factor ISL1 is essential for pacemaker development and function. *J. Clin. Invest.* 125, 3256–3268. doi: 10.1172/jci68257

Liu, C., Liu, W., Palie, J., Lu, M. F., Brown, N. A., and Martin, J. F. (2002). Pitx2c patterns anterior myocardium and aortic arch vessels and is required for local cell movement into atrioventricular cushions. *Development* 129, 5081–5091. doi: 10.1242/dev.129.21.5081

Mifsud, B., Tavares-Cadete, F., Young, A. N., Sugar, R., Schoenfelder, S., Ferreira, L., et al. (2015). Mapping long-range promoter contacts in human cells with high-resolution capture Hi-C. *Nat. Genet.* 47, 598–606. doi: 10.1038/ng.3286

Molkentin, J. D., Lin, Q., Duncan, S. A., and Olson, E. N. (1997). Requirement of the transcription factor GATA4 for heart tube formation and ventral morphogenesis. *Genes Dev.* 11, 1061–1072. doi: 10.1101/gad.11.8.1061

Mommersteeg, M. T., Hoogaars, W. M., Prall, O. W., de Gier-de Vries, C., Wiese, C., Clout, D. E., et al. (2007b). Molecular pathway for the localized formation of the sinoatrial node. *Circ. Res.* 100, 354–362. doi: 10.1161/01.res.0000258019.74591.b3

Mommersteeg, M. T. M., Brown, N. A., Prall, O. W. J., De Gier-De Vries, C., Harvey, R. P., Moorman, A. F. M., et al. (2007a). Pitx2c and Nkx2-5 are required for the formation and identity of the pulmonary myocardium. *Circ. Res.* 101, 902–909. doi: 10.1161/circresaha.107.161182

Montefiori, L. E., Sobreira, D. R., Sakabe, N. J., Aneas, I., Joslin, A. C., Hansen, G. T., et al. (2018). A promoter interaction map for cardiovascular disease genetics. *eLife* 7:e35788.

Moskowitz, I. P., Kim, J. B., Moore, M. L., Wolf, C. M., Peterson, M. A., Shendure, J., et al. (2007). A molecular pathway including Id2, Tbx5, and Nkx2-5 required for cardiac conduction system development. *Cell* 129, 1365–1376. doi: 10.1016/j.cell.2007.04.036

Nikolaidou, T., Aslanidi, O. V., Zhang, H. I, and Efimov, R. (2012). Structure-function relationship in the sinus and atrioventricular nodes. *Pediatr. Cardiol.* 33, 890–899. doi: 10.1007/s00246-012-0249-0

Opthof, T., de Jonge, B., Mackaay, A. J., Bleeker, W. K., Masson-Pevet, M., Jongsma, H. J., et al. (1985). Functional and morphological organization of the guinea-pig sinoatrial node compared with the rabbit sinoatrial node. *J. Mol. Cell Cardiol.* 17, 549–564. doi: 10.1016/s0022-2828(85)80024-9

Pashmforoush, M., Lu, J. T., Chen, H., Amand, T. S., Kondo, R., Pradervand, S., et al. (2004). Nkx2-5 pathways and congenital heart disease; loss of ventricular myocyte lineage specification leads to progressive cardiomyopathy and complete heart block. *Cell* 117, 373–386.

Ramirez, J., Duijvenboden, S. V., Ntalla, I., Mifsud, B., Warren, H. R., Tzanis, E., et al. (2018). Thirty loci identified for heart rate response to exercise and recovery implicate autonomic nervous system. *Nat. Commun.* 9:1947.

Ren, J., Han, P., Ma, X., Farah, E. N., Bloomekatz, J., Zeng, X. I., et al. (2019). Canonical Wnt5b signaling directs outlying Nkx2.5+ mesoderm into pacemaker cardiomyocytes. *Dev. Cell* 50, 729–743.e5.

Roselli, C., Chaffin, M. D., Weng, L. C., Aeschbacher, S., Ahlberg, G., Albert, C. M., et al. (2018). Multi-ethnic genome-wide association study for atrial fibrillation. *Nat. Genet.* 50, 1225–1233.

Sati, S., and Cavalli, G. (2017). Chromosome conformation capture technologies and their impact in understanding genome function. *Chromosoma* 126, 33–44. doi: 10.1007/s00412-016-0593-6

Schoenfelder, S., Furlan-Magaril, M., Mifsud, B., Tavares-Cadete, F., Sugar, R., Javierre, B. M., et al. (2015). The pluripotent regulatory circuitry connecting promoters to their long-range interacting elements. *Genome Res.* 25, 582–597. doi: 10.1101/gr.185272.114

Sun, Y., Liang, X., Najafi, N., Cass, M., Lin, L., Cai, C. L., et al. (2007). Islet 1 is expressed in distinct cardiovascular lineages, including pacemaker and coronary vascular cells. *Dev. Biol.* 304, 286–296. doi: 10.1016/j.ydbio.2006.12.048

Tessadori, F., van Weerd, J. H., Burkhard, S. B., Verkerk, A. O., de Pater, E., Boukens, B. J., et al. (2012). Identification and functional characterization of cardiac pacemaker cells in zebrafish. *PLoS One* 7:e47644. doi: 10.1371/journal.pone.0047644

Thomas, K., Henley, T., Rossi, S., Costello, M. J., Polacheck, W., Griffith, B. E., et al. (2021). Adherens junction engagement regulates functional patterning of the cardiac pacemaker cell lineage. *Dev. Cell* 56, 1498–1511e7. *1498-1511 e7

van Eif, V. W., Protze, S., Bosada, F. M., Yuan, X., Sinha, T., van Duijvenboden, K., et al. (2020). Genome-wide analysis identifies an essential human TBX3 pacemaker enhancer. *Circ. Res.* 127, 1522–1535. doi: 10.1161/circresaha.120.317054

van Eif, V. W. W., Stefanovic, S., van Duijvenboden, K., Bakker, M., Wakker, V., de Gier-de Vries, C., et al. (2019). Transcriptome analysis of mouse and human sinoatrial node cells reveals a conserved genetic program. *Development* 146:dev173161.

van Steensel, B., and Belmont, A. S. (2017). Lamina-associated domains: links with chromosome architecture, heterochromatin, and gene repression. *Cell* 169, 780–791. doi: 10.1016/j.cell.2017.04.022

Vedantham, V., Evangelista, M., Huang, Y., and Srivastava, D. (2013). Spatiotemporal regulation of an Hcn4 enhancer defines a role for Mef2c and HDACs in cardiac electrical patterning. *Dev. Biol.* 373, 149–162. doi: 10.1016/j.ydbio.2012.10.017

Vedantham, V., Galang, G., Evangelista, M., Deo, R. C., and Srivastava, D. (2015). RNA sequencing of mouse sinoatrial node reveals an upstream regulatory role for Islet-1 in cardiac pacemaker cells. *Circ. Res.* 116, 797–803. doi: 10.1161/circresaha.116.305913

Weinberger, F., Mehrkens, D., Friedrich, F. W., Stubbendorff, M., Hua, X., Muller, J. C., et al. (2012). Localization of Islet-1-positive cells in the healthy and infarcted adult murine heart. *Circ. Res.* 110, 1303–1310. doi: 10.1161/circresaha.111.259630

Wiese, C., Grieskamp, T., Airik, R., Mommersteeg, M. T., Gardiwal, A., de Gier-de Vries, C., et al. (2009). Formation of the sinus node head and differentiation of sinus node myocardium are independently regulated by Tbx18 and Tbx3. *Circ. Res.* 104, 388–397. doi: 10.1161/circresaha.108.187062

Ye, W., Wang, J., Song, Y., Yu, D., Sun, C., Liu, C., et al. (2015). A common Shox2-Nkx2-5 antagonistic mechanism primes the pacemaker cell fate in the pulmonary vein myocardium and sinoatrial node. *Development* 142, 2521–2532.

Zhang, M., Hill, M. C., Kadow, Z. A., Suh, J. H., Tucker, N. R., Hall, A. W., et al. (2019). Long-range Pitx2c enhancer-promoter interactions prevent predisposition to atrial fibrillation. *Proc. Natl. Acad. Sci. U.S.A.* 116, 22692–22698. doi: 10.1073/pnas.1907418116

Conflict of Interest: VV received research support from Amgen and a consulting fee from Merck for an unrelated project.

The remaining authors declare that the research was conducted in the absence of any commercial or financial relationships that could be construed as a potential conflict of interest.

frontiers
in Physiology

ORIGINAL RESEARCH
published: 06 January 2021
doi: 10.3389/fphys.2020.588679

Toward Biological Pacing by Cellular Delivery of Hcn2/SkM1

Anna M. D. Végh[1,2†], Arie O. Verkerk[2,3†], Lucía Cócera Ortega[3†], Jianan Wang[2], Dirk Geerts[2], Mischa Klerk[2], Kirsten Lodder[1], Ruby Nobel[1], Anke J. Tijsen[3], Harsha D. Devalla[2], Vincent M. Christoffels[2], Max Medina-Ramírez[2], Anke M. Smits[1], Hanno L. Tan[3,4], Ronald Wilders[2], Marie José T. H. Goumans[1†] and Gerard J. J. Boink[2,5*†]

[1] Department of Cell and Chemical Biology, Leiden University Medical Center, Leiden, Netherlands, [2] Department of Medical Biology, Amsterdam Cardiovascular Sciences, Amsterdam UMC, University of Amsterdam, Amsterdam, Netherlands, [3] Department of Experimental Cardiology, Amsterdam Cardiovascular Sciences, Amsterdam UMC, University of Amsterdam, Amsterdam, Netherlands, [4] Netherlands Heart Institute, Utrecht, Netherlands, [5] Department of Clinical Cardiology, Heart Center, Amsterdam Cardiovascular Sciences, Amsterdam UMC, University of Amsterdam, Amsterdam, Netherlands

Edited by:
*Victor A. Maltsev,
National Institute on Aging, National Institutes of Health (NIH), United States*

Reviewed by:
*Flavien Charpentier,
INSERM U1087 L'Unité de Recherche de l'Institut du Thorax, France
Mark Richard Boyett,
University of Copenhagen, Denmark*

***Correspondence:**
*Gerard J. J. Boink
g.j.boink@amsterdamumc.nl*

† These authors have contributed equally to this work

Specialty section:
This article was submitted to Cardiac Electrophysiology, a section of the journal Frontiers in Physiology

Received: *29 July 2020*
Accepted: *08 December 2020*
Published: *06 January 2021*

Citation:
Végh AMD, Verkerk AO, Cócera Ortega L, Wang J, Geerts D, Klerk M, Lodder K, Nobel R, Tijsen AJ, Devalla HD, Christoffels VM, Medina-Ramírez M, Smits AM, Tan HL, Wilders R, Goumans MJTH and Boink GJJ (2021) Toward Biological Pacing by Cellular Delivery of Hcn2/SkM1. Front. Physiol. 11:588679. doi: 10.3389/fphys.2020.588679

Electronic pacemakers still face major shortcomings that are largely intrinsic to their hardware-based design. Radical improvements can potentially be generated by gene or cell therapy-based biological pacemakers. Our previous work identified adenoviral gene transfer of Hcn2 and SkM1, encoding a "funny current" and skeletal fast sodium current, respectively, as a potent combination to induce short-term biological pacing in dogs with atrioventricular block. To achieve long-term biological pacemaker activity, alternative delivery platforms need to be explored and optimized. The aim of the present study was therefore to investigate the functional delivery of Hcn2/SkM1 via human cardiomyocyte progenitor cells (CPCs). Nucleofection of Hcn2 and SkM1 in CPCs was optimized and gene transfer was determined for Hcn2 and SkM1 *in vitro*. The modified CPCs were analyzed using patch-clamp for validation and characterization of functional transgene expression. In addition, biophysical properties of Hcn2 and SkM1 were further investigated in lentivirally transduced CPCs by patch-clamp analysis. To compare both modification methods *in vivo*, CPCs were nucleofected or lentivirally transduced with GFP and injected in the left ventricle of male NOD-SCID mice. After 1 week, hearts were collected and analyzed for GFP expression and cell engraftment. Subsequent functional studies were carried out by computational modeling. Both nucleofection and lentiviral transduction of CPCs resulted in functional gene transfer of Hcn2 and SkM1 channels. However, lentiviral transduction was more efficient than nucleofection-mediated gene transfer and the virally transduced cells survived better *in vivo*. These data support future use of lentiviral transduction over nucleofection, concerning CPC-based cardiac gene delivery. Detailed patch-clamp studies revealed Hcn2 and Skm1 current kinetics within the range of previously reported values of other cell systems. Finally, computational modeling indicated that CPC-mediated delivery of Hcn2/SkM1 can generate stable pacemaker function in human ventricular myocytes. These modeling studies further illustrated that SkM1 plays an essential role in the final stage of diastolic depolarization, thereby enhancing biological pacemaker functioning delivered by Hcn2. Altogether these studies support further development of CPC-mediated delivery of Hcn2/SkM1 and functional testing in bradycardia models.

Keywords: biological pacemaker, gene therapy, cell therapy, progenitor cells, HCN channels, SkM1 channels

INTRODUCTION

At present, electronic pacemaker therapy is the standard of care for patients with heart block and/or sinus node dysfunction. Despite the life-saving success of this therapy and more than 60 years of research and development, electronic pacemakers still have major shortcomings, such as inadequate sensitivity to autonomic modulation, suboptimal cardiac output, and a limited battery life time that requires surgical replacement every 8–10 years. Moreover, electronic pacemakers are prone to other hardware-related issues such as lead dislodgement or fracture, magnetic interference, and potentially lethal device-related infections (Rosen et al., 2004; van Rees et al., 2011; Kotsakou et al., 2015).

With the development of biological pacemakers, the ultimate goal is to overcome these hardware-related issues and provide a more physiologic mode of pacing that generates optimal cardiac output and is directly sensitive to autonomic modulation. Short-term proof-of-concept studies have demonstrated that this is feasible either via direct gene transfer or via transplantation of stem cells. With the latter approach, cells are either coaxed into a lineage of pacemaker cells, or are merely used as a vehicle for delivery of ion channel function, following *ex vivo* gene transfer. The approach of *ex vivo* gene transfer to stem cells and subsequent transplantation has extensively been studied with human mesenchymal stem cells (hMSCs) (Potapova et al., 2004; Plotnikov et al., 2007; Jun et al., 2012; Lu et al., 2013). These studies evaluated pacing properties of Hcn2 overexpressing hMSCs that were transplanted into the hearts of dogs with complete heart block and showed a degree of function that was largely similar to adenoviral gene transfer. Yet unfortunately, function deteriorated after 6–8 weeks post-transplantation and was thus not sustained much beyond the expression window of adenoviral gene transfer (i.e., 2–4 weeks) (Kass-Eisler et al., 1993; Tripathy et al., 1996). To explore potential alternative cell sources that can provide function over a much longer follow-up period we have previously explored the use of human cardiomyocyte progenitor cells (CPCs). These CPCs have previously been shown to reside in the mouse heart for at least 12 weeks after transplantation and are able to functionally couple to mouse cardiomyocytes, without manifesting unwanted proliferation or differentiation beyond the cardiac lineage (Smits et al., 2009a; Végh et al., 2019). In contrast to MSCs, transplanted CPCs appear not to migrate away from the injection site, enhancing their potential as biological pacemakers by generating pacemaker activity from a more localized position (Gyöngyösi et al., 2008; Smits et al., 2009a; Bruzauskaite et al., 2016). Moreover, *in vitro* studies have demonstrated that CPCs can function as an effective vehicle for HCN-based biological pacing (Végh et al., 2019).

Over the past decade, several alternative gene transfer strategies have been explored to optimize HCN-based biological pacing. Overexpression of alternative HCN isoforms (i.e., HCN1, HCN2, and HCN4) and HCN2-based variants have been explored, but these resulted in only minor improvement (e.g., mHcn2-E324A) or, in marked contrast, lead to excessive outcomes with recurrent ventricular tachycardia in case of the Hcn2/Hcn1 chimera Hcn212 (Bucchi et al., 2006; Plotnikov et al., 2008; Shlapakova et al., 2010; Boink et al., 2012b, 2013). On the other hand, substantial improvements in baseline and maximal beating rates have been obtained by combined overexpression of Hcn2 and the skeletal muscle sodium channel SkM1. This previous study showed that combined overexpression of Hcn2 with SkM1 improved pacemaker function compared to Hcn2 alone, by hyperpolarization of the action potential threshold (Boink et al., 2013). In an effort to engineer a long-term biological pacemaker, the present study therefore investigated cellular delivery of Hcn2/SkM1 and further explored the mechanism of action of this transgene combination.

MATERIALS AND METHODS

Cell Culture

Human fetal hearts were obtained after elective abortion under informed consent, with approval of the Medical Ethics Committee of the Leiden University Medical Center (number P08.087). The research was performed in accordance with the principles of the Declaration of Helsinki. Human CPCs were isolated from these hearts using magnetic activated cell sorting (MACS) as previously described (Smits et al., 2009b). In short, second trimester hearts were collected, and a single cell suspension was obtained by cutting the heart in small pieces and digesting the pieces with 500 ng/mL collagenase-A (Roche, 10103578001). Single cells were incubated with anti-Sca-1-FITC antibody [Miltenyi Biotec, Anti-Sca-1 MicroBead Kit (FITC), 130-092-529, 1:10 in M-buffer], and subsequently with anti-FITC microbeads [Miltenyi Biotec, Anti-Sca-1 MicroBead Kit (FITC), 130-092-529 1:10 in M-buffer]. Cells bound to the microbeads were isolated using a MiniMACS separation column (Miltenyi Biotec, type MS+, 130-042-201) and taken in culture in 0.1% gelatin coated wells with SP++ medium: EGM-2 (Lonza, CC-3162) with M199 (Gibco, 31150-030) in a 1:3 mixture, supplemented with 10% FBS and 1% non-essential amino acids (Gibco, 11140-035) complemented with 10 ng/mL basic fibroblast growth factor (bFGF, Sigma F0291). Cells were cultured at 37°C and 5% CO_2 in SP++ medium and passaged at a confluency of ≈80% using trypsin (Gibco, 25200-056).

Transduction and Nucleofection of CPCs

Nucleofection

Cardiomyocyte progenitor cells were nucleofected using the Lonza Amaxa 2b Nucleofector Device and the Human Stem Cell Nucleofector I Kit according to manufacturers' protocol. For protocol optimization, GFP was nucleofected using the pmaxGFP plasmid (Amaxa, Cologne, Germany). Briefly, 1×10^6 cells were resuspended in 100 μL of nucleofection buffer and 2 μg of pmaxGFP. To determine the optimal nucleofection condition, several programs were tested. Each program differs in duration and intensity of the pulsation as described by the manufacturer. After nucleofection, cells were seeded in six well plates with SP++ medium. Program X001 was selected and used in further nucleofections. For the comparison of GFP expression with or without Woodchuck Hepatitis Virus Posttranscriptional Regulatory Element (WPRE), and for FACS measurements, cells were nucleofected with 1 μg of plasmid.

For the optimization of the construct, 0.5 μg pmaxGFP, 2 μg mouse(m)Hcn2-IRES-DsRed, and 2 μg rat(r)SkM1-IRES-GFP plasmid was used. For the combination of mHcn2 and rSkM1, 2 μg of each plasmid was co-nucleofected in the CPCs. Four days after nucleofection, cells were seeded on coverslips for immunocytochemistry.

For patch-clamp experiments, 2 μg of mHcn2 or 2 μg of rSkM1 plasmid (both without reporter markers) was co-nucleofected with 0.5 μg of GFP plasmid.

Transduction

For patch-clamp experiments, CPCs were transduced with VSVg pseudotyped LV-CMV-mHcn2-P2a-GFP-WPRE or LV-CMV-rSkM1-P2a-GFP-WPRE at an MOI of 5.0 and used after 2 days in culture. For the *in vivo* experiments, CPCs were transduced with VSVg pseudotyped LV-CMV-GFP-HPRE at an MOI of 5.0 and were used for transplantation experiments after two passages.

Immunocytochemistry

Cells were fixed in 4% paraformaldehyde for 10 min at room temperature and washed 3 times in PBS. Cells were permeabilized with 0.1% Triton X-100 for 8 min and incubated overnight with the following antibodies diluted in 4% goat serum: mouse α-SkM1 antibody (Sigma-Aldrich, S9568, 1: 200) and rabbit α-HCN2 antibody (Alomone, APC-030, 1:200). The next day, cells were washed three times in PBS with 0.05% Tween 20, and incubated for 1 h at room temperature with the following secondary antibodies: goat- α-mouse-488 (Invitrogen, A-11001, 1:250) or goat α-rabbit-568 (Invitrogen, A-11011, 1:250) in PBS with 4% goat serum. Cells were washed three times in PBS with 0.05% Tween 20. Nuclei were counterstained with DAPI (1:5000) for 5 min and mounted in Mowiol (Sigma, 81381).

Patch-Clamp Experiments

Data Acquisition

The Hcn2 and SkM1 currents (I_{Hcn2} and I_{SkM1}, respectively) were measured in the whole-cell configuration of the patch-clamp technique using an Axopatch 200B amplifier (Molecular Devices Corporation, Sunnyvale, CA, United States). CPCs were harvested, stored in SP++ medium at room temperature (20°C), and studied within 4 h. Cell suspensions were put into a recording chamber on the stage of an inverted microscope (Nikon Diaphot), and single CPCs that visibly formed branches with the bottom of the recording chamber and exhibited green fluorescence were selected for electrophysiological measurements. Voltage control, data acquisition, and analysis were accomplished using custom software. Potentials were corrected for the estimated change in liquid-junction potential (Barry and Lynch, 1991). Signals were low-pass filtered with a cut-off frequency of 5 kHz and digitized at 5 and 20 kHz for I_{Hcn2} and I_{SkM1}, respectively. Series resistance was compensated by ≥80%. Cell membrane capacitance (C_m) was calculated by dividing the time constant of the decay of the capacitive transient after a −5 mV voltage step from −40 mV by the series resistance, and amounted to 24.8 ± 2.5 pF (*n* = 18).

Hcn2 Current

I_{Hcn2} was recorded using the amphotericin-perforated patch-clamp technique at 36 ± 0.2°C. Bath solution contained (in mM): NaCl 140, KCl 5.4, $CaCl_2$ 1.8, $MgCl_2$ 1.0, glucose 5.5, HEPES 5.0; pH 7.4 (NaOH). Laboratory-made pipettes [2.5–3.5 MΩ; borosilicate glass (Harvard Apparatus, United Kingdom)] were filled with solution containing (in mM): K-gluc 125, KCl 20, NaCl 10, amphotericin-B 0.44, HEPES 5; pH 7.2 (KOH). In general, I_{Hcn2} was measured during 6-s hyperpolarizing voltage clamp steps (test potentials ranging from −30 to −140 mV) from a holding potential of −30 mV. Next, a 6-s step to −120 mV was applied to record tail current followed by a 1-s pulse to 10 mV to ensure full deactivation (see **Figure 5A** for protocol; cycle length 18-s). In the experiments presented in **Figure 3**, depolarizing steps were limited up to −120 mV and were followed by an 8-s step to −120 mV for recording of tail currents. Activation kinetics were measured during the 6-s hyperpolarizing steps. The current-voltage (I–V) relation was constructed from the current measured at the end of the 6-s hyperpolarizing steps. Currents were normalized to C_m. Tail current, plotted against test voltage, provided the activation-voltage relationship. The activation-voltage relation was normalized by maximum conductance and fitted with the Boltzmann function $I/Imax = A/\{1.0 + \exp[(V-V_{1/2})/k]\}$ to determine the half-maximum activation voltage ($V_{1/2}$) and slope factor (k). Deactivation kinetics and reversal potential (E_{rev}) were measured during depolarizing voltage clamp steps (test potentials ranging from −80 to −10 mV, duration 6 s) after a 5-s prepulse to −120 mV to ensure full activation (see **Figure 5D** for protocol; cycle length 15 s). The time course of I_{Hcn2} (de)activation was fitted by the mono-exponential equation $I/Imax = A \times [1 - \exp(-t/\tau)]$, ignoring the variable initial delay in Hcn2 (de)activation (Végh et al., 2019), to determine the time constant of (de)activation τ .

SkM1 Current

I_{SkM1} was measured at room temperature using the ruptured patch-clamp technique with patch pipettes (2.0–2.5 MΩ) containing (in mM): CsCl 10, CsF 110, NaF 10, EGTA 11, $CaCl_2$ 1.0, $MgCl_2$ 1.0, Na_2ATP 2.0, HEPES 10, pH 7.2 (CsOH). Bath solution contained (in mM): NaCl 140, CsCl 10, $CaCl_2$ 1.8, $MgCl_2$ 1.0, glucose 5.5, HEPES 5.0, pH 7.4 (NaOH). The current density of the peak of I_{SkM1} and voltage dependence of (in)activation were determined using the voltage protocols as shown in **Figure 6**. The holding potential was −120 mV (except when mentioned otherwise) and the voltage clamp steps were applied with a 5 s cycle length. Peak I_{SkM1} was defined as the difference between peak and steady-state current. Current density was calculated by dividing the measured currents by C_m. To determine the activation characteristics of I_{SkM1}, I–V curves were corrected for differences in driving force and normalized to maximum peak current. The time course of I_{SkM1} inactivation and steady-state (in)activation curves were fitted using the above-mentioned mono-exponential and Boltzmann equations, respectively.

In vivo Experiments

All mouse experiments were performed in accordance with the Guide for the Care and Use of Laboratory Animals and the protocols were approved by the Animal Ethics Committee of Leiden University Medical Center. Male immunocompromised NOD-SCID mice were chosen to minimize immune rejection against the transplanted cells. Mice aged 3–6 months were anesthetized with 4% isoflurane, intubated and maintained under 1.5–2% isoflurane during the procedure. Mice were given 0.05 mg/kg Buprenorphine prior to and 8–12 h after the procedure. After thoracotomy, 10 μL PBS containing ≈500.000 CPCs was divided over two injection-sites in the left ventricle near the left anterior descending coronary artery. Mice were randomly assigned to one of the three groups: untreated CPCs ($n = 4$), LV-GFP transduced CPCs (CPC LV-GFP) ($n = 4$) or GFP nucleofected CPCs (CPC NF-GFP) ($n = 5$). Seven days after the procedure, mice were sacrificed and hearts were collected. All procedures and injections were performed by a blinded investigator. The hearts were flushed with ice-cold PBS, fixed in 4% ice-cold paraformaldehyde, dehydrated with 30% sucrose overnight and embedded in Tissue-Tek O.C.T. compound (Sakura, 4583). After snap-freezing, the hearts were stored at −80°C, before they were cryosectioned. Whole mouse hearts were cryosectioned at 7 μm thickness from apex to base, and divided in 10 fractions of five sections each with equal distance (60 sections apart) from each other for immunostaining. In total, 50 sections throughout each heart were stained and analyzed.

Immunohistochemistry

Sections were incubated overnight with the following primary antibodies in 1% bovine serum albumin (Sigma, 9048-46-8) in PBS with 0.1% Tween 20: chicken α-GFP (Abcam, ab13970, 1:200), human-specific rabbit α-Collagen-1 (Abcam, ab138492, 1:200), and mouse α-β1-integrin (Santa Cruz, SC-53711, 1:500). The next day, sections were washed and incubated with the following secondary antibodies: goat α-chicken IgG-488 (Life Technologies, A11039, 1:250), donkey α-rabbit IgG-647 (Life Technologies, A31573, 1:250), and donkey α-mouse IgG-555 (Life Technologies, A31570, 1:250).

Computer Model

Functional effects of the electrical coupling of a human cardiomyocyte to CPCs expressing Hcn2 and/or SkM1 channels were assessed by computer simulations using the human ventricular cell model by Ten Tusscher et al. (2004), as updated by Ten Tusscher and Panfilov (2006), with its strong inward rectifier K^+ current (I_{K1}) downscaled by 65%, based on patch-clamp data obtained from single ventricular cardiomyocytes that were enzymatically dissociated from non-diseased human donor hearts (Jost et al., 2013). Coupling of the model cell to a single CPC was implemented as a gap junctional conductance of 10 nS, as observed between heterologous cell pairs, such as hMSCs and myocytes (Valiunas et al., 2009). The membrane capacitance of a single CPC was set to 24.8 pF, in line with the aforementioned data. The Hcn2 current as expressed in a single CPC was included as $I_{\mathrm{Hcn2}} = y \times g_{\mathrm{Hcn2}} \times (V_m - E_{\mathrm{Hcn2}})$, in which V_m denotes membrane potential and the fully activated conductance g_{Hcn2} and reversal potential E_{Hcn2} amount to 0.4 nS/pF and −39.8 mV, respectively, as observed in our patch-clamp experiments. The kinetics of the gating variable y were determined by the steady-state activation curve and time constant of (de)activation, as obtained in these experiments. The equations for the I_{SkM1} of the CPC were identical to those for the sodium current (I_{Na}) of the ventricular cell model, but with a +10.6 mV shift in steady-state activation as well as a +18.8 mV shift in steady-state inactivation, based on our patch-clamp data on I_{SkM1}. The fully activated conductance of I_{SkM1} was set to 7.0 nS/pF, estimated from our experimental observations, corrected for temperature.

Statistical Analysis

For the *in vivo* expression, of β1-integrin and Collagen-1, non-parametric Kruskal-Wallis tests were carried out, followed by Dunn's test for multiple comparisons. Since no GFP expression was measured in the untreated CPC group, statistics in this experiment were carried out by performing a non-parametric Mann–Whitney test between transduced and nucleofected CPCs. All data are presented as mean ± SEM. $P < 0.05$ was considered statistically significant.

RESULTS

Nucleofection of CPCs Is Improved by the Addition of a WPRE-Element

To explore nucleofection as a gene delivery method in CPCs, different programs (as pre-defined by the manufacturer) were tested to evaluate gene transfer and survival, where program X001 turned out to be superior in terms of GFP expression and cell survival (**Figure 1**). Next, this nucleofection program was used for the delivery of the functional genes Hcn2 and SkM1. Plasmids containing IRES reporter markers (GFP for SkM1 and DsRed for Hcn2) were used to assess efficiency of transfection and identify transfected cells for further experiments. However, the efficiency of nucleofection of Hcn2 and SkM1 was rather low in comparison with gene transfer of GFP alone (**Figure 2A**). In order to improve gene expression, the Woodchuck Hepatitis Virus Posttranscriptional Regulatory Element (WPRE) was added, which should enhance stability of the mRNA and therefore improve expression in the setting of nucleofection. Indeed, GFP was higher expressed when a plasmid containing the WPRE motif

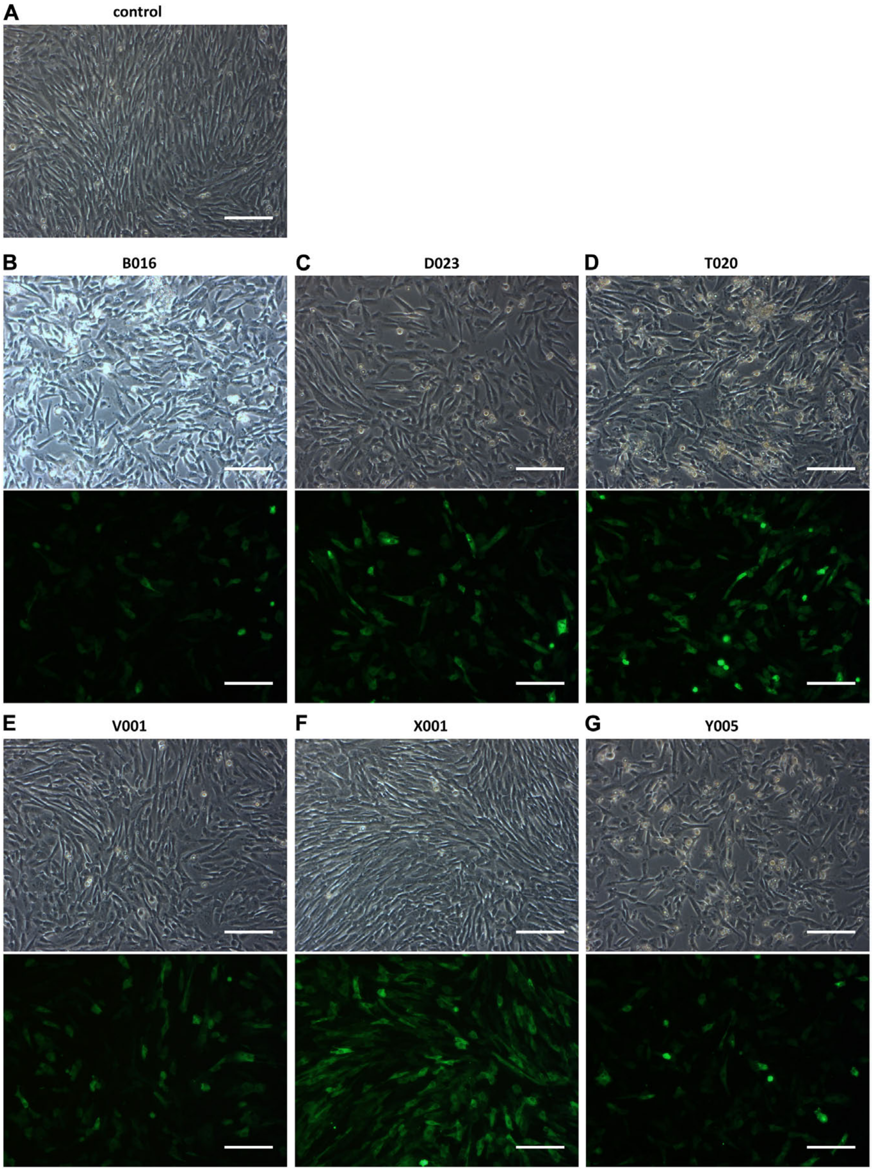

FIGURE 1 | Nucleofection optimization of CPCs with different programs. **(A)** Control figure shows nucleofected CPCs with no DNA. **(B–G)** GFP expression in CPCs as a result of different nucleofection programs. Upper rows show bright field images of nucleofected CPCs and lower rows show GFP expression. Images shown are representative examples of duplicate experiments. Scale bars represent 200 μM.

was used (**Figure 2B**). This was also the case when this was applied to the expression of Hcn2 (**Figure 2C**). Furthermore, we were able to achieve high efficiency of co-expression of Hcn2 or SkM1 together with GFP, which allowed us to visualize the cells that were efficiently transfected (**Figure 2D**, top two rows). In addition, high co-expression of Hcn2 and SkM1 was achieved with no detrimental effect on cell viability.

Nucleofection of CPCs Results in Hcn2 and SkM1 Currents

Next, we assessed whether DNA transfer by nucleofection of the Hcn2 gene and SkM1 gene resulted in functional membrane currents. CPCs transduced with only GFP neither express currents upon hyperpolarization nor on depolarization (**Figures 3A,B**), which agrees with our previous study (Végh et al., 2019). **Figure 3A**, bottom panel, shows membrane currents in an Hcn2-nucleofected, GFP-positive CPC. Typical for an HCN-encoded "funny"-current (I_f), an inward current was activated following hyperpolarizing steps from a holding potential of −30 mV, and this hyperpolarization-activated current became larger and activated more rapidly at increasingly negative potentials. In this particular example, activation threshold was around −70 mV (red trace) and full activation was reached at a potential of −110 mV (green trace). **Figure 3B**, bottom panel, shows membrane currents in

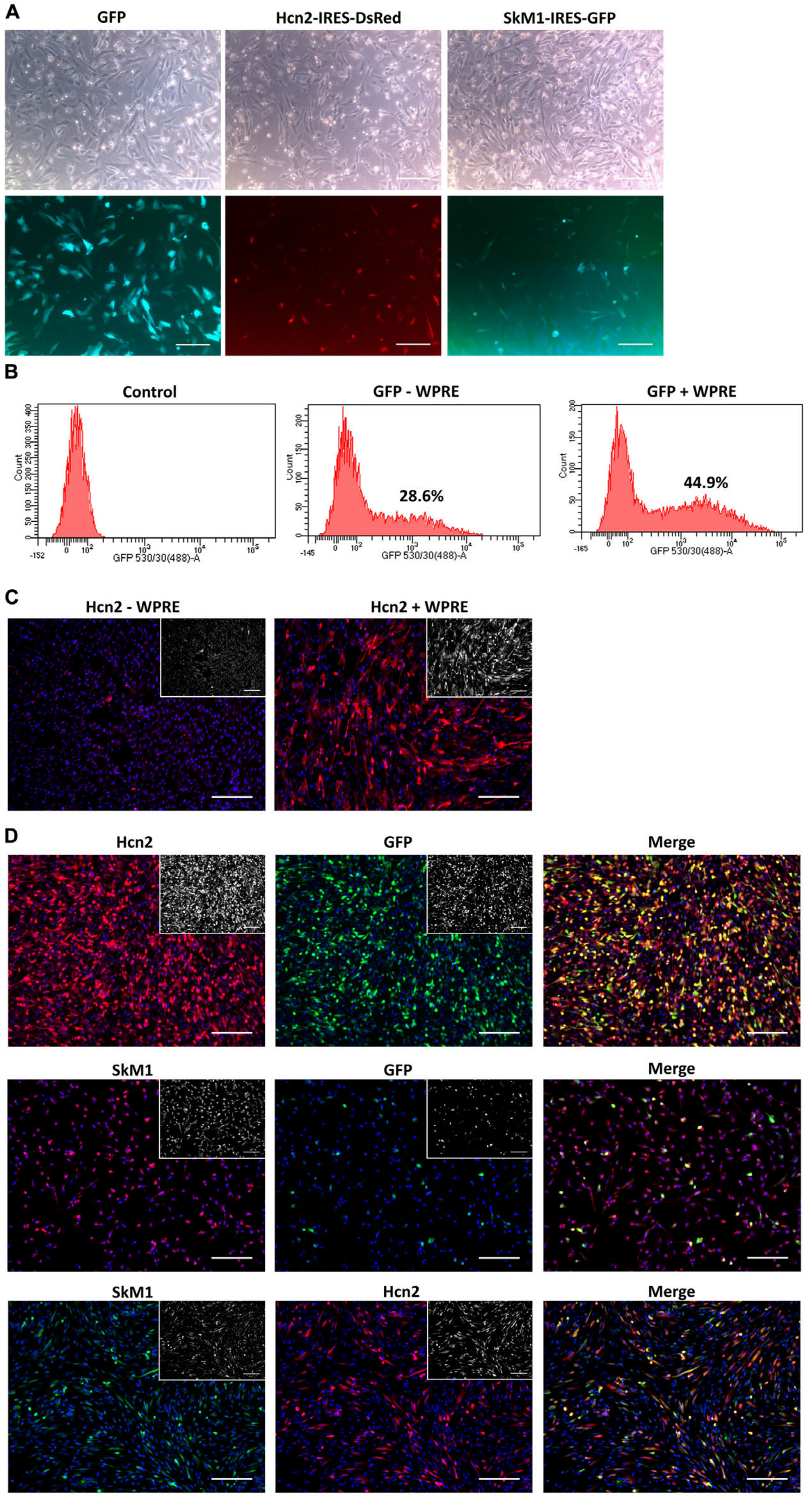

FIGURE 2 | Nucleofection optimization of CPCs. **(A)** Nucleofection with GFP (left panels), Hcn2 (middle panels) or SkM1 (right panels) plasmids with IRES driven reporter markers. Upper panels show bright field images of nucleofected CPCs and lower panels show expression of reporter markers (DsRed in red and GFP in green). Scale bars represent 200 μM. **(B)** FACS data of GFP expression in nucleofected CPCs with a GFP plasmid with (right panel) or without (middle panel) the WPRE motif. Control cells (left panel) do not express GFP. Percentages indicate the % GFP-positive counted cells. **(C)** Immunocytochemistry of nucleofected CPCs with an Hcn2 plasmid, without or with WPRE motif (left and right panel, respectively). Hcn2 is stained in red and nuclei are counterstained in blue. Staining without DAPI is shown in the insets. **(D)** Immunocytochemistry of co-expression of Hcn2 (upper panels) and SkM1 (middle panels) with GFP nucleofected CPCs in 4:1 ratio. Lower panels show co-expression of Hcn2 and SkM1 in 1:1 ratio. Staining without DAPI is shown in the insets. Scale bars represent 200 μM, *n* = 2.

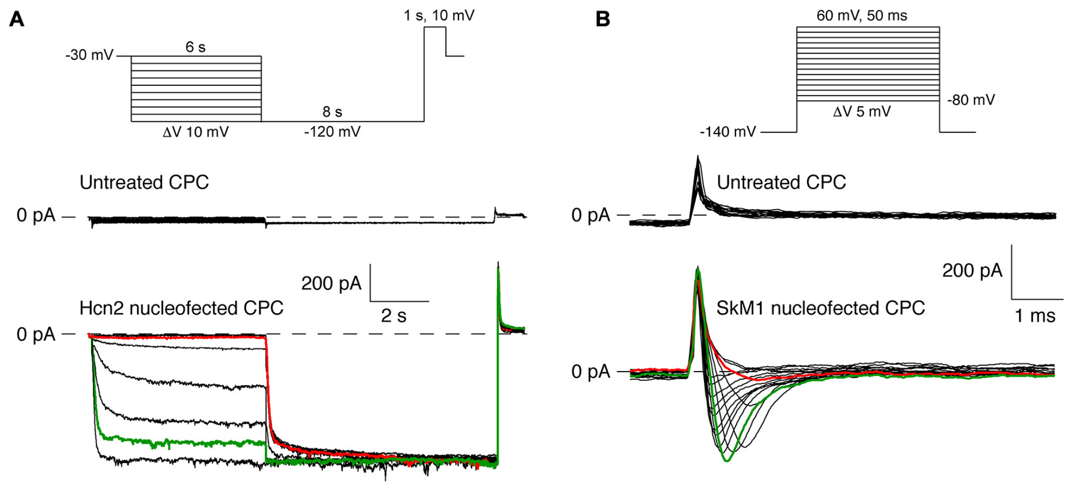

FIGURE 3 | Pilot experiments of Hcn2 and SkM1 currents measured at 36°C and room temperature, respectively, in single nucleofected CPCs. **(A)** Top panel, protocol used. Middle panel, recording of an empty CPC. Bottom panel, Hcn2-encoded "funny current" (at test potentials ranging from –30 to –120 mV) in an Hcn2 nucleofected CPC. **(B)** Top panel, protocol used. Middle panel, recording of an empty CPC. Bottom panel, skeletal fast sodium current (at test potentials ranging from –50 to +20 mV) in a SkM1 nucleofected CPC. SkM1 was measured from a holding potential of –140 mV.

an SkM1-nucleofected, GFP-positive CPC. Upon depolarizing voltage steps from −140 mV, a fast activating and inactivating inward current was activated, typical for a fast sodium current (I_{Na}). In this particular example, the current activated at −40 mV (red trace), and was maximal at −20 mV (green trace).

Although nucleofection of the Hcn2 gene and SkM1 gene resulted in functional membrane currents, GFP expression was relatively low and difficult to detect by eye in the patch-clamp set-up. We therefore continued the patch-clamp experiments in lentivirally transduced CPCs which resulted in sufficient GFP expression in a relatively large number of CPCs.

Biophysical Characterization of Lentivirally Transduced CPCs Expressing Hcn2 and SkM1

The next step was to transduce CPCs with lentiviral constructs. First, CPCs were transduced with LV-CMV-GFP-HPRE, which lead to high GFP expression *in vitro* (**Figure 4**). Then, CPCs were transduced with LV-CMV-mHcn2-P2a-GFP-WPRE or LV-CMV-rSkM1-P2a-GFP-WPRE to study the properties of the Hcn2- and SkM1-encoded currents using patch-clamp methodology. **Figure 5A** shows typical Hcn2 recordings from a single lentivirally transduced CPC. The average I–V relationship of I_{Hcn2} is summarized in **Figure 5B**. CPCs expressing Hcn2 showed large time-dependent inward currents in response to the hyperpolarizing voltage steps, typical for Hcn2 (**Figures 5A,B**). To analyze voltage-dependence of Hcn2 activation, we plotted the normalized tail current amplitude against the preceding hyperpolarizing potential and fitted a Boltzmann function to the data. The average curve is shown in **Figure 5C**. The average $V_{1/2}$ and k of the Boltzmann fit to the data were −81.4 ± 7.6 and −6.2 ± 0.8 mV (n = 9), respectively. The voltage-dependence of the fully activated current was evaluated over a large range of potentials (−80 to −10 mV) by measuring the tail current amplitudes after a hyperpolarizing pulse to −120 mV. **Figure 5D** shows a typical example, and **Figure 5E** shows the average I–V relationship of the fully activated I_{Hcn2}. The average reversal potential was −39.8 ± 1.1 mV (n = 8). Activation and deactivation time constants (**Figure 5F**) were obtained from mono-exponential fits of the step (**Figure 5A**) and tail (**Figure 5D**) currents, respectively.

Figure 6A shows representative SkM1 currents in a lentivirally transduced CPC activated by 50-ms depolarizing voltage clamp steps of 5 mV increment. The current starts to activate around −50 mV, peaks around −10 mV, and subsequently decreases in amplitude due to the reduction in Na^+ driving force. **Figure 6B** summarizes the average time constants of I_{Na} inactivation, which typically is faster at more depolarized potentials. **Figure 6C** shows average data for the I–V relationship. The average maximal current density was −217 ± 22 pA/pF (n = 9). **Figure 6D** shows the average voltage-dependency of activation. The average $V_{1/2}$ and k of the voltage-dependency of activation were −27.3 ± 2.5 and 5.6 ± 0.5 mV (n = 9), respectively. The voltage-dependency of inactivation was measured using a two-pulse protocol where a 500-ms conditioning prepulse to membrane potentials between −120 and 20 mV, to induce steady-state inactivation, was followed by a 50-ms test pulse (**Figure 6E**, inset). The average $V_{1/2}$ and k of the voltage-dependency of inactivation were −65.1 ± 1.3 and −4.6 ± 0.1 mV (n = 9), respectively.

Lentiviral Transduced CPCs Survive Better *in vivo*

Encouraged by the initial *in vitro* experiments we proceeded with an *in vivo* comparison between GFP-nucleofected and GFP-lentivirally transduced cells. One week after transplantation, the presence of CPCs and GFP expression was determined in the mouse heart. GFP was highly expressed after transplantation of transduced CPCs, whereas the nucleofected CPC group

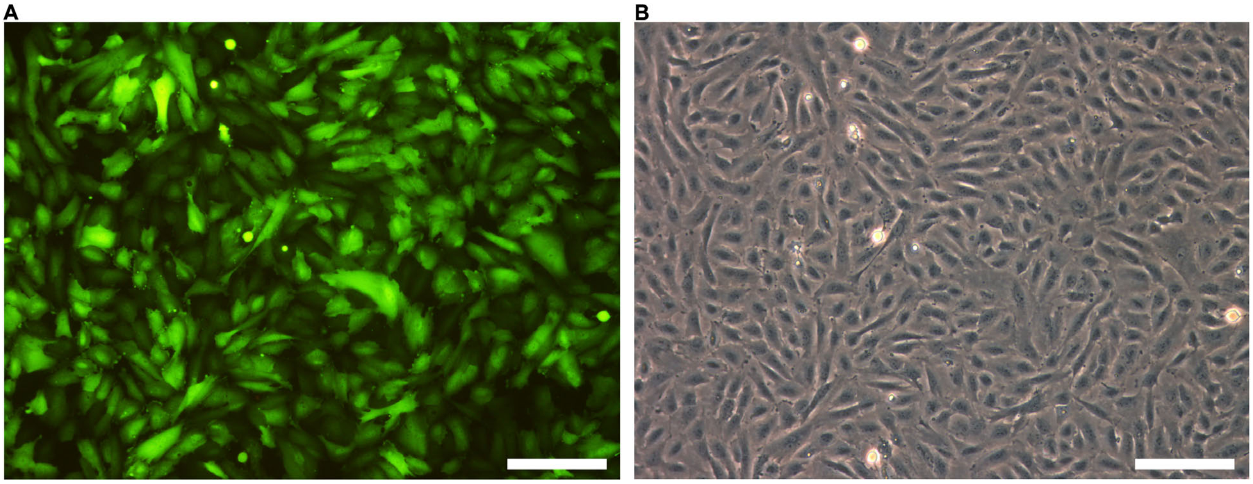

FIGURE 4 | GFP is highly expressed after lentiviral transduction. **(A)** GFP expression of LV-GFP transduced CPCs. **(B)** Bright field picture of CPCs. Scale bars represent 100 μM, *n* = 5.

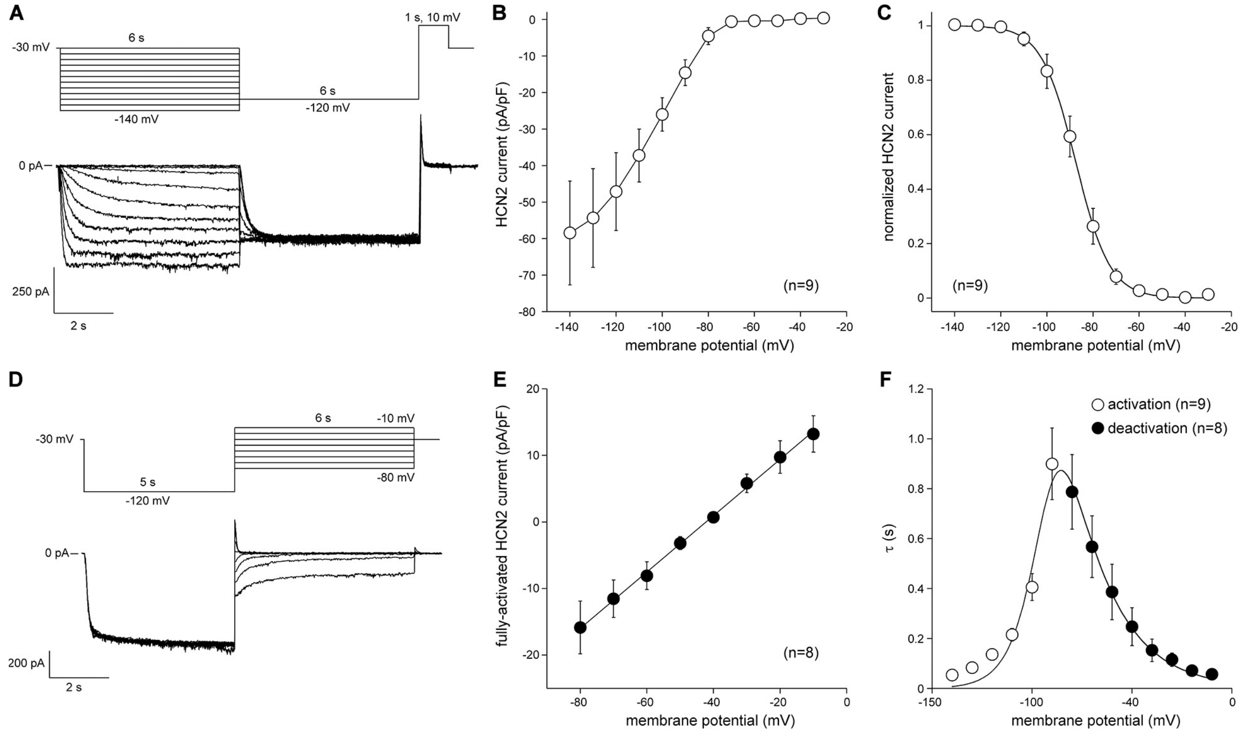

FIGURE 5 | Hcn2 current measured at measured at 36°C in single LV-transduced CPCs. **(A)** Typical Hcn2 current traces (bottom panel) activated with a double pulse voltage clamp protocol (top panel) to determine current density and activation properties. **(B)** Average current-voltage (I–V) relationship of the Hcn2 current. **(C)** Voltage dependence of Hcn2 current activation. Solid line is the Boltzmann fit to the experimental data. **(D)** Typical Hcn2 current traces (bottom panel) activated with a double pulse voltage clamp protocol (top panel) to determine the reversal potentials and deactivation properties. **(E)** I–V relationship of the fully activated Hcn2 current. Solid line is the linear fit to the experimental data. **(F)** Time constants of (de)activation. Solid line is the best fit curve to the equation $\tau = 1/[A1 \times \exp(-V/B1) + A2 \times \exp(V/B2)]$, where τ is the activation or deactivation time constant (s), and A1, A2, B1, and B2 are calculated fitting parameters, which amount to $3.2164 \cdot 10^{-8}$ s^{-1}, 9.2311 s^{-1}, 0.041248 mV, and 21.724 mV, respectively (Qu et al., 2004).

showed almost no GFP expression after transplantation (**Figures 7A–D**). The human-specific β1-integrin was used as a measure for the presence of the human-derived CPCs after transplantation (Smits et al., 2009a). Since the same number of cells is transplanted in every group, β1-integrin expression can be used as a measure for survival of the cells at a certain time point.

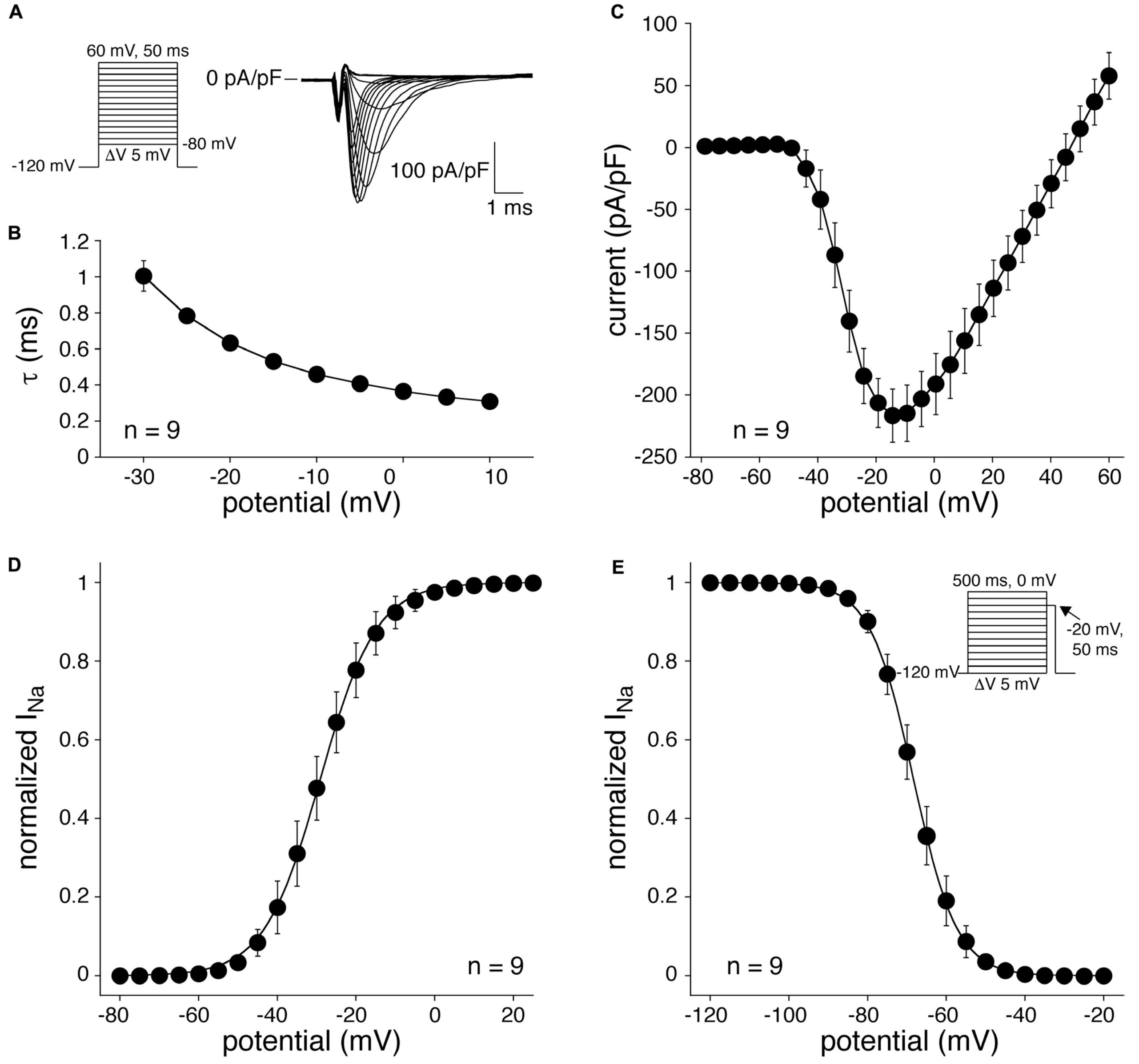

FIGURE 6 | SkM1 current measured at room temperature in single CPCs. **(A)** Left: voltage clamp protocol used. Right: Typical example of SkM1 current in response to 50-ms depolarizing voltage steps ranging from –50 and +20 mV, from a holding potential of –120 mV. **(B)** Average time constants of fast and slow SkM1 current inactivation. **(C)** Average I–V relationship. **(D)** Average steady-state activation curve. The solid line is the Boltzmann fit to the average data. **(E)** Average steady-state inactivation curve. The solid line is the Boltzmann fit to the average data. Inset: voltage clamp protocol for determination of inactivation.

The analysis clearly indicated a trend toward lowest expression of β1-integrin in the nucleofection group (**Figure 7E**). Secretion of matrix protein human collagen-1 was also lower in nucleofected CPCs. Visualization of secreted collagen-1 allows for detection of human cell grafts even beyond cell death and is therefore a measure for cumulative human cell engraftment (Bax et al., 2019) (**Figure 7F**). Collectively, these data suggest both engraftment and survival are compromised with nucleofected cells compared to unmodified or lentivirally transduced CPCs. As a result, GFP gene delivery was also higher with lentivirally transduced CPCs. We therefore proceeded with computer modeling studies, based on the biophysical characterization obtained from lentivirally transduced cells.

Contribution of SkM1 to Diastolic Depolarization

To investigate how the biophysical properties of Hcn2 and SkM1, as recorded in lentivirally transduced CPCs, would impact on action potential morphology and spontaneous activity we proceeded with computer simulation studies. These studies indicated that significant diastolic depolarization can be induced

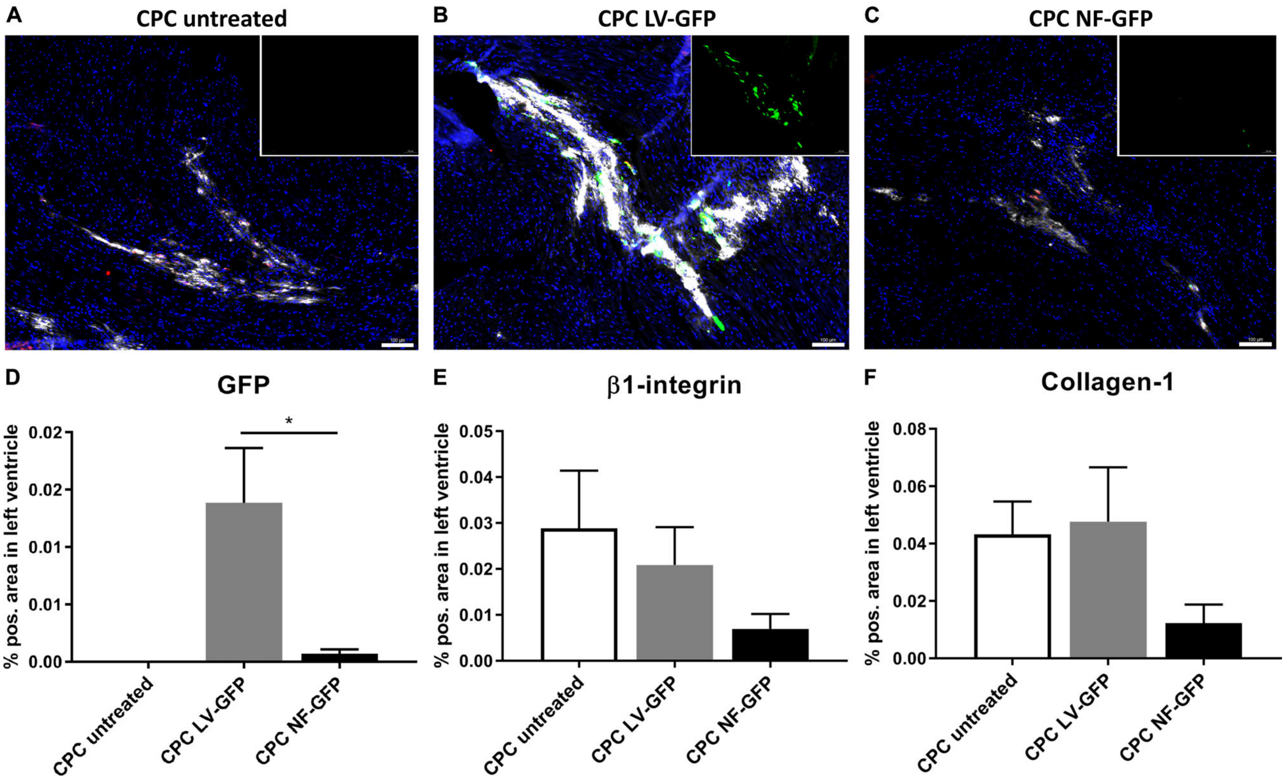

FIGURE 7 | GFP expression and CPC engraftment 1 week after transplanting CPCs to the left ventricle near the left anterior descending artery. **(A–C)** Typical examples of expression of GFP (green), β1-integrin (red), and Collagen-1 (white) in mouse hearts injected with **(A)** unmodified CPCs, **(B)** LV-GFP transduced CPCs or **(C)** GFP nucleofected (NF) CPCs. Inset: GFP expression alone. Scale bars represent 100 μM. **(D–F)** Expression of GFP, β1-integrin, and Collagen-1 in mice injected with unmodified CPCs (*n* = 4), lentivirally transduced CPCs (*n* = 4) or nucleofected CPCs (*n* = 5), measured as% positive area of total left ventricular area. * indicates $P < 0.05$.

when a moderate number of CPCs is coupled to one ventricular working cardiomyocyte, as illustrated for 10 CPCs in the left panels of **Figure 8**. However, stable automaticity could only be obtained if at least 14 CPCs were coupled to the ventricular working cardiomyocyte. The mechanism underlying this stable automaticity is illustrated in the right panels of **Figure 8** for a total of 20 CPCs.

These simulations with a total of 20 CPCs illustrated stable automaticity upon ending external stimulation exclusively with Hcn2/SkM1-expressing CPCs and not with Hcn2 alone (**Figure 8**, right panels). Interestingly, SkM1 contributed to the final stage of diastolic depolarization, supporting depolarization toward the voltage range of L-type Ca^{2+}-channel activation. In this setting, mere Hcn2-mediated diastolic depolarization was insufficient to reach the threshold for Ca^{2+}-channel opening.

The intriguing increase in action potential duration upon coupling the myocyte to 10 CPCs (**Figure 8A**, left), and even more so with 20 CPCs (**Figure 8A**, right), is the result of the junctional current (**Figure 8C**), which is inward to the myocyte during the repolarization phase of the action potential. The voltage changes of the CPCs closely follow those of the myocyte (**Figures 8A,B**), but during repolarization the myocyte is in the lead, with the CPCs lagging behind. As a consequence, the membrane potential of the CPCs is more positive than that of the myocyte during early repolarization and less negative during late repolarization, so that the junctional current acts as an inward current for the myocyte and slows its repolarization.

DISCUSSION

In the present study, we investigated cellular gene delivery of Hcn2 and SkM1 in an effort toward engineering long-term biological pacemaker activity. Although both nucleofection and lentiviral transduction were effective gene transfer tools to manipulate CPCs, lentiviral transduction was superior with regard to survival of gene-modified cells in the context of *in vivo* transplantation. Subsequent patch-clamp studies on lentivirally transduced Hcn2/SkM1-expressing cells demonstrated robust functional transgene expression that appeared sufficient to induce biological pacemaker activity in computer modeling studies, provided that I_{K1} was substantially reduced as compared to the original model (Ten Tusscher et al., 2004; Ten Tusscher and Panfilov, 2006), based on more recent comprehensive patch-clamp data on the amplitude of I_{K1} in human ventricular cardiomyocytes (Jost et al., 2013).

Both nucleofection and transduction of CPCs resulted in robust functional expression of Hcn2 and SkM1 *in vitro*. Previous

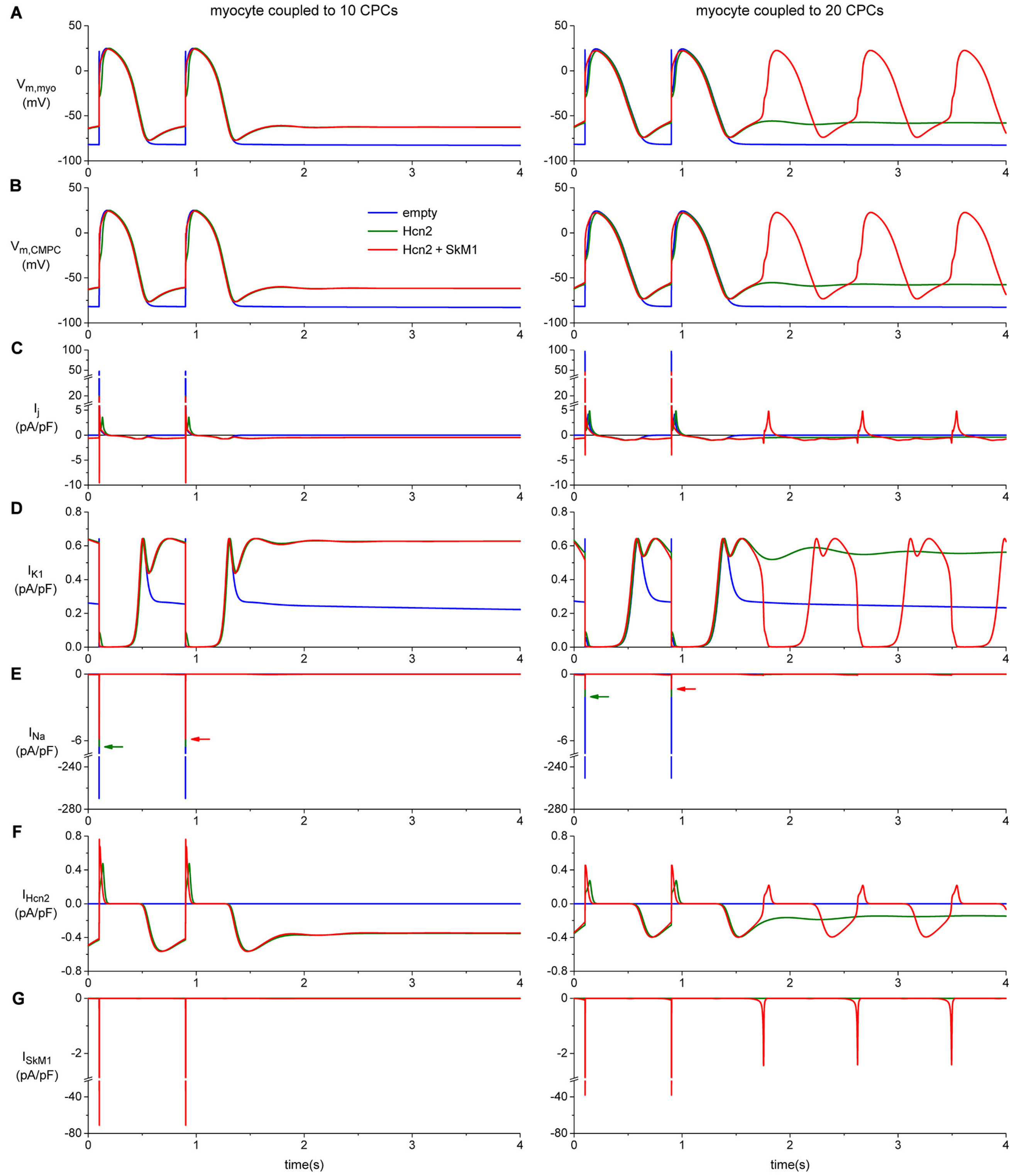

FIGURE 8 | Computer simulation of action potentials of a human ventricular myocyte coupled to 10 (left panels) or 20 CPCs (right panels) overexpressing Hcn2 alone (green line), or Hcn2 + SkM1 (red line). The blue line shows the action potentials of the myocyte coupled to 10 (left) or 20 (right) empty CPCs. **(A)** Last two action potentials of a train of 100, induced by a 1 ms, ≈50% suprathreshold stimulus. Formation of stable pacemaker function after ending the train of stimuli is found only with the larger number of CPCs and only in the Hcn2 + SkM1 group and not in the simulation with Hcn2 alone. **(B)** Corresponding membrane potential of each of the CPCs. **(C)** Total junctional current flowing from the myocyte to the CPCs. Positive junctional current is outward for the myocyte, but inward for the CMPCs, and vice versa. **(D,E)** Membrane ion currents I_{K1} and I_{Na} of the myocyte. **(F,G)** Membrane ion currents I_{Hcn2} and I_{SkM1} of each of the CPCs.

studies have shown that lentiviral transduction or electroporation of MSCs was sufficiently effective to provide robust outcomes in terms of biological pacing and restoration of impulse propagation in the epicardial border zone (Potapova et al., 2004; Plotnikov et al., 2007; Jun et al., 2012; Lu et al., 2013). However, our results indicate that delivery of GFP *in vivo* is superior with lentivirally transduced cells. This appears primarily driven by higher gene-delivery efficiency *in vitro* and better survival of the lentivirally transduced CPCs after transplantation. Other studies that compare gene-transfer efficiency and *in vitro* survival of several (stem) cell types also showed results in favor of lentiviral transduction over electroporation/nucleofection (Dullaers et al., 2004; Mcmahon et al., 2006; Li and Lu, 2009; Cao et al., 2010).

Transplantation efficiency of CPCs showed moderate engraftment of unmodified and LV-transduced CPCs after 1 week. This was also found in a previous study, where CPC survival was around 3.5% 2 days after MI and transplantation of the cells (Smits et al., 2009a). In comparison, MSC survival was found to be less than 0.44% in SCID mice 4 days after myocardial infarction (MI) (Toma et al., 2002), and ≈1% in rats 24 h after MI (McGinley et al., 2013). Although engraftment rates were low in MI models, the effect on cardiac function of transplanting (cardiac) stem cells was still significant (Zwetsloot et al., 2016). One of the advantages over restoring damaged heart muscle after MI, is that the development of a biological pacemaker expectedly requires a lower degree of cell engraftment. In dog hearts, the minimum required amount of MSCs to create stable biological pacing was estimated to 700.000 cells, which adds to the feasibility of such a stem cell-based approach (Plotnikov et al., 2007).

The comparison between biological pacemaker strategies based on undifferentiated cells (i.e., CPCs and MSCs) and those that are based on pluripotent stem cells coaxed into a lineage of pacemaker cells remains difficult at this stage. The transplantation of human embryonic stem cell derived cardiomyocytes (ESC-CMs) in guinea pigs or pigs with atrioventricular (AV)-block resulted in ectopic activity at the site of transplantation (Kehat et al., 2004; Xue et al., 2005). However, difficulties in obtaining pure hESC-CM cultures, potential risk of teratoma formation and immunological issues have hampered further translational development of this technology for biological pacemaker applications. Human induced pluripotent stem cell-derived cardiomyocytes (hiPSC-CMs) represent a promising alternative given their potential use in autologous stem cell transplantation, thereby holding important promise to bypass immune rejection. Moreover, long term biological pacing has been encouraging as stable function was maintained throughout a 13 week canine study (Chauveau et al., 2017). Yet in terms of pacemaker function, further improvements appear still to be necessary, as beating rates were relatively low, and dependency on back-up pacing was still substantial (Chauveau et al., 2017). Ongoing efforts therefore focus on optimization of hiPSC differentiation, maturation and purification protocols (Protze et al., 2017). How these improvements will eventually compare to biological pacemakers that are made from undifferentiated cells, such as CPCs, remains to be determined by follow-up studies.

Detailed biophysical studies illustrate comparable, or even potentially more favorable kinetics for I_{Hcn2} and I_{SkM1} in lentivirally transduced CPCs vs. previously reported values in MSCs. The voltage of half-maximal activation of Hcn2 (−86 mV) falls well within the physiological range of cardiomyocyte membrane potentials and appears to be more positive than the value previously reported for Hcn2-expressing MSCs (−96 mV) (Potapova et al., 2004; Plotnikov et al., 2007). Moreover, the I_{Hcn2} density also appears to be relatively high in CPCs compared to MSCs (58 pA/pF at −140 mV vs. 31 pA/pF at −150 mV). For SkM1, the comparison was slightly more complicated as the voltage of half-maximal inactivation was more negative (−65 mV) than the value reported in MSCs (−59 mV). On the other hand, the SkM1 peak current density was again much higher in CPCs than in MSCs (217 vs. 39 pA/pF) (Boink et al., 2012a). Yet, it remains difficult to draw any definitive conclusions from these numbers due to the concomitant differences in recording conditions that were used in the different laboratories.

Our computer simulations provide further mechanistic insight into Hcn2/SkM1-based biological pacing following CPC-mediated delivery. These simulations suggest that transplantation of Hcn2/SkM1-expressing CPCs to working myocardium may be insufficient to generate stable pacemaker function, given the relatively large number of CPCs required to generate stable pacemaker activity. This was a surprising finding, given the substantial *in vivo* pacing after transplantation of Hcn2-expressing MSCs to the left ventricle of AV-block dogs (Potapova et al., 2004; Plotnikov et al., 2007; Jun et al., 2012; Lu et al., 2013). It is therefore conceivable that additional factors are involved that contribute to Hcn2-based biological pacing which are not well recapitulated by our computer model. Alternatively, it could suggest that a higher expression levels of Hcn2 and SkM1 are needed for appropriate functionality. Nonetheless, biological pacing improved in the context of lowering I_{K1} as compared to the original human ventricular cell model (Ten Tusscher et al., 2004; Ten Tusscher and Panfilov, 2006), which is in line with our previous work that demonstrated superior biological pacemaker activity after adenoviral gene transfer to the left bundle branch (lower I_{K1} environment) vs. subepicardial working myocardium (higher I_{K1}) (Boink et al., 2013). This setting also allowed us to further investigate the mechanistic contribution of SkM1 to Hcn2-based biological pacing. The associated computer simulations illustrate that SkM1 can generate additional inward current during late phase 4 depolarization, thereby facilitating spontaneous activity. This represents a new mechanism of action that further supports the robustness of Hcn2/SkM1-based biological pacemaker activity and can act synergistically with the previously demonstrated hyperpolarization of action potential threshold (Boink et al., 2013).

In conclusion, the present work identified lentiviral transduction as the method of choice to manipulate CPCs for long-term biological pacemaker applications. In this respect, CPC-mediated delivery of Hcn2/Skm1 appears promising, but functional animal studies are still needed to fully characterize this approach and make head-to-head comparisons to related strategies that rely on viral gene transfer or hiPSC-CMs.

DATA AVAILABILITY STATEMENT

The raw data supporting the conclusions of this article will be made available by the authors, without undue reservation.

ETHICS STATEMENT

The studies involving human participants were reviewed and approved by the Medical Ethics Committee of the Leiden University Medical Center. The patients/participants provided their written informed consent to participate in this study. The animal study was reviewed and approved by Animal Ethics Committee of Leiden University Medical Center.

AUTHOR CONTRIBUTIONS

AMV, AS, AOV, AT, GB, HT, LC, MG, RN, RW, and VC contributed to conception and design of the study. AMV and AOV performed the statistical analysis. AMV wrote the first draft of the manuscript. AOV, LC, and RW wrote sections of the manuscript. DG, HD, JW, KL, LC, MK, MM-R, and RN contributed to data acquisition. All authors contributed to manuscript revision, read and approved the submitted version.

FUNDING

GB was supported by personal grants from the Dutch Heart Foundation (2014T065), the Netherlands Organization for Scientific Research (ZonMw Veni 016.156.162), and the European Research Council (ERC Starting Grant 714866). This work was further supported by the Rembrandt Institute for Cardiovascular Research (to GB, MG, and HT) and Health Holland LSHM16027 and LentiPace II (to GB and HT).

ACKNOWLEDGMENTS

We would like to thank Dr. Ing. Berend van Meer for helping us with *in vitro* measurements on the CPCs. Furthermore, we like to thank Prof. Dr. Ira Cohen and Prof. Dr. Dario DiFrancesco for their critical reading of the manuscript and valuable suggestions.

REFERENCES

Barry, P. H., and Lynch, J. W. (1991). Liquid junction potentials and small cell effects in patch-clamp analysis. *J. Membr. Biol.* 121, 101–117. doi: 10.1007/BF01870526

Bax, N. A. M., Duim, S. N., Kruithof, B. P. T., Smits, A. M., Bouten, C. V. C., and Goumans, M. J. (2019). *In vivo* and *in vitro* approaches reveal novel insight into the ability of epicardium-derived cells to create their own extracellular environment. *Front. Cardiovasc. Med.* 6:81. doi: 10.3389/fcvm.2019.00081

Boink, G. J. J., Duan, L., Nearing, B. D., Shlapakova, I. N., Sosunov, E. A., Anyukhovsky, E. P., et al. (2013). HCN2/SkM1 gene transfer into canine left bundle branch induces stable, autonomically responsive biological pacing at physiological heart rates. *J. Am. Coll Cardiol.* 61, 1192–1201. doi: 10.1016/j.jacc.2012.12.031

Boink, G. J. J., Lu, J., Driessen, H. E., Duan, L., Sosunov, E. A., Anyukhovsky, E. P., et al. (2012a). Effect of skeletal muscle Na^+ channel delivered via a cell platform on cardiac conduction and arrhythmia induction. *Circ. Arrhythm Electrophysiol.* 5, 831–840. doi: 10.1161/CIRCEP.111.969907

Boink, G. J. J., Nearing, B. D., Shlapakova, I. N., Duan, L., Kryukova, Y., Bobkov, Y., et al. (2012b). Ca^{2+}-stimulated adenylyl cyclase AC1 generates efficient biological pacing as single gene therapy and in combination with HCN2. *Circulation* 126, 528–536. doi: 10.1161/CIRCULATIONAHA.111.083584

Bruzauskaite, I., Bironaite, D., Bagdonas, E., Skeberdis, V. A., Denkovskij, J., Tamulevicius, T., et al. (2016). Relevance of HCN2-expressing human mesenchymal stem cells for the generation of biological pacemakers. *Stem Cell Res. Ther.* 7:67. doi: 10.1186/s13287-016-0326-z

Bucchi, A., Plotnikov, A. N., Shlapakova, I., Danilo, P., Kryukova, Y., Qu, J., et al. (2006). Wild-type and mutant HCN channels in a tandem biological-electronic cardiac pacemaker. *Circulation* 114, 992–999. doi: 10.1161/CIRCULATIONAHA.106.617613

Cao, F., Xie, X., Gollan, T., Zhao, L., Narsinh, K., Lee, R. J., et al. (2010). Comparison of gene-transfer efficiency in human embryonic stem cells. *Mol. Imaging Biol.* 12, 15–24. doi: 10.1007/s11307-009-0236-x

Chauveau, S., Anyukhovsky, E. P., Ben-Ari, M., Naor, S., Jiang, Y.-P., Danilo, P., et al. (2017). Induced pluripotent stem cell-derived cardiomyocytes provide *in vivo* biological pacemaker function. *Circ. Arrhythm Electrophysiol.* 10:e004508. doi: 10.1161/CIRCEP.116.004508

Dullaers, M., Breckpot, K., Van Meirvenne, S., Bonehill, A., Tuyaerts, S., Michiels, A., et al. (2004). Side-by-side comparison of lentivirally transduced and mRNA-electroporated dendritic cells: implications for cancer immunotherapy protocols. *Mol. Ther.* 10, 768–779. doi: 10.1016/j.ymthe.2004.07.017

Gyöngyösi, M., Blanco, J., Marian, T., Trón, L., Petneházy, O., Petrasi, Z., et al. (2008). Serial noninvasive *in vivo* positron emission tomographic tracking of percutaneously intramyocardially injected autologous porcine mesenchymal stem cells modified for transgene reporter gene expression. *Circ. Cardiovasc. Imaging* 1, 94–103. doi: 10.1161/CIRCIMAGING.108.797449

Jost, N., Virág, L., Comtois, P., Szuts, V., Seprényi, G., Bitay, M., et al. (2013). Ionic mechanisms limiting cardiac repolarization reserve in humans compared to dogs. *Authors J. Physiol. C* 591, 4189–4206. doi: 10.1113/jphysiol.2013.261198

Jun, C., Zhihui, Z., Lu, W., Yaoming, N., Lei, W., Yao, Q., et al. (2012). Canine bone marrow mesenchymal stromal cells with lentiviral mHCN4 gene transfer create cardiac pacemakers. *Cytotherapy* 14, 529–539. doi: 10.3109/14653249.2012.654490

Kass-Eisler, A., Falck-Pedersen, E., Alvira, M., Rivera, J., Buttrick, P. M., Wittenberg, B. A., et al. (1993). Quantitative determination of adenovirus-mediated gene delivery to rat cardiac myocytes *in vitro* and *in vivo*. *Proc. Natl. Acad. Sci. U.S.A.* 90, 11498–11502. doi: 10.1073/pnas.90.24.11498

Kehat, I., Khimovich, L., Caspi, O., Gepstein, A., Shofti, R., Arbel, G., et al. (2004). Electromechanical integration of cardiomyocytes derived from human embryonic stem cells. *Nat. Biotechnol.* 22, 1282–1289. doi: 10.1038/nbt1014

Kotsakou, M., Kioumis, I., Lazaridis, G., Pitsiou, G., Lampaki, S., Papaiwannou, A., et al. (2015). Pacemaker insertion. *Ann. Transl. Med.* 3:42. doi: 10.3978/j.issn.2305-5839.2015.02.06

Li, G. B., and Lu, G. X. (2009). Gene delivery efficiency in bone marrow-derived dendritic cells: comparison of four methods and optimization for lentivirus transduction. *Mol. Biotechnol.* 43, 250–256. doi: 10.1007/s12033-009-9197-1

Lu, W., Yaoming, N., Boli, R., Jun, C., Changhai, Z., Yang, Z., et al. (2013). mHCN4 genetically modified canine mesenchymal stem cells provide biological pacemaking function in complete dogs with atrioventricular block. *Pacing Clin. Electrophysiol.* 36, 1138–1149. doi: 10.1111/pace.12154

McGinley, L. M., McMahon, J., Stocca, A., Duffy, A., Flynn, A., O'Toole, D., et al. (2013). Mesenchymal stem cell survival in the infarcted heart is enhanced by lentivirus vector-mediated heat shock protein 27 expression. *Hum. Gene Ther.* 24, 840–851. doi: 10.1089/hum.2011.009

Mcmahon, J. M., Conroy, S., Lyons, M., Greiser, U., O'shea, C., Strappe, P., et al. (2006). *Gene transfer into rat mesenchymal stem cells: a comparative study of viral and nonviral vectors. Stem Cells Dev.* 15, 87–96. doi: 10.1089/SCD.2006.15.87

Plotnikov, A. N., Bucchi, A., Shlapakova, I., Danilo, P., Brink, P. R., Robinson, R. B., et al. (2008). HCN212-channel biological pacemakers manifesting ventricular tachyarrhythmias are responsive to treatment with I_f blockade. *Heart Rhythm* 5, 282–288. doi: 10.1016/j.hrthm.2007.09.028

Plotnikov, A. N., Shlapakova, I., Szabolcs, M. J., Danilo, P., Lorell, B. H., Potapova, I. A., et al. (2007). Xenografted adult human mesenchymal stem cells provide a platform for sustained biological pacemaker function in canine heart. *Circulation* 116, 706–713. doi: 10.1161/CIRCULATIONAHA.107.703231

Potapova, I., Plotnikov, A., Lu, Z., Danilo, P., Valiunas, V., Qu, J., et al. (2004). Human mesenchymal stem cells as a gene delivery system to create cardiac pacemakers. *Circ. Res.* 94, 952–959. doi: 10.1161/01.RES.0000123827.60210.72

Protze, S. I., Liu, J., Nussinovitch, U., Ohana, L., Backx, P. H., Gepstein, L., et al. (2017). Sinoatrial node cardiomyocytes derived from human pluripotent cells function as a biological pacemaker. *Nat. Biotechnol.* 35, 56–68. doi: 10.1038/nbt.3745

Qu, J., Kryukova, Y., Potapova, I. A., Doronin, S. V., Larsen, M., Krishnamurthy, G., et al. (2004). MiRP1 modulates HCN2 channel expression and gating in cardiac myocytes. *J. Biol. Chem.* 279, 43497–43502. doi: 10.1074/jbc.M405018200

Rosen, M. R., Brink, P. R., Cohen, I. S., and Robinson, R. B. (2004). Genes, stem cells and biological pacemakers. *Cardiovasc. Res.* 64, 12–23. doi: 10.1016/j.cardiores.2004.05.012

Shlapakova, I. N., Nearing, B. D., Lau, D. H., Boink, G. J. J., Danilo, P., Kryukova, Y., et al. (2010). Biological pacemakers in canines exhibit positive chronotropic response to emotional arousal. *Heart Rhythm* 7, 1835–1840. doi: 10.1016/j.hrthm.2010.08.004

Smits, A. M., van Laake, L. W., den Ouden, K., Schreurs, C., Szuhai, K., van Echteld, C. J., et al. (2009a). Human cardiomyocyte progenitor cell transplantation preserves long-term function of the infarcted mouse myocardium. *Cardiovasc. Res.* 83, 527–535. doi: 10.1093/cvr/cvp146

Smits, A. M., van Vliet, P., Metz, C. H., Korfage, T., Sluijter, J. P., Doevendans, P. A., et al. (2009b). Human cardiomyocyte progenitor cells differentiate into functional mature cardiomyocytes: an *in vitro* model for studying human cardiac physiology and pathophysiology. *Nat. Protoc.* 4, 232–243. doi: 10.1038/nprot.2008.229

Ten Tusscher, K. H. W. J., Noble, D., Noble, P. J., and Panfilov, A. V. (2004). A model for human ventricular tissue. *Am. J. Physiol. Hear Circ. Physiol.* 286, 1573–1589. doi: 10.1152/ajpheart.00794.2003

Ten Tusscher, K. H. W. J., and Panfilov, A. V. (2006). Alternans and spiral breakup in a human ventricular tissue model. *Am. J. Physiol. Hear Circ. Physiol.* 291, H1088–H1100. doi: 10.1152/ajpheart.00109.2006

Toma, C., Pittenger, M. F., Cahill, K. S., Byrne, B. J., and Kessler, P. D. (2002). Human mesenchymal stem cells differentiate to a cardiomyocyte phenotype in the adult murine heart. *Circulation* 105, 93–98. doi: 10.1161/hc0102.101442

Tripathy, S. K., Black, H. B., Goldwasser, E., and Leiden, J. M. (1996). Immune responses to transgene-encoded proteins limit the stability of gene expression after injection of replication-defective adenovirus vectors. *Nat. Med.* 2, 545–550. doi: 10.1038/nm0596-545

Valiunas, V., Kanaporis, G., Valiuniene, L., Gordon, C., Wang, H. Z., Li, L., et al. (2009). Coupling an HCN2-expressing cell to a myocyte creates a two-cell pacing unit. *J. Physiol.* 587, 5211–5226. doi: 10.1113/jphysiol.2009.180505

van Rees, J. B., de Bie, M. K., Thijssen, J., Borleffs, C. J. W., Schalij, M. J., and van Erven, L. (2011). Implantation-related complications of implantable cardioverter-defibrillators and cardiac resynchronization therapy devices: a systematic review of randomized clinical trials. *J. Am. Coll Cardiol.* 58, 995–1000. doi: 10.1016/j.jacc.2011.06.007

Végh, A. M. D., Den Haan, A. D., Cócera Ortega, L., Verkerk, A. O., Sluijter, J. P. G., Bakker, D., et al. (2019). Cardiomyocyte progenitor cells as a functional gene delivery vehicle for long-term biological pacing. *Molecules* 24:181. doi: 10.3390/molecules24010181

Xue, T., Cho, H. C., Akar, F. G., Tsang, S.-Y., Jones, S. P., Marbán, E., et al. (2005). Functional integration of electrically active cardiac derivatives from genetically engineered human embryonic stem cells with quiescent recipient ventricular cardiomyocytes: insights into the development of cell-based pacemakers. *Circulation* 111, 11–20. doi: 10.1161/01.CIR.0000151313.18547.A2

Zwetsloot, P. P., Végh, A. M. D., Jansen of Lorkeers, S. J., van Hout, G. P. J., Currie, G. L., Sena, E. S., et al. (2016). Cardiac stem cell treatment in myocardial infarction: a systematic review and meta-analysis of preclinical studies. *Circ. Res.* 118, 1223–1232. doi: 10.1161/CIRCRESAHA.115.307676

Conflict of Interest: HT and GB report ownership interest in PacingCure B.V.

The remaining authors declare that the research was conducted in the absence of any commercial or financial relationships that could be construed as a potential conflict of interest.

frontiers in Physiology

ORIGINAL RESEARCH
published: 04 March 2021
doi: 10.3389/fphys.2021.592229

Structural and Functional Properties of Subsidiary Atrial Pacemakers in a Goat Model of Sinus Node Disease

Luca Soattin[1]*†, Zoltan Borbas[1,2,3]*†, Jane Caldwell[2,4,5], Brian Prendergast[2‡], Akbar Vohra[1,2], Yawer Saeed[1,2,6], Andreas Hoschtitzky[7,8,9], Joseph Yanni[1], Andrew Atkinson[1], Sunil Jit Logantha[1,10], Balint Borbas[1], Clifford Garratt[1,2], Gwilym Matthew Morris[1,2§] and Halina Dobrzynski[1,11]*§

[1] Division of Cardiovascular Sciences, Faculty of Biology, Medicine and Health, Manchester Academic Health Science Centre, University of Manchester, Manchester, United Kingdom, [2] Manchester Heart Centre, Central Manchester University Foundation Trust, Manchester Academic Health Science Centre, Manchester, United Kingdom, [3] Liverpool Heart and Chest Hospital, Liverpool, United Kingdom, [4] Hull University Teaching Hospitals, Hull, United Kingdom, [5] Hull York Medical School, Hull, United Kingdom, [6] Department of Medicine, Aga Khan University, Karachi, Pakistan, [7] Adult Congenital Heart Disease Unit, Manchester Royal Infirmary, Manchester Academic Health Science Centre, Manchester, United Kingdom, [8] Royal Brompton Hospital, London, United Kingdom, [9] Imperial College London, London, United Kingdom, [10] Liverpool Centre for Cardiovascular Sciences, Department of Cardiovascular and Metabolic Medicine, University of Liverpool, Liverpool, United Kingdom, [11] Department of Anatomy, Jagiellonian University, Krakow, Poland

Edited by:
Gerard J. J. Boink,
University of Amsterdam, Netherlands

Reviewed by:
Tong Liu,
Tianjin Medical University, China
Alexey V. Glukhov,
University of Wisconsin-Madison, United States
Brian Hansen,
The Ohio State University, United States

****Correspondence:***
Luca Soattin
luca.soattin@manchester.ac.uk
Zoltan Borbas
zborbas@gmail.com
Halina Dobrzynski
halina.dobrzynski@manchester.ac.uk

† These authors share first authorship

‡ Deceased

§ These authors share last authorship

Specialty section:
This article was submitted to Cardiac Electrophysiology, a section of the journal Frontiers in Physiology

Received: *06 August 2020*
Accepted: *18 January 2021*
Published: *04 March 2021*

Citation:
Soattin L, Borbas Z, Caldwell J, Prendergast B, Vohra A, Saeed Y, Hoschtitzky A, Yanni J, Atkinson A, Logantha SJ, Borbas B, Garratt C, Morris GM and Dobrzynski H (2021) Structural and Functional Properties of Subsidiary Atrial Pacemakers in a Goat Model of Sinus Node Disease. Front. Physiol. 12:592229. doi: 10.3389/fphys.2021.592229

Background: The sinoatrial/sinus node (SAN) is the primary pacemaker of the heart. In humans, SAN is surrounded by the paranodal area (PNA). Although the PNA function remains debated, it is thought to act as a subsidiary atrial pacemaker (SAP) tissue and become the dominant pacemaker in the setting of sinus node disease (SND). Large animal models of SND allow characterization of SAP, which might be a target for novel treatment strategies for SAN diseases.

Methods: A goat model of SND was developed (n = 10) by epicardially ablating the SAN and validated by mapping of emergent SAP locations through an ablation catheter and surface electrocardiogram (ECG). Structural characterization of the goat SAN and SAP was assessed by histology and immunofluorescence techniques.

Results: When the SAN was ablated, SAPs featured a shortened atrioventricular conduction, consistent with the location in proximity of atrioventricular junction. SAP recovery time showed significant prolongation compared to the SAN recovery time, followed by a decrease over a follow-up of 4 weeks. Like the SAN tissue, the SAP expressed the main isoform of pacemaker hyperpolarization-activated cyclic nucleotide-gated channel 4 (HCN4) and Na^+/Ca^{2+} exchanger 1 (NCX1) and no high conductance connexin 43 (Cx43). Structural characterization of the right atrium (RA) revealed that the SAN was located at the earliest activation [i.e., at the junction of the superior vena cava (SVC) with the RA] and was surrounded by the paranodal-like tissue, extending down to the inferior vena cava (IVC). Emerged SAPs were localized close to the IVC and within the thick band of the atrial muscle known as the crista terminalis (CT).

Conclusions: SAN ablation resulted in the generation of chronic SAP activity in 60% of treated animals. SAP displayed development over time and was located within the previously discovered PNA in humans, suggesting its role as dominant pacemaker in SND. Therefore, SAP in goat constitutes a promising stable target for electrophysiological modification to construct a fully functioning pacemaker.

Keywords: sinus node ablation, sinus node disease, subsidiary atrial pacemaker tissue, paranodal area, SND goat model, site of earliest activation, HCN4

INTRODUCTION

Discovered by Martin Flack and Sir Arthur Keith in 1906, the sinoatrial/sinus node (SAN) is the primary pacemaker of the mammalian heart. Structurally and functionally, the SAN has unique properties, different from those of the working myocardium (Keith and Flack, 1907; Linscheid et al., 2019). The mammalian SAN is a crescent-shaped structure located at the junction of the superior vena cava (SVC) and the right atrium (RA) (Boyett et al., 2000; Dobrzynski et al., 2007). The extent of the SAN shows significant variation among mammalian species. In small laboratory animals, the SAN extends inferiorly and occupies the full thickness of the intercaval region adjacent to the crista terminalis (CT), almost reaching the inferior vena cava (IVC). By contrast, in humans, it is confined to a relatively short portion of the cranial intercaval region abutting the CT and separating from the endocardium by a layer of atrial cardiomyocytes (Boyett et al., 2000). In large mammals, the SAN comprises a wide body and a narrower head and tail (He et al., 1991). Recent reconstruction studies of human specimens have shown a much broader SAN, extending down at the posterolateral RA (Boyett et al., 2000; Dobrzynski et al., 2005, 2013; Sanchez-Quintana et al., 2005; Chandler et al., 2011; Atkinson et al., 2013). Various observations, both in animal models and in human patients, suggested the existence of a larger area involved in pacemaking. We have previously reported a detailed anatomical model of the human SAN (Chandler et al., 2011), showing that it begins at the SVC and extends down the CT about one-third of the distance to the IVC. Despite this, the whole CT in humans is commonly associated with physiological and pathophysiological pacemaking (focal atrial tachycardias) (Boineau et al., 1990; Fedorov et al., 2006; Morris et al., 2013, 2019). It is possible that in *Homo sapiens*, the discrepancy between anatomy and function might be explained by a novel paranodal area (PNA), which we have identified to be located within the CT and adjacent to the SAN (Dobrzynski et al., 2005; Chandler et al., 2009, 2011; Morris et al., 2013). Most importantly, the PNA appears to be much more extensive than the conventional SAN tissue (Monfredi et al., 2010; Chandler et al., 2011). Displaying unique features, the PNA might have a pivotal function in generating hierarchical subsidiary atrial pacemaker (SAP) tissue in pathophysiological conditions, such as the sinus node disease (SND) (Monfredi et al., 2010).

SND, sometimes also known as sick sinus syndrome, is an abnormality of action potential generation within the SAN and electrical impulse propagation from the SAN to its surrounding atrial muscle and/or at the interface of the SAN with the working atrial myocardium (Dobrzynski et al., 2013), causing severe sinus bradycardia, sinus pause, sinus arrest, and sinus exit block (Ferrer, 1968; Kaplan et al., 1973; Wu et al., 1992). The prevalence is in one of every 600 cardiac patients over 65 years of age and accounts for ∼20%–50% of pacemaker implants (Benditt et al., 2011; Mond and Proclemer, 2011). In clinical practice, SND commonly affects the elderly population and is often associated with heart failure, diabetes, and atrial fibrillation (Boyett et al., 2009).

Due to its SAN-like properties, PNA might be an interesting target for attempting the generation of biological atrial pacemakers, which can potentially circumvent specific limitations of electronic pacemakers (Rosen et al., 2004). In fact, in both clinical setting and animal studies, it has been demonstrated that, irrespective of the pathological process, once the SAN has failed, SAP tissue takes over as the leading pacemaker (Randall et al., 1978; Rozanski et al., 1983; Littmann et al., 1990; Kalman et al., 1995; Matsuo et al., 2010).

The ion channel expression within the SAN is highly specialized and very different from the atrial muscle (Chandler et al., 2009). Nodal cells and working myocytes present peculiar differences in terms of morphology, ion channel repertoire, and electrophysiological function. While working myocytes have a stable negative resting membrane potential, mainly due to the inward rectifier K^+ (I_{K1}) current, pacemaker cells show a less negative membrane potential, which arises during the diastole and culminates in a propagating excitation wave (Stanfield et al., 2002; Dhamoon and Jalife, 2005; Choudhury et al., 2015). Although the pacemaking theory remains in part still debated, the SAN automatic electrical activity relies on a combined interaction between specific membrane ion currents (membrane clock) and mechanisms regulating intracellular Ca^{2+}-handling (Ca^{2+} clock) (Boyett, 2009; Lakatta and Maltsev, 2012; Choudhury et al., 2015). A key role in pacemaker function is played by the funny (I_f) current, named after its unusual feature to conduct an inward depolarizing current when activated on hyperpolarization of the resting membrane potential (Brown et al., 1979). I_f is generated by the hyperpolarization-activated cyclic nucleotide-gated (HCN) channel—predominantly HCN4 (Brown et al., 1979; DiFrancesco, 1995; Azene et al., 2003). The second messenger cyclic adenosine monophosphate (cAMP) directly activates HCN channels at the cytoplasmic side (DiFrancesco and Tortora, 1991). β-Adrenergic stimulation elevates intracellular cAMP, increasing the pacemaker slope and positively affecting chronotropy (Scicchitano et al., 2012). By contrast, muscarinic or purinergic stimulation (adenosine-1 receptor) reduces cAMP availability, generating a profound negative chronotropic effect

(Mesirca et al., 2013; Soattin et al., 2017, 2020). Although PNA shows nodal-like features, the ion channel expression in the PNA appears different from both the SAN and the surrounding atrial muscle (Chandler et al., 2009). Some PNA cell clusters express atrial-specific markers, such as connexin-43 (Cx43) and atrial natriuretic peptide (ANP), while others present a nodal-like phenotype. The expression pattern of ion channels in the PNA is intermediate between SAN and atrial muscle; for example, the expression of the cardiac Na^+ channel ($Na_V1.5$) and the inward rectifier K^+ channel ($K_{ir}2.1$) is intermediate between that of the SAN and the atrial tissue (Boyett et al., 2000, 2009).

Currently, little is known in humans and in large animal models about the structural and functional properties of PNA and the subsidiary pacemakers. The relatively poor expression of I_{K1} currents would suggest that these regions may be depolarized, compared to the RA, and therefore capable of pacemaker activity. It is vital to understand their micro-anatomy, histology, electrophysiology, and any possible adaptation the SAP may undergo substituting the SAN. Investigation of the function of the PNA would require the use of a large animal model. Thus, in our study, we developed a goat model of SND by ablating the SAN and characterized the emerging SAP using histology and immunofluorescence methods. Aims of this study were to (1) functionally identify the primary and subsidiary pacemaker regions in the goat RA, (2) structurally characterize these regions, and (3) determine if the PNA exists in this species and evaluate its role as a subsidiary pacemaker in SND.

MATERIALS AND METHODS

Species Used

Adult female goats (n = 15) were used. All animal care and usage was according to standards and practices approved by the University of Manchester Animal Welfare and Ethical Review Body and in accordance with the Animals (Scientific Procedures) Act, 1986 (license number: PPL 40/3364). Flow chart of the research protocol is presented in **Supplementary Material 1.**

Surgical Technique to Expose the Heart and Gross Anatomical Location of the Sinoatrial Node Region

Anesthesia was induced and maintained with isoflurane (1–3%) in 1:2 mixture of oxygen and nitrous oxide, respectively. The goats were ventilated using positive pressure and placed in the left lateral position. Intraoperative monitoring was continuous throughout the procedure by means of pulse oximetry, non-invasive blood pressure monitoring placed on the tail, and single-lead electrocardiogram (ECG). A lateral thoracotomy was performed and the pericardium opened to expose the sulcus terminalis on the posterolateral RA. At this stage, heart rate was recorded as pre-ablation baseline.

Epicardial Pacemaker Implantation

An electronic pacemaker (Medtronic Inc.) was implanted to ensure adequate heart rate in the immediate post-operative period. A bipolar epicardial lead was implanted on the RA appendage and the pulse generator inserted in a subcutaneous pocket. The pacemaker was tested *via* a pacing system analyzer (Medtronic Inc.) and was considered satisfactory if pacing threshold was less than 1.5 V and sensed atrial amplitude >2 mV. For assessment of the SAN/SAP recovery time, programmed extra-stimuli were performed *via* the pacemaker during the follow-up period.

Mapping and Ablation

Mapping the Earliest Activation Within the Sinoatrial Node—Procedure I

Epicardial mapping was performed to determine the site of earliest activation (SEA). A quadripolar ablation catheter (3.5-mm tip; electrode spacing 2, 5, and 2 mm; Biosense Webster) was used to map the epicardial RA in a systematic manner guided by a virtual grid constructed using anatomical landmarks to aid reproducibility (**Supplementary Material 2**). During the mapping process, the RA pacemaker electrode was used as a stable fiducial reference for timing. The earliest local electrogram, preceding the onset of the ECG P-wave, was defined as the SEA. Confirmation of the aforementioned site was obtained by placing the mapping electrode at the putative SEA. Slight shift of the electrode to any direction from the indicated location resulted in a delayed premature local activation time. To display SAN potentials, it was necessary to use a cut-off below 0.5 Hz (Reiffel et al., 1980). In **Supplementary Material 3**, the RAA bipole, proximal mapping bipole, distal mapping bipole, and the surface ECG are represented. Electrograms were acquired using a filtering and preamplifier system (Digitimer Ltd.) and a PowerLab data acquisition system (AD Instruments) at a sampling rate of 1 kHz. Band-pass filters of 0.3–300, 0.1–30, and 30–300 Hz were applied to the surface ECG, mapping electrode, and RA reference electrode, respectively.

Ablation of the Sinoatrial Node

Following identification of the SEA, radiofrequency energy was delivered at the SAN region, utilizing a temperature-controlled, power feedback ablation system (max temperature: 45–50°C, max delivered power: 50–60 W, Boston Scientific Inc.) in experimental goats (n = 10). To avoid premature excessive temperature rise at the catheter tip and allow sufficient radiofrequency energy delivery to the tissue, we applied a continuous irrigation at room temperature of 0.9% saline solution at 17–30 ml/min during the ablation procedure. The earliest atrial activation during spontaneous rhythm was remapped after each ablation, the endpoint for radiofrequency application being a conventional decrease in spontaneous heart rate by 50% and/or the emergence of atrioventricular junctional rhythm (Kalman et al., 1995; **Supplementary Material 4**). Additionally, if the SEA moved away from the accessible epicardial RA (e.g., to the intra-atrial septum or LA), this was an ablation endpoint. In the immediate postoperative period, a pacing rate of 60–80 beats per minute (bpm) was maintained for 24 h. The thoracotomy wound was closed in layers and the animals recovered.

Follow-Up Period

After 24–48 h, the electronic pacemakers were reprogrammed to 30 bpm (demand AAI pacing) to allow the emergence of the intrinsic rhythm. After a further 48 h, once an established intrinsic atrial rhythm had emerged, the pacemakers were reprogrammed to sensing-only mode. All experimental goats were followed up for 4 weeks before procedure II. Single-lead ECGs were recorded weekly. Corrected sinus node recovery time (CSNRT) or SAP recovery time (CART) were determined in the resting conscious state.

Mapping of the Leading Pacemaker–Procedure II

The perioperative steps leading to exposure of the right atrial free wall were the same as during procedure I. Once visualized, the pacing leads were disconnected from the pacemaker generator and a 5-min ECG was recorded, intrinsic pacemaker recovery time (CSNRT or CART) was determined in the anesthetized state, then mapping of the SEA followed. The site of earliest activation was marked with two fine surgical sutures (2 mm cranial and caudal from SEA). In case the SEA had moved away from the site of the SAN identified in procedure I, then the SAN ablation was deemed successful and the animal was analyzed in the SAP group. By contrast, if the SEA was at the same site as the SAN from procedure I, then the animal was analyzed in the recovered SAN (rSN) group (**Supplementary Material 4**).

Methods of Functional Characterization

Surface Electrocardiogram

In the experimental group, following the ablation of the SAN (procedure I), ECGs were recorded every 7 days, over the 4-week follow-up. Leads were placed above the bony prominence on the right and left shoulder and the left hip. Bipolar recordings of 30 s were performed consecutively between left to right shoulder, left hip to left shoulder, and left hip to right shoulder (analogous to human ECG leads I, II, and III, respectively). Then, a continuous 5-min recording was created using the left hip–right shoulder bipole (lead II). The leads were connected through a bioamplifier to an analog–digital converter (PowerLab Data acquisition system, ADInstruments) and displayed on a PC using LabChart software (ADInstruments). Beat-to-beat heart rate was calculated in a consecutive 4 min of recording and cleaned from noise/baseline movement with a combination of digital filtering (1–100 Hz band-pass filter) and by rejecting distorted sections using a semi-automatic method (Beat Classifier, LabChart ADInstruments). The mean PR-interval was calculated from 30 consecutive beats.

Overdrive Pacing, SAN, and SAP Recovery Time

Sinus node recovery time (SNRT) was assessed by RA stimulation through the epicardial electrodes for 30 s at cycle lengths of 600, 500, 450, 400, and 350 ms. Upon cessation of pacing, the interval between the last paced beat and the first return of the sinus beat (SNRT) was measured three times at each cycle length and averaged. CSNRT was calculated as the difference between SNRT and the base sinus cycle length. The longest averaged CSNRT value was considered the maximal CSNRT. The corrected recovery time of the subsidiary pacemaker (CART) was measured using the method described above. CART was assessed every week in the post-ablation period in the conscious animals and during the second SAP mapping procedure under general anesthesia (Narula et al., 1972).

Monitoring the Mean Heart Rate

An implantable loop recorder (Reveal Dx, Medtronic Inc.) was inserted at the end of procedure I in three goats. On the opposite ends of the recorder, there were two electrodes acting as a bipolar recorder, capable of automatically recording a 1-min ECG, when heart rate was either lower than 30 bpm or in the presence of a pause longer than 2 s. The recorder was inserted in a superficial subcutaneous pocket overlying the heart.

Processing of the Right Atrial Tissue With Primary and Subsidiary Atrial Pacemaker Regions

Harvesting and Dissection of the Heart

After *in vivo* experiments (as shown in **Supplementary Material 1**), the goats were again anesthetized with isoflurane (1–3%) in 1:2 mixture of oxygen and nitrous oxide. The heart was exposed through the previous lateral thoracotomy. Following this, the goats were humanely euthanized with a lethal dose of intravenous pentobarbital injection, in accordance with the Home Office Animals (Scientific Procedures) Act, 1986. Immediately after cessation of cardiac activity, the heart, along with the proximal portions of the IVC and SVC, was removed and placed in ice-cold Tyrode solution. The atrial region, where the SAN (ablated and non-ablated) and SAP regions were identified as described above, was dissected. The final preparation contained the pectinate muscle and CT of the RA and intercaval region proximal segments of the SVC and IVC (**Figure 1A**). Before freezing the tissue, the preparations (due to their size) were divided perpendicularly to the CT into two segments for cryosectioning. Preparations were frozen by submerging in isopentane (Sigma-Aldrich), cooled to −50°C in liquid nitrogen, and tissue segments were stored at −80°C.

Cryosectioning

The SAN/PNA/SAP preparations were mounted and sectioned perpendicular to the CT. For each millimeter of the tissue, four consecutive sections at 10 μm (for histology) and 20 consecutive sections at 20 μm thickness (for immunofluorescence staining) were collected and placed in pairs on Superfrost Plus Microscope Slides. Slides were then stored at −80°C.

Histology and Light Microscopy

Masson's trichrome histology staining was used as previously described (Chandler et al., 2009, 2011). For detailed analysis of cell morphology within the RA, PNA, SAN, and SAP, light microscopy was used with a motorized stage (Zeiss) utilizing a high-power magnification (× 63) immersion objective. To delineate the boundaries of the SAN (with PNA region) or SAP regions within the RA, a panoramic automated light microscope

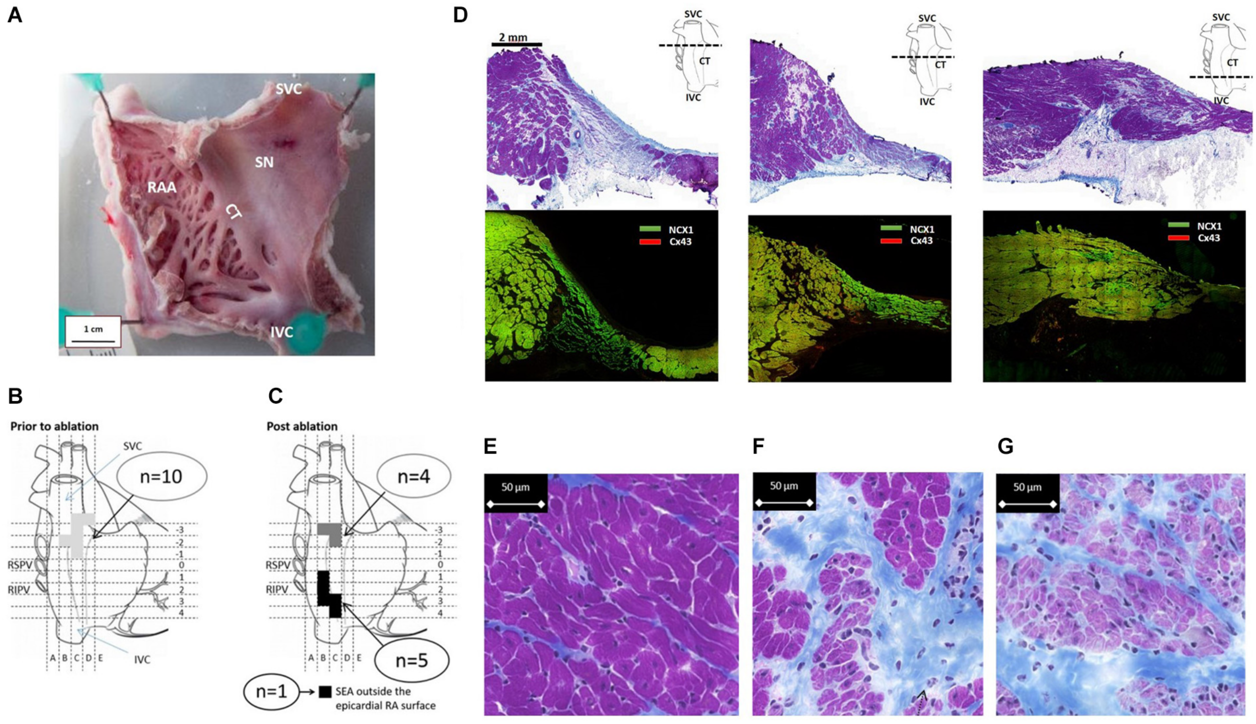

FIGURE 1 | Functional evaluation of the SAP region and the SAN in goats. **(A)** Fresh preparation of the posterior wall of the right atrium (RA) from a control goat. CT, crista terminalis; SAN, sinus node; IVC, inferior vena cava; SVC, superior vena cava. Schematic diagrams **(B,C)** depict the locations of the site of earliest activation during mapping and ablation experiments. **(B)** Location of the site of earliest activation (SEA) prior to ablation (n = 10) is represented by the shaded area (light gray). **(C)** After ablation, the shaded squares correspond to regions of the RA where each individual SEA shifted to. Two well-separated areas are defined: one cluster is close to the IVC/RA junction (black), while the second cluster remained close to the RA/SVC junction (dark gray); n = 6 are shown; one SEA was outside the accessible epicardial RA surface and is therefore presumed to be either on the interatrial septum or left atrium. **(D)** Cross-sections of the SAN and PNA, taken perpendicular to the CT at the levels displayed by the dashed line in the schematic. The top row shows Masson's trichrome (connective tissue stains royal blue, the cytoplasm pink, and the nuclei dark blue). The area of the SAN is identifiable by its pale appearance. The SAN occupies the full thickness of the intercaval region in the superior sections. The PNA appears as a loosely packed bundle, which is localized between the SAN and the working atrial myocardium. The bottom panels in panel **(D)** shows adjacent sections double labeled for NCX1 protein (green) and Cx43 protein (red); SAN tissue is characterized by the presence of NCX1 but the absence of Cx43 and thus appears bight green on these images due to the absence of red signal from Cx43. Regions of nodal tissue can be identified in all sections including the most inferior part of tissue. **(E–G)** High-magnification images of Masson's trichrome-stained atrium **(E)**, PNA **(F)**, and SAN **(G)**. The SAN cells are smaller, paler (stained purple), and embedded in a rich connective tissue (royal blue) compared to the atrial myocardial cells.

was used for this purpose creating a single digital slide at ×20 magnification covering the whole section (3DHISTECH).

Immunofluorescence and Microscopy

Immunofluorescence (IF) experiments were carried out according to an established protocol previously described (Chandler et al., 2009; Yanni et al., 2010; Morris et al., 2013). Slides were removed from the freezer and tissue sections were demarcated with a hydrophobic PAP pen (Sigma-Aldrich). To fix the tissue, sections were then immersed in 10% buffered formalin (Sigma-Aldrich) for 30 min and rinsed three times in 10 mM phosphate buffered saline (PBS). Permeabilization of the cell membrane was achieved with detergent (0.1% Triton-X100, Sigma-Aldrich), followed by repeated rinses in PBS. To reduce non-specific binding, preparations were treated with 1% bovine serum albumin (BSA). Primary antibodies (diluted in a range of 1:50–1:800, **Supplementary Table 1**) were applied within the boundaries of the circles created by the PAP pen and incubated overnight at 4°C. Following the incubation period, antibodies were removed by washing the slides in PBS three times before and after the secondary antibodies were applied (**Supplementary Table 2**) and incubated for 90 min at room temperature. FITC-conjugated antibodies were diluted to 1:100 and Cy3-conjugated ones to 1:400 (**Supplementary Table 3**). Finally, the IF-labeled slides were mounted in VECTASHIELD anti-fade medium (Vector Labs). To avoid fading of the fluorochrome, the slides were kept in a refrigerator at 4°C in the dark after staining. A laser confocal scanning microscope (Zeiss LSM5) and a scanner (with an epifluorescent objective, 3DHISTECH) were used to visualize the immunolabeled sections at a magnification range between ×10 and ×63. Pairs of slides prepared for immunofluorescence and light microscopy histology were compared.

To avoid differences in intensity and specificity of staining, sections were of equal thickness and were stained simultaneously using the same batch of primary and secondary antibodies. Immunolabeled slides were imaged within 1 day, keeping a constant pinhole size and laser energy output (Chandler et al., 2009).

Intracellular Action Potential Recordings

Sharp microelectrodes were used to record intracellular action potentials in one freshly isolated right atrial tissue preparation as previously reported (Logantha et al., 2019). Borosilicate glass capillaries were filled with KCl (3 M) and coupled to an Ag–AgCl holder (Model E45P-M15N, Harvard Apparatus, United Kingdom). Resistance developed by the microelectrode ranged between 20 and 40 MΩ. A disk electrode made of Ag–AgCl (Model E242, Harvard Apparatus, United Kingdom) placed in the bath functioned as ground return. Atrial tissue was superfused with Tyrode buffer solution with 0.05 μM isoprenaline (Sigma-Aldrich) at 37°C, bubbled with a mixture of oxygen/carbon dioxide (95:5).

Data and Statistical Analysis

Data are reported as the mean ± SEM. Statistical significance was evaluated using one-way ANOVA and/or unpaired T-test. In all statistical analyses, p-values < 0.05 were considered statistically significant and indicated with an asterisk (*). Illustrations in **Supplementary Material** were created with BioRender[1].

RESULTS

Sinus Node Ablation and Location of the Subsidiary Atrial Pacemaker Region

In all animals ($n = 10$), the SEA was found in a 1.5-cm^2 area at the SVC/RA junction (**Figure 1B**), where typically the SAN tissue localizes (**Figure 1D**). The endpoint of minimum heart rate 50% reduction and a shift of pacemaker away from the initial SEA were acutely achieved in all animals. There were 40 ± 27 (range: 18–77 min) ablation lesions created and the mean time of power delivery was 27 ± 20 min (range: 5–68 min). After a follow-up of 4 weeks, the location of the leading pacemaker was mapped during the surgical procedure II and the SEA was accurately located in nine out of 10 goats (**Figure 1C**); in one goat, the SEA was not found at the accessible epicardium. In five goats, the SEA locations clustered along the caudal portion of the CT adjacent to the IVC. In four goats, the SEA had not changed location from the pre-ablation SAN pacemaker region. There was a trend to an inverse correlation between time of applied ablation power and the success of the ablation procedure ($p = 0.09$, **Supplementary Material 5**). Histological sections confirmed the ablation of the SAN region in experimental animals. By contrast, the caudal regions were not ablated and contained nodal-like loosely packed cells within the CT (**Supplementary Material 6**).

Histological and Immunofluorescence Features of the Sinus Node

Analysis of serial histological sections showed that the SAN tissue occupies the full thickness of the intercaval region from the endocardium and epicardium abutting the CT (**Figure 1D** and **Supplementary Material 7**). Three Masson's trichrome-stained tissue sections (**Figure 1D**) are from the superior, mid, and inferior parts of the preparation shown in **Figure 1A**. In this species, the SAN is composed of the body (left panel), tail (middle panel), and the nodal-like bundles (right panel) within the PNA. Masson's trichrome-stained tissue section revealed pacemaker tissue, which stains paler when compared with working myocardium (see **Figure 1A**). The SAN appeared lightly stained with Masson's trichrome compared to the surrounding atrial muscle and is embedded in a network of blue connective tissue. This is more obvious at high-power magnification (**Figures 1E–G**). Cell diameter within the SAN was significantly smaller than in the surrounding atrial myocardium (SAN cells 10.1 ± 0.7 μm vs. RA cells 13.8 ± 0.6 μm, $p < 0.05$). Double labeling of the adjacent histological sections for Cx43 and NCX1 by IF technique confirmed the accuracy of the histological location of the SAN, showing a low expression of Cx43 and high expression of NCX1 compared to the atrial muscle (**Supplementary Material 8**). The SAN and PNA, but not the atrial muscle, also expressed HCN4 and reverse was observed for Cx43 (**Figure 2**). Similar histological and IF pattern was observed in $n = 4$ tissues (**Figures 1**, **2** and **Supplementary Table 4**). Semi-quantification of IF images (**Figure 2A**) showed that there was significantly more expression of HCN4 (as well as NCX1) in the SAN and PNA vs. RA, and the reverse is true for Cx43 expression (**Figure 2B**).

Histological and Immunofluorescence Features of the SAP Tissue: The "Witch" Fingers

In control goats, the SAP tissue (similar to the previously described PNA in human) was detected at the interface of the SAN with the RA. As shown in **Figure 1D**, the PNA in the goats localized within the CT close to the SAN and appeared as an extensive structure extending the length of the pacemaker complex caudally as well as dorsally. Masson's trichrome showed inter-digitations or "witch" fingers of nodal-like cells with atrial cells in histological images (**Figure 3A**). IF on the sister section confirmed that these "witch" fingers were indeed of nodal nature by being Cx43 negative and HCN4/NCX1 positive (**Figures 3B,F**).

Figure 4 also shows the "witch" fingers within the CT. Here, the SAP tissue was double-labeled for HCN4 (green) and Cx43 (red) proteins (**Figure 4A**) or NCX1 (red) and Cx43 (green) proteins (**Figure 4B**). The nodal-like cells are positive for HCN4 and NCX1, but negative for Cx43. However, the "witch" fingers were embedded within the Cx43-positive atrial tissue and this is why there is no difference in Cx43 expression between the RA and SAP in ablated animals as shown in **Figure 2B**. HCN4 and NCX1 are significantly higher (**Figure 2B**).

Histological and Immunofluorescence Features of the SAP Tissue: The "Lonely" Islands

In the successful ablation group, the location of the SAP was found in the caudal half of the intercaval region adjacent to the CT. Histological features of the SAP showed similarities with

---

[1] https://biorender.com/

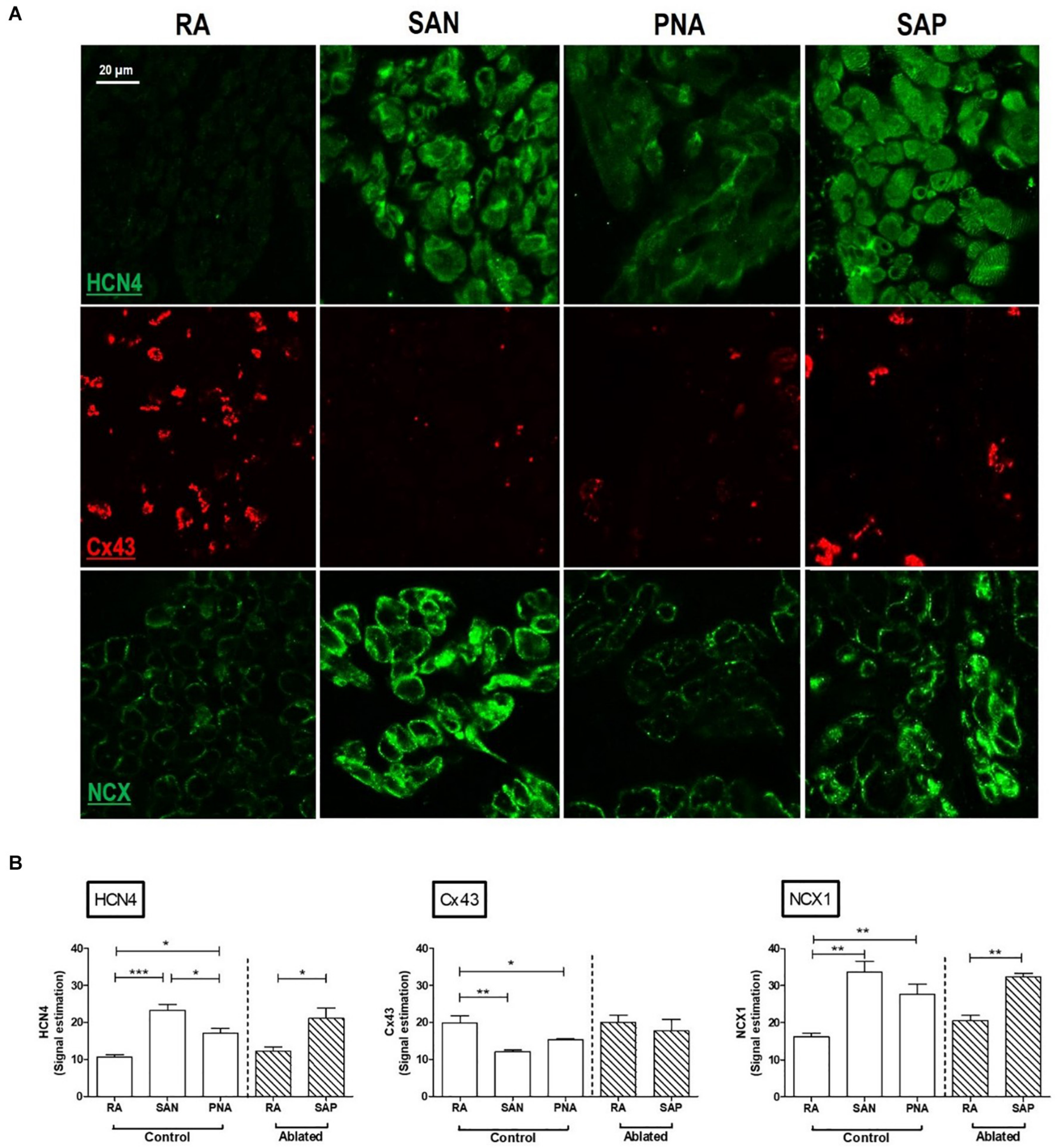

FIGURE 2 | Immunofluorescence comparison of the right atrium with the pacemaker regions. SAN, sinus node; PNA, paranodal area; SAP, subsidiary atrial pacemaker. **(A)** Immunofluorescence (IF) signal is shown for HCN4 protein in green (top rows), Cx43 protein in red (middle rows), and NCX1 protein in green (bottom rows). Sections were taken from RA, SAN, PNA, and SAP. **(B)** Semi-quantification of immunofluorescence signal intensities is shown, allowing comparison among RA, SAN, and PNA in control animals and the RA and SAP (leading pacemaker after ablation) in ablated animals $^{*}p < 0.05$, $^{**}p < 0.01$, and $^{***}p < 0.001$.

the PNA. Embedded in a large mass of atrial myocardium there were thin "lonely" islands of nodal-like cells and an intimate large-surface connection with the surrounding atrial myocytes recognizable at the level of the mapped SEA (**Figures 3C,D**). With IF technique, nodal-like islands showed HCN4/NCX1-positive labeling within Cx43/NCX1-positive labeling within the surrounding myocardium (**Figures 3D,E**).

Features on Recovered SAN Group

The failed ablated SAN tissue was used for electrophysiological investigation (**Figure 5A**). Glass microelectrode analysis of one fresh rSN preparation showed spontaneous diastolic depolarization in post-ablated regions, consistent with its pacemaker activity (**Figure 5B**). Histological analysis confirmed the presence of surviving *clusters* enriched of nodal cells close to

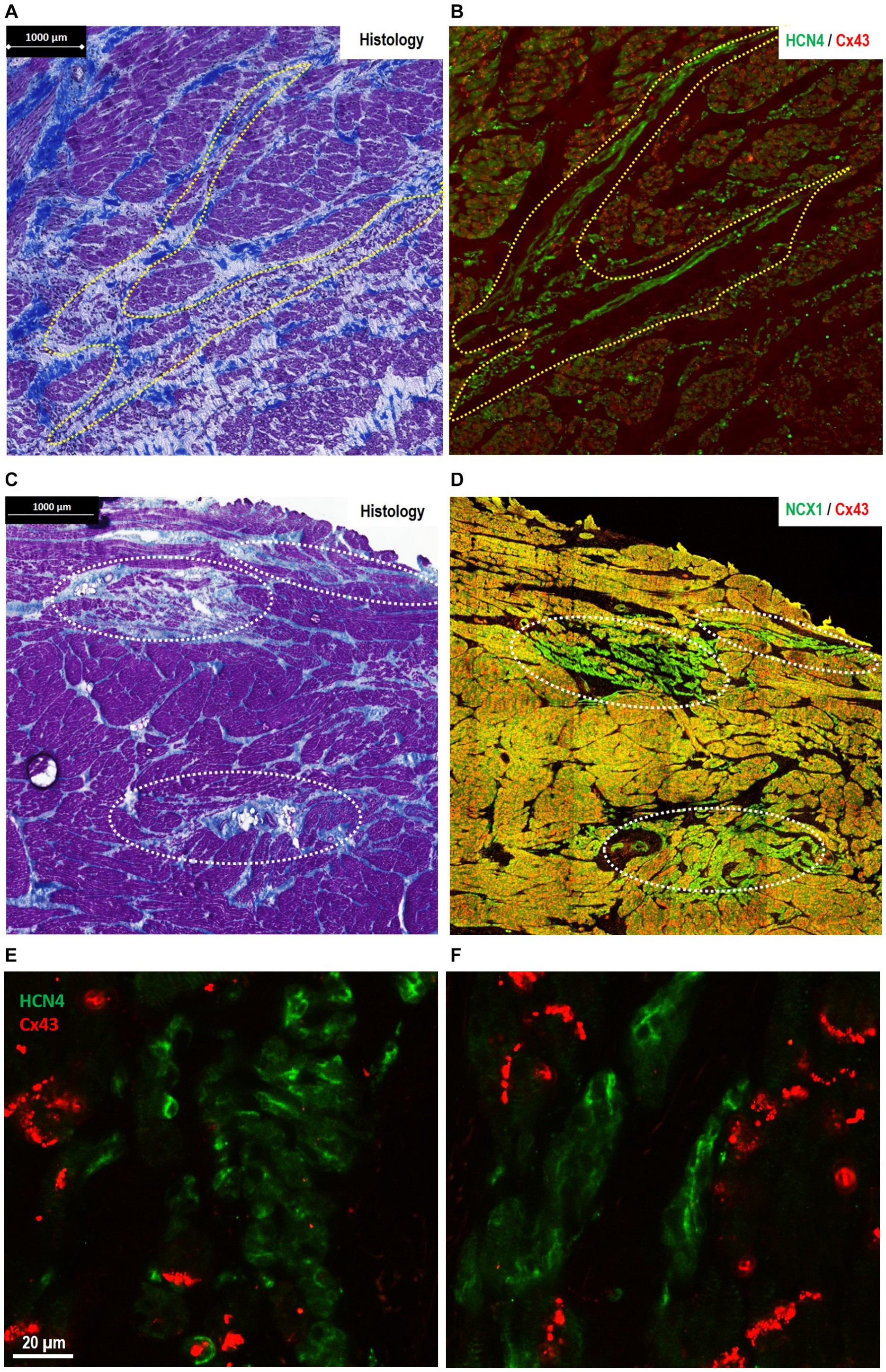

FIGURE 3 | Morphological features of pacemaker/sinus node (SAN)-like tissue in regions other than the primary SAN [where the site of earliest activation (SEA) is detected in healthy hearts]. **(A,B)** The finger-like projections of pacemaker-like tissue in the paranodal area (PNA)—"witch fingers." **(A)** Histology (Masson's trichrome) section of the PNA from a control goat (outlined in yellow, A). **(B)** Location of nodal-like cells are confirmed by immunofluorescence labeling of an adjacent section double labeled for Cx43 (red) and HCN4 (green). The nodal-like "witch" fingers in the PNA are predominantly HCN4$^+$/Cx43$^-$. **(C,D)** Islands of pacemaker-like cells within the subsidiary atrial pacemaker (SAP) regions—"lonely islands." **(C)** Masson's trichrome staining showed that cells with nodal-like phenotype in the SAP region formed well-defined islands in sections taken from the CT. **(D)** These "lonely islands" are confirmed to have "nodal"-like phenotype by IF labeling of an adjacent section Cx43 (red) and NCX1 (green). The nodal-like island SAP are predominantly NCX1$^+$/Cx43$^-$. Corresponding high-power images of sections stained for HCN4/Cx43 are shown for SAP islands in panel **(E)** and "witch fingers" in panel **(F)** demonstrating clusters of HCN4$^+$/Cx43$^-$ pacemaker-like cells (green) among the Cx43$^+$ atrial myocytes (red).

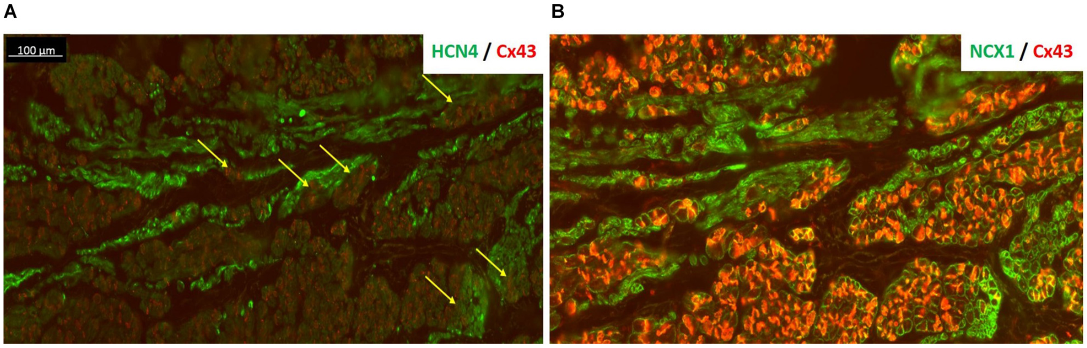

FIGURE 4 | HCN4 is present in the subsidiary atrial pacemaker (SAP) tissue. **(A)** The SAP tissue was double labeled for HCN4 (green) and Cx43 (red) proteins. The nodal-like cells are very distinct within the atrial muscle cells showing a strong HCN4 signal. The very tight contact among SAP and atrial cells is more pronounced in regions shown by the yellow arrows. **(B)** An adjacent section of SAP tissue was double labeled for NCX1 (green) and Cx43 (red). NCX1 labels all myocytes and highlights the region of nodal tissue, which has no red signal for Cx43. Note that in panel **(B)**, Cx43 signal is brighter than panel **(A)** due to the use of a different antibody [rabbit in panel **(B)** rather than mouse in panel **(A)**].

the endocardium (**Figure 5C**). Interesting to notice that despite the visible lesions to the SAN due to ablation, a relatively small nodal tissue appeared working and able to maintain a pacemaker function. On the other hand, in the histological section of successfully ablated animals (**Figure 5D** and **Supplementary Material 6**), the ablated region incorporates a full-thickness radiofrequency ablation lesion extending from the epicardium to endocardium (**Figure 5D**).

By averaging $n = 30$ consecutive beats, PR-intervals were measured in each experiment before (pre) and after (post) the ablation procedure (**Figure 6A**). In the goats where the SEA was mapped in proximity of IVC (SAP group), PR-interval was significantly reduced after ablation (pre 136 ± 24 ms vs. post 117 ± 21 ms, $n = 6$, $p < 0.05$). This was consistent with the anatomically different location of the SAP compared to the SAN. By contrast, no difference was detected among goats in which ablation had failed (rSN group, **Figure 6B**). These data confirmed the assumption that the closer the dominant pacemaker is to the AV node, the shorter the PR-interval will become. In three out of the six SAP goats, the first right atrial component of the P-wave morphology appeared inverted in a caudo-cranial fashion (**Figure 6C**). On the contrary, no change in P-wave morphology was assessed in the rSN group (**Figure 6D**).

Heart Rate During Follow-Up

Following SAN ablation, the mean heart rate (HR) was reduced by ∼50% in the majority of the experiments. Thereafter, atrial rhythm quickly recovered and no statistically significant difference was observed between the pre-ablation and post-ablation state (**Supplementary Material 9**). Among SAP ($n = 6$) and rSN ($n = 4$) goats, no significant difference in HR was observed. However, HR was significantly reduced from week 1 toward week 4 in SAP goats (**Figure 7A**). By contrast, no significant changes were detected in rSN goats' HR (**Figure 7B**).

Recovery Time and Long-Term Events

Overdrive pacing from the RA briefly suppressed the native pacemaker. Corrected SAP recovery time (CART) and corrected SAN recovery time (CSNRT) were calculated both intraoperatively and weekly in the 4-week follow-up period. In the first week, CART became more prolonged in all SAP goats (**Figure 8A**). By contrast, CSNRT was very short (84.3 ± 16.6 ms) at baseline (**Figure 8B**). CART prolongation trend normalized over 2–4 weeks follow-up. Among SAP goats with implanted loop recorders, pauses up to 6 s (**Figure 8C**) and multiple episodes of significant junctional bradycardia (<30 bpm) were detected (**Figure 8D**). These abnormalities were only in the first 3 weeks after ablation, with no pauses or bradycardia <30 bpm detected in the 4th week (data not shown).

DISCUSSION

The majority of SND is idiopathic, and despite the frequency that the condition occurs, the underlying primary pathophysiology of SND is not well known (Kalman and Morris, 2018). Possible pathological processes include fibrosis and degeneration (Morris and Kalman, 2014; Csepe et al., 2015), but recent data have suggested a prominent role of electrical remodeling, *via* changes in ion channel expression and function (D'Souza et al., 2013; Morris and Kalman, 2014). Due to the difficulty of studying disease in humans, large animal models may help translation of fundamental research findings to clinical benefit (Clauss et al., 2019). In this study, we described the SAN morphology (using a traditional histology method) in the goat, which is a common model for atrial arrhythmia. We also present data regarding the physiology and subsidiary pacemaker areas of a large animal model of SND and provide insight into the well-described challenges of sinus node ablation in humans (Marrouche et al., 2002).

The Sinus Node and Paranodal Area of the Goat

Though the anatomically determined SAN in humans is described as a compact node at the junction of the SVC and the RA, the leading cardiac pacemaker can be found at many

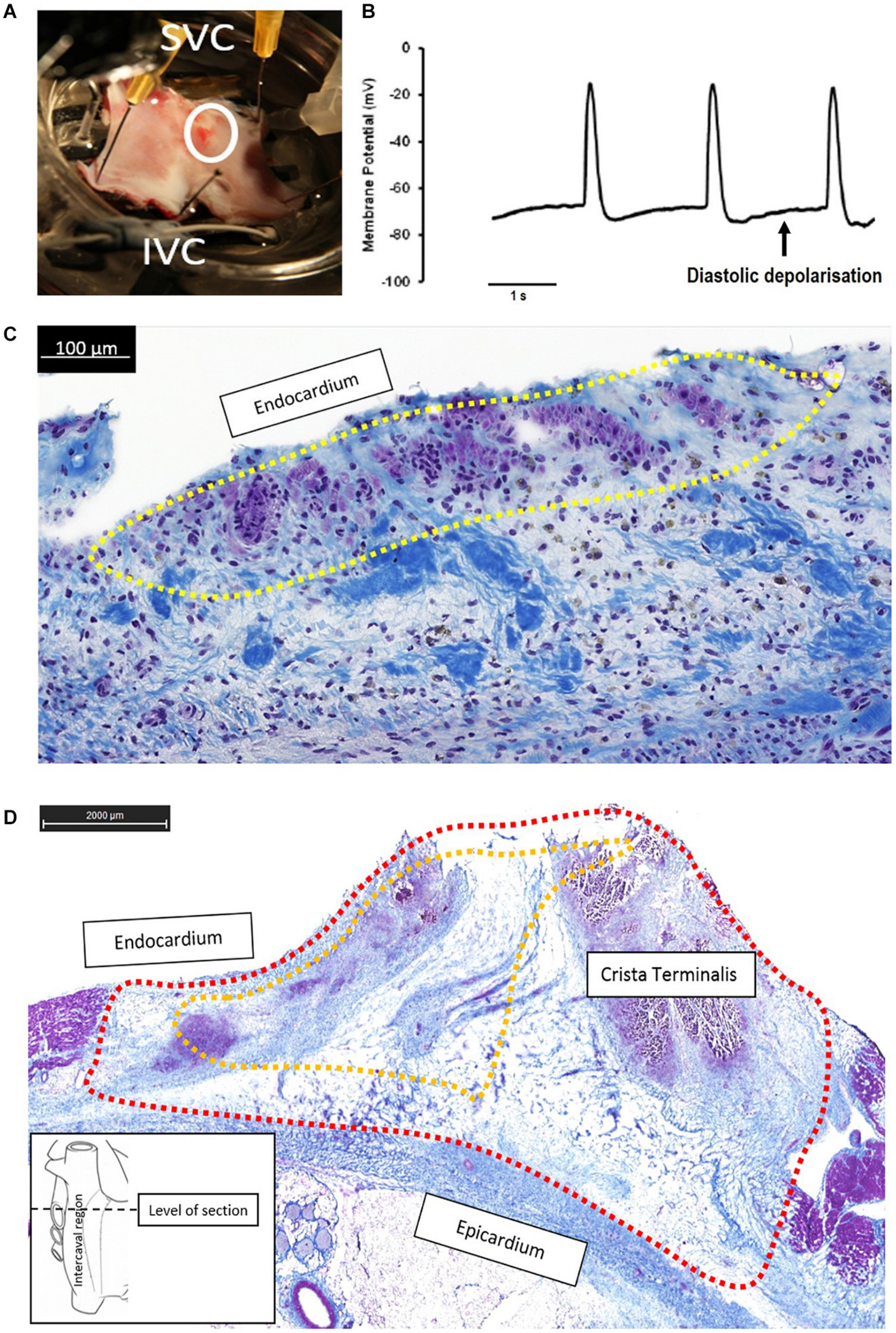

FIGURE 5 | Continued pacemaker function in the failed ablation goat (recovered sinus node, rSN) may be due to small areas of surviving "peripheral" sinus node (SAN) cells that are able to generate diastolic depolarization and thus pacemaker function. **(A)** Right atrial preparation taken from a goat in the rSN group. The ablated area is shown by the white circle, and the superior and inferior vena cava (SVC, IVC) are annotated for orientation. *In vivo* epicardial mapping had confirmed that the leading pacemaker was in this region indicating recovery of SAN function. **(B)** Spontaneous action potentials showing diastolic depolarization was recorded by means of sharp microelectrodes in the region indicated by the white circle in panel **(A)**, the apparently ablated SAN. **(C)** The corresponding histological section (Masson's trichrome) from this region confirms a thin endocardial strip of surviving nodal cells (shown encircled by yellow dotted line) surrounded by a region of fibrosis (blue) and dark nuclei presumably of necrotic cells. In this example, the application of endocardial radiofrequency energy was not able to generate a full-thickness ablation lesion, meaning a small region of endocardial cells were spared. **(D)** Histology section (Masson's trichrome) at the level of the ablated SAN from a successfully ablated animal (subsidiary atrial pacemaker, SAP group). The ablated region is circled by the red dashed line and incorporates a full-thickness radiofrequency ablation lesion extending from the epicardium to the endocardium and encompasses the whole area where the SAN would be expected to be found (yellow dashed line). The section shows dense fibrosis (blue staining) with disrupted myocardium (purple staining) and no identifiable clusters of nodal cells.

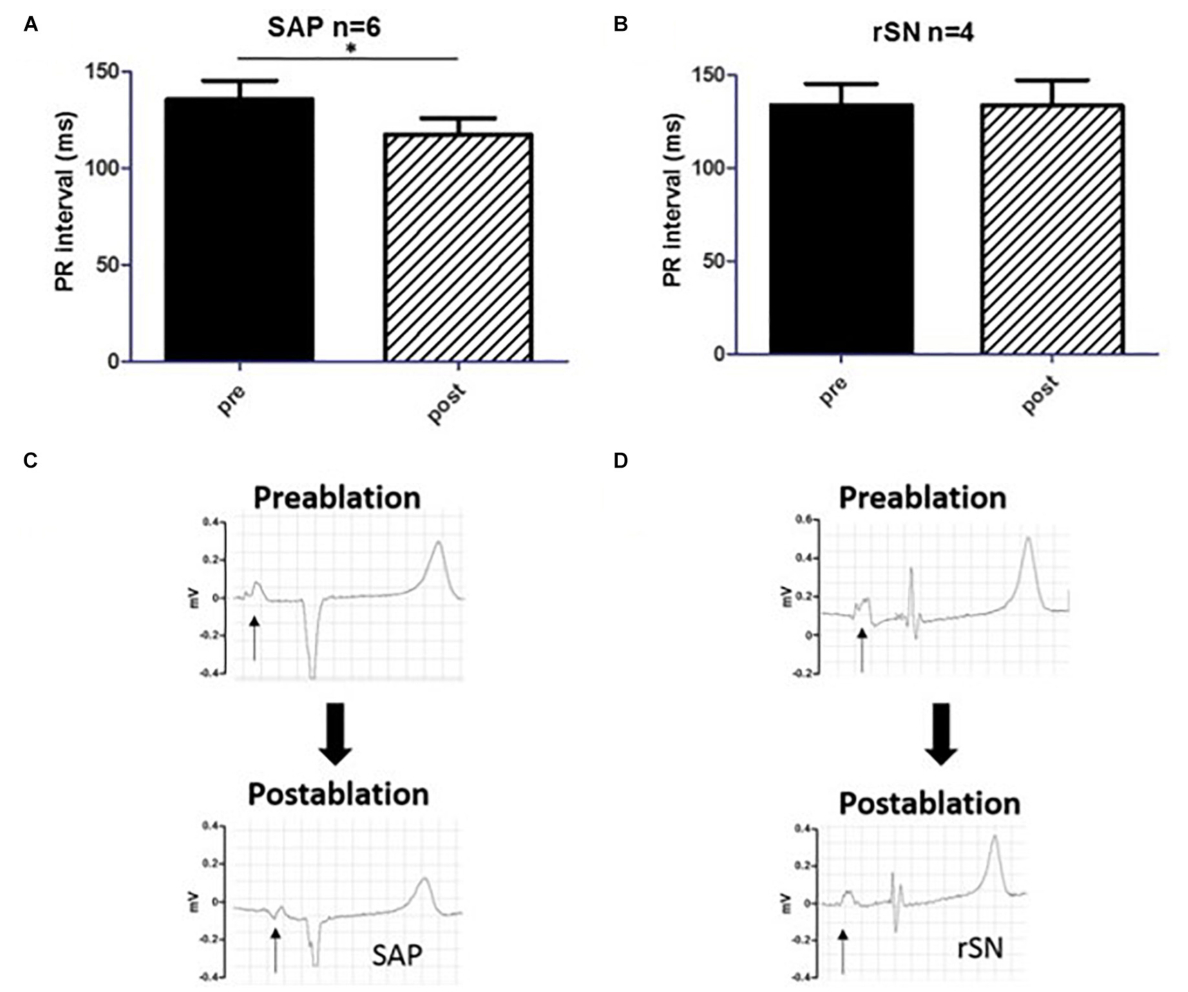

FIGURE 6 | PR-interval and P-wave morphology. **(A,B)** The comparison of PR-intervals pre and post the ablation procedure, respectively. **(A)** The PR-interval shortened significantly in the subsidiary atrial pacemaker (SAP) group (pre vs. post, $p < 0.05$, $n = 6$). **(B)** By contrast, no difference was detectable among the experimental animals [recovered sinus node (rSN), $n = 4$] in which ablation was not successful. **(C,D)** P-wave morphology change before and after the ablation procedure in SAP and rSN goats, respectively. **(C)** Surface electrocardiogram (ECG) shows a significant inversion of the first portion of the P-wave (arrow) post-ablation in the SAP. **(D)** No such shift and P-wave morphology change are observed in rSN goats. $^*P < 0.05$.

points along the CT, from the SVC to the IVC (Boineau et al., 1988). Animal studies proposed that this may be due to leading pacemaker shift within the SAN itself (Boyett et al., 2000), but contemporary optical mapping studies of human heart suggest that this may be at least in part due to discrete exit pathways from the SAN along the CT (Fedorov et al., 2010). It has also been shown that when the SAN is quiescent or removed, SAP tissue outside of the SAN region can act as the primary cardiac pacemaker (Morris et al., 2013).

Histological and molecular investigations have shown that the functional human SAN is extensive, spanning one-third of the distance to the IVC, and is surrounded by paranodal cells, which constitute the PNA, a distinct micro-anatomical structure extending toward the IVC. The PNA occupies a larger area than the anatomic SAN and could function as a subsidiary pacemaker in pathophysiological conditions (Chandler et al., 2009, 2011). Although the goat is a well-established and widely used model of atrial arrhythmia (Wijffels et al., 1995; van Hunnik et al., 2018), the structure and organization of the SAN in goats are not well known. Data presented here show that the SAN was located in the intercaval region occupying its full thickness from the endocardium to the epicardium and running parallel to the cranial half of the CT as in other smaller animals, like rabbits (Coppen et al., 1999; Zhang et al., 2003). As previously described, the SAN in the goat consisted of small and lightly stained cells, when compared to atrial myocytes. Moreover, nodal cells were embedded in a network of connective tissue. In fact, histological observations have shown that the SAN presents a higher collagen content than the surrounding working myocardium (Csepe et al., 2016). As in other species, all nodal cells expressed high levels of HCN4, which is an important component of the pacemaking I_f current (Li et al., 2015). In addition, goat SAN cells expressed NCX1 but not Cx43. It is interesting to notice that the PNA in goats, which we have identified as a possible SAP tissue,

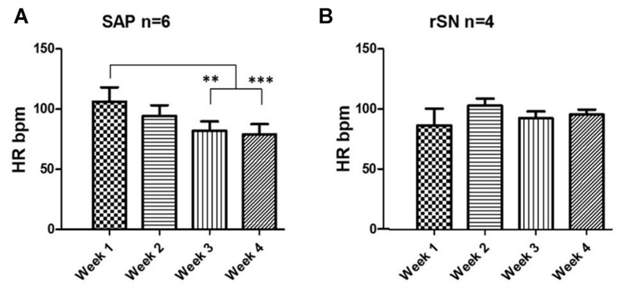

FIGURE 7 | Heart rate change during long-term follow-up. **(A)** Telemetry heart rate (HR) monitoring indicates a significant HR drop in the third and fourth week of the post-ablation in the goats where emergence of subsidiary atrial pacemaker (SAP) was found (repeated measures ANOVA, $^{**}P < 0.001$ and $^{***}P < 0.0001$, respectively). **(B)** No significant change was observed in the goats with recovery of SAN function (rSN).

resembles the same anatomical features as in humans. In fact, the PNA/SAP tissue arises on the endocardial side of the CT, extending caudally beyond the SAN as in the human heart (Chandler et al., 2009, 2011). Moreover, the PNA in the goat heart within the CT contained nodal cells (HCN4- and NCX1-positive and Cx43-negative cells) and atrial myocytes (HCN4-negative and NCX1- and Cx43-positive cells). These data suggest that goats and humans share a similar molecular architecture of the PNA and SAP (Chandler et al., 2009). Finally, whereas the SAN was located close to the SVC, the PNA extended along the entire length of the CT from the SVC to the IVC. Interestingly, we also observed nodal-like islands and inter-digitations within the CT, expressing HCN4- and NCX1-positive cells.

Subsidiary Pacemaker Regions

In order to investigate the primary and subsidiary pacemakers in goats, in this work for the first time, we generated a functional goat model of SND by ablating the SAN at the SEA. Our data show that following successful ablation, subsidiary pacemaker regions (SAP) emerge as the leading pacemaker, and the demonstrated characteristics of these pacemakers share features with human SND; they are inferiorly located within the RA, relatively bradycardic, show increased overdrive suppression, and demonstrate sinus pauses.

Radiofrequency ablation of the SAN is a complex procedure with poor outcomes in humans; in patients with inappropriate sinus tachycardia, the clinical recurrence rate was between 23 and 70% following SAN ablation (Lee et al., 1995; Man et al., 2000; Marrouche et al., 2002; Shen, 2002). As described above, the SAN is an extensive structure, which would require a large area to be ablated. In addition, in humans, the SAN is epicardial, so it's protected from the endocardial application of radiofrequency energy heating effect by a layer of atrial myocardium as well as by the heat sink effect of high blood flow within the central SAN artery (Lee et al., 1995; Yokokawa et al., 2012). If the SAN is successfully ablated, the RA can be driven by a SAP at a slower cycle length (Matsuo et al., 2010). SAP tissue is functionally distinct from the SAN and it gives rise to a slower resting and exertional HR (Ardell et al., 1991). Over time, these differences subside and the SAP pacemaker becomes functionally more similar to the native SAN (Rozanski et al., 1984; Kalman et al., 1995).

However, classic annotation at the voltage maxima has shown to bias activation detection from the atrial tissue and not the smaller intramural structure of the SAN (Parameswaran et al., 2020; Yamabe and Orita, 2020). Both in clinical studies and in optical mapping systems of human atria, SAN activation has been detected by a positioned bipolar catheter as a low-amplitude deflection preceding the sharp atrial upstroke (Gomes et al., 1982; Li et al., 2017). Since the SEA represents the origin of the depolarization wavefront, it should precede any local electrogram and needs to be premature to the onset of the P-wave. In our work, we considered the SEA as the most premature local activation. In fact, the distal bipole showed a premature signal to both the intracardiac reference as well as the onset of the P-wave (**Supplementary Material 3**). It has been also suggested that SAN pathways would contain transitionary tissues (Csepe et al., 2016), which could be mechanistically explained by the presence of discrete pacemaker clusters within the SAN connecting to the surrounding atrial myocardium *via* specialized sinoatrial conduction pathways. Ablation, neuro-hormonal functional suppression, or dysfunction of superior conduction pathways would result in different atrial activation patterns *via* inferior conduction pathways (Li et al., 2017, 2020). It might be possible that activation mapping from the endocardial or epicardial surface could potentially miss the small potentials generated by the SAN prior to exit and capture of the atrial myocardium. This indeed may partly explain the low clinical success rates in SAN ablation. Despite the plurality of mechanisms, we have excluded the conducted regions by directly mapping the supposed SEA regions.

In our experiments, the acute endpoint of 50% reduction in HR or a pacemaker shift away from the epicardially accessible RA was successfully achieved during the radiofrequency ablation procedure in all cases (**Supplementary Table 5**). In all experimental goats, after the ablation procedure, the HR recovered promptly (**Figure 7**). Following this, over the 4 weeks follow-up period, a significant HR reduction was seen in those goats in which the ablation procedure was successful, but not in those in which the SAN ablation had failed. These functional data suggest that in goats, by silencing the SAN, a new leading SAP tissue can take over as the dominant pacemaker. In six experimental goats with successful ablation, five SAP tissues clustered along the caudal part of the CT adjacent to the IVC. These data would confirm previous similar findings in rat and dog, as well as being similar to the leading pacemaker site in humans with SND (Rozanski et al., 1984; Sanders et al., 2004; Morris et al., 2013).

Subsidiary pacemaker tissue was also functionally evaluated by a change in P-wave morphology and PR-interval, which was not detectable in those animals where the ablation procedure had failed. There was a significant shortening of the PR-interval in the SAP group as previously demonstrated in a canine model of SND (Kim et al., 1986). Further analysis of the P-wave before and after the ablation showed profound changes immediately after reaching the endpoint of procedure I. In

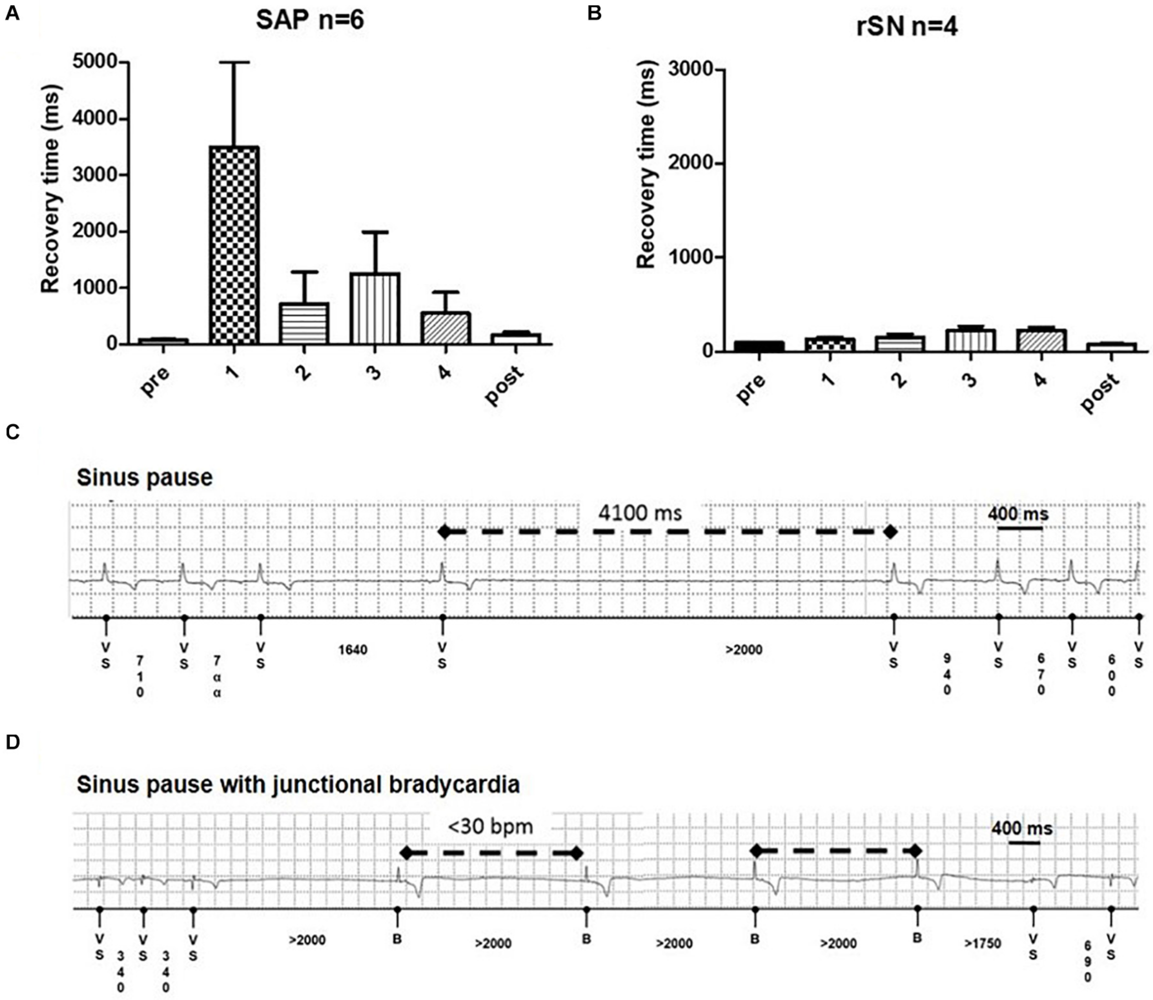

FIGURE 8 | Recovery time and junctional events on long term. **(A)** Subsidiary atrial pacemaker (SAP) group (*n* = 6) shows a profound recovery time (CART) prolongation in the first week of follow-up (**p* = 0.04). **(B)** No such prolongation is detectable in the recovered sinus node (rSN) group (*n* = 4). From the second week on, the CART values diminished and became no longer significantly longer than sinus node recovery time (SNRT) at baseline. Examples of **(C)** profound sinus pause and **(D)** sinus pause with junctional bradycardia in ablated goats.

fact, P-wave duration was significantly prolonged ($p < 0.001$, $n = 10$) in paired T-test (**Supplementary Material 10**). In addition, an inversion of the first portion of the P-wave appeared on the post-ablated ECG traces. A proper evaluation of any caudal–cranial switch activation pattern would have required precordial leads for accessing to the 12-lead ECG. In fact, no such changes in P-wave morphology in SND patients have been described yet. However, the pacemaker shift both in animal models and in healthy humans has been widely demonstrated to show P-wave inversion according to the location of the leading pacemaker (Boineau et al., 1988; Boyett et al., 2000; Monfredi et al., 2010). Moreover, in refractory inappropriate tachycardia patients, aside from the decrease in sinus rate, a typical endpoint during SAN ablation procedure is the inversion of the P-wave axis (Jacobson et al., 2014; Rodriguez-Manero et al., 2017). According to our results, the interatrial conduction time (defined by the first component of the PR-interval) had shortened with the emergence of the SAP, which was in closer distance to the atrioventricular node (**Supplementary Material 11**). Historically, the Bachmann's bundle represents the main interatrial accessory for impulse-conducting pathways. Delay in this pathway may lead to either prolongation of the P-wave or interatrial block. More recently, catheter ablation technology and also the ability of treating specific arrhythmic targets with micro-anatomical precision have shown that, in addition to Bachmann's bundle, other interatrial muscular bundles exist on the inferior atrial surface in close distance to the coronary sinus and also posteriorly in proximity of right upper and lower pulmonary veins (Ho et al., 1999; Chauvin et al., 2000; Kozłowski et al., 2002; Platonov et al., 2002; Mitrofanova et al., 2005). Furthermore, in previous works we showed that, in rat hearts, there is an extensive area in continuation of the SAN head toward the dorsal interatrial groove that appears HCN4 and Cx45 positive, suggesting that the cells in this region may have pacemaker activity (Yamamoto et al., 2006). Together with the SAN, it forms an inverted U-shaped atrial pacemaker complex. It was demonstrated that the isolation of SAN from the interatrial groove did not prevent this region to beat, hence proving that the SEA directly originated from within and its capability as a SAP (Yamamoto et al., 2006). In the goat heart, we confirmed the presence of a very similar inverted U-shaped atrial pacemaker complex, consisting of the compact SAN (located next to the CT) and the PNA area at both of its ends (**Supplementary Material 12**).

Previous works have showed that the new SAP tissue, immediately after the ablation procedure, not only reduces HR but is also readily suppressed by the overdrive pacing (Randall et al., 1982). We observed that the recovery time in the SAP group was longer than in the failed ablation group (rSN), suggesting that the degree of pacemaker suppression was greater in the SND model than in rSN group (**Figures 8A,B**). A prolonged recovery time of the SAN is indeed one diagnostic test for SND (Narula et al., 1972). In addition, the implantable loop recorder analyses showed in SAP goats the presence of transient junctional bradycardia and sinus pauses.

The Heart Rate and the Autonomic Drive

Intrinsic properties of the SAN and the autonomic nervous system modulate HR. Although sympathetic and parasympathetic components were not directly investigated in this manuscript, we did not observe a significant autonomic drive in this context. As also reported in previous studies (Reimann et al., 1972; Hydbring et al., 1999), our data showed that the HR mean in the conscious vs. anesthetized animals was 87 ± 20 bpm and 84 ± 15 bpm ($n = 15$), respectively. Although HR mean did not vary significantly, HR variation revealed interesting differences. Under isoflurane, the beat- to- beat rate was uniform with a narrow deviation around the mean HR. By contrast, HR recorded in conscious animals showed a more dispersed distribution (**Supplementary Material 13**). General anesthesia depresses both cardiac parasympathetic and sympathetic drives resulting in a decreased HR variability (Vicenzi et al., 1995; Toader et al., 2011). ECGs in conscious animals were recorded in the presence of human operators, who might affect profoundly (observer effect) the autonomic balance of each individual goat (Kovacs et al., 2014). In the first post-operative 48 h, ECG recordings were unsuitable for valid analysis since the animals required artificial pacing for stabilizing rhythm. After the goats became independent from the pacemaker, HR was also evaluated by telemetry to observe HR changes over the course of 4 weeks. By comparing telemetry data with 4-min ECG recordings, we performed a linear regression analysis: unlike in the goats with an intact SAN, no strong correlation between HR assessed under general anesthesia was found. However, the 4-min conscious HR and the pacemaker telemetry data showed a significant correlation (**Supplementary Material 14**). Since no change in HR between anesthetized successfully ablated animals before and after 4 weeks procedure I was observed, we interpreted these findings as a SAP development over time as leading pacemaker. Lack of such a "maturation" of SAP tissue would lead to a significant lower heart rate in anesthetized animals, where parasympathetic and sympathetic components are abolished by general anesthesia. Also, we detected a significant tendency in reducing HR over time in conscious ablated animals.

Insights Into Mechanisms for the Failure of Sinus Node Ablation

In six goats, the SAN was successfully ablated (described above). The remaining four goats had their SEA in an area identical to where all the pre-ablation leading pacemakers had been situated indicating ablation failure. In the rSN group, surviving islands of the SAN tissue were found on histological analysis (**Figure 6C**) and regions were found that showed a defined diastolic depolarization (**Figure 6B**). The aim of these observations was not to identify the "leading pacemaker" site of the SAN but just an interrogation of the ablated area for spontaneous action potentials. It was previously shown that moving away from the leading pacemaker, nodal action potentials present hyperpolarized membrane potentials, a longer cycle length, and change in action potential duration in transitional tissue and especially in the presence of "peripheral nodal cells" (Boyett et al., 1999, 2000). This would possibly explain the morphological features of the action potentials in our recording. Functionally, these small regions of surviving tissue were able to provide normal physiological pacemaker function with normal heart rate and minimal overdrive suppression (**Figure 8**).

The total ablated area within each experimental animal did not change, but we observed that in the failed ablated goats (rSN), the ablation time was greater when compared to the successful ablation (SAP) (**Supplementary Material 5**). We did not have force-sensing capability in the ablation catheter, so it may be that in the rSN group, the initial ablation lesions were ineffective and subsequent radiofrequency delivery was inhibited by tissue edema (Kolandaivelu et al., 2010; Yokokawa et al., 2011). In ablated animals, the SAN appeared completely and clearly fibrotic in histological sections. On the other hand, sections at the caudal level revealed that there was no change in the PNA structure between control and ablated goats (**Supplementary Material 6**). In this work, we were able to map the SEA in nine out of ten animals. In one goat, no signal was found to be premature both to the intracardiac reference electrode and to the onset of the P-wave on the surface ECG. This event could be explained by a new SEA, which emerged from the inter-atrial septum or from the left atrium (LA), which we were unable to map, as we did not have access to the LA.

STUDY LIMITATIONS

Detailed investigation of the molecular architecture at mRNA level was limited by availability of primers for goat tissue and at protein level due to lack of specific antibodies.

In order to comply ethical and animal welfare, control animals were euthanized after locating the SEA in the SAN (procedure I). Thus, there has been no possibility to compare the follow-up in successful ablated animals with the controls.

In our microelectrode experiment, the simple superfusion was not strictly physiological. Thus, it would probably lead to transmural ischemia and increase in spontaneous beating cycle length. However, presented data aimed to show pacemaker potentials from within the ablated area of "failed ablation" animals to demonstrate qualitatively that there could be surviving, functioning pacemaker cells.

In this study, we could not rule out a change in SAN exit pathways; this would be impossible to do without optical mapping. However, a change in HR would be unlikely if it were only the exit to be ablated rather than the nodal tissue. Moreover, even though we directly mapped the SEA and not the conducted regions from the exit pathways, we could not exclude that small SAN potentials have not been missed. However, it is less likely with epicardial mapping than endocardial mapping.

CONCLUSION

In this study, we generated a detailed description of the SAN region in goats and generated a model of SND in a large animal by ablating the SAN by applying radiofrequency energy. Moreover, the model allowed to map not only the SAN but also the PNA and the SAP tissues. Through histological and IF imaging, we revealed the presence of "nodal-like" clusters within the CT. These nodal clusters might have a key role as subsidiary pacemakers in pathophysiological conditions, becoming the dominant cardiac pacemaker. In addition, by expressing a mixture of an intermediate pattern of currents within the CT, similar to those typical of the SAN or RA, the SAP tissues might be prone to ectopic activity (Kalman et al., 1998; Tellez et al., 2006). Our model provides insight into the reasons for the difficulty and frequent failure of SAN ablation in humans. Indeed, in some goats, we demonstrated the persistence of small islands of SAN tissue, which were sufficient to support continued normal SAN function.

DATA AVAILABILITY STATEMENT

The raw data supporting the conclusions of this article will be made available by the authors, without undue reservation.

ETHICS STATEMENT

The animal study was reviewed and approved by the University of Manchester Animal Welfare and Ethical Review Body in accordance with the "Animals (Scientific procedures) Act, 1986." Written informed consent was obtained from the owners for the participation of their animals in this study.

AUTHOR CONTRIBUTIONS

LS: planning and manuscript writing of manuscript; re-analyzing data, creating, formatting and modifying figures and illustrations; discussion with senior authors (HD and GM) on format of manuscript and figures; incorporating all authors comments into final draft; and submitting manuscript. ZB: planning and execution of large animals' sinus node ablation and subsidiary pacemaker mapping; carry out all *in vivo* electrophysiology and all *ex vivo* histology and immunohistochemistry experiments; analyzing all data and performing statistics; and producing initial figures and initiating writing of manuscript. JC: co-PI on funding; supervising ZB to carry out *in vivo* experiments; and contributing to analysis of data. BP, AV, AH, and YS: helping to plan and/or carry out *in vivo* electrophysiology experiments. YS, JY, and AA: helping with histology and proteins experiments. SL: carry out *ex vivo* electrophysiology experiments. BB: helping with initial draft of manuscript and figures. CG: holding licence for large animal research; co-PI on funding; supervising ZB with vivo experiments. GM: contributing to planning and writing of manuscript, re-analyzing, and formatting of figures and illustrations. HD: conceiving research; PI on funding; supervising ZB, AA, JY, and SL; and contribute to planning and writing of manuscript, re-analyzing, formatting of figures and illustrations. All authors approved the manuscript and data supplement.

FUNDING

This work was supported by the *British Heart Foundation*, grants numbers RG/18/2/33392 and FS/18/47/33669 and the *Leducq Foundation*, grant number 19CVD03.

ACKNOWLEDGMENTS

The authors would like to express their thankfulness to *Boston Scientific* and *Medtronic Inc*., for providing key elements of the pacing and ablation setup. The authors would also like to thank Mark R. Boyett for his valuable comments and valuable discussions over the course of the study.

SUPPLEMENTARY MATERIAL

The Supplementary Material for this article can be found online at: https://www.frontiersin.org/articles/10.3389/fphys.2021.592229/full#supplementary-material

REFERENCES

Ardell, J. L., Randall, W. C., Pomeroy, G., Lawton, M., and Kim, T. (1991). Autonomic regulation of subsidiary atrial pacemakers during exercise. *J. Appl. Physiol.* 70, 1175–1183. doi: 10.1152/jappl.1991.70.3.1175

Atkinson, A. J., Logantha, S. J., Hao, G., Yanni, J., Fedorenko, O., and Sinha, A. (2013). Functional, anatomical, and molecular investigation of the cardiac conduction system and arrhythmogenic atrioventricular ring tissue in the rat heart. *J. Am. Heart Assoc.* 2:e000246.

Azene, E. M., Xue, T., and Li, R. A. (2003). Molecular basis of the effect of potassium on heterologously expressed pacemaker (HCN) channels. *J. Physiol.* 547, 349–356. doi: 10.1113/jphysiol.2003.039768

Benditt, D. G., Sakaguchi, S., Lurie, K. G., and Lu, F. (2011). *@Sinus Node Dysfunction*. Berlin: Springer.

Boineau, J. P., Canavan, T. E., Schuessler, R. B., Cain, M. E., Corr, P. B., and Cox, J. L. (1988). Demonstration of a widely distributed atrial pacemaker complex in the human heart. *Circulation* 77, 1221–1237. doi: 10.1161/01.cir.77.6.1221

Boineau, J. P., Schuessler, R. B., Canavan, T. E., Corr, P. B., Cain, M. E., and Cox, J. L. (1990). The human atrial pacemaker complex. *J. Electrocardiol.* 22, 189–197. doi: 10.1016/s0022-0736(07)80122-1

Boyett, M. R. (2009). 'And the beat goes on.' the cardiac conduction system: the wiring system of the heart. *Exp. Physiol.* 94, 1035–1049. doi: 10.1113/expphysiol.2009.046920

Boyett, M. R., Honjo, H., and Kodama, I. (2000). The sinoatrial node, a heterogeneous pacemaker structure. *Cardiovasc. Res.* 47, 658–687. doi: 10.1016/s0008-6363(00)00135-8

Boyett, M. R., Honjo, H., Yamamoto, M., Nikmaram, M. R., Niwa, R., and Kodama, I. (1999). Downward gradient in action potential duration along conduction path in and around the sinoatrial node. *Am. J. Physiol.* 276, H686–H698.

Boyett, M. R., Tellez, J. O., and Dobrzynski, H. (2009). "The sinoatrial node - its complex structure and unique ion channel gene programme," in *Cardiac Electrophysiology: from Cell to Brdside*, ed. D. P. Zipes and J. Jalife. Amsterdam: Elsevier

Brown, H. F., DiFrancesco, D., and Noble, S. J. (1979). How does adrenaline accelerate the heart? *Nature* 280, 235–236. doi: 10.1038/280235a0

Chandler, N. J., Greener, I. D., Tellez, J. O., Inada, S., Musa, H., and Molenaar, P. (2009). Molecular architecture of the human sinus node: insights into the function of the cardiac pacemaker. *Circulation* 119, 1562–1575. doi: 10.1161/circulationaha.108.804369

Chandler, N., Aslanidi, O., Buckley, D., Inada, S., Birchall, S., and Atkinson, A. (2011). Computer three-dimensional anatomical reconstruction of the human sinus node and a novel paranodal area. *Anat. Rec.* 294, 970–979. doi: 10.1002/ar.21379

Chauvin, M., Shah, D. C., Haissaguerre, M., Marcellin, L., and Brechenmacher, C. (2000). The anatomic basis of connections between the coronary sinus musculature and the left atrium in humans. *Circulation* 101, 647–652. doi: 10.1161/01.cir.101.6.647

Choudhury, M., Boyett, M. R., and Morris, G. M. (2015). Biology of the sinus node and its disease. *Arrhythm. Electrophysiol. Rev.* 4, 28–34.

Clauss, S., Bleyer, C., Schuttler, D., Tomsits, P., Renner, S., and Klymiuk, N. (2019). Animal models of arrhythmia: classic electrophysiology to genetically modified large animals. *Nat. Rev. Cardiol.* 16, 457–475. doi: 10.1038/s41569-019-0179-0

Coppen, S. R., Kodama, I., Boyett, M. R., Dobrzynski, H., Takagishi, Y., and Honjo, H. (1999). Connexin45, a major connexin of the rabbit sinoatrial node, is co-expressed with connexin43 in a restricted zone at the nodal-crista terminalis border. *J. Histochem. Cytochem.* 47, 907–918. doi: 10.1177/002215549904700708

Csepe, T. A., Kalyanasundaram, A., Hansen, B. J., Zhao, J., and Fedorov, V. V. (2015). Fibrosis: a structural modulator of sinoatrial node physiology and dysfunction. *Front. Physiol.* 6:37.

Csepe, T. A., Zhao, J., Hansen, B. J., Li, N., Sul, L. V., and Lim, P. (2016). Human sinoatrial node structure: 3D microanatomy of sinoatrial conduction pathways. *Prog. Biophys. Mol. Biol.* 120, 164–178. doi: 10.1016/j.pbiomolbio.2015.12.011

D'Souza, A., Bucchi, A., Johnsen, A., Monfredi, O., Logantha, S., and Prehar, S. (2013). Downregulation of HCN4 and the pacemaker current (If) underlies exercise training-induced sinus bradycardia. *Circulation* 128:A11048.

Dhamoon, A. S., and Jalife, J. (2005). The inward rectifier current (IK1) controls cardiac excitability and is involved in arrhythmogenesis. *Heart Rhythm* 2, 316–324. doi: 10.1016/j.hrthm.2004.11.012

DiFrancesco, D. (1995). The onset and autonomic regulation of cardiac pacemaker activity: relevance of the f current. *Cardiovasc. Res.* 29, 449–456. doi: 10.1016/s0008-6363(96)88518-x

DiFrancesco, D., and Tortora, P. (1991). Direct activation of cardiac pacemaker channels by intracellular cyclic AMP. *Nature* 351, 145–147. doi: 10.1038/351145a0

Dobrzynski, H., Anderson, R. H., Atkinson, A., Borbas, Z., D'Souza, A., and Fraser, J. F. (2013). Structure, function and clinical relevance of the cardiac conduction system, including the atrioventricular ring and outflow tract tissues. *Pharmacol. Ther.* 139, 260–288. doi: 10.1016/j.pharmthera.2013.04.010

Dobrzynski, H., Boyett, M. R., and Anderson, R. H. (2007). New insights into pacemaker activity: promoting understanding of sick sinus syndrome. *Circulation* 115, 1921–1932. doi: 10.1161/circulationaha.106.616011

Dobrzynski, H., Li, J., Tellez, J., Greener, I. D., Nikolski, V. P., and Wright, S. E. (2005). Computer three-dimensional reconstruction of the sinoatrial node. *Circulation* 111, 846–854. doi: 10.1161/01.cir.0000152100.04087.db

Fedorov, V. V., Glukhov, A. V., Chang, R., Kostecki, G., Aferol, H., and Hucker, W. J. (2010). Optical mapping of the isolated coronary-perfused human sinus node. *J. Am. Coll. Cardiol.* 56, 1386–1394. doi: 10.1016/j.jacc.2010.03.098

Fedorov, V. V., Hucker, W. J., Dobrzynski, H., Rosenshtraukh, L. V., and Efimov, I. R. (2006). Postganglionic nerve stimulation induces temporal inhibition of excitability in rabbit sinoatrial node. *Am. J. Physiol. Heart Circ. Physiol.* 291, H612–H623.

Ferrer, M. I. (1968). The sick sinus syndrome in atrial disease. *JAMA* 206, 645–646. doi: 10.1001/jama.206.3.645

Gomes, J. A., Kang, P. S., and El-Sherif, N. (1982). The sinus node electrogram in patients with and without sick sinus syndrome: techniques and correlation between directly measured and indirectly estimated sinoatrial conduction time. *Circulation* 66, 864–873. doi: 10.1161/01.cir.66.4.864

He, B. M., Tan, Y. X., Cheng, M., and Cui, Y. Q. (1991). The surgical anatomy of the sinoatrial node. *Surg. Radiol. Anat.* 13, 123–128. doi: 10.1007/bf01623885

Ho, S. Y., Sanchez-Quintana, D., Cabrera, J. A., and Anderson, R. H. (1999). Anatomy of the left atrium: implications for radiofrequency ablation of atrial fibrillation. *J. Cardiovasc. Electrophysiol.* 10, 1525–1533. doi: 10.1111/j.1540-8167.1999.tb00211.x

Hydbring, E., Cvek, K., and Olsson, K. (1999). Telemetric registration of heart rate and blood pressure in the same unrestrained goats during pregnancy, lactation and the non-pregnant, non-lactating period. *Acta Physiol. Scand.* 165, 135–141. doi: 10.1046/j.1365-201x.1999.00498.x

Jacobson, J. T., Kraus, A., Lee, R., and Goldberger, J. J. (2014). Epicardial/endocardial sinus node ablation after failed endocardial ablation for the treatment of inappropriate sinus tachycardia. *J. Cardiovasc. Electrophysiol.* 25, 236–241. doi: 10.1111/jce.12318

Kalman, J. M., and Morris, G. M. (2018). "Sinus node disease: pathophysiology and natural history," in *the ESC textbook of Cardiovascular Medicine*, 3rd Edn, eds A. J. Camm, T. F. Luscher, G. Maurer, and P. W. Serruys (Oxford: Oxford University Press).

Kalman, J. M., Lee, R. J., Fisher, W. G., Chin, M. C., Ursell, P., and Stillson, C. A. (1995). Radiofrequency catheter modification of sinus pacemaker function guided by intracardiac echocardiography. *Circulation* 92, 3070–3081. doi: 10.1161/01.cir.92.10.3070

Kalman, J. M., Olgin, J. E., Karch, M. R., Hamdan, M., Lee, R. J., and Lesh, M. D. (1998). "Cristal Tachycardias": origin of right atrial tachycardias from the crista terminalis identified by intracardiac echocardiography. *J. Am. Coll. Cardiol.* 31, 451–459. doi: 10.1016/s0735-1097(97)00492-0

Kaplan, B. M., Langendorf, R., Lev, M., and Pick, A. (1973). Tachycardia-bradycardia syndrome (so-called "sick sinus syndrome"). *Am. J. Cardiol.* 31, 497–508. doi: 10.1016/0002-9149(73)90302-0

Keith, A., and Flack, M. (1907). The form and nature of the muscular connections between the primary divisions of the vertebrate heart. *J. Anat. Physiol.* 41, 172–189.

Kim, K. S., Ardell, J. L., Randall, W. C., Pomeroy, G., and Calderwood, D. (1986). Cardiac responses to exercise in the dog before and after destruction of the sinoatrial node. *Eur. J. Appl. Physiol. Occup. Physiol.* 55, 253–258. doi: 10.1007/bf02343796

Kolandaivelu, A., Zviman, M. M., Castro, V., Lardo, A. C., Berger, R. D., and Halperin, H. R. (2010). Noninvasive assessment of tissue heating during cardiac radiofrequency ablation using MRI thermography. *Circ. Arrhythm. Electrophysiol.* 3, 521–529. doi: 10.1161/circep.110.942433

Kovacs, L., Jurkovich, V., Bakony, M., Szenci, O., Poti, P., and Tozser, J. (2014). Welfare implication of measuring heart rate and heart rate variability in dairy cattle: literature review and conclusions for future research. *Animal* 8, 316–330. doi: 10.1017/s1751731113002140

Kozłowski, D., Kamiński, R., Piwko, G., Gawrysiak, M., Owerczuk, A., and Piszczatowska, G. (2002). Preliminary study of external interatrial muscle fascicles. *Folia Morphologica* 61, 97–101.

Lakatta, E. G., and Maltsev, V. A. (2012). Rebuttal: what I(f) the shoe doesn't fit? "The funny current has a major pacemaking role in the sinus node". *Heart Rhythm* 9, 459–460. doi: 10.1016/j.hrthm.2011.09.024

Lee, R. J., Kalman, J. M., Fitzpatrick, A. P., Epstein, L. M., Fisher, W. G., and Olgin, J. E. (1995). Radiofrequency catheter modification of the sinus node for "inappropriate" sinus tachycardia. *Circulation* 92, 2919–2928. doi: 10.1161/01.cir.92.10.2919

Li, N., Csepe, T. A., Hansen, B. J., Dobrzynski, H., Higgins, R. S., and Kilic, A. (2015). Molecular mapping of sinoatrial node HCN channel expression in the human heart. *Circ Arrhythm. Electrophysiol.* 8, 1219–1227. doi: 10.1161/circep.115.003070

Li, N., Hansen, B. J., Csepe, T. A., Zhao, J., Ignozzi, A. J., and Sul, L. V. (2017). Redundant and diverse intranodal pacemakers and conduction pathways protect the human sinoatrial node from failure. *Sci. Transl. Med.* 9:eaam5607 doi: 10.1126/scitranslmed.aam5607

Li, N., Kalyanasundaram, A., Hansen, B. J., Artiga, E. J., Sharma, R., and Abudulwahed, S. H. (2020). Impaired neuronal sodium channels cause intranodal conduction failure and reentrant arrhythmias in human sinoatrial node. *Nat. Commun.* 11:512.

Linscheid, N., Logantha, S., Poulsen, P. C., Zhang, S., Schrolkamp, M., and Egerod, K. L. (2019). Quantitative proteomics and single-nucleus transcriptomics of the sinus node elucidates the foundation of cardiac pacemaking. *Nat. Commun.* 10:2889.

Littmann, L., Svenson, R. H., Gallagher, J. J., Bharati, S., Lev, M., Linder, K. D., et al. (1990). Modification of sinus node function by epicardial laser irradiation in dogs. *Circulation* 81, 350–359. doi: 10.1161/01.cir.81.1.350

Logantha, S., Kharche, S. R., Zhang, Y., Atkinson, A. J., Hao, G., Boyett, M. R., et al. (2019). Sinus node-like pacemaker mechanisms regulate ectopic pacemaker activity in the adult rat atrioventricular ring. *Sci. Rep.* 9:11781.

Man, K. C., Knight, B., Tse, H. F., Pelosi, F., Michaud, G. F., and Flemming, M. (2000). Radiofrequency catheter ablation of inappropriate sinus tachycardia guided by activation mapping. *J. Am. Coll. Cardiol.* 35, 451–457. doi: 10.1016/s0735-1097(99)00546-x

Marrouche, N. F., Beheiry, S., Tomassoni, G., Cole, C., Bash, D., and Dresing, T. (2002). Three-dimensional nonfluoroscopic mapping and ablation of inappropriate sinus tachycardia. Procedural strategies and long-term outcome. *J. Am. Coll. Cardiol.* 39, 1046–1054. doi: 10.1016/s0735-1097(02)01703-5

Matsuo, S., Yamane, T., Date, T., and Yoshimura, M. (2010). Spontaneously isolated sinus node activation in sick sinus syndrome as revealed by a three-dimensional mapping system. *Heart Rhythm* 7, 856–857. doi: 10.1016/j.hrthm.2009.10.013

Mesirca, P., Marger, L., Toyoda, F., Rizzetto, R., Audoubert, M., and Dubel, S. (2013). The G-protein-gated K+ channel, IKACh, is required for regulation of pacemaker activity and recovery of resting heart rate after sympathetic stimulation. *J. Gen. Physiol.* 142, 113–126. doi: 10.1085/jgp.201310996

Mitrofanova, L., Ivanov, V., and Platonov, P. G. (2005). Anatomy of the inferior interatrial route in humans. *Europace* 7(Suppl. 2), 49–55.

Mond, H. G., and Proclemer, A. (2011). The 11th world survey of cardiac pacing and implantable cardioverter-defibrillators: calendar year 2009–a world society of arrhythmia's project. *Pacing Clin. Electrophysiol.* 34, 1013–1027. doi: 10.1111/j.1540-8159.2011.03150.x

Monfredi, O., Dobrzynski, H., Mondal, T., Boyett, M. R., and Morris, G. M. (2010). The anatomy and physiology of the sinoatrial node–a contemporary review. *Pacing Clin. Electrophysiol.* 33, 1392–1406. doi: 10.1111/j.1540-8159.2010.02838.x

Morris, G. M., and Kalman, J. M. (2014). Fibrosis, electrics and genetics. perspectives in sinoatrial node disease. *Circ. J.* 78, 1272–1282. doi: 10.1253/circj.cj-14-0419

Morris, G. M., D'Souza, A., Dobrzynski, H., Lei, M., Choudhury, M., and Billeter, R. (2013). Characterization of a right atrial subsidiary pacemaker and acceleration of the pacing rate by HCN over-expression. *Cardiovasc. Res.* 100, 160–169. doi: 10.1093/cvr/cvt164

Morris, G. M., Segan, L., Wong, G., Wynn, G., Watts, T., and Heck, P. (2019). Atrial Tachycardia arising from the crista terminalis, detailed electrophysiological features and long-term ablation outcomes. *JACC Clin. Electrophysiol.* 5, 448–458. doi: 10.1016/j.jacep.2019.01.014

Narula, O. S., Samet, P., and Javier, R. P. (1972). Significance of the sinus-node recovery time. *Circulation* 45, 140–158. doi: 10.1161/01.cir.45.1.140

Parameswaran, R., Lee, G., Morris, G. M., Royse, A., Goldblatt, J., and Larobina, M. (2020). Simultaneous epicardial-endocardial mapping of the sinus node in humans with structural heart disease: impact of overdrive suppression on sinoatrial exits. *Heart Rhythm* 17, 2154–2163. doi: 10.1016/j.hrthm.2020.06.034

Platonov, P. G., Mitrofanova, L. B., Chireikin, L. V., and Olsson, S. B. (2002). Morphology of inter-atrial conduction routes in patients with atrial fibrillation. *Europace* 4, 183–192. doi: 10.1053/eupc.2002.0221

Randall, W. C., Rinkema, L. E., Jones, S. B., Moran, J. F., and Brynjolfsson, G. (1982). Overdrive suppression of atrial pacemaker tissues in the alert, awake dog before and chronically after excision of the sinoatrial node. *Am. J. Cardiol.* 49, 1166–1175. doi: 10.1016/0002-9149(82)90041-8

Randall, W. C., Talano, J., Kaye, M. P., Euler, D., Jones, S., and Brynjolfsson, G. (1978). Cardiac pacemakers in absence of the SA node: responses to exercise and autonomic blockade. *Am. J. Physiol.* 234, H465–H470.

Reiffel, J. A., Gang, E., Gliklich, J., Weiss, M. B., Davis, J. C., and Patton, J. N. (1980). The human sinus node electrogram: a transvenous catheter technique and a comparison of directly measured and indirectly estimated sinoatrial conduction time in adults. *Circulation* 62, 1324–1334. doi: 10.1161/01.cir.62.6.1324

Reimann, C., Lluch, S., and Glick, G. (1972). Development and evaluation of an experimental model for the study of the cerebral circulation in the unanesthetized goat. *Stroke* 3, 322–328. doi: 10.1161/01.str.3.3.322

Rodriguez-Manero, M., Kreidieh, B., Al Rifai, M., Ibarra-Cortez, S., Schurmann, P., and Alvarez, P. A. (2017). Ablation of inappropriate sinus tachycardia: a systematic review of the literature. *JACC Clin. Electrophysiol.* 3, 253–265.

Rosen, M. R., Brink, P. R., Cohen, I. S., and Robinson, R. B. (2004). Genes, stem cells and biological pacemakers. *Cardiovasc. Res.* 64, 12–23. doi: 10.1016/j.cardiores.2004.05.012

Rozanski, G. J., Lipsius, S. L., and Randall, W. C. (1983). Functional characteristics of sinoatrial and subsidiary pacemaker activity in the canine right atrium. *Circulation* 67, 1378–1387. doi: 10.1161/01.cir.67.6.1378

Rozanski, G. J., Lipsius, S. L., Randall, W. C., and Jones, S. B. (1984). Alterations in subsidiary pacemaker function after prolonged subsidiary pacemaker dominance in the canine right atrium. *J. Am. Coll. Cardiol.* 4, 535–542. doi: 10.1016/s0735-1097(84)80098-4

Sanchez-Quintana, D., Cabrera, J. A., Farre, J., Climent, V., Anderson, R. H., and Ho, S. Y. (2005). Sinus node revisited in the era of electroanatomical mapping and catheter ablation. *Heart* 91, 189–194. doi: 10.1136/hrt.2003.031542

Sanders, P., Morton, J. B., Kistler, P. M., Spence, S. J., Davidson, N. C., and Hussin, A. (2004). Electrophysiological and electroanatomic characterization of the atria in sinus node disease: evidence of diffuse atrial remodeling. *Circulation* 109, 1514–1522.

Scicchitano, P., Carbonara, S., Ricci, G., Mandurino, C., Locorotondo, M., and Bulzis, G. (2012). HCN channels and heart rate. *Molecules* 17, 4225–4235.

Shen, W. K. (2002). Modification and ablation for inappropriate sinus tachycardia: current status. *Card. Electrophysiol. Rev.* 6, 349–355.

Soattin, L., Lubberding, A. F., Bentzen, B. H., Christ, T., and Jespersen, T. (2020). Inhibition of adenosine pathway alters atrial electrophysiology and prevents atrial fibrillation. *Front. Physiol.* 11:493.

Soattin, L., Lubberding, A., Bentzen, B. H., and Jespersen, T. (2017). P1025Adenosine 1 receptor activation plays a proarrhythmic role in rat atrium. *EP Europace* 19, iii219–iii220.

Stanfield, P. R., Nakajima, S., and Nakajima, Y. (2002). Constitutively active and G-protein coupled inward rectifier K+ channels: Kir2.0 *and Kir*3.0. *Rev. Physiol. Biochem. Pharmacol.* 145, 47–179.

Tellez, J. O., Dobrzynski, H., Greener, I. D., Graham, G. M., Laing, E., Honjo, H., et al. (2006). Differential expression of ion channel transcripts in atrial muscle and sinoatrial node in rabbit. *Circ. Res.* 99, 1384–1393.

Toader, E., Cividjian, A., and Quintin, L. (2011). Isoflurane suppresses central cardiac parasympathetic activity in rats: a pilot study. *Minerva Anestesiol* 77, 142–146.

van Hunnik, A., Zeemering, S., Podziemski, P., Simons, J., Gatta, G., and Hannink, L. (2018). Stationary atrial fibrillation properties in the goat do not entail stable or recurrent conduction patterns. *Front. Physiol.* 9:947.

Vicenzi, M. N., Woehlck, H. J., Bajic, J., Sokolyk, S. M., Bosnjak, Z. J., and Atlee, J. L. (1995). Anesthetics and automaticity of dominant and latent atrial pacemakers in chronically instrumented dogs. III. automaticity after sinoatrial node excision. *Anesthesiology* 82, 469–478.

Wijffels, M. C., Kirchhof, C. J., Dorland, R., and Allessie, M. A. (1995). Atrial fibrillation begets atrial fibrillation. a study in awake chronically instrumented goats. *Circulation* 92, 1954–1968.

Wu, D., Yeh, S.-J., Lin, F.-C., Wang, C.-C., and Cherng, W.-J. (1992). Sinus automaticity and sinoatrial conduction in severe symptomatic sick sinus syndrome. *J. Am. Coll. Cardiol.* 19, 355–364.

Yamabe, H., and Orita, Y. (2020). Demonstration of the anatomical tachycardia circuit in sinoatrial node reentrant tachycardia: analysis using the entrainment method. *J. Am. Heart Assoc.* 9:e014472.

Yamamoto, M., Dobrzynski, H., Tellez, J., Niwa, R., Billeter, R., Honjo, H., et al. (2006). Extended atrial conduction system characterised by the expression of the HCN4 channel and connexin45. *Cardiovasc. Res.* 72, 271–281.

Yanni, J., Tellez, J. O., Sutyagin, P. V., Boyett, M. R., and Dobrzynski, H. (2010). Structural remodelling of the sinoatrial node in obese old rats. *J. Mol. Cell Cardiol.* 48, 653–662.

Yokokawa, M., Sundaram, B., Oral, H., Morady, F., and Chugh, A. (2012). The course of the sinus node artery and its impact on achieving linear block at the left atrial roof in patients with persistent atrial fibrillation. *Heart Rhythm* 9, 1395–1402.

Yokokawa, M., Tada, H., Koyama, K., Ino, T., Naito, S., and Oshima, S. (2011). The change in the tissue characterization detected by magnetic resonance imaging after radiofrequency ablation of isthmus-dependent atrial flutter. *Int. J. Cardiol.* 148, 30–35.

Zhang, H., Dobrzynski, H., Holden, A. V., and Boyett, M. R. (2003). “Heterogeneous sinoatrial node of rabbit heart - molecular and electrical mapping and biophysical reconstruction,” in *Proceedings of the Functional Imaging and Modeling of the Heart. FIMH 2003*. Berlin: Springer.

Conflict of Interest: The authors declare that the research was conducted in the absence of any commercial or financial relationships that could be construed as a potential conflict of interest.

frontiers
in Physiology

ORIGINAL RESEARCH
published: 20 January 2021
doi: 10.3389/fphys.2020.519382

Genetic Ablation of G Protein-Gated Inwardly Rectifying K^+ Channels Prevents Training-Induced Sinus Bradycardia

Isabelle Bidaud[1,2], Alicia D'Souza[3], Gabriella Forte[3], Eleonora Torre[1,2], Denis Greuet[1], Steeve Thirard[1], Cali Anderson[3], Antony Chung You Chong[1,2], Angelo G. Torrente[1,2], Julien Roussel[1], Kevin Wickman[4], Mark R. Boyett[5], Matteo E. Mangoni[1,2] and Pietro Mesirca[1,2]*

[1] Institut de Génomique Fonctionnelle, Université de Montpellier, CNRS, INSERM, Montpellier, France, [2] LabEx Ion Channels Science and Therapeutics, Montpellier, France, [3] Division of Cardiovascular Sciences, University of Manchester, Manchester, United Kingdom, [4] Department of Pharmacology, University of Minnesota, Minneapolis, MN, United States, [5] Division of Biomedical Sciences, University of Copenhagen, Copenhagen, Denmark

Edited by:
Sami Noujaim,
Morsani College of Medicine,
USF Health, United States

Reviewed by:
Vadim V. Fedorov,
The Ohio State University,
United States
Robert Alan Rose,
University of Calgary, Canada
Alexey V. Glukhov,
University of Wisconsin-Madison,
United States

***Correspondence:**
Pietro Mesirca
pietro.mesirca@igf.cnrs.fr

Specialty section:
This article was submitted to
Cardiac Electrophysiology,
a section of the journal
Frontiers in Physiology

Received: 11 December 2019
Accepted: 17 December 2020
Published: 20 January 2021

Citation:
Bidaud I, D'Souza A, Forte G,
Torre E, Greuet D, Thirard S,
Anderson C, Chung You Chong A,
Torrente AG, Roussel J, Wickman K,
Boyett MR, Mangoni ME and
Mesirca P (2021) Genetic Ablation
of G Protein-Gated Inwardly
Rectifying K^+ Channels Prevents
Training-Induced Sinus Bradycardia.
Front. Physiol. 11:519382.
doi: 10.3389/fphys.2020.519382

Background: Endurance athletes are prone to bradyarrhythmias, which in the long-term may underscore the increased incidence of pacemaker implantation reported in this population. Our previous work in rodent models has shown training-induced sinus bradycardia to be due to microRNA (miR)-mediated transcriptional remodeling of the HCN4 channel, leading to a reduction of the "funny" (I_f) current in the sinoatrial node (SAN).

Objective: To test if genetic ablation of G-protein-gated inwardly rectifying potassium channel, also known as I_{KACh} channels prevents sinus bradycardia induced by intensive exercise training in mice.

Methods: Control wild-type (WT) and mice lacking GIRK4 ($Girk4^{-/-}$), an integral subunit of I_{KACh} were assigned to trained or sedentary groups. Mice in the trained group underwent 1-h exercise swimming twice a day for 28 days, 7 days per week. We performed electrocardiogram recordings and echocardiography in both groups at baseline, during and after the training period. At training cessation, mice were euthanized and SAN tissues were isolated for patch clamp recordings in isolated SAN cells and molecular profiling by quantitative PCR (qPCR) and western blotting.

Results: At swimming cessation trained WT mice presented with a significantly lower resting HR that was reversible by acute I_{KACh} block whereas $Girk4^{-/-}$ mice failed to develop a training-induced sinus bradycardia. In line with HR reduction, action potential rate, density of I_f, as well as of T- and L-type Ca^{2+} currents (I_{CaT} and I_{CaL}) were significantly reduced only in SAN cells obtained from WT-trained mice. I_f reduction in WT mice was concomitant with downregulation of HCN4 transcript and protein, attributable to increased expression of corresponding repressor microRNAs (miRs) whereas reduced I_{CaL} in WT mice was associated with reduced $Ca_v1.3$ protein levels. Strikingly, I_{KACh} ablation suppressed all training-induced molecular remodeling observed in WT mice.

Conclusion: Genetic ablation of cardiac I_{KACh} in mice prevents exercise-induced sinus bradycardia by suppressing training induced remodeling of inward currents I_f, I_{CaT} and I_{CaL} due in part to the prevention of miR-mediated transcriptional remodeling of HCN4 and likely post transcriptional remodeling of $Ca_v1.3$. Strategies targeting cardiac I_{KACh} may therefore represent an alternative to pacemaker implantation for bradyarrhythmias seen in some veteran athletes.

Keywords: G-protein-gated inwardly rectifying potassium 4 (Girk4), hyperpolarization-activated cyclic nucleotide-gated 4 (HCN4) channel, bradycardia, sinoatrial node, endurance athletes

INTRODUCTION

The pacemaker activity of sinoatrial node (SAN) permanently controls the heart rate (HR) in everyday life (Mangoni and Nargeot, 2008). SAN pacemaking is generated by diastolic depolarization, a slow depolarizing phase of the action potential driving the membrane voltage from the end of the repolarization phase of the preceding action potential to the threshold of the following action potential. A complex and robust interplay between the activity of ion channels of the plasma membrane and the intracellular dynamics of Ca^{2+} underlies diastolic depolarization (Mangoni and Nargeot, 2008; Lakatta et al., 2010).

Among ion channels, hyperpolarization-activated cyclic nucleotide gated 4 (HCN4) channels underlying the "funny" current (I_f) play an important role in SAN automaticity (DiFrancesco, 2010). In addition to I_f, voltage-gated L- and T-type Ca^{2+} channels mediating L- and T-type Ca^{2+} currents (I_{CaL} and I_{CaT}) contribute to the generation of SAN impulse. Indeed, they supply inward current at voltages spanning diastolic depolarization (Hagiwara et al., 1988; Verheijck et al., 1999; Mangoni et al., 2003, 2006b; Torrente et al., 2016). Together with type 2 ryanodine receptors (RyR2) of the sarcoplasmic reticulum (SR), I_f and I_{CaL} mediate the positive chronotropic effect of catecholamines on SAN activity. In addition, the parasympathetic branch of the autonomic nervous system negatively regulates SAN pacemaker activity via two predominant pathways. First, vagally released acetylcholine activates muscarinic (M2) receptors to induce opening of G protein-gated inwardly rectifying K^+ (GIRK) channels mediating the cardiac I_{KACh} current (Wickman et al., 1998). Second, activated M2 receptors promote down regulation of intracellular cAMP concentration, which reduces the amplitudes of I_f (DiFrancesco and Tromba, 1988a,b), I_{CaL} (Petit-Jacques et al., 1993), as well as intracellular RyR2-mediated Ca^{2+} release and cycling (Lyashkov et al., 2009; van Borren et al., 2010). The cardiac I_{KACh} current is mediated by heteromeric GIRK1/GIRK4 channel subunits (Krapivinsky et al., 1995). However, since GIRK1 subunits require GIRK4 to be properly targeted to the cell membrane, knockout of the *Girk4* gene induces genetic ablation of I_{KACh} in the heart (Wickman et al., 1998) and in the SAN (Mesirca et al., 2013).

In spite of its intrinsic robustness, several genetic- or disease-related factors may induce chronic slowing of pacemaker activity, a condition referred to as primary or secondary SAN (sinus node) dysfunction, respectively [SND, see Monfredi and Boyett (2015), Mesirca et al. (2020) for review]. SAN bradycardia, which can be associated with atrial tachyarrhythmia or atrioventricular block, characterizes SND (Brignole et al., 2013). Chronic symptomatic SND necessitates the implantation of an electronic pacemaker (Brignole et al., 2013). Intriguingly, there is now evidence that some veteran endurance athletes represent a subpopulation of acquired SND manifesting as bradyarrhythmia, and increased incidence of electronic pacemaker implantation (Northcote et al., 1989a,b) as well as AV node dysfunction (Stein et al., 2002) and atrial fibrillation (Andersen et al., 2013).

In rodent models of endurance training (D'Souza et al., 2014) and in human athletes (D'Souza et al., 2017), we have previously demonstrated an intrinsic slowing of SAN pacemaking attributable to training-induced transcriptional remodeling of key pacemaking ion channels. Specifically, in mice trained by swimming, we identified a role for transcriptional downregulation of the HCN4 channel (and a corresponding reduction in I_f) in the development of training-induced bradycardia. As such, swim-training in rodents may be regarded as a model of secondary HCN4-mediated SND.

In previous work, we also showed that genetic ablation of I_{KACh} by knockout of *Girk4* rescued SAN bradycardia and prevented associated arrhythmias in mice expressing dominant negative non-conductive HCN4 subunits (Mesirca et al., 2014). Furthermore, we showed that ablation of I_{KACh} restores normal HR and rhythm in mice lacking L-type $Ca_v1.3$ channels ($Ca_v1.3^{-/-}$) (Mesirca et al., 2016a; Bidaud et al., 2020). Finally, work on human SAN maintained *ex vivo* showed that pharmacologic block of I_{KACh} prevents failure of impulse generation and conduction induced by adenosine (Li et al., 2017). Taken together, these data have suggested that genetic or pharmacological targeting of I_{KACh} may constitute promising concepts to improve HR and rhythm in SND [see Mesirca et al. (2016b, 2020), for review].

However, evidence showing that genetic ablation of I_{KACh} can improve *in vivo* HR in secondary forms of bradycardia and SND are lacking. We thus investigated the consequences of I_{KACh} ablation on training-induced SAN bradycardia in mice and hypothesized that I_{KACh} channels are required for the development of training-induced bradycardia. We show that I_{KACh} ablation protects mice from training induced SAN bradycardia. I_{KACh} knockout blocked down-regulation of I_f, I_{CaT} and I_{CaL}, explaining protection of *Girk4*$^{-/-}$ mice from training-induced bradycardia. Our study provides first evidence that genetic deletion of I_{KACh} can prevent bradycardia in an *in vivo* model of secondary SND.

MATERIALS AND METHODS

Wild-type (WT) and *Girk4*$^{-/-}$ (Mesirca et al., 2013) mice were bred and maintained under the C57Bl/6J genetic background. The investigation conforms to the Guide for the Care and Use of Laboratory Animals published by the US National Institute of Health (NIH Publication No. 85–23, revised 1996) and European directives (2010/63/EU). The experimental procedure was approved by the Ethical committee of the University of Montpellier and the French Ministry of Agriculture (protocol n°: 2017010310594939). Animals were housed in individual cages with free access to food and water and were exposed to 12-h light/dark (light, 8:00 h to 20:00 h) in a thermostatically controlled room.

Training Protocol

68 WT and 67 *Girk4*$^{-/-}$ mice were assigned to a sedentary or trained group. Mice in the trained group first underwent a ramp-up period, in which the duration of swimming was increased in daily increments of 10 min, to finally reach 1 h. Mice in the trained group then underwent 1-h exercise swimming twice a day (morning session: 09:30–10:30, afternoon session 15:30–16:30) for 28 days, 7 days per week. Sedentary mice underwent 5-min swimming in the same period, to account for stress-related effects. The temperature of the water was set to 35°C (3 ppm Cl). After each session, mice were dried manually and then exposed to a warming red light source for 30 min.

ECG Recordings in Conscious Mice and Heart Rate Variability Analysis

Mice undergoing telemetric ECG recordings were anesthetized with 2% isoflurane (Forene®, Abbott, United Kingdom). A midline incision was made on the back along the spine to insert a telemetric transmitter (ETA-F10, Data Sciences International) into a subcutaneous pocket. Paired wire electrodes were placed over the thorax (chest bipolar ECG lead) in DII derivation against the heart axis. Mice were left to recover for 14 days before ECG recordings. ECG signals were recorded using a telemetry receiver and an analog-to-digital conversion data acquisition system for display and analysis by Dataquest^{TM} A.R.T.^{TM} software (Data Sciences International). We recorded ECG for 12 h, before the ramp-up period (basal conditions) and daily (from 20:00 to 08:00 dark period) after ramp-up period until the 28th day of training. Heart rates (HR) were measured from ventricular RR intervals. ECG parameters were measured with ECG Auto 1.5.7 software (EMKA Technologies). HRV analysis was performed on telemetric ECGs by sampling four different 5-min periods of stable ECG segments (first 5-min period 22:55–23:00; second 5-min period 01:55–02:00; third 5-min period 04:55–05:00, and fourth 5-min period 07:55–08:00) at day 0 and at day 28 in WT and *Girk4*$^{-/-}$ sedentary and trained animals. The standard deviation of intervals between two consecutive heart beats (SDNN), power spectral density (PSD) of HRV determined by Fast Fourier Transformation analysis (Welch Periodogram method), spectral frequency bands (low frequency spectra 0.15–1.5 Hz, high-frequency spectra 1.5–5 Hz and ratio between LF and HF values), percentage of successive intervals that differ by more than 6 ms (pNN6), standard deviation of instantaneous beat-to-beat interval variability (SD1) and continuous long-term R-R interval variability (SD2) provided by ellipse-fitting technique of the Poincaré scatter-gram obtained in each of the four 5 min period were averaged.

ECGs were also recorded from conscious restrained mice using the non-invasive ecgTUNNEL® device (Emka Technologies). ECG signals were continuously recorded for 15 min using iOX Software v2.10.5.14 (Emka Technologies) and the heart rate was analyzed with ecgAUTO v3.3.5.12 (Emka Technologies). Each mouse underwent habituation to the setup for 10 min before data collection. ECG measurements started 40 min after intraperitoneal injection of saline or atropine (0.5 mg/kg, Aguettant) and propranolol (5 mg/kg, Sigma Aldrich) solution. This delay was considered as a good compromise between the absence of the artifact due to the stress of the injection and the measurement of the amplitude of the drug effect.

Echocardiography and Arterial Pressure Recordings

Anesthetized mice (1–1.2% isoflurane) underwent transthoracic two-dimensional echocardiography. Images were obtained in parasternal long-axis view and short-axis view at the midpapillary muscle level. Cardiac morphology and function were assessed using high frequency, high-resolution echocardiographic system consisting of a VEVO ultrasound machine (2100) equipped with a 22–55 MHz bifrequencial transducer (VisualSonics B.V.), with continuous temperature and ECG monitoring.

Blood pressure was recorded using the CODA mouse tail-cuff system (Kent Scientific) in conscious restrained mice. Systolic and diastolic blood pressure were measured using volume pressure recording (VPR) to determine the tail blood volume (Daugherty et al., 2009) and recorded using the Coda 3.4 software (Kent Scientific). Pressure measurements started after 3 days of adaptation during which mice become accustomed to the holders and to tail cuff procedure. Recordings were always performed by the same investigator. Each session started with animals installed for 15 min in the holders placed on the warmed measurement platform. Following the 15-min habituation period, a set of 30 consecutive measurements was used for determining the blood pressure in each mouse.

SAN Cell Isolation

Sinoatrial node cells were isolated as previously described (Mangoni and Nargeot, 2001). Briefly, SAN tissue strips were immersed into a "low-Ca^{2+}" Tyrode's solution containing 140 mM NaCl, 5.4 mM KCl, 0.5 mM $MgCl_2$, 0.2 mM $CaCl_2$, 1.2 mM KH_2PO_4, 50 mM taurine, 5.5 mM D-glucose, 1 mg/mL BSA, and 5 mM Hepes-NaOH (pH 6.9 with NaOH) for 5 min. The tissue was then transferred into a low-Ca^{2+} containing solution, washed 3 times and then transferred to a low-Ca^{2+} solution containing purified collagenase and protease mix (Liberase TM; 229 U/mL; Roche) and 1.9 U/ml elastase (Boehringer Mannheim). Digestion was carried out for 15–20 min at 36°C. SAN strips were then washed in a modified "Kraftbrühe" (KB) medium containing 70 mM L-glutamic acid, 20 mM KCl, 80 mM KOH, 10 mM KH_2PO_4, 10 mM taurine, 1 mg/ml BSA, and 10 mM Hepes-KOH (adjusted to pH 7.4 with KOH). Single cells were isolated from the tissue by manual agitation using a flame-forged Pasteur pipette in KB solution at 36°C. For recovering of pacemaker activity, Ca^{2+} was gradually reintroduced into the cell storage solution to a final concentration of 1.8 mM. Normal Tyrode solution containing 1 mg/ml BSA was added to the storage solution. Cells were then stored at room temperature until use.

Patch-Clamp Recordings

We employed the whole-cell variation of the patch-clamp technique to investigate the effects of the training or sedentary regimen on I_f, I_{CaT} and I_{CaL} in SAN cells from wild-type or *Girk4*$^{-/-}$ mice (Hamill et al., 1981). To this aim, cells were harvested in recording chambers (working volume 500 μl) allowing controlled unidirectional solution flow and mounted on the stage of an Olympus X71 inverted microscope. Cells were continuously perfused with normal Tyrode solution. Actions potentials and ionic currents were recorded using an Axon multiclamp patch-clamp 700B amplifier (Axon Instruments Inc.), grounded by an agar bridge filled with 150 mM KCl. Pacemaker activity was recorded by the perforated patch technique with escin (50 μM). Recording electrodes were pulled from borosilicate glass, using a DMZ-Universal Electrode Puller (Zeitz Instruments). For recording cell automaticity, as well as I_f, we used an intracellular solution containing (mM): K^+-aspartate, 130; NaCl, 10; ATP-Na^+ salt, 2; creatine phosphate, 6.6; GTP-Mg^{2+}, 0.1; $CaCl_2$, 0.04 (pCa = 7); Hepes-KOH, 10 (adjusted to pH = 7.2 with KOH). Electrodes had a resistance of about 5 MΩ. The extracellular solution contained (in mM): NaCl, 140; KCl, 5.4; $CaCl_2$, 1.8; $MgCl_2$, 1; Hepes-NaOH, 5; and D-glucose, 5.5 (adjusted to pH = 7.4 with NaOH). Data was acquired with pClamp software (ver. 9, Axon Instruments Inc.). For recordings of I_{CaL}, we used an extracellular solution containing (in mM): 135 tetraethylammonium chloride (TEA-Cl), 10 4-aminopyridine (4-AP), 1 $MgCl_2$, 0.03 tetrodotoxin (TTX), 1 g/l glucose, 2 $CaCl_2$, 10 Hepes (adjusted to pH = 7.2 with CsOH) (Mangoni et al., 2003). Electrodes had a resistance of about 3 MΩ when filled with an intracellular solution containing (in mM): 125 CsOH, 20 TEA-Cl, 1.2 $CaCl_2$, 5 Mg-ATP, 0.1 Li_2-GTP, 5 EGTA, and 10 HEPES (pH adjusted to 7.2 with aspartate). When recording I_f or I_{CaL}, seal resistances were in the range of 2–5 GΩ.

The I_f steady-state activation curve was calculated as previously described (DiFrancesco and Mangoni, 1994). Briefly, an hyperpolarizing voltage ramp starting from an holding potential of −35 mv to −135 mV with 100 mV/80s rate was applied. The I_f activation curve was then calculated as the voltage dependence of probability of f-channels' opening $P(V)$, by calculating the ratio between the current steady-state waveform and fully-activated I-V relationship (Mangoni and Nargeot, 2001). The fully activated I-V relationship was calculated by extrapolating the straight line passing through the point of zero current (fixed at −40 mV) and the point of maximal current (at −135 mV). Averaged I_f activation curve was then fitted according to a modified Boltzmann equation: $P(V) = 1/[1 + exp(V\text{-}V_{1/2})/k]$, where $P(V)$ is the voltage dependency of the f-channels open probability, $V_{1/2}$ is the half-activation voltage and k is the slope factor. Analysis was performed using Prism software (v 8.4.1 GraphPad). Current densities and activation of I_{CaT} and I_{CaL} were calculated as described previously (Mangoni et al., 2003). Half-activation voltages were calculated by fitting current I-V curves by using the Boltzmann relation: $I/I_{max} = g_{max}(V - V_{rev})\{1 + exp[(V_{1/2} - V)/k]\}$, where V_{rev} is the current reversal potential, V is the membrane voltage, I is the peak current, g_{max} is the maximal conductance, $V_{1/2}$ is the voltage for half activation, and k is the slope factor.

Numerical Modeling of Pacemaker Activity

Numerical simulations of pacemaker activity of mouse SAN cells were performed using a model that we developed previously (Christel et al., 2012). To simulate the effects of the training regimen on pacemaker activity, we entered the conductance of I_f and I_{CaL} recorded in sedentary and trained WT and *Girk4*$^{-/-}$ mice. Equations to simulate I_f and I_{CaL} were the same as in Christel et al. (2012). Calculations were performed in the Jsim environment for integration of differential equations[1]. The integration step was set to 200 μs. Simulations were analyzed using the Graph Prism software (ver. 5.03).

RNA Isolation and qPCR

Tissue biopsies were collected from the SAN of trained and sedentary mice approximately at the level of the main branch from the *crista terminalis*. Biopsies were frozen in liquid N_2 and stored at −80°C until use. RNA was isolated using a Qiagen RNEasy kit following manufacturer's instructions. For mRNA quantitation of HCN4, Ca^{2+} channel accessory subunits and miRs, cDNA was generated using the miScript II RT kit (Qiagen), using the HiFlex buffer option, to allow analysis of miRs and mRNAs in the same cDNA sample. The reaction mixture for mRNA comprised 1 μl of cDNA, 1 × Qiagen assay, 1 × SYBR Green Master Mix (Applied Biosystems) and DNase-free water. mRNA expression was calculated by the ΔCt method and normalization to the expression of *Tbp* which was determined as the optimal endogenous control (*Polr2a*, *Tbp* and

---

[1] http://nsr.bioeng.washington.edu/jsim/

Ubc were tested) using the algorithm geNorm (qBaseplus, version 2.0, Biogazelle). The miScript SYBR green PCR kit was used to measure miR expression. The reaction comprised 1 μl cDNA, 1 × miScript universal primer, 1 × primer assay and DNAse-free water.

Primers were purchased from Qiagen (formerly Exiqon, miR-10b-5p, 205637; miR-486-3p, 204107; miR423-5p, 205624; miR-676-3p, 205098; miR-181b-5p, 204530; Let-7e-5p, 205711; Let-7d-5p, and 204124). Primer set for mmu-miR-5099 was custom designed according to previously published sequences. miR expression was calculated by the ΔCt method with normalization to expression of *Snord65* and *Snord91* (geNorm-determined optimal reference gene combination, *Snord65* and *Snord91* and *Rnu1a1* tested). All samples were run in duplicate. mRNA expression of L-type Ca^{2+} channel subunits as well as GIRK1 and GIRK4 was carried out using custom-designed TaqMan Low Density Array microfluidic cards (Applied Biosystems, cat. no. 2549025; format 96A) as described in detail elsewhere (D'Souza et al., 2014). mRNA expression for these transcripts was calculated by the ΔCt method and normalized to the expression of *Tbp*.

Western Blots

Snap frozen sinus node biopsies were homogenized with RIPA buffer (Sigma Aldrich) with protease inhibitors in FastPrep lysing matrix D ceramic bead (1.4 mm) 2 mL tubes (MPBio) using an MP FastPrep-24. Pierce BCA protein assays were used to estimate total protein concentration following which samples were denatured in 5× laemmli buffer and 6 M urea and heated to 37°C for 15 min. Proteins were separated using a 4–20% or 7.5% stain-free SDS-polyacrylamide gel electrophoresis (PAGE; Bio-Rad) system with Precision Plus Unstained Protein Standards, *Strep*-tagged recombinant (Bio-Rad) running at 110V for ∼70 min in SDS running buffer (25 mM Tris, 192 mM glycine, 0.1% SDS). Stain-free gels were imaged using ChemiDoc MP and proteins transferred to PVDF (polyvinyl difluoride) membranes using the *Trans*-Blot Turbo transfer system and buffers (Bio-Rad) at 25 V/1Amp for 30 min according to the manufacturer's instructions. For $Ca_v1.2$ the ethanol in the transfer buffer was reduced to 10%. Successful transfer was confirmed by imaging using the ChemiDoc MP and an image was obtained for total protein quantification. PVDF membranes were washed in Tris-buffered saline containing 0.1% v/v Tween 20 (TBS-Tween) and blocked in 4% BSA in TBS-Tween and incubated with primary antibodies in 2% BSA. Rabbit polyclonal anti-HCN4 (Alomone Labs, APC-052, Lot #APC052AN2802), anti-$Ca_v1.2$ (ACC-003, Lot #ACC003AN6802), anti-GIRK1 (APC-005, Lot #APC005AN1125) and anti-GIRK4 (APC-027, Lot #APC027AN0725), were used at 1:200. anti-$Ca_v1.3$ (Christel et al., 2012) was used at 1/2000. After washing, membranes were then incubated with horseradish peroxidase (HRP)-linked secondary antibody (HRP-linked anti-rabbit IgG, Cell Signaling, 1:3000) and Precision Protein StrepTactin-HRP conjugate (Bio-Rad, 1:5000) in milk-TBS-Tween. Unbound secondary antibody was removed by washing in TBS-Tween following which membranes were treated with Clarity Western ECL substrate (Bio-Rad) and imaged with a Bio-Rad ChemiDoc MP system. The chemiluminescent signal intensity was normalized to quantification of total protein, calculated and volume-adjusted using Image Lab 6.0 by selection of equivalent lane segments across the blot on the total protein image. All samples were run in duplicate. For HCN4, $Ca_v1.2$ and $Ca_v1.3$, wild-type and *Girk4*$^{-/-}$ samples were run on separate gels and data given as% reduction from corresponding sedentary control (set as 100%).

Data Analysis and Statistics

Data analysis and statistical assessing were performed using Prism 8.0 (GraphPad Software). Data are represented as mean ± SEM unless differently stated. Statistical tests used in each experiment are specified throughout the figure legends. In the text and in the legends, statistical significance was defined as $p < 0.05$. $^{*}p < 0.05$, $^{**}p < 0.01$, $^{***}p < 0.001$, and $^{****}p < 0.0001$.

RESULTS

Genetic Ablation of I_{KACh} Prevented Training-Induced SAN Bradycardia

We compared the HR of mice assigned to the trained group to that of the sedentary group (**Figure 1**). The HR of trained WT mice decreased with training progression and was significantly reduced by day 17 (550 ± 7 bpm vs 522 ± 4 bpm, $p < 0.05$, day 0 and day 17, respectively, **Figure 1A**). In contrast, the HR rate of trained *Girk4*$^{-/-}$ mice remained stable throughout the training regimen (**Figure 1B**). As expected, the HR of sedentary WT or *Girk4*$^{-/-}$ mice remained unaltered (**Figures 1A,B**). As such, a significant change in the slope of the regression line between HR and days of regimen only in the group of trained WT mice (**Figure 1C**). At swimming cessation (day 28), the HR of trained WT mice was significantly lower that of sedentary counterparts. In contrast, we failed to observe a statistically significant difference in HR between trained and sedentary *Girk4*$^{-/-}$ mice (**Figure 1D**).

The effect of tertiapine-Q on HR was investigated in sedated mice using echocardiography (see Methods). Sedated WT mice presented with slightly reduced basal heart rate (**Figure 1E**) in comparison to conscious animals (**Figure 1D**). Administration of tertiapin-Q increased the HR of sedentary mice, in line with inhibition of tonic regulation of HR by I_{KACh}, as we reported previously (Mesirca et al., 2016a). In addition, tertiapin-Q increased the HR of trained WT (**Figure 1E**), but not *Girk4*$^{-/-}$ mice (**Figure 1F**). The HR of sedentary and trained WT mice after administration of 5 mg/Kg tertiapin-Q was similar, showing that pharmacologic inhibition of I_{KACh} compensated for the decrease in HR induced by the training regimen.

Absence of significant training-induced bradycardia in *Girk4*$^{-/-}$ mice could not be attributed to reduced training activity of mutants compared to WT animals, because the difference in body weight between sedentary and trained mice at the end of training regimen was similar in both strains-(**Supplementary Figure 1**).

Besides HR, the training regimen also prolonged the atrioventricular conduction (PR) interval in WT mice

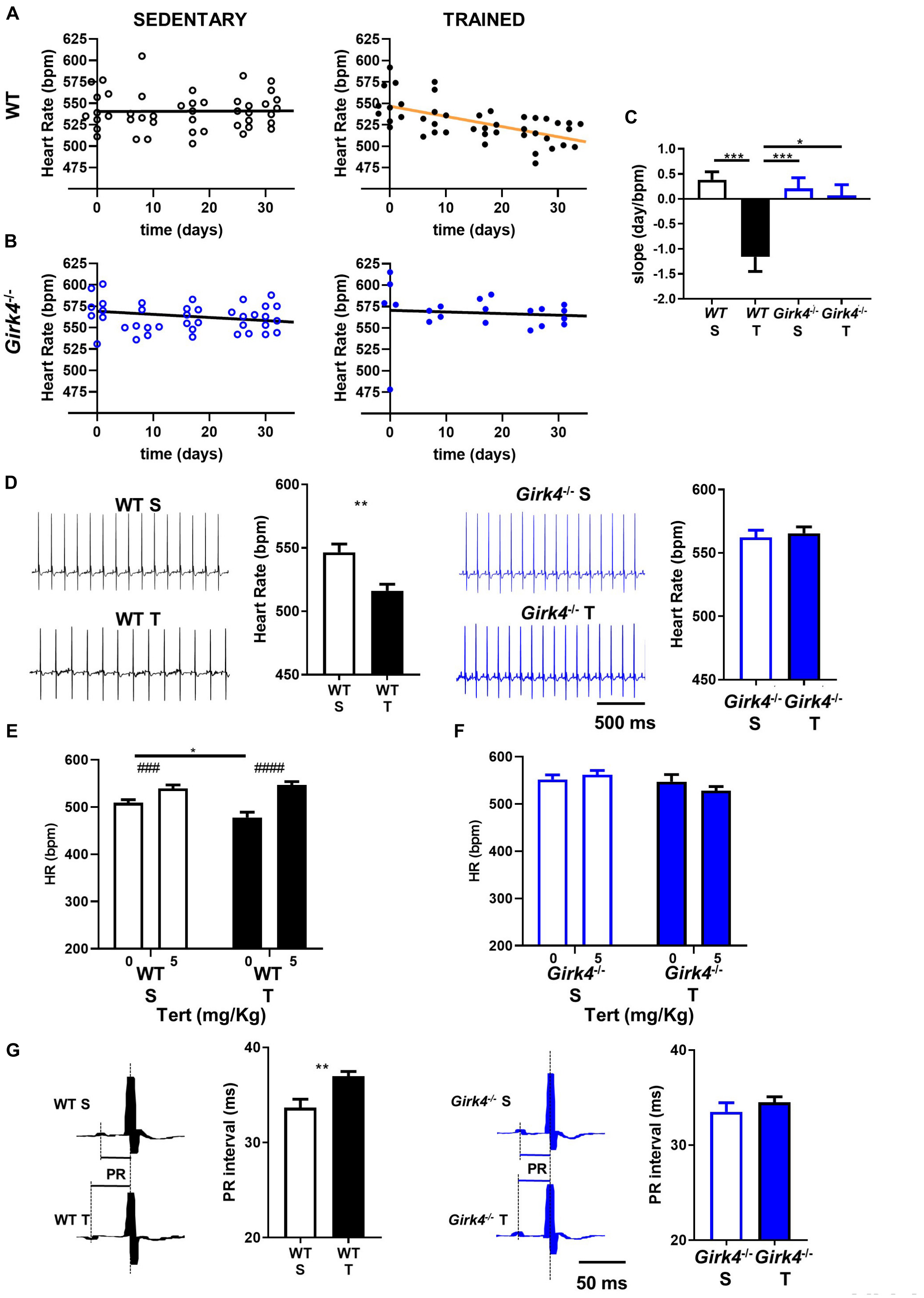

FIGURE 1 | Heart rate recorded in sedentary (left panel) and trained (right panel) WT **(A)** and *Girk4*$^{-/-}$ mice **(B)** at different days during 5 min sham-training (WT and *Girk4*$^{-/-}$ sedentary, see methods) and training (WT and *Girk4*$^{-/-}$ trained) protocol. **(C)** Histogram of the average values of the slopes of the regression line between time and heart rate. Statistics: one-way analysis of variance followed by Tukey's multiple comparisons test. **(D)** Representative examples of ECG traces and averaged heart rate recorded at day 28 from sedentary (top) and trained (bottom) WT (left panel) and *Girk4*$^{-/-}$ mice (right panel). Statistics: unpaired Student's *t*-test. Tertiapin-Q (Tert, 5 mg/kg) effect in WT **(E)** and *Girk4*$^{-/-}$ **(F)** sedentary (empty bar) and trained (filled bars) mice. Statistics: two-way analysis of variance followed by Sidak multiple comparisons test. **(G)** Close-up of ECG traces and averaged PR interval recorded at day 28 from sedentary (top) and trained (bottom) WT (left panel) and *Girk4*$^{-/-}$ mice (right panel). Statistics: unpaired Student's *t*-test. $^{*}p < 0.05$, $^{**}p < 0.01$, $^{***}p < 0.001$, $^{\#\#\#}p < 0.001$, $^{\#\#\#\#}p < 0.0001$. Error bars indicate s.e.m. WTS: WT sedentary; WTT: WT trained; *Girk4*$^{-/-}$ S: *Girk4*$^{-/-}$ sedentary and *Girk4*$^{-/-}$ T: *Girk4*$^{-/-}$ trained.

(33.6 ± 0.9 ms vs 37.0 ± 0.5 ms, $p < 0.01$). In contrast, the PR intervals of *Girk4*$^{-/-}$ mice did not change significantly upon training (**Figure 1G**). We did not detect statistically significant differences in QRS, QT and QTc intervals of the ECG waveform between WT and *Girk4*$^{-/-}$ mice, either in the sedentary condition or after 28 days of training (**Supplementary Table 1**). *In vivo* echocardiographic imaging of sedentary and trained WT and *Girk4*$^{-/-}$ mice showed slowing of HR in trained WT animals to be associated with hallmarks of ventricular hypertrophy (**Supplementary Figure 2**). Particularly, the training regimen significantly increased the left ventricular mass diameter and volume, as well as wall thickness. These changes were accompanied by an increase in ventricular stroke volume and a decrease in ejection fraction. Remarkably, the training regimen did not affect ventricular morphology, stroke volume or ejection fraction in *Girk4*$^{-/-}$ mice (**Supplementary Figure 2**). Finally, no changes in arterial systolic or diastolic pressure in WT and *Girk4*$^{-/-}$ mice were noted (**Supplementary Figure 3**). Cumulatively, these data demonstrate, for the first time, the requirement of I_{KACh} in the development of training-induced sinus bradycardia as well as canonical structural and functional remodeling characteristics commonly referred to as the 'athlete's heart.'

Mechanisms underlying the prevention of training-induced bradycardia in *Girk4*$^{-/-}$ mice were investigated. The heart rate adaptation to training is widely attributed to high parasympathetic (vagus) activity and therefore we studied the impact of training on heart rate variability (HRV, a surrogate measure of autonomic activity) in WT and *Girk4*$^{-/-}$ mice (**Figures 2A–D**). Genetic ablation of I_{KACh} reduced the standard deviation of the RR interval (SDNN) in comparison to WT counterparts (**Figures 2A,B**), as previously reported for this mouse strain (Wickman et al., 1998; Mesirca et al., 2013). However, the measured SDNN was similar at day 0 and day 28 in WT and in *Girk4*$^{-/-}$ mice (**Figures 2A,B**), suggesting that the training regimen did not affect the autonomic innervation of the SAN. Consistent with this hypothesis, training did not affect the integral of the low-frequency (LF) or high-frequency (HF) fractions of the HRV spectrum in WT or *Girk4*$^{-/-}$ mice (**Supplementary Figures 4A,B**). Furthermore, the LF/HF ratio did not differ between WT and *Girk4*$^{-/-}$ mice and was unaffected by training (**Supplementary Figure 4C**). The training regimen significantly augment the power spectral density (PSD) in WT but not in *Girk4*$^{-/-}$ mice (**Figures 2C,D**). Finally, training did not affect other HRV parameters (pNN6, SD1 and SD2, **Supplementary Figures 5A–C**). We did not see significant sex differences in the HR, PR interval and in the power spectral density of heart rate variability neither in WT nor in *Girk4*$^{-/-}$ animals under basal conditions (**Supplementary Dataset 1**). We then tested if decrease in HR observed in WT mice following the training regimen was maintained after pharmacologic inhibition of autonomic nervous system input. To this aim, we compared the HR (recorded non-invasively by TUNNEL-ECG see methods) of sedentary and trained WT and *Girk4*$^{-/-}$ mice under control conditions or following concomitant injection of atropine (0.5 mg/Kg) and propranolol (5 mg/Kg). Concomitant injection of atropine and propranolol decreased HR in both sedentary and trained WT and *Girk4*$^{-/-}$ mice (**Figures 2E–H**). However, the HR of trained WT mice was significantly lower than that recorded in sedentary counterparts (**Figures 2E,F**), which indicates that training induced slowing of intrinsic SAN pacemaker activity, as previously shown (D'Souza et al., 2014). In contrast, the training regimen did not significantly change the intrinsic SAN rate of *Girk4*$^{-/-}$ mice (**Figures 2G,H**). Taken together, our results show that the training regimen induced SAN bradycardia, increased the AV conduction interval and reduced the intrinsic SAN rate in WT, but not in *Girk4*$^{-/-}$ mice. In addition, our data show that training induces slowing of intrinsic SAN pacemaking at the end of training regimen, in the absence of a change in the sympathovagal balance.

Genetic Ablation of I_{KACh} Abolished Training-Induced Reduction in Spontaneous Firing of SAN Cells

Since the training regimen induced slowing of intrinsic SAN pacemaker activity in trained WT but not in *Girk4*$^{-/-}$ mice, we recorded spontaneous action potentials from isolated pacemaker cells (**Figure 3A**). Consistent with recordings of resting HR *in vivo* under control conditions or following inhibition of autonomic nervous system input, the averaged spontaneous beating rate of SAN cells from trained WT mice was significantly lower than the rate of cells from the SAN of sedentary WT mice (135 ± 9 vs 220 ± 10 bpm, $p < 0.0001$, i.e., 39%, **Figure 3B**). The rate of spontaneous action potentials of *Girk4*$^{-/-}$ SAN cells did not differ between the sedentary and trained group (223 ± 17 vs 229 ± 10 bpm, **Figure 3B**). Consistent with the effect on the rate of spontaneous action potentials, the slope of the linear part of the diastolic depolarization (SLDD) was significantly reduced by the training regimen (44%) in WT but not in *Girk4*$^{-/-}$ mice (**Figure 3C**). The training regimen also significantly prolonged the action potential duration in WT but not in *Girk4*$^{-/-}$ mice (**Supplementary Table 2**). No significant difference was observed in the rate of spontaneous action potentials of SAN cells obtained from sedentary WT and *Girk4*$^{-/-}$ mice (**Figure 3B**). Finally, in sedentary or trained WT and *Girk4*$^{-/-}$ mice, we did not record significant differences in the maximum diastolic potential, action potential threshold, slope of the exponential fraction of diastolic depolarization, action potential upstroke, and action potential amplitude (**Supplementary Table 2**). In conclusion, our data show that the training regimen slowed the HR by reducing the intrinsic spontaneous activity of SAN pacemaker cells and that genetic ablation of I_{KACh} prevented the reduction in spontaneous pacemaker activity.

Genetic Ablation of I_{KACh} Prevented Training-Induced Down Regulation of I_f, I_{CaT} and I_{CaL} in SAN Cells

Previous work showed that SAN bradycardia induced by training is due to downregulation of I_f (D'Souza et al., 2014). We thus compared the density of I_f in SAN cells from trained and sedentary WT and *Girk4*$^{-/-}$ mice (**Figure 4**). I_f density in SAN cells from trained WT mice was significantly lower than

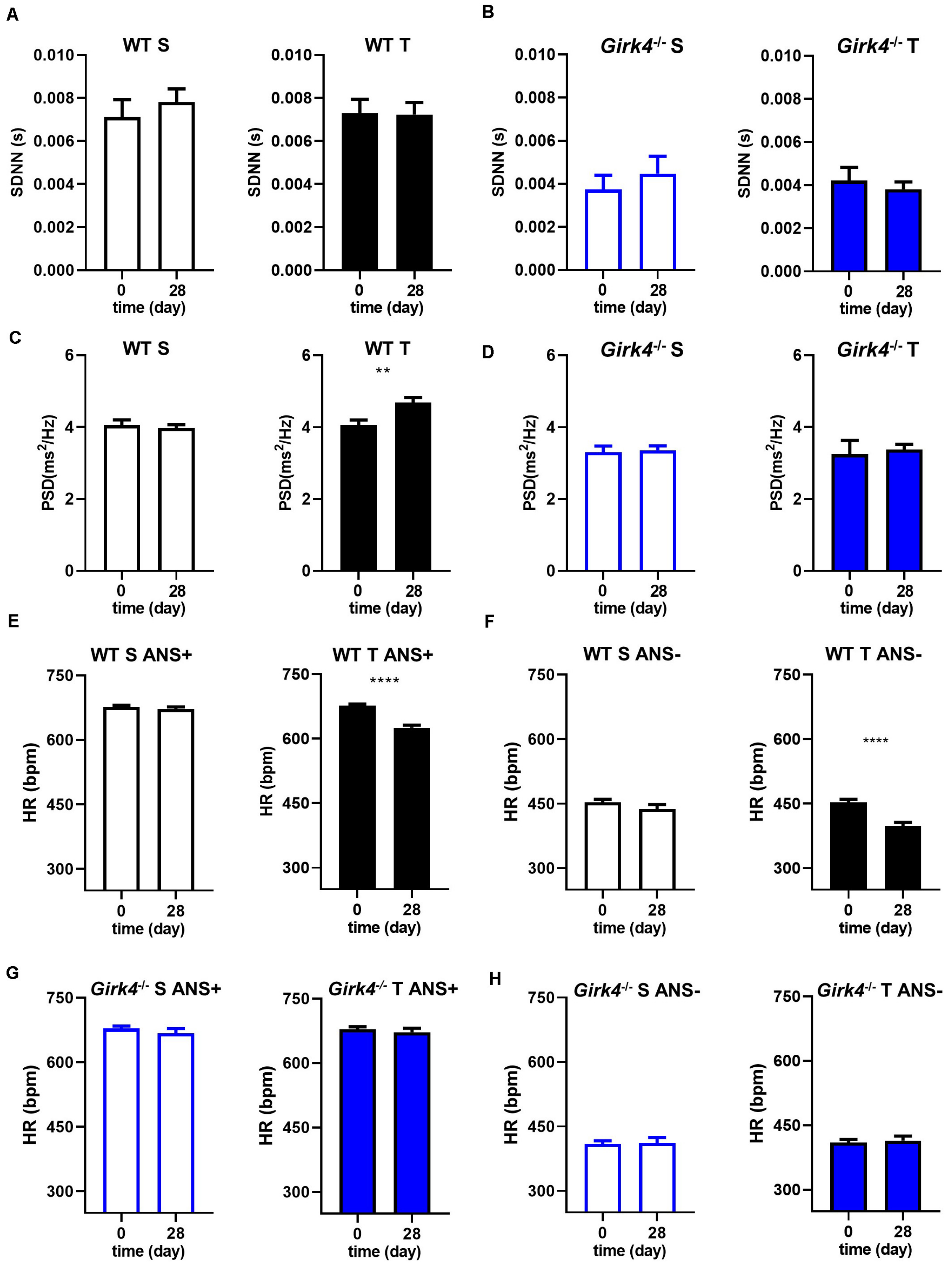

FIGURE 2 | Standard deviation of intervals between two consecutive heart beats (SDNN) calculated in 5-min stable ECG periods at day 0 and at day 28 in WT **(A)** and *Girk4*$^{-/-}$ **(B)** sedentary (open bars) and trained (filled bars) animals. Power spectral density (PSD) of heart rate variability determined by Fast Fourier Transformation analysis of 5-min of stable ECG segments at day 0 and at day 28 in WT **(C)** and *Girk4*$^{-/-}$ **(D)** sedentary (open bars) and trained (filled bars) animals. Heart rate (non-invasive ECG recordings) measured in sedentary (open bars, left panel) and trained (filled bars, right panel) WT mice before (day 0) and after (day 28) training period in control condition (ANS + , **E**) or following intraperitoneal injection of atropine (0.5 mg/kg) and propranolol (5 mg/kg) to inhibit the input of the autonomic nervous system (ANS-, **F**). **(G,H)** same as **(E,F)** but in *Girk4*$^{-/-}$ animals. Statistics: unpaired Student's *t*-test. $^{**}p < 0.01$, $^{****}p < 0.0001$. Error bars indicate s.e.m.

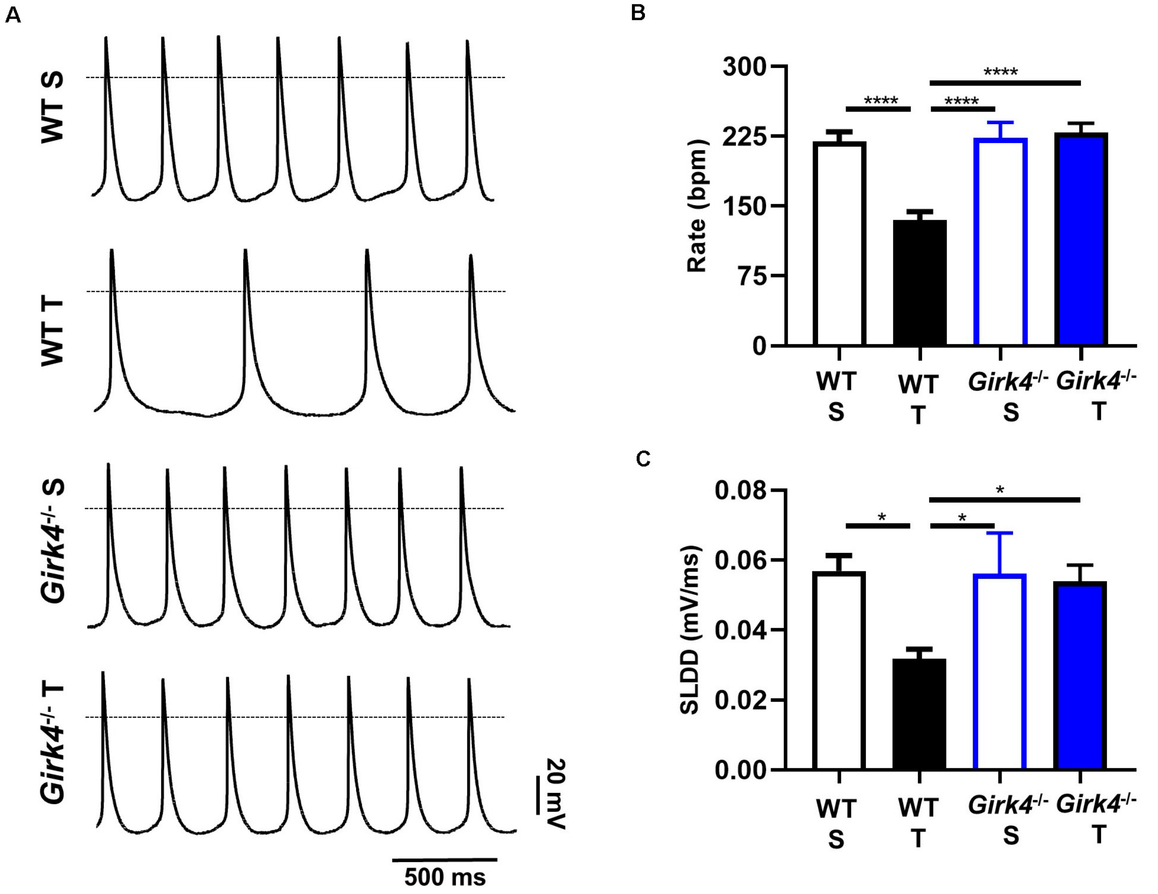

FIGURE 3 | Action potential recordings of SAN myocytes isolated from WT sedentary (WT S), WT trained (WT T), *Girk4*$^{-/-}$ sedentary (*Girk4*$^{-/-}$ S) and *Girk4*$^{-/-}$ trained (*Girk4*$^{-/-}$ T) in Tyrode's solution at the end of training, or sham-training protocol (day 28) **(A)**. The dotted line indicates the 0 mV. Rate of spontaneous action potentials **(B)** and slope of the linear part of the diastolic depolarization (SLDD, **C**) recorded at day 28 in SAN myocytes in Tyrode's solution (n = 6 WT S, n = 10 WT T, n = 7 *Girk4*$^{-/-}$ S and n = 8 *Girk4*$^{-/-}$ T). Statistics: one-way analysis of variance followed by Tukey's multiple comparisons test. $^{*}p < 0.05$, $^{****}p < 0.0001$. Error bars indicate s.e.m.

in cells from sedentary mice (**Figures 4A,B**). I_f was reduced by about 40% at voltages spanning the range of diastolic depolarization (**Figure 4B**, inset). In contrast, the training regimen did not significantly affect I_f density in *Girk4*$^{-/-}$ SAN cells (**Figures 4C,D**). I_f half-activation voltage was unaffected by the training regimen and was similar in both genotypes (**Figure 4E**). We then measured the density of I_{CaL} and I_{CaT} in SAN cells isolated from trained and sedentary WT and *Girk4*$^{-/-}$ mice (**Figure 5**). The training regimen significantly reduced peak I_{CaL} density in WT but not in *Girk4*$^{-/-}$ mice (**Figures 5A–D**). In addition, the training regimen shifted the current half-activation to more positive voltages (**Supplementary Figure 6A**). We then measured I_{CaT} in sedentary and trained WT and *Girk4*$^{-/-}$ (**Figures 5E–G**). We separated I_{CaT} from I_{CaL} by subtracting traces recorded by stepping from a holding potential of −80 mV from those recorded from a holding potential of −55 mV, which completely inactivates I_{CaT} (**Figures 5E,F**; Mangoni et al., 2006b). The training regimen significantly reduced I_{CaT} density in WT but not in *Girk4*$^{-/-}$ SAN cells (**Figures 5G,H**), leaving unaffected the current half-activation voltage (**Supplementary Figure 6B**). We did not find significant differences in densities of I_{CaL} and I_{CaT} between sedentary WT and *Girk4*$^{-/-}$ mice (**Figures 5B,D,G**). Finally, the density of I_{KACh} was similar in sedentary and trained WT mice (**Supplementary Figure 7**), which indicated that HR slowing in trained WT animals could not be attributed to alterations in this current.

Genetic Ablation of I_{KACh} Suppressed Training-Induced Molecular Remodeling of the SAN

We investigated the molecular underpinnings of the observed training-induced reduction in the density of the aforementioned inward currents and its abolition on I_{KACh} ablation. Consistent with previous findings (D'Souza et al., 2014, 2017), we confirmed that the training-induced reduction in I_f seen in WT mice was concomitant with a significant reduction in *Hcn4* (**Figure 6A**, $p < 0.05$) that translated into a reduced expression of HCN4 protein as determined by western blot

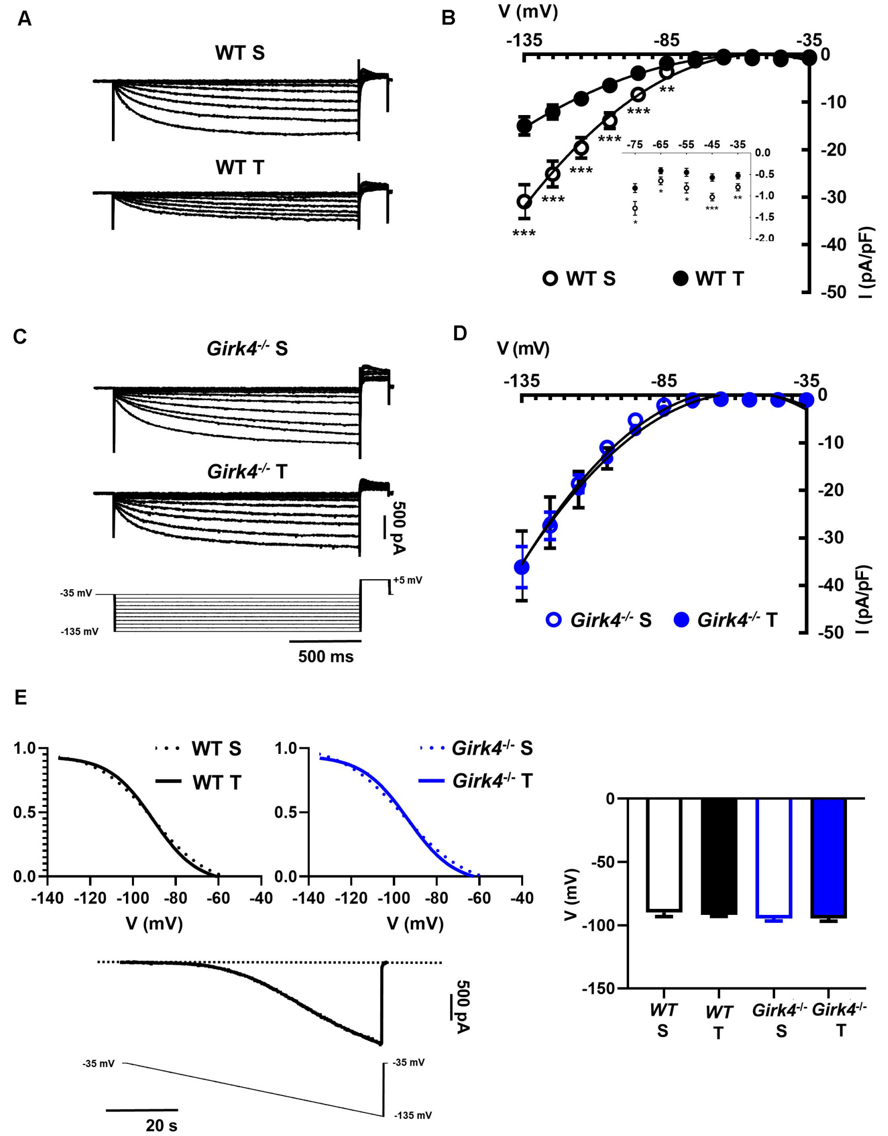

FIGURE 4 | Representative traces of I_f recordings **(A)** and averaged current-to-voltage (I-V) curve **(B)** in sedentary (open black circles, $n = 15$) and trained (filled black circles, $n = 23$) WT SAN myocytes. I_f recordings **(C)** and I-V curve **(D)** in SAN myocytes from sedentary (open blue circles, $n = 12$) and trained (filled blue circles, $n = 18$) isolated *Girk4*$^{-/-}$ SAN pacemaker cells. The voltage-clamp protocol used for all the recordings is shown at the bottom of panel **(C)**. Statistical significance was tested at each voltage using the unpaired Student's *t*-test. $^*p < 0.05$, $^{**}p < 0.01$, $^{***}p < 0.001$. (**E**, left panel) Steady state I_f activation curves in isolated SAN cells from sedentary (dotted line) and trained (continuous line), WT (black) and *Girk4*$^{-/-}$ (blue) mice. Representative ramp current trace recorded in a WT sedentary SAN cell and corresponding voltage protocol are shown under the curves. (**E**, right panel) Histograms representing averaged half-activation voltages ($V_{1/2}$) values for I_f recorded in SAN cells from WT (black bars) and *Girk4*$^{-/-}$ (blue bars) sedentary (open bars) and trained (filled bars) animals. Data have been collected at day 28 (end of training, or sham-training, protocol). Statistics: one-way analysis of variance. Error bars indicate s.e.m.. WT S: WT sedentary; WT T: WT trained; *Girk4*$^{-/-}$ S: *Girk4*$^{-/-}$ sedentary and *Girk4*$^{-/-}$ T: *Girk4*$^{-/-}$ trained.

(**Figure 6B**, $p < 0.05$). A representative western blot is shown in **Figure 6B-left** (top panel) and corresponding stain free total-protein gel used for quantification is given in the lower panel. In line with an unchanged I_f density in trained *Girk4*$^{-/-}$mice (**Figures 4C,D**), training-induced HCN4 modulation was not detectable in *Girk4*$^{-/-}$mice at either transcript (**Figure 6A**) or protein level (**Figure 6B**). From a separate set of experiments, it was determined that unlike mRNA, HCN4 protein levels did not vary between sedentary WT and *Girk4*$^{-/-}$mice (**Supplementary Figure 8**).

We previously demonstrated that induction of a repressive miR signature (with specific emphasis on miR-423-5p, D'Souza et al., 2017) is a candidate mechanism for *Hcn4* downregulation in the trained WT SAN. Therefore, the consequences of I_{KACh} ablation for selected (previously investigated D'Souza et al., 2017) miRs were tested. Strikingly, induction of *Hcn4*-repressor miRs

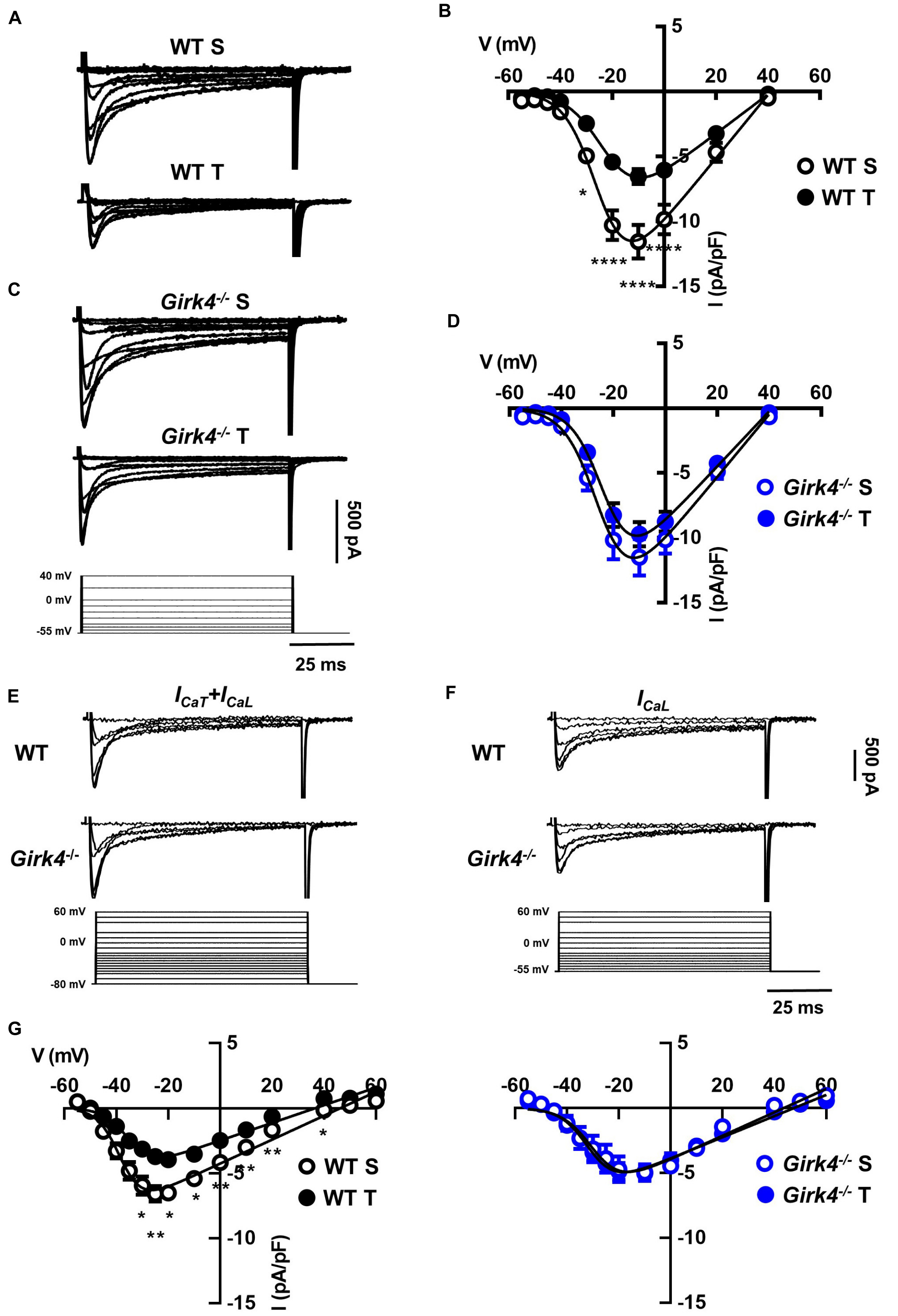

FIGURE 5 | Representative Ca^{2+} current traces of the L-type Ca^{2+} current (I_{CaL}) measured from a holding potential (HP) of −55 mV **(A)** and current-to-voltage (I-V) relationships **(B)** from sedentary (open black circles, $n = 14$) and trained (filled black circles, $n = 13$) WT SAN myocytes. Traces of I_{CaL} **(C)** and I-V curves **(D)** from sedentary (open blue circles, $n = 15$) compared with trained (filled blue circles, $n = 22$) *Girk4*$^{-/-}$ SAN myocytes. Data, collected at day 28 were fitted with a modified Boltzmann equation. Voltage protocol is shown in panel C (bottom). **(E)** Sample traces of I_{Ca} ($I_{CaT} + I_{CaL}$) recorded from a HP of −80 mV in WT and *Girk4*$^{-/-}$SAN myocytes. **(F)** Sample I_{Ca} traces for same myocytes as in **(E)**, but after switching to HP = −55 to inactivate I_{CaT}. **(G)** Net peak I_{CaT} I-V curves measured following subtraction of traces recorded from HP = −55 mV from traces obtained at HP = −80 mV in WT (left panel) and in *Girk4*$^{-/-}$ (right panel) SAN myocytes from sedentary and trained mice. Statistical significance was tested at each voltage using the unpaired Student's *t*-test. $^{*}p < 0.05$, $^{**}p < 0.01$, $^{****}p < 0.0001$. Error bars indicate s.e.m. WT S: WT sedentary; WT T: WT trained; *Girk4*$^{-/-}$ S: *Girk4*$^{-/-}$ sedentary, and *Girk4*$^{-/-}$ T: *Girk4*$^{-/-}$ trained.

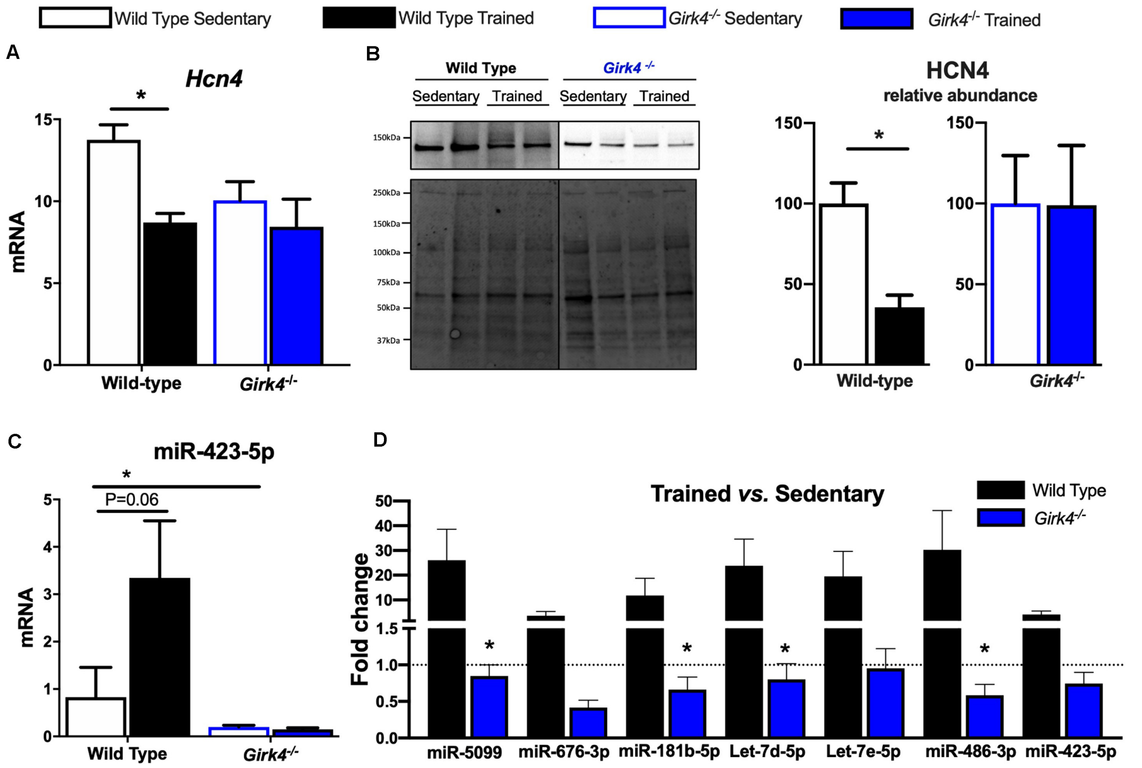

FIGURE 6 | Expression of HCN4 mRNA **(A)** normalized to expression of *Tbp* in SAN biopsies of from WT sedentary (n = 8), WT trained (n = 8), *Girk4*$^{-/-}$ sedentary (n = 7), and *Girk4*$^{-/-}$ trained (n = 6) mice. Statistics: two-way analysis of variance with Sidak's multiple comparisons test. Representative HCN4 western blot (**B**, left panel) with corresponding stain-free total protein gel used for quantification (lower left panel). (**B**, right panel) Protein expression determined by western blot in individual SAN biopsies isolated from WT sedentary (n = 4), WT trained (n = 4) sedentary *Girk4*$^{-/-}$ mice (n = 5) and trained *Girk4*$^{-/-}$mice (n = 4). Statistics: Students *t*-test. SAN Expression of miR-423-5p **(C)** in WT sedentary (n = 8), WT trained (n = 7) sedentary *Girk4*$^{-/-}$ mice (n = 8) and trained *Girk4*$^{-/-}$mice (n = 7). **(D)** Fold change in expression of selected miRs in the SAN of WT trained (n = 8) and *Girk4*$^{-/-}$ trained mice (n = 7) relative to respective WT sedentary (n = 8) and *Girk4*$^{-/-}$ sedentary mice (n = 7). Statistics: one-way analysis of variance with Tukey's multiple comparisons test. *p < 0.05. miR expression in **(C,D)** was normalized to expression of Snord61 and Snord95.

including miR-423-5p (**Figure 6C**) observed in trained WT mice was largely abrogated by *Girk4* silencing (**Figure 6D**). An intriguing baseline reduction in the expression levels of *Hcn4*, miR-423-5p, miR-676-3p and miR-181b-5p in sedentary WT vs sedentary *Girk4*$^{-/-}$ mice was also noted but not investigated further (data not shown). Nevertheless, our findings highlight a new and complex association between I_{KACh} ablation and miR-mediated transcriptional regulation of *Hcn4* in the mouse SAN.

Next, we assessed whether a similar transcriptional control mechanism extended to observed changes in I_{CaL} and I_{CaT}. In contrast to *Hcn4,* mRNA expression of the α subunits of voltage-gated T- and L-type Ca^{2+} channels, $Ca_v1.2$, $Ca_v1.3$, $Ca_v3.1$, and $Ca_v3.2$ (**Figure 7A**) in trained and sedentary WT and *Girk4*$^{-/-}$ mice were unaltered by training or *Girk4* silencing. Furthermore, expression of L-type Ca^{2+} channel $\alpha_2\delta$ and β subunit isoforms also remained unchanged (**Supplementary Figure 9**). At the protein level, western blotting demonstrated a significant training-induced reduction in the SAN expression levels of $Ca_v1.3$ (**Figure 7C**, $p < 0.05$), but not of $Ca_v1.2$ (**Figure 7B**) in WT mice. Consistent with **Figures 5C,D,G** (right panel) the training regimen did not significantly alter the expression levels of either ion channel subunit in the *Girk4*$^{-/-}$ SAN, although there was a trend toward reduction in both cases. Commercially sourced antibodies against I_{CaT} subunits $Ca_v3.1$ and $Ca_v3.2$ could not be validated. In sum, the available data from these pilot molecular investigations indicate a potential role for post-transcriptional and/or post-translational modifications in explaining the reduction of the L- type Ca^{2+} current in the trained WT SAN.

Finally, and in keeping with the finding that I_{KACh} density was unaffected by training (**Supplementary Figure 7**), there were no detectable training-induced changes to GIRK1 or GIRK4 at transcript or protein levels (**Supplementary Figure 10**) in WT or *Girk4*$^{-/-}$mice.

Numerical Modeling of Training-Induced Effects on SAN Pacemaking

The training regimen in WT mice affected I_f, I_{CaT} and I_{CaL} (**Figures 4**, **5**). Dissection of the contribution of these currents to training-induced decrease in automaticity of SAN cells, either

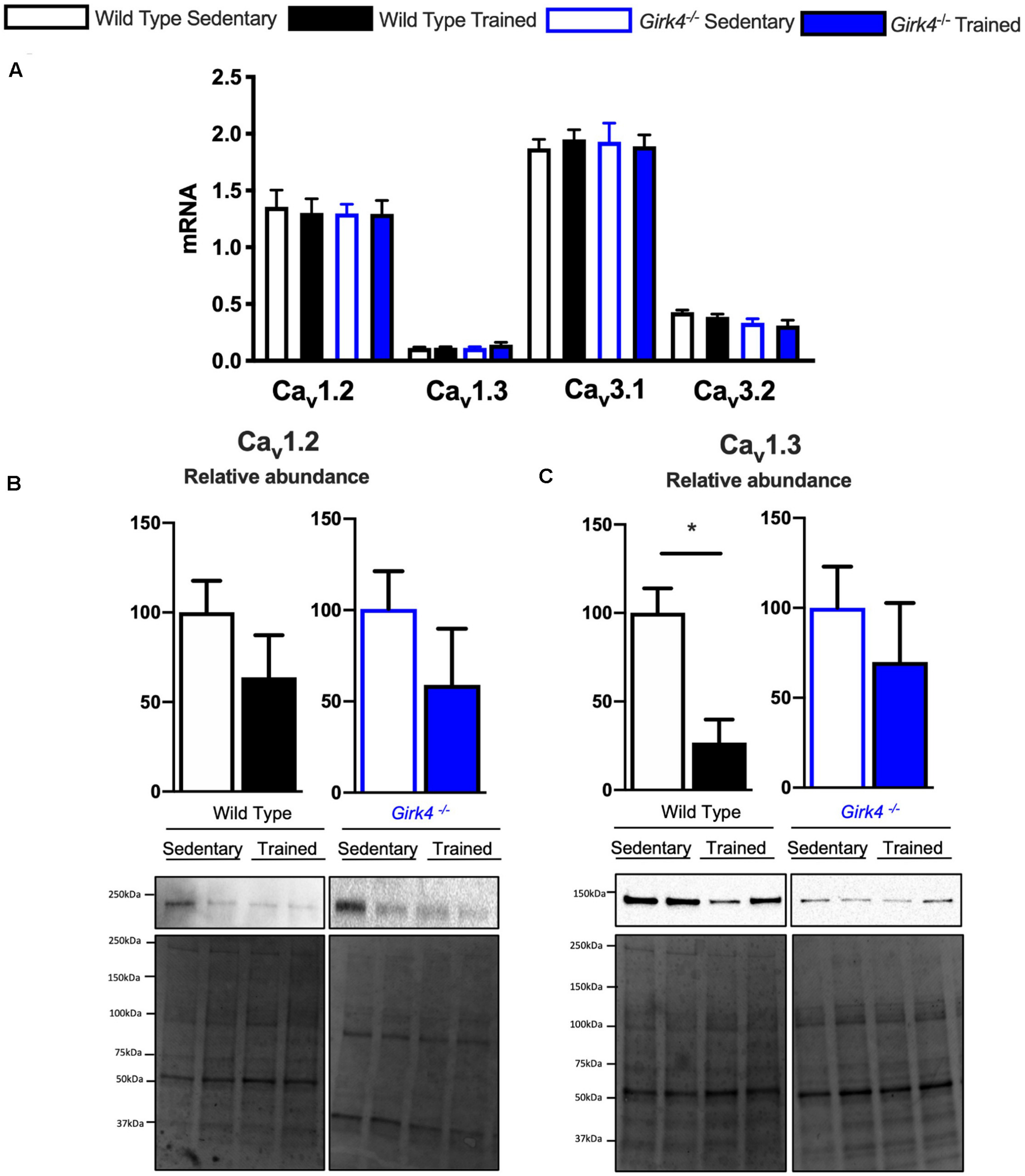

FIGURE 7 | mRNA expression of L-type calcium channel subunits $Ca_v1.2$, $Ca_v1.3$, $Ca_v3.1$, and $Ca_v3.2$ **(A)** (normalized to expression of Tbp) in SAN biopsies from from WT sedentary ($n = 10$), WT trained ($n = 10$), *Girk4*$^{-/-}$ sedentary ($n = 9$) and *Girk4*$^{-/-}$ trained ($n = 10$) mice. Protein expression determined by western blot using antibodies directed against $Ca_v1.2$ **(B)** and $Ca_v1.3$ **(C)** in individual sinus node biopsies isolated from sedentary WT ($n = 6$), trained WT ($n = 4$) sedentary *Girk4*$^{-/-}$ mice ($n = 6$) and trained *Girk4*$^{-/-}$mice ($n = 6$). Representative western blots with corresponding stain-free total protein blot used for quantification shown in lower panel. Statistics: Students *t*-test. $^{*}p < 0.05$.

individually or in combination, would be difficult to achieve using pharmacologic agents, as specific $Ca_v1.3$ inhibitor or gating modifiers are yet to be identified. We thus attempted to predict the impact of training-induced regulation of these currents using a numerical model of mouse SAN cell automaticity that we developed previously (Christel et al., 2012; **Figures 8A–E**). Our model of pacemaker activity includes both L-type $Ca_v1.3$ and $Ca_v1.2$ isoform to calculate total I_{CaL}, as the sum of $Ca_v1.3$-mediated and $Ca_v1.2$-mediated I_{CaL}, respectively (Christel et al., 2012). When values for I_f, I_{CaT} and I_{CaL} measured in sedentary

WT SAN cells were used for calculations, the model generated basal pacemaking of 226 bpm, which compares to what recorded in native sedentary WT SAN cells (220 bpm, **Figure 3B**). To simulate the effects of training-induced reduction in I_f and I_{CaT} magnitudes in WT SAN cells, we used corresponding values of averaged densities and activation measured experimentally (**Figures 4, 5** and **Supplementary Figure 6**). Because we observed decrease in protein expression of $Ca_v1.3$ but not $Ca_v1.2$ (**Figure 7**), we attributed the change in I_{CaL} magnitude and shift of the voltage for half activation to $Ca_v1.3$-mediated I_{CaL}. When all changes in I_f, I_{CaT} and I_{CaL} are included the model predicted a 38% slowing of predicted pacemaker activity, which compares to 39% observed in native trained WT SAN cells (from 226 to 140 bpm, **Figure 8E**). We then calculated the predicted relative effect of changes in each current individually (**Supplementary Figure 11**). The model predicted a 15% slowing of automaticity when only the training-induced reduction in I_f density was included in the simulation. Similarly, computed automaticity predicted 13% slowing of pacemaking when only the training-induced change in I_{CaT} magnitude was included in calculations. A very limited (1%) prolongation of the computed pacemaker cycle length was obtained when changes in I_{CaL} magnitude and in voltage for half activation were included. Change in total I_{CaL} also reduced the predicted action potential amplitude. However, analysis of diastolic depolarization phase showed that the diastolic interval (DI) was prolonged by 11%, by concomitant reduction in I_{CaL} magnitude and the + 4 mV positive shift in the current voltage for half activation, which indicates slowing of the computed pacemaker mechanism. In contrast, predicted action potential duration was reduced by training-induced changes in I_{CaL} explaining in part the lack of significant slowing of pacemaker cycle length despite the effect on diastolic interval. In contrast, when changes in I_{CaL} magnitude corresponding to values recorded in sedentary and trained $Girk4^{-/-}$ cells were included in the model, no significant training-induced slowing in the rate of pacemaker activity was predicted (**Supplementary Figure 12**), in line with experimental data. Taken together, these results show that genetic ablation of I_{KACh} prevents training-induced remodeling of ionic currents in SAN cells and that remodeling of I_f, I_{CaT} and I_{CaL} contribute to this effect.

DISCUSSION

Impact of the Study

This is the first demonstration that that genetic ablation of I_{KACh} prevents sinus bradycardia, slowing of atrioventricular conduction and development of ventricular hypertrophy in a murine model of athletic training. The novel findings of this study accumulate along three lines: First, we report that endurance exercise downregulates not only I_f but also I_{CaT} and I_{CaL} and the *combination* of these changes predicts HR reduction *in silico.* Second, we show that training-induced remodeling of I_f, I_{CaT} and I_{CaL} is suppressed by I_{KACh} ablation, explained in part by: (i) a previously unsuspected transcriptional interaction with HCN4 and its repressor miRs and (ii) likely post-transcriptional regulation of $Ca_v1.3$. Finally, we also demonstrate that acute I_{KACh} block reverses training-induced SAN bradycardia.

Training-Induced Bradycardia in Wild-Type Mice Is Due to Remodeling of Intrinsic SAN Automaticity

Consistent with our previous studies in rodent models and in human athletes (D'Souza et al., 2014, 2017), we found that training regimen affects the sinus rate and the atrioventricular conduction time (**Figure 1**). We cannot completely exclude that, because of the decrease of expression of $Ca_v1.3$ in the SAN, trained mice may present with increased susceptibility to inducible atrial arrhythmia. However, we have previously reported that ablation of I_{KACh} prevents arrhythmias in $Ca_v1.3^{-/-}$ mice (Mesirca et al., 2016a). Ablation of I_{KACh} concomitantly rescued SAN automaticity and atrioventricular conduction (**Figure 1**). We have shown that $Girk4^{-/-}$ mice have reduced HF and LF integrals of the HRV spectrum (Wickman et al., 1998; Mesirca et al., 2013). This reduction is arguably due to loss of the fast G protein dependent pathway of HR regulation by the parasympathetic branch of the autonomic nervous system (Wickman et al., 1998). In the present study, despite a reduction in total HRV, we do not find evidence of a differential sympatho-vagal balance in WT and $Girk4^{-/-}$ mice. Indeed, the heart rates of WT and $Girk4^{-/-}$ mice *in vivo* similarly responded to atropine or propranolol, an observation that indicates that $Girk4^{-/-}$ mice do not present with sympathetic or parasympathetic overdrive secondary to global *Girk4* knockout (Mesirca et al., 2013). Consistent with these previous results, the training regimen did not affect the rate independent HRV parameters of HR of WT and $Girk4^{-/-}$ mice. Indeed, training did not affect either the SDNN or the LF/HF ratio of HR of WT and $Girk4^{-/-}$ mice, suggesting similar degrees of vagal input in the two mouse strains (**Figure 2** and **Supplementary Figure 5**). However, the training regimen augmented the power spectral density in WT but not in $Girk4^{-/-}$ mice (**Figure 2**). Although this could be argued to be evidence of a change in autonomic innervation following training, HRV has been shown to be strongly influenced by HR (Zaza and Lombardi, 2001; Monfredi et al., 2014; Dias da Silva et al., 2015), and the training-induced increase in PSD in WT mice could be the result of the concomitant decrease in HR. Taken together, the effects of the training regimen on HRV, together with our observation that the difference between the HR recorded in sedentary and trained WT mice is maintained after pharmacologic inhibition of autonomic nervous system input, show that intrinsic remodeling of SAN automaticity mediated by regulation of expression of ion channels involved in pacemaking is the predominant mechanism of HR adaptation to training. Consequently, the absence of reduction in I_f, I_{CaL}, I_{CaT} with accompanying transcriptional remodeling in $Girk4^{-/-}$ mice is unlikely to be due to a differential degree of vagal input in the two mouse strains.

Our previous findings in human athletes (D'Souza et al., 2017) and that of others (Lewis et al., 1980; Katona et al., 1982;

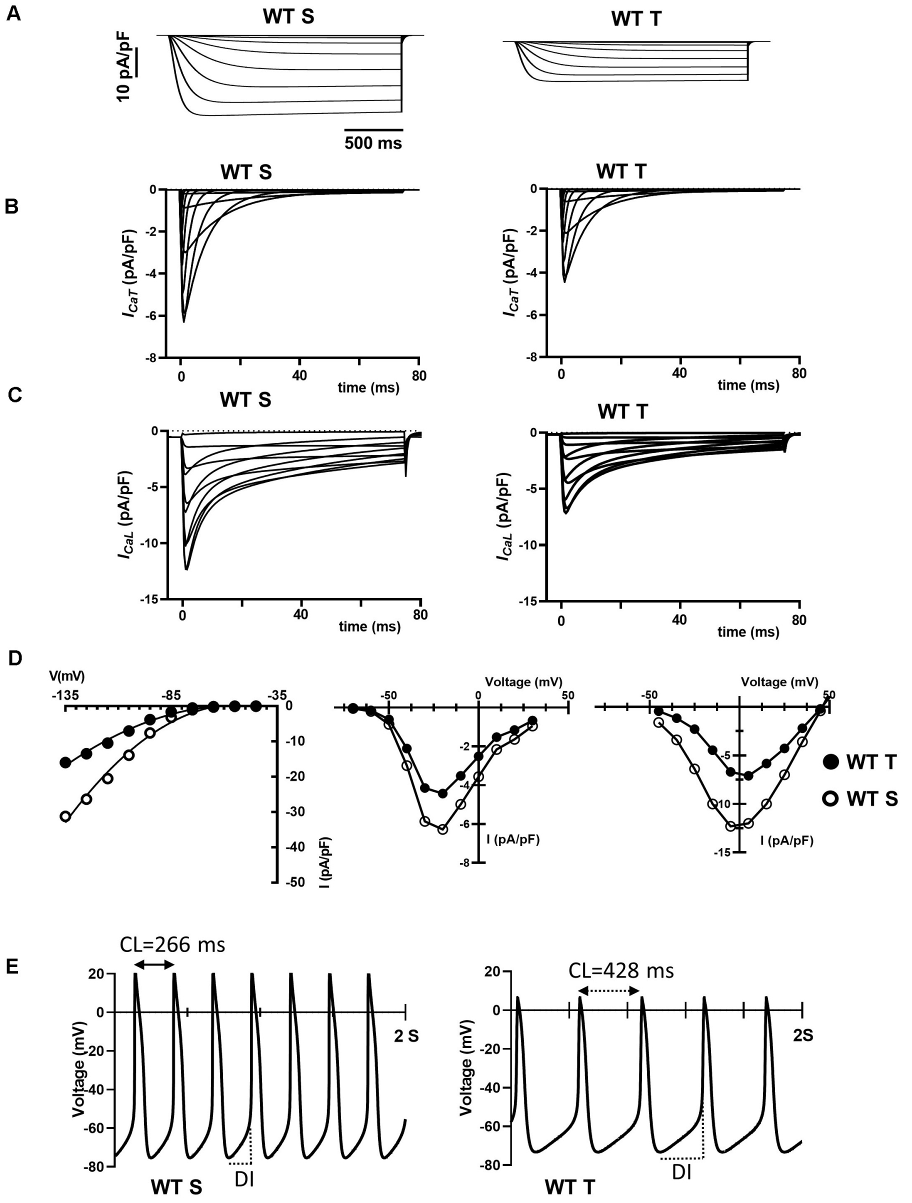

FIGURE 8 | Numerical simulation of current traces for I_f **(A)**, I_{CaT} **(B)**, and I_{CaL} **(C)** calculated using current density and activation parameters recorded in WT sedentary (WT S), WT trained (WT T), *Girk4*$^{-/-}$ sedentary (*Girk4*$^{-/-}$ S) and *Girk4*$^{-/-}$ trained (*Girk4*$^{-/-}$ T) at day 28 of experimental protocol. **(D)** Corresponding predicted I-V curves of I_f (left panel), I_{CaT} (central panel) and I_{CaL} (right panel), calculated at the peak of current density from simulations in **(A–C)**. In I-V curves, open circles show predicted current densities of WT sedentary SAN cells and black circles densities of WT trained SAN cells. **(E)** Comparison between predicted pacemaker activities simulated for control (sedentary) condition (left panel), or including training-dependent changes of I_f, I_{CaT} and I_{CaL}. Abbreviations: CL, pacemaker activity cycle length; DI, diastolic interval.

Maciel et al., 1985; Dickhuth et al., 1987; Stein et al., 2002) demonstrated intrinsic HR slowing accompanied training-induced bradycardia. These findings are contested by studies in rodents (e.g., Aschar-Sobbi et al., 2015) and dogs (Billman et al., 2015) where training induced intrinsic slowing was not observed and instead a role for high vagal tone was determined. The evidence for intrinsic vs. autonomic mechanisms in underlying training-induced sinus bradycardia has been extensively reviewed by our group (Boyett et al., 2013, 2017; D'Souza et al., 2015, 2019) and we posit that non-uniform methodology (species, drug doses, and training modalities) contribute to the reported discrepancies. Furthermore, based on our present results we advance that both vagally mediated and intrinsic SAN remodeling-based mechanisms of the HR adaptation to training may be reconciled: we speculate that (currently uncharacterized) training-induced alterations in sympathetic and/or parasympathetic input may trigger transcriptional remodeling of SAN ion channels, leading to a decrease in intrinsic automaticity as observed. This hypothesis is consistent with one of the main observations of the present study, that genetic deletion of I_{KACh}, an important downstream effector of the parasympathetic nervous system, prevents training-induced remodeling of SAN automaticity. Our model of training induced secondary SAN bradycardia differs from the one used by Long et al. of a canine model of SAN dysfunction associated with heart failure (Long et al., 2020). The pathological mechanisms underlying secondary SAN dysfunction can differ among forms, so the role of I_{KACh}. Indeed, while it appears that remodeling of GIRK1 and GIRK4 expression is an important pathophysiological mechanism in SAN dysfunction associated with heart failure (Long et al., 2020), we did not find evidence for I_{KACh} remodeling by the training regimen. However, these studies combined underscores the importance of I_{KACh} has an important physiopathological mechanism in several forms of SAN dysfunction.

Genetic Ablation of I_{KACh} Prevents Training-Induced Remodeling of SAN Ion Channels Involved in Automaticity

The observation that genetic ablation of I_{KACh} prevented training induced remodeling of I_f, I_{CaT} and I_{CaL} is striking. Indeed, it could have been expected that I_{KACh} abolition would have compensated for decrease in inward ionic currents involved in pacemaking, thereby leading to a lack of net effect on pacemaking by the training regimen. We previously described this mechanism of diastolic inward/outward current balance in mice lacking I_f conductance or after genetic ablation of $Ca_v1.3$ and $Ca_v3.1$ channels (Mesirca et al., 2014, 2016a; Bidaud et al., 2020). This compensatory effect of acute I_{KACh} inhibition was observed also in this study in trained WT mice (**Figure 1E**), in which three important inward currents contributing to diastolic depolarization are downregulated (**Figures 4**, **5**). The mechanism linking constitutive loss of I_{KACh} to suppression of protein downregulation or miR-mediated ion channel remodeling (**Figures 6**, **7**) is at present unknown. However, it raises some important issues. Indeed, it indicates that *Girk4* knockout has complex transcriptional consequences for HCN4 and its repressor miRs. Such a role for *Girk4* is surprising and new. Could I_{KACh} channels be important signaling molecules? As a parasympathetic nervous system effector, it is at the interface of the vagus and the heart and this could be an important position for a signaling molecule. An attractive possibility is that GIRK4 may have nuclear functions as a transcription factor, as has been previously described for cardiac KCHIP2, the accessory subunit defining $I_{to,f}$ (Nassal et al., 2017). Alternatively, GIRK4 could be a key signaling hub wherein genetic ablation of I_{KACh} *per se*, or deletion of GIRK4 from the plasma membrane, blocks a signaling pathway that triggers miR-mediated remodeling of the expression of a particular set of genes including *Hcn4*. Another intriguing development from this work is the differential regulation of HCN4 vs. the L- and T-type calcium channels in response to training. Whereas *Hcn4* downregulation explains I_f reduction in wild-type animals, reduced I_{CaT} and I_{CaL} could not be attributed to reduced expression of mRNAs coding for pore forming Ca^{2+} channel α1 subunits (**Figure 7**) or accessory subunits of voltage-gated Ca^{2+} channels (**Supplementary Figure 9**). Whether the observed reduction in $Ca_v1.3$ and its restoration on *Girk4* knockout is due to (albeit less well established) miR-mediated translational inhibition without mRNA degradation (Eulalio et al., 2007) or other ion channel modulators such as protein kinases merits further study.

Training-Induced Slowing of SAN Cells Pacemaker Activity Is Due to Downregulation of I_f, I_{CaT} and I_{CaL}

In the present study, we report that I_f, I_{CaL} and I_{CaT} amplitudes are diminished by the training regimen (**Figures 4**, **5**). In addition, training positively shifted I_{CaL} half-activation (**Supplementary Figure 6**). While this study is consistent with previous work showing that training induces I_f down-regulation (D'Souza et al., 2014), the role of I_{CaT} and I_{CaL} in mediating training induced bradycardia is an emerging one. We showed previously that $Ca_v3.1$-mediated I_{CaT} contributes to pacemaker activity of adult mouse SAN cells. Genetic ablation of $Ca_v3.1$-mediated I_{CaT} reduced basal automaticity of SAN cells by 16% in comparison to wild-type counterparts (Baudot et al., 2020), a value that is comparable to the predicted 13% slowing of basal automaticity, calculated by reducing I_{CaT} maximal conductance of 30%, as observed experimentally (**Figure 5** and **Supplementary Figure 11**). SAN cells express distinct L-type Ca^{2+} channel isoforms, $Ca_v1.3$ and $Ca_v1.2$ (Mangoni et al., 2003; Marionneau et al., 2005). One of the key differences between $Ca_v1.3$- and $Ca_v1.2$-mediated I_{CaL} is their voltage-dependence for activation (Mangoni et al., 2006a). $Ca_v1.3$-mediated I_{CaL} activates at negative voltages and contributes to the generation of diastolic depolarization by supplying inward current (Mangoni et al., 2003; Toyoda et al., 2017) and controlling diastolic RyR-dependent Ca^{2+} release during pacemaking (Torrente et al., 2016). $Ca_v1.2$-mediated I_{CaL} activates at more positive voltages than $Ca_v1.3$, contributes to the action potential upstroke phase and to regulation of SR Ca^{2+} load (Torrente et al., 2016). Because of the importance of $Ca_v1.3$-mediated I_{CaL} in the generation of diastolic depolarization, we may expect that the decrease in the amplitude of I_{CaL} induced by the training regimen would lead to slowing of SAN spontaneous activity. Our numerical simulations predict that a decrease of 48% of I_{CaL} peak density and a 4 mV positive shift in activation does not prolong the calculated cycle length (**Supplementary Figure 11**). This inconsistency could be explained, in part by predicted shortening of action potential duration following decreased I_{CaL} magnitude (**Figure 8**). A similar prediction was reported by Zhang et al. in modeling the negative chronotropic effect of ACh in the central part of the rabbit SAN (Zhang et al., 2002). However, our model does predict prolongation of the diastolic interval by concomitant I_{CaL} down-regulation and positive shift of I_{CaL} activation (**Supplementary Figure 11**), in line with the importance of $Ca_v1.3$-mediated I_{CaL} in the generation pacemaker activity. In particular, our model predicts slowing of diastolic interval by positive shifting the voltage for half activation of $Ca_v1.3$-mediated I_{CaL} (**Supplementary Figure 13**). Furthermore, our recent work showed that $Ca_v1.3$ is an essential molecular determinant of the sustained inward current I_{st} (Toyoda et al., 2017). In addition, the density of I_{st} positively correlates with that of I_{CaL} and mRNA coding for $Ca_v1.3$ in guinea-pig SAN cells (Toyoda et al., 2018). It is thus possible that since the training regimen down-regulated $Ca_v1.3$, this could also have affected also I_{st} density, further contributing to slowing of automaticity. Even if our model predicts slowing of diastolic depolarization when I_{st} is reduced (data not shown), we did not include this in our calculations, as we did not directly measure the effects of training regimen on I_{st} expression in this study.

When training-induced changes in I_f, I_{CaT} and I_{CaL} are combined, the predicted magnitude of slowing is higher than the sum of the predicted individual contributions of I_f, I_{CaT} and I_{CaL} (**Figure 8** and **Supplementary Figure 11**), which suggests a non-linear quantitative impact of predicted loss of the cell depolarization reserve. This is consistent with our recent observation that the relative HR slowing observed after administration of the I_f inhibitor ivabradine is higher in mice lacking both $Ca_v1.3$ and $Ca_v3.1$ ($Ca_v1.3^{-/-}/Ca_v3.1^{-/-}$) channels, than in wild-type counterparts (Baudot et al., 2020). Previous work showed that administration of the I_f inhibitor ivabradine negated the difference in HR between sedentary and trained mice (D'Souza et al., 2014). However, the present study does not contradict these data. Indeed, we cannot exclude that, while I_f, I_{CaT} and I_{CaL} jointly contribute to slowed cellular automaticity *ex vivo* conditions (**Figure 3**), the permanent action of the autonomic nervous system and mechanical hemodynamic forces regulating SAN activity and HR *in vivo,* modulates the relative contribution of HCN4, $Ca_v3.1$ and $Ca_v1.3$ to pacemaking in trained animals. Moreover, previous work in rabbit SAN cells has showed that I_f block by ivabradine reduces diastolic RyR-dependent Ca^{2+} release (Yaniv et al., 2013). It has thus been proposed that I_f inhibition slows pacemaker activity not only via a reduction in inward current via funny channels, but also via reduction in the speed of the Ca^{2+} clock/NCX1 pacemaker mechanism (Yaniv et al., 2013). This proposal would be consistent also with the hypothesis that slowing of diastolic depolarization by ivabradine alters the kinetics of recruitment of I_{CaT} and $Ca_v1.3$-mediated I_{CaL} in the pacemaker potential range, thereby indirectly contribute to the effect of ivabradine on pacemaker activity *in vitro* and on HR *in vivo*. In conclusion, our study indicates that the training regimen slows the HR via regulation of three ionic currents important for pacemaker activity: I_f, I_{CaT} and I_{CaL}. Future studies will be required to understand how these currents interact to generate pacemaking, mechanisms that current models of automaticity cannot reproduce fully.

CONCLUSION

Athletes are considered to be part of the healthiest fraction of the population. However, in the long term there is emerging evidence for SAN dysfunction leading to an increased incidence of electronic pacemaker implantation in this population (Baldesberger et al., 2008). For the first time, our studies show that genetic targeting of I_{KACh} is an effective strategy to control remodeling of ionic currents and sinus bradycardia in a murine model of training-induced SAN dysfunction. Gene therapy or pharmacological targeting of I_{KACh} may therefore represent a viable alternative to pacemaker implantation for the management of pathological bradyarrhythmias seen in some veteran athletes.

DATA AVAILABILITY STATEMENT

The raw data supporting the conclusions of this manuscript will be made available by the authors, without undue reservation, to any qualified researcher.

ETHICS STATEMENT

The animal study was reviewed and approved by Ethical committee of the University of Montpellier and the French Ministry of Agriculture (protocol no: 2017010310594939).

AUTHOR CONTRIBUTIONS

PM, IB, AD'S, KW, MB, and MM designed the research and wrote the manuscript. PM, IB, AD'S, GF, ET, DG, ST, CA, AC, AT, JR, and MM performed the experiments. PM, IB, AD'S, ET, MB, and MM analyzed the results. All authors contributed to the article and approved the submitted version.

FUNDING

The IGF research group is a member of the Laboratory of Excellence "Ion Channel Science and Therapeutics" supported by a grant from ANR (ANR-11-LABX-0015). Research has been supported by the Fondation pour la Recherche Medicale "Physiopathologie Cardiovasculaire" (DPC20171138970 to MM), by the Agence Nationale de la Recherche (ANR-15-CE14-0004-01 to MM), the National Institutes of Health (HL105550 to KW), the British Heart Foundation Intermediate Basic Science Research Fellowship (FS/19/1/34035 to AD'S), the British Heart Foundation Program Grant (RG/18/2/333912 to MB), and the Fondation Leducq (TNE FANTASY 19CVD03 to MM and MB).

ACKNOWLEDGMENTS

We thank the Réseau d'Animaleries de Montpellier (RAM) of Biocampus facility for the management of mouse lines. We thank all the personnel of the PCEA mouse breeding facility in Montpellier and of the iExplore platform for help in functional exploration of the mouse SND lines. We also thank Dr. Amy Lee (University of Iowa), for sharing the anti-rabbit Cav1.3 antibody.

SUPPLEMENTARY MATERIAL

The Supplementary Material for this article can be found online at: https://www.frontiersin.org/articles/10.3389/fphys.2020.519382/full#supplementary-material

REFERENCES

Andersen, K., Farahmand, B., Ahlbom, A., Held, C., Ljunghall, S., Michaelsson, K., et al. (2013). Risk of arrhythmias in 52 755 long-distance cross-country skiers: a cohort study. *Eur. Heart J.* 34, 3624–3631. doi: 10.1093/eurheartj/eht188

Aschar-Sobbi, R., Izaddoustdar, F., Korogyi, A. S., Wang, Q., Farman, G. P., Yang, F., et al. (2015). Increased atrial arrhythmia susceptibility induced by intense endurance exercise in mice requires TNFα. *Nat. Commun.* 6:6018. doi: 10.1038/ncomms7018

Baldesberger, S., Bauersfeld, U., Candinas, R., Seifert, B., Zuber, M., Ritter, M., et al. (2008). Sinus node disease and arrhythmias in the long-term follow-up of former professional cyclists. *Eur. Heart J.* 29, 71–78. doi: 10.1093/eurheartj/ehm555

Baudot, M., Torre, E., Bidaud, I., Louradour, J., Torrente, A. G., Fossier, L., et al. (2020). Concomitant genetic ablation of L-type Cav1.3 (α1D) and T-type Cav3.1 (α1G) Ca2+ channels disrupts heart automaticity. *Sci. Rep.* 10:18906.

Bidaud, I., Chong, A. C. Y., Carcouet, A., Waard, S., Charpentier, F., Ronjat, M., et al. (2020). Inhibition of G protein-gated K(+) channels by tertiapin-Q rescues sinus node dysfunction and atrioventricular conduction in mouse models of primary bradycardia. *Sci. Rep.* 10:9835.

Billman, G. E., Cagnoli, K. L., Csepe, T., Li, N., Wright, P., Mohler, P. J., et al. (2015). Exercise training-induced bradycardia: evidence for enhanced parasympathetic regulation without changes in intrinsic sinoatrial node function. *J. Appl. Physiol.* 118, 1344–1355. doi: 10.1152/japplphysiol.01111.2014

Boyett, M. R., D'Souza, A., Zhang, H., Morris, G. M., Dobrzynski, H., and Monfredi, O. (2013). Viewpoint: Is the resting bradycardia in athletes the result of remodeling of the sinoatrial node rather than high vagal tone? *J. Appl. Physiol.* 114, 1351–1355. doi: 10.1152/japplphysiol.01126.2012

Boyett, M. R., Wang, Y., Nakao, S., Ariyaratnam, J., Hart, G., Monfredi, O., et al. (2017). Point: exercise training-induced bradycardia is caused by changes in intrinsic sinus node function. *J. Appl. Physiol.* 123, 684–685. doi: 10.1152/japplphysiol.00604.2017

Brignole, M., Auricchio, A., Baron-Esquivias, G., Bordachar, P., Boriani, G., Breithardt, O. A., et al. (2013). 2013 ESC Guidelines on cardiac pacing and cardiac resynchronization therapy: the Task Force on cardiac pacing and resynchronization therapy of the European Society of Cardiology (ESC). Developed in collaboration with the European Heart Rhythm Association (EHRA). *Eur. Heart J.* 34, 2281–2329. doi: 10.1093/eurheartj/eht150

Christel, C. J., Cardona, N., Mesirca, P., Herrmann, S., Hofmann, F., Striessnig, J., et al. (2012). Distinct localization and modulation of Cav1.2 and Cav1.3 L-type Ca2+ channels in mouse sinoatrial node. *J. Physiol.* 590(Pt 24), 6327–6342. doi: 10.1113/jphysiol.2012.239954

Daugherty, A., Rateri, D., Hong, L., and Balakrishnan, A. (2009). Measuring blood pressure in mice using volume pressure recording, a tail-cuff method. *J. Vis. Exp.* 27:1291.

Dias da Silva, V. J., Tobaldini, E., Rocchetti, M., Wu, M. A., Malfatto, G., Montano, N., et al. (2015). Modulation of sympathetic activity and heart rate variability by ivabradine. *Cardiovasc. Res.* 108, 31–38. doi: 10.1093/cvr/cvv180

Dickhuth, H. H., Lehmann, M., Auch-Schwelk, W., Meinertz, T., and Keul, J. (1987). Physical training, vegetative regulation, and cardiac hypertrophy. *J. Cardiovasc. Pharmacol.* 10(Suppl. 6), S71–S78.

DiFrancesco, D. (2010). The role of the funny current in pacemaker activity. *Circ. Res.* 106, 434–446. doi: 10.1161/circresaha.109.208041

DiFrancesco, D., and Mangoni, M. (1994). Modulation of single hyperpolarization-activated channels (i(f)) by cAMP in the rabbit sino-atrial node. *J. Physiol.* 474, 473–482. doi: 10.1113/jphysiol.1994.sp020038

DiFrancesco, D., and Tromba, C. (1988a). Inhibition of the hyperpolarization-activated current (if) induced by acetylcholine in rabbit sino-atrial node myocytes. *J. Physiol.* 405, 477–491. doi: 10.1113/jphysiol.1988.sp017343

DiFrancesco, D., and Tromba, C. (1988b). Muscarinic control of the hyperpolarization-activated current (if) in rabbit sino-atrial node myocytes. *J. Physiol.* 405, 493–510. doi: 10.1113/jphysiol.1988.sp017344

D'Souza, A., Bucchi, A., Johnsen, A. B., Logantha, S. J., Monfredi, O., Yanni, J., et al. (2014). Exercise training reduces resting heart rate via downregulation of the funny channel HCN4. *Nat. Commun.* 5:3775.

D'Souza, A., Pearman, C. M., Wang, Y., Nakao, S., Logantha, S., Cox, C., et al. (2017). Targeting miR-423-5p reverses exercise training-induced HCN4 channel remodeling and sinus Bradycardia. *Circ. Res.* 121, 1058–1068. doi: 10.1161/circresaha.117.311607

D'Souza, A., Sharma, S., and Boyett, M. R. (2015). CrossTalk opposing view: bradycardia in the trained athlete is attributable to a downregulation of a pacemaker channel in the sinus node. *J. Physiol.* 593, 1749–1751. doi: 10.1113/jphysiol.2014.284356

D'Souza, A., Trussell, T., Morris, G. M., Dobrzynski, H., and Boyett, M. R. (2019). Supraventricular arrhythmias in athletes: basic mechanisms and new directions. *Physiology* 34, 314–326. doi: 10.1152/physiol.00009.2019

Eulalio, A., Rehwinkel, J., Stricker, M., Huntzinger, E., Yang, S. F., Doerks, T., et al. (2007). Target-specific requirements for enhancers of decapping in miRNA-mediated gene silencing. *Genes Dev.* 21, 2558–2570. doi: 10.1101/gad.443107

Hagiwara, N., Irisawa, H., and Kameyama, M. (1988). Contribution of two types of calcium currents to the pacemaker potentials of rabbit sino-atrial node cells. *J. Physiol.* 395, 233–253. doi: 10.1113/jphysiol.1988.sp016916

Hamill, O. P., Marty, A., Neher, E., Sakmann, B., and Sigworth, F. J. (1981). Improved patch-clamp techniques for high-resolution current recording from cells and cell-free membrane patches. *Pflugers Arch. Eur. J. Physiol.* 391, 85–100. doi: 10.1007/bf00656997

Katona, P. G., McLean, M., Dighton, D. H., and Guz, A. (1982). Sympathetic and parasympathetic cardiac control in athletes and nonathletes at rest. *J. Appl. Physiol. Respir. Environ. Exerc. Physiol.* 52, 1652–1657. doi: 10.1152/jappl.1982.52.6.1652

Krapivinsky, G., Gordon, E. A., Wickman, K., Velimirovic, B., Krapivinsky, L., and Clapham, D. E. (1995). The G-protein-gated atrial K+ channel IKACh is a heteromultimer of two inwardly rectifying K(+)-channel proteins. *Nature* 374, 135–141. doi: 10.1038/374135a0

Lakatta, E. G., Maltsev, V. A., and Vinogradova, T. M. (2010). A coupled SYSTEM of intracellular Ca2+ clocks and surface membrane voltage clocks controls the timekeeping mechanism of the heart's pacemaker. *Circ. Res.* 106, 659–673. doi: 10.1161/circresaha.109.206078

Lewis, S. F., Nylander, E., Gad, P., and Areskog, N. H. (1980). Non-autonomic component in bradycardia of endurance trained men at rest and during exercise. *Acta Physiol. Scand.* 109, 297–305. doi: 10.1111/j.1748-1716.1980.tb06600.x

Li, N., Hansen, B. J., Csepe, T. A., Zhao, J., Ignozzi, A. J., Sul, L. V., et al. (2017). Redundant and diverse intranodal pacemakers and conduction pathways protect the human sinoatrial node from failure. *Sci. Transl. Med.* 9:eaam5607. doi: 10.1126/scitranslmed.aam5607

Long, V. P. III, Bonilla, I. M., Baine, S., Glynn, P., Kumar, S., Schober, K., et al. (2020). Chronic heart failure increases negative chronotropic effects of adenosine in canine sinoatrial cells via A1R stimulation and GIRK-mediated IKado. *Life Sci.* 240:117068. doi: 10.1016/j.lfs.2019.117068

Lyashkov, A. E., Vinogradova, T. M., Zahanich, I., Li, Y., Younes, A., Nuss, H. B., et al. (2009). Cholinergic receptor signaling modulates spontaneous firing of sinoatrial nodal cells via integrated effects on PKA-dependent Ca(2+) cycling and I(KACh). *Am. J. Physiol. Heart Circ. Physiol.* 297, H949–H959.

Maciel, B. C., Gallo Junior, L., Marin Neto, J. A., Lima Filho, E. C., Terra Filho, J., and Manco, J. C. (1985). Parasympathetic contribution to bradycardia induced by endurance training in man. *Cardiovasc. Res.* 19, 642–648. doi: 10.1093/cvr/19.10.642

Mangoni, M. E., Couette, B., Bourinet, E., Platzer, J., Reimer, D., Striessnig, J., et al. (2003). Functional role of L-type Cav1.3 Ca2+ channels in cardiac pacemaker activity. *Proc. Natl. Acad. Sci. U.S.A.* 100, 5543–5548. doi: 10.1073/pnas.0935295100

Mangoni, M. E., Couette, B., Marger, L., Bourinet, E., Striessnig, J., and Nargeot, J. (2006a). Voltage-dependent calcium channels and cardiac pacemaker activity: from ionic currents to genes. *Prog. Biophys. Mol. Biol.* 90, 38–63. doi: 10.1016/j.pbiomolbio.2005.05.003

Mangoni, M. E., and Nargeot, J. (2001). Properties of the hyperpolarization-activated current (I(f)) in isolated mouse sino-atrial cells. *Cardiovasc. Res.* 52, 51–64. doi: 10.1016/s0008-6363(01)00370-4

Mangoni, M. E., and Nargeot, J. (2008). Genesis and regulation of the heart automaticity. *Physiol. Rev.* 88, 919–982. doi: 10.1152/physrev.00018.2007

Mangoni, M. E., Traboulsie, A., Leoni, A. L., Couette, B., Marger, L., Le Quang, K., et al. (2006b). Bradycardia and slowing of the atrioventricular conduction in mice lacking CaV3.1/alpha1G T-type calcium channels. *Circ. Res.* 98, 1422–1430. doi: 10.1161/01.res.0000225862.14314.49

Marionneau, C., Couette, B., Liu, J., Li, H., Mangoni, M. E., Nargeot, J., et al. (2005). Specific pattern of ionic channel gene expression associated with pacemaker activity in the mouse heart. *J. Physiol.* 562(Pt 1), 223–234. doi: 10.1113/jphysiol.2004.074047

Mesirca, P., Alig, J., Torrente, A. G., Muller, J. C., Marger, L., Rollin, A., et al. (2014). Cardiac arrhythmia induced by genetic silencing of 'funny' (f) channels is rescued by GIRK4 inactivation. *Nat. Commun.* 5:4664.

Mesirca, P., Bidaud, I., Briec, F., Evain, S., Torrente, A. G., Le Quang, K., et al. (2016a). G protein-gated IKACh channels as therapeutic targets for treatment of sick sinus syndrome and heart block. *Proc. Natl. Acad. Sci. U.S.A.* 113, E932–E941.

Mesirca, P., Bidaud, I., and Mangoni, M. E. (2016b). Rescuing cardiac automaticity in L-type Cav1.3 channelopathies and beyond. *J. Physiol.* 594, 5869–5879. doi: 10.1113/jp270678

Mesirca, P., Fedorov, V. V., Hund, T. J., Torrente, A. G., Bidaud, I., Mohler, P. J., et al. (2020). Pharmacologic approach to sinoatrial node dysfunction. *Annu. Rev. Pharmacol. Toxicol.* doi: 10.1146/annurev-pharmtox-031120-115815 [Epub ahead of print].

Mesirca, P., Marger, L., Toyoda, F., Rizzetto, R., Audoubert, M., Dubel, S., et al. (2013). The G-protein-gated K+ channel, IKACh, is required for regulation of pacemaker activity and recovery of resting heart rate after sympathetic stimulation. *J. Gen. Physiol.* 142, 113–126. doi: 10.1085/jgp.201310996

Monfredi, O., and Boyett, M. R. (2015). Sick sinus syndrome and atrial fibrillation in older persons - A view from the sinoatrial nodal myocyte. *J. Mol. Cell. Cardiol.* 83, 88–100. doi: 10.1016/j.yjmcc.2015.02.003

Monfredi, O., Lyashkov, A. E., Johnsen, A. B., Inada, S., Schneider, H., Wang, R., et al. (2014). Biophysical characterization of the underappreciated and important relationship between heart rate variability and heart rate. *Hypertension* 64, 1334–1343. doi: 10.1161/hypertensionaha.114.03782

Nassal, D. M., Wan, X., Liu, H., Maleski, D., Ramirez-Navarro, A., Moravec, C. S., et al. (2017). KChIP2 is a core transcriptional regulator of cardiac excitability. *eLife* 6:e17304.

Northcote, R. J., Canning, G. P., and Ballantyne, D. (1989a). Electrocardiographic findings in male veteran endurance athletes. *Br. Heart J.* 61, 155–160. doi: 10.1136/hrt.61.2.155

Northcote, R. J., Rankin, A. C., Scullion, R., and Logan, W. (1989b). Is severe bradycardia in veteran athletes an indication for a permanent pacemaker? *BMJ* 298, 231–232. doi: 10.1136/bmj.298.6668.231

Petit-Jacques, J., Bois, P., Bescond, J., and Lenfant, J. (1993). Mechanism of muscarinic control of the high-threshold calcium current in rabbit sino-atrial node myocytes. *Pflugers Arch.* 423, 21–27. doi: 10.1007/bf00374956

Stein, R., Medeiros, C. M., Rosito, G. A., Zimerman, L. I., and Ribeiro, J. P. (2002). Intrinsic sinus and atrioventricular node electrophysiologic adaptations in endurance athletes. *J. Am. Coll. Cardiol.* 39, 1033–1038. doi: 10.1016/s0735-1097(02)01722-9

Torrente, A. G., Mesirca, P., Neco, P., Rizzetto, R., Dubel, S., Barrere, C., et al. (2016). L-type Cav1.3 channels regulate ryanodine receptor-dependent Ca2+ release during sino-atrial node pacemaker activity. *Cardiovasc. Res.* 109, 451–461. doi: 10.1093/cvr/cvw006

Toyoda, F., Ding, W. G., and Matsuura, H. (2018). Heterogeneous functional expression of the sustained inward Na(+) current in guinea pig sinoatrial node cells. *Pflugers Arch.* 470, 481–490. doi: 10.1007/s00424-017-2091-y

Toyoda, F., Mesirca, P., Dubel, S., Ding, W. G., Striessnig, J., Mangoni, M. E., et al. (2017). CaV1.3 *L-type Ca*2+ channel contributes to the heartbeat by generating a dihydropyridine-sensitive persistent Na+ current. *Sci. Rep.* 7: 7869.

van Borren, M. M., Verkerk, A. O., Wilders, R., Hajji, N., Zegers, J. G., Bourier, J., et al. (2010). Effects of muscarinic receptor stimulation on Ca2+ transient, cAMP production and pacemaker frequency of rabbit sinoatrial node cells. *Basic Res. Cardiol.* 105, 73–87. doi: 10.1007/s00395-009-0048-9

Verheijck, E. E., van Ginneken, A. C., Wilders, R., and Bouman, L. N. (1999). Contribution of L-type Ca2+ current to electrical activity in sinoatrial nodal myocytes of rabbits. *Am. J. Physiol.* 276(3 Pt 2), H1064–H1077.

Wickman, K., Nemec, J., Gendler, S. J., and Clapham, D. E. (1998). Abnormal heart rate regulation in GIRK4 knockout mice. *Neuron* 20, 103–114. doi: 10.1016/s0896-6273(00)80438-9

Yaniv, Y., Sirenko, S., Ziman, B. D., Spurgeon, H. A., Maltsev, V. A., and Lakatta, E. G. (2013). New evidence for coupled clock regulation of the normal automaticity of sinoatrial nodal pacemaker cells: bradycardic effects of ivabradine are linked to suppression of intracellular Ca(2)(+) cycling. *J. Mol. Cell. Cardiol.* 62, 80–89. doi: 10.1016/j.yjmcc.2013.04.026

Zaza, A., and Lombardi, F. (2001). Autonomic indexes based on the analysis of heart rate variability: a view from the sinus node. *Cardiovasc. Res.* 50, 434–442. doi: 10.1016/s0008-6363(01)00240-1

Zhang, H., Holden, A. V., Noble, D., and Boyett, M. R. (2002). Analysis of the chronotropic effect of acetylcholine on sinoatrial node cells. *J. Cardiovasc. Electrophysiol.* 13, 465–474.

Conflict of Interest: The authors declare that the research was conducted in the absence of any commercial or financial relationships that could be construed as a potential conflict of interest.

Advantages of publishing in Frontiers

OPEN ACCESS
Articles are free to read
for greatest visibility
and readership

FAST PUBLICATION
Around 90 days
from submission
to decision

HIGH QUALITY PEER-REVIEW
Rigorous, collaborative,
and constructive
peer-review

TRANSPARENT PEER-REVIEW
Editors and reviewers
acknowledged by name
on published articles

Frontiers
Avenue du Tribunal-Fédéral 34
1005 Lausanne | Switzerland

Visit us: www.frontiersin.org
Contact us: frontiersin.org/about/contact

REPRODUCIBILITY OF RESEARCH
Support open data
and methods to enhance
research reproducibility

DIGITAL PUBLISHING
Articles designed
for optimal readership
across devices

FOLLOW US
@frontiersin

IMPACT METRICS
Advanced article metrics
track visibility across
digital media

EXTENSIVE PROMOTION
Marketing
and promotion
of impactful research

LOOP RESEARCH NETWORK
Our network
increases your
article's readership